Identification of time-varying models for flapping-wing micro aerial vehicles

Armanini, Sophie

Important note
To cite this publication, please use the final published version (if applicable).
Please check the document version above.

IDENTIFICATION OF TIME-VARYING MODELS FOR FLAPPING-WING MICRO AERIAL VEHICLES

IDENTIFICATION OF TIME-VARYING MODELS FOR FLAPPING-WING MICRO AERIAL VEHICLES

Proefschrift

ter verkrijging van de graad van doctor
aan de Technische Universiteit Delft,
op gezag van de Rector Magnificus prof. dr. ir. T.H.J.J. van der Hagen,
voorzitter van het College voor Promoties,
in het openbaar te verdedigen op donderdag 22 februari 2018 om 15:00 uur

door

Sophie Franziska ARMANINI

Diplomingenieurin Luft- und Raumfahrttechnik,
Technische Universität München, Duitsland
geboren te Padua, Italïe.

Dit proefschrift is goedgekeurd door de promotor:
Prof. dr. ir. M. Mulder

Copromotor:
Dr. ir. C.C. de Visser

Samenstelling promotiecommissie:

Rector Magnificus,	voorzitter
Prof. dr. ir. M. Mulder,	Technische Universiteit Delft, promotor
Dr. ir. C.C. de Visser,	Technische Universiteit Delft, copromotor

Onafhankelijke leden:

Prof. Dr.-Ing. F. Holzapfel	Technische Universität München
Prof. dr. ir. L.L.M. Veldhuis	Technische Universiteit Delft
Prof. dr. ir. M. Verhaegen	Technische Universiteit Delft
Dr. ir. F.T. Muijres	Wageningen University and Research
Dr. ir. B.W. van Oudheusden	Technische Universiteit Delft

Dr. G.C.H.E de Croon heeft als begeleider in belangrijke mate aan de totstandkoming van het proefschrift bijgedragen.

*I set limits to my work, which would in time
be ended, though not completed.*

Samuel Johnson, 1755, preface to 'A Dictionary of the English Language'

CONTENTS

SUMMARY

The ever-increasing interest in unmanned aircraft, for applications ranging from the traditional military to commercial and civilian, has fuelled the exploration of novel and unconventional solutions, to respond to increasingly challenging new requirements. One strong trend is the demand for always smaller, more manoeuvrable and versatile vehicles, which could be used in complex, tight and possibly dangerous environments. This demand cannot be met with conventional manned flight approaches and has led engineers to seek inspiration in nature, giving rise to the biologically-inspired flapping-wing micro aerial vehicle – the FWMAV. FWMAVs achieve a remarkable flight performance at low airspeeds and small scales, displaying high manoeuvrability, hover-capability, and a considerable potential for further miniaturisation. In spite of their favourable properties, however, FWMAVs are almost exclusively used as research objects and their development continues to pose a considerable challenge. While several FWMAVs have been constructed, knowledge of their flight mechanics, and particularly their aerodynamics, remains limited, which hinders the development of effective dynamic and aerodynamic models. Such models are essential for realistic dynamic simulation, more efficient design and advanced control system development, which would greatly enhance the performance and autonomy of such vehicles. At present, few models are available for flapping-wing flight, and these are typically either too complex for practical applications, or too simplified for control design, or not fully validated.

This thesis addresses the challenge of modelling time-varying flapping-wing dynamics on the basis of free-flight and wind tunnel data, with the aim of developing new modelling approaches, while providing new insight into flapping-wing flight mechanics in the process. In particular, the objective is to devise models that are accurate but also suitable for control and simulation applications, i.e. not excessively complex or computationally expensive. The results should support the further development of FWMAVs, bringing them one step closer to full integration in the aerospace field. The overall approach taken is data-driven – this allows both for realistic results and inherent validation opportunities, and for insight to be derived despite limited a priori knowledge of the studied system. In view of the experimental methodology, the presented research is based on a test vehicle, i.e., the DelFly II, developed at TU Delft. Hence, the approach taken is first to analyse, model and better understand the flight mechanics of a specific FWMAV, and then to generalise the devised approaches and the gained insight. To meet the stated objectives, two high-level modelling approaches are developed, and discussed in the two parts of this thesis.

The first modelling approach is based on system identification using free-flight data, and leads to linear time-varying grey-box state-space models of the vehicle dynamics. A time-scale separation approach, involving a two-part model structure and a frequency-domain decomposition of the identification data into high and low-frequency components, is proposed to include time-varying flapping-related effects in these models. These effects are typically neglected in FWMAV dynamics models, but are considered a useful asset not

only for a fuller characterisation of the vehicle, but also to test on-board instrumentation and novel control and navigation algorithms requiring high precision. Despite the considerable accuracy of the time-varying model component of the studied test platform, there appear to be effects the model cannot account for during manoeuvres. These effects are minor, nonetheless a further investigation of potential time-scale couplings is advocated before assuming decoupling for vehicles, like the DelFly, where the flapping frequency is close to the body mode frequencies. The chosen model structure involves few parameters and measurements, and the resulting model is accurate in representing both the time-averaged and the time-varying aerodynamic forces and moments. It also allows for accurate dynamic simulation, thus improving on previously available results for the DelFly specifically.

The grey-box modelling approach is subsequently applied in a range of different flight conditions and used to characterise the dynamics of the test platform more fully, focusing on the more significant flap cycle-averaged component. The results of this analysis are used to devise a linear parameter-varying (LPV) model of the dynamics covering the explored flight envelope, hereby demonstrating a global model identification approach for FWMAVs. This involves determining a set of scheduling functions expressing the dependency of the local models on the corresponding flight condition. Using a low-order, interpretable model structure and a small number of parameters, the LPV model yields a continuous and accurate description of the dynamics over a considerable part of the typical flight envelope, providing new opportunities for control and simulation work. This again addresses a gap in the literature, where most models are developed or validated for a single flight condition. The global modelling process also yields new insight into the vehicle dynamics, highlighting and clarifying the changes that occur in different flight conditions. While these changes are on a small scale for the DelFly, they are nonetheless significant and modelled effectively. Both the local and the global grey-box models are shown to be accurate as well as computationally inexpensive and easy to obtain, interpret and apply – hereby meeting the stated objectives. The model structures defined and modelling approaches developed are applicable to other FWMAVs, with similar actuation mechanisms and flight properties.

In the context of the free-flight system identification process used within the first modelling approach, it was to some extent necessary to adapt existing flight testing, data acquisition and data processing methods to the flapping-wing case. FWMAVs are characterised by low flight speeds, periodic oscillations of the body during flight, small sizes, and unconventional flight properties – and hence pose different challenges from conventional aircraft. Recommendations for effective flapping-wing vehicle flight testing are therefore also put forth in this thesis. In addition to experiment design and test execution guidelines, a data fusion method is developed to combine on-board inertial sensor data with off-board optical motion tracking data. The fusion approach yields more informative and reliable measurements compared to the separate sensors, largely avoiding the drawbacks of these, such as noise amplification, limited resolution at small scales, drift and bias. A wind tunnel-comparable quality of data is achieved without the drawback of clamping, particularly at the high frequencies relevant for flapping-wing flyers. In this way, high-quality measurements can be obtained in realistic free-flight conditions, during manoeuvres and at high frequencies. These data are valuable not only for model identification, but also for theoretical analysis, e.g., of the time-resolved aerodynamics.

In the second part of this thesis the focus is shifted from the high-level system dynam-

ics to the aerodynamics, particularly considering the variation occurring within the single flap cycles. While the first modelling approach is aimed primarily at developing low-order and easily applicable models, the second approach aims to obtain phenomenological models, which still exploit experimental data but are more detailed and informative, and more closely related to the physics of the system. The wings and tail are considered separately, to isolate their respective effects and obtain a better understanding. To allow for a greater level of detail, these models are derived from wind tunnel data.

A quasi-steady model is derived to represent the wing aerodynamics, with particular emphasis on capturing the unsteady clap-and-fling effect and assessing its importance. For this, existing quasi-steady formulations are extended with an additional circulatory component to represent clap-and-fling. The added term leads to considerable accuracy and a clear improvement compared to existing formulations, hereby demonstrating the importance of considering the clap-and-fling mechanism when present. The developed model also differs from existing approaches as it uses flight-measured, as opposed to prescribed, wing kinematics. Additionally, the model is extended so as to be applicable in different flight regimes, by expressing the force coefficients as a function of vehicle states. Accurate results are achieved without resorting to excessive complexity or computational burden. While more complex than the previously described grey-box models, this type of model offers the benefit of more detail, insight and flexibility, thanks to its more physically meaningful structure. In the modelling process, it is moreover shown that a quasi-steady formulation can sometimes still be applicable at relatively high reduced frequencies, suggesting that the typically accepted applicability ranges may be extendible, at least in specific cases.

To complement the aforementioned wing model, lastly, the tail aerodynamics are considered. While the majority of existing FWMAVs are equipped with a conventional tailplane, to provide passive stability and facilitate the actuation mechanism, the tail is rarely considered explicitly in FWMAV models. When it is, its interaction with the flapping-wing wake is either neglected or extremely simplified. To allow for the flapping-wing wake influence on the tail to be considered, a model of the wake is identified from PIV data. The wake model describes the spatio-temporal variation of the flow behind the flapping wings with high accuracy, without resorting to high-order terms thanks to its piecewise formulation. The time-varying tail forces are then modelled with a two-dimensional quasi-steady aerodynamic model, where the local flow conditions at the tail are computed from the aforementioned wing-wake model, combined with the influence of the free stream. The tail aerodynamics model is novel in taking into account the effect of the wing wake at a time-resolved level. At the same time it is to some extent physically interpretable and requires only light computations, while the tail forces it predicts are in a plausible order of magnitude. The proposed approach both constitutes an effective method to predict FWMAV tail forces, useful for modelling, design and control work, and yields a better understanding of the tail-wing wake interaction and the tail aerodynamics. The flapping-induced flow is shown to heavily influence the flow conditions at the tail, reaching the same order of magnitude as the typical forward velocity of the test platform. The local velocity at the tail peaks at $50-70\%$ of the tail span, suggesting the tail is most effective in this region.

Like the previously described grey-box approaches, the proposed phenomenological aerodynamic modelling methods are generalisable to other vehicles – in this case, if aerodynamic similarity is ensured. Furthermore, the latter models do not strictly require flight

testing, which makes them more widely and easily usable, and they provide more extensive and detailed physical insight. This comes at the price of a more complex structure and interpretation, and a higher effort required for derivation and implementation. In considering which model to use, the desired accuracy must be weighed against the complexity required to achieve it. The grey-box models are generally recommended for control applications due to their overall simplicity; the phenomenological aerodynamic models are potentially more suited for advanced controllers, which exploit the time-varying mechanisms. The latter models are also recommended for in-depth theoretical analysis and design studies at the phase where no flight-capable platform is available. Once a flight-capable FWMAV is available, however, the grey-box modelling process is easier to implement and is considered a more effective approach to gain immediate qualitative insight for a novel vehicle.

Finally, while the modelling methods developed in this thesis can to some extent be generalised, they are derived from measurements on the DelFly II and hence also specifically contribute towards a fuller understanding of this particular platform. The work described results in the following new models for the DelFly: (i) an accurate and simulation-capable dynamic model, including time-varying effects; (ii) a global dynamic model; (iii) a quasi-steady wing aerodynamics model including the clap-and-fling effect; and (iv) a time-varying tail aerodynamics model.

From the obtained results, several recommendations for future work can be derived. The grey-box models could be extended by considering the effect of flapping frequency excitation and the lateral component should be improved. Free-flight testing in the wind tunnel could be exploited to explore a wider flight envelope, resulting in a more complete global model. Furthermore, explicitly considering aggressive manoeuvres in the dynamic modelling process would be beneficial, as manoeuvrability is one of the key assets of FW-MAVs. In view of the manual construction of most FWMAVs, it would also be useful to account for small variations in the same vehicle, by incorporating geometric parameters in the model structures. On the theoretical side, current results suggest that potential couplings between the body and flapping dynamics should be further investigated for vehicles where the flapping frequency and body mode frequencies have a similar magnitude.

The quasi-steady wing aerodynamics model can be extended to account for wing flexibility and the wing 'clap' effect. It would also be of interest to evaluate different wing geometries and kinematics, and better assess the generalisability of the model. Deriving the model parameters from free-flight data would additionally allow for more realistic results and improved drag estimation. The tail force model requires more comprehensive validation, which encompasses experimental challenges. The tail model could also be improved by further investigating the interaction between free stream and wing wake, for instance with the help of PIV measurements in forward flight. Such measurements may also provide an improved theoretical understanding of the complex tail-wing wake interaction. Combining the wing and tail aerodynamic models, accounting for the effect of control inputs and inserting the result into suitable equations of motion, would yield a full phenomenological system dynamics model, as alternative to the grey-box dynamic models.

Lastly, all of the developed models pave the way for new work in design, simulation, and control, and various potential applications are envisaged. Particularly new control approaches could be explored, for instance, ones that explicitly exploit the flapping-wing mechanism to achieve an enhanced performance.

NOMENCLATURE

Latin letters

$\mathbf{A}$	System matrix
$\mathbf{A}_{ij}, \mathbf{B}_{ij}$	Constant matrices of LPV model parameters (scheduling coefficients)
A	Wave amplitude, with respect to the mean
a_0	Lift curve slope for two-dimensional airfoil
a_{x_w}, a_{z_w}	Relative acceleration of wing blade element along x_W and z_W axes, ms^{-2}
a_x, a_y, a_z	Linear accelerations measured by IMU, ms^{-2}
$\mathbf{B}$	Input matrix
$\mathbf{B}$	Regressor matrix in barycentric coordinates
b	Average thickness of wing blade element, m
b	Span width, m
b_{ax}, b_{ay}, b_{az}	Accelerometer biases, ms^{-2}
b_p, b_q, b_r	Gyroscope biases, $deg \cdot s^{-1}$
b_{t_j}	Local barycentric coordinates with respect to simplex t_j
C_D	Drag coefficient
C_{D_0}	Drag coefficient at 0° angle of attack
$C_{D\frac{\pi}{2}}$	Drag coefficient at 90° angle of attack
$C_{D,t}$	Tail drag coefficient
$C_{D0,t}$	Tail drag coefficient at 0° angle of attack
$C_{D\frac{\pi}{2},t}$	Tail drag coefficient at 90° angle of attack
C_F	Fling coefficient
C_L	Lift coefficient
$C_{L,t}$	Tail lift coefficient
C_l	Dimensionless lift coefficient
C_T	Coefficient of translational circulation
C_R	Coefficient of rotational circulation
$C_{\theta_{w_0}}, C_{\theta_{w_\zeta}}, C_{\theta_{w_{\dot\zeta}}}$	Coefficients used to approximate wing pitch angle

c	B-coefficient vector
c	Chord length, m
c_{eff}	Effective chord length, considering only peeled part of wing blade element, m
D	Drag force, N
d	Model polynomial degree
d	Wing pitch rotation axis position, m
d_c	Chordwise distance from wing trailing edge, m
d_s	Spanwise distance from wing root, m
$d\mathbf{F}$	Total force acting on blade element, N
$d\mathbf{F}_{centrip}$	Centripetal force acting on blade element, N
$d\mathbf{F}_{circ}$	Circulatory force acting on blade element, N
$d\mathbf{F}_{addmass}$	Added mass force acting on blade element, N
$d\mathbf{F}_{visc}$	Viscous force acting on blade element, N
F	Vector of aerodynamic forces, N, and moments, Nm
F_u, M_u	Control derivatives in standard notation: partial derivative of force F/moment M with respect to control input u
F_x, M_x	Stability derivatives in standard notation: partial derivative of force F/moment M with respect to state x
F	F-statistic
f	Frequency, Hz
f_f	Flapping frequency, Hz
g	Acceleration due to gravity, ms^{-2}
H	Smoothness matrix
H	Jacobian matrix
h	Fourier series harmonics number
I_{xx}, I_{yy}, I_{zz}	Body moments of inertia, $kg \cdot m^2$
I_{xy}, I_{yz}, I_{xz}	Body products of inertia, $kg \cdot m^2$
J	Cost function
J	Number of simplices in triangulation
K	Kalman gain
k	Reduced frequency
L	Lift force, N

L, M, N	Aerodynamic moments around x_B, y_B and z_B axes, Nm
M_{wing}	Wing mass, kg
m	Mass, kg
m_{11}, m_{22}	Mass of surrounding fluid accelerated along x_W and z_W axes, kg
n_k	Number of measurement points
n_u	Number of inputs
n_x	Number of states
n_y	Number of outputs
P	Estimated measurement error covariance matrix
p, q, r	Angular rates in body-fixed reference frame, $deg \cdot s^{-1}$
Q	Process noise covariance matrix
R	Measurement error covariance matrix
$\mathscr{R}_\epsilon$	Autocorrelation of model residuals
R^2	Coefficient of determination
S	Surface area, m^2
T	Wing flapping period, s
t^*	Non-dimensional time with respect to wing flapping period
t	Time, s
u	System input vector
u, w	Velocity in x and z directions of corresponding frame, ms^{-1}
u, v, w	Linear velocities in body-fixed frame, ms^{-1}
V	Velocity magnitude, ms^{-1}
V_∞	Free-stream velocity, ms^{-1}
v_{ub}, v_{vb}, v_{wb}	Measurement noise in velocity measurements, ms^{-1}
v_{x_w}, v_{z_w}	Relative velocities of wing blade element along x_W and z_W axes, ms^{-1}
$v_{x_{w_l}}, v_{z_{w_l}}$	Relative velocity perceived by lower wing blade element along x_W and z_W axes, ms^{-1}
$v_{x_{w_u}}, v_{z_{w_u}}$	Relative velocity perceived by upper wing blade element along x_W and z_W axes, ms^{-1}
v_Φ, v_Θ, v_Ψ	Measurement noise in attitude measurements, deg
w_{ax}, w_{ay}, w_{az}	Process noise in accelerations, ms^{-2}
w_p, w_q, w_r	Process noise in angular velocities, $deg \cdot s^{-1}$
X	Regressor matrix

$\mathbf{x}$	System state vector
(x, y, z)	Position, m
x_0	Chordwise position of wing section rotation axis, m
x_h	Horizontal tail longitudinal position with respect to wings, m
x_B, y_B, z_B	Unit axes of body reference frame
x_A, y_A, z_A	Unit axes of aerodynamic reference frame
X, Y, Z	Aerodynamic forces along x_B, y_B and z_B axes, N
$\mathbf{y}$	Model-predicted system output
$\mathbf{z}$	Measured system output

Greek letters

α	Angle of attack, deg
β	Angle of sideslip, deg
Γ	Discrete input matrix
Γ_{trans}	Translatory circulation, $m^2 s^{-1}$
Γ_{rot}	Rotational circulation, $m^2 s^{-1}$
Δ	Difference with respect to equilibrium condition
δ_e	Elevator deflection, deg
$\delta_{e,CMD}$	Commanded elevator deflection, deg
δ_r	Rudder deflection, deg
$\delta_{r,CMD}$	Commanded rudder deflection, deg
ϵ	Least squares error
ζ_0	Wing dihedral angle, deg
ζ	Wing flap angle, deg
$\dot{\zeta}$	Wing flap angular velocity, $deg \cdot s^{-1}$
$\hat{\boldsymbol{\Theta}}$	Vector of parameter estimates
θ_w	Wing pitch angle, deg
θ_u	Upper wing pitch angle, deg
θ_l	Lower wing pitch angle, deg
κ, γ	Multi-indices
ρ	Fluid density, $kg \cdot m^{-3}$
$\boldsymbol{\rho}$	Vector of scheduling variables

σ^2	Variance
Φ	Wave phase, s
Φ, Θ, Ψ	Euler angles, deg
$\mathbf{\Psi}$	Discrete state transition matrix

Subscripts

A	Expressed in aerodynamic reference frame
B	Expressed in body reference frame
b	Referring to the body
I	Expressed in inertial reference frame
loc	Local
$glob$	Global
t	Referring to the tail
W	Expressed in wing reference frame
w	Referring to the wing
0	Referring to a steady condition
∞	Free-stream

Acronyms

AOA	Angle of attack
AR	Aspect ratio
BE	Blade element
CFD	Computational fluid dynamics
CG	Centre of gravity
DFT	Discrete Fourier transform
DOF	Degree of freedom
EKF	Extended Kalman filter
EOM	Equations of motion
FFT	Fast Fourier transform
FS	Fourier series
FWMAV	Flapping-wing micro aerial vehicle
GPS	Global positioning system

IMU	Inertial measurement unit
LEV	Leading edge vortex
LPV	Linear parameter-varying
LQR	Linear quadratic regulator
LTI	Linear time-invariant
MAV	Micro aerial vehicle
MEMS	Micro-electromechanical systems
ML	Maximum likelihood
OLS	Ordinary least squares
OT	OptiTrack system
PID	Proportional-integral-derivative (control)
PIV	Particle image velocimetry
PSD	Power spectral density
QS	Quasi-steady
RMSE	Root mean square error
TA	Time-averaged
TEV	Trailing edge vortex
TV	Time-varying
UAV	Unmanned aerial vehicle
WT	Wind tunnel

1

INTRODUCTION

Flying animals have at their disposal an impressive and widely varied arsenal of flight capabilities. Skilled at feats ranging from hover all the way to dives, sharp turns and complex aggressive manoeuvres, they master the art of flying to a degree that human-built flying machines cannot compete with. The rapid technological advances of the past decades have engendered a rapid growth of the unmanned aerial vehicle industry – with it, an always greater demand for smaller, more efficient and more agile vehicles has ensued, which cannot be met with conventional approaches designed for manned flight. One strategy to meet this challenge is to seek inspiration in nature. Flapping-wing mechanisms achieve a high performance at very low Reynolds numbers and thus represent a promising solution to the miniaturisation challenge in unmanned flight. Before flapping-wing robots can establish their presence in the air, however, many theoretical and practical challenges must be tackled. This chapter introduces and motivates the concept of flapping-wing micro aerial vehicle, placing it into context in the unmanned flight landscape. A concise overview of the fundamental mechanisms of flapping flight is provided and the literature most relevant to the research presented in this thesis is reviewed. The motivation and objectives of the presented research are then discussed in the final sections.

1

1.1. FLAPPING-WING MICRO AERIAL VEHICLES

Flapping-wing flight evolved millions of years ago, with the oldest known fossil of a flying insect to date being approximately 400 million years old [1]. Their ability to fly and remarkable flight performance may explain why insects and birds have been so successful in an evolutionary sense and still exist on earth today. At present, over a million types of insects and approximately 13,000 vertebrates are capable of flight [2], and all of these use active wing flapping as part of their flight mechanism. It is therefore unsurprising that mankind's timeless fascination with flight should have focused first on flapping-wing flight, drawing inspiration from the extraordinary aerial feats of natural flyers.

(a) 'The Fall of Icarus' by Jacob Peter Gowy, showing an early example of human fascination with flapping wings.

(b) Otto Lilienthal's *Kleiner Schlagflügelapparat* ornithopter, which was only tested in gliding flight.

(c) Lippisch's ornithopter (1929): a rare example of successful man-powered flapping-wing flight [3].

Figure 1.1: Early examples of man's theoretical and practical interest in artificial flapping-wing flight.[1]

Already the ancient Greeks envisaged, in their mythology, man-made wings of wax and feathers, allowing humans to lift off, however it would take centuries for the idea to be reconsidered more scientifically, and longer yet for it to be put into practice with even marginal success. The concept of a flapping-wing machine was mentioned in a somewhat scientific context circa 1260, when the Franciscan monk and scholar Roger Bacon wrote, *It is possible to make engines for flying, a man sitting in the midst whereof, onely turning about an instrument, which moves artificial wings made to beat the aire, much after the fashion of a bird's flight* [4]. The idea would then notoriously be taken up again, two hundred years later, by Leonardo da Vinci, who developed several detailed theoretical designs of human-powered flapping-wing machines [5]. In the time that followed, there have been numerous

---

[1]Figures taken from: (a)http://www.museodelprado.es/imagen/alta_resolucion/P01540_01.jpg; (b)http://www.lilienthal-museum.de/olma/213.htm

scientific and amateurish attempts to imitate flight in nature by mechanical means, however, most vehicles failed to take off, displayed a highly limited performance, or conveyed their pilot to death (e.g., the many examples of so-called 'tower jumpers').

Only the significant technological progress of the twentieth century, fuelled by two world wars, finally led to a breakthrough in the field of aviation, after the first human-built aircraft were able to take off successfully in the early nineteen hundreds. Despite centuries of fascination with flapping-wing flight, these vehicles were either lighter-than-air or had fixed wings. Only recently, the idea of flapping-wing flight was reconsidered, this time for unmanned aircraft. In fact, the flapping-wing approach, which had proved largely unsuccessful for human transport, was found to represent a highly promising solution to the novel challenges of miniaturisation encountered in the budding unmanned aerial vehicle (UAV) field.

Unmanned aerial vehicles (UAVs) were initially conceived as military tools for 'dull, dirty and dangerous' tasks disagreeable to humans. In time, as technology facilitated the development of such vehicles, their production and use began to spread into the commercial and even the hobby sector, and the interest in UAVs continues to grow rapidly. Nowadays, UAVs are being used or considered for a large variety of applications, next to the original military ones, e.g., for crop supervision, pipeline inspection, surveillance, data collection, package delivery and aerial photography. Unmanned flight holds many attractions and allows for unprecedented freedom in exploring new designs and flight mechanisms. However, it also entails challenges – above all, the developed vehicles must achieve a level of safety that allows for them to be used in everyday life. Thus, research in this field focuses, on the one hand, on developing platforms with improved or novel flight capabilities and increased performance for the intended application, and, on the other hand, on increasing the safety, reliability and autonomy of these platforms.

One of the current major trends in the UAV industry, is to develop increasingly small vehicles, which fall into the class of so-called micro aerial vehicles (MAVs). In practice, however, this is challenging. Next to the difficulty of designing and constructing platforms that are as small and light as possible but can still carry a means of propulsion and a useful payload, the perhaps greatest hurdle is to achieve flight at all, at the low Reynolds numbers ensuing when miniature vehicles fly at low velocities. It was the latter requirement, in particular, that led to the flapping-wing micro aerial vehicle (FWMAV)[2]. While, historically, flapping-wing flight has predominantly been considered as a means of human conveyance, it is in fact significantly better suited to small, light bodies travelling at relatively low speeds.

FWMAVs (e.g., [6–12]) are a sub-category of UAVs, characterised by small sizes [13] and generating lift and thrust by means of wing flapping. FWMAVs are typically very light, potentially highly manoeuvrable and versatile, and capable of hovering and of efficient flight at low speeds. Given their favourable flight properties, several practical applications can be envisaged for such vehicles, such as search and rescue operations or inspection of damaged buildings or machinery. In particular, FWMAVs are expected to fill in the gap between fixed-wing and rotary-wing MAVs. Compared to fixed-wing MAVs, they are able to hover and take off and land vertically (VTOL), display a significantly greater manoeuvrability and higher performance at low Reynolds numbers. This makes FWMAVs more

---

[2]In this book, as in the literature, the term ornithopter is used as synonymous to FWMAV, even when referring to smaller vehicles more akin to insects than to birds.

1

(a) University of Toronto's Mentor [11], 2002

(b) AeroVironment's Nano Hummingbird [7], 2011

(c) University of Maryland's Small Bird [14], 2009

(d) TU Delft's DelFly I, 2005

(e) Tamkang University's Golden Snitch [10], 2009

(f) Berkeley University's ibird [15], 2010
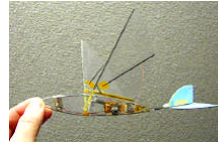
(g) Caltech's Micro-Bat [9], 2001
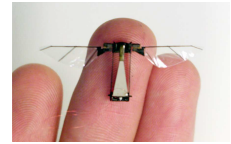
(h) Harvard University's microrobotic fly [8], 2008

Figure 1.2: Examples of flight-capable FWMAVs.

versatile and suited for flight in complex, cluttered environments. Rotating-wing MAVs share some of the advantages of FWMAVs, e.g. hover and VTOL capability, however, they have a lower efficiency and performance at low Reynolds numbers, and are generally noisier and heavier.

Several flight-capable FWMAVs have been developed in recent years, as for instance shown in Fig. 1.2. Common criteria used to classify flapping-wing robots include their size, their flapping configuration, their stability properties and their control mechanism. All of the aforementioned criteria are linked to each other.

The most common wing configuration in nature involves a single pair of wings: i.e., one wing on each side of the body. This mechanism is widely used also for FWMAVs [7–10, 14, 16, 17]. It is the most straightforward in terms of design and construction, however the resulting wing motion often leads to considerable inertial oscillations of the body, which are for instance disadvantageous for on-board cameras or sensors.

Alternatively, some FWMAVs make use of two pairs of wings, which leads to additional lift production and a high potential for precise and versatile control. When occurring in nature, four wings are arranged in a tandem configuration. This mechanism is known to yield remarkable flight capabilities, as for instance demonstrated by dragonflies [18], however it is highly elaborate and difficult to mimic in robotic flyers, which explains why efforts in this direction remain scarce [19–21]. A more widespread alternative, in the FWMAV field, is to arrange the two wing pairs in a biplane (or 'X-wing') configuration. This solution cannot be found in nature[3], but is attractive for robotic flyers. Opposite-phase flapping of the upper and lower wing pairs drastically reduces flapping-induced oscillations of the body, leading to a more stable flight motion – amenable for carrying optical payload or sensors. X-wing

---

[3]It has, however, been hypothesised that it existed in prehistoric times [22]

configurations have also generally been suggested to result in more stable dynamics [23]. Moreover, the X-wing design lends itself to exploitation of the lift-enhancing clap-and-fling mechanism (explained in Sec. 1.2.3), if the two wings on each side of the body are made to touch each other during each flap cycle. Although X-wings cannot be found in nature, the clap-and-fling mechanism itself occurs – in a different form – in the flight of many birds and insects, whose left and right wings touch at the end of the outstroke. Examples of biplane FWMAVs include the University of Toronto's Mentor [11], Berkeley University's i-Bird [15], Chiba University's FWMAV [24] and TU Delft's DelFly, which is the test subject used in this thesis (discussed further in Sec. 1.4.1).

A different type of distinction can be made between passively stable and unstable configurations – typically corresponding to tailed and tailless designs, respectively. Tailed FWMAVs are equipped with a tailplane, based on conventional fixed-wing aircraft design, which provides static stability and can be used to control the vehicle. Key advantages of this configuration include static stability and simpler control mechanisms avoiding complex active wing control. Tailed designs are also generally larger and involve simpler flapping mechanisms, e.g. having only a single active degree of freedom (DOF). The increased simplicity and stability come at the cost of a somewhat lower manoeuvrability, nonetheless the performance of tailed FWMAVs remains high compared to their non-flapping counterparts.

By contrast, the vast majority of tailless vehicles are inherently unstable, and typically smaller and lighter than their tailed counterparts, more closely resembling insects. Thanks to their instability, they are extremely agile and capable of rapid aggressive manoeuvres. They are also considered more adept at handling gusts and turbulence. However, instability calls for stabilisation mechanisms, which, in the absence of a tailplane, require active wing control. Flapping-wing actuation mechanisms are significantly more complex compared to fixed-wing flight ones, representing a challenge both in terms of design and fabrication, and in terms of control law design, particularly considering the small scales of tailless FWMAVs. Tailless vehicles are less widespread, however a small number of such vehicles have successfully taken off and displayed controlled flight capability, including the Nano Hummingbird [7], the RoboBee [25] and Festo's BionicOpter [19], and significant progress can be expected in this direction in the coming years.

As evident from the preceding overview, FWMAVs are now being widely researched, however, they are not yet being used commercially. In fact there are still many obstacles to this development, arising from a combination of the high complexity of flapping-wing flight mechanisms (cf. Sec. 1.2) and the practical difficulties of constructing micro-scale robots that make use of such mechanisms. Many complications already arise from the small scale alone, and are thus common to all MAVs. Extremely light but efficient batteries are for instance required to allow for a useful flight time. On-board instruments must be as light as possible, but still sufficiently precise. Controllers can only rely on simple computations, given the limited payload availability, but also have to be highly effective, particularly for unstable platforms. Developing effective actuation mechanisms at small scales is also highly complex. In view of these points, the development of MAVs, and FWMAVs in particular, remains an open field of research.

A final point to note is that MAVs vary widely amongst each other. Being small, light and unmanned, they are relatively easy and inexpensive to produce, and so far relatively unconstrained by certification requirements and safety regulations – indeed safety concerns

1

are inherently limited due to the low kinetic energy of such vehicles. All of this allows for remarkable freedom in designing new platforms, but likewise leads to the production of many entirely different vehicles in small numbers. This in turn complicates the development of general methodologies in every field from design and construction all the way to simulation and control, and introduces many new challenges, whereas the alternative solution of devising bespoke methods for each vehicle entails high costs. This thesis will address some of the aforementioned challenges and investigate modelling methods for flapping-wing MAVs, as well as consider to what extent these methods can be generalised.

1.2. FLAPPING-WING FLIGHT

This section briefly discusses the basic mechanisms of flapping-wing flight, which this thesis aims to model.

1.2.1. KINEMATICS

Flapping-wing flyers use the motion of their wings to generate both lift and thrust, thus simultaneously maintaining themselves aloft and either propelling themselves forward or maintaining an approximately fixed hovering position. To achieve this, different flyers move their wings in different ways, i.e. according to distinct kinematic patterns. In general, the movement of rigid wings is described in terms of three distinct motions around different axes, viz.: (i) plunging (or flapping, or heaving): up-down motion, i.e. rotation around the wing root; (ii) pitching: rotation around a spanwise axis; and (iii) sweeping (or feathering, or lead-lag motion): forward-backward motion. These motions are clarified in Fig. 1.3. The motion of wings during one stroke is generally considered to occur within a plane, known as stroke plane, whose orientation can be adjusted by some flyers to influence the orientation of the resulting force vector [26].

(a) Rear view, showing plunging motion
(b) Side view, showing pitching motion
(c) Top view, showing sweeping motion
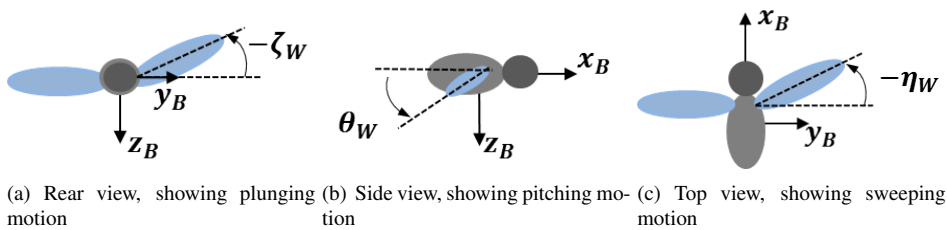
Figure 1.3: Schematic overview of the three motions of a generic rigid wing. Body frame axes (x_B, y_B, z_B) are shown for reference.

Typically, each wing flap cycle (illustrated in Fig. 1.4) can be divided into two phases, upstroke and downstroke, during which the wings accelerate in opposite directions. Between the two translatory phases, at what is known as stroke reversal, the wings rotate (i.e. pitch) rapidly about a spanwise axis, a movement called pronation when performed between upstroke and downstroke, and supination in the opposite case. This motion ensures that, despite opposite translatory motions during the upstroke and downstroke, the geometric leading edge of the wings always corresponds to the aerodynamic leading edge [27].

This in turn implies that the wing can maintain a positive angle of attack (AOA) during the entire flap cycle, hence generating lift throughout. Both the positioning of the rotation axis and the timing of the rotation influence the aerodynamic force generation process, as clarified in Sec. 1.2.3. It should also be noted that while wing rotation predominantly occurs at stroke reversal, some pitching motion may also occur throughout the flap cycle, depending on the specific flyer. The particular wing flapping motion leads to unique aerodynamic phenomena, an overview of which is given in the following subsections.
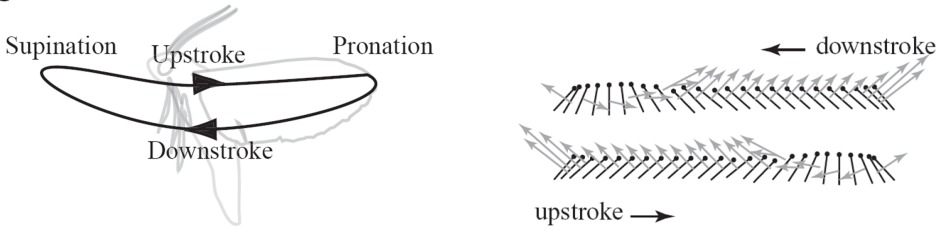
Figure 1.4: Main phases of the flap cycle (left, figure adapted from [28]), and example of wing chord orientation and translation throughout the cycle (right, figure adapted from [29]).

1.2.2. NON-DIMENSIONAL PARAMETERS

Three important non-dimensional parameters must be considered when analysing flapping-wing aerodynamics, viz. the Reynolds number, the Strouhal number and the reduced frequency. Together these can be used to define aerodynamic similarity [29]. These parameters also determine the main characteristics of the aerodynamics and hence determine which particular assumptions are acceptable and what modelling approaches are most suitable for a particular flyer.

The Reynolds number (Re) describes the ratio between inertial and viscous forces and is given by:

$$Re = \frac{\rho L_{ref} V_{ref}}{\mu},$$

(1.1)

where ρ is the fluid density, μ is the fluid viscosity, L_{ref} is the reference length and V_{ref} is the reference fluid velocity. Typically, the mean aerodynamic chord $\bar{c}$ is used as reference length, as in classical aerodynamics. The reference velocity can be defined in different ways for the flapping-wing case. In forward flight, it is common to use the forward flight velocity of the body, whereas for slow forward velocities and hover conditions, the mean wing tip velocity is typically used instead [29], i.e.:

$$V_{m,wingtip} = 2\pi f_f R,$$

(1.2)

where f_f is the flapping frequency and R is the span of one wing. A possible alternative approach is to use the velocity induced by the flapping wings, if this value can be measured or estimated, e.g. from actuator disk theory [30]. Reynolds number values for flapping flyers at hover are typically between 10 and 10,000.

1

The Strouhal number (St) characterises the relation between flapping-related oscillations and forward motion:

$$St = \frac{f_f L_{ref}}{V_{ref}}. \tag{1.3}$$

The reference distance in this case is the distance travelled by the wing during one half-stroke.

The reduced frequency (k) is a parameter quantifying the unsteadiness in flapping-wing airfoils, and is defined as:

$$k = \frac{\omega \bar{c}}{2 V_{ref}}, \tag{1.4}$$

where ω is the wing angular velocity in radians per second. Again, the reference velocity can be defined in different ways. In forward flight, the reference velocity is typically defined as the free-stream velocity, while in hover conditions, the mean wing tip velocity is often used instead. As for the Reynolds number, however, different definitions of the reference velocity are conceivable, particularly in low-speed and hover flight regimes. As it quantifies unsteadiness, the reduced frequency is a useful metric to determine what type of model is applicable to describe the aerodynamics of a particular flapping-wing flyer. Thus, for instance, quasi-steady models (cf. Sec. 1.3.1) are only strictly considered applicable for forward flight when the reduced frequency is low (e.g. below 0.1 [31]).

1.2.3. AERODYNAMIC MECHANISMS

Flapping-wing aerodynamics involves a number of different phenomena, many of these unsteady and not explicable by classical aerodynamic theory. Next to free-stream circulation, the following force generation mechanisms have been identified [32]: (i) delayed stall and leading edge vortex (LEV), (ii) rotational circulation (Kramer effect), (iii) Wagner effect, (iv) wing-wake interaction, (v) clap-and-fling [33] and (vi) added mass. Additionally, flapping wings typically generate inertial forces due to their rotational motion. This section briefly explains the aforementioned mechanisms, based on Refs. [26, 27, 29, 32, 34–36]. It must be noted that not all flapping-wing flyers make use of all the mechanisms discussed.

DELAYED STALL AND LEADING EDGE VORTEX FORMATION

The delayed stall phenomenon is connected to the translatory motion of the wings at high angles of attack. When a wing accelerates from rest at a high AOA, as happens in flapping-wing flight during the translatory phases, the flow over the wing surface separates at the leading edge, forming what is known as a leading edge vortex (LEV). In two-dimensional translating wings, the LEV stays attached to the wing for a number of chord lengths, until the wing eventually stalls (hence the term 'delayed stall'). In three-dimensional flapping wings, by contrast, the LEV remains stably attached to the wing [37] and the flow reattaches to the surface before reaching the trailing edge, so that the Kutta condition is maintained. Hence, the wing does not stall during translation and can transmit a larger downward momentum to the surrounding fluid. This in turn leads to additional lift generation compared to the steady case. The stabilisation of the LEV in flapping wings has been attributed to a spanwise flow along the wing, first observed by Ellington et al [37].

Delayed stall and LEV formation were first observed in insect flight by Maxworthy [39], on mechanical model wings, and later observed in the flow around hawkmoth (*Manduca*

(a) LEV visualisation on a hawkmoth wing; figure adapted from Ellington et al. [37]

(b) LEV visualisation on a butterfly wing; figure adapted from Srygley et al. [38]

Figure 1.5: Example of LEV formation visualised experimentally on insect wings.

sexta) wings by Ellington et al [37], using smoke visualisation techniques (cf. Fig. 1.5(a)). Since then, a number of studies have reported experimental observation of these phenomena in both natural flyers (e.g. cf. Fig. 1.5) and robotic flapping-wing setups [27, 38, 40–43].

ROTATIONAL CIRCULATION (KRAMER EFFECT)

As described in Sec. 1.2.1, between opposing half-strokes flapping wings rotate rapidly around a spanwise axis, thus maintaining a positive AOA throughout the flap cycle. When a translating wing rotates around a spanwise axis, the flow velocity is increased on one side of the wing and decreased on the other. This leads to violation of the Kutta condition, shifting the stagnation point away from the trailing edge, and results in a force perpendicular to the wing chord. To counter this effect and re-establish the Kutta condition, the wing generates additional circulation. Given that the Kutta effect is not re-established immediately, the wing thus generates additional circulation until the stagnation point has been shifted back to the trailing edge, which in turn leads to additional forces being generated. This phenomenon is known as the Kramer effect [44].

The rotational circulation is proportional to the angular velocity of the wing's rotation [32], and the direction and magnitude of the resulting forces depend on the direction and duration of the wing rotation, on its timing with respect to the translatory motion, and on the location of the wing rotation axis [27, 37]. It was found experimentally [27] that if the wing rotates before it changes direction of translation ('advance rotation'), an upward force is produced, which increases the lift. If rotation is delayed with respect to the stroke reversal, a downward force is produced, which reduces the lift. In the symmetrical case, the wing first generates an upward force, before stroke reversal, then a downward force, after stroke reversal. In hover conditions, rotational circulation has been found to account for up to 35% of the total lift force in robotic fruit flies, and up to 50% in robotic hoverflies [27].

WAGNER EFFECT

The Wagner effect [45] is the delay in growth of circulation observed when an inclined wing accelerates impulsively from rest. In this situation, the circulation around the wing does not

immediately reach the steady value required to establish the Kutta condition, but increases gradually. Next to an inherent latency in the establishment of steady circulation, the process is influenced by the vortex formations around the wings. As the wing accelerates from rest, a TEV is generated and shed, eventually rolling up into a starting vortex. The starting vortex induces a velocity field that further opposes the growth of bound circulation as long as the starting vortex is in the vicinity of the wing. The Wagner effect is unusual in that it attenuates rather than enhances aerodynamic force generation. However, studies suggest that this effect is not very significant for most insects [27] and, consequently, it is frequently neglected in the modelling of flapping-wing aerodynamics.

WING-WAKE INTERACTION

Through their periodic motion, flapping wings interact with their own wake, i.e. they come into contact with vortices shed during prior strokes. This effect, also known as 'wake capture', is mainly visible after stroke reversal and is believed to lead to an increase in aerodynamic force production directly following stroke reversal [27]. At stroke reversal the wing generates leading and trailing edge vortices, inducing a velocity field. When the wing moves back through this region after reversing, it travels through the increased velocity field, thus generating larger forces. The magnitude of the force increase is significantly influenced by the wing kinematics [32]. Wake capture was first shown to be present in insect flight by Dickinson et al. [27], through experiments on a robotic fruit fly, however it is generally difficult to isolate this effect and so far no effective approaches have been suggested to model it.

CLAP-AND-FLING (WING-WING INTERACTION)

Clap-and-fling denotes the interaction (typically touching) of two wings, observed in some insect species at dorsal stroke reversal. As the wings move towards each other, they come into contact with each other, starting at the leading edges. The gap between them closes gradually until the trailing edges are in contact ('clap' phase). As the gap closes, the air in this space is pushed downwards, imparting additional thrust to the insect [46]. Additionally, as the wings move closer together, their opposite circulations cancel out, which significantly attenuates the TEVs shed at the subsequent wing stroke. This in turn reduces the delay in circulation growth (Wagner effect), allowing for increased lift production [33, 47]. After the clap, the wings pronate and move apart again, starting at the leading edges ('fling' phase). The gap between them gradually opens up again, and the surrounding air moves into this low-pressure region, supporting the growth of circulation and the formation of an augmented LEV [48]. The clap-and-fling process if clarified in Fig. 1.6.

This effect was first described by Weis-Fogh [33] to explain the high lift generation in the *Encarsia formosa* wasp, and has since been studied in detail, theoretically, experimentally and through numerical simulation [39, 47, 49–53]. All studies found the combination of the described effects to lead to a significant lift force enhancement.

Variations of the clap-and-fling mechanism have also been identified, for instance the equivalent phenomenon occurring with flexible wings, sometimes known as 'clap-and-peel' [54]. In this case, the wings peel, rather than fling, apart, with the upper portions of the wings already peeling apart while the lower parts are still clapping together. The flexible peeling is believed to reduce drag [55] and wake-capture effects [48]. Moreover, flexibility decreases the effect of the clap phase, and decreases the added mass effect (for
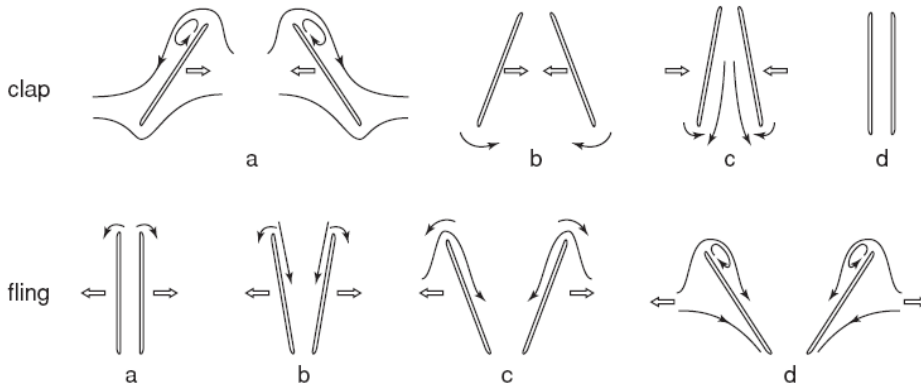
Figure 1.6: Schematic representation of clap-and-fling interaction between two interacting wing sections: thin arrows represent the flow, thick arrows indicate the direction of motion of the wings (sections). Figure adapted from [29].

less of the wing is accelerating during the upstroke). Finally, the TEVs shed during the peeling are reduced, supporting the growth of circulation [32].

ADDED MASS

In the course of each flap cycle, flapping wings undergo significant accelerations, and in so doing they accelerate the fluid they displace. The resulting reaction force is known as added mass effect. As this force occurs at the same time as the circulatory forces, it is difficult to measure in isolation. In quasi-steady aerodynamic models, the force resulting from the added mass effect is often modelled as a time-variant increase in wing inertia [32, 56].

1.3. MODELLING AND CONTROL OF FLAPPING FLIGHT

As evident from Sec. 1.2, flapping-wing flight is highly complex. This, combined with the practical limitations discussed in Sec. 1.1, explains why FWMAVs are not yet being used in practice. Particularly the modelling, design and control of such vehicles are open, and interrelated, areas of research. This thesis focuses on modelling, which can be seen as an important initial step in the development and functional understanding process. Mathematical models are helpful preliminary design tools, allow for simulation prior to time-consuming and potentially damaging real-world testing, support the development of controllers, and sometimes yield new insight.

A complete model of flapping-wing flight comprises different components. Firstly, the aerodynamic forces must be modelled. Secondly, a model of the system dynamics, or so-called equations of motion (EOM), must be defined, describing how the forces act on the body. Thirdly, the wing kinematics must be considered (or neglected based on suitable assumptions). Lastly, in an aerospace context, the control/actuation mechanism must be modelled. Depending on the approach taken, all of the aforementioned components may be considered separately, or merged with one or more of each other.

1

This section presents an overview of the literature on modelling flapping-wing flight, and particularly FWMAVs, establishing the foundations for the research presented in this thesis. In the interest of clarity, a distinction is made between aerodynamic and dynamic modelling where possible. A brief overview of control-related work is also provided, as this represents one of the main applications of FWMAV models. Following the review, the main challenges identified are summarised.

1.3.1. AERODYNAMIC MODELLING

The most widely used approach for aerodynamic modelling of flapping-wing vehicles, be they natural or human-built, is quasi-steady modelling. The underlying idea is to assume that the instantaneous forces on a flapping wing are equal to the forces that would act on a wing moving steadily at the same free-stream velocity and angle of attack [34]. These models are often implemented in a framework based on blade element theory, borrowed from helicopter studies, whereby the forces acting at each spanwise section of the wing are integrated along the span to obtain the total forces acting on the wing, thus allowing for the local flow conditions at each section to be considered. Since the first quasi-steady analyses of insect aerodynamics (e.g. cf. the review by Weis-Fogh and Jensen [57]), the quasi-steady approach has been discussed and applied extensively, with notable contributions by Weis-Fogh [57, 58] and, later, Ellington [34]. In their most basic form, quasi-steady models account only for translatory effects, which can be considered to include the LEV contribution [59]. Subsequent models have been extended to include additional effects that were previously neglected or wholly unknown, e.g. wing rotation [28].

One of the most widely-applied models in the literature is that developed by Sane and Dickinson [28, 56] using measurements performed on a dynamically scaled mechanical model of the fruit fly. Empirical expressions were obtained for the translatory lift and drag coefficients as functions of the wing AOA, based on the forces measured on a robotic wing moving with constant velocity at different AOAs. After Dickinson et al. [27] identified wing rotation as an additional mechanism of flapping-wing lift production, Sane and Dickinson included a term to represent rotational forces in a revised version of their original model [28]. In addition to translatory effects, the revised model also explicitly considers added mass effects and suggests that wake capture effects should be included in a complete model. Another widely-used quasi-steady model is that developed by the group of Wang at Cornell University [60–63], originally devised for falling plates with different kinematic patterns. This model is based on blade element theory, and captures the translatory and rotational forces, viscous effects, and added mass.

Quasi-steady models present a number of limitations and their validity is sometimes called into question in the literature. One of the first to do so was Ellington [34, 46, 54], who concluded that quasi-steady theory cannot explain the hovering flight of hawkmoths and underestimates the aerodynamic forces by up to 30%. Nonetheless, in many cases the quasi-steady approach yields a useful first approximation of the aerodynamic forces, and thus represents an attractive compromise between sufficient accuracy and low computational effort. In general, quasi-steady theory is considered applicable when the reduced frequency is low (cf. Sec. 1.2.2). Hence, in recent years, quasi-steady models have been widely used to describe flapping-wing aerodynamics of both natural flyers and FWMAVs [27, 31, 62, 64–71], and have frequently been found to achieve a high accuracy, especially for two-winged

flyers with low reduced frequencies and rigid wings. While quasi-steady models cover many of the aerodynamic mechanisms of flapping-wing flight, some effects have so far not been included in simplified models, most notably wake capture and clap-and-fling.

To cover more of the unsteady mechanisms of flapping-wing aerodynamics, several more complex models have been proposed. Zbikowski suggested two different approaches to model hovering flight aerodynamics, one based on circulation and the other based on von Karman-Sears unsteady wing theory [72]. Ansari et al. [73, 74] extended the latter approach to obtain a three-dimensional unsteady model for hovering flight, including wake capture as well as vortex effects. Due to its high complexity, however, this model is not suitable for most applications. The vast majority of more advanced flapping-flight models are implemented numerically using computational fluid dynamics (CFD) [75–81]. While such models can achieve a high accuracy, and are therefore useful for fundamental aerodynamic insight, they tend to be complex and computationally inefficient. Hence, they are inadequate for practical applications such as control system design [65] and dynamic simulation.

Yet another alternative was suggested by Taylor and Zbikowski [82], who used Fourier series to represent the forces produced by tethered desert locusts. While most of the models described previously incorporate some empirical component, typically in the aerodynamic force coefficient expressions, they are clearly linked to the physics of the system. This approach, by contrast, loses all physical connection. This in turn implies a diminished flexibility, as the resulting model only constitutes an accurate description of one particular system (here, the desert locust) in one particular flight regime. Nonetheless, this approach achieves extremely high accuracy and can for instance be useful for accurate simulation of one particular system[4]. This method can also be seen as a precursor of the system identification approach to dynamic modelling, discussed in Sec. 1.3.3.

Clearly, the central challenge and limiting factor in aerodynamic modelling is given by the conflicting accuracy and simplicity requirements. An additional limitation common to many of the current flapping-wing aerodynamic models is the fact that they are developed and validated for a single flight condition, often hover. This is often done to simplify the modelling process or due to experimental constraints, however it limits the applicability of such models in a flight dynamics context, as it can be expected that the aerodynamics change significantly in different flight regimes.

Finally, for evident reasons, the flapping-wing literature focuses on the wing aerodynamics, however, most robotic flyers (and many birds) are equipped with tailplanes, which play a crucial role on the dynamics. While FWMAV tail surfaces are typically modelled after conventional fixed-wing aircraft ones, their position in the wake of the flapping wings results in complex aerodynamics. Tailed FWMAV studies typically incorporate the tail in an overall model of the vehicle aerodynamics, without differentiating between tail and wings [15, 83, 84], which is convenient for dynamic modelling but yields no insight into the specific role of the tail. Rare studies that consider the tail, do not explicitly account for the effect of the wing wake on it [85]. Hence, this is another aspect that is understudied.

---

[4]Appendix A compares a similar type of black-box approach to a quasi-steady approach.

1

1.3.2. DYNAMIC MODELLING

Like the aerodynamics, the body dynamics of flapping-wing flyers are highly complex, time-varying and typically nonlinear, hence they are also difficult to model. The flapping motion implies that flapping-wing flyers are multi-body systems. The flapping motion can also lead to significant flexibility [86] and inertia effects [87], both typically negligible in fixed-wing aircraft. To narrow down the problem, in many cases simplifications are considered acceptable, e.g. neglecting inertia effects or neglecting the changes occurring within each flap cycle altogether [87, 88]. Both assumptions are generally considered acceptable when the flapping frequency is significantly higher than the natural frequency of the body modes.

One distinction can be made between single-body and multi-body formulations. Some researchers, opting for a more realistic representation, treat flapping-wing flyers as multi-body systems. Different mechanical formalisms have been applied to derive EOM for flapping-wing flyers, e.g., Newtonian methods [89, 90], d'Alembert's principle of virtual work [67, 91], the Gibbs-Appel equations [92, 93], the Boltzmann-Hamel equations [94], and Kane's equations [95]. Multi-body models allow for consideration of inertial effects of the wings on the body, and involve explicit consideration of the flapping kinematics. Such formulations can be considered necessary particularly when the wing mass is high compared to the body mass [87], and for larger flyers, e.g. birds or bird-inspired FWMAVs, where the flapping frequency is lower and inertia changes over each flap cycle are therefore slower. Some models also include flexibility effects [86, 96]. Due to the added complexity of multi-body models, when the wing mass is small compared to the body mass, typically wing inertia effects are neglected and single-body models are preferred [64, 66, 88, 97, 98].

Another widespread assumption in the context of flapping-wing modelling, especially in control-related work, is time-scale separation. Based on the assumption that the body and flapping dynamics are related to significantly different frequencies and hence decoupled, averaging over the flap cycle is used to cancel out time-varying effects [65, 88, 97, 99–103]. It has been suggested that this assumption is not always justified and that there may be significant interactions between the aforementioned components of the dynamics [31, 71, 104, 105]. However, neglecting such potential interactions remains the most common approach, and is considered acceptable when the flapping frequency is significantly higher than the body mode frequencies (e.g. ten times higher [98]).

In the context of controller design, simulation and stability analysis, simple and computationally efficient models are desirable, and hence the assumptions of negligible inertia and time-scale separation are both widespread. Additionally, linear time-invariant (LTI) models are often favoured, as they allow for straightforward stability analysis through the eigenvalues of the system matrix, and are compatible with a wide compendium of established control synthesis techniques. Hence, several studies have employed considerably simplified, low-order linear models, nonetheless achieving effective results [84, 88, 106–110].

1.3.3. SYSTEM IDENTIFICATION

An alternative to the mostly physics-derived modelling approaches discussed so far is system identification, i.e. extracting a model of a dynamic system from experimental data. In the aerospace context, this typically involves assuming a model structure, based on a priori knowledge and hypotheses, and determining the model parameters such that the data are

represented as accurately as possible. Some methods also allow for the model structure itself to be determined starting from a pool of candidate terms [111, 112]. A prerequisite for obtaining a meaningful result is that the data should be collected in conditions that are as similar as possible to the real operating conditions of the system to be represented, and in which the system dynamics are being excited.

Being based on data, the obtained models are more closely tied to the test platform and less easy to generalise, compared to theoretically-derived models. However, this type of approach potentially allows for models both computationally efficient and highly accurate, and hence it represents an attractive alternative to both simplified physical models and highly complex numerical models. The direct connection to experimental data also allows for straightforward validation. While the model parameters have to be adapted to the specific vehicle, the identification approach and, in some cases, the model structure, are transferable to other vehicles.

The model structures used in system identification work range from black-box formulations [113] to physically-derived ones where the parameters to estimate have a clear meaning [114]. For flapping-wing flight, intermediate solutions are common, where the model structure is not fully derived from first principles but retains some physical interpretability. In general, linear-in-the-parameters model structures are favoured, often similar to ones used to represent fixed-wing aircraft [84, 110, 115–117]. Some studies have also used identification methods to determine the model structure as well as the parameters contained in it [85]. While system identification is typically used to model the aerodynamics, it is also possible to directly identify a model of the dynamics that incorporates the aerodynamics in a black-box type structure [113].

Due to the technological challenges involved in obtaining accurate flight data for FW-MAVs (cf. Sec. 1.4.2), relatively limited system identification work has been performed with such vehicles so far. Collecting suitable free-flight data, in particular, has only recently become possible, hence models identified from free-flight data are still scarce. Nonetheless, efforts to date [84, 106, 110, 113–118] have shown that this type of approach can yield accurate, realistic and simple models, as well as new insight for novel and complex types of vehicles that have not yet been extensively studied. Some studies have also identified models from simulation data, for instance to derive simpler model structures from complex nonlinear ones [107, 119].

1.3.4. EXPERIMENTAL DATA

Regardless of the chosen modelling approach, ultimately, any model must be validated with experimental data. While a significant portion of the insight we have on flapping-wing flight derives from observing birds and insects, and – more recently – from experimenting on mechanical models of FWMAVs, collecting realistic data for flapping-wing flyers can still be difficult, and this is one of the current obstacles in flapping-wing modelling.

The majority of experiments, especially in earlier studies, involved tethering the flyer or parts of it [24, 40, 88, 120–123]. Wind-tunnel tests with tethered flyers provide a significant amount of insight, and allow for easier and more accurate monitoring and control of the test conditions. Due to the increased repeatability and the reduced impact of external factors such as air draughts, tethered tests are for instance often preferred for the study of aerodynamic phenomena [30]. In studying flapping-wing robots, specifically, clamped test-

1

ing is also often preferred because it is feasible before a vehicle is flight-capable, and thus can be used to guide the design process, or to obtain fundamental insight without having to construct a fully-fledged vehicle. Nevertheless, clamping constrains the body of the vehicle, hindering certain oscillations that would occur in free flight. It has been shown that tethering can lead to aerodynamic forces that differ from the free-flight situation [124–126], and therefore realistic insight for free flight should be obtained in free-flight conditions.

However, free-flight testing presents challenges. In the FWMAV case, the most crucial one is, as already mentioned, that it is necessary to first develop a flight-capable vehicle. Even once a flight-capable vehicle is available, it is not straightforward to collect adequate and informative free-flight data. Systematic flight testing requires specific facilities and/or sensors that are not widely available, due to the small scale and unusual flight mechanisms. Data acquisition options include the use of optical motion tracking systems [16, 83, 116, 127] or on-board sensors [115, 128, 129]. Motion tracking systems are not always available and entail space restrictions [130]. By contrast, effective on-board sensing requires very small, light-weight sensors that do not significantly affect the flight properties of the vehicle but nonetheless provide accurate measurements – these are also not widely available. To analyse the aerodynamics, in particular, it may also be of interest to obtain reliable measurements at the sub-flap cycle level, which requires a high level of accuracy as well as a high resolution, often difficult to achieve in standard setups [126]. Additionally, FWMAVs are often inherently unstable, which renders them difficult to control in free flight and limits the possibility of open-loop experiments. This also impacts the repeatability of experiments, as it can be difficult to replicate the same test conditions repeatedly.

Recently, particle image velocimetry (PIV) measurements have been conducted on a free-flying FWMAV, kept in position in the wind-tunnel flow by a PID controller [131]. The setup implemented in this work paves the way for new opportunities, with the potential of combining the high accuracy of PIV measurements and highly controlled flow in the wind tunnel with realistic free-flight test conditions.

A number of flight test-based studies have been reported in the literature, analysing different aspects of flapping-wing flight, e.g. flight performance [132], kinematics and dynamics [16, 130, 133–135], and aerodynamics [116, 129, 136]. Nonetheless, while flight experiments with flapping-wing flyers are rapidly increasing, obtaining accurate free-flight data, especially at high model frequencies, remains challenging.

1.3.5. FLIGHT CONTROL APPROACHES

One of the main applications of FWMAV models is in the context of designing and developing control systems. Tasks for FWMAV controllers range from fulfilling obvious low-level objectives, such as stabilisation or gust resistance, to autonomously performing high-level tasks, e.g. tracking a trajectory [100], avoiding obstacles [137] or flying through narrow spaces [106]. A variety of control approaches have been suggested for FWMAVs. The majority of these are linear [65, 66, 97, 101, 138–142] , e.g. involving simple PID or PD controllers or LQR-based control laws, while nonlinear control methods are less common [99, 100, 143, 144]. Examples of control techniques based on machine learning have also appeared in the literature, but with rare exceptions [145], have not been tested in flight [146, 147]. Additionally, studies looking at the internal control

behaviour of insects [148–150] may provide inspiration for control approaches in flapping-wing robots [151].

Based on the concept of time-scale separation, most controllers are developed based on the time-averaged system dynamics, although they are then applied to the time-varying system. Moreover, most controllers are based on linearised formulations of the dynamics [65, 138]. This in part explains why, with some exceptions [139], control-related FWMAV work often only considers a single flight condition [65, 99, 101, 138], which implies that the vehicle can only be controlled effectively in a limited part of its flight envelope.

Furthermore, most of the controllers proposed so far do not foresee the possibility of control inputs changing within the flap cycle. While this possibility can be considered unnecessary when the flapping frequency is high, it may constitute an interesting strategy for vehicles with a slower flapping motion. Typically, the flapping is either neglected altogether, or the control signal is only allowed to vary once per flap cycle [101]. A step towards 'sub-flap cycle' control has been proposed by Oppenheimer et al. [97], who developed a control approach based on split-cycle frequency modulation, where the flapping frequency can be varied at the end of either the upstroke or the downstroke.

1.3.6. Modelling challenges
Based on the preceding discussion, this section summarises some of the main challenges in the field of flapping-wing modelling, particularly of robotic flyers.

To begin with, flapping-wing flight is a highly complex physical process, and both the unsteady aerodynamics and the time-varying, multi-body dynamics are challenging to model. While a significant amount of knowledge is available thanks to studies on biological and robotic flyers, there are still open questions, and some phenomena, such as clap-and-fling, have not yet been modelled in a simplified way. Moreover, representing highly complex mechanisms remains difficult – frequently leading to computationally intractable or physically unobservable models – even when such mechanisms are fully understood. While simplifying assumptions can be made, it is important to ensure that a sufficient level of realism and accuracy is retained, and to investigate the justifiability of such assumptions as are made.

A particular difficulty is to represent the aforementioned physical processes in a meaningful and useful way, i.e. such that insight can be obtained and/or such that the resulting models can be applied in practice, e.g. for design or control work. Ideally, models should be both easily interpretable and computationally efficient. The latter point is especially important for models used on board, as the payload of FWMAVs is extremely limited. High accuracy can be achieved through black-box approaches or CFD methods, however the practical applicability of such models is limited – with the former being highly sensitive to small deviations from the tested flight conditions and the latter computationally intractable for real-time use. Additionally, the interpretation of both types of models is mostly arduous.

An additional challenge is the obtaining of useful experimental data, especially in realistic, free-flight conditions. The combination of highly complex mechanisms and miniature scales implies that flight testing FWMAVs is challenging and requires bespoke instrumentation that is not readily available. It is particularly difficult to conduct repeatable controlled flight tests that excite particular dynamic modes of a vehicle. However, experimental data are not only useful to obtain insight and construct better models, but also indispensable

1

for validation. The small scale itself is an obstacle not only in terms of data acquisition, but also limits the availability of on-board computational power and instrumentation, and complicates the development of actuation mechanisms.

Furthermore, the modelling and design problem constitutes a loop – models are helpful for designing new and flight-capable vehicles, while at the same time it is helpful to already have flight-capable vehicles in order to develop better models. This is particularly relevant in the FWMAV case, in view of the difficulty of constructing flight-capable vehicles, the still limited availability of FWMAVs and the substantial variation between different designs. The final two points are limiting factors in their own right.

Flapping-wing flight, particularly in the context of robotic vehicles, is still a young field of research, and relatively few flight-capable FWMAVs have been developed. Hence, so far there is limited prior experience to draw from. Conventional methods that have been extensively tested on conventional aircraft and honed for this purpose, must be reassessed and adapted to novel, flapping-wing configurations, which in many cases entail very different requirements.

Finally, compared to fixed-wing aircraft, FWMAVs are significantly more varied in their structural design and actuation mechanisms, and hence in the resulting kinematics, aerodynamics and dynamics. This makes it difficult to generalise results and establish generally applicable methods. Indeed, additional challenges depend on the specific FWMAV considered, as elaborated further in Sec. 1.5.

The combination of the aforementioned factors explains why modelling flapping-wing flight represents a challenge and why the availability of both realistic experimental data and accurate models is still limited. These points constitute the basis for the motivation of this thesis, which is discussed in Sec. 1.5 after an overview of the experimental setup used.

1.4. EXPERIMENTAL SETUP AND PRELIMINARIES

This section provides a brief overview of the main experimental setup used in this thesis, viz. the test vehicle and flight data acquisition systems. More specific details are provided in subsequent thesis chapters.

1.4.1. THE DELFLY TEST PLATFORM

The work presented in this thesis was developed for and tested on the 'DelFly II', an FWMAV developed at Delft University of Technology [152]. The first DelFly design (DelFly I, cf. Fig. 2.1) was conceived and constructed in 2005, with a number of iterations following in the subsequent years, most notably the DelFly Explorer, the first FWMAV capable of autonomous flight [153], and the DelFly Micro, the world's smallest and lightest FWMAV carrying a camera and a video transmitter [152]. Different DelFly configurations vary in size, actuation mechanisms and payload, and are used for different purposes.

The specific configuration used in this thesis is known as DelFly II[5]. It has a mass of approximately 16g and a wing span of approximately 28cm, with some variation depending on the particular specimen, and is equipped with two pairs of wings, arranged in an 'X'-configuration, and a conventional styrofoam inverted T-tail. The wings are constructed out of thin Mylar foil, attached to carbon rods representing the leading edges. In a neutral

---

[5]In the remainder of this thesis, the 'II' will be dropped for conciseness.

position, the upper and lower wings meet at a dihedral angle of approximately 15°. During each flap cycle, the wings perform a large-amplitude passive rotation, which results in the lift-enhancing clap-and-fling mechanism[6] (cf. Sec. 1.2.3). Stiffeners are used to stiffen the Mylar foil, nonetheless the wings remain highly flexible, which enhances their passive rotation movement.

The wing configuration is advantageous in a number of ways. Firstly, it allows for exploitation of the clap-and-fling effect, through interaction of the upper and lower wings on each side of the fuselage at the start and end of each flap cycle. Secondly, it minimises oscillations of the body, thanks to the opposite movement of the upper and lower wings, and is therefore favourable for carrying a camera. Thirdly, it entails a highly simplified flapping mechanism, involving only a single active DOF, i.e. rotation of the wing leading edges around the fuselage axis.

Thanks to the tailplane, the vehicle is passively stable in its common flight regimes. The tail is also equipped with conventional fixed-wing moving surfaces (elevator and rudder), and hence allows for conventional control mechanisms, avoiding complex wing actuation. In addition to elevator and rudder deflections, also the flapping frequency can be adjusted during flight. The DelFly II flies using flapping frequencies in the range of 10-15Hz and most typically moves at velocities ranging from hover to 1.5m/s. Velocities up to 7m/s have been demonstrated [83], however these are only achievable through shifting of the CG, e.g. by physically re-arranging the payload.

Different DelFly designs have been the subject of many studies, in domains including structural optimisation and design [154, 155], experimental and computational aerodynamics [30, 48, 156–159], autonomous exploration [137, 153] and control [128, 147, 160]. The flight dynamics of the DelFly only began to be modelled and studied recently, when it became possible to collect free-flight data. The main contributions in this field were made by Caetano et al., and included developing methods to extract useful information out of motion tracking data [83, 117], comparing wind-tunnel and free-flight data [126], comparing different kinematic formulations [161], and devising initial aerodynamic models [117]. The research presented in this thesis continues on this track, building on the aforementioned work and results.

While the DelFly configuration used in this thesis was always the same, different specimens were used at different times. Additionally, the occasional occurrence of damage, combined with uncontrollable external factors and in-flight disturbances, implies that even between separate flights conducted on the same vehicle, small changes may occur in the vehicle. These changes are mostly involuntary and not easily quantifiable. In view of this, the geometric properties of the specific vehicle used in every experiment are mentioned in the relevant chapters.

1.4.2. FREE-FLIGHT DATA ACQUISITION ENVIRONMENTS
Two different experimental setups were used to collect the flight data used in this study. These are briefly introduced here, while details are given subsequently in the text.

The earlier phase of the presented research made use of an extensive available dataset, collected in 2013 in the Vicon motion tracking chamber of the US Air Force Research Laboratory at Wright-Patterson Air Force Base [83]. This is a 22m×17m×10m indoor

---

[6]More precisely, the flexible-wing equivalent of clap-and-fling, known as clap-and-peel, occurs in the DelFly

1
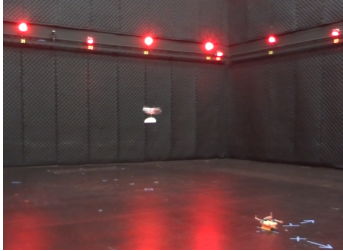
(a) DelFly II

(b) US AFRL motion tracking chamber

(c) TU Delft *CyberZoo* motion tracking chamber

Figure 1.7: The DelFly II FWMAV test platform and two flight testing environments used to collect the flight data in this thesis.

flight arena equipped with 60 Vicon cameras, which was used to track the positions of retro-reflective markers on a flying DelFly II vehicle, at 200Hz. From these positions, the states of the rigid body, and finally the forces and moments acting on it, were reconstructed as described in Refs. [83, 117]. These flight tests were primarily intended to characterise the performance of the vehicle, and hence involved a large variety of manoeuvres. Typical system identification manoeuvres were also performed, however, limited prior knowledge was available at the time to systematically design these inputs.

After the TU Delft *CyberZoo* flight arena became functional in 2014, new flight data could be acquired in this facility. The *CyberZoo* is a 10m×10m×7m motion tracking facility, equipped with 24 OptiTrack Flex13 cameras, tracking the position of active or reflective markers on moving objects, at sampling frequencies of up to 120Hz. The smaller size and lower sampling frequency posed some limitations, compared to the aforementioned AFRL tests, with the former point constraining the maximum flight test velocity. Regarding the latter point, however, since 2015, it has been possible to install an inertial measurement unit (IMU) on the DelFly [129], providing additional on-board measurements of the accelerations and angular rates, at 512Hz. Further details on the data acquisition are given in Chapter 2. Several test campaigns were conducted in the *CyberZoo*, as detailed subsequently.

(a) Coordinate frame B1 (Chapters 3, 5, 6)

(b) Coordinate frame B2 (Chapters 2, 4)
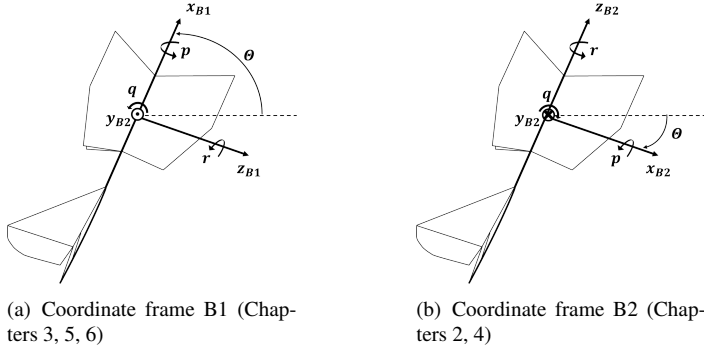
Figure 1.8: Main body-fixed coordinate systems used in this thesis.

1.4.3. COORDINATE SYSTEMS

Two different sets of body-fixed coordinate systems are used in this thesis. Initially, coordinate frames were defined according to aerospace convention, where the inertial frame x-axis points forwards, the y-axis to the right, and the z-axis downwards ('north-east-down' system). The corresponding body-fixed frame ($B1$), shown in Fig. 1.8, is obtained in a standard way from the Euler angles. In the course of the research process, however, it was found that the standard coordinate system leads to singularity issues due to the typically large pitch angle of the test platform, which can easily exceed 90° during manoeuvres. To avoid such issues but retain an intuitive representation, hence avoiding quaternions, an alternative coordinate frame was introduced for data processing and dynamic modelling. This second coordinate frame, indicated as $B2$ in Fig. 1.8, is more suited to flapping-wing applications, and is rotated with respect to the original system ($B1$) by the following matrix,

$$M_{B2 \leftarrow B1} := \begin{bmatrix} 1 & 0 & 0 \\ 0 & \cos\pi & \sin\pi \\ 0 & -\sin\pi & \cos\pi \end{bmatrix} \begin{bmatrix} \cos\frac{\pi}{2} & 0 & \sin\frac{\pi}{2} \\ 0 & 1 & 0 \\ -\sin\frac{\pi}{2} & 0 & \cos\frac{\pi}{2} \end{bmatrix} = \begin{bmatrix} 0 & 0 & 1 \\ 0 & -1 & 0 \\ 1 & 0 & 0 \end{bmatrix} \quad (1.5)$$

As shown in the figure, in the new system the z-axis is aligned with the fuselage and the x-axis normal to it. The newly-defined pitch angle is thus considerably smaller in the most commonly-occurring flight attitudes of the vehicle. This change was introduced in the second phase of the presented research, thus different coordinate systems are used in different chapters. Each chapter explicitly mentions which coordinate frame has been used. Additional frames used for specific purposes, e.g. relative to moving components, are introduced throughout the text where required.

1.5. THESIS MOTIVATION AND OVERVIEW

1.5.1. RESEARCH SCOPE

The main research question addressed in this thesis is the following:

1

> ## Research question
>
> How can experimental data be used to model the complex, time-varying flight mechanics of flapping-wing micro aerial vehicles in a way that is accurate, insightful, and suitable for simulation, control and design problems?

This is a broad question, warranting further elaboration, however it clearly highlights the two main aspects that connect all the work presented in this thesis. Firstly, the high-level goal pursued throughout this thesis is stated, i.e. fulfilling the conflicting requirements of high accuracy and high efficiency, such that the resulting models are accurate, insightful and practically applicable. All of the more detailed research objectives specified subsequently are subordinate to this overall aim. Secondly, the experimental character of the thesis is underlined. The main boundary condition that was set a priori and established the main direction of this work, was the focus on data-driven modelling. This was identified as a promising approach to achieve the desired modelling results, and was additionally found to represent a gap in the current body of knowledge (cf. Sec. 1.3.1), where the majority of work is theoretical or based on simulations. In view of the experimental approach, the research presented is based on a test vehicle, the DelFly II (cf. Sec. 1.4.1). The overall objective is therefore always twofold: on the one hand, to analyse, model and better understand the flight mechanics of the DelFly II specifically, and, on the other hand, to extend some of the obtained insight and approaches to similar vehicles, and possibly flapping-wing flyers generally. These two aspects are considered in parallel throughout the thesis.

The test platform is not only a test object – it also determines which particular aspects of flapping-wing flight can be studied. In fact, in addition to the numerous general difficulties involved in FWMAV modelling (cf. Sec. 1.3.6), there are more specific ones that are particularly relevant to the test platform. These include: (i) considering the clap-and-fling effect, (ii) modelling and analysing the tail aerodynamics, (iii) considering the closeness between the body natural frequencies and the flapping frequencies. All three of these aspects are not only relevant to the test platform, but also highly challenging and under-investigated in the literature, and therefore considered further within this thesis.

In order to answer the main research question, two different modelling approaches are developed in this thesis, and a number of subordinate research questions are addressed in the process.

The first modelling approach, presented in Chapters 3 and 4, aims primarily at developing as simple and interpretable as possible a model of the system dynamics, addressing the general problem of accuracy versus simplicity. In addition, more specific objectives are to (i) include time-varying effects in the model and (ii) cover different flight conditions. Both of these aspects are typically neglected in existing work (cf. Sec. 1.3.2). Lastly, the model is to include not only the forces acting on the vehicle, as is customary in the literature, but also the moments – which are essential for simulation and control system design. The modelling approach is based on system identification and uses data gathered in free-flight tests to arrive at time-varying grey-box models of the dynamics. A simple but effective approach is suggested to include time-varying, flapping-related effects in the model, which involves adapting the model structure, data processing and identification process. The inclusion of time-varying effects in the model is further exploited as a means of assessing

possible couplings between time-averaged and time-varying dynamics in the test platform used. The developed identification approach is implemented to obtain, assess and validate local models of the DelFly dynamics.

Subsequently, the modelling approach is applied, in combination with a new set of flight test data, to investigate the dynamics of the test vehicle in a range of different flight conditions. This offers some insight into the properties of the test platform studied. Furthermore, guided by the results of this analysis, a linear-parameter-varying (LPV) approach is developed to construct a global model accounting for differences across the explored part of the flight envelope. The devised model constitutes a continuous representation of the vehicle over a large part of the operating domain, and thereby provides new opportunities for control and simulation studies, which are typically focused on a single flight condition.

The modelling approaches developed in the first part of this thesis required adapting existing system identification, flight testing and data processing methods to the FWMAV case. While many such methods exist and have been widely tested in the aerospace field, the guidelines derived from work on standard fixed-wing or rotary-wing aircraft are often not directly applicable to unconventional micro-scale vehicles, particularly FWMAVs, which have significantly different flight properties. Thus, in addition to the modelling itself, this thesis also discusses the experimental methods used in the experimental phase. In the context of system identification, this phase involves designing manoeuvres that adequately excite the system dynamics, obtaining useful measurements from the available data acquisition setup, and extracting accurate information from the raw measurements. Each of these aspects is discussed, however the main focus is placed on the data processing phase.

The main contribution of this thesis, on the experimental side, is a sensor fusion method developed to advantageously merge motion-tracking data and on-board inertial measurements. Based on extended Kalman filtering, the fusion algorithm yields more accurate, informative and reliable free-flight data than was previously achievable, particularly at high frequencies, which are of interest in flapping-wing flight. The fusion approach is applied to obtain free-flight data for system identification, but is also shown to be useful for more fundamental studies, e.g. involving detailed analysis of the aerodynamics. An additional aspect that is discussed in this thesis, albeit to a lesser extent, is the experiment design process – again, well-established for fixed-wing and rotary-wing aircraft, but relatively unexplored for FWMAVs. Input signals are designed for identification of the DelFly II, and are used to derive general recommendations for FWMAV experiment design. As a clarification, it should be noted that the main contributions of this thesis, on the experimental side, are connected with free-flight testing. Given that the second modelling approach, discussed subsequently, predominantly employs tethered wind-tunnel measurements, the aforementioned experimental methods developed are thematically linked to the first modelling approach.

The following research sub-questions are answered in the first part of this thesis (Chapters 2–4):

> **Research sub-questions: part I (Ch. 2–4)**
>
> 1.1 How can accurate and informative free-flight data for model identification and analysis of FWMAVs be obtained using *on-board and off-board sensors*? (Ch. 2)
>
> 1.2 How can *low-order and time-varying* models of flapping-wing dynamics be developed using free-flight data? (Ch. 3)
>
> 1.3 How can a *low-order global model* be obtained, representing the changing dynamic properties of FWMAVs across their flight envelope? (Ch. 4)

The second modelling approach, presented in Chapters 5 and 6, also involves experimental data, but moves a step closer to physical aerodynamic modelling and attempts to shed more light on the force generation processes. The high-level objective in investigating this alternative route is to obtain models that are more closely related to the physics of the investigated system, and that explicitly account for specific aerodynamic effects, rather than incorporating all of these implicitly in an overall, to some extent arbitrary, model structure. The focus is narrowed down from the system level to the aerodynamic force generation level, and from the full vehicle to the separate wing and tail sub-systems. Additionally, a number of specific challenges are addressed, i.e. (i) modelling the clap-and-fling mechanism, and (ii) modelling the time-varying aerodynamics of the tailplane and the interaction between tail and wing wake. Both aspects had not previously been included in simplified aerodynamic models (cf. Sec. 1.2.3).

The wing aerodynamics are modelled using a quasi-steady approach, extended to account for the clap-and-fling effect. In particular, the model is developed for a flexible clap-and-peel mechanism. Additional contributions include the extension of the developed aerodynamic model to different flight conditions, achieved by relating the model parameters to the steady flow conditions, and the consideration of the real, data-derived wing kinematics as opposed to prescribed formulations. The tail aerodynamics are modelled using a quasi-steady aerodynamic model combined with an identified model of the complex, unsteady wing wake. A mathematical representation of the wing wake is derived from particle image velocimetry (PIV) data, using a multivariate splines-based identification method, and is used to estimate the complex wing-induced flow on the tail. The effect of the wing wake is then combined with the effect of the free stream, within a conventional aerodynamic model, in order to predict the forces generated by the tailplane. In particular, the spatio-temporal variation of the tail forces under the influence of both free stream and wing wake is obtained. Both wing and tail aerodynamic models retain a clear physical connection despite including some empirical components, and thus yield not only an accurate representation of the underlying processes, but also improved insight into the force generation processes. Moreover, combining the proposed wing and tail aerodynamic models with EOM yields a full description of the system dynamics, which may be usable for dynamic simulation and control, and thus potentially represents a fully-fledged alternative to the first modelling approach.

The following main research sub-questions are addressed in the second part of this

thesis:

> **Research sub-questions: part II (Ch. 5–6)**
>
> 2.1 How can the wing aerodynamics of a *clap-and-fling* FWMAV be modelled in a physically meaningful way?
>
> 2.2 How can the *time-varying tail aerodynamics* of a FWMAV be modelled?

1.5.2. THESIS OUTLINE

With the exception of the introduction and conclusion, the chapters in this thesis are based on papers published (or submitted for publication) independently. They can therefore be read separately, while an introductory text at the beginning of each places it into the context of the full thesis. This also implies that there is some overlap in the introductory sections – minor adjustments were made to reduce the overlap where possible. Fig. 1.9 shows a schematic layout of the rest of this thesis, which is structured as follows.
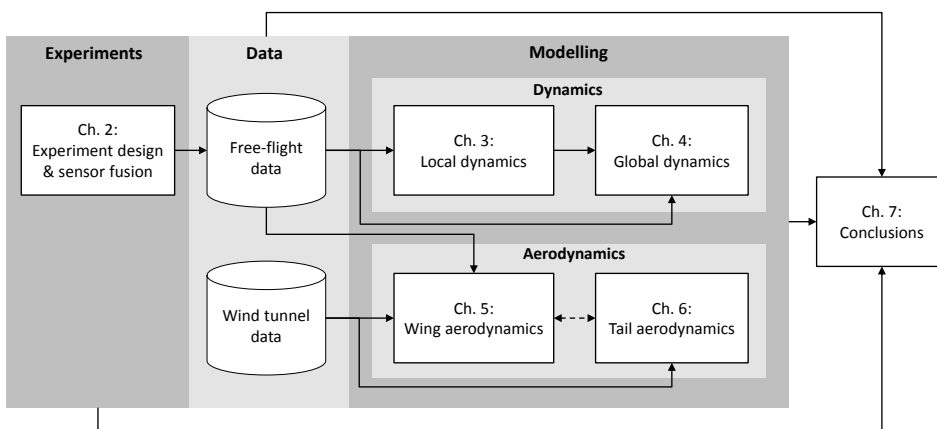
Figure 1.9: Diagram schematically illustrating the layout of this thesis.

Chapter 1 reviews the most relevant literature and describes the background of the project, placing it in a context within the broader field.

Chapter 2 describes the methodologies used within this thesis, i.e. methods for data collection (flight/wind tunnel testing), data processing, system identification and modelling of flapping-wing vehicles. This includes new methodologies developed within this thesis and adaptations of existing methods to the flapping-wing case. In particular, a sensor fusion method is developed, combining motion tracking and on-board sensor measurements to obtain high-accuracy FWMAV data. The experiment design process is also discussed, in the FWMAV context.

Chapters 3 and 4 discuss the first flapping-wing modelling approach considered, i.e.

1

grey-box system identification from free-flight data. The former chapter describes the local modelling by means of linear time-invariant (LTI) models, extended with a time-varying flapping component, whilst the latter chapter focuses on the extension of the modelling approach to the full flight envelope. Models are developed for the test platform and validated with flight data. Further, they are used to evaluate the dynamics of the system, the effects of flapping on the flight behaviour and the extent of decoupling between body and flapping dynamics.

Chapters 5 and 6 present an alternative modelling approach that is more physically meaningful and based more closely on the system aerodynamics. Chapter 5 derives a model of the wing aerodynamics, which is based on quasi-steady aerodynamic theory and for the first time accounts for the unsteady clap-and-fling effect. Chapter 6 then addresses the tail aerodynamics, proposing a novel approach to model the tail aerodynamics accounting for its interaction with the flapping-wing wake. Both models are derived from high-accuracy force and flow field measurements on the tethered platform.

Finally, **Chapter 7** closes this thesis, with an overview and concise discussion of the main contributions and findings, and recommendations for future work.

Additional minor contributions and intermediate results can be found in the appendix. Appendix A compares the quasi-steady and black-box aerodynamic modelling approaches developed in Chapters 3 and 5, respectively; Appendix B is a study on tail design, showing an example of how the models developed in this thesis can be used for both dynamic analysis and design evaluations; and Appendix C presents a precursor of the local model in Chapter 3.

REFERENCES

[1] M. S. Engel and D. A. Grimaldi, *New light shed on the oldest insect,* Nature **427**, 627 (2004).

[2] W. Shyy, C.-k. Kang, P. Chirarattananon, S. Ravi, and H. Liu, *Aerodynamics, sensing and control of insect-scale flapping-wing flight,* Proceedings of the Royal Society A **472** (2016).

[3] A. M. Lippisch, *Man powered flight in 1929,* Aeronautical Journal **64**, 395 (1960).

[4] R. Bacon, *Epistolae Fratris Rogerii Baconis, De Secretis Operibus Artis et Naturae, et De Nullitate Magiae* (Frobenius, Hamburg, 1618).

[5] L. da Vinci, *Manuscript B* (1488–1490).

[6] G. C. H. E. de Croon, K. M. E. de Clercq, R. Ruijsink, B. D. W. Remes, and C. de Wagter, *Design, aerodynamics, and vision-based control of the DelFly,* International Journal of Micro Air Vehicles **1**, 71 (2009).

[7] M. Keennon, K. Klingebiel, and H. Won, *Development of the nano hummingbird: A tailless flapping wing micro air vehicle,* in *50TH AIAA Aerospace Sciences Meeting incl. New Horizons Forum and Aerospace Exposition*, AIAA Paper 2012-0588 (2012).

[8] R. Wood, *The first takeoff of a biologically-inspired at-scale robotic insect,* IEEE Transactions on Robotics **24(2)**, 341 (2008).

[9] T. N. Pornsin-Sirirak, Y.-C. Tai, C.-M. Ho, and M. Keennon, *Microbat: A Palm-Sized Electrically Powered Ornithopter,* in *Proceedings of NASA/JPL Workshop on Biomorphic Robotics* (2001).

[10] F. Y. Hsiao, T. M. Yang, and W. C. Lu, *Dynamics of flapping-wing MAVs: Application to the tamkang golden snitch,* Journal of Applied Science and Engineering **15**, 227 (2012).

[11] P. Zdunich, D. Bilyk, M. MacMaster, D. Loewen, J. DeLaurier, R. Kornbluh, T. Low, S. Stanford, and D. Holeman, *Development and Testing of the Mentor Flapping-Wing Micro Air Vehicle,* Journal of Aircraft **44**, 1701 (2007).

[12] C.-K. Hsu, J. Evans, S. Vytla, and P. Huang, *Development of flapping wing micro air vehicles - design, CFD, experiment and actual flight,* in *48th AIAA Aerospace Sciences Meeting Including the New Horizons Forum and Aerospace Exposition* (2010).

[13] J. M. McMichael and M. S. Francis, *Micro Air Vehicles - Toward a New Dimension in Flight*, Tech. Rep. (Defense Advanced Research Projects Agency (DARPA), 1997) (accessed on 24/05/2017).

[14] W. Bejgerowski, A. Ananthanarayanan, D. Mueller, and S. Gupta, *Integrated product and process design for a flapping wing drive-mechanism,* Journal of Mechanical Design **131** (2009).

[15] S. Baek and R. Fearing, *Flight forces and altitude regulation of 12 gram i-bird,* in *IEEE RAS and EMBS International Conference on Biomedical Robotics and Biomechatronics (BioRob)* (2010).

[16] G. Lim, S. Shkarayev, Z. Goff, and P. Beran, *Studies of flight kinematics of ornithopters,* in *International Competition and Conference on Micro Air Vehicles* (2012).

[17] L. Hines, D. Campolo, and M. Sitti, *Liftoff of a motor-driven, flapping-wing micro aerial vehicle capable of resonance,* IEEE Transactions on Robotics **30**, 220 (2014).

[18] X. Sun, X. Gong, and D. Huang, *A review on studies of the aerodynamics of different types of maneuvers in dragonflies,* Archive of Applied Mechanics **87** (2017).

[19] N. Gaissert, R. Mugrauer, G. Mugrauer, A. Jebens, K. Jebens, and E. M. Knubben, *Inventing a micro aerial vehicle inspired by the mechanics of dragonfly flight,* in *Towards Autonomous Robotic Systems. TAROS 2013.*, Lecture Notes in Computer Science, Vol. 8069, edited by A. Natraj, S. Cameron, C. Melhuish, and M. Witkowski (Springer, Berlin, Heidelberg, 2014) pp. 90–100.

[20] C. Dileo and X. Deng, *Design of and experiments on a dragonfly-inspired robot,* Advanced Robotics **23:7-8, 1003-1021** (2009).

1

[21] J. M. Kok and J. S. Chahl, *Design and manufacture of a self-learning flapping wing-actuation system for a dragonfly-inspired MAV,* in *AIAA Atmospheric Flight Mechanics Conference* (2016).

[22] R. J. Wootton and J. Kukalova-Peck, *Flight adaptations in palaeozoic palaeoptera (insecta),* Biological Reviews **75**, 129 (1999).

[23] C. T. Orlowski, A. R. Girard, and W. Shyy, *Four wing flapping micro air vehicles - dragonfies or X-wings?* in *AIAA Guidance, Navigation, and Control Conference*, AIAA Paper 2010-7707 (Toronto, Ontario, Canada, 2010).

[24] T. Nakata, H. Liu, Y. Tanaka, N. Nishihashi, X. Wang, and A. Sato, *Aerodynamics of a bio-inspired flexible flapping-wing micro air vehicle,* Bioinspiration & Biomimetics **6** (2011).

[25] K. Ma, P. Chirarattananon, S. Fuller, and R. Wood, *Controlled flight of a biologically inspired, insect-scale robot,* Science **340**, 603 (2013).

[26] Z. J. Wang, *Dissecting Insect Flight,* Annual Review of Fluid Mechanics **37**, 183 (2005).

[27] M. H. Dickinson, F.-O. Lehmann, and S. P. Sane, *Wing Rotation and the Aerodynamic Basis of Insect Flight,* Science **284**, 1954 (1999).

[28] S. P. Sane and M. H. Dickinson, *The aerodynamic effects of wing rotation and a revised quasi-steady model of flapping flight.* Journal of Experimental Biology **205**, 1087 (2002).

[29] W. Shyy, Y. Lian, and J. Tang, *Aerodynamics of low Reynolds number flyers*, Cambridge aerospace series (Cambridge University Press, 2008).

[30] M. Perçin, *Aerodynamic Mechanisms of Flapping Flight*, Ph.D. thesis, Delft University of Technology (2015).

[31] H. E. Taha, M. R. Hajj, and P. S. Beran, *State-space representation of the unsteady aerodynamics of flapping flight,* Aerospace Science and Technology **34**, 1 (2014).

[32] S. P. Sane, *The aerodynamics of insect flight,* Journal of Experimental Biology **206**, 4191 (2003).

[33] T. Weis-Fogh, *Quick estimates of flight fitness in hovering animals, including novel mechanisms for lift production,* Journal of Experimental Biology **59** (1973).

[34] C. P. Ellington, *The Aerodynamics of Hovering Insect Flight. I. The Quasi-Steady Analysis,* Philosophical Transactions of the Royal Society B: Biological Sciences **305**, 1 (1984).

[35] D. D. Chin and D. Lentink, *Flapping wing aerodynamics: from insects to vertebrates,* Journal of Experimental Biology **219**, 920 (2016).

[36] A. Azuma, *The biokinetics of flying and swimming*, 2nd ed. (AIAA, Reston, 2006) iSBN 1563477815 9781563477812.

[37] C. P. Ellington, C. van den Berg, A. P. Willmott, and A. L. R. Thomas, *Leading-edge vortices in insect flight,* Nature **384**, 626 (1996).

[38] R. B. Srygley and A. L. R. Thomas, *Unconventional lift-generating mechanisms in free-flying butterflies,* Nature **420** (2002).

[39] T. Maxworthy, *Experiments on the Weis-Fogh mechanism of lift generation by insects in hovering flight. Part 1. Dynamics of the fling,* Journal of Fluid Mechanics **93** (1979).

[40] A. P. Willmott and C. P. Ellington, *The mechanics of flight in the hawkmoth Manduca Sexta II. Aerodynamic consequences of kinematic and morphological variation,* Journal of Experimental Biology **200**, 2723 (1997).

[41] R. J. Bomphrey, G. K. Taylor, and A. L. R. Thomas, *Smoke visualization of free-flying bumblebees indicates independent leading-edge vortices on each wing pair,* Experiments in Fluids **46**, 811 (2009).

[42] F.-o. Lehmann and M. H. Dickinson, *The control of wing kinematics and flight forces in fruit flies (Drosophila spp.),* Journal of Experimental Biology **201**, 385 (1998).

[43] F. T. Muijres, L. C. Johansson, R. Barfield, M. Wolf, G. R. Spedding, and A. Hedenstr om, *Leading-edge vortex improves lift in slow-flying bats,* Science **319**, 1250 (2008).

[44] M. Kramer, *Die Zunahme des Maximalauftriebes von Tragflügeln bei plötzlicher Anstellwinkelvergrösserung (Böeneffekt).* Zeitschrift für Flugtechnik und Motorluftschiffahrt **23**, 185 (1932).

[45] H. Wagner, *Über die Entstehung des dynamischen Auftriebes von Tragflügeln,* Zeitschrift für Angewandte Mathematik und Mechanik **5**, 17 (1925).

[46] C. P. Ellington, *The aerodynamics of hovering insect flight. iv. aerodynamic mechanisms,* Philosophical Transactions of the Royal Society of London. Series B, Biological Sciences **305**, 79 (1984).

[47] M. J. Lighthill, *On the Weis-Fogh mechanism of lift generation,* Journal of Fluid Mechanics **60**, 1 (1973).

[48] M. Perçin, Y. Hu, B. W. van Oudheusden, B. Remes, and F. Scarano, *Wing Flexibility Effects in Clap-and-Fling,* International Journal of Micro Air Vehicles **3**, 217 (2011).

[49] L. Bennett, *Clap and fling aerodynamics-an experimental evaluation,* Journal of Experimental Biology **69**, 261 (1977).

[50] G. R. Spedding and T. Maxworthy, *The generation of circulation and lift in a rigid two-dimensional fling,* Journal of Fluid Mechanics **165**, 247 (1986).

1

1

[51] S. Sunada, K. Kawachi, I. Watanabe, and A. Azuma, *Fundamental analysis of three-dimensional 'near fling',* Journal of Experimental Biology **183**, 217 (1993).

[52] F.-O. Lehmann, S. P. Sane, and M. Dickinson, *The aerodynamic effects of wing–wing interaction in flapping insect wings,* Journal of Experimental Biology **208**, 3075 (2005).

[53] D. Kolomenskiy, H. K. Moffatt, M. Farge, and K. Schneider, *The Lighthill-Weis-Fogh clap-fling sweep mechanism revisited,* Journal of Fluid Mechanics **676**, 572 (2011).

[54] C. P. Ellington, *The aerodynamics of hovering insect flight. iii. kinematics,* Philosophical Transactions of the Royal Society of London B: Biological Sciences **305**, 41 (1984).

[55] L. A. Miller and C. S. Peskin, *Flexible clap and fling in tiny insect flight,* Journal of Experimental Biology **212**, 3076 (2009).

[56] S. P. Sane and M. H. Dickinson, *The control of flight force by a flapping wing: lift and drag production,* Journal of Experimental Biology **2626**, 2607 (2001).

[57] T. Weis-Fogh and M. Jensen, *Biology and physics of locust flight. i basic principles in insect flight. a critical review.* Philosophical Transactions of the Royal Society B: Biological Sciences **239**, 415 (1956).

[58] T. Weis-Fogh, *Energetics of hovering flight in hummingbirds and in drosophila,* Journal of Experimental Biology **56**, 79 (1972).

[59] C. P. Ellington, *The novel aerodynamics of insect flight: Applications to micro-air vehicles,* Journal of Experimental Biology **202**, 3439 (1999).

[60] A. Andersen, U. Pesavento, and Z. J. Wang, *Unsteady aerodynamics of fluttering and tumbling plates,* Journal of Fluid Mechanics **541**, 65 (2005).

[61] A. Andersen, U. Pesavento, and Z. J. Wang, *Analysis of transitions between fluttering, tumbling and steady descent of falling cards,* Journal of Fluid Mechanics **541**, 91 (2005).

[62] U. Pesavento and Z. J. Wang, *Falling paper: Navier-Stokes solutions, model of fluid forces, and center of mass elevation,* Physical Review Letters **93**, 144501 (2004), the American Physical Society.

[63] G. J. Berman and Z. J. Wang, *Energy-minimizing kinematics in hovering insect flight,* Journal of Fluid Mechanics **582**, 153 (2007).

[64] Z. A. Khan and S. K. Agrawal, *Wing Force and Moment Characterization of Flapping Wings for Micro Air Vehicle Application,* in *Proceedings of the American Control Conference*, Vol. 3 (2005).

[65] X. Deng, L. Schenato, W. C. Wu, and S. Shankar Sastry, *Flapping Flight for Biomimetic Robotic Insects : Part I - System Modeling,* IEEE Transactions on Robotics **22**, 776 (2006).

[66] J. M. Dietl and E. Garcia, *Stability in Ornithopter Longitudinal Flight Dynamics,* Journal of Guidance, Control, and Dynamics **31**, 1157 (2008).

[67] C. T. Orlowski, A. R. Girard, and W. Shyy, *Derivation and simulation of the nonlinear dynamics of a flapping wing micro-air vehicle,* in *International Micro Air Vehicle Conference and Competition (IMAV)* (2009).

[68] D. B. Doman, M. W. Oppenheimer, and D. O. Sigthorsson, *Dynamics and control of a minimally actuated biomimetic vehicle: part i - aerodynamic model,* in *AIAA Guidance, Navigation and Control Conference* (2009).

[69] D. O. Sigthorsson, M. W. Oppenheimer, and D. B. Doman, *Flapping Wing Micro Air Vehicle Aerodynamic Modeling Including Flapping and Rigid Body Velocity,* in *50th AIAA Aerospace Sciences Meeting* (2012).

[70] M. Perçin and B. van Oudheusden, *Three-dimensional flow structures and unsteady forces on pitching and surging revolving flat plates,* Experiments in Fluids **56**, 47 (2015).

[71] S. F. Armanini, J. V. Caetano, G. C. H. E. de Croon, C. C. de Visser, and M. Mulder, *Quasi-steady aerodynamic model of clap-and-fling flapping MAV and validation with free-flight data,* Bioinspiration & Biomimetics **11**, 046002 (2016).

[72] R. Żbikowski, *On aerodynamic modelling of an insect-like flapping wing in hover for micro air vehicles,* Philosophical Transactions of the Royal Society of London A: Mathematical, Physical and Engineering Sciences **360**, 273 (2002).

[73] S. A. Ansari, R. Żbikowski, and K. Knowles, *Non-linear unsteady aerodynamic model for insect-like flapping wings in the hover. Part 2: implementation and validation,* Proceedings of the Institution of Mechanical Engineers, Part G: Journal of Aerospace Engineering **220**, 169 (2006).

[74] S. A. Ansari, K. Knowles, and R. Żbikowski, *Aerodynamic modelling of insect-like flapping flight for micro air vehicles,* Progress in Aerospace Sciences **42**, 129 (2006).

[75] H. Nagai, K. Isogai, T. Fujimoto, and T. Hayase, *Experimental and Numerical Study of Forward Flight Aerodynamics of Insect Flapping Wing,* AIAA Journal **47**, 730 (2009).

[76] R. Ramamurti and W. C. Sandberg, *A three-dimensional computational study of the aerodynamic mechanisms of insect flight,* **1518**, 1507 (2002).

[77] W. Su and C. E. S. Cesnik, *Nonlinear aeroelastic simulations of a flapping wing micro air vehicle using two unsteady aerodynamic formulations,* in *51st AIAA/ASME/ASCE/AHS/ASC Structures, Structural Dynamics, and Materials Conference, Structures, Structural Dynamics, and Materials and Co-located Conferences*, AIAA Paper 2010-2887 (2010).

1

1

[78] A. Gogulapati and P. P. Friedmann, *Approximate Aerodynamic and Aeroelastic Modeling of Flapping Wings in Hover and Forward Flight,* in *52nd AIAA/ASME/AHS/ASC Structures, Structural Dynamics and Materials Conference* (2011).

[79] C. Kang, H. Aono, and C. E. Cesnik, *Effects of flexibility on the aerodynamic performance of flapping wings,* in *6th AIAA Theoretical Fluid Mechanics Conference*, AIAA Paper 2011-3121 (2011).

[80] M. S. Vest and J. Katz, *Unsteady Aerodynamic Model of Flapping Wings,* in *AIAA 33rd Aerospace Sciences Meeting and Exhibit* (1995).

[81] M. Sun and J. Tang, *Lift and power requirements of hovering flight in Drosophila virilis.* Journal of experimental biology **205**, 2413 (2002).

[82] G. K. Taylor and R. Żbikowski, *Nonlinear time-periodic models of the longitudinal flight dynamics of desert locusts Schistocerca gregaria.* Journal of the Royal Society Interface **2**, 197 (2005).

[83] J. V. Caetano, C. C. de Visser, B. D. Remes, C. De Wagter, E.-J. Van Kampen, and M. Mulder, *Controlled Flight Maneuvers of a Flapping Wing Micro Air Vehicle: a Step Towards the Delfly II Identification,* AIAA Atmospheric Flight Mechanics Conference (2013).

[84] S. F. Armanini, C. C. de Visser, G. C. H. E. de Croon, and M. Mulder, *Time-varying model identification of flapping-wing vehicle dynamics using flight data,* Journal of Guidance, Control, and Dynamics **39**, 526 (2016).

[85] J. Grauer, E. Ulrich, J. H. Jr, D. Pines, and J. S. Humbert, *Model Structure Determination of an Ornithopter Aerodynamics Model from Flight Data,* in *48th AIAA Aerospace Sciences Meeting Including the New Horizons Forum and Aerospace Exposition* (2010).

[86] J.-H. Han, J.-Y. Lee, and D.-K. Kim, *Ornithopter modeling for flight simulation,* International Conference on Control, Automation and Systems (2008).

[87] C. T. Orlowski and A. R. Girard, *Averaging of the nonlinear dynamics of flapping wing micro air vehicles for symmetrical flapping,* in *AIAA Aerospace Sciences Meeting including the New Horizons Forum and Aerospace Exposition* (2011).

[88] G. K. Taylor and A. L. R. Thomas, *Dynamic flight stability in the desert locust Schistocerca gregaria,* Journal of Experimental Biology **206**, 2803 (2003).

[89] G. Gebert and P. Gallmeier, *Equations of motion for flapping flight,* in *AIAA Atmospheric Flight Mechanics Conference and Exhibit*, AIAA Paper 2002-4872 (2002).

[90] K. H. Loh and M. V. Cook, *Flight dynamic modelling and control design for a flapping wing micro aerial vehicle at hover,* in *AIAA Atmospheric Flight Mechanics Conference* (2003).

[91] J. V. Caetano, S. F. Armanini, C. C. de Visser, G. C. H. E. de Croon, and M. Mulder, *Data-Informed Quasi-Steady Aerodynamic Model of a Clap-and-Fling Flapping Wing MAV,* in *International Conference on Intelligent Unmanned Systems (ICIUS)* (2015).

[92] W. Buler, L. Loroch, and K. Sibilski, *Modeling and simulation of the nonlinear dynamic behavior of a flapping wings micro-aerial-vehicle,* in *42nd AIAA Aerospace Sciences Meeting and Exhibit* (2004).

[93] M. Lasek and K. Sibilski, *Modelling and simulation of flapping wing control for a micromechanical flying insect (entomopter),* in *AIAA Modeling and Simulation Technologies Conference and Exhibit* (2002).

[94] J. A. Grauer and J. E. Hubbard, *Multibody Model of an Ornithopter,* Journal of Guidance, Control, and Dynamics **32**, 1675 (2009).

[95] M. A. Bolender, *Rigid multi-body equations-of-motion for flapping wing MAVs using Kane equations,* in *AIAA Guidance, Navigation, and Control Conference*, AIAA Paper 2009-6158 (2009).

[96] A. T. Pfeiffer, J.-S. Lee, J.-H. Han, and H. Baier, *Ornithopter Flight Simulation Based on Flexible Multi-Body Dynamics,* Journal of Bionic Engineering **7**, 102 (2010).

[97] M. W. Oppenheimer, D. B. Doman, and D. O. Sigthorsson, *Dynamics and Control of a Biomimetic Vehicle Using Biased Wingbeat Forcing Functions,* Journal of Guidance, Control, and Dynamics **34**, 204 (2011).

[98] G. Taylor, R. Bomphrey, and J. 't Hoen, *Insect flight dynamics and control,* in *44th AIAA Aerospace Sciences Meeting and Exhibit* (2006).

[99] H. Rifai, N. Marchand, and G. Poulin, *Bounded control of a flapping wing micro drone in three dimensions,* in *IEEE International Conference on Robotics and Automation* (2008).

[100] Z. A. Khan and S. K. Agrawal, *Control of Longitudinal Flight Dynamics of a Flapping-Wing Micro Air Vehicle Using Time-Averaged Model and Differential Flatness Based Controller,* in *Proceedings of the 2007 American Control Conference* (2007).

[101] L. Schenato, D. Campolo, and S. Sastry, *Controllability issues in flapping flight for biomimetic Micro Aerial Vehicles (MAVs),* in *42nd IEEE Conference on Decision and Control (CDC)* (2003).

[102] S. Mao and J. K. Wang, *Flight stabilization control of a hovering model insect,* Journal of Experimental Biology **210**, 2714 (2007).

[103] H. Duan and Q. Li, *Dynamic model and attitude control of Flapping Wing Micro Aerial Vehicle,* in *IEEE International Conference on Robotics and Biomimetics (RoBio)* (2009).

1

1

[104] H. E. Taha, C. A. Woolsey, and M. R. Hajj, *A Geometric Control Approach for the Longitudinal Flight Stability of Hovering Insects / FWMAVs,* in *AIAA Atmospheric Flight Mechanics Conference*, AIAA Paper 2015-1552 (2015).

[105] S. Zeyghami and H. Dong, *Coupling of the wings and the body dynamics enhances damselfly maneuverability,* ArXiv e-prints (2015), arXiv:1502.06835 [physics.flu-dyn] .

[106] R. C. Julian, C. J. Rose, H. Hu, and R. S. Fearing, *Cooperative Control and Modeling for Narrow Passage Traversal with an Ornithopter MAV and Lightweight Ground Station,* in *International Conference on Autonomous Agents and Multi-Agent Systems* (2013).

[107] I. Faruque and J. Sean Humbert, *Dipteran insect flight dynamics. Part 1 Longitudinal motion about hover.* Journal of Theoretical Biology **264**, 538 (2010).

[108] I. Faruque, P. Samuel, and J. S. Humbert, *Yaw dynamics identification of an insect-inspired flapping wing micro air vehicle,* in *AIAA Guidance, Navigation and Control Conference* (2014).

[109] M. Sun and Y. Xiong, *Dynamic flight stability of a hovering bumblebee,* Journal of Experimental Biology **208**, 447 (2005).

[110] H. Gim, S. Kim, J. Suk, and S. Cho, *Longitudinal system identification of ornithopter with automated flight tests,* in *IFAC Conference* (2016).

[111] V. Klein and J. G. Batterson, *Determination of airplane model structure from flight data using splines and stepwise regression*, Tech. Paper 2126 (NASA, 1983).

[112] T. Lombaerts, E. V. Oort, Q. Chu, J. Mulder, and D. Joosten, *Online aerodynamic model structure selection and parameter estimation for fault tolerant control,* Journal of Guidance, Control, and Dynamics **33** (2010).

[113] S. F. Armanini, C. C. de Visser, and G. C. H. E. de Croon, *Black-box LTI Modelling of Flapping-wing Micro Aerial Vehicle Dynamics,* in *AIAA Atmospheric Flight Mechanics Conference* (2015) AIAA Paper 2015-0234.

[114] J. Dietl, T. Herrmann, G. Reich, and E. Garcia, *Dynamic Modeling, Testing, and Stability Analysis of an Ornithoptic Blimp,* Journal of Bionic Engineering **8**, 375 (2011).

[115] A. N. Chand, M. Kawanishi, and T. Narikiyo, *Parameter Estimation for the Pitching Dynamics of a Flapping-Wing Flying Robot,* in *IEEE International Conference on Advanced Intelligent Mechatronics (AIM)* (2015).

[116] J. Grauer, E. Ulrich, J. E. Hubbard, D. Pines, and J. S. Humbert, *Testing and System Identification of an Ornithopter in Longitudinal Flight,* Journal of Aircraft **48**, 660 (2011).

[117] J. V. Caetano, C. C. de Visser, G. C. H. E. de Croon, B. Remes, C. De Wagter, and M. Mulder, *Linear Aerodynamic Model Identification of a Flapping Wing MAV Based on Flight Test Data,* International Journal of Micro Air Vehicles (2013).

[118] B. M. Finio, N. O. Perez-Arancibia, and R. J. Wood, *System identification and linear time-invariant modeling of an insect-sized flapping-wing micro air vehicle,* in *2011 IEEE/RSJ International Conference on Intelligent Robots and Systems (IROS)* (2011).

[119] I. Faruque and J. S. Humbert, *Dipteran insect flight dynamics. part 2 lateral-directional motion about hover,* Journal of Theoretical Biology **265**, 306 (2010).

[120] M. Jensen, *Biology and physics of locust flight. iii the aerodynamics of locust flight.* Philosophical Transactions of the Royal Society B: Biological Sciences **239**, 511 (1956).

[121] R. Dudley and C. P. Ellington, *Mechanics of forward flight in bumblebees II. Quasi-steady lift and power requirements,* Journal of Experimental Biology **148**, 53 (1990).

[122] M. Dickinson and K. G. Götz, *Unsteady aerodynamic performance of model wings at low reynolds numbers,* Journal of Experimental Biology **174**, 45 (1993).

[123] S. Vogel, *Flight in drosophila. iii. aerodynamic characteristics of fly wings and wing models,* Journal of Experimental Biology **46**, 431 (1967).

[124] C. Rose and R. S. Fearing, *Comparison of ornithopter wind tunnel force measurements with free flight,* in *2014 IEEE International Conference on Robotics & Automation (ICRA)* (2014).

[125] A. Jennings, M. Mayhew, and J. Black, *Video measurements of instantaneous forces of flapping wing vehicles,* Mechanical Systems and Signal Processing **64–65**, 325 (2015).

[126] J. V. Caetano, M. Percin, B. W. van Oudheusden, B. D. W. Remes, C. de Wagter, G. C. H. E. de Croon, and C. C. de Visser, *Error analysis and assessment of unsteady forces acting on a flapping wing micro air vehicle: Free-flight versus wind tunnel experimental methods,* Bioinspiration & Biomimetics **10** (2015).

[127] L. Ristroph, G. J. Berman, A. J. Bergou, Z. J. Wang, and I. Cohen, *Automated hull reconstruction motion tracking (HRMT) applied to sideways maneuvers of free-flying insects,* Proceedings of the National Academy of Sciences **107**, 1324 (2009).

[128] J. L. Verboom, S. Tijmons, C. De Wagter, B. Remes, R. Babuska, and G. C. H. E. de Croon, *Attitude and altitude estimation and control on board a flapping wing micro air vehicle,* in *IEEE International Conference on Robotics and Automation (ICRA)* (2015).

[129] M. Karásek, A. J. Koopmans, S. F. Armanini, B. D. W. Remes, and de Croon G. C. H. E., *Free flight force estimation of a 23.5 g flapping wing MAV using an on-board IMU,* in *IEEE International Conference on intelligent robots and systems (IROS)* (2016).

1

[130] S. F. Armanini, M. Karásek, C. C. de Visser, G. C. H. E. de Croon, and M. Mulder, *Flight testing and preliminary analysis for global system identification of ornithopter dynamics using on-board and off-board data,* in *AIAA Atmospheric Flight Mechanics Conference*, AIAA Paper 2017-1634 (2017).

[131] M. Karásek, M. Percin, T. Cunis, B. W. van Oudheusden, C. D. Wagter, B. D. W. Remes, and G. C. H. E. de Croon, *First free-flight flow visualisation of a flapping-wing robot,* arXiv preprint: 1612.07645 (2017).

[132] J.-H. Kim, C.-Y. Park, S.-M. Jun, D.-K. Chung, J.-R. Kim, H.-C. Hwang, B. Stanford, P. Beran, G. Parker, and D. Mrozinski, *Flight Test Measurement and Assessment of a Flapping Micro Air Vehicle,* International Journal of Aeronautical and Space Sciences **13**, 238 (2012).

[133] G. Maniar, R. Randall, S. Shkarayev, Z. Goff, and P. Beran, *Kinematics of Free-flight Ornithopters,* in *50th AIAA Aerospace Sciences Meeting* (2012).

[134] R. Krashanitsa, D. Silin, and S. Shkarayev, *Flight Dynamics of Flapping-Wing Air Vehicle,* AIAA Atmospheric Flight Mechanics (AFM) Conference (2008).

[135] J.-S. Lee and J.-H. Han, *Experimental study on the flight dynamics of a bioinspired ornithopter: free flight testing and wind tunnel testing,* Smart Materials and Structures **21**, 094023 (2012).

[136] J. V. Caetano, C. C. de Visser, B. D. W. Remes, C. de Wagter, and M. Mulder, *Modeling a Flapping Wing MAV: Flight Path Reconstruction of the DelFly II,* in *AIAA Modeling and Simulation Technologies Conference*, AIAA Paper 2013-4597 (2013).

[137] S. Tijmons, G. de Croon, B. Remes, C. De Wagter, R. Ruijsink, E.-J. van Kampen, and Q. Chu, *Stereo vision based obstacle avoidance on flapping wing MAVs,* in *Advances in Aerospace Guidance, Navigation and Control*, edited by Q. Chu, B. Mulder, D. Choukroun, E.-J. van Kampen, C. de Visser, and G. Looye (Springer Berlin Heidelberg, 2013).

[138] X. Deng, L. Schenato, and S. Sastry, *Hovering Flight Control of a Micromechanical Flying Insect,* in *Proceedings of the 40th IEEE Conference on Decision and Control (CDC)* (2001).

[139] J. Geder, *Onboard Stability Control System for a Flapping Wing Nano Air Vehicle*, Tech. Rep. (Naval Research Laboratory, 2009).

[140] B. Cheng and X. Deng, *Mathematical modelling of near-hover insect flight dynamics,* in *Proceedings of the ASME 2010 Dynamics Systems and Control Conference* (2010).

[141] M. Bhatia, M. Patil, C. Woolsey, B. Stanford, and P. Beran, *LQR controller for stabilization of flapping wing MAVs in gust environments,* in *AIAA Atmospheric Flight Mechanics Conference*, AIAA Paper 2012-4867 (2012).

[142] A. N. Chand, M. Kawanishi, and T. Narikiyo, *Adaptive pole placement pitch angle control of a flapping-wing flying robot,* Advanced Robotics **30** (2016).

[143] A. Serrani, *Robust nonlinear control design for a minimally-actuated flapping-wing mav in the longitudinal plane,* in *European Control Conference (ECC)* (2011).

[144] A. N. Chand, M. Kawanishi, and T. Narikiyo, *Non-linear model-free control of flapping wing flying robot using ipid,* in *IEEE International Conference on Robotics and Automation (ICRA)* (2016).

[145] K. Y. W. Scheper, S. Tijmons, C. C. de Visser, and G. C. H. E. de Croon, *Behavior trees for evolutionary robotics,* Artificial Life **22**, 23 (2016).

[146] R. Tedrake, Z. Jackowski, R. Cory, J. W. Roberts, and W. Hoburg, *Learning to Fly like a Bird*, Tech. Rep. (Massachusets Institute of Technology, 2009) (accessed 23/05/2017).

[147] M. W. Goedhart, E.-J. van Kampen, S. F. Armanini, C. C. de Visser, and Q. P. Chu, *Machine learning for flapping wing flight control,* in *AIAA Intelligent Systems Conference*, AIAA Paper 2018-2135 (2018).

[148] S. C. Whitehead, T. Beatus, L. Canale, and I. Cohen, *Pitch perfect : how fruit flies control their body pitch angle,* Journal of Experimental Biology **218**, 3508 (2015).

[149] T. Beatus, J. M. Guckenheimer, and I. Cohen, *Controlling roll perturbations in fruit flies,* Journal of the Royal Society Interface **12** (2015).

[150] T. L. Hedrick, *Flight control in the hawkmoth Manduca sexta: the inverse problem of hovering,* Journal of Experimental Biology **209**, 3114 (2006).

[151] H. Rifai, F. Guerrero-Castellanos, N. Marchand, and G. Poulin, *Biomimetic-based output feedback for attitude stabilization of a flapping-wing micro aerial vehicle,* Robotica **31**, 955 (2013).

[152] G. C. H. E. de Croon, M. Perçin, B. D. W. Remes, R. Ruijsink, and C. De Wagter, *The DelFly Design, Aerodynamics, and Artificial Intelligence of a Flapping Wing Robot* (Springer Netherlands, 2016).

[153] C. De Wagter, S. Tijmons, B. D. W. Remes, and G. C. H. E. de Croon, *Autonomous Flight of a 20-gram Flapping Wing MAV with a 4-gram Onboard Stereo Vision System,* in *IEEE International Conference on Robotics & Automation (ICRA)* (2014).

[154] B. Bruggeman, *Improving flight performance of DelFly II in hover by improving wing design and driving mechanism*, Master's thesis, Delft University of Technology (2010).

[155] J. A. Koopmans, S. Tijmons, C. de Wagter, and G. C. H. E. de Croon, *Passively stable flapping flight from hover to fast forward through shift in wing position,* in *International Micro Air Vehicles Conference* (2015).

1

[156] K. De Clercq, R. de Kat, B. Remes, B. van Oudheusden, and H. Bijl, *Flow Visualization and Force Measurements on a Hovering Flapping-Wing MAV DelFly II,* 39th AIAA Fluid Dynamics Conference (2009).

[157] M. Perçin, H. Eisma, B. van Oudheusden, B. Remes, R. Ruijsink, and C. de Wagter, *Flow Visualization in the Wake of the Flapping-Wing MAV 'DelFly II' in Forward Flight,* in *AIAA Applied Aerodynamics Conference* (2012).

[158] W. B. Tay, B. W. van Oudheusden, and H. Bijl, *Numerical simulation of X-wing type biplane flapping wings in 3D using the immersed boundary method.* Bioinspiration & Biomimetics **9**, 036001 (2014).

[159] S. Deng, M. Percin, B. van Oudheusden, B. Remes, and H. Bijl, *Experimental investigation on the aerodynamics of a bio-inspired flexible flapping wing micro air vehicle,* International Journal of Micro Air Vehicles **6**, 105 (2014).

[160] T. Cunis, M. Karásek, and G. C. H. E. de Croon, *Precision Position Control of the DelFly II Flapping-wing Micro Air Vehicle in a Wind-tunnel,* in *International Micro Air Vehicle Conference and Competition (IMAV)* (2016).

[161] J. V. Caetano, M. B. Weehuizen, C. C. de Visser, G. C. H. E. de Croon, and M. Mulder, *Rigid-Body Kinematics Versus Flapping Kinematics of a Flapping Wing Micro Air Vehicle,* Journal of Guidance, Control, and Dynamics **38**, 2257 (2015).

I

DYNAMIC MODEL IDENTIFICATION

2

FLIGHT TESTING AND DATA FUSION FOR FLAPPING FLIGHT MODELLING

While system identification is well-established in the aeronautical field, the application of data-driven modelling methods to unconventional flapping-wing micro aerial vehicles is at present considerably under-explored. One of the main reasons for this is the difficulty of obtaining experimental data suitable for such purposes. System identification requires, firstly, adequate data acquisition techniques, secondly, suitable processing techniques to render the data meaningful and usable, and thirdly, effective experiment design to ensure that informative data will be collected in the specific flight tests conducted. This chapter investigates these three aspects for the specific case of flapping-wing vehicles, focusing predominantly on the first two. First, data acquisition and processing are considered and a sensor fusion method is developed to combine motion tracking and on-board inertial sensor data. The resulting fused data are more reliable and informative compared to the measurements obtained from the separate sources, particularly at high frequencies relevant for flapping-wing flight. This represents the main contribution of this chapter. Subsequently, the flight testing process is discussed in a flapping-wing system identification context, and recommendations are derived for experiment design and for the practical execution of flight tests. The developed techniques are demonstrated on the DelFly II, and were applied to obtain the measurements used in Chapter 4 (and in Appendix B), however they are also applicable to other comparable flapping-wing vehicles.

2

2.1. Introduction

As discussed in Chapter 1, flapping-wing flyers have a remarkable performance at very low Reynolds numbers: they are highly manoeuvrable, potentially power-efficient and versatile, typically being able to fly in a wide range of different conditions, extending from hover to fast forward flight. Hence bio-inspired flapping-wing micro aerial vehicles (FWMAVs) are being researched extensively, and are expected to allow for novel applications that are not achievable with conventional fixed-wing or rotary-wing aircraft. However, flapping-wing mechanisms are highly complex, due to (i) the unsteady aerodynamics, involving phenomena such as wake-capture and leading edge vortices, and (ii) the time-varying dynamics. While significant insight is now available on both fronts, thanks to studies on insects and birds [3–6], and, more recently, increasingly on robotic test platforms [7–17], the high complexity of flapping flight still poses a considerable challenge to FWMAV development. In addition to this, it is still considerably difficult to obtain realistic experimental data, particularly in free flight and in different flight regimes. Studies have found discrepancies between free-flight and wind tunnel data [18–20], suggesting that wind tunnel measurements approximate free-flight data only for specific clamping positions and flight conditions, so that realistic insight for free flight ideally should be obtained in free-flight conditions.

For these reasons, the analysis and modelling of flapping-wing flight remain challenging, especially obtaining simple, computationally efficient models that can yield basic insight and be used for design and control in real-life applications. When flight data is obtainable, an appealing modelling option, in alternative to often complex and computationally expensive theoretical or numerical models, is system identification. Previous FWMAV system identification efforts [10, 21–26] showed that a data-driven approach can yield both realistic and simple models, as well as new insight on a novel and complex type of flying vehicle. However limited work has been done in this field so far, largely due to the difficulty of obtaining suitable flight data. Similarly, many low-order dynamic and aerodynamic models currently available have not been validated with free-flight data, and particularly not in different flight regimes [27–30].

Thus, a significant limitation in the analysis, modelling and design of flapping-wing vehicles, is the limited amount of free-flight data available, particularly data suited for modelling. Obtaining such data requires effective design of experiments, flight test procedures, data acquisition methods and data processing techniques. On the data acquisition front, particular challenges include obtaining accurate free-flight data: (i) at the high frequencies relevant for flapping flight, (ii) in different flight regimes and (iii) during manoeuvres. Such data would for instance support the development of more realistic models, possibly covering different flight regimes, a better understanding of manoeuvring flight, and a better evaluation of free flight as opposed to the tethered wind tunnel case. This in turn would support improved understanding and further development of flapping-wing vehicles. A range of further challenges arise in the experiment design phase and during the flight testing process itself. The flight testing of small-scale unmanned vehicles is still in its early stages, and free-flight tests for system identification of flapping-wing platforms have been particularly scarce [10, 24–26], hence there is limited prior experience to draw from. Very small and unconventional vehicles also have unusual flight properties and differ significantly amongst each other, therefore standard methods may not be applicable or may require adjustments, and these adjustments may be difficult to generalise. A critical element in the system iden-
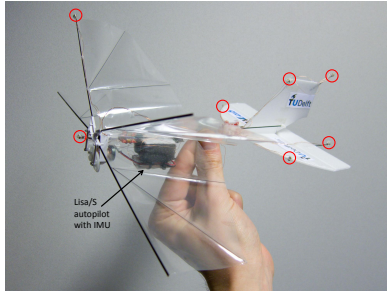
(a) Test platform (DelFly II [31]), with LED markers for optical tracking circled.
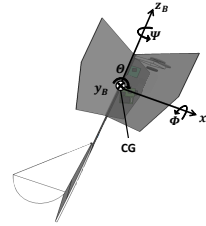
(b) Body-fixed coordinate frame, centered at the CG; a typical flight attitude is shown (side view).

Figure 2.1: Test platform used in this study and body-fixed coordinate system x_B, y_B, z_B

tification cycle is the design of experiments that will sufficiently excite the studied platform dynamics and result in data that are informative and can be used for modelling. Connected to this, but also on a more general level, the practical aspects of flight testing need to be considered, to ensure an optimal yield of any test flights.

This chapter discusses the development and testing of approaches for data acquisition, experiment design and flight testing using flapping-wing platforms. A sensor fusion approach is proposed to support effective data acquisition: by combining on-board and off-board sensor measurements, it yields more informative and reliable data at higher resolutions than was previously possible, and avoiding the main drawbacks of the separate sensors. Additionally, the input design process and flight testing are briefly discussed, highlighting the main challenges identified and suggesting guidelines to support the testing process for similar FWMAVs. The combination of methods and recommendations developed constitute a valuable starting point for further work in system identification of flapping-wing flyers and, in particular, for some of the subsequent work presented in this thesis (cf. Chapter 4 and Appendix B).

The rest of this chapter is structured as follows. Section 2.3 presents the sensor fusion approach developed to combine on-board and off-board measurements, including synchronisation and filter design. Examples of results are provided in Section 2.4 to illustrate the functioning and and effectiveness of the method. The resulting fused measurements are also compared to high-resolution wind tunnel data for further evaluation. Section 2.5 discusses the design and execution of flight tests for system identification purposes, closing the experimental data-acquisition loop. Section 2.6 summarises the main conclusions drawn.

2.2. EXPERIMENTAL SETUP

2.2.1. TEST VEHICLE

The experimental methods discussed in this chapter were derived for and implemented on the DelFly II ornithopter described in Chapter 1 (cf. Sec. 1.4.1). The mass and inertia properties of the specific FWMAV used in the specific flight tests relevant to this chapter

Table 2.1: Mass and inertia properties of the test platform

Property	Value
$m[kg]$	23.5×10^{-3}
$x_{CG}[m]$ (below fuselage)	9.6×10^{-3}
$y_{CG}[m]$	0
$z_{CG}[m]$ (from wing leading edge)	-7.0×10^{-2}
$I_{xx}, I_{yy}, I_{zz}[Nm^2]$	$(7.5, 6.6, 1.9) \times 10^{-5}$
$I_{xy}, I_{yz}, I_{xz}[Nm^2]$	$(0, 0, 8.5) \times 10^{-6}$

are presented in Table 2.1. The inertia values were estimated from the mass and positioning of the separate components of the vehicle. Fig. 4.1 shows the orientation of the body-fixed coordinate system used in this chapter, defined to be centred at the centre of gravity (CG) of the platform. In contrast to convention, the z-axis is aligned with the fuselage – this was done to avoid attitude singularities, given the typically large pitch angle assumed in flight by this FWMAV (cf. Sec. 1.4.3: coordinate frame $B2$).

2.2.2. In-flight data acquisition

The test platform was flown in a 10m×10m×7m motion tracking facility (TU Delft *Cyberzoo*), equipped with 24 OptiTrack Flex13 cameras, and relevant measurements were acquired during flight using two different methods.

Firstly, the aforementioned optical tracking system (hereafter: 'OptiTrack') was used to measure the positions of 7 active LED markers attached to the FWMAV at the locations illustrated in Fig. 2.1(a). The four markers attached to the fuselage and tail allowed for reconstruction of the position and orientation (quaternions) of the rigid body, while the remaining markers, on the wing leading edge, rudder and elevator allowed for reconstruction of the control surface deflections, and of the wing leading edge movement, hence the wing flap angle (ζ). The obtained measurements were transformed from the OptiTrack (i.e. inertial) coordinate system to the body-fixed coordinate frame shown in Fig. 4.1, and quaternions were transformed to Euler angles for easier interpretation. Note that the CG location does not coincide with the centre of the OptiTrack-defined body-coordinate system, which is based on geometry. This difference was considered when processing the data (cf. also Fig. 2.2). The LED markers have a mass of 0.035g each, and high-speed imagery suggests that such a small mass has a negligible effect on the wing kinematics.

Secondly, on-board measurements were acquired by means of an inertial measurement unit (IMU). For the flight tests presented, the FWMAV was equipped with a 2.8g Lisa/S autopilot [32], which includes a 6-axis MEMS IMU and a microcontroller unit (ARM Cortex-M3), allowing for open-source drone autopilot framework Paparazzi-UAV [33] to be run. The IMU was used to measure the linear accelerations and angular velocities of the vehicle, at a chosen sampling frequency of 512Hz. While sampling up to 1024Hz is possible, internal low-pass filtering at 256Hz implies that such sampling frequencies would not yield accurate additional information, and it was also found that at higher rates, significant numbers of frames were being lost, presumably as a result of CPU overloading. Moreover, previous work with similar ornithopters showed that very high-frequency content becomes

Table 2.2: Overview of relevant data obtained from each data acquisition system.

Data acquisition means	Measurements provided
OptiTrack	Position (x, y, z) Attitude quaternions (q_0, q_1, q_2, q_3) Control surface deflections (δ_e, δ_r) Wing flap angle (ζ)
IMU	Angular velocities (p, q, r) Linear accelerations (a_x, a_y, a_z)
On-board additional	Servo commands $(\delta_{e,CMD}, \delta_{r,CMD})$ Motor speed (RPM)

Table 2.3: IMU specifications.

Parameter	Gyroscope	Accelerometer
Measurement range	$\pm 2000°/s$	$\pm 16g$
Sensitivity	2%	2%
Bandwidth*	$256 Hz$	$256 Hz$
Noise density	$0.005 \mathrm{deg}/\sqrt{Hz}$	$400 \mu g/\sqrt{Hz}$

* As determined by the internal low-pass filtering, cf. Sec. 4.2.2

increasingly difficult to distinguish from noise [18].

The IMU was attached to the body. Following the initial finding that the attachment mode influenced the measurements made, a block of foam was added between IMU and fuselage, to introduce damping and reduce unwanted vibrations. Small residual effects that remain despite the foam are being studied further, however these effects were found to be small after the aforementioned modification. To account for the fact that the IMU was not completely aligned with the body frame, a static calibration procedure was conducted prior to each flight. By comparing the accelerometer and optical tracking output at a number of different body orientations, the rotation between IMU and body frames was determined, and subsequently used to transform the in-flight IMU data to the body frame.

The IMU measurements, as well as servo commands and motor speed, were logged using a microSD card added to the autopilot. Table 2.2 provides an overview of the measurements obtained, and Table 2.3 presents the main specifications of the IMU. Further details on the hardware and flight test setup can be found in [34].

2.3. SENSOR FUSION

This section proposes a sensor fusion-based method for the acquisition of accurate free-flight data for flapping-wing vehicles. Fusion of on-board inertial measurement unit (IMU) data and off-board optical tracking data is suggested as an approach to obtain high quality, more reliable measurements, that are also accurate at high frequencies and can be used for in-depth analysis of time-resolved flapping effects in free flight and during manoeuvres.

External optical tracking systems [10, 35, 36], such as are often used for FWMAVs,

2

provide accurate position measurements, but typically have a relatively low bandwidth if the intention is to consider processes happening during each flap cycle. Additionally, linear and angular velocities and accelerations have to be computed via numerical differentiation, which introduces considerable noise [18]. It can also be expected that as platforms become increasingly small, attitude data obtained from tracking alone will decrease in quality due to the limited resolution. By contrast, IMU sensors have a high bandwidth, which allows for high-frequency measurements. Accelerations and angular velocities are measured directly, however both are affected by integration drift – when used to determine attitude or velocity – and high noise levels. Hence, it is suggested that combining the approaches will yield more accurate and reliable data than either of the two approaches alone, and, in particular, data providing insight into what is happening during each flap cycle.

The forces computed from the obtained data are compared with wind tunnel measurements, to provide an initial idea of their accuracy and reliability. Additionally, implications of the suggested data processing approach for time-resolved modelling are discussed. We argue that our approach is advantageous for analysis of time-resolved aerodynamics and dynamics, giving results that are qualitatively comparable to wind tunnel ones, but more realistic since representing free flight, and providing the opportunity of considering dynamic manoeuvres. The resulting data allow for the forces acting on the FWMAV in free flight (including manoeuvres) to be reconstructed with high accuracy and resolution, at smaller time scales than previously considered. Meaningful information is obtained at frequencies up to five times the flapping frequency of the test vehicle, i.e. approximately 70Hz. As a comparison, previous work on a similar test platform showed that 200Hz-sampled optical tracking data only resulted in reliable information up to 32Hz in the accelerations obtained from double differentiation [18]. The high resolution attained is relevant not only for the forces and moments, but also for the states themselves, and especially the body velocities, which cannot be estimated as effectively by either IMU or optical tracking alone. In this respect, the measurements can be considered highly valuable for analysis and system identification of FWMAVs. The suggested method is applicable to other similarly equipped FWMAV, and hence is also a valuable contribution to the FWMAV modelling community.

This section discusses the data fusion process, focusing on filter design. The main results obtained on the test platform are presented, and potential uses of the collected data for time-resolved modelling and analysis are mentioned. The overall approach proposed, from raw data to fused and processed data, is illustrated in Fig. 2.2. The logic in this diagram is followed throughout this section.

2.3.1. MOTIVATION FOR DATA FUSION
The flight test setup described allowed us to combine on-board IMU measurements and external optical tracking measurements, thus obtaining a highly accurate and informative dataset, suitable specifically for analysing and modelling flapping-wing vehicles. In particular, this not only leads to the usual favourable results of sensor fusion, e.g. higher accuracy and reliability, but also allows for accurate high-frequency measurements, indispensable for in-depth analysis of flapping-wing flight and the short time-scale mechanisms involved. Additionally, unknown IMU biases can be estimated, further increasing the overall accuracy.

Optical tracking yields precise (typical mean tracking error approximately 1-2mm) and reliable measurements, whose accuracy does not deteriorate over time. The main draw-
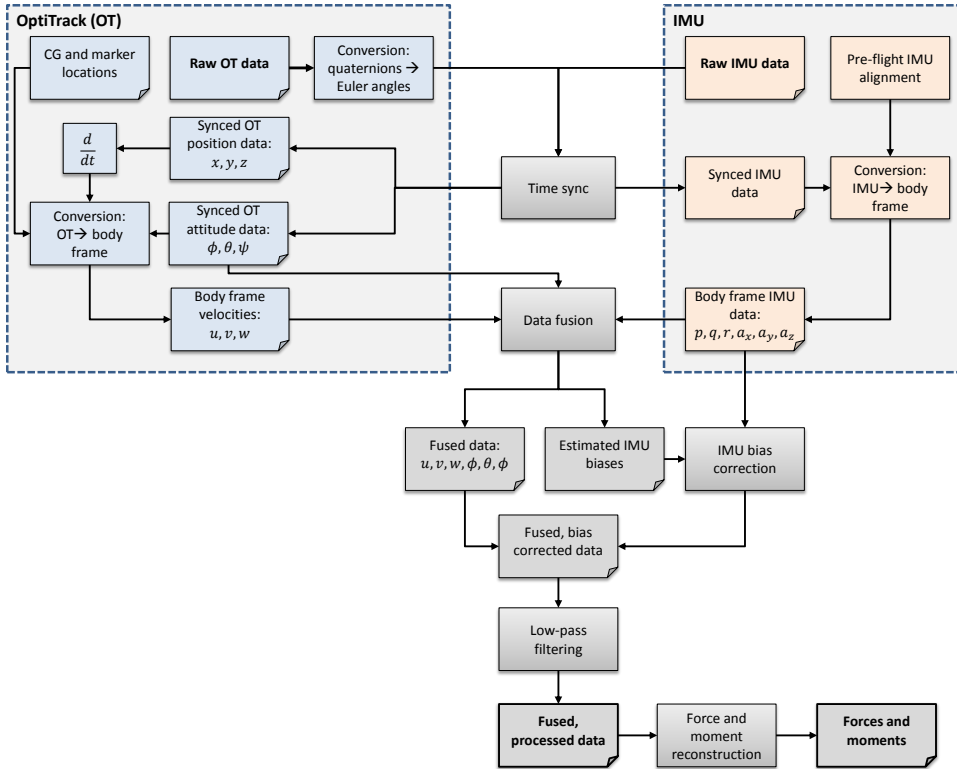
Figure 2.2: Diagram illustrating the proposed data processing and fusion process.

backs include: (i) relatively low sampling frequencies for the considered purpose, e.g. here 120Hz; (ii) presence of glitches and occasionally untracked or misattributed markers, e.g. due to light disturbance; and (iii) exclusive measurement of position and attitude, meaning rates must be computed via numerical differentiation, which amplifies the noise by a factor of $\frac{1}{(\Delta t)^n}$, with n the order of differentiation and Δt the time step [18]. The low acquisition frequency, in particular, means that even for the relatively low flapping frequency of the studied ornithopter (10-15Hz), only approximately 8-12 measurements are made during each flap cycle. As can be seen in Fig. 2.4, this leads to a relatively low resolution, hence accurate analysis at a sub flap-cycle time scale is possible only with great limitations.

By contrast, IMU measurements are typically gathered at very high sampling frequencies, here 512Hz. This represents a significant advantage for looking at the sub flap-cycle level. Additionally, IMU devices provide relatively accurate measurements over short time scales – all of which can be exploited to generally enhance the reliability of the resulting dataset. The major drawback is drift integration, as well as increased noise and the possibility of biases, which must be computed during calibration procedures and/or estimated in flight. Additionally, in the current experimental setup the way the IMU is attached to the body also represents a potential source of error. While it is possible to investigate the

2

effects of the foam attachment, the extremely low mass of the platform, as well as its shape, implies that however the IMU is attached, there will be an effect that may influence the results. In this sense, an additional advantage of a fusion approach is that the impact of such effects can be minimised through comparison with optical tracking data.

While each of the used measurement devices has limitations, combining their output allows for improved reliability, thanks to redundant information, the availability of more direct measurements, fewer issues with noise propagation, glitches and missing data, and more accurate and informative high-frequency data. In the rest of this section the data fusion approach is outlined and the resulting data are briefly discussed.

2.3.2. SYNCHRONISATION

In order to be used together, the datasets given by IMU and OptiTrack, respectively, first had to be synchronised. This was done using one of the LED markers on the FWMAV body. This marker is switched on when the on-board logging starts, and off when it ends, thus allowing for synchronisation of the measurement devices. However, the different sampling rates of the two data acquisition systems (120Hz for OptiTrack, 512Hz for IMU), still entail a seemingly random time shift of up to 1/120s=8.3ms (10% of a flap cycle). To counter this effect, the time shift is estimated by shifting the IMU roll angle estimate by up to half a flap cycle (app. 41ms) in both directions until a minimum sum of squared errors is found between IMU and adequately resampled (using spline interpolation) OptiTrack signals. The data are then shifted accordingly prior to subsequent computations and filtering. The roll angle was used for synchronisation because the best match between OptiTrack and IMU amplitude was observed in this angle, suggesting the roll axis is the most reliable, possibly due to the foam between IMU and body being stiffer in this direction. Additionally, in the current data there is limited excitation of the roll dynamics, and hence there are also less external factors influencing the time history of this variable. An alternative approach could be the direct application of a multi-rate filter, accounting for the different sampling rates. This will be considered in future work.

2.3.3. FILTER DESIGN

An extended Kalman filter (EKF) was designed to fuse the IMU and optical tracking-provided data. The EKF is an extension of the linear Kalman filter that is applicable to nonlinear systems, with the drawback that a global optimal solution cannot be guaranteed, and divergence may occur, e.g. due to inadequate initialisation. Improvements can be attained e.g. by using iterated Kalman filters, however, for the present application, an EKF was found to provide accurate results. The EKF is documented comprehensively in the literature (e.g. [37]), thus only the main equations are given here, for a nonlinear state-space system of the form:

$$x(t_{k+1}) = f(x_k, u_k, t_k) + g(u_k, t_k) + w(t_k) \qquad (2.1)$$

$$z(t_k) = h(x, u, t_k) + v(t_k) \qquad (2.2)$$

where x denotes the states, u the input, z the measured output, w the process noise and v the measurement noise. The process and measurement noise are assumed to be white and Gaussian, and are characterised by covariance matrices Q and R, respectively. The filter is

then given by the following equations.
Prediction:

$$\hat{x}_{k+1,k} = \hat{x}_{k,k} + \int_{t_k}^{t_{k+1}} f(\hat{x}_{k,k}, u_k, t)\,dt \tag{2.3}$$

$$P_{k+1,k} = \Phi_{k+1,k} P_{k,k} \Phi_{k+1,k}^T + \Gamma_{k+1,k} Q_{k+1} \Gamma_{k+1,k}^T \tag{2.4}$$

Innovation:

$$K_{k+1} = P_{k+1,k} H_k^T [H_k P_{k+1,k} H_k^T + R_{k+1}]^{-1} \tag{2.5}$$

$$\hat{x}_{k+1,k+1} = \hat{x}_{k+1,k} + K_{k+1}[z_{k+1} - h(\hat{x}_{k+1,k}, u_{k+1})] \tag{2.6}$$

$$P_{k+1,k+1} = P_{k+1,k} - K_{k+1} H_k P_{k+1,k}^T \tag{2.7}$$

where Φ and Γ are the discretised state transition and input matrices for the linearised system at step k, P is the estimated measurement error covariance matrix, K is the Kalman gain, and H is the Jacobian of the measurement equation.

The filter designed in this study estimates the body attitude and velocities, as well as accelerometer and gyro biases, using IMU data as input variables and OptiTrack data as output measurements. Given that on the test platform, as on most current FWMAVs, no onboard velocity measurement was available, the velocities fed to the EKF as measurements (u_b^*, v_b^*, w_b^*) were in fact calculated from the OptiTrack-measured positions, via numerical differentiation and necessary coordinate transforms, using the attitude computed from the OptiTrack-measured quaternions. Assuming the OptiTrack reference frame also has an upwards-pointing z-axis, the body-frame velocities are given by:

$$\begin{bmatrix} u_b^* \\ v_b^* \\ w_b^* \end{bmatrix} = \begin{bmatrix} \cos\Psi\cos\Theta & \cos\Theta\sin\Psi & -\sin\Theta \\ \cos\Psi\sin\Phi\sin\Theta - \cos\Phi\sin\Psi & \cos\Phi\cos\Psi + \sin\Phi\sin\Psi\sin\Theta & \cos\Theta\sin\Phi \\ \sin\Phi\sin\Psi + \cos\Phi\cos\Psi\sin\Theta & \cos\Phi\sin\Psi\sin\Theta - \cos\Psi\sin\Phi & \cos\Phi\cos\Theta \end{bmatrix} \begin{bmatrix} \dot{x} \\ \dot{y} \\ \dot{z} \end{bmatrix}_{OT}$$

The required numerical derivatives were computed using a three point central difference method. The Euler angles were calculated from the quaternions which the OptiTrack software computes from the marker positions. Nonetheless, the attitude data were considered measurements, as they are a direct output of the OptiTrack. Moreover, the conversion from quaternions to Euler angles can be considered a matter of notation. The states, inputs, outputs and noise terms of the filter, according to Eqs. 2.3–2.4, are thus,

$$x = [\Phi \ \ \Theta \ \ \Psi \ \ u_b \ \ v_b \ \ w_b \ \ b_p \ \ b_q \ \ b_r \ \ b_{ax} \ \ b_{ay} \ \ b_{az}]^T$$
$$u = [p \ \ q \ \ r \ \ a_x \ \ a_y \ \ a_z]^T$$
$$z = [\Phi_m \ \ \Theta_m \ \ \Psi_m \ \ u_b^* \ \ v_b^* \ \ w_b^*]^T$$
$$v = [v_\Phi \ \ v_\Theta \ \ v_\Psi \ \ v_{ub} \ \ v_{vb} \ \ v_{wb}]^T$$
$$w = [w_p \ \ w_q \ \ w_r \ \ w_{ax} \ \ w_{ay} \ \ w_{az}]^T$$

and the process and measurement equations are:

2

Process equations:

$$\dot{\Phi} = (p - b_p) + (q - b_q)\sin\Phi\tan\Theta + (r - b_r)\cos\Phi\tan\Theta \qquad (2.8)$$

$$\dot{\Theta} = (q - b_q)\cos\Phi - (r - b_r)\sin\Phi \qquad (2.9)$$

$$\dot{\Psi} = (q - b_q)\sin\Phi\sec\Theta + (r - b_r)\cos\Phi\sec\Theta \qquad (2.10)$$

$$\dot{u}_B = (r - b_r)v_b - (q - b_q)w_b - g\sin\Theta + a_x - b_{ax} \qquad (2.11)$$

$$\dot{v}_B = -(r - b_r)u_b + (p - b_p)w_b + g\sin\Phi\cos\Theta + a_y - b_{ay} \qquad (2.12)$$

$$\dot{w}_B = (q - b_q)u_b - (p - b_p)v_b + g\cos\Phi\cos\Theta + a_z - b_{az} \qquad (2.13)$$

$$\dot{b}_p = 0 \qquad (2.14)$$

$$\dot{b}_q = 0 \qquad (2.15)$$

$$\dot{b}_r = 0 \qquad (2.16)$$

$$\dot{b}_{ax} = 0 \qquad (2.17)$$

$$\dot{b}_{ay} = 0 \qquad (2.18)$$

$$\dot{b}_{az} = 0 \qquad (2.19)$$

Measurement equations

$$\Phi_m = \Phi + v_\Phi \qquad (2.20)$$

$$\Theta_m = \Theta + v_\Theta \qquad (2.21)$$

$$\Psi_m = \Psi + v_\Psi \qquad (2.22)$$

$$u_b^* = u_b + v_{ub} \qquad (2.23)$$

$$v_b^* = v_b + v_{vb} \qquad (2.24)$$

$$w_b^* = w_b + v_{wb}, \qquad (2.25)$$

where $[\Phi, \Theta, \Psi]$ are the Euler angles, $[p, q, r]$ are the roll, pitch and yaw rates, $[u_b, v_b, w_b]$ are the body-frame velocities[1], $[a_x, a_y, a_z]$ are the accelerometer-measured accelerations, $[b_p, b_q, b_r, b_{ax}, b_{ay}, b_{az}]$ are the sensor biases of the gyroscope and accelerometer, $[v_{ub}, v_{vb}, v_{wb}, v_\Phi, v_\Theta, v_\Psi]$ are the measurement noise in the measured velocities and attitudes, and $[w_p, w_q, w_r, w_{ax}, w_{ay}, w_{az}]$ are the process noise in the rates and accelerations. Asterisk superscripts indicate terms that are not directly measured but obtained from Opti-Track measurements, as discussed.

The process and measurement noise matrices, Q and R, were initially based on the actual noise characteristics of the available measurements. In a subsequent step, the matrices were adjusted further to achieve more effective results, based on the known or expected behaviour of OptiTrack and IMU (cf. Sec. 2.3.1), on the desired outcome (i.e. accurate results also at relatively high frequencies), and (iteratively) on intermediate results obtained. Based on the previous discussion, a desirable solution is one where sufficient high-frequency content is left in the fused data, thanks to the IMU contribution, while the slow time-scale evolution largely follows that of the OptiTrack. Thus the underlying idea is to use the optical tracking data as a basis, particularly on a cycle-averaged and long-term level, while

---

[1]Note that, unlike in the rest of the thesis, the subscript 'b', standing for 'body', is added to the velocities: this is to differentiate more clearly between the velocity components and the measurement noise terms.

using IMU data to (i) compensate for glitches in the tracking and (ii) provide accurate high-frequency content. Additionally, the IMU provides useful direct measurements of the rates and accelerations, unavailable from the tracking system.

The primary goal in further tuning the Q and R matrices was to ensure a sufficiently strong preference for the OptiTrack, except at high frequencies, while also retaining as realistic results as possible. Hence, adjustments were made in order to give additional weight to the OptiTrack data. In particular, the R matrix was chosen to be slightly smaller (finally: ×0.8) than the noise characteristics of the OptiTrack, as estimated from measurements, suggested. On the other hand, the Q matrix entries were selected to be somewhat larger (finally: ×2) than what inferred from the data, to reduce the confidence in the IMU.

Within the range of values where the resulting flap-averaged time evolution approximately corresponded to that of the OptiTrack, the final values, i.e. the extent to which the baseline matrices estimated from the data were adjusted, were selected experimentally, by considering, firstly, the amplitude of the resulting flapping-related oscillations, and, secondly, the innovation errors and convergence behaviour. The first point involved ascertaining that the high-frequency content was still predominantly taken over from the IMU. Prior to this, preliminary evaluations were made to investigate to what extent the IMU high-frequency data are reliable. It was observed that in some cases the flapping-related oscillations had larger amplitudes in IMU than in OptiTrack measurements. This may be due to the effect of the IMU mount, and, for the velocities, different sensitivities of the accelerometer along different axes may also have an effect. Nonetheless, comparing forces estimated from the IMU alone to wind tunnel data [34] showed an overall adequate agreement, with minor discrepancies. While no true values are available for validation, and there are known to be some differences between wind tunnel and free-flight forces [15], this observation nonetheless suggests that at sub-flap cycle level, the IMU information can be considered sufficiently reliable.

The second step involved comparing the innovation errors to the uncertainty bounds predicted by the EKF. It was found that while reducing R and increasing Q leads to increasingly small innovation errors and faster filter convergence, this can eventually lead to a significant discrepancy between innovation errors and error bounds predicted by the filter. Thus, a compromise was found, where the errors and estimated error bounds are small, but the former are still largely contained within the latter. Even a very significant higher weighting of the OptiTrack measurements (cf. Eqs. 2.26, 2.27) was found to allow for high-frequency content to be taken over from the IMU measurements, while also leading to small innovation errors and rapid convergence.

The final covariance matrices were set to the following values.

$$Q = \mathrm{diag}(3.06, 7.30, 7.12, 44.21, 14.80, 24.20) \tag{2.26}$$

$$R = \mathrm{diag}(9.94 \times 10^{-4}, 1.07 \times 10^{-3}, 8.33 \times 10^{-4}, 9.80 \times 10^{-3}, 2.47 \times 10^{-3}, 6.82 \times 10^{-3}) \tag{2.27}$$

(a) Φ (b) Θ (c) Ψ

(d) u_b (e) v_b (f) w_b
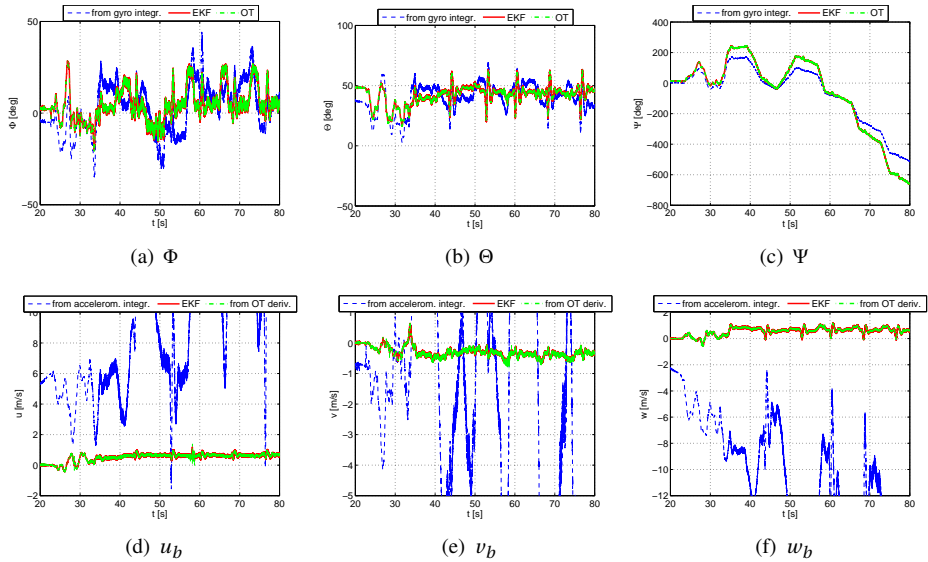
Figure 2.3: Comparison of OptiTrack (OT) measurements, IMU integration-obtained values, and EKF-obtained values, during free flight.

2.4. SENSOR FUSION RESULTS

2.4.1. FUSED STATES

Figure 2.3 shows an example of fused data, compared to data obtained from the OptiTrack and from the IMU directly. Note that the IMU-calculated values are still computed using OptiTrack measurements for the initial conditions and to convert to the body frame where required. It can be seen that an accurate result is achieved. In the long term there is significant agreement between the OptiTrack data and the EKF result, avoiding typical IMU drawbacks such as drift integration that lead to inaccurate attitude and position reconstruction. At small time scales, on the other hand, the IMU sensor readings are used to obtain a high-resolution, accurate result, that improves significantly on what could be achieved with the the OptiTrack alone. The detailed views in Fig. 2.4 further highlight the increased information that can be obtained at high frequencies. Note that in the closest view provided in subfig. 2.4(a) the gyro measurement is no longer visible as it has drifted above the other two signals, as seen in the remaining subfigures. The overall result can also be evaluated in the frequency domain, e.g. using fast Fourier transforms (FFT), as for instance shown in Fig. 2.5 for the pitch attitude. Here it can be clearly seen which measurement source is favoured in which frequency range.

Figure 2.6 shows that the innovation errors ($z_{k+1} - h(\hat{x}_{k+1,k}, u_{k+1})$, cf. Eq. 2.6) are mostly contained within the estimated error bounds, suggesting an effective filter implementation. As can be observed in the figure, the errors in the estimated attitude are typically approximately 1-2° during flight, and below 0.2° in the static case, however errors in the velocities are still relatively high during flight, reaching up to 0.1m/s, possibly due to

(a) $t \in [40.93, 41.17]\,s$ (b) $t \in [40, 41]\,s$ (c) $t \in [34, 40]\,s$
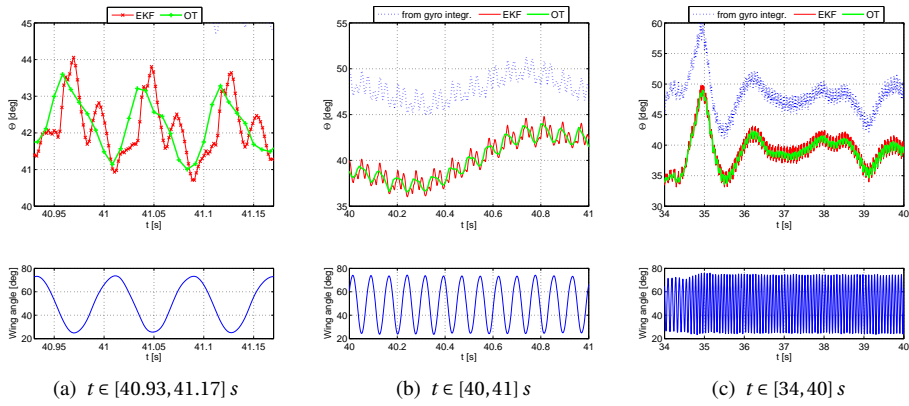
Figure 2.4: Detail of EKF and OptiTrack-obtained results: high-frequency content in pitch attitude, with corresponding wing flap angle below (increasingly small time scale view of the same measurements from right to left).

(a) Full view   (b) Detailed view
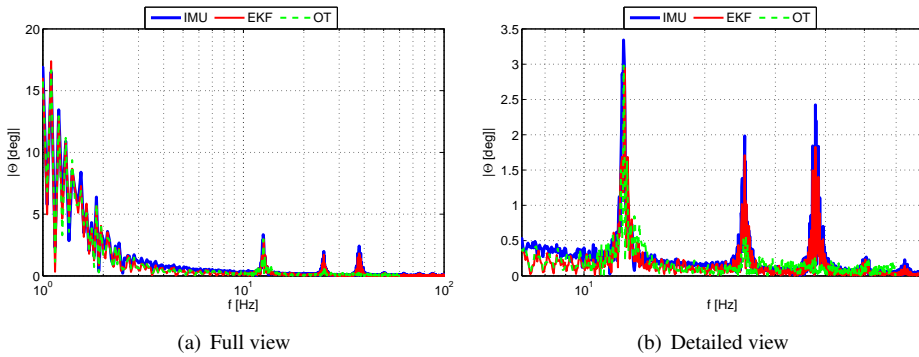
Figure 2.5: FFT of the pitch attitude computed from OptiTrack, EKF and IMU.

the numerical derivatives used as measurements in Eqs. 2.23–2.25. As can be observed in the plots, errors are also slightly higher during dynamic manoeuvres, however they either remain within the estimated bounds, or venture only slightly beyond these. More effective tuning will be explored to improve this result further.

Bias terms (cf. Eqs. 2.8–2.19) were found to converge in the static case, while during flight they vary to a limited extent, typically in conjunction with manoeuvres. It can for instance be observed in Fig. 2.8, that the bias estimates, particularly the ones for the lateral acceleration measurement, change somewhat when turns are being flown (i.e. in conjunction with long rudder input signals). To some extent, these changes may reflect a real, small movement of the IMU relative to the body, which cannot be excluded in the current setup. Nonetheless, these effects are at a very small scale, and typically only connected to large, long-lasting manoeuvres, whereas rapid longitudinal inputs mostly appear to have only a slight transient effect. The similar bias values estimated from different datasets (cf. Fig. 2.7), suggest reliable results, and all the values were found to be small, so that neglecting the bias terms may not have a significant impact. Nonetheless, the possibility of biases should be considered in a general setup. Indeed, the possibility of estimating such biases is another advantage of using data fusion.

Further testing and analysis of the sensors is required to draw conclusions on the remaining discrepancies between IMU and OptiTrack measurements mentioned above. Additionally, the velocity estimation can still be improved, e.g. by further fine-tuning of the filter and perhaps the use of higher-order differencing schemes and perhaps the use of higher-order differencing schemes to compute the velocities from the position data. The current setup should however be suitable for most modelling and identification work. The obtained data are accurate, contain detailed high-frequency information, and entail increased reliability due to the merging of separate data sources.

2.4.2. FORCES AND MOMENTS: OUTLOOK FOR TIME-RESOLVED FLAPPING FLIGHT ANALYSIS

The suggested experimental setup and data fusion approach allow for effective analysis of sub-flap cycle processes. It becomes possible, in free flight, to consider higher frequency content than can be achieved with optical tracking alone (cf. Fig. 2.4), and to consider dynamic manoeuvres, which is not possible in open-loop wind tunnel experiments.

Accurate and realistic high-frequency content can be useful for dynamic analysis, e.g. considering the effect of the flapping-related oscillations in the states, however it is particularly essential in aerodynamic studies. It has for instance been shown that some unsteady effects, such as clap-and-fling, are visible clearly only at very high frequencies [16], which are typically only accurately observable in wind tunnel tests. At the same time, as mentioned in Sec. 4.1, wind tunnel and free-flight data are only identical in limited and very specific cases[18], hence it is valuable to have the ability to obtain qualitatively comparable data in free-flight conditions. The suggested filter yields results that are close to wind tunnel results in terms of detail and information content, while also more realistic and practically useful, as they represent free flight.

As an example, Figs. 2.9 and 2.10 show a comparison of the aerodynamic forces in body frame x and z axes (i.e. the forces relevant for longitudinal manoeuvres) computed from EKF data, OptiTrack data and wind tunnel data, for four different flight conditions.

2

(a) Attitude, static condition

(b) Attitude, free flight

(c) Velocity, static condition

(d) Velocity, free flight
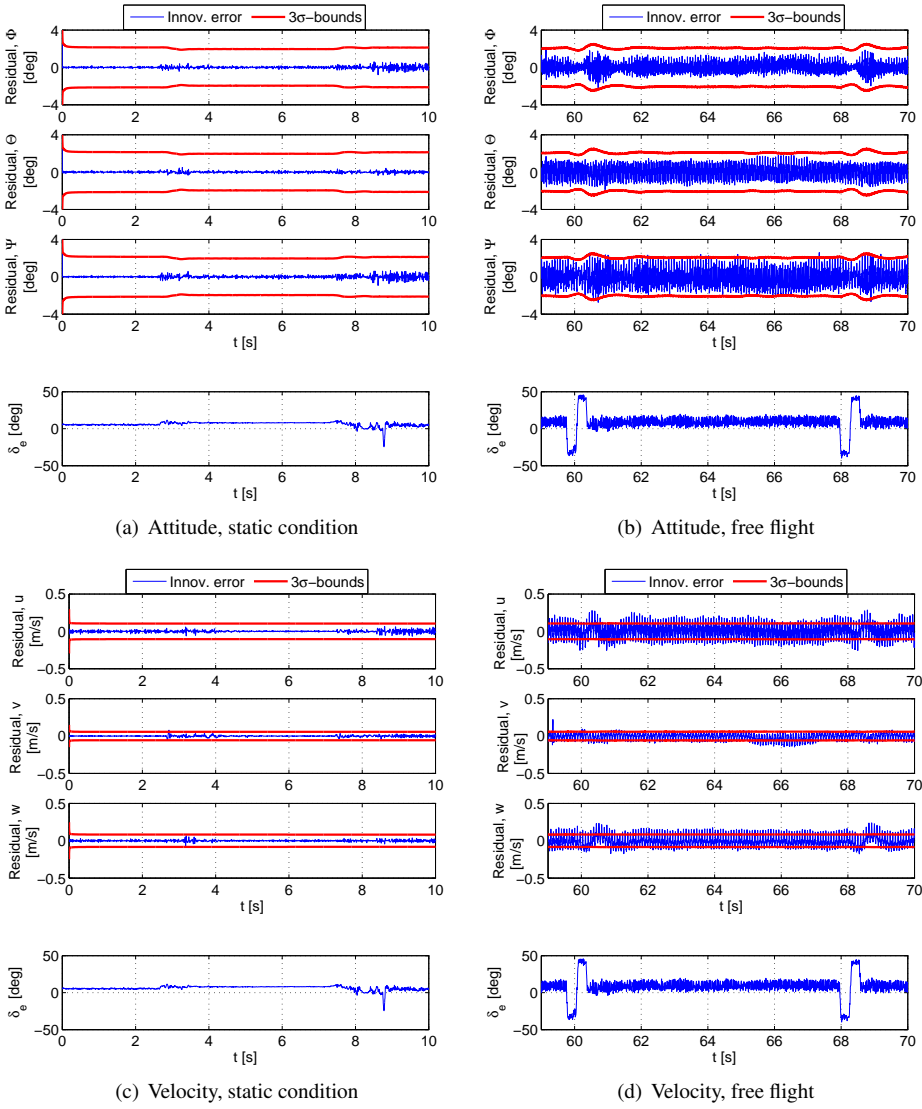
Figure 2.6: EKF innovation errors and predicted error variance bounds ($\pm 3\sigma$) in static and free flight segments; and corresponding measured elevator deflection.

2

(a) Accelerometer bias, static

(b) Accelerometer bias, free-flight

(c) Gyroscope bias, static

(d) Gyroscope bias, free-flight
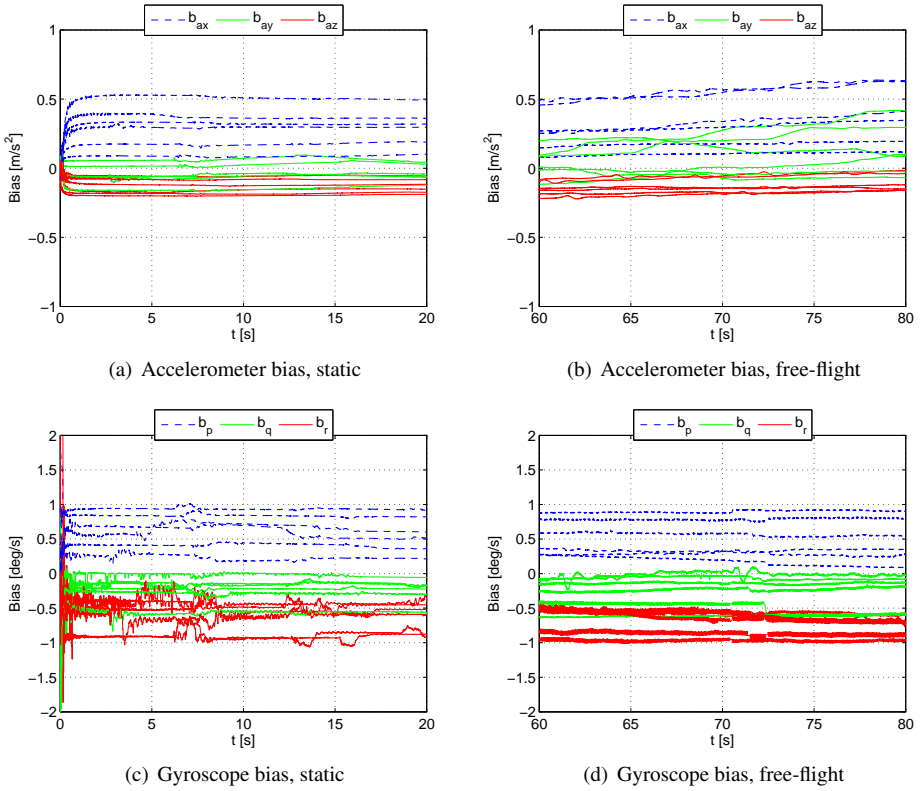
Figure 2.7: Estimated sensor biases, in static conditions and during manoeuvring flight (for six datasets).

(a) Accelerometer bias

(b) Gyroscope bias
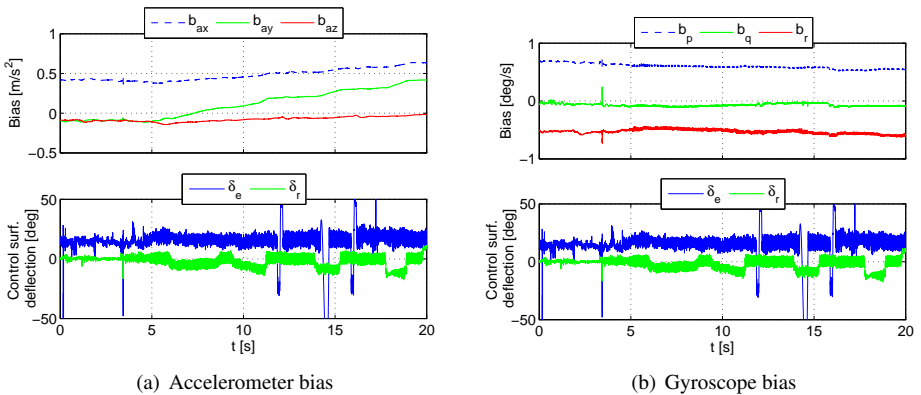
Figure 2.8: Estimated sensor biases for a single dataset (free-flight conditions) and corresponding measured elevator deflection.

The wind tunnel measurements [34] were conducted in conditions similar to the conditions observed in flight (in terms of angle of attack, forward velocity and flapping frequency), however it must be considered that small differences in the test conditions are inevitable, given the experimental setting. The data are shown for two different filter cutoff frequencies, chosen just above three times and five times the flapping frequency, respectively. In the considered range of flight conditions, flapping frequencies vary between approximately 10Hz and 14Hz. The plots show two flap cycles, and the data are plotted against non-dimensional time, $t^* := t/T_{cycle}$. Qualitatively, it can be seen that there is considerable agreement between EKF and wind tunnel forces, particularly for the force component parallel to the fuselage (Z). Slight discrepancies, particularly in the normal force component (X), are in line with previous results suggesting differences between wind tunnel and free-flight forces in this component particularly [18]. In fact the wind tunnel and free-flight cases cannot be considered entirely equal, as the clamping has a significant impact on the recorded forces [18]. Hence complete equality cannot be expected even in an ideal case. Nonetheless, the considerable agreement suggests that the remaining discrepancies between wind tunnel and fused free flight forces are at least partly due to actual differences between the free-flight and the clamped wind tunnel situation, rather than due to measurement error. This is also suggested by the similar trend in the forces measured for different flight conditions, in wind tunnel and free flight data. In terms of information content, the EKF and wind tunnel forces display a similar resolution and smoothness, and indeed can be considered of comparable quality. By contrast, the OptiTrack derived forces have a visibly lower resolution, as evident from the more abrupt and discontinuous evolution. While the evolution generally echoes that of the EKF and wind tunnel, details are not recognisable due to the insufficient number of measurement points. Clearly, a higher sampling frequency is required for accurate capturing of sub-flap forces in free flight. It can be seen (cf. Fig. 2.10) that even with relatively high filter cutoff frequencies, leaving five flapping frequency harmonics in the data, there is still a considerable level of agreement between wind tunnel and EKF results, and a comparable level of detail, suggesting that the suggested data fusion approach allows for high frequencies to be considered.

Finally, the possibility of considering manoeuvres is also of interest, as manoeuvring flight is essential for a real flying vehicle, and particularly for flapping-wing flyers, which boast high manoeuvrability as one of their pivotal advantages. Furthermore, previous work has hypothesised that additional interactions may occur at the sub-flap level during manoeuvres [26, 38], that are not observable in steady flight. Again, this cannot be studied in the wind tunnel.

Thus, the suggested combination of different data sources yields a more comprehensive and in-depth overview of time-resolved flapping behaviour that constitutes a useful stepping stone for further work in this field.

2.5. FLIGHT TESTING FOR SYSTEM IDENTIFICATION

In order to obtain data suitable for modelling and system identification, not only the data acquisition and processing are important, but also the flight test itself, and especially the input signal that is applied to the studied system. In the course of this thesis, several flight tests were conducted to extract data for modelling purposes. To ensure that the obtained data were useful and informative, a study of input design was conducted and the flight tests

2

(a) $V \approx 0.4 m/s$

(b) $V \approx 0.7 m/s$

(c) $V \approx 0.8 m/s$

(d) $V \approx 1.3 m/s$
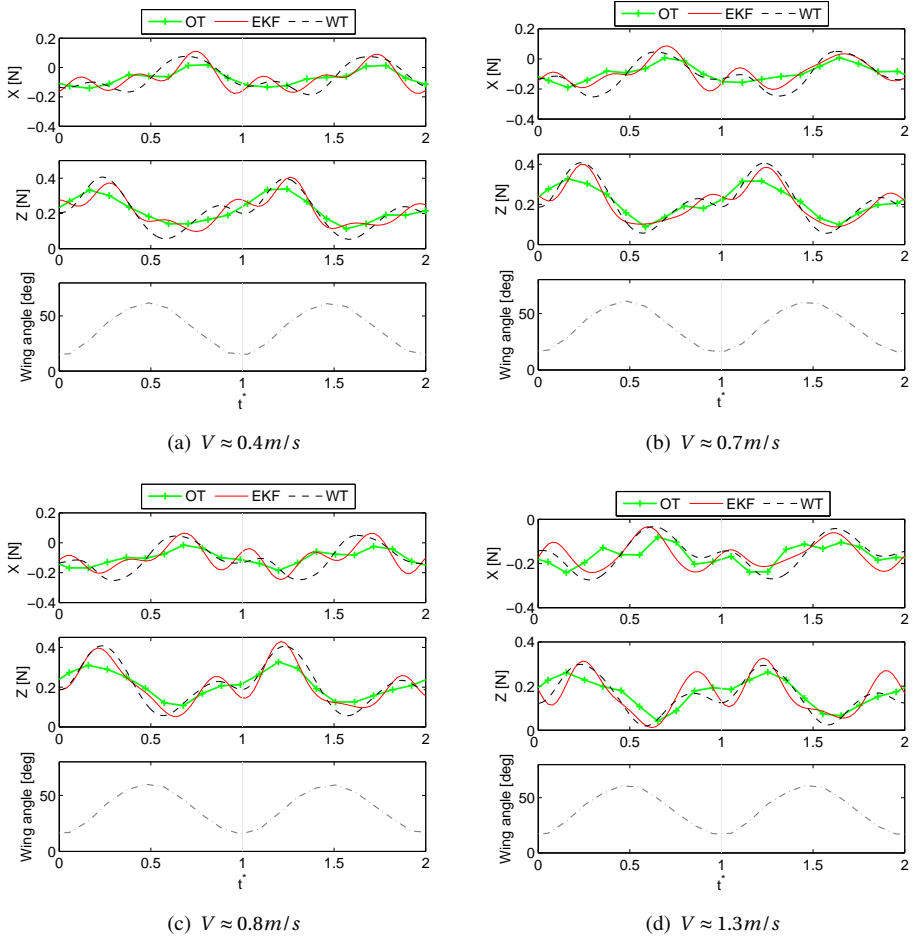
Figure 2.9: Aerodynamic forces obtained from OptiTrack (OT), EKF and wind tunnel (WT); low-pass filtered above the third flapping frequency harmonic. The corresponding wing flapping angle is also shown, for reference.
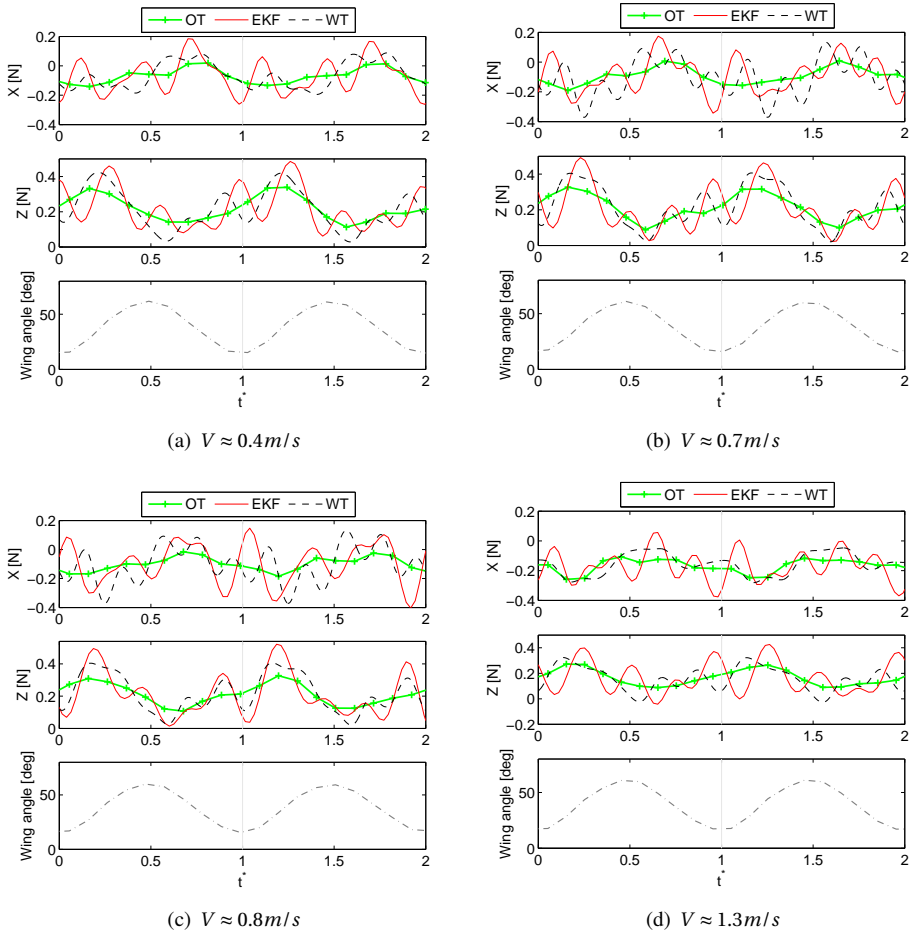
Figure 2.10: Aerodynamic forces obtained from OptiTrack (OT), EKF and wind tunnel (WT); low-pass filtered above the fifth flapping frequency harmonic. The corresponding wing flapping angle is also shown, for reference.

2

(a) Forces from fused free-flight data   (b) Forces from wind tunnel data
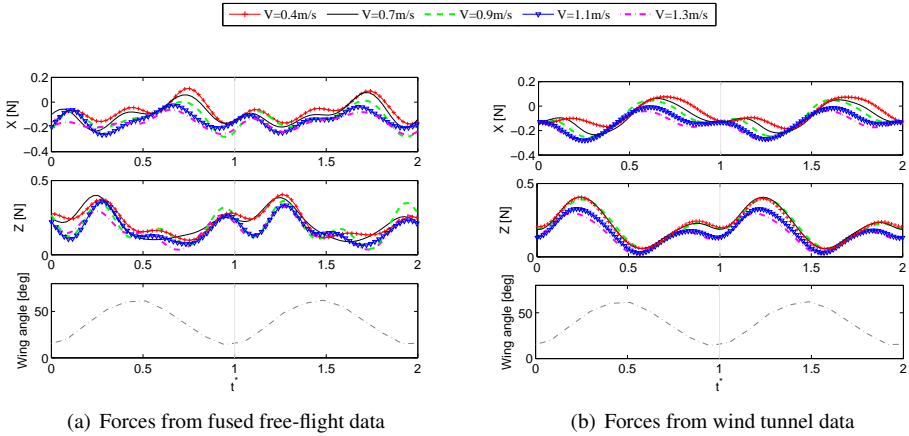
Figure 2.11: Aerodynamic forces for different total velocities; filtering above the third flapping frequency harmonic. The corresponding wing flapping angle is also shown, for reference.

were specifically designed a priori. This was partly based on existing theory, partly based on available knowledge of the system at hand, and partly an iterative process, with the experience assimilated during earlier tests being used to improve later tests. The rest of this section discusses the experiment design and flight testing process used in this thesis, and general recommendations derived from it that can also be applied to comparable flapping-wing robots. First, general aspects to consider are outlined; then specific recommendations are derived in particular for the DelFly and the local linear modelling approach used in thesis (Chapters 3 and 4). It should be noted that most of the considerations in this chapter are generally relevant for tailed FWMAVs, such as the DelFly – FWMAVs with different actuation mechanisms involve different requirements. Nonetheless, some remarks and procedures may be transferable – with some adjustment – to platforms with different actuation mechanisms.

As a clarification, it should be noted that the data used in Chapter 3 were collected prior to the start of this research project – these data represented a baseline to improve upon and were evaluated to derive general recommendations, however the recommendations made in this chapter were only applied to subsequent flight tests, i.e., those used in this same chapter, in Chapter 4 and in Appendix B. The flight tests used to evaluate the sensor fusion approach in this same chapter did not have to meet system identification requirements, nonetheless, some general remarks on flight testing still apply to them.

2.5.1. EXPERIMENT DESIGN
Experiment design is essential for any kind of test, however, it is a particularly crucial element for the system identification process, ensuring that the collected data contain sufficient and useful information to allow for models to be extracted from them. Inputs for system identification must excite the dynamics of the system in the range of interest, while remaining compatible with the constraints dictated by the available experimental setup and the modelling approach. While input design is a well-established field and many guidelines

exist for aircraft system identification experiments, novel systems can present a challenge, due to the more limited *a priori* knowledge and experience. This is the case for flapping-wing robots, where (i) the dynamics are not known in great detail, (ii) free-flight data are not easily obtainable and thus there is still little experience with – and data from – flight testing, and (iii) the flapping motion introduces additional complications.

Different approaches for input design include: computing in some way optimal inputs based on a priori knowledge of the system [39–42], choosing input signals based on approximate or qualitative prior knowledge and trial and error testing, or simply exciting as many frequencies as possible using heuristic signals such as frequency sweeps. In the interest of simplicity, and given that some, but not comprehensive, prior knowledge was available on the studied ornithopter, an engineering approach was chosen to design simple multistep inputs. To devise suitable manoeuvres for the flight tests conducted in this thesis, we started from standard aircraft guidelines [43, 44], and adjusted these with the help of insight from previous work and preliminary flight tests to obtain more effective results.

Firstly, the type of input has to be selected. Inputs that are somehow optimized may provide effective results, however they typically require extensive prior knowledge of the system and are complex to design and implement. Given the complexity of flapping-wing flight, the difficulties and limitations involved in the flight testing process, and the limited prior knowledge available, this approach was considered unfavourable as a starting point, and is not recommended for new platforms. In view of the limited knowledge of the DelFly test platform, frequency sweeps were also considered, as these allow for a wide range of frequencies to be covered, so that accurate prior knowledge of the system dynamics is dispensable. However, frequency sweeps have a relatively long duration if a wide frequency band is to be covered – which can be a hindrance when the flight space is limited, as is typically the case for indoor testing of FWMAVs. Moreover, these signals cannot excite several axes simultaneously, which limits the possibility of modelling coupled dynamics, should this be desired.

Finally, simple, multistep inputs were chosen as a favourable solution for the test platform considered. These can be easily programmed and executed, are relatively rapid, can be used to excite several axes simultaneously if applied to different actuators in sequence, and can be tailored to the system and setup with relative ease, even when the dynamics are not yet well known. Initial flight tests also proved that such signals can provide suitable excitation for the DelFly [36], while simultaneously presenting fewer challenges e.g. compared to frequency sweeps. In general, when a new vehicle is tested, multistep inputs are a straightforward but effective solution.

Different types of multi-step inputs have been applied in the aerospace literature, ranging from steps to more complex sequences of pulses, e.g. 3211 or Koehler inputs [45]. The latter can excite a somewhat wider range of frequencies, however they involve longer execution times, which can be a problem when flight space – hence time – is limited, particularly when the platform dynamics are fast. These signals are also asymmetric, which can be a limitation. In view of this, doublets were considered the most effective solution for the DelFly, and are also considered an effective signal for a typical flapping-wing flight testing setup, especially as a starting point. Doublets are simple to execute, even manually, relatively simple to design, shorter in duration compared to 211 and 3211 inputs with equally long pulses, and symmetrical, which is advantageous if linear modelling approaches are to

2

be applied, as the vehicle is more likely to remain close to its initial steady flight condition following the excitation. Compared to 211 or 3211 signals with equally long pulses, doublets are also shorter in duration, and given the limited size of the flight arena, this is advantageous as it allows for longer response times. Previous tests with a similar ornithopter also showed that doublets provided sufficient excitation [36].

The majority of the tests presented in this thesis involved elevator deflections. This was found to be the most effective and straightforward way of exciting most of the longitudinal dynamics, and hence a useful starting point. A small number of tests involved excitation signals based on throttle input (i.e. variation of the flapping frequency), in order to obtain a complete model of the actuation component, and based on rudder input, to consider the lateral dynamics. In the rest of this discussion, the focus is placed on the design of the elevator signals, however the considerations are general and the procedure was analogous for the design of the other input signals. The specific signals used in the different tests are mentioned again in the relevant sections of this thesis.

Analogously, it should be noted that while the observations in this chapter are based on the testing of tailed FWMAVs, the same high-level procedures can be applied to tailless platforms, using the available actuation mechanisms and possibly considering additional limitations and particularities. In some designs it is for instance possible that a particular axis can only be excited using several actuators simultaneously: in this case the input design process remains analogous but additional complications may arise. Furthermore, unstable configurations may require closed-loop testing, which again entails additional constraints to accommodate. Finally, some of the considerations made also apply to non-flapping-wing MAVs.

Once a type of signal has been chosen, it must be tuned based on a number of considerations, some unique to the flapping-wing case. In particular, the following points must be considered: (i) input duration, (ii) input amplitude, (iii) input shape, (iv) input type, i.e. decision of which actuator to activate. The duration and amplitude of the doublet input signals used in the flight tests conducted for this thesis were tuned based on a number of interrelated considerations.

Firstly, the input signal must provide adequate excitation of the frequency range of interest. Evidently, a larger, longer input provides more information, as long as it continues to excite the aircraft, but it also requires more time (hence, longer tests) and takes the vehicle further away from its steady condition, possibly violating linearity assumptions. By contrast, small, rapid signals can lead to unclear responses and significant noise influence. These problems can be accentuated in the flapping-wing case, as, depending on the flapping frequency, the flapping motion can introduce considerable body oscillations, that one may not wish to consider when modelling the dynamics.

Secondly, and related to the previous point, to allow the cycle-averaged dynamics to be identified effectively on their own, the input must be such that the body dynamics are distinct from the flapping-related oscillations. The flapping motion induces oscillations of the body, that, depending on the amount of filtering and the particular state, can have significant amplitudes (e.g., as shown in Fig. 2.12). If only the cycle-averaged dynamics are considered, as is done in many flapping-wing dynamics studies (cf. Chapter 1, Sec. 1.3.2), then the flapping-related dynamics effectively represent a disturbance – and can imply a low signal-to-noise ratio, which can negatively impact the identification process. This, for

(a) Low-pass filter cutoff at 50Hz

(b) Low-pass filter cutoff at 15Hz, just above the flapping frequency
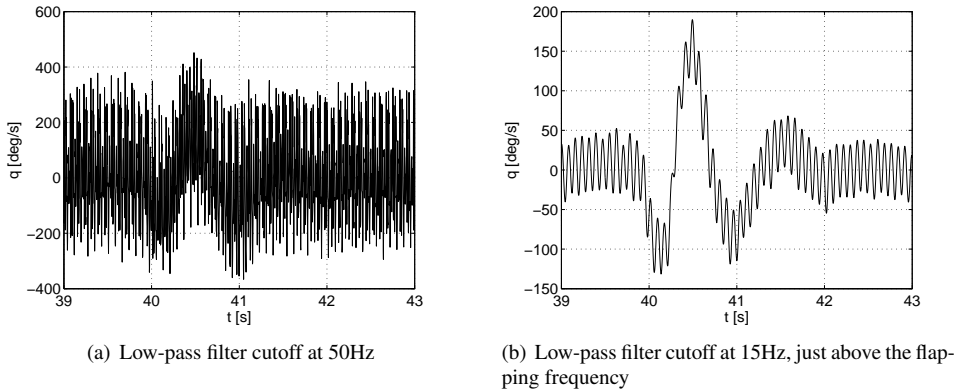
Figure 2.12: Sample of IMU-measured pitch rate q, low-pass filtered at different frequencies, highlighting the sometimes large flapping-induced oscillations, as compared to the body oscillations.

instance, can lead to large input signals being required. Indeed it was found that, because of this and the particular dynamics of the system, relatively large inputs are required compared to typical inputs used for linear model identification with fixed-wing aircraft [46–48]. This, however, may conflict with particular modelling requirements, e.g. linearity (in this thesis). Alternatively, a solution may be to minimise this problem by completely filtering out the flapping content prior to identification [26]. The latter solution is preferable when linear models are to be identified.

Thirdly, if a linear modelling approach is considered, as in the first part of this thesis, the aircraft must remain close to its initial, steady condition. This implies that the chosen manoeuvre must be somewhat symmetrical and not excessively long or large. Additionally and lastly, to allow for linear modelling, it is important to fly in a steady condition in the first place, i.e. to achieve and maintain a sufficiently steady initial condition prior to execution of the manoeuvres. In practice this can be challenging to do manually, particularly for a vehicle that is continually oscillating and flying in a limited space, and particularly considering the effect of air draughts and the need to re-stabilise after every turn. Trimming manually means that the initial condition is not always completely steady, and that it is difficult to re-create the exact same conditions repeatedly. This is enhanced by the fact that slightly different velocity/flapping-frequency/attitude combinations are possible with the same elevator trim.

Finally, the space restrictions inherent in indoor flight testing, the most common approach for FWMAVs, impose additional constraints. The time available for each manoeuvre is limited, and this time must be sufficient for the input to be executed and its effects observed, otherwise parts of the dynamics may not be captured effectively in the data, resulting in more variation in the identified dynamics. At the same time, linear identification approaches require a sufficiently steady condition prior to the excitation, which also requires some time. Insufficient measurement time leads to more variation in the identified dynamics, as some components may not be observed effectively. At the same time, the

edge of the flight space is reached rapidly, which implies frequent sharp turns that take the vehicle away from its steady condition, requiring time for a steady state to be reached again. Large rudder inputs for instance led to considerable disturbances in the DelFly test platform, often making the successive manoeuvre unusable for identification. These requirements are in conflict – more time to stabilise leaves less time for the response, and the problem becomes increasingly significant in faster flight. Spatial restrictions are therefore an important point to consider when designing input signals for FWMAVs, to ensure that the chosen signal is executable and remains effective. A possible alternative solution may be to fly in non-restricted space, using on-board measurements only. However, this necessitates sensor fusion algorithms that are based on on-board measurements alone [49], possibly at the cost of a lower quality, and would also require an approach for velocity estimation, as integrated accelerometer measurements alone are not suitable for this. A further alternative may be to still only track in the limited tracking area, but use additional, untracked space to *reach* steady conditions, thus using the tracking space exclusively for the useful manoeuvre.

In view of the different requirements, the detailed design process is somewhat iterative. If any information is available on the platform, an approximate duration for the signal [45] can be derived from frequency-domain analysis, such that the power content is highest around the expected natural frequency. Similar vehicles can be used to provide initial tentative values for entirely new platforms. Further adjustments may then be required to account for the aforementioned restrictions in the experimental setup, and a better result can be obtained through iterative adjustments once more information on the vehicle becomes available in the testing process. Adjustments may also be necessary depending on the particular flight condition, e.g., if some of the actuators are also used to maintain a specific flight condition, less manoeuvring space remains available for excitation. Moreover, it should be considered that the vehicle dynamics are likely to vary in different flight conditions (e.g., hover versus forward flight), by adjusting the input amplitude if a more aggressive response is anticipated.

2.5.2. INPUT SIGNALS FOR THE DELFLY EXAMPLE

The amplitude and duration of the input signals used in this thesis were selected on the basis of all the above considerations, and resulted in signals similar to that shown in Fig. 2.13. Previous work on the same ornithopter suggested natural frequencies of approximately 1Hz [25, 50] in the most typical flight conditions – while this is an indicative value and will change in different flight regimes and with slightly different configurations/ vehicle specimens, it gives an initial reference for input design. Based on frequency-domain analysis, suitable durations for a signal [45] can be approximately derived, such that the power content peaks around the expected natural frequency. From this type of analysis combined with initial tests, a duration of 0.35s per pulse in the doublet was selected for all flight tests. This was also found to be suitably short for the time and space constraints discussed, and generally allowed for the vehicle not to move away from its stationary condition. While different values will be more effective in different flight conditions, to minimise the test times and since no quantitative information was available on this, the same duration was used in all tests.

The amplitude was then chosen to provide sufficient excitation, while considering the restrictions discussed. $20°-30°$ elevator deflections were used in the final tests, with smaller
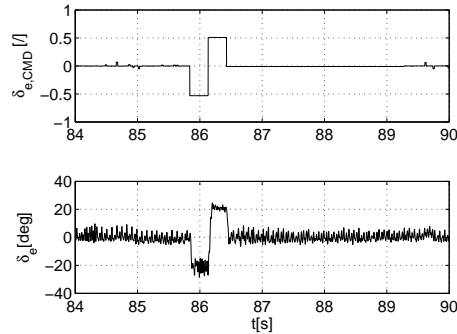
Figure 2.13: Example of elevator signal used for model identification of the DelFly, in terms of command (top) and resulting deflection (bottom).

amplitudes becoming necessary where more of the elevator deflection range was needed to maintain the trimmed condition. Both deflections and responses are larger than is typical for standard aircraft in a linear modelling context. On the one hand, inputs of a few degrees lead to responses in the same order of magnitude as the flapping-related oscillations, particularly in the linear and angular velocities, and were found to be less effective. On the other hand, the different dynamics play a role – FWMAVs easily reach extremely large angular velocities, i.e. even a small input will lead to small but extremely rapid changes in attitude. Compared to a standard aircraft, the same change in attitude may be achieved an order of magnitude more rapidly. Nonetheless, while the current, fairly large inputs were found to yield accurate results, future work should investigate how this dynamic behaviour affects linearity assumptions. To improve the signal-to-noise ratio, when analysing the cycle-averaged dynamics, the flapping-related content was wholly filtered out for the model identification work in this thesis, as discussed more thoroughly in Chapter 3. This was found to improve the results, and was significantly less likely to lead to convergence problems in the estimation algorithm.

2.5.3. REMARKS ON FLIGHT TESTING PROCEDURES

Once an input signal has been designed, it can either be applied manually or pre-programmed and applied automatically by an autopilot. Manual input can be favourable as it typically introduces more excitation, manual movements being inherently less regular. For the same reason, however, manual inputs are less repeatable, which can represent a drawback. Moreover, manual execution does not allow for highly complex manoeuvres. Finally, for small and unconventional vehicles such as FWMAVs, manual flight may be challenging *per se*, making manual input a less attractive solution. Adequate execution of the input signal is particularly important considering the space limitations discussed previously in this chapter. Hence, in this thesis, inputs were executed using the autopilot, when triggered by the pilot.

To maximise the available time for each manoeuvre, diagonal trajectories were flown across the tracking space. Manoeuvres were conducted in the central part of the flight arena,

allowing enough time for the vehicle to stabilise after precedent turns, but still providing enough time for the effects to be observed.

2.6. CONCLUDING REMARKS

2

This chapter discussed flight testing and data processing methods for system identification and experimental analysis of flapping-wing vehicles, and highlighted important aspects and limitations to consider. All methods proposed were originally developed for, and applied to, the DelFly II FWMAV. The emphasis was placed on the obtaining of informative, realistic and accurate data, and two specific aspects were investigated, viz. data acquisition/fusion and experiment design.

An extended Kalman filter-based approach was suggested to fuse data from on-board inertial sensors and off-board optical tracking measurements on a flapping-wing micro aerial vehicle (FWMAV). Compared to both the separate measurement methods, this approach was found to provide more reliable and accurate data and, in particular, to yield more extensive and accurate insight into the behaviour of the vehicle during each flap cycle, in terms of both the vehicle's states and the forces acting on it. Other advantages include the possibility of estimating the velocities more effectively than with either the inertial measurement unit (IMU) or optical tracking alone, and the possibility of obtaining accurate attitude data also for very small platforms, where the information provided by tracking alone decreases in quality due to the limited resolution. The proposed approach is considered generally useful for studying flapping-wing vehicles in free flight, as it avoids the tethering inherent in wind tunnel testing and also allows for manoeuvring and different flight conditions to be easily considered, while still providing a comparable degree of detail. Both slow and fast time-scale processes can be captured in detail, supporting the modelling process and providing better insight into the properties of novel, flapping-wing vehicles. The method is expected to remain effective also for smaller vehicles. A similar approach could also be used to combine on-board data with GPS data in an outdoor flight setting, opening up new possible applications, provided that the effect of gusts is considered. Finally, while the suggested data fusion setup can only be implemented offline, with the considered instrumentation, it allows for more accurate and detailed models to be constructed and validated, and therefore can be considered a useful basis also for advanced, sub-flap cycle control in the future.

The flight testing process itself was then discussed, with emphasis on the design of manoeuvres suitable for system identification, i.e. exciting the dynamics of the system. Recommendations were derived for FWMAVs specifically, and particular challenges to bear in mind were highlighted, including the effect of flapping and the typically constrained test space.

The combination of experimental methods discussed is considered to provide adequate datasets for data-driven model identification, hence represents a basis for a significant part of the modelling work presented in the following chapters.

REFERENCES

[1] S. F. Armanini, M. Karásek, d. G. C. H. E., and C. C. de Visser, *Onboard/ offboard sensor fusion for high-fidelity flapping-wing robot flight data,* Journal of Guidance,

Control and Dynamics **40** (2017).

[2] S. F. Armanini, M. Karásek, C. C. de Visser, G. C. H. E. de Croon, and M. Mulder, *Flight testing and preliminary analysis for global system identification of ornithopter dynamics using on-board and off-board data,* in *AIAA Atmospheric Flight Mechanics Conference*, AIAA Paper 2017-1634 (2017).

[3] C. P. Ellington, *The Aerodynamics of Hovering Insect Flight. I. The Quasi-Steady Analysis,* Philosophical Transactions of the Royal Society B: Biological Sciences **305**, 1 (1984).

[4] C. P. Ellington, C. van den Berg, A. P. Willmott, and A. L. R. Thomas, *Leading-edge vortices in insect flight,* Nature **384**, 626 (1996).

[5] G. K. Taylor and A. L. R. Thomas, *Dynamic flight stability in the desert locust Schistocerca gregaria,* Journal of Experimental Biology **206**, 2803 (2003).

[6] S. P. Sane, *The aerodynamics of insect flight,* Journal of Experimental Biology **206**, 4191 (2003).

[7] M. H. Dickinson, F.-O. Lehmann, and S. P. Sane, *Wing Rotation and the Aerodynamic Basis of Insect Flight,* Science **284**, 1954 (1999).

[8] J. Dietl, T. Herrmann, G. Reich, and E. Garcia, *Dynamic Modeling, Testing, and Stability Analysis of an Ornithoptic Blimp,* Journal of Bionic Engineering **8**, 375 (2011).

[9] D. B. Doman, M. W. Oppenheimer, and D. O. Sigthorsson, *Dynamics and control of a minimally actuated biomimetic vehicle: part i - aerodynamic model,* in *AIAA Guidance, Navigation and Control Conference* (2009).

[10] J. Grauer, E. Ulrich, J. E. Hubbard, D. Pines, and J. S. Humbert, *Testing and System Identification of an Ornithopter in Longitudinal Flight,* Journal of Aircraft **48**, 660 (2011).

[11] J.-s. Han, J. W. Chang, J.-k. Kim, and J.-H. Han, *Experimental Study on the Unsteady Aerodynamics of a Robotic Hawkmoth Manduca sexta model,* in *AIAA SciTech Aerospace Sciences Meeting* (2014).

[12] J.-S. Lee and J.-H. Han, *Experimental study on the flight dynamics of a bioinspired ornithopter: free flight testing and wind tunnel testing,* Smart Materials and Structures **21**, 094023 (2012).

[13] T. Nakata, H. Liu, Y. Tanaka, N. Nishihashi, X. Wang, and A. Sato, *Aerodynamics of a bio-inspired flexible flapping-wing micro air vehicle,* Bioinspiration & Biomimetics **6** (2011).

[14] M. Perçin, H. Eisma, B. van Oudheusden, B. Remes, R. Ruijsink, and C. de Wagter, *Flow Visualization in the Wake of the Flapping-Wing MAV 'DelFly II' in Forward Flight,* in *AIAA Applied Aerodynamics Conference* (2012).

[15] J. V. Caetano, M. B. Weehuizen, C. C. de Visser, G. C. H. E. de Croon, and M. Mulder, *Rigid-Body Kinematics Versus Flapping Kinematics of a Flapping Wing Micro Air Vehicle,* Journal of Guidance, Control, and Dynamics **38**, 2257 (2015).

[16] S. F. Armanini, J. V. Caetano, G. C. H. E. de Croon, C. C. de Visser, and M. Mulder, *Quasi-steady aerodynamic model of clap-and-fling flapping MAV and validation with free-flight data,* Bioinspiration & Biomimetics **11**, 046002 (2016).

[17] A. M. DeLuca, M. F. Reeder, and R. G. Cobb, *An experimental investigation into the effect of flap angles for a piezo-driven wing,* International Journal of Micro Air Vehicles **5** (2013).

[18] J. V. Caetano, M. Percin, B. W. van Oudheusden, B. D. W. Remes, C. de Wagter, G. C. H. E. de Croon, and C. C. de Visser, *Error analysis and assessment of unsteady forces acting on a flapping wing micro air vehicle: Free-flight versus wind tunnel experimental methods,* Bioinspiration & Biomimetics **10** (2015).

[19] A. Jennings, M. Mayhew, and J. Black, *Video measurements of instantaneous forces of flapping wing vehicles,* Mechanical Systems and Signal Processing **64–65**, 325 (2015).

[20] C. Rose and R. S. Fearing, *Comparison of ornithopter wind tunnel force measurements with free flight,* in *2014 IEEE International Conference on Robotics & Automation (ICRA)* (2014).

[21] B. M. Finio, N. O. Perez-Arancibia, and R. J. Wood, *System identification and linear time-invariant modeling of an insect-sized flapping-wing micro air vehicle,* in *2011 IEEE/RSJ International Conference on Intelligent Robots and Systems (IROS)* (2011).

[22] H. Duan and Q. Li, *Dynamic model and attitude control of Flapping Wing Micro Aerial Vehicle,* in *IEEE International Conference on Robotics and Biomimetics (RoBio)* (2009).

[23] A. N. Chand, M. Kawanishi, and T. Narikiyo, *Parameter Estimation for the Pitching Dynamics of a Flapping-Wing Flying Robot,* in *IEEE International Conference on Advanced Intelligent Mechatronics (AIM)* (2015).

[24] J. V. Caetano, C. C. de Visser, G. C. H. E. de Croon, B. Remes, C. De Wagter, and M. Mulder, *Linear Aerodynamic Model Identification of a Flapping Wing MAV Based on Flight Test Data,* International Journal of Micro Air Vehicles (2013).

[25] S. F. Armanini, C. C. de Visser, and G. C. H. E. de Croon, *Black-box LTI Modelling of Flapping-wing Micro Aerial Vehicle Dynamics,* in *AIAA Atmospheric Flight Mechanics Conference* (2015) AIAA Paper 2015-0234.

[26] S. F. Armanini, C. C. de Visser, G. C. H. E. de Croon, and M. Mulder, *Time-varying model identification of flapping-wing vehicle dynamics using flight data,* Journal of Guidance, Control, and Dynamics **39**, 526 (2016).

[27] Y. Xiong and M. Sun, *Stabilization control of a bumblebee in hovering and forward flight,* Acta Mechanica Sinica **25**, 13 (2009).

[28] J. Wu and M. Sun, *Control for going from hovering to small speed flight of a model insect,* Acta Mechanica Sinica **25**, 295 (2009).

[29] G. J. Berman and Z. J. Wang, *Energy-minimizing kinematics in hovering insect flight,* Journal of Fluid Mechanics **582**, 153 (2007).

[30] C. T. Orlowski and A. R. Girard, *Averaging of the nonlinear dynamics of flapping wing micro air vehicles for symmetrical flapping,* in *AIAA Aerospace Sciences Meeting including the New Horizons Forum and Aerospace Exposition* (2011).

[31] G. C. H. E. de Croon, M. Perçin, B. D. W. Remes, R. Ruijsink, and C. De Wagter, *The DelFly Design, Aerodynamics, and Artificial Intelligence of a Flapping Wing Robot* (Springer Netherlands, 2016).

[32] B. D. W. Remes, P. Esden-Tempskiy, F. van Tienen, E. Smeur, C. De Wagter, and G. C. H. E. de Croon, *Lisa-s 2.8g autopilot for gps-based flight of mavs,* in *International Micro Air Vehicle Conference and Competition (IMAV)* (2014).

[33] *Paparazzi UAV,* http://wiki.paparazziuav.org, (retrieved 7 Dec. 2016).

[34] M. Karásek, A. J. Koopmans, S. F. Armanini, B. D. W. Remes, and de Croon G. C. H. E., *Free flight force estimation of a 23.5 g flapping wing MAV using an on-board IMU,* in *IEEE International Conference on intelligent robots and systems (IROS)* (2016).

[35] P. Chirarattananon and R. J. Wood, *Identification of flight aerodynamics for flapping-wing microrobots,* in *IEEE International Conference on Robotics and Automation (ICRA)* (2013).

[36] J. V. Caetano, C. C. de Visser, B. D. Remes, C. De Wagter, E.-J. Van Kampen, and M. Mulder, *Controlled Flight Maneuvers of a Flapping Wing Micro Air Vehicle: a Step Towards the Delfly II Identification,* AIAA Atmospheric Flight Mechanics Conference (2013).

[37] A. Gelb, ed., *Applied Optimal Estimation*, 16th ed. (MIT Press, Cambridge, MA, 1974) pp. 180–190.

[38] S. Zeyghami and H. Dong, *Coupling of the wings and the body dynamics enhances damselfly maneuverability,* ArXiv e-prints (2015), arXiv:1502.06835 [physics.flu-dyn] .

[39] J. A. Mulder, *Design and evaluation of dynamic flight test manoeuvres*, Phd, Delft University of Technology (1986).

[40] E. Plaetschke and G. Schulz, *Practical input signal design,* in *Parameter Identification AGARD-LS-104* (NATO, 1979).

2

2

[41] E. A. Morelli and V. Klein, *Optimal input design for aircraft parameter estimation using dynamic programming principles,* in *AIAA Atmospheric Flight Mechanics Conference* (1990).

[42] E. Morelli, *Flight test validation of optimal input design and comparison to conventional inputs,* in *AIAA Atmospheric Flight Mechanics Conference* (1997).

[43] R. Maine and K. Iliff, *Application Of Parameter Estimation To Aircraft Stability And Control: The Output-Error Approach*, NASA Reference Publication 1168 (NASA, 1986).

[44] V. Klein and E. Morelli, *Aircraft System Identification* (AIAA Education Series, 2006).

[45] R. Jategaonkar, *Flight Vehicle System Identification A Time Domain Methodology* (AIAA Progress in Astronautics and Aeronautics, Reston, VA, USA, 2006).

[46] K. W. Iliff, *Identification of Aircraft Stability and Control Derivatives in the Presence of Turbulence*, Tech. Rep. (NASA TN D-7647, 1974).

[47] G. W. Milne, J. A. Mulder, M. W. Soijer, S. Juliana, and Hermansyah, *Maximum Likelihood Stability and Control Derivative Identification of a Cessna Citation II,* in *AIAA Atmospheric Flight Mechanics Conference and Exhibit*, AIAA Paper 2001-4013 (2001).

[48] M. Napolitano, A. Paris, B. Seanor, and A. Bowers, *Parameter Estimation for a Cessna U-206 Aircraft Using the Maximum Likelihood Method,* in *AIAA Atmospheric Flight Mechanics Conference*, 94-3481 (1994).

[49] J. L. Verboom, S. Tijmons, C. De Wagter, B. Remes, R. Babuska, and G. C. H. E. de Croon, *Attitude and altitude estimation and control on board a flapping wing micro air vehicle,* in *IEEE International Conference on Robotics and Automation (ICRA)* (2015).

[50] A. Koopmans, *Delfly Freeflight: Autonomous flight of the DelFly in the wind tunnel using low-cost sensors*, Master's thesis, Delft University of Technology (2012).

3

LOCAL TIME-VARYING GREY-BOX DYNAMIC MODELLING

Following the establishing of suitable flight testing and data processing methods for flapping-wing vehicles in Chapter 2, this chapter focuses on the subsequent step in the system identification process, i.e., modelling. Using the DelFly II as an example, the problem of identifying models of flapping-wing dynamics from free-flight data is addressed. The aim is to determine a suitable modelling procedure and, in particular, to devise a method to include the flapping-related oscillations. Such oscillations are typically neglected in the literature, yet their magnitude can be significant, especially for flyers with lower flapping frequencies. A local model for the dynamics of the DelFly II in a slow forward flight condition is identified and validated using free-flight data, based on a maximum likelihood estimator. The model is shown to be highly accurate and applicable for dynamic simulation. Furthermore, the selected linear time-invariant grey-box model structure is amenable for control applications and dynamics analysis at a system level, while still allowing for a degree of physical interpretation. An approach is then proposed to include time-varying flapping effects in the model, based on the assumed decoupling of the body and wing dynamics and involving a frequency-domain decomposition of the identification data. The resulting model constitutes a more accurate and realistic representation of the observed flight behaviour without incurring excessive complexity. Additionally, the model is used to assess the validity of the widely-applied time-scale separation assumption in the specific case where the flapping frequency is low compared to the frequencies of the body dynamics modes.

A time-varying model for the forward flight dynamics of a flapping-wing micro aerial vehicle is identified from free-flight optical tracking data. The model is validated and used to assess the validity of the widely-applied time-scale separation assumption. Based on this assumption, each aerodynamic force and moment is formulated as a linear addition of decoupled time-averaged and time-varying sub-models. The resulting aerodynamic models are incorporated in a set of linearised equations of motion, yielding a simulation-capable full dynamic model. The time-averaged component includes both the longitudinal and the lateral aerodynamics and is assumed to be linear. The time-varying component is modelled as a third-order Fourier series, which approximates the flapping dynamics effectively. Combining both components yields a more complete and realistic simulation. Results suggest that while in steady flight the time-scale separation assumption applies well, during manoeuvres the time-varying dynamics are not fully captured. More accurate modelling of flapping-wing flight during manoeuvres may require considering coupling between the time scales.

3.1. INTRODUCTION

The recent surge of interest in unmanned aircraft, for both civilian and military applications, has propelled extensive exploration of new and unconventional configurations. One of these is the biologically-inspired Flapping-Wing Micro Aerial Vehicle (FWMAV) [2–4]. FWMAVs combine a small size and mass with the numerous favourable flight properties of flapping-wing flyers, such as high manoeuvrability and agility, power efficiency, an extensive flight envelope, and the ability to fly at low speeds and hover.

In view of these properties, FWMAVs are expected to have useful applications in the future, e.g. for ISR (intelligence, surveillance and reconnaissance) operations, or inspecting damaged buildings or machines. However, at present the development of such vehicles is challenging due to the complex phenomena involved in flapping-wing flight. Flapping-wing flyers operate at low Reynolds numbers and are characterised by unsteady aerodynamics, our understanding of which is incomplete [5, 6]. A few models have been proposed to capture some of these unsteady effects, based on computational fluid dynamics and first principles [7–9]. These models however, tend to be complex and computationally inefficient, and are typically inadequate for practical applications such as control system design [10] and dynamic simulation.

A more viable alternative from this perspective is given by quasi-steady models, combined with coefficients derived from either first principles or experimental data [11–14]. Quasi-steady, linear-in-the-parameters models have also been obtained from flight data by means of system identification [15, 16]. The advantage is a strong link between model and physical system and the direct possibility for validation with real data. By contrast, first-principles and numerical models are often not fully validated, or validated indirectly with data collected with other platforms [11, 17].

The flapping motion also results in complex time-varying kinematics and dynamics, and flapping-wing vehicles are often represented as multi-body dynamic systems [18–23]. However, some studies suggest that flapping-wing kinematics have a negligible effect on the cycle-averaged aerodynamics when either the flapping frequency is significantly higher than that of the rigid body modes [24], or the wing mass is low compared to the body mass [25]. These findings may justify simpler single-body formulations of the dynamics [25].

Specifically for stability analysis, control system design and simulation, simple and computationally efficient models are desired. In this context, several significantly simplified, low-order dynamic models have been applied [24, 26–28], often based on the linearised fixed-wing aircraft equations of motion (EOM) [24, 27]. Control work on FWMAVs also often applies averaging techniques to cancel time-varying effects [10, 29–31]. Under the assumption of *time-scale separation*, such studies consider the body and flapping dynamics to be decoupled. Whether or not this is the case is under debate, as there may be non-negligible interactions between the two components [32]. Taha et al. suggest that particularly where the ratio between flapping frequency and body natural frequency is low, the high-frequency periodic forcing due to flapping can influence the stability of hovering insects, and hence separating the fast and slow time scales is sometimes questionable [32, 33]. However, at present the most widespread approach is to neglect time-varying effects at a body dynamics level.

The development of simple but accurate models for FWMAVs remains an open field of research, and particularly models based on free-flight data are scarce [15, 26, 34, 35], owing to the limited availability of testing facilities and the restrictions imposed by the limited size, payload and controllability of FWMAVs. Extensive modelling work on the DelFly FWMAV was done by Caetano et al., who obtained linear aerodynamic models from flight data [35] using the two-step method [36]. These models capture the platform cycle-averaged aerodynamics fairly well, but result in divergence when used in a nonlinear simulation, which contrasts with the observed flight behaviour.

More recently, linear time-invariant (LTI) structures were used to model the dynamics of the DelFly via black-box system identification [37] (cf. Appendix C). The resulting models are fairly accurate, but include unphysical terms to account for effects that could not be captured otherwise, and due to their structure do not provide information on the aerodynamics. Despite limitations, the aforementioned studies suggest that within bounded regions of the flight envelope, linear model structures can provide acceptable approximations of both the aerodynamics and dynamics of the DelFly.

This chapter discusses the identification and validation of grey-box models for the DelFly, based on free-flight optical tracking data. The models include flapping effects and are sufficiently accurate for control system design and realistic flight simulation, within a small but representative region of the flight envelope. Low-order models are first developed for the longitudinal and lateral flap cycle-averaged dynamics. Subject to a number of assumptions, these models accurately describe the vehicle's time-averaged behaviour in forward flight and can be used to simulate it. Subsequently, a simple model for the flapping component is proposed under the assumption of time-scale separation. The model is considered an effective first approximation and is combined with the aforementioned cycle-averaged model to yield a time-varying description for the longitudinal system dynamics.

Our modelling approach additionally allows us to investigate the fast time-scale dynamics and assess the validity of the time-scale separation assumption. Any discrepancies between the suggested model and the measurements give insight into the limitations of the assumption, and into the magnitude and timing of possible couplings between the cycle-averaged and time-varying components.

The chosen grey-box formulation provides useful insight into the Delfly dynamics, while the simple model structure allows for the development of new control and guidance

systems [38]. The inclusion of flapping effects in particular, is important for the design and testing of on-board sensors, cameras, and vision-based control algorithms. Finally, the obtained model is the first simulation-capable and partially physically meaningful model of the DelFly, and thus enhances the potential for further work on this platform.

This chapter is structured as follows. Section 3.2 explains the proposed overall modelling approach. Section 3.3 presents the DelFly platform and the experimental setup used to obtain the flight data. Sections 3.4 and 3.5 outline the cycle-averaged and time-varying modelling processes, respectively, and discuss the main results obtained; Section 3.6 discusses the combined model. Section 3.7 summarises the main conclusions and suggestions for further work.

3.2. APPROACH

We aim to investigate the time-averaged and time-varying components of the dynamics of the DelFly. Neglecting fast time-scale effects and focusing on a cycle-averaged level is common in the modelling of flapping-wing flyers. There is no clear consensus, however, on whether or not the flapping and body dynamics are decoupled, and this also depends on the specific platform. In the case of the DelFly, the flapping frequency ($\approx$10Hz) is only one order of magnitude larger than the body mode frequencies ($\approx$1Hz), [37, 39] hence the validity of the decoupling assumption is not self-evident.

To begin with, the principle of time-scale separation was investigated as a means of obtaining a model for each the time-averaged and the time-varying component. Whereas time-scale separation is typically used to justify omitting flapping effects when modelling the overall dynamics, it was used here also as a means to consider flapping effects. For this, the assumption was reformulated to signify that if the cycle-averaged and time-varying components are indeed decoupled, then two distinct models can be developed for the two components, and these models can then be combined linearly to yield a full model of the system that includes flapping effects. Applying this modelling approach is a way to evaluate how effectively time-scale separation allows for the system's behaviour to be represented, and, if necessary, to identify shortcomings of this approach and the need for more advanced alternatives.

In this context, in addition to the cycle-averaged modelling, an investigation into the fast time-scale processes was undertaken, with the initial objective of determining a first approximation of the flapping dynamics to combine with the cycle-averaged model, e.g., to allow for more realistic simulation. The aim was also, however, to acquire further knowledge on the flapping process, and particularly to investigate whether there are any interactions between the two time scales, and, if so, how significant these are.

Hence, a model for the DelFly was developed in terms of a superposition of a time-averaged and a time-varying sub-model, as illustrated in Fig. 3.1. The total aerodynamic forces and moments, collectively denoted by F in the diagram, were defined to consist of the sum of a time-averaged, low-frequency component, F_{TA}, and a time-varying, higher-frequency component, F_{TV}, each generated by a separate sub-model, driven by a separate input signal u_i. Adding both parts yields the total force F, which can then be fed into the EOM, as defined in Sec. 3.4.1, to run a complete simulation of the system, that also includes a time-varying component. Each sub-model is independent and can be used on its own to represent one of the two components of the aerodynamics and dynamics. The de-
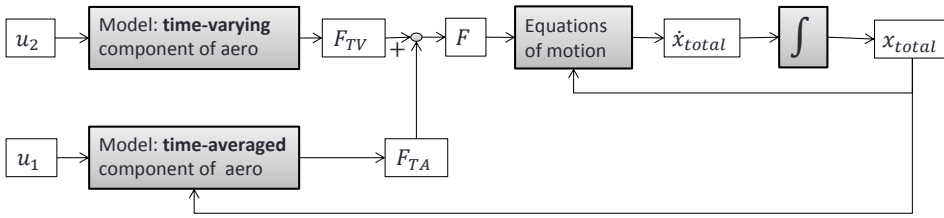
Figure 3.1: Overall modelling approach based on time-scale separation.

composition into sub-models was defined in terms of the aerodynamic forces and moments rather than the states, because the time-varying behaviour in the states can be considered a *consequence* of the time-varying behaviour in the aerodynamics.

3.3. EXPERIMENTAL SETUP

3.3.1. PLATFORM AND DATA

The subject of the work presented in this chapter is the DelFly II, shown in Fig. 3.2 together with the coordinate frame used, and described previously in Chapter 1 (Sec. 1.4.1). The particular vehicle used in this study has a mass of approximately 18g. It can be piloted remotely, but is also equipped with an autopilot that allows for control inputs to be pre-programmed and executed. This is particularly useful for system identification purposes. In contrast to fixed-wing vehicles, the DelFly typically flies at very large pitch angles (~70°-80° in slow forward flight), which leads to a high degree of roll-yaw coupling and adds to the complexity of the platform. This also implies that many of the small angle assumptions typically made for fixed-wing aircraft are not applicable.
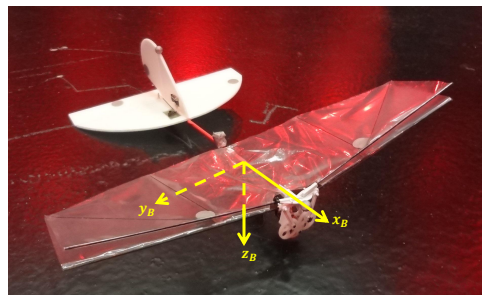
Figure 3.2: The DelFly II and definition of the body-fixed coordinate system (corresponding to frame $B1$, as defined in Sec. 1.4.3).

The flight data used in this chapter were collected in the Vicon optical tracking chamber

of the US Air Force Research Laboratory at Wright-Patterson Air Force Base [40]. The flight tests involved typical system identification manoeuvres, such as pulses, doublets and 211 inputs, on the elevator and the rudder. In previous work, the resulting data were pre-processed to ensure consistency, remove outliers and reduce noise, and the vehicle states were reconstructed from the measured positions of eight markers attached to the DelFly at various locations [16]. The aerodynamic forces and moments, not measurable directly in flight, were reconstructed from the states assuming rigid-body dynamics [16]. It was shown that for the DelFly this gives almost identical results as using a multi-body model that considers flapping effects [25]. The flight testing and initial data-processing are described in Refs. [16, 40].

For this study, sixteen datasets for slow forward flight were used, containing short elevator and rudder manoeuvres. While the initial steady conditions prior to the application of the test inputs differed somewhat between samples, they covered a relatively small area of the flight envelope, as shown in Fig. 3.3, and were thus assumed to correspond to the same approximate flight regime. This allowed, firstly, for a comparison between models estimated from different samples, and secondly, for the samples not used to estimate a particular model to be used for its validation.
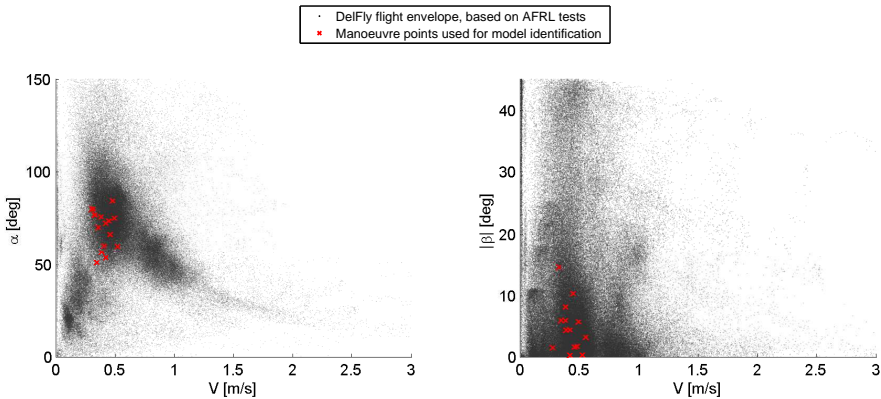
Figure 3.3: DelFly flight envelope coverage: velocity magnitude combined with angle of attack (left) and angle of sideslip (right), at the test points used for the collection of the estimation data (crosses), together with the full flight envelope (dots).

3.3.2. DATA DECOMPOSITION
To identify separate models for the time-averaged and time-varying components of the aerodynamics, it was first necessary to obtain adequate estimation data. For this, the measured flight data were decomposed in an analogous way as the model, i.e. into a time-averaged and a time-varying component, used to identify models for the time-averaged and time-varying components of the aerodynamics, respectively.

The data were decomposed by means of linear filtering. The raw measurements were first low-pass filtered to remove noise. Given that the flapping frequency ranged from 11Hz to 13Hz in the chosen datasets, a 40Hz cutoff was used, based on the observation that in
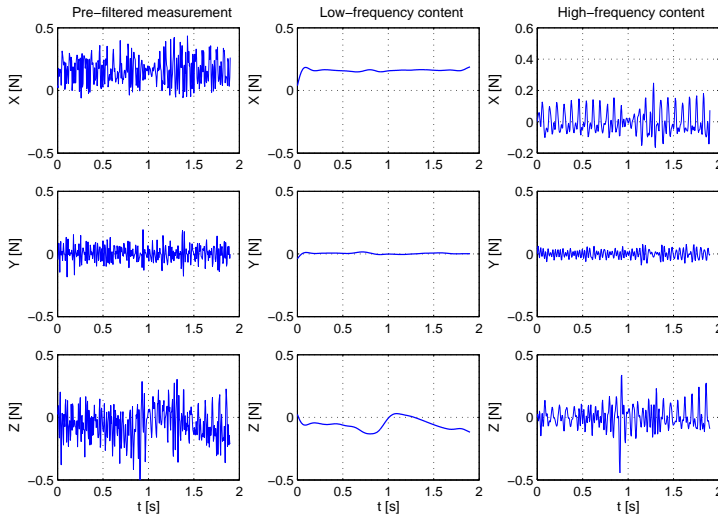
(a) Time-domain
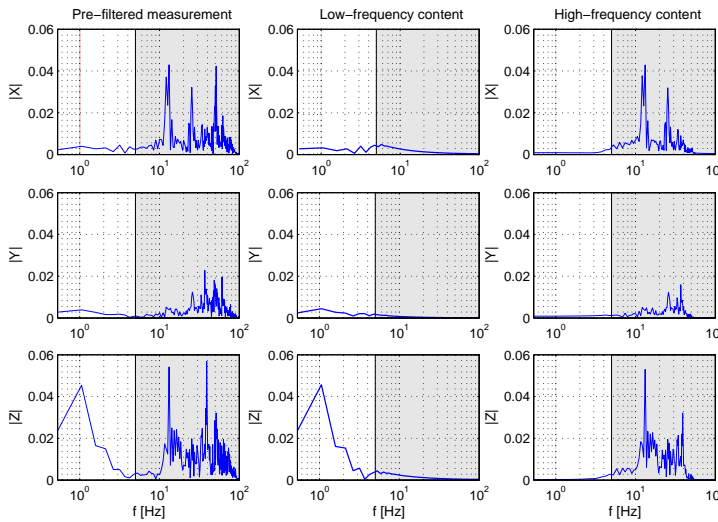
(b) Frequency-domain; the white area indicates the low-frequency region, the shaded area the high-frequency region

Figure 3.4: Decomposition of the aerodynamic forces calculated from the measurements, previously low-pass filtered at 40Hz to remove noise, into time-averaged and flapping-related components. The flapping frequency for this example is in the range $12.5 Hz - 13.3 Hz$.

free-flight data only the first three flapping harmonics can be clearly recognised as distinct from noise.

Next, a cutoff between the frequency ranges relevant for the body dynamics and for the flapping dynamics was chosen. The Delfly body dynamics are characterised by frequencies in the order of 1Hz (cf. Sec. 3.2); the flapping frequency is approximately 12Hz. On the basis of free-flight and wind tunnel measurements, 5Hz was found to constitute an adequate cutoff between the two time scales. Note that any cutoff represents a compromise. Although frequency peaks are recognisable in the data, there is some frequency content in-between these that may belong to neither component, or to both due to coupling effects. A low cutoff, close to the body mode frequencies, will lead to more frequency content in the flapping component that may be unrelated to the flapping dynamics. Likewise, a cutoff just below the flapping frequency will lead to more disturbance in the time-averaged component. Similarly, whilst low-pass filtering is necessary to remove noise, it may also remove some flapping-related content, again requiring an adequate compromise.

Fig. 3.4 presents an example of the decomposition of the aerodynamic forces in x_B, y_B and z_B direction (as defined in Fig. 3.2) computed from the measured data, into a cycle-averaged and a flapping-related component. All measurements used for estimation were decomposed similarly. In the measurements, it can already be seen that the flapping component of the aerodynamics is not perfectly periodic and is to some extent affected by the platform low-frequency dynamics, or by external factors. Hence, the data alone already cast doubt upon the periodicity of the fast time-scale component, and whether or not it is coupled to the body dynamics. The modelling process was expected to shed further light on this aspect.

3.4. TIME-AVERAGED MODELLING

Here we discuss the modelling and identification of the DelFly cycle-averaged dynamics, starting with the longitudinal component and then summarising the lateral component.

3.4.1. MODEL STRUCTURE DEFINITION

The chosen identification approach requires the definition of a model structure for the system at hand. Whilst data can be fitted to any arbitrary structure, it is desirable for the model to have some connection to the physics of the system it represents. Hence, a grey-box identification approach was chosen, allowing for a priori system knowledge to be included in the model. The cycle-averaged dynamics of the DelFly are here represented by means of a linearised model structure derived from the general nonlinear fixed-wing rigid-body aircraft EOM. Whilst the DelFly differs in many ways from conventional aircraft, previous research showed these equations to be an adequate description for the considered flight conditions, at a cycle-averaged level [25].

A linearised model was opted for because this represents the simplest solution and one that offers many practical advantages. Further to this, previous work on the DelFly suggests that the time-averaged component of the dynamics, in a forward flight regime and within a limited part of the flight envelope, can be represented reasonably well by means of simple, linear models. It also shows that decoupled lateral and longitudinal models provide an adequate description in the aforementioned flight conditions [37].

Hence, the nonlinear fixed-wing rigid-body EOM were linearised around a typical forward flight condition of the DelFly. The standard small perturbations assumptions were

made, and additionally, to account for the large pitch attitude characterising the typical steady forward flight of the DelFly, the pitch attitude and the forward and vertical body-frame velocities were assumed to be non-zero at the linearisation point.

A linear model structure was then defined for each of the aerodynamic forces and moments, in the light of previous work suggesting that linear models describe a significant part of the DelFly aerodynamics in slow forward flight [16]. Only measurable and physically plausible states were included in the models, and the assumption of decoupling made for the dynamics was assumed to apply equally to the aerodynamics, resulting in the following equations,

$$X = X_q \Delta q + X_u \Delta u + X_w \Delta w + X_{\delta_e} \Delta \delta_e + mg \sin \Theta_0 \tag{3.1}$$

$$Y = Y_p \Delta p + Y_r \Delta r + Y_v \Delta v + Y_{\delta_r} \Delta \delta_r \tag{3.2}$$

$$Z = Z_q \Delta q + Z_u \Delta u + Z_w \Delta w + Z_{\delta_e} \Delta \delta_e - mg \cos \Theta_0 \tag{3.3}$$

$$L = L_p \Delta p + L_r \Delta r + L_v \Delta v + L_{\delta_r} \Delta \delta_r \tag{3.4}$$

$$M = M_q \Delta q + M_u \Delta u + M_w \Delta w + M_{\delta_e} \Delta \delta_e \tag{3.5}$$

$$N = N_p \Delta p + N_r \Delta r + N_v \Delta v + N_{\delta_r} \Delta \delta_r, \tag{3.6}$$

where all states and aerodynamic forces and moments are cycle-averaged. Control surface deflections are also cycle-averaged, to prevent the oscillations caused in them by the flapping from entering the model through the input. Finally, the DelFly was assumed to fly symmetrically, so that the only inertial components in the aerodynamics are those counterbalancing the weight, i.e., the mass-dependent terms in the X and Z equations.

Applying the simplifications discussed to obtain the system dynamics equations and substituting Eqs. (3.1)-(3.6) into the thus obtained EOM yields the following grey-box state-space model structures, for the DelFly cycle-averaged longitudinal dynamics,

$$
\begin{bmatrix} \Delta \dot{q} \\ \Delta \dot{u} \\ \Delta \dot{w} \\ \Delta \dot{\Theta} \end{bmatrix}
=
\begin{bmatrix}
\frac{M_q}{I_{yy}} & \frac{M_u}{I_{yy}} & \frac{M_w}{I_{yy}} & 0 \\
\frac{X_q}{m} - w_0 & \frac{X_u}{m} & \frac{X_w}{m} & -g\cos(\Theta_0) \\
\frac{Z_q}{m} + u_0 & \frac{Z_u}{m} & \frac{Z_w}{m} & -g\sin(\Theta_0) \\
1 & 0 & 0 & 0
\end{bmatrix}
\begin{bmatrix} \Delta q \\ \Delta u \\ \Delta w \\ \Delta \Theta \end{bmatrix}
+
\begin{bmatrix}
\frac{M_{\delta e}}{I_{yy}} & b_{\dot{q}} \\
\frac{X_{\delta e}}{m} & b_{\dot{u}} \\
\frac{Z_{\delta e}}{m} & b_{\dot{w}} \\
0 & b_{\dot{\Theta}}
\end{bmatrix}
\begin{bmatrix} \Delta \delta_e \\ 1 \end{bmatrix}, \tag{3.7}
$$

and lateral dynamics,

$$
\begin{bmatrix} \Delta \dot{p} \\ \Delta \dot{r} \\ \Delta \dot{v} \\ \Delta \dot{\Phi} \end{bmatrix}
=
\begin{bmatrix}
\frac{I_{zz}}{I_c} L_p + \frac{I_{xz}}{I_c} N_p & \frac{I_{zz}}{I_c} L_r + \frac{I_{xz}}{I_c} N_r & \frac{I_{zz}}{I_c} L_v + \frac{I_{xz}}{I_c} N_v & 0 \\
\frac{I_{xz}}{I_c} L_p + \frac{I_{xx}}{I_c} N_p & \frac{I_{xz}}{I_c} L_r + \frac{I_{xx}}{I_c} N_r & \frac{I_{xz}}{I_c} L_v + \frac{I_{xx}}{I_c} N_v & 0 \\
\frac{Y_p}{m} + w_0 & \frac{Y_r}{m} - u_0 & \frac{Y_v}{m} & g\cos\Theta_0 \\
1 & \tan\Theta_0 & 0 & 0
\end{bmatrix}
\begin{bmatrix} \Delta p \\ \Delta r \\ \Delta v \\ \Delta \Phi \end{bmatrix}
$$
$$
+
\begin{bmatrix}
\frac{I_{zz}}{I_c} L_{\delta_r} + \frac{I_{xz}}{I_c} N_{\delta_r} & b_{\dot{p}} \\
\frac{I_{xz}}{I_c} L_{\delta_r} + \frac{I_{xx}}{I_c} N_{\delta_r} & b_{\dot{r}} \\
\frac{Y_{\delta_r}}{m} & b_{\dot{v}} \\
0 & b_{\dot{\Phi}}
\end{bmatrix}
\begin{bmatrix} \Delta \delta_r \\ 1 \end{bmatrix} \tag{3.8}
$$

with $I_c = I_{xx} I_{zz} - I_{xz}^2$, and where Δ denotes perturbation values. In accordance with the linearised formulation, the states are perturbations from the steady condition, and the inertial components in Eqs. (3.1)-(3.6) are not included. The unknown parameters in the equations
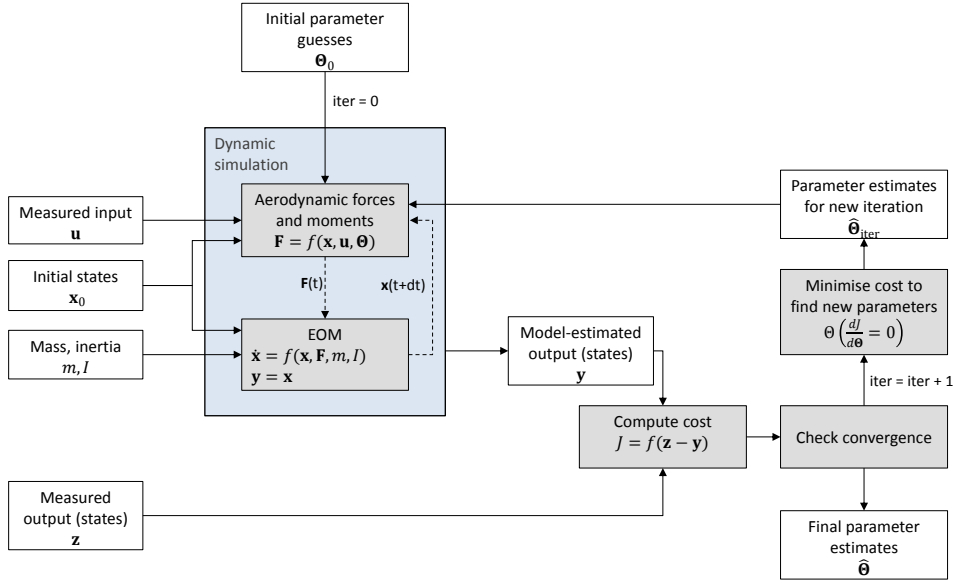
Figure 3.5: Parameter estimation framework: output error approach with maximum likelihood estimator.

represent the aerodynamic contribution. Additionally, a bias term was introduced in each equation by means of a unit input to compensate for possible measurement biases, and in particular for inaccuracies in the calculation of the trim condition and the perturbation values. Given that the mass and inertia of the platform are known [16], estimating the unknown parameters yields models for each of the aerodynamic terms as well as an overall linearised model for the DelFly.

To allow for simulation of the estimated models, in addition to the state-space systems in Eqs. (3.7)-(3.8), an equation for the yaw dynamics was required. Linearising the known kinematic expressions relating Euler angles and body rates under the same assumptions used previously yields:

$$\Delta\dot{\Psi} = \frac{\Delta r}{\cos\Theta_0 - \sin\Theta_0\Delta\Theta} \tag{3.9}$$

Finally, note that at this stage of the modelling process the measured data used for estimation are cycle-averaged and yield models for the cycle-averaged aerodynamic forces and moments only. Hence, running a simulation with the identified aerodynamic models will result in states that are likewise only cycle-averaged.

3.4.2. PARAMETER ESTIMATION

The unknown parameters in Eqs. (3.1)-(3.6) were estimated using a maximum likelihood (ML) estimator and an output error approach, as illustrated in Fig. 3.5 and described in this section. This estimation approach allows for measurement error in the states to be

considered, under the assumption that it is white and Gaussian, whereas process noise is not taken into account. The cost function for this type of problem can be defined as the negative logarithm of the likelihood function expressing the probability p of an observation $\mathbf{z}$ occurring at a particular time point k, given the parameter vector Θ:

$$J(\mathbf{\Theta}, \mathbf{R}) = -\ln p(\mathbf{z}|\mathbf{\Theta}) = \frac{1}{2}\sum_{k=1}^{n_k}[\mathbf{z}(k) - \mathbf{y}(k)]^T\mathbf{R}^{-1}[\mathbf{z}(k) - \mathbf{y}(k)] + \frac{n_k}{2}\ln(\det(\mathbf{R})) + \frac{n_k n_y}{2}\ln(2\pi)$$
(3.10)

where $\mathbf{R}$ is the measurement noise covariance matrix, n_k is the number of samples, n_y is the number of outputs, and $\mathbf{z}(k)$ and $\mathbf{y}(k)$ are the measured and model-predicted outputs, respectively, at time point k. The model-predicted outputs are a function of the parameter vector.

The matrix $\mathbf{R}$ appearing in the Eq. (5.22) is typically unknown, and can for instance be determined within each iteration step through a relaxation technique [41]. For this, the parameters are fixed at the value found in the previous iteration and the cost function is minimised with respect to $\mathbf{R}$, which gives the following estimate for $\mathbf{R}$:

$$\hat{\mathbf{R}} = \frac{1}{n_k}\sum_{k=1}^{n_k}[\mathbf{z}(k) - \mathbf{y}(k)][\mathbf{z}(k) - \mathbf{y}(k)]^T$$
(3.11)

Substituting the above expression into the cost function in Eq. (5.22) yields the cost at the current iteration step, which is used to determine whether the convergence criteria have been met. To estimate a new set of parameters for the successive iteration step, the noise covariance matrix determined from the previous set of parameters by means of Eq. (5.23) is substituted into the cost function in Eq. (5.22), and the cost function is now minimised with respect to the parameters, which are assumed to be unknown again. The minimisation of the cost yields the parameter update step and a new set of parameters for the following iteration. The minimisation process can be performed using any suitable algorithm; here, a Gauss-Newton technique was applied. More exhaustive information on ML-based estimation can be found in the literature [41–43], as well as in Appendix C (Sec. C.4).

For the estimation work presented here, the system states were used as outputs, and the system equations were formulated in state-space form, as in Eqs. (3.7-3.8) in Sec. 3.4.1. The longitudinal and lateral components of the model were estimated separately but using an analogous approach. In each case, the relevant states were used as outputs, leading to an output equation of the form: $\mathbf{z} = diag\{1,\ldots,1\}\mathbf{x}$. Thus, the cost function J in Eq. (5.22) was a function of the difference between measured and model-predicted states. The propagation of the states required within the estimation process was computed using Eqs. (3.7) and (3.8) for the longitudinal and lateral dynamics, respectively, by means of a fourth-order Runge-Kutta integrator. In the diagram in Fig. 3.5, this happens within the *dynamic simulation* block, where the known input, initial states, and mass and inertia properties are used to calculate the model-predicted states during each iteration. The two sub-blocks clarify that the aerodynamic models (*aerodynamic forces and moments* sub-block) are incorporated in the state-space model (*EOM* sub-block). Least squares regression was used to obtain initial guesses for the parameters (cf. Appendix C, Sec. C.4, for an overview of the least squares estimation process).

Table 3.1: Parameter estimates $\hat{\Theta}$ and estimated standard deviations $\hat{\sigma}$ for the identified cycle-averaged longitudinal model. A non-dimensional form of each parameter, computed as explained in Appendix E, is also presented.

Param.	$\hat{\Theta}$	$|\hat{\sigma}|$	$100|\hat{\sigma}/\hat{\Theta}|$	Non-dim. form	$\hat{\Theta}_{\text{nondim}}$
X_q	3.05×10^{-3}	2.90×10^{-5}	0.95	C_{xq}	1.10
X_u	-3.39×10^{-2}	1.48×10^{-4}	0.44	C_{xu}	-0.95
X_w	1.81×10^{-2}	8.58×10^{-5}	0.47	C_{xw}	0.51
X_{δ_e}	2.53×10^{-2}	2.23×10^{-4}	0.88	$C_{x\delta_e}$	0.26
Z_q	-1.31×10^{-2}	2.87×10^{-5}	0.22	C_{zq}	-4.71
Z_u	-3.21×10^{-2}	2.18×10^{-4}	0.68	C_{zu}	-0.90
Z_w	-7.74×10^{-2}	1.29×10^{-4}	0.17	C_{zw}	-2.16
Z_{δ_e}	-9.67×10^{-2}	1.93×10^{-4}	0.20	$C_{z\delta_e}$	-0.98
M_q	-1.03×10^{-3}	1.46×10^{-6}	0.14	C_{mq}	-4.80
M_u	3.90×10^{-3}	8.76×10^{-6}	0.22	C_{mu}	1.42
M_w	2.59×10^{-3}	4.15×10^{-6}	0.16	C_{mw}	0.94
M_{δ_e}	-6.96×10^{-3}	1.19×10^{-5}	0.17	$C_{m\delta_e}$	-0.91

3.4.3. TIME-AVERAGED MODELLING RESULTS

As several datasets were available, a number of separate models could be estimated. These were first evaluated separately, then compared to each other, considering the limitations dictated by the modelling approach. For both the longitudinal and the lateral dynamics, one model is discussed in some detail as a representative example, and a brief comparison is then made to the other models.

LONGITUDINAL MODELLING

The estimated parameters and corresponding estimated standard deviations obtained for the longitudinal example model are presented in Table 3.1. The estimated standard deviations are all below 1% of the corresponding parameter estimate values, suggesting an overall effective estimation process. Similarly, the correlation between the separate parameters was found to be acceptably low, mostly below 0.7, again pointing to an unproblematic estimation. Fig. 3.6 shows that the model-predicted states and aerodynamic forces and moment match the estimation data effectively, and the metrics reported in Table 3.2 corroborate the visual assessment. The model residuals were found to have approximately a zero mean and not to be excessively correlated to the measurements (cf. Appendix D for a brief evaluation of the residuals).

The exception to some of the above observations is the model for the X force, which appears to be less effective. In part this may be due to the relatively limited excitation of X in the data, however it can also be seen that the X response to the input seems to be somewhat nonlinear, so that the current model structure is insufficient to accurately represent it. Despite these limitations, the visible inaccuracy of the model for X is not noticeably reflected in the states, presumably because the constant component of the force that is counterbalancing the weight of the platform by far predominates over the transient effects.

The estimated model was also found to be fairly effective in predicting the response to validation manoeuvres in a comparable flight regime, as for instance shown in Fig. 3.7.

(a) States

(b) Aerodynamic forces and moments
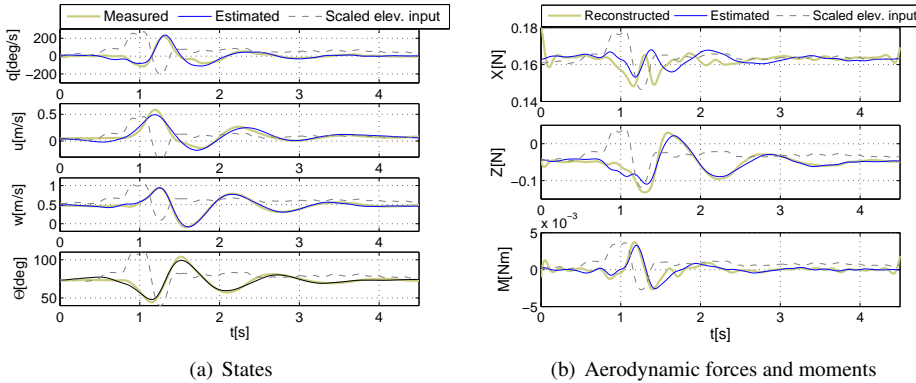
Figure 3.6: **Estimation** results for the time-averaged longitudinal model: measured identification data and model-estimated values for the states and the aerodynamic forces and moments.

(a) States

(b) Aerodynamic forces and moments
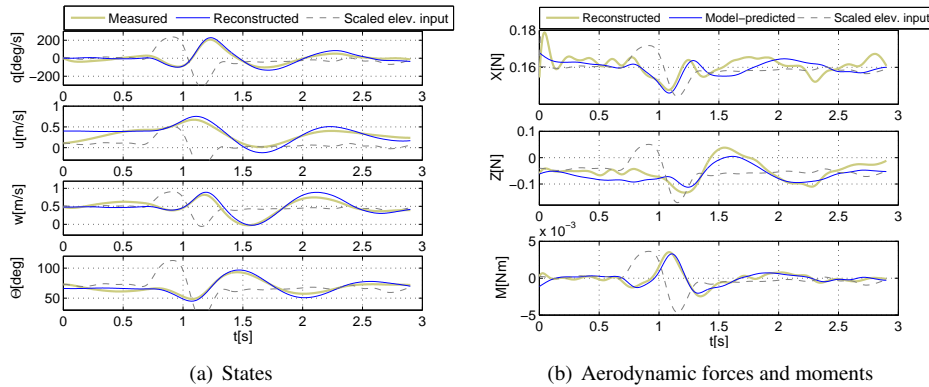
Figure 3.7: **Validation** example for the time-averaged longitudinal model: measured (or measurement-reconstructed) validation data and model-predicted values for the states and the aerodynamic forces and moments.

There are a number of small but noticeable discrepancies between measured and model-predicted values, particularly in the velocity u and in the force X. These differences may be partly due to a reduced excitation of certain components in the estimation data, as suggested earlier, or may stem from the inclusion of superfluous parameters or the absence of necessary parameters in the model, however this must be investigated further.

Further to the ability to reproduce the system behaviour effectively, it is useful to assess the physical plausibility of the model, in the light of what is known or expected of the system. Table 3.3 reports the eigenvalues of the estimated longitudinal model. The model is stable, which agrees with the observed flight behaviour of the DelFly, and is characterised by one high-frequency oscillatory mode and two aperiodic modes. The resulting dynamics, as for instance evaluated in terms of simulated responses to small elevator deflections, were found to be plausible, and the oscillatory mode in particular can be considered analogous

Table 3.2: Metrics quantifying the performance of the time-averaged longitudinal model as applied to the estimation dataset shown in Fig. 3.6 and to the validation dataset shown in Fig. 3.7.

Output variable	Match with estimation data				Match with validation data			
	Output corr.	R^2	RMSE	RMSE (% of meas. range)	Output corr.	R^2	RMSE	RMSE (% of meas. range)
q	0.95	0.87	$18.62\frac{\circ}{s}$	5.55%	0.95	0.90	$0.39\frac{\circ}{s}$	6.65%
u	0.96	0.91	$0.04\frac{m}{s}$	5.39%	0.88	-0.32	$0.19\frac{m}{s}$	25.64%
w	0.99	0.98	$0.02\frac{m}{s}$	2.39%	0.93	0.84	$0.10\frac{m}{s}$	9.34%
Θ	0.98	0.96	$1.99°$	3.34%	0.96	0.76	$0.12°$	10.83%

3

to the short period mode in fixed-wing aircraft.

The obtained estimates (cf. Table 3.1), many of which can be attributed a physical meaning, also largely seem plausible, particularly those of the more influential parameters. The pitch damping M_q is for instance negative, indicating a stable platform. There are a few anomalies, e.g., a positive M_u, which may be related to possible limitations in the estimation data and the model structure, but may also hint at dynamic behaviours specific to the DelFly. More extensive testing would be required for a better evaluation.

In a final stage a comparison was drawn between the models estimated from different datasets. Evidently, linear models are only valid for a particular flight condition and small differences between manoeuvres may have an effect on the resulting model. However, a comparison of the high-level dynamics of the models was considered justifiable as the manoeuvres were all recorded in similar flight conditions (cf. Fig. 3.3).

Table 3.3: Eigenvalues of the estimated time-averaged longitudinal model

$$-10.9638$$
$$-1.3538 + 5.6483i$$
$$-1.3538 - 5.6483i$$
$$-3.3945$$
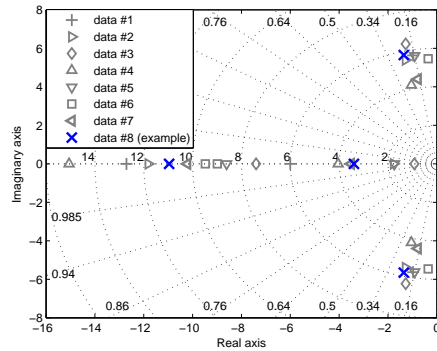
Figure 3.8: Eigenvalues of the time-averaged longitudinal models identified from 8 different elevator manoeuvres; the discussed example is indicated.

Fig. 3.8 shows the eigenvalues of the longitudinal models estimated from eight different datasets. All the models are stable, in agreement with the observed flight behaviour. In addition, they are all characterised by one very similar oscillatory mode. By contrast, the two aperiodic modes of the separate models differ more widely. This may be a consequence of the previously discussed possible limitations in the estimation data, which may have led to an increased uncertainty in the estimation process. It is also possible that the datasets,

Table 3.4: Parameter estimates $\hat{\Theta}$ and estimated standard deviations $\hat{\sigma}$ for the identified cycle-averaged lateral model. A non-dimensional form of each parameter, computed as explained in Appendix E, is also presented.

Param.	$\hat{\Theta}$	$|\hat{\sigma}|$	$100|\hat{\sigma}/\hat{\Theta}|$	Non-dim. form	$\hat{\Theta}_{\text{nondim}}$
Y_p	6.54×10^{-4}	2.42×10^{-4}	36.90	C_{yp}	0.14×10^{0}
Y_r	-2.59×10^{-3}	1.20×10^{-3}	46.22	C_{yr}	-5.35×10^{-1}
Y_v	-9.92×10^{-2}	2.37×10^{-3}	2.39	C_{yv}	-0.28×10^{0}
Y_{δ_r}	-6.96×10^{-2}	3.51×10^{-3}	5.04	$C_{y\delta_r}$	-7.17×10^{-1}
L_p	-7.14×10^{-6}	3.80×10^{-7}	5.33	C_{lp}	-5.38×10^{-3}
L_r	3.09×10^{-5}	1.81×10^{-6}	5.86	C_{lr}	2.33×10^{-2}
L_v	-4.47×10^{-5}	2.84×10^{-6}	6.36	C_{lv}	-4.62×10^{-3}
L_{δ_r}	6.89×10^{-5}	3.91×10^{-6}	5.67	$C_{l\delta_r}$	0.26×10^{-3}
N_p	-1.98×10^{-5}	3.61×10^{-6}	18.18	C_{np}	-1.49×10^{-2}
N_r	-4.79×10^{-4}	1.43×10^{-5}	2.98	C_{nr}	-3.61×10^{-1}
N_v	-1.45×10^{-3}	2.46×10^{-5}	1.70	C_{nv}	-1.50×10^{-1}
N_{δ_r}	-2.10×10^{-3}	2.81×10^{-5}	1.34	$C_{n\delta_r}$	-7.89×10^{-2}

3

which were all shorter than 5 seconds, were too short for slower dynamic modes to fully develop. However, the two aperiodic modes are still discernible, which suggests that the modes of the actual system should be somewhere within the range defined by the current values, and that more complete data might yield improved results.

Despite the limitations mentioned, the clear similarities in the high-level dynamics of all estimated models constitute a basic form of validation for the results. Furthermore, taken separately the models all display a fairly effective performance, analogous to that of the example model discussed, and validation results such as those in Fig. 3.7 show that the models obtained are effective at predicting the response to different manoeuvres in a similar flight regime. These observations suggest that the chosen approach and model structure are adequate, and that by means of more comprehensive estimation data more reliable results could be obtained, that address the current shortcomings.

LATERAL MODELLING

The estimated lateral cycle-averaged model is able to capture the basic progression of both the estimation data (Fig. 3.9) and validation data (e.g., Fig. 3.10), with output correlations ranging from 0.77 to 0.97. However, there are a number of discrepancies, which may indicate an insufficient amount of information in the estimation data or an inadequate model structure. Similarly, the estimated standard deviations of some of the parameters, presented in Table 3.4 are relatively high (up to 46%), suggesting that the estimation process can be improved. The roll rate in particular is estimated poorly. A possible explanation is that the rudder manoeuvres used for estimation did not sufficiently excite the roll dynamics. Since the DelFly configuration used for these tests had no direct roll input possibility, the roll dynamics could only be excited indirectly by means of rudder inputs, via roll-yaw coupling effects. It can also be observed that the rolling moment displays limited movement and hardly appears to be affected by the manoeuvre, which is presumably reflected in the poorly estimated roll rate.

3

(a) States

(b) Aerodynamic forces and moments
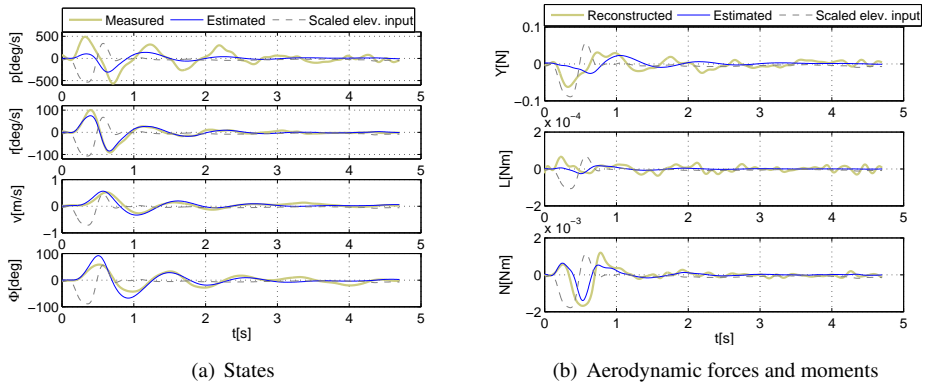
Figure 3.9: **Estimation** results for the time-averaged lateral model: measured (or measurement-reconstructed) identification data and model-estimated values for the states, and the aerodynamic forces and moments.

(a) States

(b) Aerodynamic forces and moments
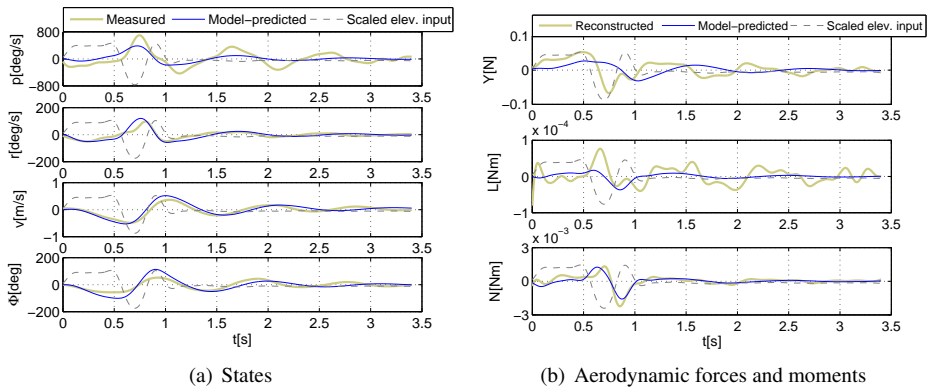
Figure 3.10: **Validation** example for the time-averaged lateral model: measured validation data and model-predicted values for the states and the aerodynamic forces and moments.

Table 3.5: Metrics quantifying the performance of the time-averaged lateral model as applied to the estimation dataset shown in Fig. 3.6 and to the validation dataset shown in Fig. 3.7.

Output variable	Match with estimation data				Match with validation data			
	Output corr.	R^2	RMSE	RMSE (% of meas. range)	Output corr.	R^2	RMSE	RMSE (% of meas. range)
p	0.77	0.48	$127.20\frac{°}{s}$	12.02	0.80	0.55	$143.24\frac{°}{s}$	12.91
r	0.97	0.94	$6.88\frac{°}{s}$	3.47	0.89	0.59	$16.62\frac{°}{s}$	11.15
v	0.90	0.75	$0.07\frac{m}{s}$	8.64	0.92	0.76	$0.09\frac{m}{s}$	10.66
Φ	0.90	0.69	$11.46°$	11.50	0.87	0.36	$23.49°$	21.62

The obtained model is stable and characterised by one oscillatory and two aperiodic eigenmodes (Table 3.6). The modes to some extent correspond to what has been observed in flight. Rudder input is for instance known to cause oscillatory roll-yaw motion, and a similar behaviour to the coordinated turn found in response to rudder steps has also been observed. However, given the previously discussed limitations in the estimation process, and considering the known complexity of the lateral dynamics and control mechanism of the DelFly, additional testing is required to obtain a more comprehensive and reliable picture.

The limitations in the discussed example model also appear in the models obtained from other datasets, and it can additionally be noted that the estimated models vary more significantly among themselves than in the longitudinal case. This is probably a consequence of the diminished quality of the estimation process and resulting models. The higher estimated standard deviation that characterises some of the parameter estimates regardless of the dataset they are estimated from, limits the confidence that can be placed in any one estimated value and is likely to lead to a larger overall variation. In spite of this, the poles of the separate models still display two visible clusters. As in the longitudinal case, the oscillatory eigenmode is similar for all the estimated models, and with one exception all models are stable, as expected. The aperiodic modes are scattered and it is difficult to determine even ranges to characterise them.

Table 3.6: Eigenvalues of the estimated time-averaged lateral model

$-1.3186 + 5.7559i$
$-1.3186 - 5.7559i$
-5.0708
-9.1591
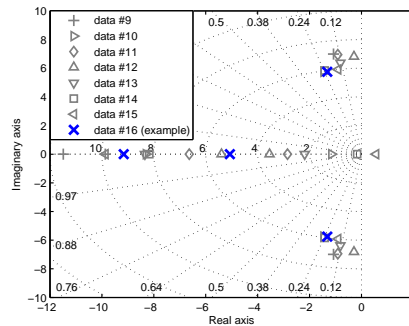
Figure 3.11: Eigenvalues of the time-averaged lateral models identified from 8 different rudder manoeuvres; the discussed example is indicated.

The overall less satisfactory performance of the lateral models compared to the longitudinal ones has several possible explanations. Firstly, lateral excitation through the rud-

der only may be insufficient. Secondly, the chosen model structures may not sufficiently account for roll-yaw coupling effects, which are known to be significant for the DelFly. Thirdly, the model structure does not account for coupling between the longitudinal and lateral dynamics, and flight test measurements suggest that an elevator input does have at least a small effect on the lateral states.

In particular, it was found to be difficult to excite the lateral dynamics without also exciting the longitudinal dynamics, possibly because the elevator is always oscillating due to the flapping motion. In all the rudder manoeuvres there is still considerable movement of the elevator, sometimes of a comparable order of magnitude. This leads to effects that are not accounted for in the model structure. This issue may be resolvable by including some degree of coupling in the model, which however would require more complex model structures.

Finally, the diminished performance of the lateral models may be related to the chosen *aerodynamic* model structure. These models were defined based on engineering judgement and it is possible that including additional terms or using more complex model structures would provide a more accurate result. Further investigation into the aerodynamic model structure is advisable.

3.5. TIME-VARYING MODELLING

This section outlines the modelling of the fast time-scale dynamics, and the insight and results obtained in the process. To limit the scope of this investigation, only the longitudinal component of the flapping dynamics is considered at this stage.

As mentioned in Sec. 3.2, the cycle-averaged and time-varying components were defined in terms of the aerodynamic forces and moments. Whereas the time-averaged component was still modelled as a full dynamic system, comprising both the aerodynamics and the body dynamics, the time-varying component was modelled exclusively in terms of the aerodynamics. Furthermore, the chosen model structure for the time-varying component, which will be presented below, is not affected by the time-averaged model states, hence there is no need to include the system dynamics in the estimation process. The time-varying component was thus defined only for the aerodynamics. In a final step, the models for the time-varying and time-averaged aerodynamics were combined and inserted into the EOM defined in Eq. (3.7) to give a model of the full, time-varying system.

3.5.1. IDENTIFICATION OF FAST TIME-SCALE DYNAMICS

A Fourier series expansion was selected as the model structure to represent the time-varying component of the aerodynamics. Time-scale separation implies that as long as there is no excitation at a sub-flap cycle level, the behaviour within each flap cycle is exactly the same, regardless of what is happening in the body dynamics. In the absence of disturbances, the global behaviour is therefore assumed to be periodic and can be modelled with a Fourier series. A drawback of this approach is that the model is not physical, however at this stage our knowledge of the flapping dynamics is limited, and the aim of the current study was to obtain an initial data-based model. The time-varying component of the aerodynamic forces and moments was thus assumed to be representable by a trigonometric Fourier series

Table 3.7: Parameter estimates $\hat{\Theta}$ and estimated standard deviations $\hat{\sigma}$ for the identified fast time-scale longitudinal model

	X_{TV} **equation parameters**				Z_{TV} **equation parameters**				M_{TV} **equation parameters**		
Param.	$\hat{\Theta}$	$|\hat{\sigma}|$	$100|\hat{\sigma}/\hat{\Theta}|$	Param.	$\hat{\Theta}$	$|\hat{\sigma}|$	$100|\hat{\sigma}/\hat{\Theta}|$	Param.	$\hat{\Theta}$	$|\hat{\sigma}|$	$100|\hat{\sigma}/\hat{\Theta}|$
$a_{x,1}$	-7.09×10^{-3}	5.13×10^{-3}	72.35	$a_{z,1}$	4.02×10^{-2}	5.63×10^{-3}	14.00	$a_{m,1}$	-3.58×10^{-4}	2.84×10^{-4}	79.23
$b_{x,1}$	8.89×10^{-2}	5.09×10^{-3}	5.72	$b_{z,1}$	-5.64×10^{-2}	5.58×10^{-3}	9.88	$b_{m,1}$	3.20×10^{-3}	2.81×10^{-4}	8.81
$a_{x,2}$	3.09×10^{-2}	5.12×10^{-3}	16.57	$a_{z,2}$	-5.51×10^{-3}	5.61×10^{-3}	101.96	$a_{m,2}$	-5.15×10^{-4}	2.83×10^{-4}	55.02
$b_{x,2}$	2.75×10^{-2}	5.10×10^{-3}	18.51	$b_{z,2}$	4.24×10^{-2}	5.59×10^{-3}	13.17	$b_{m,2}$	2.69×10^{-3}	2.82×10^{-4}	10.49
$a_{x,3}$	7.32×10^{-3}	5.10×10^{-3}	69.69	$a_{z,3}$	1.42×10^{-2}	5.60×10^{-3}	39.36	$a_{m,3}$	5.44×10^{-4}	2.83×10^{-4}	51.94
$b_{x,3}$	1.83×10^{-2}	5.11×10^{-3}	27.86	$b_{z,3}$	1.29×10^{-2}	5.61×10^{-3}	43.49	$b_{m,3}$	8.35×10^{-4}	2.83×10^{-4}	33.90

expansion:

$$F_{TV}(t) = \sum_{n=1}^{h} \left[a_n \sin\left(2\pi n f t\right) + b_n \cos\left(2\pi n f t\right) \right], \tag{3.12}$$

where F_{TV} represents the time-varying component of any one of the aerodynamic forces and moments, h is the number of harmonics chosen, f is equal to the flapping frequency, t is time, and a_n and b_n are the nth Fourier coefficients.

A Fourier series expansion up to the third harmonic, $h = 3$, was selected based on the frequency content of the measured data [44]. In order to apply this type of model, the only measurement required is the flapping frequency, which can be considered the 'input' signal. This does not pose a problem as the flapping frequency is measurable in flight. Moreover, defining the flapping frequency as an input can be considered acceptable on a theoretical plane, given that the frequency can indeed be actively influenced in flight to adjust the amount of lift created. A minor issue with this formulation is that it focuses on capturing the frequency content and may result in phase-shifted time-domain results, e.g., if the model is validated with data that begins at a different stage of the flap cycle. However, this can be rectified by means of subsequent phase-shifting to align the model-predicted values with the measurements.

The unknown parameters appearing within the proposed models were determined through system identification, applied exclusively to the time-varying component of the data, computed as outlined in Sec. 3.3.2. An ML estimator was used for the estimation process, analogous to that for the time-averaged modelling described in Sec. 3.4.2. Here, the output measurements are the time-varying components of the aerodynamics forces X and Z and moment M, and the output equation is given directly by the Fourier series in Eq. (3.12). The estimation process is considerably simplified because the model is a pure input-output model and there is no need for dynamic simulation within the estimation process. As for the time-averaged modelling, initial guesses for the parameters were determined using an ordinary least squares estimator.

3.5.2. TIME-VARYING MODELLING RESULTS

This section presents the models identified for the flapping component of the longitudinal aerodynamics of the DelFly, using the suggested approach and the same example dataset as used for the time-averaged modelling. The flapping frequency for this sample was 12.5Hz. The estimated parameters are reported in Table 3.7.

Fig. 3.12 shows the match of the estimated Fourier series models with the corresponding estimation data, in the time domain and the frequency domain. It can be observed that the

model is effective at capturing particularly the first frequency peak, representing the flapping frequency, and the second peak, but even the third peak is estimated fairly effectively. At higher frequencies, it becomes increasingly difficult to distinguish flapping-related peaks from noise, nonetheless it can be seen that the Fourier series approximation provides the potential for representing possible higher harmonics. Although non-periodic components cannot be captured, periodic ones are captured effectively.
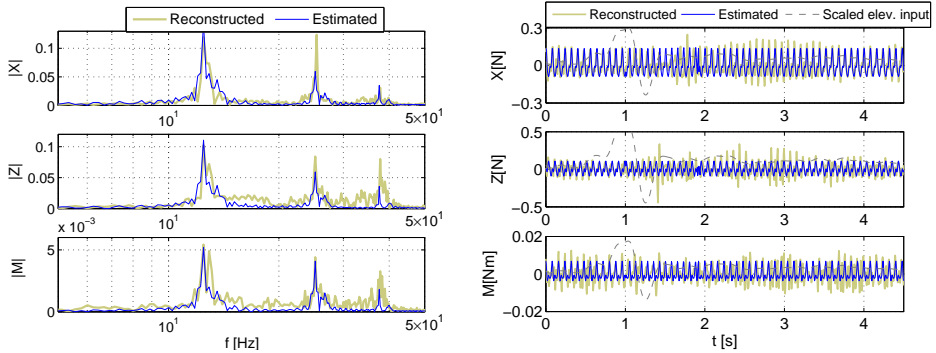
Figure 3.12: **Estimation** result: model-estimated values for the time-varying component of the longitudinal aerodynamic forces X and Z and moment M, versus measurement-reconstructed values obtained via filtering (cf. Sec. 3.3.2). The scaled input signal shows where the manoeuvre begins in the time domain.

At the same time it is evident, considering the observations made previously regarding the measured data, that the chosen model structure does not allow for all the content in the measurement-reconstructed aerodynamics to be replicated. The identified models match the time-varying component of the data effectively, providing a useful approximation for it, but they also underline that there seems to be a non-periodic component in the fast time-scale dynamics. It may well be that the non-periodic component has no significant effect on the low-frequency body dynamics, however this is not demonstrated and will be investigated in future research.

The time-domain match in Fig. 3.12 also suggests that the input manoeuvre may have some influence on the aforementioned non-periodic effect. Particularly in the two force components, the measurement-obtained progression seems to become more irregular following the elevator deflection. The same effect can also be observed in the validation example in Fig. 3.13(b). Note that to allow for a clearer comparison to the validation data, the time-domain results were phase-shifted to be aligned with the measurements at the start of the dataset, and the flapping frequency was the same (12.5Hz) in both estimation and validation data.

In a first attempt to investigate the issue, but also to obtain more accurate models for a steady flight condition, the identification process was repeated using only steady-state flight data, involving no significant control surface deflections. The initial assumption that the two time scales are decoupled implies that manoeuvring should not affect the fast time-scale dynamics, hence this is a way of assessing whether the non-periodicity in the original estimation dataset indeed appears to be a consequence of the manoeuvre being flown, or

(a) Validation example with **steady-state data**

(b) Validation example with **manoeuvre data**
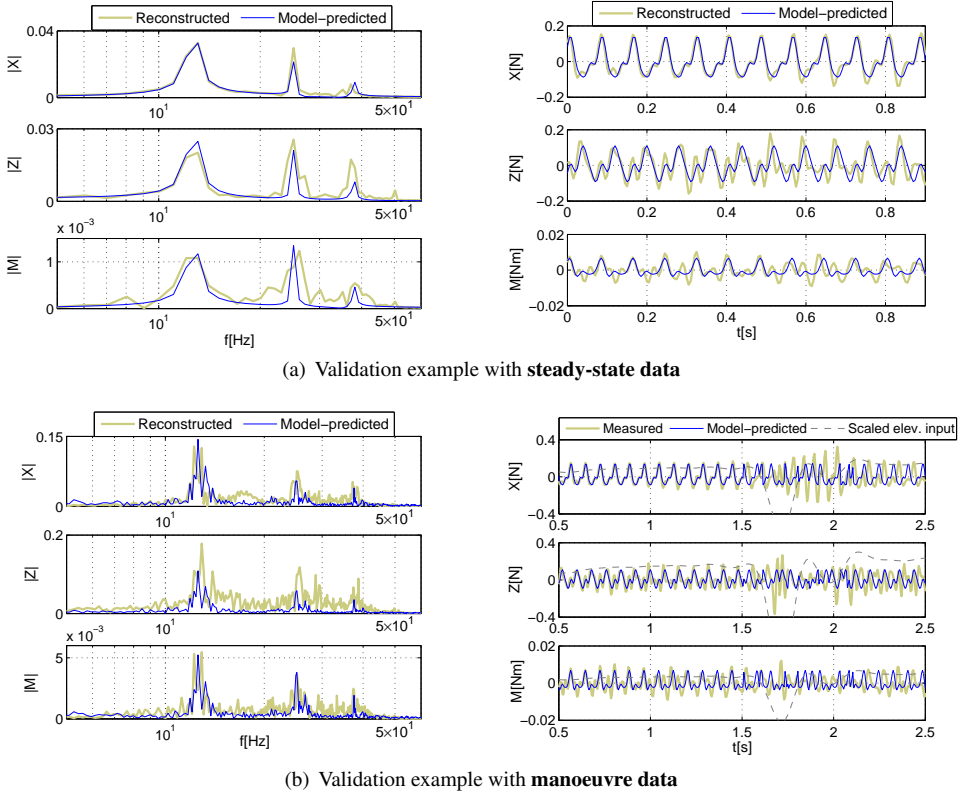
Figure 3.13: **Validation** examples for the time-varying component of the aerodynamics alone. The top row shows the validation with steady-state data, the bottom row the validation with manoeuvre data. The scaled input signal shows where the manoeuvre begins in the time domain.

whether it can be attributed to other causes. Additionally, given that the chosen model structure is designed to capture periodic components and cannot account for possible interactions between the time scales, a more accurate and theoretically sound result, valid at least for steady-state flight, may be obtained using steady-state data only.

The results of this test are presented in Fig. 3.14. The estimation data alone already show that, in a steady state, the fast time-scale progression is highly periodic and the assumption of decoupling applies very effectively. This is particularly evident in the frequency spectrum, where the peaks are much clearer than for manoeuvre datasets, underlining the pronounced periodicity of the aerodynamic force and moment progression in steady flight. It is possible that in steady-state flight there is also less measurement noise, which would also lead to a more regular progression, however this would manifest itself mostly in the higher frequency range.

Regardless of the cause, steady-state data were found to yield a significantly more accurate model of the time-varying component of the aerodynamics, which is at least valid in steady flight. In view of the previous results, this suggests that manoeuvring may have
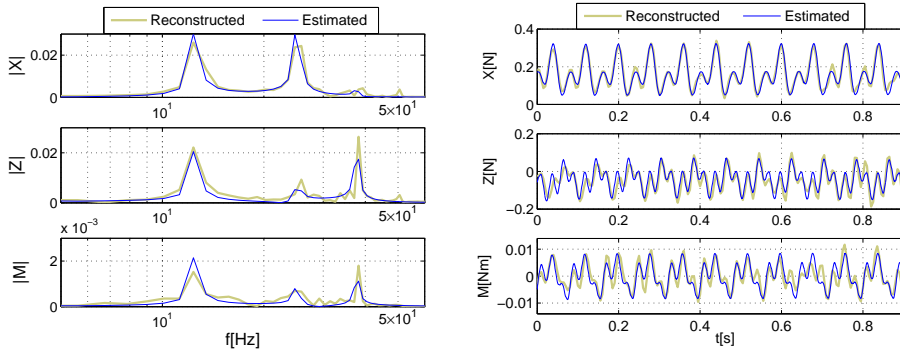
Figure 3.14: **Estimation** result: model-estimated values for the time-varying component of the longitudinal aerodynamic forces *X* and *Z* and moment *M*, versus real values obtained via filtering (cf. Sec. 3.3.2), for approximately **steady-state flight** and a flapping frequency of 12.5Hz.

some effect on the flapping process and that there may be some interaction between the two time scales. It should also be remarked, however, that whilst manoeuvring appears to influence the flapping, it remains difficult to evaluate whether, and to what extent, the flapping influences the body dynamics, and this must be researched. Slow changes in the flapping mechanism clearly affect the aerodynamics, but at this stage it cannot be evaluated whether changes occurring only within the single flap cycle have any significant effect on the body dynamics. Some form of systematic excitation at sub-flap cycle level would be required to make a better evaluation.

The steady-state evaluation highlights possible time-scale couplings and suggests that the current approach, using Fourier series and assuming time-scale separation, is more suited, theoretically and practically, to obtain models for steady-state flight. However, given that the final aim is to model manoeuvring flight, we retain the models identified from manoeuvre data for our final evaluation. Although models estimated from steady-state data are a more accurate representation of steady-state flight than models estimated from manoeuvre data, they are not necessarily a more accurate representation of manoeuvring flight. Rather, in manoeuvring flight different *model structures* may provide more accurate results.

With the current setup, the use of manoeuvre data for estimation is still considered preferable, as well as being necessary in view of the suggested overall approach. System identification generally requires estimation data to be collected in conditions as similar as possible to those the model should describe. In this sense, manoeuvre data are more relevant and informative, as they represent the conditions we are attempting to model. Although with the current model structure time-scale coupling effects cannot be captured, it is our intention to investigate such effects starting from the current results, and it is therefore considered more convenient to use manoeuvre data for both components. Finally, the suggested methodology of using *the same* dataset to estimate both the time-averaged and the time-varying component in fact requires the estimation dataset to include manoeuvring, as otherwise the time-averaged component cannot be estimated due to lack of excitation. Hence, all further evaluations refer to the model estimated from manoeuvre data.

On a practical level, the estimated models perform adequately (cf. Table 3.8) in both the

Table 3.8: Residual RMS of the time-varying longitudinal model when applied to the estimation dataset and to a validation dataset.

	Match with estimation data			Match with validation data	
Output	RMSE[N]	[% of meas. range]		RMSE[N]	[% of meas. range]
X_{TV}	0.07	16.6		0.10	25.2
Z_{TV}	0.08	9.8		0.11	13.0
M_{TV}	0.004	17.9		0.01	17.0

frequency domain and the time domain, when applied to validation datasets, as for instance shown in Fig. 3.13. Particularly the forces are predicted accurately. It is interesting to observe the effect of the elevator deflection on model performance. In steady flight, i.e., in Fig. 3.13(a) and in the first 1.5 seconds of Fig. 3.13(b), the model-estimated values replicate the highly periodic validation data with significant accuracy. Once the elevator is deflected, however, the data display some form of response which interferes with their periodicity and no longer allows the models to reproduce them as accurately.

In spite of this effect, RMSE values remain below 25%, which can be considered satisfactory particularly considering the small order of magnitude of the outputs. Thus, despite the limited accuracy of the models during manoeuvres and the small discrepancies that can be observed even in the steady state, the models can be considered effective as a first approximation.

3.6. THE COMBINED MODEL

The final step in evaluating our approach consists of combining the time-averaged and time-varying models derived in the previous sections and simulating the resulting full system. This was done according to a superposition approach, as illustrated in Fig. 3.1. Again, the flapping frequency was assumed to be measurable in flight at each time step and was therefore considered a known system input. Each aerodynamic term was calculated as a sum of the time-averaged component (cf. Eq. (3.1)) and the time-varying component (cf. Eq. (3.12)), resulting in the following overall equations,

$$X = X_{TA} + X_{TV} \tag{3.13}$$

$$= X_q \Delta q + X_u \Delta u + X_w \Delta w + X_{\delta_e} \Delta \delta_e + mg \sin \Theta_0 + \sum_{n=1}^{3} \left[a_{x,n} \sin(2\pi n f t) + b_{x,n} \cos(2\pi n f t) \right]$$

$$Z = Z_{TA} + Z_{TV} \tag{3.14}$$

$$= Z_q \Delta q + Z_u \Delta u + Z_w \Delta w + Z_{\delta_e} \Delta \delta_e - mg \cos \Theta_0 + \sum_{n=1}^{3} \left[a_{z,n} \sin(2\pi n f t) + b_{z,n} \cos(2\pi n f t) \right]$$

$$M = M_{TA} + M_{TV} \tag{3.15}$$

$$= M_q \Delta q + M_u \Delta u + M_w \Delta w + M_{\delta_e} \Delta \delta_e + \sum_{n=1}^{3} \left[a_{m,n} \sin(2\pi n f t) + b_{m,n} \cos(2\pi n f t) \right]$$

To clarify, note that the time-varying component, as currently defined, depends wholly on measured input values, thus the simulation process and the estimated time-averaged

states have no effect on it. However, at each time step, once the total aerodynamic terms have been computed from the aforementioned superposition, these are inserted into the EOM (Eq. (3.7)) and used to calculate the propagation of the system states. In this way, the time-varying nature of the aerodynamics is transmitted to the states.
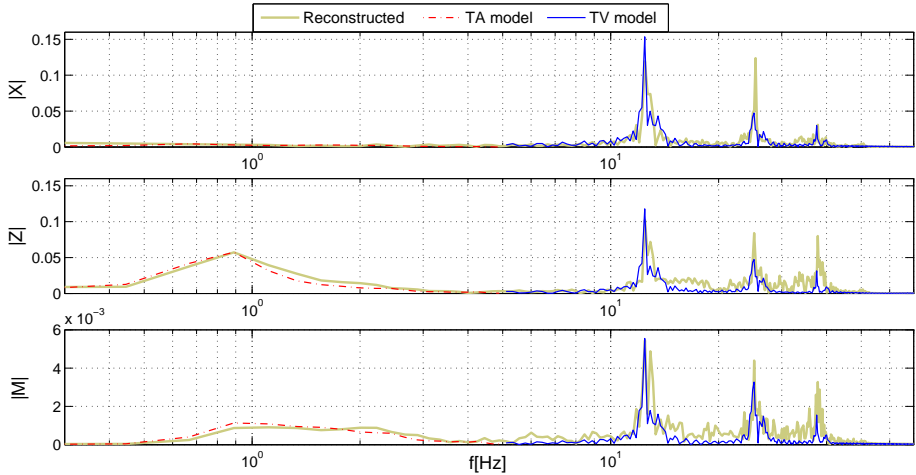
Figure 3.15: Linear addition of the separate time-averaged (TA) and time-varying (TV) models in the frequency domain.

Fig. 3.15 visually illustrates how the components are combined. As shown, the cycle-averaged sub-model accurately captures the low-frequency content of the measurements, and the time-varying sub-model provides a good approximation for the high-frequency content, so that combined the two sub-models yield a complete, straightforward and fairly accurate description of the full aerodynamic measurements. The results of the simulation process for the longitudinal dynamics are shown in Fig. 3.16. The time-averaged component is that identified in Sec. 3.4.3, and the time-varying component is modelled using the Fourier series model suggested in Sec. 3.5.2.

These results allow a more practical evaluation of the models to be made. Whilst it was previously pointed out that the time-varying sub-models do not capture the non-periodic content in the measurements, e.g., components that result from control surface deflections, it can be observed that the effect of this on the overall outcome is small. In fact, the Fourier series models provide a good first approximation of the flapping behaviour, sufficient for purposes of simulation. The agreement with validation data, Fig. 3.17, is also adequate and displays similar properties. The first three frequency peaks in the aerodynamics and in the states are replicated with adequate accuracy, and this can also be clearly seen in the time response. The measurements display one main peak and one smaller peak within each flap cycle, and both of these are captured well by the model. Looking at the data also suggests that whilst it may be theoretically interesting to model more peaks, these may have no significant impact, as already the third peak is hardly visible in the time response, particularly in the states.

From the current results and from the observed flight behaviour, it cannot be concluded

(a) States

(b) Aerodynamic forces and moments
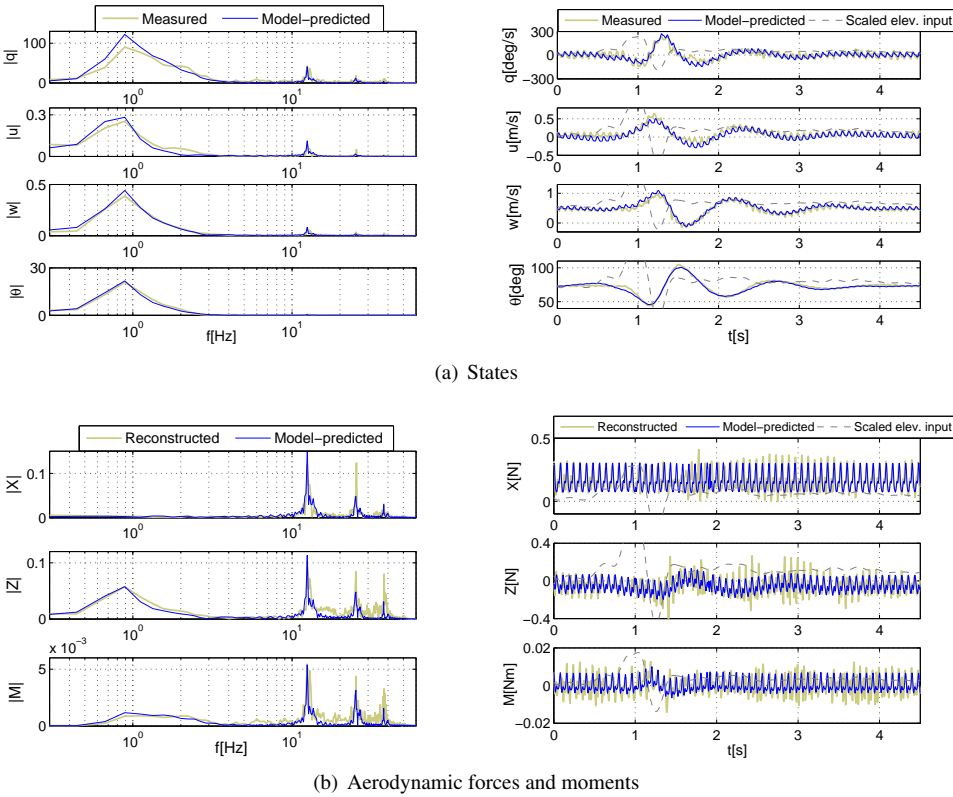
Figure 3.16: **Simulation** of the full model of the DelFly, consisting of the time-averaged sub-model presented in Sec. 3.4.3, and the time-varying sub-model presented in Sec. 3.5.2.

whether the interactions between the flapping component and the time-averaged component have a significant effect on the body dynamics: this should be investigated further. A closer look at the data also highlights that whereas the flapping dynamics have a very limited effect on the states, which are dominated by the cycle-averaged body dynamics, the flapping appears to significantly affect the aerodynamic forces and moments, which calls for further investigation.

3.7. CONCLUSIONS

System identification was used to estimate models for the aerodynamics and dynamics of a flapping-wing micro aerial vehicle (FWMAV) from optical tracking flight data. Under the assumption that the time-averaged and time-varying components can be decoupled, the aerodynamic model was formulated as a superposition of separate sub-models for each of the two aforementioned components. The time-averaged aerodynamic forces and moments were assumed to be a linear combination of states. The time-varying component was modelled as a Fourier series expansion. The models were inserted into a linearisation of the

(a) States

(b) Aerodynamic forces and moments
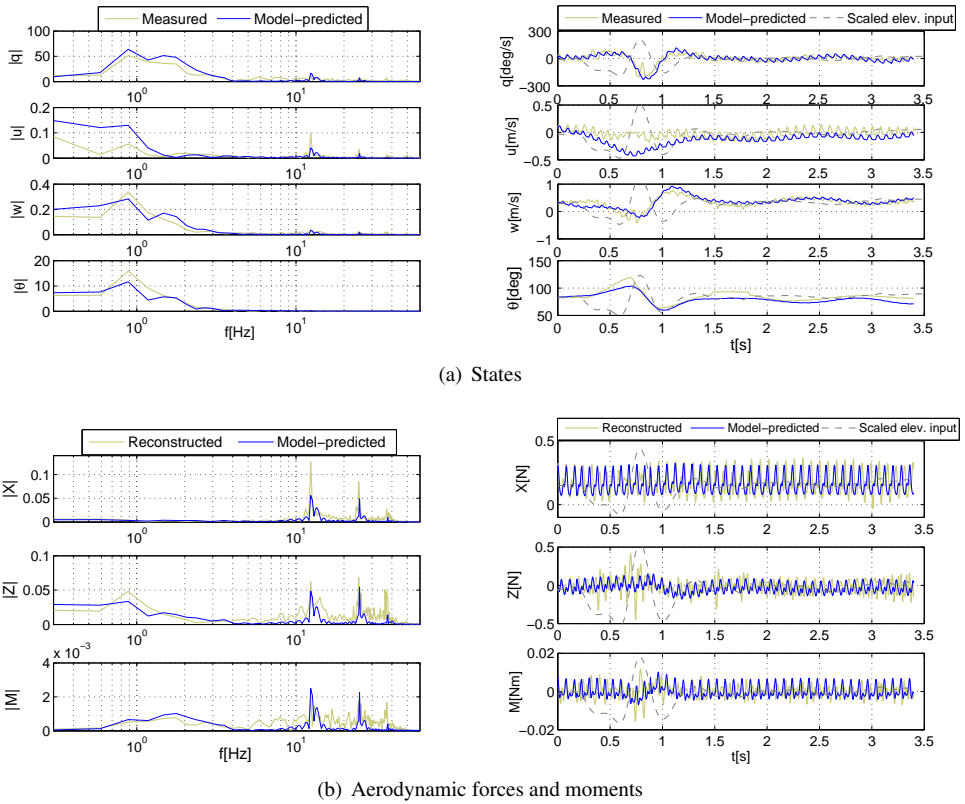
Figure 3.17: **Validation** example for the full model, consisting of the time-averaged sub-model presented in Sec. 3.4.3, and the time-varying sub-model presented in Sec. 3.5.2.

nonlinear, fixed-wing equations of motion to drive simulations.

Results show that linear time-invariant model structures can provide an effective description of the flap cycle-averaged system dynamics and aerodynamics in forward flight, particularly for the longitudinal component. This is also supported by validation results (RMSE<26%) and reflected in the low variances and correlations of the parameter estimates. The DelFly was found to have one oscillatory and two aperiodic stable eigenmodes for both the longitudinal and the lateral dynamics. The obtained system dynamics are largely plausible and agree with the observed flight behaviour of the platform. Only a small number of parameters appear to be estimated less well, possibly because they are superfluous to the model or because the estimation data contained insufficient information for their estimation. The lateral dynamics models are less accurate than the longitudinal ones and improvements may be achieved by using more adequate data, addressing coupling effects and investigating the effectiveness of the chosen model structure.

A comparison amongst models obtained from different datasets shows a good agreement in terms of the estimated system dynamics, corroborating the findings made. Whilst

the chosen model structure cannot account for nonlinearities or longitudinal-lateral coupling, its simplicity is very amenable for many purposes.

The time-varying component was found to be adequately approximated by the Fourier series models, which captured the first three harmonics in the data effectively. The time-scale separation approach was found to provide a good solution for including basic flapping effects in the overall model. However, interactions between the time-averaged and time-varying components were observed, and more complex models would be required to capture these.

Further, it was remarked that these interactions appear to be at least partly related to the manoeuvring of the vehicle at a cycle-averaged level, whereas in steady-state flight the fast time-scale behaviour is indeed almost entirely periodic. For this reason, the current time-varying model can be considered effective particularly as a representation of flapping effects in steady-state flight. Whilst the slow time-scale body dynamics appear to have a noticeable effect on the fast time-scale dynamics, the opposite cannot be assessed at this stage. This issue should be investigated further and may provide more in-depth understanding of the physical mechanism of flapping.

The combination of the identified time-varying and time-averaged sub-models yields a useful and accurate model for the aerodynamics and dynamics of the DelFly, based entirely on flight data. The model is computationally simple and well-suited for simulation and control purposes. The inclusion of the flapping component in particular is useful both for the testing of novel guidance and control algorithms and for the design of on-board instrumentation.

REFERENCES

[1] S. F. Armanini, C. C. de Visser, G. C. H. E. de Croon, and M. Mulder, *Time-varying model identification of flapping-wing vehicle dynamics using flight data,* Journal of Guidance, Control, and Dynamics **39**, 526 (2016).

[2] G. C. H. E. de Croon, K. M. E. de Clercq, R. Ruijsink, B. D. W. Remes, and C. de Wagter, *Design, aerodynamics, and vision-based control of the DelFly,* International Journal of Micro Air Vehicles **1**, 71 (2009).

[3] M. Keennon, K. Klingebiel, and H. Won, *Development of the nano hummingbird: A tailless flapping wing micro air vehicle,* in *50TH AIAA Aerospace Sciences Meeting incl. New Horizons Forum and Aerospace Exposition*, AIAA Paper 2012-0588 (2012).

[4] R. Wood, *The first takeoff of a biologically-inspired at-scale robotic insect,* IEEE Transactions on Robotics **24(2)**, 341 (2008).

[5] W. Shyy, Y. Lian, and J. Tang, *Aerodynamics of low Reynolds number flyers*, Cambridge aerospace series (Cambridge University Press, 2008).

[6] C. P. Ellington, C. van den Berg, A. P. Willmott, and A. L. R. Thomas, *Leading-edge vortices in insect flight,* Nature **384**, 626 (1996).

[7] H. Nagai, K. Isogai, T. Fujimoto, and T. Hayase, *Experimental and Numerical Study of Forward Flight Aerodynamics of Insect Flapping Wing,* AIAA Journal **47**, 730 (2009).

[8] R. Ramamurti and W. C. Sandberg, *A three-dimensional computational study of the aerodynamic mechanisms of insect flight,* **1518**, 1507 (2002).

[9] S. A. Ansari, R. Żbikowski, and K. Knowles, *Non-linear unsteady aerodynamic model for insect-like flapping wings in the hover. Part 2: implementation and validation,* Proceedings of the Institution of Mechanical Engineers, Part G: Journal of Aerospace Engineering **220**, 169 (2006).

[10] X. Deng, L. Schenato, W. C. Wu, and S. Shankar Sastry, *Flapping Flight for Biomimetic Robotic Insects : Part I - System Modeling,* IEEE Transactions on Robotics **22**, 776 (2006).

[11] J. DeLaurier, *An Aerodynamic Model For Flapping-Wing Flight,* The Aeronautical Journal of the Royal Aeronautical Society (1993).

[12] S. P. Sane, *The aerodynamics of insect flight,* Journal of Experimental Biology **206**, 4191 (2003).

[13] G. J. Berman and Z. J. Wang, *Energy-minimizing kinematics in hovering insect flight,* Journal of Fluid Mechanics **582**, 153 (2007).

[14] D. O. Sigthorsson, M. W. Oppenheimer, and D. B. Doman, *Flapping Wing Micro Air Vehicle Aerodynamic Modeling Including Flapping and Rigid Body Velocity,* in *50th AIAA Aerospace Sciences Meeting* (2012).

[15] J. Grauer, E. Ulrich, J. E. Hubbard, D. Pines, and J. S. Humbert, *Testing and System Identification of an Ornithopter in Longitudinal Flight,* Journal of Aircraft **48**, 660 (2011).

[16] J. V. Caetano, C. C. de Visser, B. D. W. Remes, C. de Wagter, and M. Mulder, *Modeling a Flapping Wing MAV: Flight Path Reconstruction of the DelFly II,* in *AIAA Modeling and Simulation Technologies Conference*, AIAA Paper 2013-4597 (2013).

[17] A. Gogulapati and P. P. Friedmann, *Approximate Aerodynamic and Aeroelastic Modeling of Flapping Wings in Hover and Forward Flight,* in *52nd AIAA/ASME/AHS/ASC Structures, Structural Dynamics and Materials Conference* (2011).

[18] W. Buler, L. Loroch, and K. Sibilski, *Modeling and simulation of the nonlinear dynamic behavior of a flapping wings micro-aerial-vehicle,* in *42nd AIAA Aerospace Sciences Meeting and Exhibit* (2004).

[19] M. Lasek and K. Sibilski, *Modelling and simulation of flapping wing control for a micromechanical flying insect (entomopter),* in *AIAA Modeling and Simulation Technologies Conference and Exhibit* (2002).

[20] M. A. Bolender, *Rigid multi-body equations-of-motion for flapping wing MAVs using Kane equations,* in *AIAA Guidance, Navigation, and Control Conference*, AIAA Paper 2009-6158 (2009).

3

[21] J. A. Grauer and J. E. Hubbard, *Multibody Model of an Ornithopter,* Journal of Guidance, Control, and Dynamics **32**, 1675 (2009).

[22] G. Gebert and P. Gallmeier, *Equations of motion for flapping flight,* in *AIAA Atmospheric Flight Mechanics Conference and Exhibit*, AIAA Paper 2002-4872 (2002).

[23] C. T. Orlowski and A. R. Girard, *Averaging of the nonlinear dynamics of flapping wing micro air vehicles for symmetrical flapping,* in *AIAA Aerospace Sciences Meeting including the New Horizons Forum and Aerospace Exposition* (2011).

[24] G. K. Taylor and A. L. R. Thomas, *Dynamic flight stability in the desert locust Schistocerca gregaria,* Journal of Experimental Biology **206**, 2803 (2003).

[25] J. V. Caetano, M. B. Weehuizen, C. C. de Visser, G. C. H. E. de Croon, and M. Mulder, *Rigid-Body Kinematics Versus Flapping Kinematics of a Flapping Wing Micro Air Vehicle,* Journal of Guidance, Control, and Dynamics **38**, 2257 (2015).

[26] R. C. Julian, C. J. Rose, H. Hu, and R. S. Fearing, *Cooperative Control and Modeling for Narrow Passage Traversal with an Ornithopter MAV and Lightweight Ground Station,* in *International Conference on Autonomous Agents and Multi-Agent Systems* (2013).

[27] M. Sun and Y. Xiong, *Dynamic flight stability of a hovering bumblebee,* Journal of Experimental Biology **208**, 447 (2005).

[28] I. Faruque and J. Sean Humbert, *Dipteran insect flight dynamics. Part 1 Longitudinal motion about hover.* Journal of Theoretical Biology **264**, 538 (2010).

[29] H. Rifai, N. Marchand, and G. Poulin, *Bounded control of a flapping wing micro drone in three dimensions,* in *IEEE International Conference on Robotics and Automation* (2008).

[30] Z. A. Khan and S. K. Agrawal, *Control of Longitudinal Flight Dynamics of a Flapping-Wing Micro Air Vehicle Using Time-Averaged Model and Differential Flatness Based Controller,* in *Proceedings of the 2007 American Control Conference* (2007).

[31] L. Schenato, D. Campolo, and S. Sastry, *Controllability issues in flapping flight for biomimetic Micro Aerial Vehicles (MAVs),* in *42nd IEEE Conference on Decision and Control (CDC)* (2003).

[32] H. E. Taha, C. A. Woolsey, and M. R. Hajj, *A Geometric Control Approach for the Longitudinal Flight Stability of Hovering Insects / FWMAVs,* in *AIAA Atmospheric Flight Mechanics Conference*, AIAA Paper 2015-1552 (2015).

[33] H. E. Taha, M. R. Hajj, and P. S. Beran, *State-space representation of the unsteady aerodynamics of flapping flight,* Aerospace Science and Technology **34**, 1 (2014).

[34] J. Dietl, T. Herrmann, G. Reich, and E. Garcia, *Dynamic Modeling, Testing, and Stability Analysis of an Ornithoptic Blimp,* Journal of Bionic Engineering **8**, 375 (2011).

3

3

[35] J. V. Caetano, C. C. de Visser, G. C. H. E. de Croon, B. Remes, C. De Wagter, and M. Mulder, *Linear Aerodynamic Model Identification of a Flapping Wing MAV Based on Flight Test Data,* International Journal of Micro Air Vehicles (2013).

[36] J. A. Mulder, Q. P. Chu, J. K. Sridhar, J. H. Breeman, and M. Laban, *Non-linear aircraft flight path reconstruction review and new advances,* Progress in Aerospace Sciences **35**, 673 (1999).

[37] S. F. Armanini, C. C. de Visser, and G. C. H. E. de Croon, *Black-box LTI Modelling of Flapping-wing Micro Aerial Vehicle Dynamics,* in *AIAA Atmospheric Flight Mechanics Conference* (2015) AIAA Paper 2015-0234.

[38] K. Y. W. Scheper, *Behaviour Trees for Evolutionary Robotics: Reducing the Reality Gap*, Master's thesis, TU Delft, The Netherlands (2014), unpublished.

[39] A. Koopmans, *Delfly Freeflight: Autonomous flight of the DelFly in the wind tunnel using low-cost sensors*, Master's thesis, Delft University of Technology (2012).

[40] J. V. Caetano, C. C. de Visser, B. D. Remes, C. De Wagter, E.-J. Van Kampen, and M. Mulder, *Controlled Flight Maneuvers of a Flapping Wing Micro Air Vehicle: a Step Towards the Delfly II Identification,* AIAA Atmospheric Flight Mechanics Conference (2013).

[41] R. Jategaonkar, *Flight Vehicle System Identification A Time Domain Methodology* (AIAA Progress in Astronautics and Aeronautics, Reston, VA, USA, 2006).

[42] R. Maine and K. Iliff, *Application Of Parameter Estimation To Aircraft Stability And Control: The Output-Error Approach*, NASA Reference Publication 1168 (NASA, 1986).

[43] V. Klein and E. Morelli, *Aircraft System Identification* (AIAA Education Series, 2006).

[44] J. V. Caetano, S. F. Armanini, C. C. de Visser, G. C. H. E. de Croon, and M. Mulder, *Data-Informed Quasi-Steady Aerodynamic Model of a Clap-and-Fling Flapping Wing MAV,* in *International Conference on Intelligent Unmanned Systems (ICIUS)* (2015).

4

GLOBAL GREY-BOX DYNAMIC MODELLING

The identification approach in Chapter 3 yielded a model that was accurate but limited to a single flight condition. Most models in the literature are likewise developed for one particular flight condition, due to the high complexity of flapping-wing flight and the limited availability of accurate free-flight data. Global models identified from flight data, in particular, are not yet available. For many applications, however, a global model is desirable, if not indispensable. In this chapter, a global modelling approach for flapping-wing dynamics is suggested and implemented on the DelFly II, using appositely collected flight data. To narrow down the scope, the main focus is placed on the time-averaged longitudinal dynamics. First, the methodology developed in Chapter 3 is applied to identify local LTI models in numerous different flight conditions, covering a significant part of the flight envelope. The obtained models are used to analyse the system dynamics and guide the global modelling process. Subsequently, a linear parameter-varying (LPV) approach is used to combine said local models into a global model. The scheduling variables in the LPV model are selected based on analysis of the flight data, while the scheduling functions are determined using a stepwise regression. The resulting model captures the most significant changes in the system dynamics due to different flight conditions, and has a low order and an easily interpretable structure. Results additionally suggest the proposed LPV approach is scalable and can be further improved in accuracy and coverage once more extensive and informative data become available.

To take full advantage of the favourable flight properties of biologically-inspired flapping-wing micro aerial vehicles, we need to have insight into their dynamics and to provide adequate control in all flight conditions. Due the high complexity of flapping flight and limited availability of accurate free-flight data, however, global models are not readily available, particularly models validated with flight data and suitable for practical applications. This paper proposes an approach for global modelling of non-linear flapping-wing dynamics, using a linear parameter-varying model derived from a set of local linear models. The model parameters and scheduling functions are determined using system identification, from free-flight data collected on a real test platform over a significant part of the flight envelope. The resulting model is significantly accurate and allows for the dominant parts of the dynamics to be predicted across the considered range of conditions. With 24 parameters overall, it greatly improves on the starting point of 46 local models with 12 parameters each. Moreover, a single model that adapts to the flight condition provides flexibility and continuous coverage, highly useful for simulation and control applications. While in the explored part of the flight envelope nonlinearity was found to be limited, the approach is scalable and expected to also cover larger variations.

4.1. INTRODUCTION

Flapping-wing micro aerial vehicles (FWMAVs) are attracting an ever-increasing interest from the aerospace community. Inspired by natural flyers, they can achieve outstanding manoeuvrability, agility and efficiency, at very small scales and low flight velocities. Thanks to their unique properties, FWMAVs are expected to fill in the gap between fixed-wing and rotating-wing vehicles, allowing for unprecedented performance, particularly for flight indoors or in complex cluttered environments. Despite the significant progress that has been made in understanding flapping-wing mechanisms [3–8], however, FWMAVs remain challenging to model, due to their unsteady aerodynamics and complex time-varying dynamics.

One particular challenge is to obtain models covering different flight conditions. Particularly low-order models of flapping-wing dynamics and aerodynamics typically have a limited applicability range and/or have not been validated in different conditions with free-flight data [9–16]. However, it is essential to know how a system behaves in all its operating conditions, in order to ensure an effective operation and maximise its performance. Furthermore, accurate global models are highly valuable and often indispensable to provide more realistic and comprehensive simulation possibilities, support the development and testing of new controllers and allow for the application of more advanced control approaches. A limited validity domain is particularly constraining in the flapping-wing case, because FW-MAVs can typically operate in different regimes, which can lead to significantly different flight properties. In the context of control and simulation, an additional challenge is that models must be not only accurate, and ideally validated with free-flight data, but also computationally efficient and suitable for practical application. Hence, simplified models are preferable when they can achieve sufficient accuracy. When flight data are available, an alternative to typically complex and computationally expensive numerical or first-principles models is therefore system identification. This approach is not yet widespread due to the difficulty of obtaining suitable data, nonetheless existing work [9–11, 17–20] has shown that it can yield models that are at the same time realistic, relatively simple and applicable

in the context of control and simulation.

This chapter addresses the challenge of global data-driven modelling of flapping-wing vehicles, using the example of an existing, flight-capable FWMAV, the DelFly II[21]. Starting from flight data, we identify a model of the cycle-averaged longitudinal vehicle dynamics that covers a range of different flight conditions, representing a significant part of the flight envelope achievable by the vehicle in a single configuration. Based on a preliminary analysis of the data and on local modelling results, the global dynamics are approximated using a linear parameter-varying (LPV) modelling approach, starting from a set of local linear time-invariant (LTI) models. LPV modelling is closely related to gain-scheduling control, and is based on the idea that a global model (or a model covering all operating conditions) can be obtained by interpolating between local models (or models valid at specific operating conditions), which are typically linear [22–24]. The LPV approach represents an attractive global modelling solution, avoiding complex high-order model structures, and also typically results in global models that are compatible with established linear control methods. LPV control and modelling methods have been applied to a variety of dynamic systems, including aircraft [25–32], but not yet to FWMAVs. Hence, in addition to the primary aim of developing an accurate low-order global model for a specific FWMAV, the current study also represents an investigation into the applicability of an LPV approach to model flapping-wing dynamics.

Given that no first principles model of the test platform is available, we opt for an identification approach, involving two steps: firstly, local linear models are identified from free-flight data collected on the vehicle; secondly, a set of interpolating functions are determined to combine these models into a global LPV model. Potential scheduling variables are selected based on analysis of the collected flight data and of the local models, while the scheduling functions defining the global model are determined using stepwise regression [33]. The resulting global model is evaluated through comparison with both flight data and local models, in conditions where local models and data are available. To evaluate the robustness and reliability of the results, evaluations are also performed using validation data that were not used in the estimation process.

This chapter is organised as follows. Section 4.2 describes the test vehicle and experimental data used in this study. Section 4.3 introduces the local models at the basis of the global modelling approach, and briefly evaluates both these models and the flight data, focusing on the observations relevant for global modelling. A simplified local model structure is also formulated. Section 4.4 outlines the LPV modelling approach used to transition from the local models to the global models and discusses the scheduling formulation. Section 4.5 presents the main results and evaluates the obtained LPV model in comparison to flight data. Section 4.6 summarises the main conclusions drawn.

4.2. METHODS AND EXPERIMENTAL DATA

4.2.1. TEST VEHICLE

The subject of this study is the DelFly II: for further information the reader is referred to Chapters 1 and 2, or to Ref. [21]. The mass and inertia properties of the specific FWMAV used in these flight tests can be found in Table 2.1, in Chapter 2. Fig. 4.1 shows the definition of the body-fixed coordinate system used in this chapter – this is coordinate system $B2$
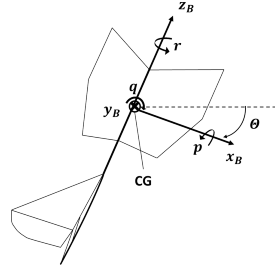
Figure 4.1: Body-fixed coordinate system x_B, y_B, z_B

4

as defined in Chapter 1, Sec. 1.4.3.

4.2.2. FLIGHT DATA ACQUISITION

The modelling work discussed in this chapter was based on a set of flight data acquired on the test vehicle described in Sec. 4.2.1. The data were collected using a motion tracking system (24 OptiTrack Flex13 cameras, covering a 10m×10m×7m motion tracking facility) in combination with an on-board inertial measurement unit (IMU) attached to the vehicle. The tracking system was used to measure the positions of seven active LED markers attached to the vehicle at the positions shown in Fig. 2.1(a), allowing for the reconstruction of body position and orientation, control surface deflections and wing leading edge movement, all at a frequency of 120Hz. The 6-axis IMU, incorporated in the vehicle's Lisa/S autopilot, was used to measure linear accelerations and angular velocities at a frequency of 512Hz. A sensor fusion approach based on extended Kalman filtering was applied to combine the different measurements, leading to high-accuracy and high-resolution measurements [34]. The flight tests were intended for identification of the longitudinal dynamics, and involved elevator input signals, executed by the autopilot when triggered by the pilot [35]. The hardware and flight test setup, data processing and sensor fusion process, and manoeuvre design are described in more detail in Chapter 2 (cf. also Refs. [36] and [35]) – the process was analogous for this study, however new tests were conducted involving a larger number of manoeuvres in different conditions, and incorporating minor practical improvements based on the previous flight test campaigns [35, 36].

4.2.3. FLIGHT TEST DATA

In line with aerospace convention, the flight envelope was initially defined in terms of possible combinations of angle of attack (AOA) and velocity. Additionally, the flapping frequency was considered as a further important variable. This could be considered an additional state, defining the flight envelope together with the AOA and velocity, but could also be seen as an input, as in the test vehicle it is almost entirely a controlled variable, controlled via the motor RPM [35]. Flight test conditions were selected on the basis of previous tests on the same platform [35, 37], and covered trim velocities ranging approximately from 0.5 to 1.3m/s, trim angles of attack (AOA) in the range of 40 to 80°, and flapping frequencies between 10 and 14Hz (cf. Fig. 4.2). While in absolute terms the covered range is limited, particularly in terms of the velocities covered, in fact this range represents a significant part

of the flight envelope achievable with the test vehicle in its current configuration. CG shifts, obtained by moving parts of the hardware (e.g. battery, wings) [37], can be used to further enlarge the flight envelope. However, in view of the restricted test flight space, and because the current work constitutes primarily an investigation into the modelling methodology, no CG shifts were considered in this study. Furthermore, flight testing showed that significant changes in the flight behaviour are already noticeable within the aforementioned range. In total, 46 short (2-5s) manoeuvres for system identification were recorded.
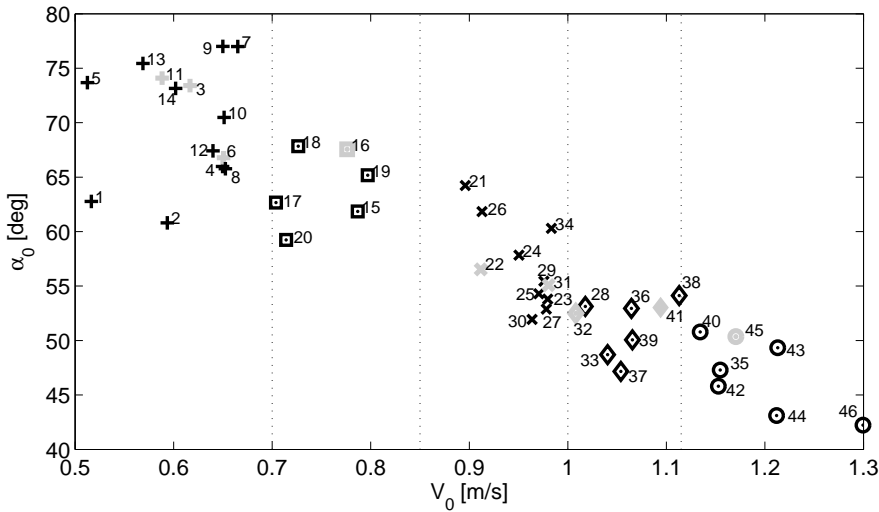
Figure 4.2: Trim conditions for each of the 46 datasets analysed in this study (angle of attack, α_0, versus velocity magnitude, $V_0 := \|V_0\|$), with validation sets in grey. Different symbols and dashed lines show grouping into similar conditions, used to select suitably distributed validation sets and for preliminary evaluations. The grouping intervals were chosen so as to obtain similarly sized groups where possible.

Due to the manual trimming procedure and inevitable slight differences between separate flights, the exact same flight condition could not be replicated repeatedly. Rather, a grid of trim conditions was covered, as shown in Fig. 4.2. This can be seen as an advantage because the full domain can be covered more effectively, allowing for small differences to be considered. To facilitate some of the subsequent evaluations, the test manoeuvres were subdivided into five groups, as shown in Fig. 4.2. It can also be observed in the figure that the flight envelope does not uniformly cover the potentially achievable rectangular domain given by the upper and lower bounds of the velocity and AOA. Instead, only a limited area around a two-dimensional line is covered. This does not point to incompleteness of the flight data, rather, it suggests that there is some correlation between velocity and AOA, and that the inherently stable FWMAV is pulled towards an equilibrium condition. Therefore, the typical operating conditions of the test platform fall within this limited range. The coverage within the range considered is also not even; in particular, there is a more sparse region in the middle, which may have some effect on the results. Finally, it should be noted

(a) Velocity, angle of attack and flapping fre- (b) Velocity, angle of attack and elevator de-
quency   flection

(c) Velocity and angle of attack (d) Velocity and flapping fre- (e) Velocity and elevator deflec-
                                   quency   tion
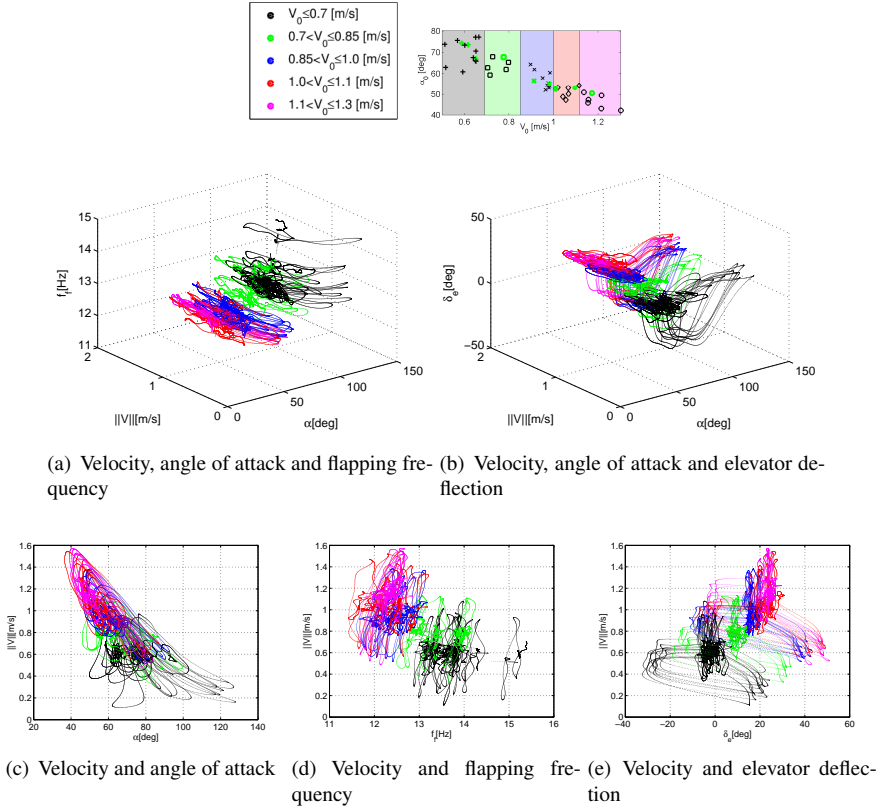
Figure 4.3: Flight envelope representations – coverage obtained in the test flights, in terms of angle of attack, velocity ($\|V\|$), elevator deflection and flapping frequency. The 2D plots (c–e) are projections of the 3D plots above (a–b).

that the choice of variables to define the flight envelope is to some extent arbitrary, and it is indeed possible that additional parameters are necessary to fully describe the envelope, however the current selection was found to represent an effective starting point.

4.3. FLIGHT ENVELOPE ANALYSIS AND LOCAL MODELLING

Two steps were performed prior to developing global models, so as to glean information on the system behaviour and select a suitable global modelling approach. Firstly, the collected flight data were evaluated, and, secondly, local linearised models were identified. Both evaluations were focused on the flap cycle-averaged behaviour, under the assumption that the flapping component can be neglected due to time-scale separation, found in previous work to be acceptable for system-level dynamic analysis of this entomopter [20]. This assumption was also introduced to simplify the evaluation of the modelling approach – the inclusion of flapping effects will be considered in future work, if the approach is found to

be promising. This section discusses the main findings of the aforementioned preliminary evaluations. The local models also constitute the basis of the global modelling process developed subsequently in this chapter.

4.3.1. LOCAL MODEL ESTIMATION

While flapping-wing dynamics are highly complex, warranting investigation into multi-body modelling [13, 38–40], several studies have demonstrated that for basic considerations, e.g. in the context of design and control work, the conventional fixed-wing aircraft equations of motion (EOM) represent a suitable description for many insects and FW-MAVs [7, 20, 41, 42]. Thus, local models were obtained using a simplified approach, shown in previous work to yield accurate local models for the studied test platform [20].

To narrow down the global modelling problem, and given that the effect of the time-varying component on the body dynamics was found to be minor (cf. Chapter 3), the time-varying component was neglected in this study. Furthermore, only the longitudinal dynamics were considered. Once a global modelling approach has been established for the time-averaged component, a similar approach as in Chapter 3 can be adopted to include the time-varying component again. Depending on the desired level of accuracy, it may be necessary to account for variation in the time-varying component across the flight envelope. Similarly, the modelling approach can be extended to include the lateral component in future work.

The time-averaged longitudinal dynamics were assumed to have the following linear time-invariant (LTI) structure [20]:

$$
\begin{bmatrix} \Delta\dot{q} \\ \Delta\dot{u} \\ \Delta\dot{w} \\ \Delta\dot{\Theta} \end{bmatrix} = \begin{bmatrix} \frac{M_q}{I_{yy}} & \frac{M_u}{I_{yy}} & \frac{M_w}{I_{yy}} & 0 \\ \frac{X_q}{m} - w_0 & \frac{X_u}{m} & \frac{X_w}{m} & g\cos(\Theta_0) \\ \frac{Z_q}{m} + u_0 & \frac{Z_u}{m} & \frac{Z_w}{m} & g\sin(\Theta_0) \\ 1 & 0 & 0 & 0 \end{bmatrix} \begin{bmatrix} \Delta q \\ \Delta u \\ \Delta w \\ \Delta\Theta \end{bmatrix} + \begin{bmatrix} \frac{M_{\delta_e}}{I_{yy}} \\ \frac{X_{\delta_e}}{m} \\ \frac{Z_{\delta_e}}{m} \\ 0 \end{bmatrix} \Delta\delta_e \qquad (4.1)
$$

As discussed in Chapter 3, the above model structure is based on the nonlinear fixed-wing flight dynamics EOM, with minor differences in the linearisation process (e.g. accounting for the large pitch attitude in flight). An LTI model of the local longitudinal dynamics was identified from each of the 46 flight manoeuvres, resulting in 46 local models, covering a significant part of the achievable flight envelope (cf. Sec. 4.2.3). For each dataset, the parameters in Eq. 4.1 were determined using a maximum likelihood estimator, as described in Chapter 3 [20].

With the exception of one case (test # 9), where the estimation data were somewhat unsteady prior to the manoeuvre and adversely affected the result, all of the identified local models were found to be accurate for the corresponding conditions, as clear from the metrics in Table 4.1 (cf. also Appendix D for an overview of the model residuals). Overall, results were comparable to those obtained in Chapter 3, with minor quantitative differences owing to the different test vehicle and data acquisition setup. As seen in the aforementioned table and discussed previously in Chapter 3, the accuracy is slightly lower for the velocities – especially for the w-velocity, for which the data appeared to be less informative. In general, the pitch dynamics are captured more accurately than the velocities, possibly because the elevator deflections used as input have a more significant effect on the former.

As stated in Sec. 4.2.2, elevator signals were used to excite the system. Such signals were found in previous work to provide suitable excitation. A number of throttle manoeuvres (causing changes in flapping frequency) were collected in addition to the discussed data, in an attempt to better excite the velocity dynamics, in particular the component related to the force parallel to the fuselage (here, Z) – however, the overall excitation provided by throttle signals was found to be significantly more limited, and did not lead to a significant increase in excitation of the Z-force component, hence the decision to focus first on elevator manoeuvres. More complex types of input signals, e.g. based on some form of optimal input design [43, 44], may allow for improved excitation and hence improved results. Such signals will be considered in future work, and may allow for a more accurate representation of the velocity dynamics, however it is also possible that the velocity dynamics do not vary as significantly as the pitch dynamics or cannot be excited independently from the pitch dynamics, which would make this component difficult to model reliably.

Table 4.1: Metrics quantifying the performance of the local models (eq. 4.1); values show average±standard deviation over all datasets. The model parameters are reported in Appendix F, in dimensional and non-dimensional form; the model residuals are shown in Appendix D.

Variable	Output corr.	RMSE (% of meas. range)
q	0.96 ± 0.10	4.2 ± 3.0
u	0.94 ± 0.10	6.2 ± 3.9
w	0.93 ± 0.15	6.8 ± 5.3
Θ	0.97 ± 0.06	3.9 ± 2.6

4.3.2. Data and local model analysis

Initially, the flight data were analysed to establish how and to what extent the system dynamics change in different flight conditions and hereby to help guide the modelling approach. Thus, for instance, an assessment was made of the change in measured responses to the same input signal in different flight conditions. Fig. 4.4(b) shows an example of this: here, the average responses of the manoeuvres conducted in each of the six groups of flight conditions (cf. Fig. 4.2), respectively, are shown together. This provides an idea of the trends in the output behaviour with the flight condition, and the magnitude of the changes. It can be seen that different trim conditions lead to visible differences in the resulting system response to the same input – in both magnitude, and especially phase. Moreover, these differences are small – they are likely to be significant, given the overall small scale considered, however they may be difficult to model accurately with real, noisy flight data. From flying experience with the studied ornithopter, it is known that there are noticeable differences in flight behaviour in the range of conditions considered. However, one additional goal of this study is to evaluate to what extent a global model is necessary in the considered range, and whether such small-scale differences can be modelled on the basis of real-world measurements.

Next, the obtained local linear models were considered. Such models constitute a helpful tool to analyse and quantify the changing dynamics of a system, which in turn is a useful starting point for global modelling. An analysis of the system dynamics was thus

(b) Average responses of the FWMAV in different regions of the flight envelope, with main trends indicated.

(c) Poles of the local models obtained in all 46 flight tests (4 poles per model). The bottom arrow indicates the main trend of *both* the aperiodic poles.
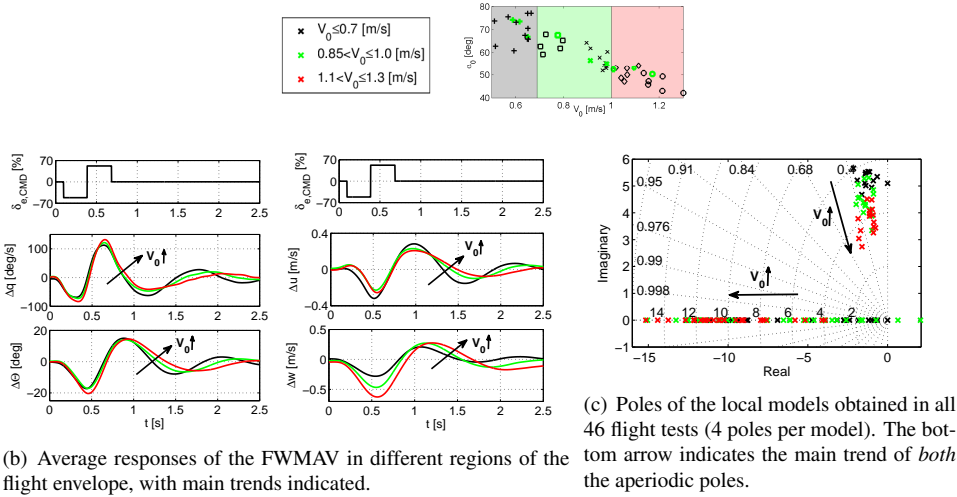
Figure 4.4: Trends in system dynamics and output, with changing flight conditions.

conducted as described in more detail in Ref. [35][1]. As anticipated from the data analysis, a number of clear trends were found in the system poles. As already observed in previous work [20, 37], the FWMAV has one oscillatory pole and two aperiodic poles. In this case, all of the poles are stable except for two of the identified local models (cf. Fig. 4.4(c)). With increasing velocity (and decreasing AOA), the oscillatory pole pair moves clearly towards lower frequencies. The damping appears to vary only to a minor extent and less clearly (cf. Sec. 4.5.3 for further discussion). The slower aperiodic pole varies from approximately -1 to -10 with increasing velocities, indicating a clear increase in stability. The faster pole, however, varies less consistently. It is interesting to note that for this particular eigenvalue, the current results do not fully agree with previous results obtained on the same vehicle [35], suggesting that this component of the dynamics cannot be reliably captured and/or may be affected by parameters other than the velocity and AOA. One likely reason for the large variation and unclear trends is insufficiently informative data. Indeed, it was found that a number of parameters – especially those connected to the w-velocity – are estimated significantly less effectively, resulting in high variances, as discussed further in Sec. 4.3.4. It is possible that better excitation of the corresponding dynamics can be obtained through different input sequences, but it is also possible that this part of the dynamics is generally less dominant compared to others, making it more challenging to excite and hence estimate. Some trends were also observed in the control behaviour, with the vehicle becoming more responsive to elevator deflections at higher velocities. As expected, this is mainly evident in the reaction of the pitch rate to the elevator, whilst the (indirect) effect on the velocities is both less significant overall, and less affected by the changing flight conditions (e.g., cf. Sec. 4.3.4).

The system dynamics will be evaluated in more detail in Sec. 4.5.3, after the final model

---

[1]Note that there are minor differences with the results in the reference as different flight test data are used here.

structure has been established. Nevertheless, the initial evaluation outlined in this section clearly suggests that changes in the dynamics are present within the operating domain considered, and already provides some information on the system dynamics and useful insight for global modelling. The main implications of the local modelling results for global modelling are summarised in the following section.

4.3.3. MAIN CONCLUSIONS FOR GLOBAL MODELLING

Based on the analysis in the previous sections, two main conclusions were drawn that are relevant for global modelling. Firstly, it was shown in Sec. 4.3 that LTI models of the suggested form (cf. Eq. 4.1) achieve a high accuracy at a local level, and can be used to describe the system dynamics in the entire region of the flight envelope analysed so far. This implies that the simplest possible approach to obtain global coverage is to somehow combine the available local models. This is also a highly advantageous approach from a control perspective, as a wide array of established control methods are available for LTI model structures. Secondly, within this region, there is a visible correlation between the local linear system dynamics and the flight conditions the respective local models refer to. Fig. 4.4 for instance highlights that with changing velocity, the eigenvalues move in a clearly defined way within the complex plane, suggesting that at least some of the system properties change in different flight conditions. The aforementioned points suggest that linearised models provide a suitable local description, but also that the flight dynamics are in fact nonlinear, at least to some extent, even within the limited domain considered so far, and hence that global modelling is relevant. Moreover, based on these observations, a linear-parameter-varying (LPV) approach appears to be a suitable and indeed advantageous way to model the observed nonlinearity.

The preceding analysis also raised a number of questions to be considered in the global modelling process. One challenge is the fact that the observed differences between different local models are, in an absolute sense, small. Given that the considered scale is itself small – as is by definition the case for any MAV – even small differences in system behaviour may have a considerable impact, however, such differences are challenging to model accurately using flight data, which are inherently affected by noise and error. Another challenge is the fact that some components appear to be less reliably estimated than others, at the local level (cf. also Sec. 4.3.4), which, clearly, will have adverse effects on the global modelling process. A similar problem may be posed by the somewhat unclear trends highlighted in some components of the dynamics: it is likely that these are mostly due to insufficient excitation, however it is also possible that the current definition of the flight envelope does not account for all the changes in the system behaviour. Alternative formulations, e.g. involving the flapping frequency, were considered but did not yield a significant improvement in the results, which, again, would seem to suggest that estimation issues are at the origin of the somewhat unclear variation in some components. The aforementioned factors may complicate the finding of an accurate global model of the system dynamics, although it is also possible that a global model will improve on the local results, by ignoring single outlier results in favour of the overall trends.

One possibility to address the challenge of unreliably-estimated components, without recurring to additional flight tests, is to adjust the local model structure and potentially exclude components that cannot be accurately determined, if these do not significantly affect

the overall accuracy of the result. Thus, prior to proceeding with the global modelling methodology, an assessment of the local model structure is made in the next section, with the object of improving the reliability and accuracy of the global modelling result.

4.3.4. SIMPLIFIED LOCAL MODEL

Despite the overall accurate local modelling results, a number of the local parameters were found to be unreliably estimated. Given that the LPV model will be constructed out of the local models, prior to proceeding to the global modelling, it is important to ensure that the local results are as accurate and reliable as possible, and to address known limitations where possible. In this context, the local model structure was revisited in an attempt to ensure a more accurate and more reliable final global model.

While the overall accuracy of the local models was found to be high, even for the less well-modelled components (w), it is possible that some of the parameters have no significant effect and therefore the parameter estimates themselves are essentially meaningless, which may influence the global model, as defined in this chapter. Thus, an important question to consider, is whether the separate local model parameters are well-estimated and whether they are all necessary in the model structure.

The simplest evaluation that can be made, is to consider the estimated model parameters themselves, how they are distributed and how much and in what way they vary. Regarding the latter point, due to the different flight conditions covered, variation is expected, nonetheless, implausible and erratic variation can serve as a further indication that a particular parameter is not estimated reliably. When the accuracy and reliability of a local parameter is particularly low, for any of the reasons mentioned, the corresponding estimates may be meaningless. It can for instance be observed that the parameters X_w and Z_{δ_e} vary significantly between different local models, not only in magnitude but also in sign. Given that the final state-output predicted by the local models was nonetheless accurate for all datasets, the significant variation implies that these parameters have no significant effect on the overall model (as determined from the current estimation data) and could be discarded from the local model structure with no significant effect. To a lesser extent, similar observations were made for all remaining Z-related parameters.

To evaluate the identifiability of single local model parameters, the estimated covariance matrices (Cramér-Rao bounds) of the original local models were considered next. Fig. 4.6 shows the estimated standard errors ($\hat{\sigma} := +\sqrt{var(\hat{\theta})}$) of the model parameters. The figure plots the distribution of the errors obtained for all local models, i.e. number of occurrences in each range of values. It can be observed that for some of the parameters, particularly those related to the Z-force and/or the w velocity, the standard errors tend to be higher, with values frequently above 10% and reaching up to 50% in some cases. This implies that a lower confidence can be placed on the estimated parameter values, which points to a lower identifiability, and at least partially explains the seemingly more random variation of said parameters with the flight condition. For the remaining parameters, standard errors are mostly low for all datasets, typically below 5% and often much lower – suggesting that the local values are reliable.

Finally, it may be insightful to consider the estimated correlation coefficient between pairs of parameters in the local models. While the correlations between parameter pairs were rarely found to exceed the critical value of 0.9 [33], the values obtained nonetheless
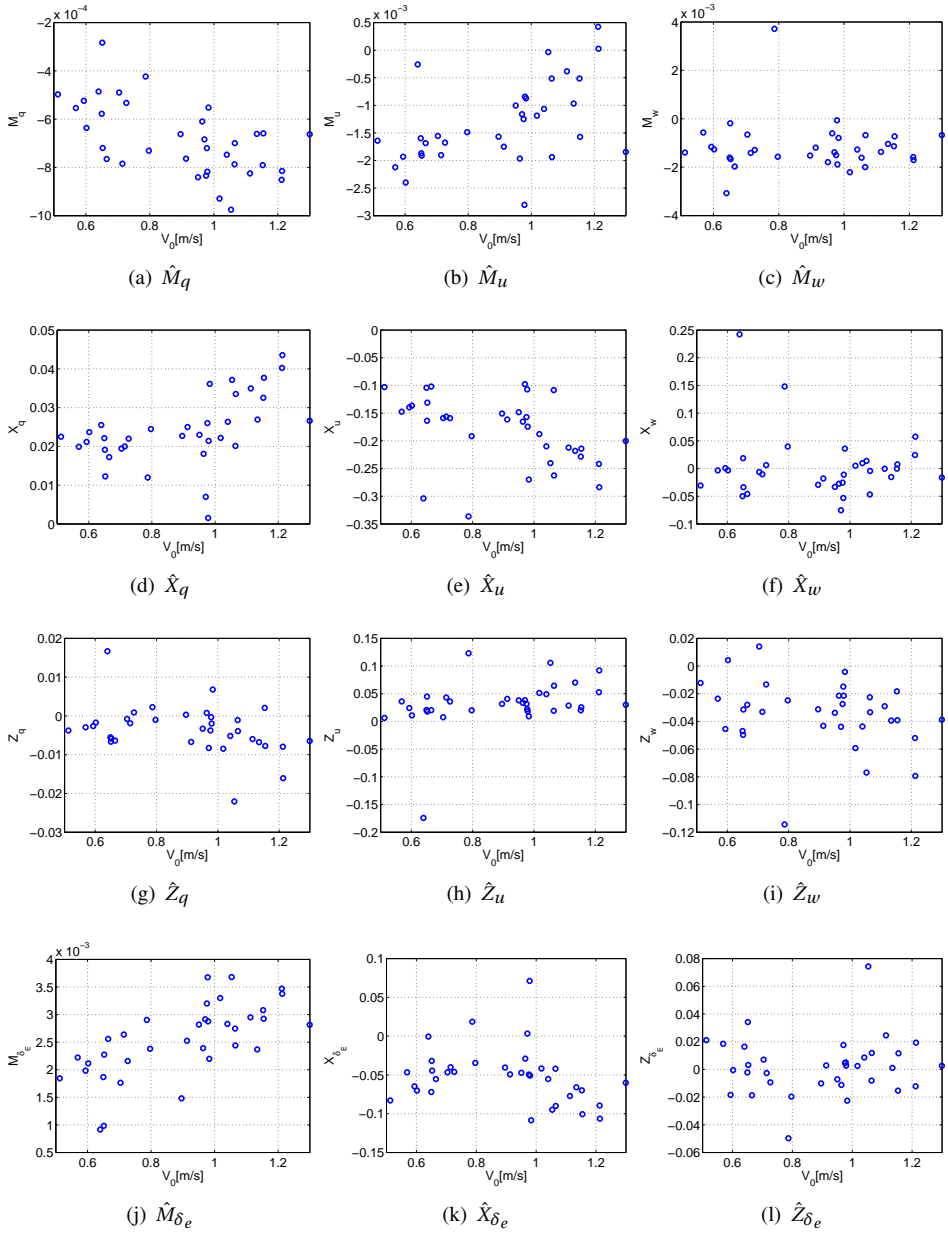
Figure 4.5: Local LTI model parameters versus flight velocity (cf. Fig. 4.2).

provide insight into which parameters have similar effects. The w velocity-related parameters, for instance, were found to be generally more correlated to other parameters. Overall, with one exception, the correlations between parameters only exceeded the critical value in isolated cases, all of these occurring in the same two local models, which presumably were not effectively estimated as a whole. The exception is the parameter pair $[Z_q, Z_{\delta_e}]$: these two parameters were found to be almost fully correlated (corr>0.98) for a significant number of the local models, suggesting that for one of the reasons discussed in Sec. 4.3.2 they cannot be estimated separately with any reliability, and hence it is advisable to drop one of the two from the model structure.

Based on the preceding discussion, a more reliable and accurate modelling result may be obtainable by fixing the less reliably estimated local parameters to zero a priori, i.e. excluding them from the local model structure, so that the main effects can be better captured by the remaining parameters, which in turn may facilitate the construction of an accurate global model. Specifically, the following parameters were discarded: X_w, Z_u, Z_{δ_e}. Note that the decision to discard Z_u rather than Z_w was to some extent arbitrary, as both parameters appeared to be unreliable to a similar extent. Z_q was retained because it was found to affect the result, despite not being estimated clearly – this parameter will be re-evaluated in Sec. 4.5.2. The resulting simplified model structure was thus the following:

$$
\begin{bmatrix} \Delta \dot{q} \\ \Delta \dot{u} \\ \Delta \dot{w} \\ \Delta \dot{\Theta} \end{bmatrix} = \begin{bmatrix} \frac{M_q}{I_{yy}} & \frac{M_u}{I_{yy}} & \frac{M_w}{I_{yy}} & 0 \\ \frac{X_q}{m} - w_0 & \frac{X_u}{m} & 0 & g\cos(\Theta_0) \\ \frac{Z_q}{m} + u_0 & 0 & \frac{Z_w}{m} & g\sin(\Theta_0) \\ 1 & 0 & 0 & 0 \end{bmatrix} \begin{bmatrix} \Delta q \\ \Delta u \\ \Delta w \\ \Delta \Theta \end{bmatrix} + \begin{bmatrix} \frac{M_{\delta e}}{I_{yy}} \\ \frac{X_{\delta e}}{m} \\ 0 \\ 0 \end{bmatrix} \Delta \delta_e \qquad (4.2)
$$

Results were found to be slightly better than for the original model, both in terms of output accuracy (cf. Table 4.2) and in terms of consistency and reliability, while requiring a smaller number of parameters. While the Z-equation parameters are still less accurately estimated than the rest, there is an improvement in the parameter covariances (cf. Fig. 4.7) even in these parameters. The remaining parameters are all estimated reliably and, as will be discussed subsequently in Sec. 4.5.2, they display clearer trends with the flight conditions, where such trends appear to be present. The previously identified problem of highly correlated parameters was also no longer found to be present.

Table 4.2: Metrics quantifying the performance of the simplified local models (eq. 4.2); values show average±standard deviation over all datasets. The model parameters are reported in Appendix F (Table F.6 in dimensional form, Table F.10 in non-dimensional form); the model residuals are shown in Appendix D.

Variable	Output corr.	RMSE (% of meas. range)
q	0.97 ± 0.02	4.0 ± 1.2
u	0.96 ± 0.02	5.7 ± 1.9
w	0.94 ± 0.07	6.9 ± 3.2
θ	0.98 ± 0.02	3.9 ± 1.2
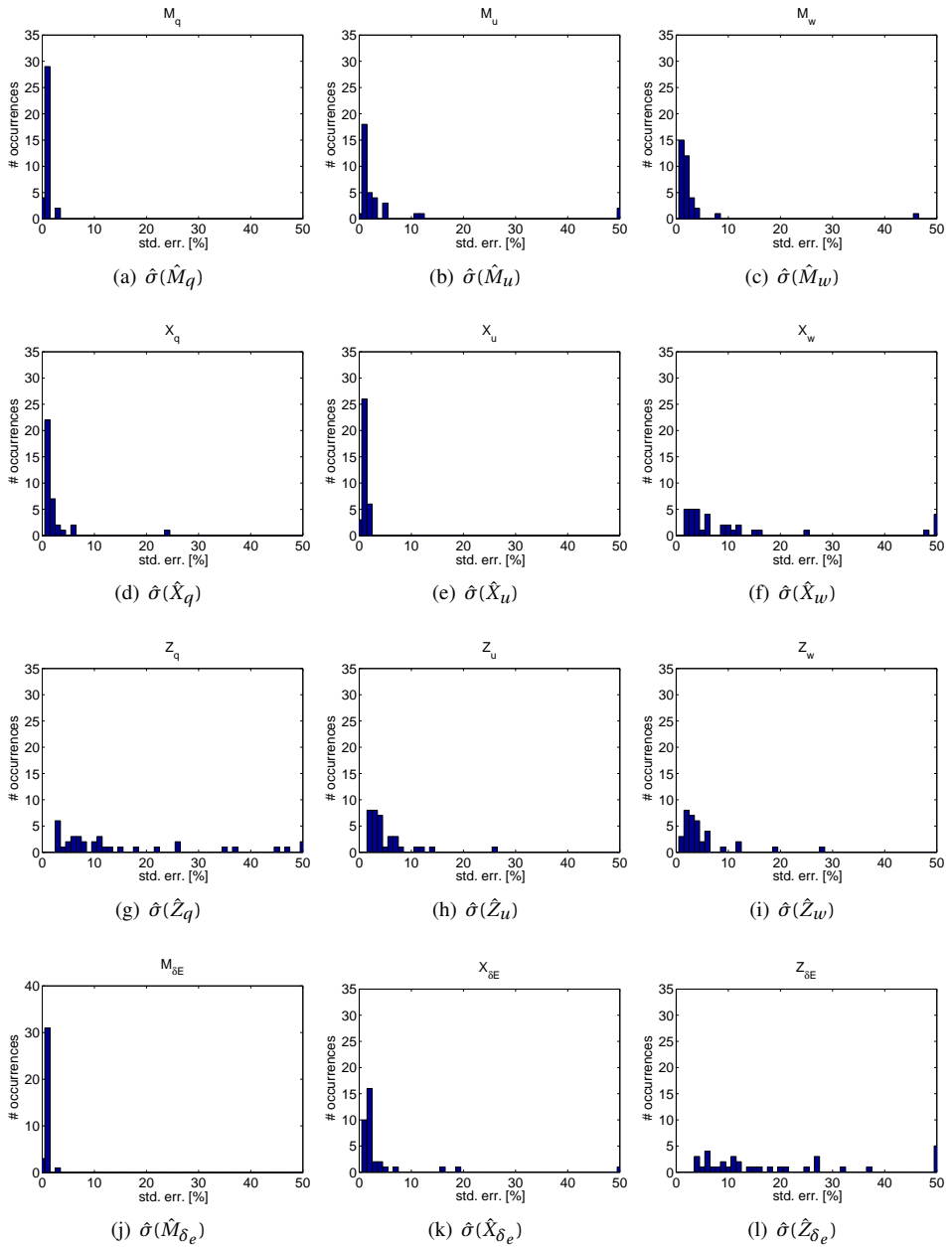
Figure 4.6: Estimated standard errors for each local LTI parameter estimate, using the **full model structure (Eq. 4.1).**
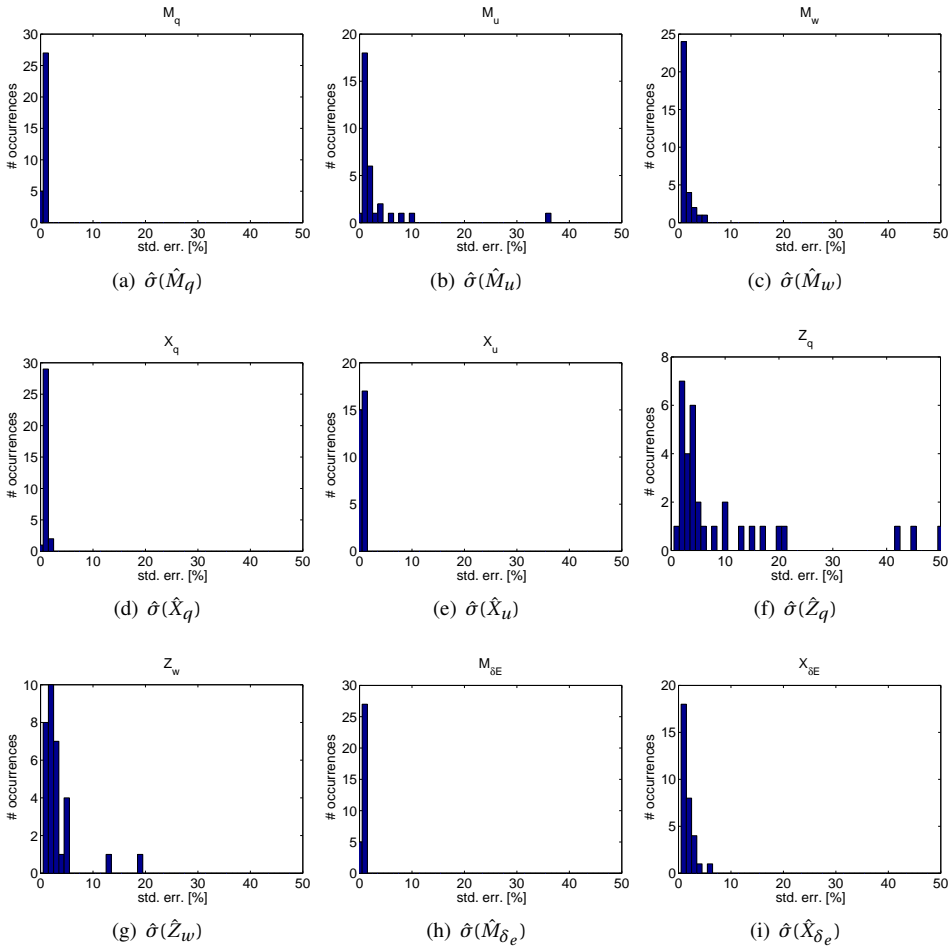
Figure 4.7: Estimated standard errors for each local LTI parameter estimate, using the **simplified model structure** (Eq. 4.2).

4.4. GLOBAL MODELLING

4.4.1. LPV APPROACH

Linear parameter-varying (LPV) modelling is closely related to the idea of gain scheduling in control [45, 46]. The underlying concept is that at every point in the operating domain of a system a linearised model can be obtained, and that a function can be found to interpolate between these linearised models, based on some arbitrary scheduling variable. As a result, the same model structure can be used to describe the entire operating domain, in dependence on a set of scheduling variables. Ideally, the scheduling variables should be exogenous and independent of the system dynamics [47, 48]. In this sense, LPV methods are best suited to systems with clearly defined, discrete operating conditions, where independent external scheduling variables can be easily defined. Nonetheless, the LPV approach has been applied to systems that do not strictly meet this requirement, including aircraft [25–28, 49]. Many aircraft applications in fact use a so-called quasi-LPV approach, where the scheduling variables are (or depend on) system states but are assumed to be independent. Furthermore, many aerospace examples of LPV modelling linearise an available nonlinear model to obtain a linearised model structure that contains the chosen scheduling variables [27, 32]. The aim is frequently to simplify the nonlinear model to allow for simpler control approaches to be applied.

In the current study, no baseline model was available, thus it was not possible to derive from first principles an LPV model structure, where the scheduling variables can be defined somewhat intuitively and related to physical parameters. Instead, the choice of scheduling variables and scheduling functions was to some degree arbitrary, as discussed subsequently. The LPV model was implemented by scheduling the individual model parameters, i.e. the state-space matrices in Eq. 4.1, as described in Sec. 4.4.2. Note that while the term scheduling is adopted to describe the functions used to approximate the changes between local models, the resulting global model will not be identical to the local models at the flight conditions the latter are estimated in. In fact, given that the baseline local models are themselves not ideal, *true* descriptions of the system, and that the observed variation in local dynamics may not depend exclusively on the chosen scheduling variables, it was considered inadvisable to interpolate between the local models. Doing so would result in highly complex functions, both counteracting the object of simplified modelling, and almost inevitably producing a global model that captures the error as well as the system dynamics. Instead, it was considered preferable to find a function that approximates the most significant trends observed in a somehow optimal way. The chosen approach is based on the assumption that the parameters are sufficiently uncorrelated to each other (cf. also Sec. 4.3.4) and that the model structure remains the same for all conditions considered. Both assumptions are already made, implicitly, in the local modelling process, and, while both are not wholly valid, the obtained local results suggest that they are acceptable. The following sections outline the LPV modelling approach formulated within this study. An in-depth treatment of the general LPV modelling framework can be found in the literature (e.g., [22, 47, 48]).

4.4.2. Scheduling formulation

As for the previously discussed local modelling, the first step in the global model identification process is to define a suitable model structure. For LPV modelling, this involves defining both a local model structure and a set of scheduling functions to combine the local models. In view of the already available local models, the structure of the LPV model was based on that of the local LTI models (cf. Eq. 4.1), however in the LPV model each parameter is a function of some of the states rather than a constant, i.e.:

$$\dot{\mathbf{x}} = \mathbf{A}(\rho)\mathbf{x} + \mathbf{B}(\rho)\mathbf{u} \tag{4.3}$$

where ρ is the vector of scheduling variables and the system matrices $\mathbf{A}$ and $\mathbf{B}$ are no longer constant but depend on ρ. Assuming the dependence on the scheduling variables is affine, this can be written out as:

$$\mathbf{A}(\rho) = \mathbf{A}_0 + \mathbf{A}_1\rho(1) + \mathbf{A}_2\rho(2) + \ldots + \mathbf{A}_n\rho(n) \tag{4.4}$$

$$\mathbf{B}(\rho) = \mathbf{B}_0 + \mathbf{B}_1\rho(1) + \mathbf{B}_2\rho(2) + \ldots + \mathbf{B}_n\rho(n) \tag{4.5}$$

where the bracketed number denotes the corresponding component in the scheduling vector ρ, and the matrices $\mathbf{A}_i$ and $\mathbf{B}_i$ are matrices of coefficients for the ith of the n elements in the scheduling vector. Note that the matrices on the right hand side do not have to be full, and in the current problem are indeed mostly sparse (cf. Eq. 4.16).

Once the underlying local model structure has been defined, the key question in devising an LPV model structure is the selection of suitable scheduling variables. In conventional fixed-wing problems, LPV models are typically scheduled based on either flight states, or configuration-related variables [25, 26, 31, 32]. Based on the analysis in Sec. 4.3.2 and on previous work [35, 37], and given that a single configuration (i.e. CG and geometry) was considered, functions of the (trim) angle of attack (AOA), total velocity and flapping frequency were considered as a basis for scheduling in the current model. Given that accurate results were found to be obtainable using only the AOA and velocity (excluding the flapping frequency), however, the remainder of this chapter focuses on these two variables only. Moving from the general notation in Eqs. 4.4–4.5 to the specific formulation used in this study, the scheduling vector ρ thus takes the form:

$$\rho_{ij}(V_0, \alpha_0) := V_0^i \alpha_0^j, \quad i \in [0, d], j \in [0, d], \tag{4.6}$$

where d is the maximum degree considered for each scheduling variable. It should be noted that the entire set of possible combinations obtainable from Eq. 4.6 was merely the starting point for model structure selection, whereas the final model structure includes only a small number of these terms (cf. Sec. 4.4.3).

Given that certain components of the local model structure are known and entirely determined by kinematic relations, the scheduling was limited to the aerodynamic terms, while the known parts of the local model structure were kept at their known values, or determined from known expressions, as clarified in Eq. 4.7. In some cases it may be more convenient, in practice, to directly interpolate the entire matrices – if this is the case, it is straightforward to adjust the current model formulation to also include the kinematic terms, particularly since all of these terms are either constant or known to be related to the chosen scheduling

4

states. The resulting LPV model, as formulated in the current study, takes the following form, where tilde superscripts denote parameters estimated from the scheduling functions.

$$\tilde{\mathbf{A}}(V_0, \alpha_0) = \begin{bmatrix} \frac{\tilde{M}_q}{I_{yy}} & \frac{\tilde{M}_u}{I_{yy}} & \frac{\tilde{M}_w}{I_{yy}} & 0 \\ \frac{\tilde{X}_q}{m} - w_0 & \frac{\tilde{X}_u}{m} & \frac{\tilde{X}_w}{m} & g\cos(\Theta_0) \\ \frac{\tilde{Z}_q}{m} + u_0 & \frac{\tilde{Z}_u}{m} & \frac{\tilde{Z}_w}{m} & g\sin(\Theta_0) \\ 1 & 0 & 0 & 0 \end{bmatrix}$$

$$:= \begin{bmatrix} 0 & 0 & 0 & 0 \\ -w_0 & 0 & 0 & g\cos(\Theta_0) \\ u_0 & 0 & 0 & g\sin(\Theta_0) \\ 1 & 0 & 0 & 0 \end{bmatrix} + \sum_{i=0}^{d}\sum_{j=0}^{d} \mathbf{A}_{ij}\rho_{ij}(V_0, \alpha_0) \qquad (4.7)$$

$$\tilde{\mathbf{B}}(V_0, \alpha_0) = \begin{bmatrix} \frac{\tilde{M}_{\delta_e}}{I_{yy}} \\ \frac{\tilde{X}_{\delta_e}}{m} \\ \frac{\tilde{Z}_{\delta_e}}{m} \\ 0 \end{bmatrix} := \sum_{i=0}^{d}\sum_{j=0}^{d} \mathbf{B}_{ij}\rho_{ij}(V_0, \alpha_0) \qquad (4.8)$$

As in Eqs. 4.4 and 4.5, $\mathbf{A}_{ij}$ and $\mathbf{B}_{ij}$ are constant matrices of coefficients[2], however, here their subscripts indicate which component of the scheduling vector they refer to. Given that not all permutations given by Eq. 4.6 are used in the final model structure, and that finally different parameters will be represented by different scheduling functions, several $\mathbf{A}_{ij}$ and $\mathbf{B}_{ij}$ matrices in the above equations will be either zero or sparse matrices. As a further clarification, the LPV component of Eqs. 4.7 and 4.8 can be written out for each parameter in the model structure (**A** and **B** matrices) as shown below for, e.g., $\tilde{M}_q$:

$$\tilde{M}_q(V_0, \alpha_0) = \sum_{i=0}^{d}\sum_{j=0}^{d} a_{Mq,ij}\rho_{ij} = a_{Mq,00} + a_{Mq,01}\rho_{01} + \ldots + a_{Mq,dd}\rho_{dd} \qquad (4.9)$$

Here $a_{Mq,ij}$ denotes the set of constant global model parameters (contained in the A_{ij} matrices in Eq. 4.7) that are used to compute $\tilde{M}_q$ at any given flight condition, given the velocity and AOA. Note that in the analogous of the above equation written for parameters in the *local* **B** matrix, the *global* model parameters are denoted by a *b* instead of an *a* (e.g. $b_{M\delta_e,ij}$). The different notation is merely used to highlight the relation between the scheduling functions and the local model structure at the basis of the global model.

The derivation of the scheduling functions, and estimation of the global model parameters they contain (A_{ij}, B_{ij}), are explained in the following section.

4.4.3. SCHEDULING FUNCTION SELECTION AND GLOBAL MODEL PARAMETER ESTIMATION

Clearly, Eqs. 4.4 and 4.5 result in a large number of terms even if a small polynomial degree d is chosen for the scheduling functions. In fact, only a small number of terms were found to be required on the right hand side of the equations, resulting in a relatively

---

[2]$\mathbf{A}_{ij}$ and $\mathbf{B}_{ij}$ contain the *global* model parameters, which are constant for all flight conditions

simple final result. To determine which of the potential terms are necessary for accurate global modelling, and to determine suitable functions to describe each term in the LPV model, a stepwise regression was implemented, starting from a candidate pool of model terms including all parameters shown in Eq. 4.6, up to a degree of $d = 3$ for each model term. The maximum model degree was limited to avoid excessively high orders that might have led to over-fitting. Additionally, lower-order functions are more likely to retain a basic level of physical plausibility.

Given that considering the LPV model output (i.e. the model-predicted states) directly in the stepwise regression would have required optimising the model structure for all scheduling functions simultaneously, as well as for all flight conditions simultaneously, potentially resulting in a computationally expensive problem, the problem was simplified by assuming that all local model parameters are entirely uncorrelated (cf. Sec. 4.4.1). This was considered an acceptable assumption based on the relatively low correlations obtained between separate parameters in the local models (cf. Sec. 4.3.4), and allows for each term in the LPV model to be considered separately. It was thus assumed that finding the optimal model structure for each sub-model would lead to a suitable global model structure, albeit not an optimal one.

A stepwise regression was thus conducted for each parameter in the $\mathbf{A}_{ij}$ and $\mathbf{B}_{ij}$ matrices ($\tilde{M}_q, \tilde{M}_u$, etc.), in order to determine a scheduling polynomial to represent the parameter as a function of the scheduling variables (V, α). This was attempted both with the AOA and velocity alone, and with the two aforementioned variables together with the flapping frequency. Initial results demonstrated that a high accuracy can be achieved even if the flapping frequency is excluded – a solution considered preferable as it results in a simpler model structure.

Details on stepwise regression can be found in the literature (e.g., Refs. [33, 50, 51]); a concise overview is given here for completeness. Stepwise regression is a model structure determination process for problems that can be expressed as a linear regression, in the form:

$$\mathbf{z} = \mathbf{X}\mathbf{\Theta} + \epsilon \qquad (4.10)$$

where Θ is a constant parameter vector, ϵ is the equation error, and $\mathbf{z}$ and $\mathbf{X}$ contain the output and regressors, respectively, at each measurement point.

Based on the previously stated assumption that the local model parameters are uncorrelated, each parameter in the local model structure was treated separately. Thus, for each local parameter (M_q, M_u, etc.), the above equation is constructed as follows: the parameter vector contains the global model parameters (e.g. the a terms in Eq. 4.9) used to represent the *local* model parameter considered; the output vector contains the values the considered local parameter takes in each of the identified local models ($\mathbf{z} \in \mathbb{R}^{n_C \times 1}$, where n_C is the number of flight conditions considered); and the regressor matrix contains functions of V and α computed from measurements at every flight condition, starting from all n_x combinations given by Eq. 4.6 ($\mathbf{X} \in \mathbb{R}^{n_C \times n_x}$). Each measurement instance (row of $\mathbf{z}$, $\mathbf{X}$ and ϵ) therefore corresponds to a different flight condition.

Thus, for instance, for M_q, Eq. 4.10 takes the form,

$$
\begin{bmatrix}
M_q(V(1),\alpha(1)) \\
M_q(V(2),\alpha(2)) \\
\vdots \\
M_q(V(n_C),\alpha(n_C))
\end{bmatrix}
=
$$

$$
\begin{bmatrix}
\rho_{00}(1)=1 & \rho_{01}(1)=\alpha(1) & \dots & \rho_{dd}(1)=V^d(1)\alpha^d(1) \\
\rho_{00}(2)=1 & \rho_{01}(2)=\alpha(2) & \dots & \rho_{dd}(2)=V^d(2)\alpha^d(2) \\
\vdots & \vdots & \ddots & \vdots \\
\rho_{00}(n_C)=1 & \rho_{01}(n_C)=\alpha(n_C) & \dots & \rho_{dd}(n_C)=V^d(n_C)\alpha^d(n_C)
\end{bmatrix}
\begin{bmatrix}
a_{Mq,00} \\
a_{Mq,01} \\
\vdots \\
a_{Mq,dd}
\end{bmatrix}
+
\begin{bmatrix}
\epsilon(1) \\
\epsilon(2) \\
\vdots \\
\epsilon(n_C)
\end{bmatrix}
\quad (4.11)
$$

The main limitation of the model formulation in Eq. 4.10 is that it cannot account for the error in the velocity and AOA measurements, and only considers the error ϵ in the local model parameters, assumed, as per convention, to be white Gaussian noise. Nonetheless, the aforementioned model formulation provides a straightforward means to derive suitable scheduling functions, and was subsequently found to yield accurate final results (cf. Sec. 4.5).

Given an equation of the form of Eq. 4.10, the goal of the stepwise regression process is to determine which of the n_x regressors in $\mathbf{X}$ need to be retained in order to obtain an accurate model. The stepwise regression thus begins from a pool of candidate regressors, constructed out of permutations of the velocity and AOA, up to the chosen maximum model degree (here, 3; cf. also Eqs. 4.6 and 4.9). At each step, the partial correlation of each regressor with the known output z is computed, accounting for any already determined model terms (i.e. we compute the correlation of the regressor to the original output z minus the contribution of the model terms included in previous steps). The regressor x_k leading to the highest partial correlation is considered for inclusion in the model structure, and the (partial) F-statistic is calculated [51] to determine whether the contribution of the selected regressor to the model is significant, i.e. whether F is above a chosen critical value:

$$
F_k = \frac{\hat{\theta}_k^2}{\sigma^2(\hat{\theta}_k)} > F_{crit} \quad (4.12)
$$

where $\hat{\theta}_k$ is the considered parameter (which is multiplied by regressor x_k in the model), and σ^2 is the estimated variance of $\hat{\theta}_k$. If Eq. 4.12 holds, then the corresponding parameter $\hat{\theta}_k$ is included in the model. Whenever a new model term has been added, the partial F-statistic of all regressors previously included in the model structure must be re-computed, to assess whether their contribution remains significant after the additional variable has been included in the model structure. Any of the previously included regressors whose F-statistic is below the chosen threshold is once again removed from the model. These steps are repeated until some criterion is met; in this case, the change in predicted square error and R^2 coefficient were considered.

Once a model structure has been selected, the global model parameters are estimated using an ordinary least squares (OLS) estimator, which lends itself well to the model formulation used in the regression. Using the same notation as in Eq. 4.10, the cost function to minimise, for each local parameter ('output' $\mathbf{z}$), is given by:

$$
\mathbf{J} = \frac{1}{2}[\mathbf{z}-\mathbf{X}\Theta]^T[\mathbf{z}-\mathbf{X}\Theta]^T \quad (4.13)
$$
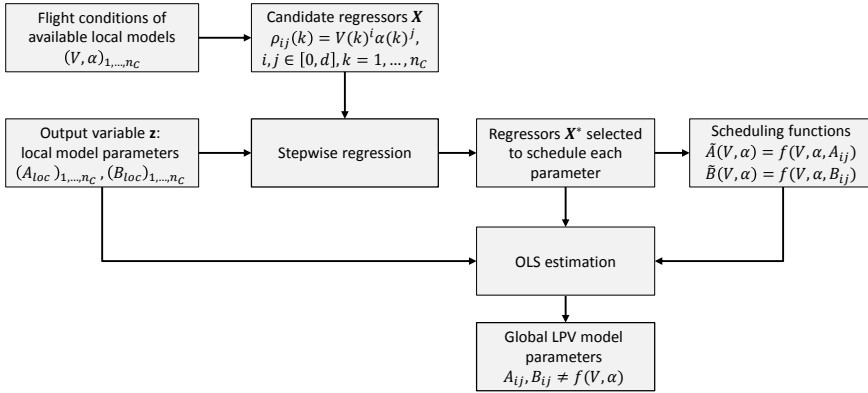
Figure 4.8: Diagram schematically illustrating the LPV model construction process. $\mathbf{X}^*$ represents the final regressor matrix obtained after the stepwise regression process.

where X^* denotes the final, optimised set of regressors resulting from the stepwise regression. The OLS estimator resulting from the minimisation process is then:

$$\hat{\boldsymbol{\Theta}} = (\mathbf{X}^T\mathbf{X})^{-1}\mathbf{X}^T\mathbf{z} \tag{4.14}$$

The set of global model parameter vectors $\hat{\Theta}$ (one per local model term) allows for an LTI model to be obtained in any part of the known flight envelope and, theoretically, also to extrapolate beyond this. The latter however requires further investigation of the boundaries of the flyable envelope and of the nonlinearity of the system outside the explored region. The high-level process to determine the scheduling functions and global model parameters is clarified in Fig. 4.8

4.4.4. AVERAGE MODEL FOR COMPARISON

The alternative to expressing each model parameter as a function of the flight condition, is to use a constant value. In order to provide a worst-case comparison for the developed LPV model, we also defined an *average* model, with a single set of parameters, which we applied to the entire flight envelope considered, to establish whether and to what extent global modelling is necessary for the considered test platform. To account for the fact that the flight test data are not distributed in a uniform manner, the average model was obtained by calculating a weighted average for each parameter in the local model structure from the parameter values of all the local models. In particular, each model parameter was weighted with its distance from the calculated geometric centre $(\bar{V}, \bar{\alpha})$ of the considered flight envelope, defined as the difference between maximum and minimum V and AOA, respectively, for each of the two spatial coordinates. Each parameter in the average model was thus defined as,

$$\theta_{avg} := \begin{cases} \frac{\sum \theta_k(V_k,\alpha_k)r_k}{\sum r_k} & \text{if} \quad r_k \neq 0 \forall k \\ \theta(\bar{V},\bar{\alpha}) & \text{if} \quad \exists r_k(r_k=0) \end{cases}, \qquad r_k := \sqrt{(V_k-\bar{V})^2 + (\alpha_k-\bar{\alpha})^2} \tag{4.15}$$

where θ represents any parameter in the **A** and **B** matrices defining the model structure (i.e. M_q, M_u, etc.). The second clause of the equation is included to account for the possibility of local models identified at the defined centre of the flight envelope. As no such models were available, effectively only the first clause of the equations was used. To ensure a fair comparison also in the validation phase, only the estimation datasets were used to compute the average model.

As discussed previously, in the global model a distinction is made between the aerodynamic and purely kinematic components of the LPV model. Thus, in an analogous way, two different average models were considered. The first average model is an overall weighted average, defined directly by Eq. 4.15. Here also the kinematics-related terms are averaged. The second average model involves averaging only the aerodynamic components according to Eq. 4.15, while the kinematic terms are assumed to be known at any flight condition. The latter model hence can be seen as a partial average – i.e. an average of the aerodynamics only. In the majority of the evaluations that follow, the partial average model is used for comparison (henceforth, this model is termed 'average', while, where mentioned, the overall average model is denoted as 'full average'). This choice was made in order to differentiate between the effects of the aerodynamics and the kinematics, thus obtaining an idea of how the aerodynamics change. The results obtained with an overall average were found to be somewhat less accurate than those obtained with a partial average, but mostly in the same order of magnitude. In this sense, comparing the LPV model to the partial average can also be considered a conservative evaluation of how useful the global model is.

4.5. LPV MODELLING RESULTS

4.5.1. PRELIMINARIES

This section presents the obtained global LPV model. Following an assessment of the scheduling results, the final LPV model is evaluated and compared to (i) the original local models, in the conditions where such models were available, (ii) the flight data collected in the same conditions, and (iii) the 'partial' average model presented in Sec. 4.4.4. Comparison to the local models represents the most basic form of evaluation, as the LPV model is based directly on the local models, and not on the flight data. Hence, this determines how accurate the LPV model is at reproducing the changing dynamics given by the local models. Comparison to flight data provides additional insight, given that while in theory the best possible outcome is for the LPV model to replicate the local models in the considered local conditions, in reality it is possible that the LPV model approximates the flight data better than the local models, as it does not represent a direct interpolation and may therefore compensate for irregularities in single local models/datasets. Finally, comparing to the average model was intended to evaluate to what extent a global model is necessary, and whether the suggested approach improves upon the worst-case option of using the same model throughout the flight envelope. Fig. 4.9 clarifies the relations between the three types of models.

Similarly, for the evaluations that follow, it is important to distinguish between (a) global model parameters, (b) estimated local model parameters, and (c) LPV model-estimated local parameters. The LPV model contains a set of global parameters (a), which are the same in all flight conditions. The LPV model can be used to estimate local parameters (b,
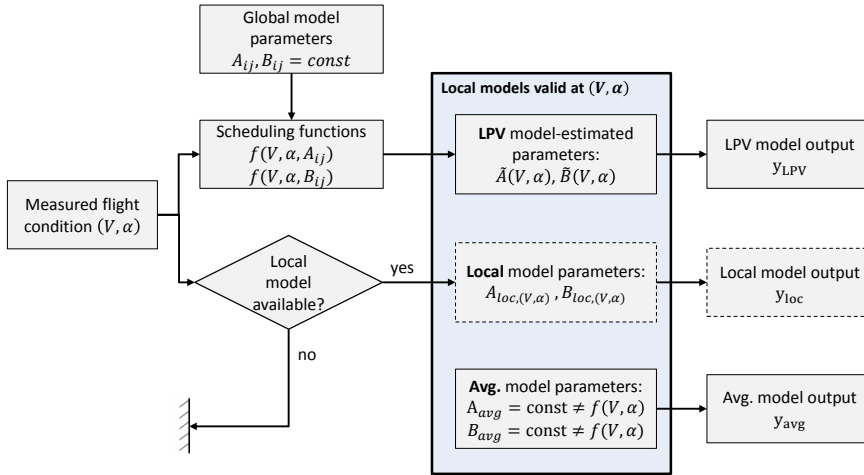
Figure 4.9: Diagram schematically illustrating the relationship between the global LPV model, and the set of local models and single average model that it is compared to.

henceforth 'LPV-estimated local parameters'): these are the values taken by the left hand side variables in Eqs. 4.7 and 4.8 (and all equations analogous to Eq. 4.9) if AOA and velocity values for a particular flight condition are substituted into the right hand side of the equations. The set of resulting calculated parameters yields an LTI model at the flight condition considered and can therefore be compared to the original estimated local model parameters (c) directly estimated in the same flight condition.

A number of flight test datasets were excluded from the model identification process and used only in the validation phase in order to assess the accuracy of the obtained model. For this, nine datasets were selected at random, distributed uniformly among the groups of datasets shown in Fig. 4.2, in relation to the group size. Several different random selections were investigated, and the comparable results obtained suggest a degree of robustness of the modelling approach. In the remainder of this chapter, results are shown for one of the estimation-validation selections (validation datasets: 3, 6, 11, 16, 22, 31, 32, 41, 45; shown in bold grey font in Fig. 4.2).

4.5.2. SCHEDULING RESULTS
Prior to considering the complete LPV model, it is useful to consider the (estimated) local model parameters in comparison to the corresponding parameters predicted by the LPV model in the same flight conditions (LPV model-estimated local parameters). This gives

a preliminary indication of the accuracy of the resulting model and also provides further insight into the adequacy of the chosen model structure. Shortcomings in the LPV model are likely to be related to one of the following causes: (i) the parameter is not estimated accurately in the local models, (ii) the chosen LPV scheduling variables are unsuited to represent the variation of the particular local parameter considered, or (iii) the local parameter is generally unaffected by the flight condition. The first point may be due to insufficient excitation in the estimation data used, or because the parameter has a limited influence on the system dynamics (i.e. is superfluous to the model), or because it is strongly correlated to other parameters and therefore cannot be identified independently from these – these points were addressed in Sec. 4.3.4. The second point is not considered at this stage, as the local analysis in Sec. 4.3 suggests that the velocity and AOA are suitable at least to capture the most significant trends in the dynamics. The third point is discussed in this section, in the context of the scheduling results. Based on this evaluation, final minor adjustments are made to the model structure, and the final LPV model is obtained, which is then discussed in depth in Sec. 4.5.

The approach outlined in Sec. 4.4 was applied, starting from the flight data presented in Sec. 4.2.3 and the local model structure defined in Sec. 4.3.4, to obtain an LPV model covering the portion of the flight envelope explored in the current flight tests (cf. Fig. 4.2). Starting from the simplified local model structure defined in Eq. 4.2, the following scheduling functions were obtained from the stepwise regression process, conducted according to Sec. 4.4.3:

$$
\begin{aligned}
\tilde{M}_q &= a_{Mq,00} + a_{Mq,10}V + a_{Mq,30}V^3 \\
\tilde{M}_u &= a_{Mu,00} + a_{Mu,10}V + a_{Mu,20}V^2 + a_{Mu,30}V^3 \\
\tilde{M}_w &= a_{Mw,00} := \bar{M}_w \\
\tilde{M}_{\delta_e} &= b_{M\delta_e,00} + b_{M\delta_e,20}V^2 + b_{M\delta_e,21}V^2\alpha + b_{M\delta_e,30}V^3 \\
\tilde{X}_q &= a_{Xq,00} + a_{Xq,21}V^2\alpha \\
\tilde{X}_u &= a_{Xu,00} + a_{Xu,11}V\alpha + a_{Xu,21}V^2\alpha \\
\tilde{X}_w &= 0 \\
\tilde{X}_{\delta_e} &= b_{X\delta_e,00} + b_{X\delta_e,10}V + b_{X\delta_e,30}V^3 \\
\tilde{Z}_q &= a_{Zq,00} := \bar{Z}_q \\
\tilde{Z}_u &= 0 \\
\tilde{Z}_w &= a_{Xw,00} + a_{Xw,01}\alpha + a_{Xw,11}V\alpha + a_{Xw,12}V\alpha^2 \\
\tilde{Z}_{\delta_e} &= 0
\end{aligned}
\tag{4.16}
$$

The bracketed expressions in the set of equations above denote parameters which were not scheduled in the final model. In fact, next to ensuring a suitable identifiability of the local model parameters at the basis of the chosen modelling approach (cf. Sec. 4.3.4), the resulting LPV model can be further improved by determining whether the local parameters are in fact significantly related to the flight conditions and only scheduling the parameters that meet this requirement. While it was mentioned in Sec. 4.3 that the dynamics of the

local models are related to the flight condition, this does not necessarily imply that each of the local parameters is correlated to the flight condition. Some parameters were found to be important for the system dynamics overall, but not to be significantly affected by different flight regimes, as defined in this chapter and within the range considered, or to be difficult to predict accurately with simple functions of the AOA and velocity. While scheduling expressions for these parameters were nonetheless obtained from the stepwise regression, owing to the liberally chosen stopping criteria, the scheduling results suggested that not scheduling these parameters would have no significant effect on the result, as discussed further below.

The scheduling results obtained are shown in Fig. 4.10, which shows the local model parameters, the LPV model-estimated parameters for the same flight conditions, and the average model parameters (based on Sec. 4.4.4). While several parameters are dependent on a function of both the velocity and the AOA, the parameters are plotted against each of these two variables separately, to provide a clearer overview. Overall, it can be observed that most of the LPV model-calculated parameters take on values that are close to those of the local models in the corresponding conditions. Where there is a trend with the flight condition, the sub-models are capable of reproducing it accurately, as, for instance, clearly seen for M_u, M_{δ_e}, X_q and X_u. The parameters connected to the Z force and w velocity are less accurately predicted by the global model – these parameters were already estimated less reliably in the local models, it is therefore unsurprising that the global modelling result is equally inaccurate. It is also clear that while some parameters display a clear correlation with the flight condition, others do not, despite being estimated effectively in the local models. This suggests that it is unnecessary to enforce on all local parameters a correlation to the flight condition, and that a similar or better result may be obtainable by keeping some parameters fixed to constant values (e.g. the value from the average model in Eq. 4.15) and only varying the remaining parameters. This would allow for simpler, smaller models that still capture the main effects. Based on a visual evaluation, local model parameters that do not appear to vary with the flight regime include M_w and Z_q.

A quantitative evaluation of the accuracy of the chosen LPV model – and, to some extent, the degree of correlation of local parameters and flight conditions – can also be obtained by computing, for each parameter, the correlation between local parameter estimates obtained in all flight conditions and corresponding LPV model-predicted parameters. Additionally, probability values (p-values) can be considered to evaluate the significance of said correlations. Based on these metrics, shown in Table 4.3, it can be observed that most of the parameters retained in the simplified local model structure are modelled effectively by the chosen LPV formulation, with the exception of M_w and Z_q, which do not display significant trends with the flight condition, and hence are not accurately predicted by the chosen LPV scheduling functions. The parameters X_δ and Z_w are also significantly less correlated to the flight conditions compared to the remaining parameters, however the obtained results suggest they may still be possible to model.

4

(a) M_q

(b) M_u

(c) (M_w – average used)

(d) M_{δ_e}

(e) X_q

(f) X_u

(g) X_{δ_e}

(h) (Z_q – average used)

(i) Z_w
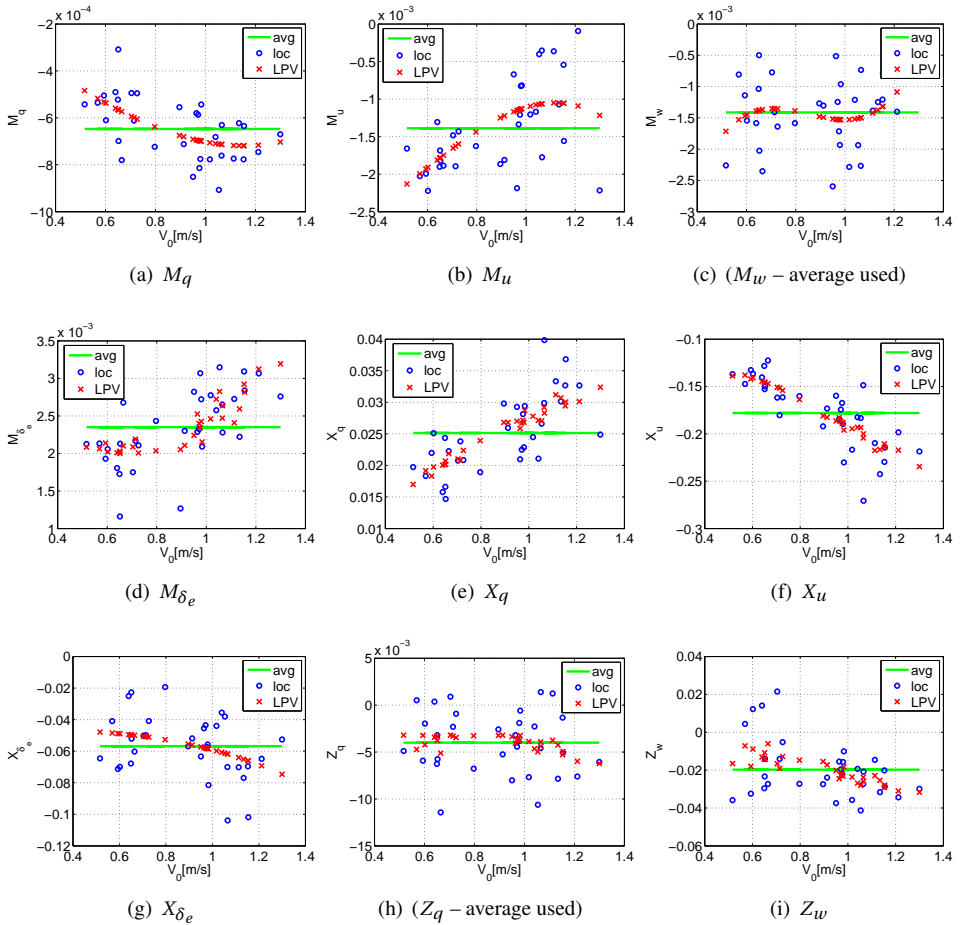
Figure 4.10: Estimated LPV parameters compared to corresponding LTI model parameters, in flight conditions where local models are available. Local LTI model parameters, and corresponding parameters estimated from the LPV model, plotted versus the trim flight velocity (cf. Fig. 4.2). The average of each parameter over all 46 LTI models is also shown for comparison.
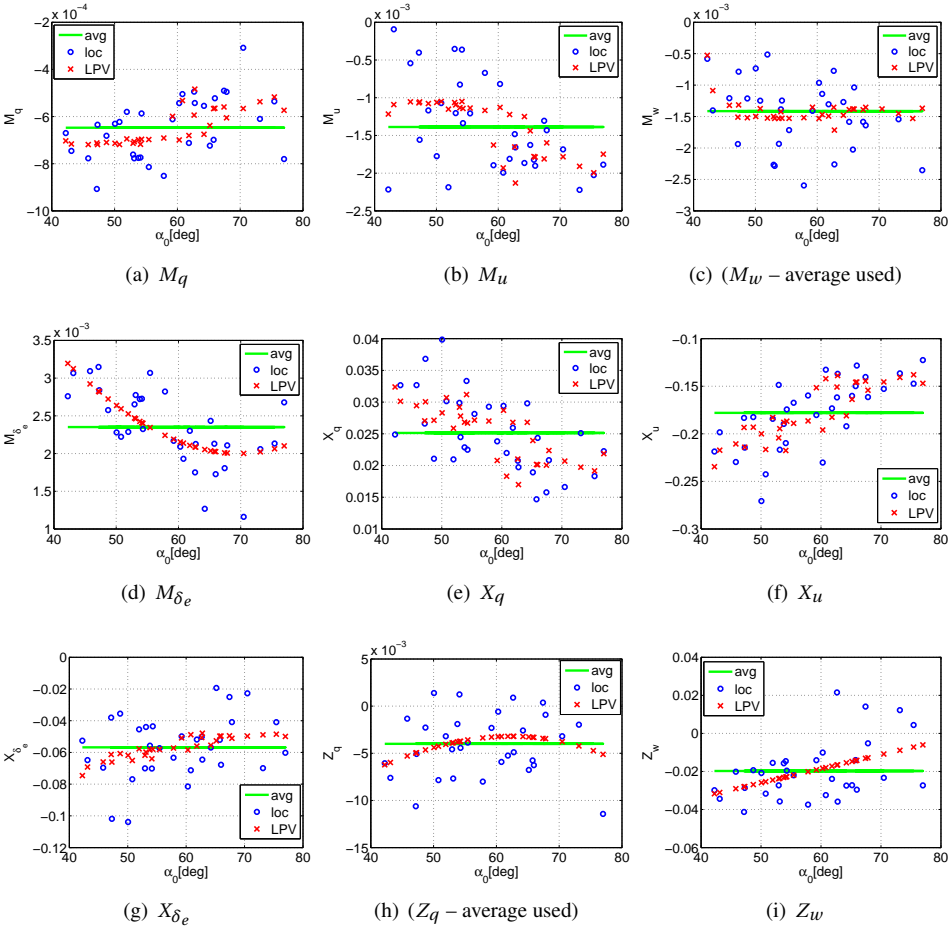
Figure 4.11: Estimated LPV parameters compared to corresponding LTI model parameters, in flight conditions where local models are available. Local LTI model parameters, and corresponding parameters estimated from the LPV model, plotted versus the trim angle of attack (cf. Fig. 4.2). The average of each parameter over all 46 LTI models is also shown for comparison.

Table 4.3: Full model structure: correlation between LPV-estimated parameters and local model values; and corresponding p-values (statistical significance).

Param.	$\mathrm{corr}(\tilde{\theta}_{\mathbf{LPV}}, \hat{\theta}_{\mathbf{loc}})$	p-value
M_q	0.61	$\ll 0.001$
M_u	0.75	$\ll 0.001$
M_w	0.22	0.23
M_{δ_e}	0.71	$\ll 0.001$
X_q	0.78	$\ll 0.001$
X_u	0.83	$\ll 0.001$
X_{δ_e}	0.52	0.003
Z_q	0.06	0.73
Z_w	0.55	0.002

4

Based on all the preceding considerations, the parameters M_w and Z_q were therefore fixed to average values (obtained from the average model in Eq. 4.15). The following LPV model structure was thus chosen for the final, simplified (subscript 'simp') global model:

$$\tilde{\mathbf{A}}_{\mathbf{simp}}(V, \alpha) = \begin{bmatrix} \frac{\tilde{M}_q(V)}{I_{yy}} & \frac{\tilde{M}_u(V)}{I_{yy}} & \frac{\bar{M}_w}{I_{yy}} & 0 \\ \frac{\tilde{X}_q(V,\alpha)}{m} - w_0 & \frac{\tilde{X}_u(V,\alpha)}{m} & 0 & g\cos(\Theta_0) \\ \frac{\bar{Z}_q}{m} + u_0 & 0 & \frac{\tilde{Z}_w(V,\alpha)}{m} & g\sin(\Theta_0) \\ 1 & 0 & 0 & 0 \end{bmatrix}, \tag{4.17}$$

$$\tilde{\mathbf{B}}_{\mathbf{simp}}(V, \alpha) = \begin{bmatrix} \frac{\tilde{M}_{\delta_e}(V,\alpha)}{I_{yy}} \\ \frac{\tilde{X}_{\delta_e}(V)}{m} \\ 0 \\ 0 \end{bmatrix} \tag{4.18}$$

where a bar superscript indicates that the corresponding parameter is fixed to the same constant value (viz. a weighted average obtained from all estimation datasets) regardless of the flight condition, rather than being computed from the scheduling functions. Note that the parameters in Eq. 4.18 are now estimated from the *global* model, as denoted by the tilde superscript, and can therefore be calculated in any flight condition. The scheduling functions used to obtain the unknown parameters in the above expression were given previously in Eq. 4.16. Substituting the estimated global model parameters into the aforementioned

equation gives the following final scheduling functions:

$$\tilde{M}_q = -7.45 \times 10^{-3} - 3.49 \times 10^{-2}V + 7.11 \times 10^{-3}V^3$$
$$\tilde{M}_u = -4.21 \times 10^{-2} - 1.80 \times 10^{-1}V + 1.64 \times 10^{-1}V^2$$
$$\tilde{M}_w = -7.21 \times 10^{-2}$$
$$\tilde{M}_{\delta_e} = 8.26 \times 10^{-2} + 2.04 \times 10^{-1}V^2 - 0.10 \times 10^{-1}V^2\alpha - 6.25 \times 10^{-2}V^3$$
$$\tilde{X}_q = 1.24 \times 10^{-2} + 1.60 \times 10^{-2}V^2\alpha$$
$$\tilde{X}_u = -1.39 \times 10^{-1} + 8.25 \times 10^{-2}V\alpha - 1.37 \times 10^{-1}V^2\alpha \qquad (4.19)$$
$$\tilde{X}_w = 0$$
$$\tilde{X}_{\delta_e} = -1.29 \times 10^{-1} + 1.56 \times 10^{-1}V - 8.10 \times 10^{-2}V^3$$
$$\tilde{Z}_q = -4.15 \times 10^{-3}$$
$$\tilde{Z}_u = 0$$
$$\tilde{Z}_w = -3.87 \times 10^{-1} + 3.46 \times 10^{-1}\alpha + 3.67 \times 10^{-1}V\alpha - 3.48 \times 10^{-1}V\alpha^2$$
$$\tilde{Z}_{\delta_e} = 0$$

Results were also computed using the original full local model (Eq. 4.1) with no further adjustments (cf. Appendix F). The simplified model structure was found to yield somewhat improved results, while requiring only approximately half the number of parameters, therefore it represents an attractive solution. Additionally, the new model structure improves on the original in terms of reliability of the results, by only including well-estimated parameters and only scheduling those parameters that vary significantly with the flight condition. The estimated local parameters, for both the original and the simplified model structures, are listed in full in Appendix F.

Ultimately, rather than by its parameters, a model must be judged by its dynamic properties and the output it predicts. These points are discussed in the next subsections.

4.5.3. SYSTEM DYNAMICS

The resulting model was first evaluated in terms of the system dynamics. This evaluation also provided more detailed insight into the dynamics of the test vehicle, which are therefore discussed again in this section. Note that the local modelling results shown in the remainder of this chapter refer to the simplified model given by Eq. 4.2.

As discussed, the local LTI systems all have one complex pole pair and two real poles. Fig. 4.12 shows the full polar plots obtained from the LPV model in the 46 different flight conditions considered, the corresponding 46 local models, and the average model (cf. Sec. 4.4.4). The poles obtained from each model are also shown separately in Fig. 4.13, with colours illustrating the changes with changing flight velocity. Finally, to facilitate the evaluation of each component of the dynamics, the poles of each of the aforementioned models (or set of models) are plotted separately in Fig. 4.14, against the flight conditions the LPV model was evaluated at (corresponding to the conditions where local models were available). In the interest of clarity, the complex pole is split into real and imaginary components. Results obtained from the validation data are highlighted in the plots. Note that in this section – and in the figures shown – the flight condition is shown only in terms of the

velocity. For the sake of clarity, it was decided to only evaluate one variable at a time. The velocity was chosen as it is the variable most correlated to most of the model parameters, however trends with the AOA were in most cases approximately inversely correlated.
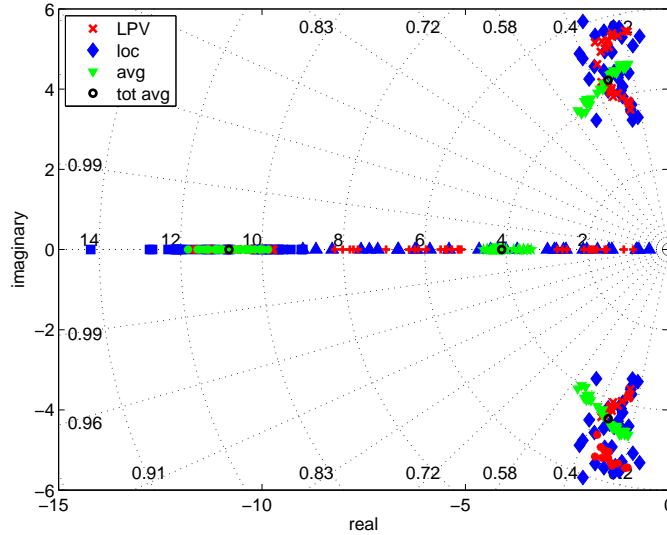
Figure 4.12: System poles in the complex plane: LPV, local and average models; overall average (with fixed kinematics) is also shown.
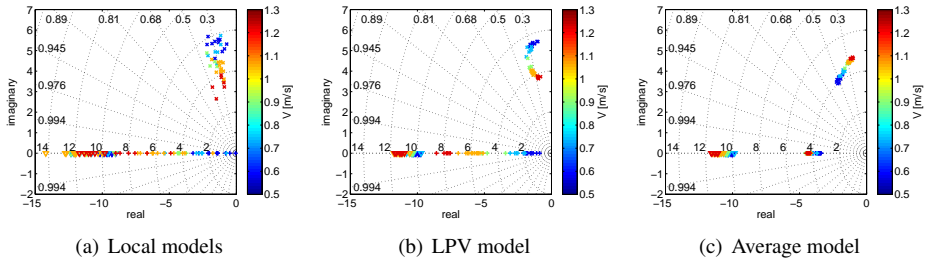
Figure 4.13: System poles in the complex plane: LPV, local and average models; with colour indicating changing flight velocity.

As already suggested in Sec. 4.3.2, there are trends between the system poles and the flight conditions, however this is not the case, to the same extent, for all of the poles. The LPV model was found to replicate most of the observed trends, albeit some more accurately than others. As expected, the trends that emerged more clearly from the local modelling are replicated more accurately by the LPV model, while unclear variations in the local modelling results led to unclear global modelling results. This points to shortcomings in the underlying local models rather than in the global model.

(a) $Re(p_1) = Re(p_2)$

(b) $Im(p_1) = -Im(p_2)$

(c) p_3

(d) p_4
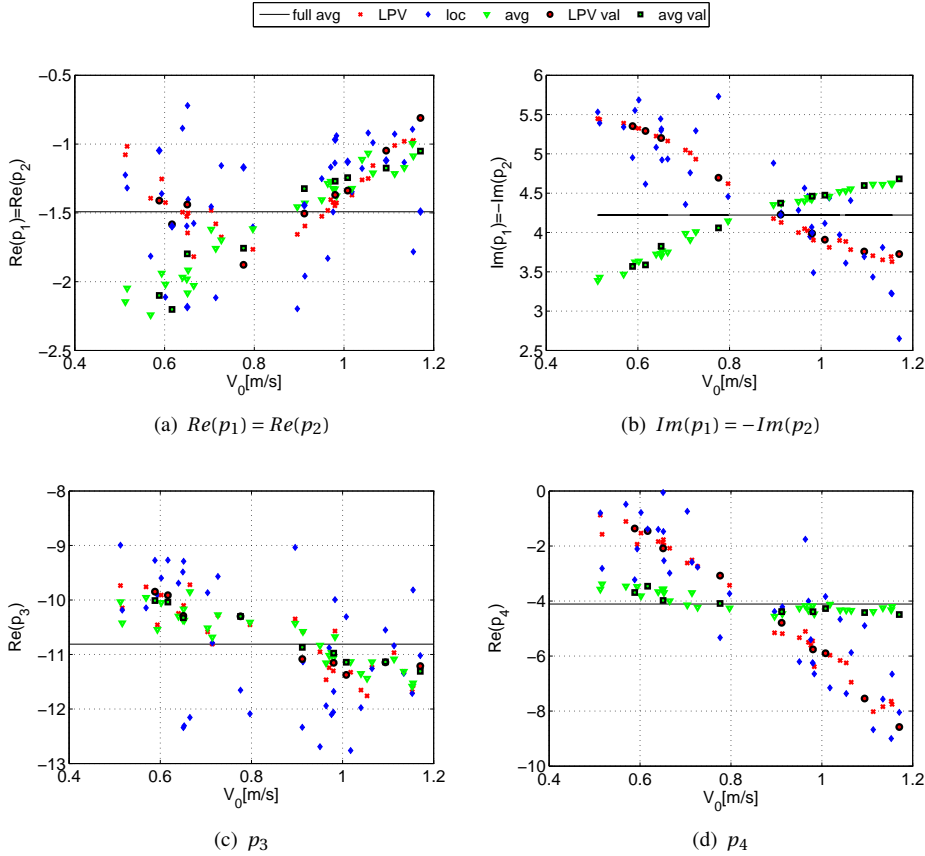
Figure 4.14: System poles versus corresponding trim velocity: LPV, local and average models (val=validation).

The complex pole displays a clear trend with the flight condition, as evident from the trends highlighted in Figs. 4.14(a) and 4.14(b), and the analogous trajectory shown in Fig. 4.13. The imaginary component in particular, clearly decreases in magnitude at higher velocities – indicating that the frequency decreases. This trend is accurately captured by the LPV model. Interestingly, the average model, which considers the changing kinematics but not the changing aerodynamics, shows an opposite trend in the imaginary component, suggesting that the trend seen in the local model oscillatory dynamics (particularly in the frequency) is predominantly determined by the aerodynamics rather than by the kinematics. By contrast, the real component of the complex pole displays a considerably smaller overall variation and the local model-obtained values are more scattered, so that the variation with the velocity is less clear, particularly in the low velocity range. Nonetheless, there appears to be a trend, which is captured by the LPV model, with the damping initially increasing, in the lower velocity range (up to $V \approx 0.8$m/s), and then clearly decreasing again at even higher velocities. The average model that only considers kinematic changes,

displays a very similar result in the high velocity range, but the trend does not reverse at low velocities, suggesting that at low velocities the aerodynamics play a more dominant role in determining the overall dynamic behaviour, compared to the (body) kinematics. It would also appear that there is a 'sweet spot' for the studied platform, where the damping is highest – and this is in agreement with piloting experience on the vehicle. However, the significant amount of seemingly random variation in the local data implies that these results must be verified and are not yet conclusive.

The faster of the two real poles (p_3) shows only a vague trend, decreasing somewhat at higher velocities, however there is a large amount of variation between the local model results, and further (and ideally better) data would be required to ascertain this trend. Given the large amount of variation, while the LPV model captures a part of the trend, the result is not clear, especially in the higher velocity range. Here, the LPV and average models are almost identical – this may be because of the parameters that were fixed to constant values or excluded from the model structure, which imply that parts of the LPV model-predicted dynamics (i.e. the parts associated with the Z-force) will be very close to those predicted by the average model. Despite the somewhat unclear result, it should be noted that since this is the fastest pole, it should play only a limited part in the overall response. The slower pole (p_4) again displays a very clear trend with the flight condition, which is captured with significant accuracy by the LPV model. The average model, by contrast, barely captures any of this trend, and closely resembles the overall average, suggesting that this component of the dynamics too is determined by the aerodynamics rather than the kinematics. It can also be observed that, based on the observed trends, this pole appears to be become unstable at very low velocities and clearly unstable at hover. For a symmetrical tailless flapper at hover, p_4 captures the vertical dynamics.

Overall, the damping decreases at very low velocities. At higher velocities, the real poles become more negative but the oscillatory pole appears to eventually become unstable. The oscillatory component decreases in frequency at high velocities – in agreement with observed flight behaviour of the test platform. The significant differences between the local (and LPV model) trends and those shown by the kinematic model highlight that the aerodynamics are indeed changing with changing flight conditions, and suggest that the overall flight behaviour resulting is predominantly influenced by the aerodynamics, as opposed to the kinematics. Overall the LPV model is accurate in capturing those trends that are clearly visible and can be used to predict the changing dynamic properties of the system in different conditions, which may itself already be useful. However, it should be considered that additional effects may become evident with more informative data, particularly data where the linear velocity dynamics are excited more effectively. The current result is mainly focused on the pitch dynamics, which for instance do not appear to have a significant effect on the fast aperiodic pole (p_3).

4.5.4. OUTPUT MATCH

Figs. 4.15 and 4.16 show examples of the output predicted by the LPV model, compared to the flight data, the output of the corresponding local LTI models, and the output of the average model (where only the kinematics vary, cf. Sec. 4.4.4). Examples of results are shown for both the estimation and the validation datasets, with the specific datasets selected from different parts of the flight envelope so as to present a basic overview. A more compre-

hensive overview is given in Figs. 4.17–4.19, which show statistical metrics (RMS errors and output correlation coefficients) evaluating the performance of the LPV model for all estimation and validation datasets. Figs. 4.17 and 4.19, in particular, show the difference in performance, respectively, between LPV and average models, and between LPV and local models, facilitating the comparison of the different types of models. The same information is also summarised in Table 4.4.

As anticipated from the scheduling results (cf. Sec. 4.5.2), it can be observed that the LPV model is able to approximate the local models, and hence the flight data, reaching a high level of accuracy for both the estimation and the validation conditions. The validation results, in particular, suggest that the model can be used to predict the flight behaviour at points where no local models are available. While the local models are consistently more accurate compared to the LPV results computed in the same conditions – as expected, given that the local models are the baseline used to construct the LPV model, and considered to be correct a priori – the differences between the set of local models and the LPV model are typically small. Generally, where the local models used for estimation have a somewhat lower accuracy, the LPV model also tends to perform less effectively, emphasising that an identified model can only be as good as the identification data it is derived from. Nevertheless, amongst the flight conditions considered, there are isolated cases where the LPV model displays a marginally better performance than the corresponding local model (cf. Fig. 4.19) – these are cases where the relevant local model is comparatively less accurate, e.g. due to less clean or informative identification data, suggesting that the LPV model is more dependable overall and can help to circumvent locally inaccurate models. In view of this observation, a better result may be obtainable if only the most accurate local models are used for estimation, rather than a random selection among the models available.

The LPV model is accurate and scalable, and hence brings a significant improvement compared to the use of a single average model. Fig. 4.18 highlights that the LPV model consistently achieves a higher accuracy than the average model, in both estimation and validation conditions (cf. also the output examples in Figs. 4.15 and 4.16). While the differences are of a small magnitude, it is important to consider that the scale of the entire problem is small, as discussed in Sec. 4.3. On the one hand, this implies that seemingly negligible changes may have a significant effect. On the other hand, the achievable accuracy – in terms of modelling and especially data acquisition – is limited and may be close in magnitude to the changes being modelled. Even small errors in the local models are for instance significant given the small global variation to be modelled. Similarly, the small scale emphasises the effect of inaccuracies in the scheduling. Indeed, it can be remarked that although the LPV scheduling is effective overall and yields results (parameters and eigenvalues) significantly closer to the local results than the average model (cf. Secs. 4.5.2 and 4.5.3), the difference in the resulting output is less noticeable. It appears that the modelling errors involved are large enough to affect the final result, even though per se they appear to be small, and all the main trends in the dynamics are replicated accurately by the LPV model.

Bearing these points in mind, an average model may be a sufficiently accurate approximation for some applications, if a limited operating domain is considered. Overall, however, the LPV model is more accurate and offers several advantages over both the average model and the set of local models. Unlike the average model, the LPV model does not

4
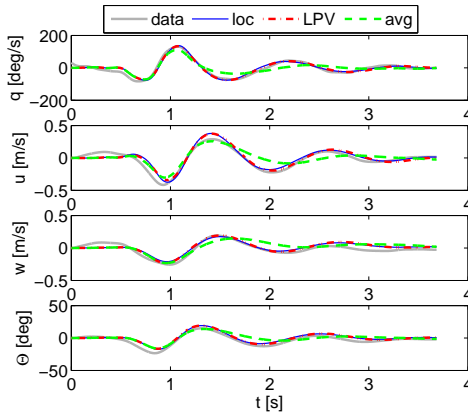
(a) Test #2 (low velocity/ high AOA condition)   (b) Test #14 (low velocity/ high AOA condition)
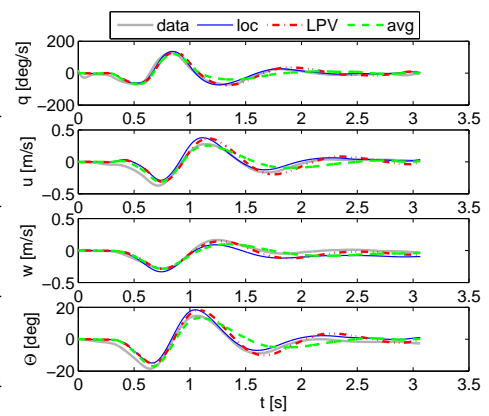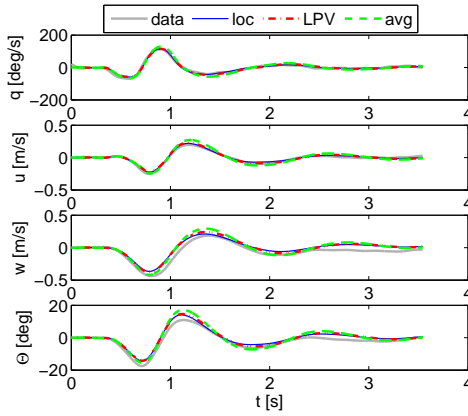
(c) Test #26 (intermediate velocity/ AOA condition)   (d) Test #38 (high velocity/ low AOA condition)
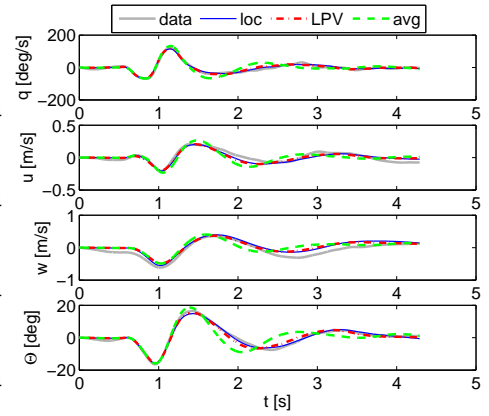
Figure 4.15: Example of output match: LPV, average and local models, versus flight test data (**estimation** sets)
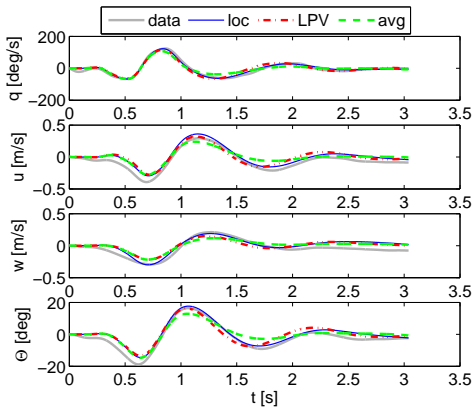
(a) Test #3 (low velocity/ high AOA condition)
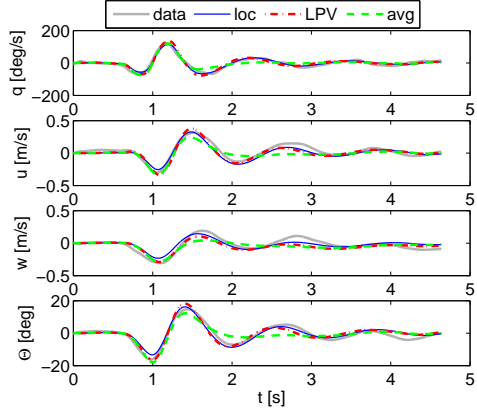
(b) Test #11 (low velocity/ high AOA condition)
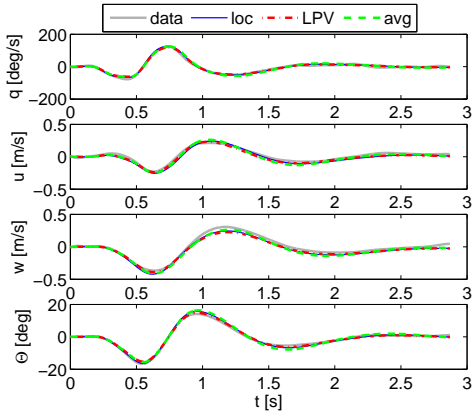
(c) Test #22 (intermediate velocity/ AOA condition)
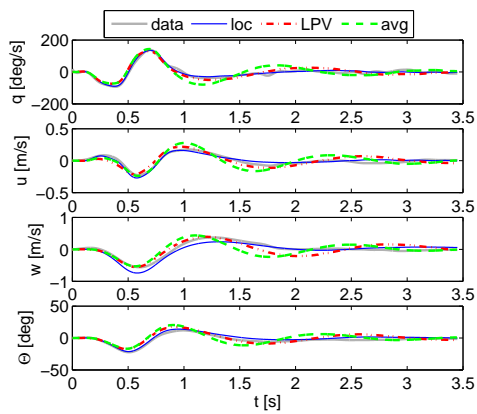
(d) Test #45 (high velocity/ low AOA condition)

Figure 4.16: Example of output: LPV, average and local models, versus flight test data (**validation** sets)

Table 4.4: Percentage of cases (flight conditions the models are evaluated at) where the LPV model has a better performance than the average and local models, respectively.

State	RMSE: % cases better than				corr: % cases better than			
	Avg.(est.)	Loc.(est.)	Avg.(val.)	Loc.(val.)	Avg.(est.)	Loc.(est.)	Avg.(val.)	Loc.(val.)
q	87	10	100	11	84	6	100	11
u	81	6	89	11	77	6	67	11
w	81	10	44	0	77	13	67	11
Θ	84	10	100	0	81	16	100	0

deteriorate in accuracy as the flight conditions change. Figs. 4.18 and 4.19 show that in the central part of the flight envelope the LPV and average model results are very similar, but that the average model increasingly loses accuracy at flight conditions increasingly different from those in the middle of the envelope. This can also be observed in the output (Fig. 4.15): especially at low velocities, the discrepancy between average model and flight data is clearly visible. This effect will become more pronounced if a wider flight envelope is considered (e.g. through changes to the vehicle configuration, cf. Sec. 4.2.1). Hence, an average model is not a robust solution, and is inadequate for high-accuracy applications.

By contrast, the LPV model retains a similar performance throughout the domain considered, with the exception of isolated outliers, whose decreased performance can be traced back to the estimation data. It is more accurate than the average model and represents a scalable solution that can be extended to cover a vaster flight envelope. The developed model can also be used effectively to predict how the dynamics of the system change, which is not possible with an average model (cf. Fig. 4.14 and Sec. 4.5.3). While less accurate than the local models – as expected, since the estimation process minimises the difference between LPV model and closest local model –, the LPV model has the advantages of higher flexibility, continuous coverage and a smaller overall model size (a total of 25 parameters, as opposed to 12 parameters per flight condition initially, or 9 per condition with the simplified model structure). Another benefit is that, whereas single local models may be inaccurate, e.g. due to inaccurate identification data, if the majority of the original local models are accurate, the LPV model can bypass local errors (e.g. single outliers) in favour of the more significant overall trends.

The modelling approach itself is therefore considered an effective and useful approach when dealing with flapping-wing vehicles that can be locally represented by LTI models (the most widespread formulation in the literature). Whether the suggested approach remains effective when considering more significant variation (e.g. including the effect of CG shifts, which would allow for considerably higher velocities) must be verified, however the approach remains theoretically applicable. Moreover, the fact that the LPV model remains accurate at the edges of the considered region suggests that some degree of further extrapolation could be handled. The benefits of using a global model as opposed to a rough single average approximation would become more evident if more significant changes were considered. Further, the currently observed effects may become more clearly discernible and easier to model if more accurate and informative data are used.
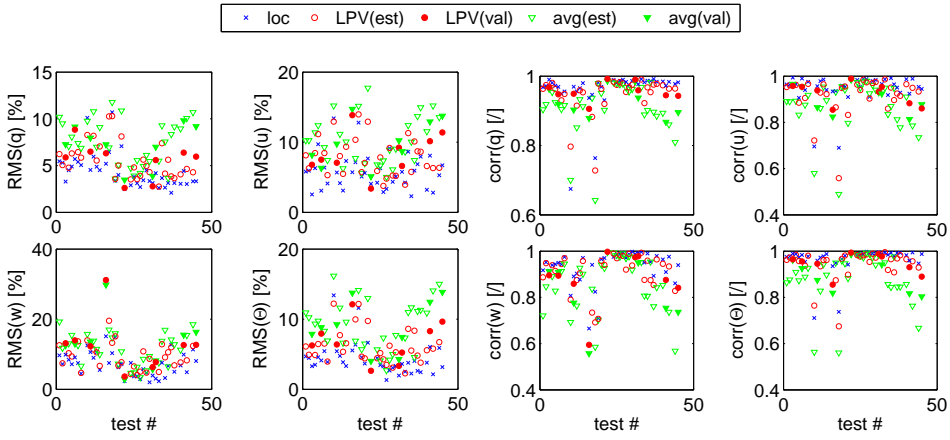
Figure 4.17: LPV, average and local model-obtained results, compared to flight data.
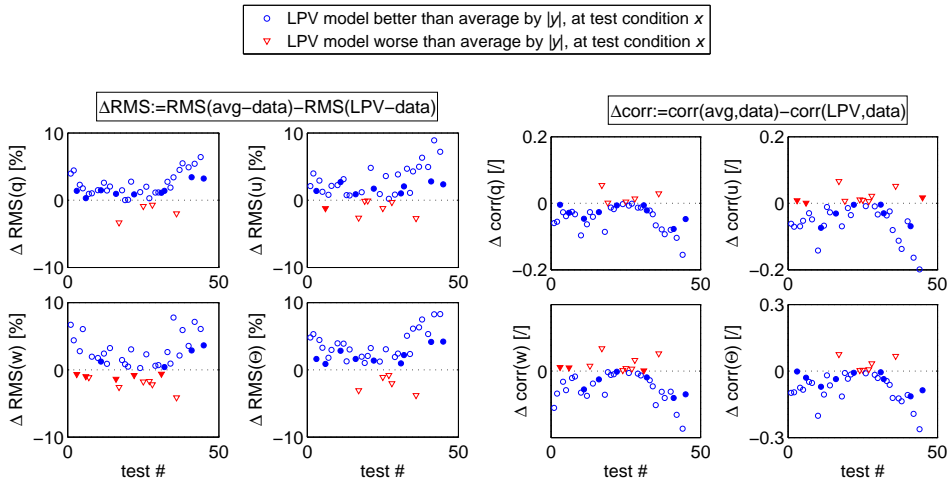
Figure 4.18: **LPV and average** model-obtained results, compared to flight data (validation sets as filled markers)
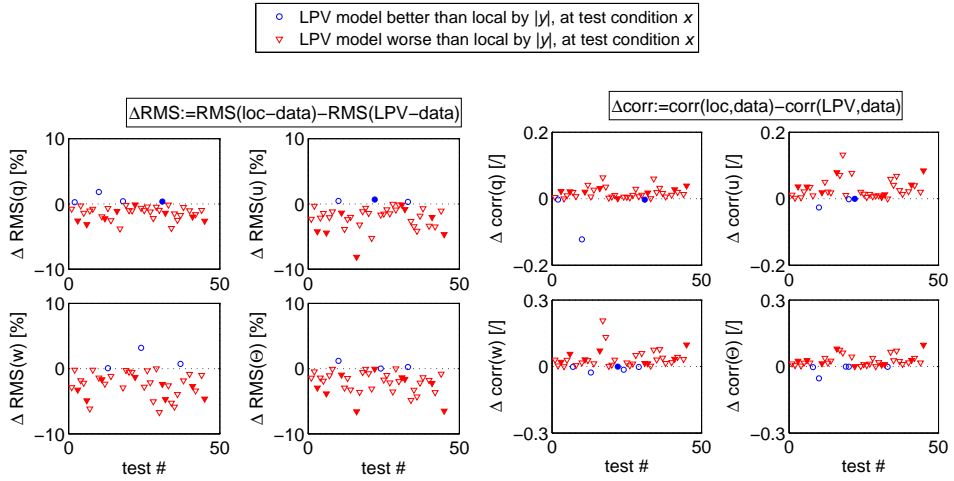
Figure 4.19: **LPV and local** model-obtained results, compared to flight data (validation sets as filled markers).

4.6. CONCLUSIONS

A linear parameter-varying (LPV) model identification approach was developed to represent the time-averaged dynamics of a flapping-wing micro aerial vehicle (FWMAV). This involved, firstly, estimating local dynamic models of the system, using 46 sets of free-flight data collected in different flight conditions, and, secondly, determining a set of scheduling functions to express the dependency of these models on the flight condition they represent. Results show that the obtained scheduling functions accurately model the key dynamic properties of the vehicle, and therefore constitute a useful means of predicting the system dynamics and simulating the system response in different flight conditions. With a significantly lower number of parameters, the global model achieves an only slightly lower accuracy than the initial set of local models, while additionally providing continuous coverage across the entire range of conditions considered, and therefore also increased flexibility. Furthermore, the model retains an approximately constant accuracy also at the edges of the covered flight envelope, suggesting that some extrapolation is possible and that the approach may be an effective solution also to represent more significant global variation, provided that linear models remain effective locally. The small physical scale of the FWMAV modelling problem was found to be a challenge, as the changes being modelled are significant for the *micro* aerial vehicle studied, but simultaneously close in magnitude to the error in the data acquisition and modelling process. In spite of this limitation, the modelling approach is promising, and yielded a global model that is accurate but requires few measurements, is computationally light and is easily interpretable. All of these properties make the resulting model highly suitable for simulation and control work. The modelling process also yielded more in depth information on the dynamic properties of the test platform, clearly showing that these vary with the angle of attack and flight velocity and providing insight into how they vary. The observed trends are consistent with flight experience, providing further

corroboration of the obtained results. Improved results may be obtainable with more informative and extensive data, leading to more accurate local models and a reduced error in the global modelling process. Furthermore, the suggested approach is considered applicable to account for different vehicle configurations in a single model. This type of extension of the model would likely involve larger changes and therefore more fully exploit the LPV approach.

REFERENCES

[1] S. F. Armanini, M. Karásek, and C. C. de Visser, *Global LPV model identification of flapping-wing dynamics using flight data,* in *AIAA Modeling and Simulation Technologies Conference*, AIAA Paper 2018-2156 (2018).

[2] S. F. Armanini, M. Karásek, and C. C. de Visser, *Global linear parameter-varying model identification of flapping-wing dynamics using flight data,* Journal of Guidance, Control and Dynamics (2018), (under review).

[3] C. P. Ellington, *The Aerodynamics of Hovering Insect Flight. I. The Quasi-Steady Analysis,* Philosophical Transactions of the Royal Society B: Biological Sciences **305**, 1 (1984).

[4] C. P. Ellington, C. van den Berg, A. P. Willmott, and A. L. R. Thomas, *Leading-edge vortices in insect flight,* Nature **384**, 626 (1996).

[5] S. P. Sane, *The aerodynamics of insect flight,* Journal of Experimental Biology **206**, 4191 (2003).

[6] M. H. Dickinson, F.-O. Lehmann, and S. P. Sane, *Wing Rotation and the Aerodynamic Basis of Insect Flight,* Science **284**, 1954 (1999).

[7] G. K. Taylor and A. L. R. Thomas, *Dynamic flight stability in the desert locust Schistocerca gregaria,* Journal of Experimental Biology **206**, 2803 (2003).

[8] T. Nakata, H. Liu, Y. Tanaka, N. Nishihashi, X. Wang, and A. Sato, *Aerodynamics of a bio-inspired flexible flapping-wing micro air vehicle,* Bioinspiration & Biomimetics **6** (2011).

[9] J. Grauer, E. Ulrich, J. E. Hubbard, D. Pines, and J. S. Humbert, *Testing and System Identification of an Ornithopter in Longitudinal Flight,* Journal of Aircraft **48**, 660 (2011).

[10] J. V. Caetano, C. C. de Visser, G. C. H. E. de Croon, B. Remes, C. De Wagter, and M. Mulder, *Linear Aerodynamic Model Identification of a Flapping Wing MAV Based on Flight Test Data,* International Journal of Micro Air Vehicles (2013).

[11] S. F. Armanini, C. C. de Visser, and G. C. H. E. de Croon, *Black-box LTI Modelling of Flapping-wing Micro Aerial Vehicle Dynamics,* in *AIAA Atmospheric Flight Mechanics Conference* (2015) AIAA Paper 2015-0234.

[12] G. J. Berman and Z. J. Wang, *Energy-minimizing kinematics in hovering insect flight,* Journal of Fluid Mechanics **582**, 153 (2007).

[13] C. T. Orlowski and A. R. Girard, *Averaging of the nonlinear dynamics of flapping wing micro air vehicles for symmetrical flapping,* in *AIAA Aerospace Sciences Meeting including the New Horizons Forum and Aerospace Exposition* (2011).

[14] Z. A. Khan and S. K. Agrawal, *Force and moment characterization of flapping wings for micro air vehicle application,* in *American Control Conference* (2005).

[15] Y. Xiong and M. Sun, *Stabilization control of a bumblebee in hovering and forward flight,* Acta Mechanica Sinica **25**, 13 (2009).

[16] J. Wu and M. Sun, *Control for going from hovering to small speed flight of a model insect,* Acta Mechanica Sinica **25**, 295 (2009).

[17] B. M. Finio, N. O. Perez-Arancibia, and R. J. Wood, *System identification and linear time-invariant modeling of an insect-sized flapping-wing micro air vehicle,* in *2011 IEEE/RSJ International Conference on Intelligent Robots and Systems (IROS)* (2011).

[18] H. Duan and Q. Li, *Dynamic model and attitude control of Flapping Wing Micro Aerial Vehicle,* in *IEEE International Conference on Robotics and Biomimetics (Ro-Bio)* (2009).

[19] A. N. Chand, M. Kawanishi, and T. Narikiyo, *Parameter Estimation for the Pitching Dynamics of a Flapping-Wing Flying Robot,* in *IEEE International Conference on Advanced Intelligent Mechatronics (AIM)* (2015).

[20] S. F. Armanini, C. C. de Visser, G. C. H. E. de Croon, and M. Mulder, *Time-varying model identification of flapping-wing vehicle dynamics using flight data,* Journal of Guidance, Control, and Dynamics **39**, 526 (2016).

[21] G. C. H. E. de Croon, M. Perçin, B. D. W. Remes, R. Ruijsink, and C. De Wagter, *The DelFly Design, Aerodynamics, and Artificial Intelligence of a Flapping Wing Robot* (Springer Netherlands, 2016).

[22] O. Sename, P. Gáspár, , and J. Bokor, eds., *Robust Control and Linear Parameter Varying Approaches*, Lecture Notes in Control and Information Sciences (Springer, Berlin Heidelberg, 2013).

[23] R. Tóth, P. M. J. Van den Hof, J. H. a. Ludlage, and P. S. C. Heuberger, *Identification of nonlinear process models in an LPV framework,* Proceedings of the 9th International Symposium on Dynamics and Control of Process Systems , 869 (2010).

[24] D. J. Leith and W. E. Leithead, *Survey of gain-scheduling analysis and design,* International Journal of Control **73**, 1001 (2000).

[25] A. Fujimori and L. Ljung, *Model identification of linear parameter varying aircraft systems,* IMechE Part G: Journal of Aerospace Engineering **220** (2006).

[26] A. Marcos and G. Balas, *Linear parameter varying modeling of the Boeing 747-100/200 longitudinal motion,* in *AIAA Guidance, Navigation, and Control Conference and Exhibit* (2001).

[27] A. Marcos and G. J. Balas, *Development of Linear-Parameter-Varying Models for Aircraft,* Journal of Guidance, Control, and Dynamics **27**, 218 (2004).

[28] A. Marcos, J. Veenman, and C. W. Scherer, *Application of LPV Modeling, Design and Analysis Methods to a Re-entry Vehicle*, Tech. Rep. (2010).

[29] G. J. Balas, I. Fiahlo, A. Packard, J. Renfrow, and C. Mullaney, *On the design of the lpv controllers for the f-14 aircraft lateral-directional axis during powered approach,* in *American Control Conference* (1997).

[30] P. Seiler, G. Balas, and A. Packard, *Control of linear parameter varying systems with applications,* (Springer, Boston, MA, 2012) Chap. Linear parameter varying control for the X-53 active aeroelastic wing.

[31] C. Westermayer, A. Schirrer, M. Hemedi, and M. Kozek, *Linear parameter-varying control of a large blended wing body flexible aircraft,* in *IFAC Proceedings*, Vol. 43 (2010).

[32] J. Weilai, D. Chaoyang, and W. Qing, *A systematic method of smooth switching lpv controllers design for a morphing aircraft,* Chinese Journal of Aeronautics **28**, 1640 (2015).

[33] V. Klein and E. A. Morelli, *Aircraft System Identification: Theory And Practice* (AIAA Education Series, Reston, VA, 2006).

[34] S. F. Armanini, M. Karásek, d. G. C. H. E., and C. C. de Visser, *Onboard/ offboard sensor fusion for high-fidelity flapping-wing robot flight data,* Journal of Guidance, Control and Dynamics **40** (2017).

[35] S. F. Armanini, M. Karásek, C. C. de Visser, G. C. H. E. de Croon, and M. Mulder, *Flight testing and preliminary analysis for global system identification of ornithopter dynamics using on-board and off-board data,* in *AIAA Atmospheric Flight Mechanics Conference*, AIAA Paper 2017-1634 (2017).

[36] M. Karásek, A. J. Koopmans, S. F. Armanini, B. D. W. Remes, and de Croon G. C. H. E., *Free flight force estimation of a 23.5 g flapping wing MAV using an on-board IMU,* in *IEEE International Conference on intelligent robots and systems (IROS)* (2016).

[37] J. V. Caetano, C. C. de Visser, B. D. Remes, C. De Wagter, E.-J. Van Kampen, and M. Mulder, *Controlled Flight Maneuvers of a Flapping Wing Micro Air Vehicle: a Step Towards the Delfly II Identification,* AIAA Atmospheric Flight Mechanics Conference (2013).

[38] C. Orlowski, A. Girard, and W. Shyy, *Derivation and simulation of the nonlinear dynamics of a flapping wing micro-air vehicle,* in *European Micro Aerial Vehicle Conference and Flight Competition* (2009).

[39] M. A. Bolender, *Rigid multi-body equations-of-motion for flapping wing MAVs using Kane equations,* in *AIAA Guidance, Navigation, and Control Conference*, AIAA Paper 2009-6158 (2009).

[40] J. A. Grauer and J. E. Hubbard, *Multibody Model of an Ornithopter,* Journal of Guidance, Control, and Dynamics **32**, 1675 (2009).

[41] M. Sun and Y. Xiong, *Dynamic flight stability of a hovering bumblebee,* Journal of Experimental Biology **208**, 447 (2005).

[42] I. Faruque and J. Sean Humbert, *Dipteran insect flight dynamics. Part 1 Longitudinal motion about hover.* Journal of Theoretical Biology **264**, 538 (2010).

[43] J. A. Mulder, *Design and evaluation of dynamic flight test manoeuvres*, Phd, Delft University of Technology (1986).

[44] E. Morelli, *Flight test validation of optimal input design and comparison to conventional inputs,* in *AIAA Atmospheric Flight Mechanics Conference* (1997).

[45] G. Papageorgiou, K. Glover, G. D'Mello, and Y. Patel, *Taking robust LPV control into flight on the VAAC harrier,* in *Proceedings of the 39th IEEE Conference on Decision and Control (CDC)*, Vol. 5 (2000).

[46] M. N. Hammoudi and M. H. Lowenberg, *Dynamic gain scheduled control of an f16 model,* in *AIAA Guidance, Navigation and Control Conference* (2008).

[47] B. Bamieh and L. Giarré, *Identification of linear parameter varying models,* International Journal of Robust and Nonlinear Control **12**, 841 (2002).

[48] R. Tóth, *Modeling and Identification of Linear Parameter-Varying Systems an Orthonormal Basis Function Approach*, Phd thesis, Delft University of Technology (2008).

[49] A. Marcos and S. Bennani, *LPV modeling, analysis and design in space systems: Rationale, objectives and limitations,* in *AIAA Guidance, Navigation, and Control Conference and Exhibit* (2009).

[50] R. Jategaonkar, *Flight Vehicle System Identification A Time Domain Methodology* (AIAA Progress in Astronautics and Aeronautics, Reston, VA, USA, 2006).

[51] V. Klein and J. G. Batterson, *Determination of airplane model structure from flight data using splines and stepwise regression*, Tech. Paper 2126 (NASA, 1983).

II

AERODYNAMIC MODELLING

5

QUASI-STEADY WING AERODYNAMIC MODELLING

The first part of this thesis focused on a considerably simplified and heavily data-driven modelling approach, where physical interpretability is limited. Particularly the flapping-related time-varying effects could only be included through a black-box formulation, offering no insight and only limited potential for generalisation (cf. Appendix A). While the previously proposed models are amenable to control design and stability analysis, a more physically meaningful and detailed representation is desirable to acquire theoretical insight, to support design and aerodynamics studies, and, potentially, as a basis for advanced controllers acting within the single flap cycles. In this chapter, the focus is shifted from the full dynamic system to the aerodynamics, and a quasi-steady model is derived for the wing aerodynamics of the studied test vehicle. The model extends existing quasi-steady theory by introducing a circulatory term to represent the unsteady clap-and-fling lift enhancement mechanism, and considering the flight-measured wing kinematics of the vehicle, rather than prescribing the wing motion, and covering different flight regimes. Additionally, the model is generalised to cover different flight regimes by expressing the model parameters, initially estimated from wind tunnel measurements, as a function of the flight condition. Validation tests performed with both free-flight and wind-tunnel data demonstrate that the model achieves a high accuracy and clearly captures the observed clap-and-fling effects. Compared to the approach proposed in Chapters 3 and 4, the approach put forth in this chapter yields more physical insight at the cost of a limited increase in complexity – it is therefore considered useful both for conceptual studies preceding the development of new platforms, and for sub-flap cycle control design.

Flapping-wing aerodynamic models that are accurate, computationally efficient and physically meaningful, are challenging to obtain. Such models are essential to design flapping-wing micro aerial vehicles and to develop advanced controllers enhancing the autonomy of such vehicles. In this work, a phenomenological model is developed for the time-resolved aerodynamic forces on clap-and-fling ornithopters. The model is based on quasi-steady theory and accounts for centripetal, circulatory, added mass and viscous forces. It extends existing quasi-steady approaches by: including a fling circulation factor to account for unsteady wing-wing interaction, and considering real platform-specific wing kinematics and different flight regimes. The model parameters are estimated from wind tunnel measurements conducted on a real test platform. Comparison to wind tunnel data shows that the model predicts the lift forces on the test platform accurately and accounts for wing-wing interaction effectively. Additionally, validation tests with real free-flight data show that lift forces can be predicted with considerable accuracy in different flight regimes. The complete parameter-varying model represents a wide range of flight conditions, is computationally simple, physically meaningful and requires few measurements. It is therefore potentially useful for both control system design and preliminary conceptual studies for developing new platforms.

5.1. INTRODUCTION

Insects and birds have unmatched flying capabilities. This unique skill has evolved over the course of millions of years, enabling them to improve their survivability, evade predators and carry food. Aside from the development at a neuromuscular level, flying species have optimised their wing shapes and beats to provide them with added performance and lift when required. An example of such evolution is the 'clap-and-fling' mechanism that typically occurs during the dorsal stroke-reversal of two-winged insects and specific birds, such as the pigeon [2]. This mechanism can be seen as the (near) touch of the wings, which begins when the leading edges of the wings touch at the end of the dorsal outstroke (clap) and proceeds with the evolution of the point of interaction between the wings down the chordwise axis of the wings, as they pronate around their trailing edges and fling apart (cf. Fig. 1.6 in Chapter 1). Since the first description of this mechanism by Weis-Fogh [3], several studies have identified variations of this motion to be present in many other species: *Trialeurodes vaporariorum* [4], *Thrips physapus* [5], and the parasitoid wasp *Muscidifurax raptor* [6]. Larger insects, such as *Lepidoptera* [7] and locusts [8], also exhibit similar behaviours.

This particular type of flapping motion has been shown to augment the generation of lift during the flap cycle and is believed to be used by flapping flyers whose wing stroke capabilities are limited by their sweeping angle [9]. Adding to the observations of Weis-Fogh, Ellington [5] further suggested that the *Chrysopa Carnea* uses clap-and-fling for lift augmentation, steering and flight control. Several experimental studies tried to prove these hypotheses by developing flapping mechanisms that promote wing-wing interaction [10–12]. More recently, experimental work [9, 13–16] and numerical simulations [17–19] concluded that the clap-and-fling mechanism can enhance lift production by 6% [14] to 50% [20] of the net average force, with most of the studies reporting lift gains of 15% to 25% [9, 16].

Inspired by the evolution of natural flyers, such clap-and-fling mechanisms have been mimicked and implemented in a multitude of flapping-wing micro aerial vehicles (FW-MAVs) [14, 21–29], using four wings. Reasons for choosing this design setup include: (i) lift augmentation, allowing the FWMAVs to carry more payload, compared to their non-wing-interacting counterparts [30]; (ii) reduced complexity of flapping mechanisms with two degrees of freedom per wing, compared to multiple-degree-of-freedom mechanisms of other designs [31, 32]; (iii) reduced flapping-induced oscillations due to mutual cancellation of opposed forces caused by counter-motion of opposed wings, which facilitates inertial measurement unit (IMU) and vision payload integration; and (iv) presence of a tail that introduces static stability and simplifies the on-board control strategies.

Despite the significant maturation of technology, such FWMAVs still have very limited on-board processing capabilities, which, in turn, limit the use of complex control strategies for automatic and autonomous operations. These control strategies are thus typically characterised by simple proportional-integral-derivative (PID) controllers [33], which limit the flight regime to conditions very close to a linearised model [34]. More complex strategies, like non-linear dynamic inversion or unsteady aerodynamic models working atop kinematic information, are currently too computationally expensive for on-board control. To avoid this complexity, some studies suggest the use of free-flight system identification for the estimation of low-order 'brute-force' models [34–36] or the use of Fourier series for the complete modelling of the aerodynamic forces of an existing FWMAV [37, 38]. However, such methods are only possible if the FWMAV is already flight-capable and typically involve expensive measurement facilities, thus they are not applicable for the prediction of the aerodynamic, and consequently, the dynamic behaviour of FWMAVs during the design phase.

As pointed out by many studies [39–44], in some cases a good compromise can be obtained through the use of quasi-steady aerodynamic models. These closely represent the aerodynamic forces of single non-interacting wings, with results matching experimental and numerical results with a high approximation. Such models offer elegant solutions for the limitations identified above. However, for the specific case of lift-augmenting clap-and-fling FWMAVs, the quasi-steady models devised so far are lacking in three aspects: (i) quasi-steady aerodynamic representation of the added lift from wing-wing interaction during clap-and-fling; (ii) accurate modelling of the wings, typically modelled as rigid flapping plates without consideration of spanwise torsion or of the added benefits of wing flexibility, shown to be responsible for most of the lift gain [6, 15]; (iii) providing model parameters for flight conditions other than hover, hence impeding the application of the models to other flight conditions, where active control is more necessary.

The present study addresses the three gaps mentioned above and presents a simple phenomenological model for flapping-wing aerodynamics, which provides a suitable first approximation of the aerodynamic forces acting on a clap-and-fling FWMAV. The model extends quasi-steady theory to include additional circulation terms that are present during and shortly after clap-and-fling. The parameters of the model are estimated, using a maximum likelihood estimator, from high-resolution wind tunnel force measurements obtained on a real FWMAV, considering the real wing kinematics of the specific platform (the DelFly II [45]) in different flight conditions. A global function of the parameters for different trimmed flight conditions is provided, which allows for fast computation of the

aerodynamic parameters for a multitude of flight regimes, ranging from close to hover to fast $2m/s$ flight. Furthermore, the model is validated by comparing the force estimation in different flight regimes with real free-flight data of the FWMAV, ensuring additional closeness to the real physical system. The proposed model is simple, computationally fast, and requires few input measurements, therefore it is potentially highly useful for control applications, being applicable as a predictor already at the design stage.

This chapter continues with the comparison of existent quasi-steady models, a theoretical background on the clap-and-fling mechanism and a discussion of the proposed model, in Section 5.2. Section 5.3 presents the experimental methods used to obtain the force data and wing kinematics, from both wind tunnel and free-flight testing. This is followed by the results, discussion and validation of the estimated aerodynamic model in Section 5.4. Section 5.5 summarises the most important conclusions and contributions.

5.2. AERODYNAMIC MODELLING

5.2.1. REVISITING QUASI-STEADY AERODYNAMIC MODELS

As identified by Sane [46], four unsteady mechanisms are present in flapping-wing flight: (1) build-up of a starting vortex from the growth of a trailing edge vortex (TEV), known as Wagner effect; (2) delayed stall and leading edge vortex (LEV); (3) rotational circulation around a rotating surface, known as Kramer effect; (4) capture of the wake of the previous stroke by the subsequent one, typically called wake capture. In addition to these, (5) centripetal effects due to circular motion, (6) added mass effect due to accelerating wings and (7) wing-wing interaction are also important force generation mechanisms [3, 41].

Under the assumption of a quasi-steady development of the aerodynamics, the instantaneous forces acting on the wing are equivalent to the forces that would act during a steady uniform motion of the wing at the same free-stream velocity and angle of attack [47]. This way, a kinematic pattern can be divided into a number of consecutive time steps at which the forces are calculated, and the time history of the forces is obtained. Despite not considering some of the mechanisms mentioned above, viz. Wagner effect, wake capture and wing-wing interaction, and being initially derived for low angles of attack under thin airfoil theory, quasi-steady models of flapping wings have been shown to approximate the aerodynamic forces with significant accuracy [39, 41–43, 48].

The applicability of quasi-steady models is limited by two aspects, as further clarified by Table 5.1. On the one hand, for hovering flight (or very slow forward velocity) regimes, quasi-steady models are only applicable if the flapping frequency is considerably higher than the natural frequency of the flapper. On the other hand, for forward flight, the reduced frequency ($k = \frac{\omega c}{V_{ref}}$) should be low (e.g., below 0.2) for quasi-steady models to be applicable. In both cases, once the time scales of the flapping and body dynamics differ sufficiently, they can be considered decoupled: at very high flapping frequencies, the body dynamics dominate over the flapping-related dynamics, while at high body velocities, the free-stream flow dominates over the unsteady flow. The proposed model attempts to extends the applicability of quasi-steady models to other regimes and flyers, and, in particular, to account for clap-and-peel. It must be noted that the test platform used in this study is at the edge of the domain where quasi-steady models are considered acceptable – its flapping frequency is only one order of magnitude larger than its body mode frequencies (cf. Chap-

Table 5.1: Applicability of existent quasi-steady and proposed models, according to reduced frequencies ($k = \frac{\omega c}{V}$) and natural frequencies (ω_n). Adapted from [48, 49].

Criteria	Hover			Forward flight		
	$\frac{\omega}{\omega_n} \gg 1$	$\frac{\omega}{\omega_n} \approx O(1)$	$k > 0.2$ $\alpha > 25°$	$k > 0.2$ $\alpha < 25°$	$k < 0.2$
Modelling techniques	Only average forces affect body dynamics; **QS aerodynamics** • QS models that include LEV, e.g.: Dickinson et al. [39], Berman & Wang [50] • **Proposed model**	Contribution of LEV; Coupling between sub-flap forces and body dynamics • Numerical methods • **Proposed model**		Methods that capture unsteady effects • UVLM • Theodorsen et al. [51] • Peters [52]	**QS Aerodynamics** • QS models that include forward flight information • **Proposed Model**

ter 3), and its reduced frequency is above 0.2 in slow forward flight. In this sense, while the main focus of this study is to capture clap-and-peel, it is also evaluated to what extent quasi-steady models are applicable at the edges of the accepted range, where unsteady effects are increasingly significant.

5.2.2. UNDERSTANDING THE CLAP-AND-PEEL MECHANISM

Following the initial description by Weis-Fogh [3], for most species the clap-and-fling mechanism starts at the end of a half-stroke – at dorsal stroke reversal, cf. subfigure A in Fig. 5.1. As the wings touch, the cleft that is formed closes under the point of contact of the wings in a 'clap' shaped movement. During this phase, the air in the cleft is pushed down, which is believed to generate extra momentum [53]. After the clap (B), the wings pronate and move away from each other, rotating about their trailing edges, which generates the rapid growth of a new cleft between the upper parts of the wings, as they 'fling' apart (C and D). During this phase, air rushes around the leading edge of each wing into the cleft, in what was observed as an augmented LEV [15]. As the flap continues, the LEV continues to grow, and when the trailing edges separate, a starting trailing vortex starts to form (E).

The particular case represented in Fig. 5.1 as an example is based on theoretical assumptions found in the literature [3, 47, 54], complemented with experimental results of important studies in the field [15, 17, 18, 46, 53].

Several studies have focused on replicating this mechanism through mathematical [54], physical [11–13] and numerical simulation [17, 55] to draw further conclusions on the force augmentation mechanisms. All verified instantaneous and net force augmentation. However, two generalisations were present in these studies: (i) the wings were modelled as rigid, and (ii) the fling phase was modelled as a pure rotation about the trailing edges of the wings, without translation.

Recent observations concluded that in some cases the mechanism is better explained and replicated by a flexible 'peel' that replaces the previously described fling phase. It is believed that flexibility allows for the reconfiguration of biological structures, which results in reduced drag [6] and wake-capture mechanisms [15]. In this updated description, the
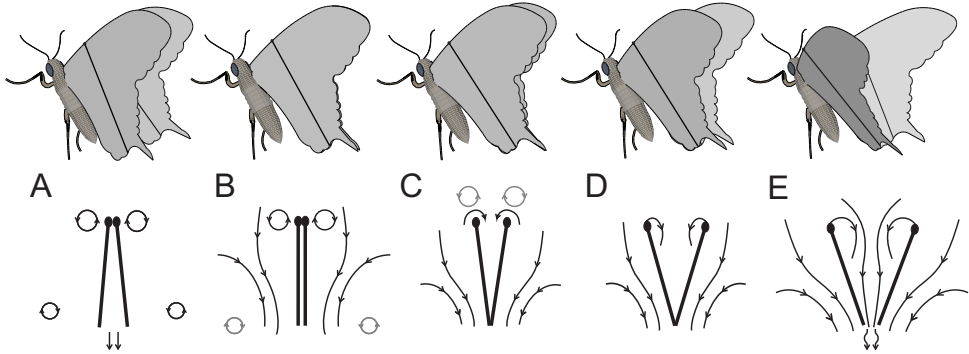
Figure 5.1: Clap-and-fling mechanism represented for a butterfly model with rigid wings. Arrows represent the direction of the flow; lines in black and grey represent current and previous subfigure vortices, respectively; detached lines are streamlines; circular shapes represent vortices; lines connected to the leading edge are starting vortices; lines at the trailing edges of subfigure E represent the interaction between the beginning of starting vortices and the flow from within the cleft.

upper parts of the wings 'peel' apart, while the lower parts are still 'clapping', due to a translatory motion induced by the wing flap reversal along the stroke plane. This reduces the effect of the clap, while it promotes the generation of stronger LEVs and a decrease of the negative effects of added mass, due to the reduction of the effective portion of the wing that is accelerating during the outstroke. Furthermore, this mechanism ensures a considerable reduction – and sometimes cancellation – of the trailing edge vorticity shed by each wing at the consequent stroke (during 'peeling'), which promotes the growth of circulation due to the absence of both the Wagner and Kramer effects – also considered to be one of the reasons for force augmentation [46].

5.2.3. PROPOSED AERODYNAMIC MODEL

In comparison to other modelling techniques, such as computational fluid dynamics (CFD) or unsteady vortex lattice methods (UVLM), quasi-steady models have the advantage of providing more physical insight, and their relatively simple form and low computational cost (cf. Table 5.2) make them suitable for physical understanding of the force generation mechanisms, design of FWMAVs, control and simulation work. Nevertheless, none of the existing quasi-steady models include the contribution of wing-wing interaction, and therefore they fail to predict the added lift present in clap-and-peel mechanisms, for both the instantaneous and the time-averaged lift augmentation.

The proposed model builds on existing quasi-steady models to include the effects listed in Sec. 5.2.1, as items (2) to (7). As a starting point, an extensive survey was performed to understand the applicability and compare the (dis)advantages of the formulations found across the literature.

GENERAL FORMULATION

The baseline of the proposed model consists of the combination of quasi-steady aerodynamics with blade element theory [41, 50, 56]. The forces acting on a wing are divided into

Table 5.2: Comparison between existent and proposed models. The focus is on non-CFD methods, as CFD models are not phenomenologically insightful or applicable for on-board control. Table adapted from Ref. [48].

	Dickinson et al.	Berman & Wang	Peters et al.	Khan & Agrawal	UVLM	Ansari et al.	**Proposed model**
# DOF	low	low	low	low	high	high	low
LEV	✓	✓	-	✓	-	✓	✓
Rot. circulation	✓	✓	✓	✓	✓	✓	✓
Added mass	✓	✓	✓	✓	✓	✓	✓
Viscous effects	-	✓	-	✓	-	-	✓
Wake capture	-	-	-	-	✓	-	-
Wing flexibility	-	-	-	-	-	-	✓
Clap-and-peel	-	-	-	-	-	-	✓
Validated in forward flight	-	-	-	-	-	-	✓
Applicability to on-board control	low	high	low	low	low	low	high

blade elementary forces, that are integrated both along the spanwise direction and in time to obtain the time history of the forces. The forces acting on a single blade element (BE), at each time instant, take the form:

$$d\mathbf{F} = d\mathbf{F}_{centrip} + d\mathbf{F}_{circ} + d\mathbf{F}_{addmass} - d\mathbf{F}_{visc} \tag{5.1}$$

which accounts for the centripetal, circulatory, added mass and viscous effects, respectively. Note that initial TEV shedding (Wagner effect) was not considered for the following reasons: (i) this effect has different contributions to the forces, depending on the Reynolds number (Re) of the system; (ii) there is no apparent agreement on the presence of such mechanisms in flapping wings [9]; (iii) clap-and-peel mechanisms considerably attenuate the starting TEV; (iv) mathematical simplicity. The centripetal term results from the Coriolis force due to the combined effect of translation and rotation of the blade element – cf. our final formulation in Eqs. 5.12 and 5.13. The other three terms we discuss in more detail in the remainder of this section, progressively building up our model until the final formulation is obtained in Sec. 5.2.3.

CIRCULATORY TERM

The circulatory term ($d\mathbf{F}_{circ}$ in Eq. 5.1) results from a combination of the translatory circulation (Γ_{trans}) and the rotational circulation (Γ_{rot}). Both are included to satisfy the Kutta condition (cf. Fig. 2 in [46]). For single, non-interacting wings (or, in this case, blade elements) Γ_{trans} includes the contribution of the free-steam circulation and the LEV, while Γ_{rot} accounts for the added circulatory term needed to maintain the Kutta condition for a rotating blade element. These terms take the form:

$$\Gamma = \Gamma_{trans} + \Gamma_{rot} = \frac{1}{2} C_L c(r) |V| + \frac{1}{2} C_R c^2(r) \dot{\theta}_w \tag{5.2}$$

where C_L is the lift coefficient function, $|V|$ is the magnitude of the velocity (vector) perceived by the blade element, C_R is the rotational coefficient, $c(r)$ is the chord as function of the spanwise radius and $\dot{\theta}_w$ the pitch rate of the wing element.

Several C_L and C_R formulations were studied from literature: viz. for C_L Fig. 2 in [39], Eq. 2.16 in [50], Eq. 31 in [57] and Eq. 17 in [48]. The values for the different parameters of each of these formulations were optimised (as explained in Sec. 5.4.1), and similar results could be obtained with all formulations by adjusting the parameters. Hence, the following formulations are recommended:

$$C_L = C_l \sin(2\alpha) \quad \text{or} \quad C_L = \frac{\pi AR}{2(1 + \sqrt{(\frac{\pi AR}{a_0})^2 + 1})} \sin(2\alpha) \tag{5.3}$$

the former [50] for simplicity, the latter [48] for preliminary design purposes, as the aspect ratio (AR) of the wing is considered. In the above equation, C_l is the lift coefficient, a_0 is the lift curve slope of a two-dimensional airfoil, and α is the angle of attack at the blade element. The rotational coefficient C_R takes the form observed in Refs. [39, 40],

$$C_R = C_r(0.75 - x_0) \tag{5.4}$$

where C_r is a constant coefficient, and x_0 is the chordwise position of the axis of rotation of the wing section.

The final circulatory term used in the model is derived in the next section, where clap-and-peel effects are discussed and incorporated in the formulation.

INCLUDING CLAP-AND-PEEL

Despite the lack of agreement on how to model the clap-and-peel mechanism, some aspects have been observed across multiple studies: (i) increased growth of circulation during clap-and-fling [3, 54, 55, 58]; (ii) prolonged effect of clap-and-fling on lift augmentation, still noticeable after the fling until half-way of the wing stroke [13, 17]; (iii) contribution of wing flexibility to increased lift augmentation and considerably reduced drag forces [6, 59]. These points are further detailed below.

Lighthill suggested the force augmentation mechanism could be described mathematically by a circulatory term of the form [54, 55]:

$$\Gamma = g(\lambda)\dot{\theta}c^2 \tag{5.5}$$

with $g(\lambda)$ being a function of the angle between the wing sections ($\lambda = \theta_{fling}/\pi$). A similar theoretical formulation was later introduced by Edwards & Cheng [60] and Wu & Hu-Chen [61], who added circulatory terms to the initial formula, with no considerable changes in the outcome. In another study, Spedding and Maxworthy [11] verified the formulation by performing a wing-wing interaction experiment with pure rotation around the trailing edge, obtaining discrete values for $g(\lambda)$ for different wing separation angles. They concluded the function $g(\lambda)$ to be different from the previous theoretical formulations, taking a somewhat constant value (≈ 2) up to $\theta_{fling} = 30°$, and then increasing linearly with the increase of the separation (cf. Fig. 17 in Ref. [11]). Sunada [12] also obtained similar results for different wing shapes. These results point to the coherence of the initial circulatory formulation of Eq. 5.5, indicating that after 30° other circulatory terms seem to dominate.

Furthermore, during fling, the trailing edges of the interacting wings are in contact, which considerably attenuates the generation of TEVs, known as starting vortices, and thus reduces the delay in bounded circulation growth [46, 53, 62]. This force augmentation

was found to be present also in the case of interacting wings that initiate a translatory motion after the fling [13, 17] – hence closer to the real flapping kinematics of the flyer considered. In particular, it was demonstrated that the clap-and-fling force augmentation still produces effects as late as mid-stroke, after the fling has occurred, suggesting that this mechanism could be considered to distort the spatio-temporal structure of the wake of the previous stroke, in what could be considered as wake-capture. Such phenomenon was later observed experimentally by Perçin et al. [15], who showed the lift-enhancing wake capture in clap-and-fling mechanisms was possible due to wing flexibility and consequent peel instead of fling. Furthermore, the same study revealed that during peeling a stronger LEV forms, which continues to grow after the peel phase, during wing translation. This is in line with the numerical results of Miller & Peskin [6] and Noda et al. [59] who observed a considerable increase in lift and a surprising reduction in drag due to the inclusion of flexibility in the model.

Others have suggested different theoretical formulations for the force augmentation. Ellington [58], for instance, proposed a circulation dependent on the velocity of the 'unzipping' of the wings ($u_z(t)$) during a modelled 'flat peel', as:

$$\Gamma = u_z(t)\, x_e\, f(\theta_{fling}), \quad f(\theta_{fling}) \approx \left(\theta_{fling} - \frac{\pi}{2}\right)^2 + 2 \tag{5.6}$$

with x_e being the effective chord length exposed ('flung part'). This formulation was tested in the current study, however simpler alternatives were found to yield effective results while requiring less complex computation, e.g., avoiding the calculation of a wing 'unzipping' velocity. Hence Eq. 5.6 was not used for the final formulation (presented subsequently).

Furthermore, actuator disk and conservation of mass theories have been suggested to explain the additional force observed during clap-and-fling: Bennett [10] proposed a formulation based on the conservation of mass around the leading edge, suggesting that the fling promotes the growth of induced velocity in the cleft between the wings. He showed this induced velocity was considerably higher in the presence of a mirror wing. Under similar assumptions, we have concluded the induced velocity to be a function of the wing flap angle (ζ), wing flap rate ($\dot{\zeta}$), wing pitch angle (θ_w)[1] and wing pitch rate ($\dot{\theta}_w$). This approach, however, results in complex formulae that were tested against the method suggested below with no considerable improvements, and hence it was not considered for implementation.

The previous observations support the following hypothesis, which addresses the three aspects (i–iii) mentioned at the beginning of this section:

As opposed to rigid-wing clap-and-fling, the flexible clap-and-peel mechanism is dominated by both the translation and the rotation of the wings around the leading edges. Hence, its dominant effects can be explained by a combination of translatory and rotational circulation, defined as functions of the wing flap rate ($\dot{\zeta}$) and wing pitch rate ($\dot{\theta}$). After the peel phase, the peel rotational circulation ceases when the wing stops rotating ($\dot{\theta}=0$), giving place to a rotational circulation needed to establish the Kutta condition after the trailing edges peel apart.

Hence, the clap-and-peel effect is included in the model by adapting the circulation equation

---

[1] θ_w is the angle between the blade element and the $y_B z_B$ plane, cf. Fig. 5.11

(Eq. 5.2) to the hypothesis in the form of a piecewise function: the first piece acts during the peel phase, until the wing reaches a constant pitch angle (i.e., $\dot{\theta}=0$) and the second piece equals the circulation of Eq. 5.2:

$$\Gamma = \begin{cases} \frac{1}{2}C_L c(r)|V| + \frac{1}{2}C_F c^2(r)\dot{\theta}_{fling} & \text{if} \quad t^* \geq 0 \quad \text{and} \quad \dot{\theta}_{fling} \geq 0 \\ \frac{1}{2}C_L c(r)|V| + \frac{1}{2}C_R c^2(r)\dot{\theta}_w & \text{else} \end{cases} \tag{5.7}$$

where C_F is the fling coefficient, $t^* = t/T$ is the dimensionless time per flap cycle of period T, and $\dot{\theta}_{fling} = -\dot{\theta}_w$. The above equation thus replaces Eq. 5.2 in the final model.

Different formulations were tested and Eq. 5.7 was found to be the simplest and still physically meaningful formulation to model clap-and-peel, as it considers: (i) circulation to be a function of the wing flap (translatory circulation) and pitch angles, as demonstrated in conservation of mass theory; (ii) different circulatory terms for each part of the motion; and (iii) cancellation of the TEV and the Kramer effect during peel. The clap part was not considered as for flexible wings its contribution is reduced [9].

The circulatory force contribution in Eq. 5.1 can now be obtained from:

$$d\mathbf{F}_{circ} = \begin{bmatrix} dF_{circ_x} \\ dF_{circ_z} \end{bmatrix} = -\rho_f \Gamma \begin{bmatrix} v_{z_w} \\ -v_{x_w} \end{bmatrix} dr \tag{5.8}$$

where ρ_f is the density of the surrounding fluid.

ADDED MASS

The added mass term ($d\mathbf{F}_{addmass}$ in Eq. 5.1) originates from the surrounding fluid during blade element acceleration. For a section of size $c \times b \times d_r$, with c the chord, b the thickness, d_r the infinitesimal length of the section, it takes the general form:

$$d\mathbf{F}_{addmass} = \begin{bmatrix} dF_{addmass_x} \\ dF_{addmass_z} \end{bmatrix} = - \begin{bmatrix} m_{11} a_{x_w} \\ m_{22} a_{z_w} \end{bmatrix} dr \tag{5.9}$$

where m_{11} and m_{22} are the masses of the surrounding fluid being accelerated along the axes of the wing section. These are obtained from the two-dimensional theory of the Joukowski airfoil profile [63]. Here, we consider the wings to be thin flat plates[2] with thickness b:

$$m_{11} = \frac{1}{4}\pi\rho_f b^2, \quad m_{22} = \frac{1}{4}\pi\rho_f c_{eff}^2(r) \tag{5.10}$$

Note that Eq. 5.10 accounts for the flexibility of the wing during peel by introducing an effective chord ($c_{eff}^2(r)$) that only considers the 'peeled' part of the chord for added mass purposes – failing to consider this may result in errors in the final model outcome.

VISCOUS EFFECTS

Viscous effects (term $d\mathbf{F}_{visc}$ in Eq. 5.1), arising from fluid viscosity and friction, were modelled as drag forces acting at each section. Similarly as for the lift coefficient function C_L, several forms were considered, cf. Refs. [39, 50, 57]. After parameter estimation, all forms were found to lead to comparable results. One particular aspect of the model (Eq.

---

[2]Formulae for other airfoil shapes can be obtained using the equations on p. 38 of [63], with wing profile information from, e.g., [64]

32) in [57] is that it should only be applied in the initial phase of the stroke. Due to the singularities present in other formulations, the following was selected [41, 48, 50]:

$$d\mathbf{F}_{visc} = \begin{bmatrix} dF_{visc_x} \\ dF_{visc_z} \end{bmatrix} = \frac{1}{2}\rho_f c(r) C_D |V| \begin{bmatrix} v_{x_w} \\ v_{z_w} \end{bmatrix} dr, \quad \text{with} \quad C_D = C_{D_0}\cos^2\alpha_w + C_{D_{\frac{\pi}{2}}}\sin^2\alpha_w$$

(5.11)

where C_{D_0} and $C_{D_{\frac{\pi}{2}}}$ are the drag coefficients for zero and 90° angle of attack of the wing, respectively; v_{x_w} and v_{z_w} are the relative velocities of the blade elements of each wing, along the $\mathbf{x}_W$ and $\mathbf{z}_W$ axes, respectively; and α_w is the element-relative angle of attack, computed from $\arctan(-v_{z_w}/v_{x_w})$.

FINAL PROPOSED MODEL

The aerodynamic forces acting along the $\mathbf{x}_W$ and $\mathbf{z}_W$ axis of each wing blade element can now be formulated as the following equations, in conjunction with Eqs. 5.7, 5.10 and 5.11:

$$d\mathbf{F} \quad = d\mathbf{F}_{centrip} \quad + d\mathbf{F}_{circ} \quad + d\mathbf{F}_{addmass} \quad - d\mathbf{F}_{visc}$$
$$dF_{x_w} = [m_1 v_{z_w}\dot{\theta}_w \quad -\rho_f \Gamma v_{z_w} - m_{11}a_{x_w}] dr - dF_{visc_x}$$
(5.12)
$$dF_{z_w} = [-m_2 v_{x_w}\dot{\theta}_w + \rho_f \Gamma v_{x_w} - m_{22}a_{z_w}] dr - dF_{visc_z}$$
(5.13)

$$m_1 = \frac{c(r)}{\bar{c}R} M_{wing} + m_{22}, \quad m_2 = \frac{c(r)}{\bar{c}R} M_{wing} + m_{11}$$
(5.14)

where M_{wing} is the wing mass and ρ_f is the fluid density. The equation terms are arranged in the same order as in Eq. 5.1, which is shown again here for better clarity.

This model is extendible to flapping species and ornithopters with: (i) two or four wings; (ii) dorsal, or dorsal and ventral wing interaction; (iii) flight conditions different from hover; (iv) a wing dihedral angle. Hence, the infinitesimal forces acting along the body reference frame can be calculated using:

$$dF_{x_b} = dF_{x_w}\sin\theta_w + dF_{z_w}\cos\theta_w$$
$$dF_{z_b} = (dF_{x_w}\cos\theta_w - dF_{z_w}\sin\theta_w)\cos\zeta$$
(5.15)

for each blade element. The total force is then computed by numerically integrating the forces acting on each blade along the span of the wing (from Eq. 5.15), considering the wing shape, real flapping kinematics, pitch and velocity of the FWMAV and relative wind perceived by each wing element. Finally, the total lift and drag forces can be obtained from the known body pitch attitude Θ_b, which in the wind tunnel setup corresponds to the body angle of attack:

$$\mathbf{L} = \mathbf{F}_{x_b}\sin\Theta_b - \mathbf{F}_{z_b}\cos\Theta_b$$
$$\mathbf{D} = -\mathbf{F}_{x_b}\cos\Theta_b - \mathbf{F}_{z_b}\sin\Theta_b$$
(5.16)

5.3. MATERIALS AND METHODS

5.3.1. THE FLAPPING-WING MICRO AERIAL VEHICLE

The test platform used in this chapter is the DelFly II FWMAV. Specifically, the two configurations flight tested in the AFRL motion tracking chamber were considered, weighing

approximately 17g (cf. Chapter 1, Sec. 1.4.2). A description of the vehicle was provided in Chapter 1, Sec. 1.4.1, while the detailed physical properties of the vehicle are reported in Table G.1 in Appendix G (configurations I and II). The test platform's most relevant feature for this study is the fact that it makes extensive use of the clap-and-fling mechanism, as further elaborated in the following subsections.

5.3.2. EXPERIMENTAL TECHNIQUES

Two experimental techniques were used to determine the forces that act on the ornithopter. Firstly, measurements were gathered during free flight of the platform in an optical tracking chamber. Secondly, tests were performed in a low-speed wind tunnel with the FWMAV clamped and the tail removed.

FREE-FLIGHT TESTING

Using a high-accuracy indoor position tracking system, the FWMAV was flown extensively at a wide range of attitudes and velocities covering all the typical conditions experienced in flight. The position of eight retro-reflective markers placed on the ornithopter (cf. Fig. 5.2) was recorded at 200Hz (cf. Chapter 1, Sec. 1.4.2): four markers were placed on the fixed structure at the nose, wing trailing edge, and horizontal and vertical stabilisers; the remaining four were placed on the moving surfaces, viz. two at the connection point between the wing leading edge spar and the foil stiffeners and one on the elevator and rudder, respectively.

The states of the ornithopter in free flight were reconstructed using the flight path reconstruction techniques explained in [65], according to the reference axes indicated in Fig. 5.11. The typical flight regimes of the ornithopter, reconstructed from free-flight position data, are represented in Fig. 5.5 in terms of angle of attack (α) versus total velocity $V := ||V||$ – each dot in the plot indicates a single measurement in time, at 200Hz, with a total of about 300,000 points, corresponding to 28 minutes of free flight. The areas of the plot in Fig. 5.5 that present a higher concentration of dots approximately indicate the trimmed flight regimes of the FWMAV, with the remaining dispersion indicating the states measured during manoeuvring. The circle markers in black represent the eight trimmed flight conditions that were replicated in the wind tunnel experiments reported below and listed in Table 5.3.

WIND TUNNEL TESTING

The wind tunnel experiments were conducted in an open-section $(0.6 \times 0.6) m^2$ wind tunnel (cf. Fig. 5.6(a)) capable of delivering laminar flows at speeds as low as 0.3m/s, with very low turbulence ($\approx 1\%$). Fig. 5.6(b) presents a simplified schematic of the setup and respective inertial and body-fixed reference axes. The ornithopter was attached to a high-accuracy force transducer (ATI Nano17 Titanium, resolution of 0.149gram-force), while its attitude, flapping frequency and flow speed were set to the eight conditions reported in Table 5.3. The point where the ornithopter is attached to the balance can significantly influence the force readings along the $\mathbf{z}_B$ direction (Z force), negatively impacting the measurements [66]. To reduce this effect, the forces were measured at a position near the average force application point, at 35mm from the nose (flapping-wing mechanism hinge). The setup was completed

Figure 5.2: Location on the ornithopter of the retro-reflective markers used to track the position.
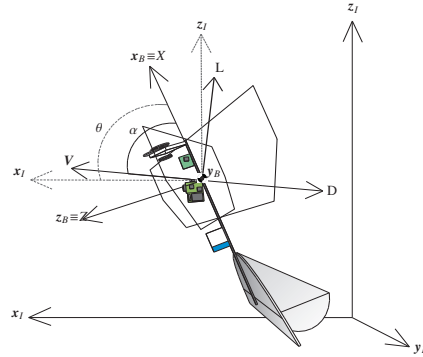
Figure 5.3: Schematic of the ornithopter in free flight, showing the inertial ($\mathbf{x_I}, \mathbf{y_I}, \mathbf{z_I}$) and body ($\mathbf{x_B}, \mathbf{y_B}, \mathbf{z_B}$) reference frames, and the velocity ($\mathbf{V}$), pitch (Θ) and angle of attack (α) of the body.

Figure 5.4: Free-flight testing experimental setup.
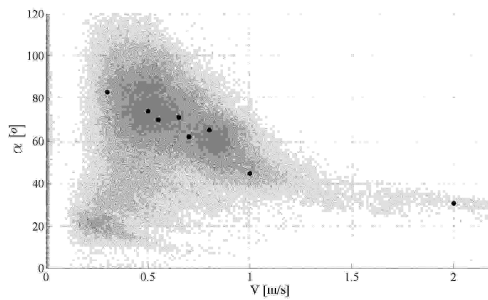
Figure 5.5: Reconstructed angle of attack (α) and total velocity $\mathbf{V}$ of the ornithopter (grey dots), representing the flight states for approximately 28 minutes of flight. The black markers indicate the flight conditions reproduced in the wind tunnel experiments.

Table 5.3: Steady flight test conditions replicated in the wind tunnel experiments.

Test #	Velocity $\mathbf{V}$[m/s]	Pitch angle Θ_b[°]	Flap freq. f_f[Hz]
1	0.30	83	13.3
2	0.50	74	12.5
3	0.55	70	12.5
4	0.65	71	12.5
5	0.70	62	11.7
6	0.80	65	13.3
7	1.00	45	11.7
8	2.00	31	10.3

with a hot-wire anemometer with thermocouple temperature compensation, for precise flow velocity measurements and a field-programmable gate array (FPGA) for force data acquisition at 12.5kHz. The phase of the wing flap was determined by combining the engine speed controller (ESC) readings, the Hall sensor mounted on the flap mechanism and high-speed imagery captured at 1.2kHz.

5.3.3. TIME-RESOLVED FORCE DATA

Fig. 5.7 presents the forces in x_B and z_B direction (X and Z) for a two-flap cycle window and different trimmed flight conditions. For clarity, only four out of the eight test conditions are shown, representing the four different flapping frequencies considered in the wind tunnel tests. The figure presents the forces determined from both experimental methods. The plot on the left shows the evolution of the forces acting on the FWMAV in free flight computed using single rigid-body kinematics [67]. The plot on the right shows the forces obtained from the force transducer in the wind tunnel. The arrows indicate the direction of the observed changes when lowering the flapping frequency and increasing the total velocity. It is worth noting that the forces from the wind tunnel present a smoother evolution given the direct force measurement and the much higher sampling frequency, as compared to the forces obtained from free flight, which are significantly more challenging to obtain [67].

As shown in Ref. [66], the raw forces obtained from both experimental methods are not easily processed, due to the significant noise at high frequencies. Particularly in the forces determined from free-flight data, the signal-to-noise ratio reduces considerably due to the double time-differentiation used to compute the accelerations. To reduce the noise level, both free-flight and wind tunnel-obtained forces were filtered using a zero-phase lag low-pass filter. A cutoff frequency of 40Hz (just above the second harmonic of the flapping frequency) was found to provide sufficient detail for a comparison between wind tunnel and free-flight forces, as well as an accurate evolution of the aerodynamic forces acting on the FWMAV. However, this filters out some of the aerodynamic force production mechanisms. In particular, a 40Hz cutoff filters out the clap-and-fling peak, which by contrast is clearly recognisable when higher cutoff frequencies are used. Fig. 5.8 shows the wind tunnel forces low-pass filtered at 67Hz (just above the fourth harmonic of the flapping frequency):

(a) Setup: a) FWMAV; b) ATI Nano-17 force transducer; c) open section wind tunnel; d) actuated strut; e) hot-wire anemometer; f) thermocouple.

(b) Schematic from a lateral perspective. Inertial (x_I, y_I, z_I) and body (x_B, y_B, z_B) reference frames.
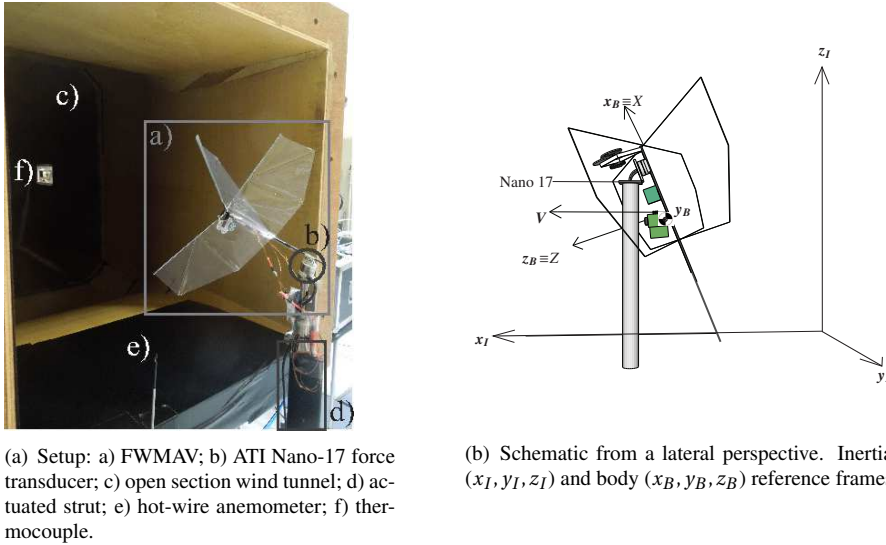
Figure 5.6: Wind tunnel experimental setup.

here the clap-and-fling peak can be clearly seen in the shaded area at the beginning of the flap cycle. Lower cutoff frequencies also filter out the initial part of the stroke reversal for non-dimensional cycle times $t^* \in [0.58, 0.70]$. One limitation of a higher filter cutoff is that in the current free-flight tests, frequency content above three harmonics was not clearly recognisable and distinct from noise [66]. For this reason, higher filter cutoffs were considered further only for the wind tunnel data.

The X forces obtained from both experimental methods exhibit a very similar evolution, with both the cycle phase and the peak amplitude decreasing with decreasing flapping frequency and increasing total velocity, as clarified by the large arrows in Fig. 5.7(b). Moreover, the sub-flap cycle level behaviour of the X forces is similar for all test conditions, and characterised by a nearly constant cycle phase and a peak amplitude that varies with changes in flapping frequency and forward velocity. The experimental data suggest that in a typical steady flight condition, the X force (parallel to the fuselage) is the main component sustaining the flight. By contrast, the Z forces vary more between the two experimental methods and between different test conditions. This is due to the restriction imposed by the clamping in the wind tunnel tests. In free flight there is an oscillatory motion around the y_B axis, which is more pronounced at higher flapping frequencies, whereas in the wind tunnel this motion is suppressed.

For the modelling process, wind tunnel data were selected over flight data for a number of reasons. Firstly, the wind tunnel measurements have a higher resolution thanks to the significantly higher sampling frequency: this allows for the unsteady effects to be clearly visualised, and thus for the suggested models to be evaluated more thoroughly. Secondly, there are fewer external disturbances acting during wind tunnel testing, and a wide range of test conditions can be selected and maintained very effectively. These conditions can
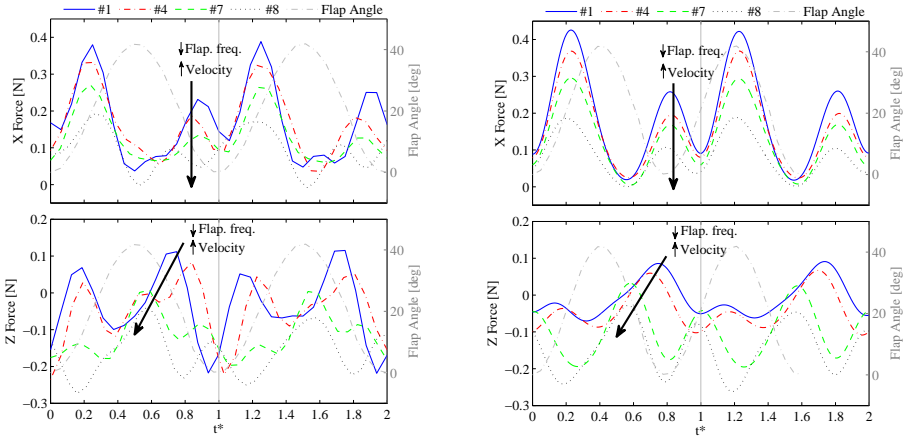
(a) Forces determined from free-flight tests, using single rigid-body kinematics.

(b) Forces determined from wind tunnel experiments.

Figure 5.7: Forces acting on the FWMAV, filtered at 40Hz, for test conditions #1, #4, #7 and #8 – cf. Table 5.3. The large arrows indicate the direction of peak phase and amplitude changes with decreasing flapping frequency and increasing total velocity.
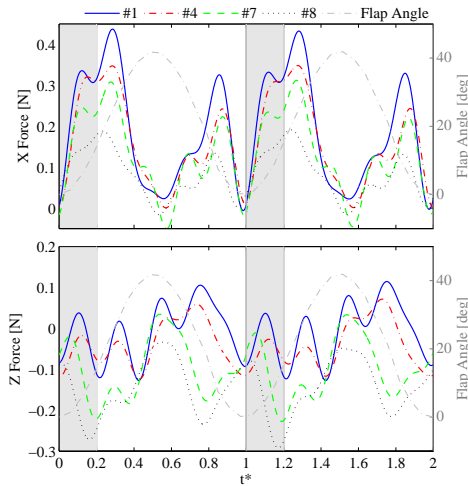
Figure 5.8: Forces acting on the FWMAV, measured in the wind tunnel and low-pass filtered at 67Hz, for test conditions #1, #4, #7 and #8 – cf. Table 5.3. Shaded areas indicate the clap-and-peel phase.

be considered realistic, as long as they are selected to correspond to existing free-flight conditions. Finally, wind tunnel testing allows for the wing aerodynamics to be considered separately from tail effects. The quasi-steady model proposed in this study accounts only for the aerodynamic forces produced by the wings, thus it is more accurate, on a theoretical level, to use force measurements conducted on the wings alone for parameter estimation. This was therefore the approach chosen here.

The discussed differences between free-flight and wind tunnel data do have to be considered. However they were found to be negligible for the X force component, which is the main contributor to lift. Given that lift is the main component of interest, this limitation was considered acceptable.

5.3.4. MODELLING THE WING KINEMATICS

The wing kinematics were obtained from experimental data, using a combination of high-speed cameras, motor rotation sampling and PIV measurements [66, 68], cf. Sec. 5.3.2. The wing has one active degree of freedom (DOF), characterised by the flapping motion along the stroke plane, which is perpendicular to the body of the FWMAV. Here, this DOF is represented by the so-called flap angle, ζ, measured as the angle between the wing leading edges and the position of closed wings, ζ_0. Passive wing pitching is a consequence of wing flexibility, and kinematic and aerodynamic forces. As an example of the real wing foil motion, Fig. 5.10 presents the shape of the wing foil at 70% of the wing span (cf. Fig. 5.9(a)) throughout one flap cycle, for a flapping frequency of 11Hz and hover conditions ($V_\infty=0$) [68].

(a) Top view: $\rho_{W1,H}$ and $\rho_{B,H}$ representation, from the body CG to the CG of each wing, with closed wings.

(b) Front view: wings open at angle ζ; the dashed line represents the position of the closed wings at ζ_0.
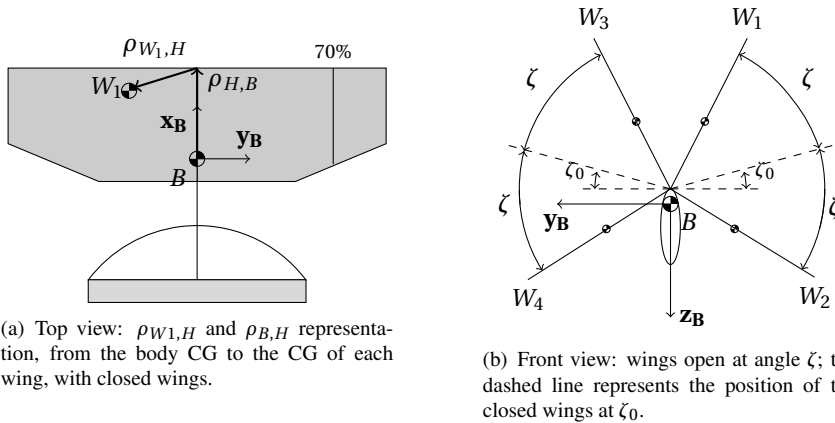
Figure 5.9: Simplified model with CG, body (B) and wing (W1 to W4) reference frames; the grey areas represent moving parts.

This information was used to compute a mathematical relation between the wing shape, the flap angle (ζ) and the flap angle rate ($\dot{\zeta}$).

$$\hat{\theta}_w = \frac{\pi}{2} + C_{\theta_{w_0}} + C_{\theta_{w_\zeta}} \zeta + C_{\theta_{w_{\dot\zeta}}} \dot{\zeta} + C_{\theta_{w_{\dot\zeta2}}} \dot{\zeta}^2 \tag{5.17}$$

Despite not considering in-flight deformations from turbulence and unsteady effects, this

mathematical formulation relates the wing shape to the wing flap phase, reducing the DOFs of the model, and hence its complexity, while still maintaining real kinematic properties. The coefficients were obtained through least squares estimation and are presented in Table 5.4.

Table 5.4: Estimated coefficients for Eq. 5.17 using two chord assumptions.

Coefficient	$\theta_{w_{100\%}}$
$C_{\theta_w,0}$	0.3139
$C_{\theta_w,\zeta}$	-1.1382
$C_{\theta_w,\dot{\zeta}}$	-0.0179
$C_{\theta_w,\dot{\zeta}^2}$	-0.0002

Wing torsion was verified to have a close to linear evolution in spanwise direction throughout the flap cycle. It was linearly interpolated, in spanwise direction, between zero wing pitch angle (θ_w) at the wing root and the wing pitch angle at 70% of the span length, observed from PIV [14]. The different relative wind perceived by each blade element is a function of the location of the considered element in spanwise direction (r), the pitch angle of the body (Θ_b) and forward velocity of the ornithopter (V_∞), the wing dihedral (ζ_0), the wing flap angle (ζ), the wing flap rate ($\dot{\zeta}$), and the wing pitch axis of rotation (d) along the chord (c), which is parallel to y_W. Lateral movement of the ornithopter is neglected and only longitudinal displacements are considered. Hence, the relative velocity perceived by the upper and lower wing elements, neglecting downwash and unsteady effects (e.g. LEV) is given by:

$$\begin{aligned}
v_{x_{w_u}} &= r_i\dot{\zeta}\cos\theta_w - V_\infty\cos(\theta_u) \quad \text{and} \\
v_{z_{w_u}} &= -r_i\dot{\zeta}\sin\theta_w - dc(r)\dot{\theta}_w + V_\infty\sin(\theta_u)\cos(\zeta_0+\zeta)
\end{aligned} \tag{5.18}$$

$$\begin{aligned}
v_{x_{w_l}} &= r_i\dot{\zeta}\cos\theta_w + V_\infty\cos(\theta_l) \quad \text{and} \\
v_{z_{w_l}} &= -r_i\dot{\zeta}\sin\theta_w - dc\dot{\theta}_w - V_\infty\sin(\theta_l)\cos(\zeta_0-\zeta)
\end{aligned} \tag{5.19}$$

where $\theta_u = \Theta_b - \theta_w + \frac{\pi}{2}$ and $\theta_l = \Theta_b + \theta_w - \frac{\pi}{2}$, and $d=0$ for the present case. The acceleration of each wing element is easily obtained by differentiating the above formulations in time – it is worth noting that d should be equal to 0.5 to compute the acceleration for the added mass effect. Furthermore, the effective chord used in Eq. 5.9 varies linearly between 0, at the beginning of the fling ($t^*=0$), and 1, when the blade elements peel apart ($t^*\approx0.17$).

The wing flap angle (ζ) was captured at 1kHz in the wind tunnel tests. While the high frequency makes the state more accurate, the numerical differentiation of this state introduces considerable error magnification [66], which adds to any discontinuities in the differentiated state. Furthermore, the wing flap motion lasts more time during the outstroke than during the instroke, due to the fling suction and latency in the motor torque. For these reasons, a biased wing beat formula was used that considers this split-cycle evolution with constant period [69]:

$$\phi_{up}(t^*) = -A_{amp}\cos((\omega-\delta)t^*) + \eta \tag{5.20}$$

$$\phi_{down}(t^*) = -A_{amp}\cos((\omega+\sigma)t^* + \zeta) + \eta \tag{5.21}$$
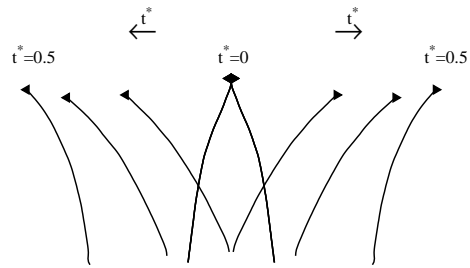
(a) Chord evolution for outstroke, nondimendional time $t^* \in [0, 0.5]$

(b) Chord evolution for instroke, $t^* \in [0.6, 1]$
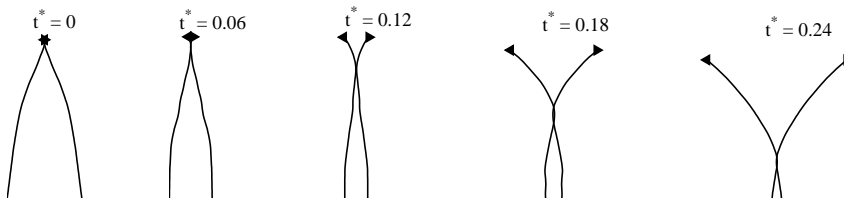
(c) Detailed chord evolution for first part of outstroke, nondimensional time $t^* \in [0, 0.24]$

Figure 5.10: Chord evolution during one flap cycle, for two flexible wings displaying clap-and-peel interaction. Subfigure (c) is a detailed representation of the chord evolution between the first and second time frames in subfigure (a).
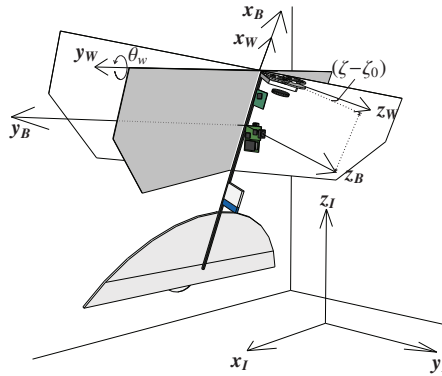
Figure 5.11: Inertial ($\mathbf{x_I}$,$\mathbf{y_I}$,$\mathbf{z_I}$), body ($\mathbf{x_B}$,$\mathbf{y_B}$,$\mathbf{z_B}$) and wing ($\mathbf{x_W}$,$\mathbf{y_W}$,$\mathbf{z_W}$) reference frames.

where ω is the fundamental frequency, η is the wing bias, δ is the split-cycle parameter, $\sigma := \delta\omega/(\omega - 2\delta)$, $\zeta := -2\pi\delta/(\omega - 2\delta)$, and A_{amp} adjusts the values to the amplitude of the flapping. The coefficients of the formula were identified as: $A_{amp} = 0.34, \delta = 0.35, \eta = 0.34$. More details on this approximation can be found in Ref. [69].

5.3.5. PARAMETER ESTIMATION APPROACH

To apply the proposed model (Eqs. 5.12-5.13), the unknown parameters flowing into it must be determined ($\Theta = \begin{bmatrix} C_l & C_r & C_{D0} & C_{D_{\frac{\pi}{2}}} & C_F \end{bmatrix}$, cf. Eqs. 5.3, 5.4, 5.7, 5.11) These parameters were estimated using a maximum likelihood (ML) estimator and an output error approach [70, 71] (cf. Chapter 3 for further details). The cost function for this type of problem can be expressed as:

$$J(\boldsymbol{\Theta}, \mathbf{R}) = \frac{1}{2} \sum_{k=1}^{n_k} [\mathbf{z}(k) - \mathbf{y}(k)]^T \mathbf{R}^{-1} [\mathbf{z}(k) - \mathbf{y}(k)] + \frac{n_k}{2} \ln(\det(\mathbf{R})) + \frac{n_k n_y}{2} \ln(2\pi), \qquad (5.22)$$

where $\mathbf{R}$ is the measurement noise covariance matrix, n_k is the number of data samples, n_y is the number of output variables, and $\mathbf{z}(k)$ and $\mathbf{y}(k)$ are the measured and model-predicted outputs, respectively, at measurement time k. The noise covariance matrix $\mathbf{R}$ was estimated in each iteration step using a relaxation technique:

$$\hat{\mathbf{R}} = \frac{1}{n_k} \sum_{k=1}^{n_k} [\mathbf{z}(k) - \mathbf{y}(k)][\mathbf{z}(k) - \mathbf{y}(k)]^T]. \qquad (5.23)$$

A Gauss-Newton algorithm was used to minimise the cost function. Initial guesses for the parameters, required to initialise the estimator, were based on values in the literature [50, 72], where available (cf. Table 5.5). However, testing showed that the result was not sensitive to the choice of these values.

The output equations were inferred from the aerodynamic model structures in Sec. 5.2.3. While the evolution of the aerodynamic forces is a dynamic process, measurements of all

Table 5.5: Initial guesses for the model parameters, based on values in the literature[50, 72].

Param.	Initial value before estimation
C_l	1
C_r	1.6
C_F	1
C_{D0}	0
$C_{D_{\frac{\pi}{2}}}$	π

required variables were obtainable, so it was not necessary to include any dynamics in the estimation process. The output is a direct function of the input and can be computed from the measurements at each time step.

Different estimation setups were investigated, as further clarified in Sec. 5.4.1. Depending on the case, the output $\mathbf{z}$ included one or both of the aerodynamic forces X and Z, which was in each case a function of a different set of parameters (out of those available, mentioned above) and measurements. The output equation was obtained via integration from Eqs. 5.12 and 5.13, which represent the forces over a single blade element. The measurements required for this model are the flap angle and its derivative, the wing pitch angle and its first and second derivatives, the flapping frequency, and the forward flight velocity. All of these could be obtained from the wind tunnel tests.

5.4. RESULTS AND DISCUSSION

5.4.1. PARAMETER ESTIMATION SETUP

Preliminary tests were conducted to establish the most plausible and effective identification approach. This involved estimating different subsets of the available parameters (cf. Table 5.5), while fixing other parameters at pre-defined values, and using the X force, Z force, or both as outputs within the estimation process.

The chosen setup uses X as sole output measurement, and estimates the parameters C_l, C_r and C_F. It was found that estimating C_{D_0} and $C_{D_{\frac{\pi}{2}}}$ as well led to an accurate output but implausible values for these two parameters. This is most likely because these parameters do not have a significant effect on the X component of the force and hence cannot be identified effectively from X force data. C_{D_0} is also typically very small and therefore difficult to estimate reliably. Hence, these parameters were fixed *a priori* at literature-based values (cf. Table 5.5) to ensure a physically realistic result.

The X force was selected as output because it is the main contributor to lift in typical flight regimes, and hence of more interest. Moreover, as discussed in Sec. 5.3, the Z forces measured in the wind tunnel are significantly affected by the clamping and, therefore, are not a realistic representation of the forces occurring in free flight. Similarly, the Z component of the forces is considerably affected by the tail of the FWMAV. This again introduces a difference between wind tunnel and free-flight measurements, and additionally implies that the current model, which considers only the wings, is inadequate for a complete representation of the Z forces. All results presented refer to the outlined setup. In the interest of clarity, results are shown in terms of lift and drag forces, as defined in Eq. 5.16.

Table 5.6: Evaluation of computed models

Test #	Lift			Drag		
	RMSE [N]	RMSE [%]	Corr.	RMSE [N]	RMSE [%]	Corr.
1	0.05	13	0.97	0.03	23	0.66
2	0.04	13	0.97	0.05	43	0.25
3	0.04	13	0.97	0.04	36	0.34
4	0.05	15	0.96	0.05	48	0.04
5	0.04	17	0.96	0.05	52	0.30
6	0.05	18	0.94	0.05	64	0.24
7	0.05	50	0.92	0.04	43	0.90
8	0.05	32	0.85	0.04	47	0.72
Avg.	0.04	21	0.94	0.04	44	0.43

5.4.2. MODELLING RESULTS

Fig. 5.12 shows the model-predicted lift and drag for four different test cases, in comparison with the corresponding wind tunnel measurements. Results are shown for the same example test cases discussed previously, which represent each of the four different flapping frequencies considered in the testing. For comparison, the plots also show one of the baseline models from the literature (Berman & Wang [50]), which does not consider clap-and-fling effects. Note that the coefficients of the baseline model were estimated in the same way as those of the proposed model.

Overall, the models replicate the lift force measurements with considerable accuracy, in terms of both phase and amplitude. The shape of the force evolution is captured effectively, with both force peaks in the 40Hz-filtered data being reproduced and the phase alignment and peak amplitudes close to the measured ones. The visual evaluation is confirmed by the low RMSE values (~ 0.04N) and output correlation coefficients up to 0.97 (cf. Table 5.6).

While all metrics indicate a satisfactory performance, it can be observed that results are most accurate for flight conditions close to hover; the correlation coefficient deteriorates slightly for increasing forward velocity and decreasing flapping frequency. This may be partly connected to the fact that a number of assumptions made in the model definition process (cf. Sec. 5.2 and 5.3.4) refer to either the hover case or a typical flight condition (close to hover, $f_f \approx 12$Hz), and therefore the more the test conditions differ from these cases, the more error is introduced into the model. Additionally, with decreasing pitch attitude, the contribution of the Z force component to the lift increases, and as discussed, the proposed model does not accurately predict the Z forces captured in the balance measurements. Nonetheless, even for test # 8, which is characterised by a high forward velocity, the model still provides an adequate approximation. While the focus of this study lies in modelling the instantaneous, 'sub-flap' forces, it can be observed in Fig. 5.12 that the cycle-averaged lift force is also predicted accurately.

The accuracy of the model is partly due to the added fling term, which substantially affects the force evolution during the first part of the flap cycle. Comparing the proposed model to available quasi-steady models in the literature that do not include clap-and-fling effects, e.g., Berman & Wang [50] (cf. Fig. 5.12), clearly highlights the impact of the supplementary term in the proposed model. The comparison also shows how unsteady

(a) Test condition # 1

(b) Test condition # 4

(c) Test condition # 7
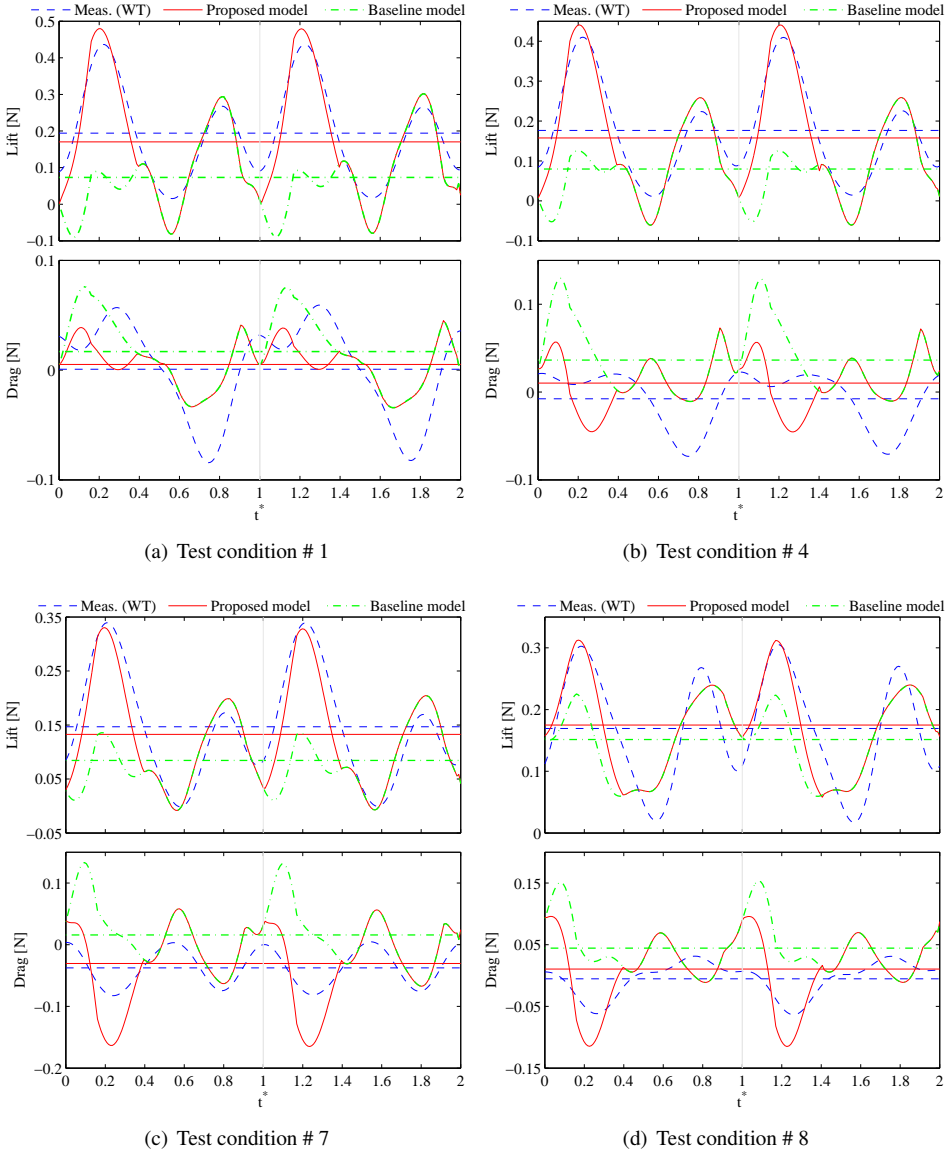
(d) Test condition # 8

Figure 5.12: Wind tunnel measurements and models estimated from wind tunnel data for test conditions # 1, # 4, # 7, #8. Cycle averages are also indicated for each force time history (horizontal lines).

effects predominantly occur while the wings are interacting, during the first part of the flap cycle (outstroke). Without the fling term, the model can replicate the second part of the flap cycle, after the wings have separated (here, for $t^* > 0.4$), with accuracy. However, it underestimates the lift during wing-wing interaction, which leads to instantaneous forces that differ significantly from experimental observation and, consequently, also to a reduced cycle-averaged lift force prediction. Hence, there is a strong need to account for clap-and-fling effects for accurate modelling of ornithopters relying on such mechanisms.

It can be observed in Fig. 5.12, particularly for test conditions #1 and #4, that there is a singularity at around $t^* = 0.4$ of the flap cycle. Due to the definition of circulation as a piecewise function (cf. Eq. 5.7), at the switching point $\dot{\theta}_{fling} = 0$ only zero-order continuity is ensured. For control applications this discontinuity could cause problems and hence it is advisable to enforce continuity and ensure a smooth transition. However, for modelling purposes, the current formulation is considered adequate and more easily interpretable as it shows clearly where fling stops being effective.

In contrast to the lift forces, the drag forces are not predicted very accurately, and there is a considerable difference between different results, as highlighted by the output match in Fig. 5.12 and the comparatively high RMS values (relative to the magnitude of the measurements). Output correlation coefficients vary significantly, ranging between 0.18 and 0.90, indicating that the model does replicate a part of the drag forces, but cannot be relied on to provide an accurate prediction. However, this result was expected, given that it is predominantly the Z force component that contributes to the drag.

Firstly, previous work [66] showed that the Z forces measured in the wind tunnel are significantly affected by the clamping and are, therefore, not a realistic representation of the forces occurring in free flight. Secondly, the Z component of the forces is considerably affected by the tail, so that the current model is in any case inadequate for a complete representation. Thirdly, the Z forces are highly influenced by the kinematics, i.e., the assumptions made regarding wing shape and torsion (cf. Sec. 5.3.4). Finally, and indeed *because of* these factors, the model parameters were optimised based on the resulting X force, further constraining the achievable accuracy of the Z and, consequently, drag force prediction. Despite the aforementioned limitations, it can be observed in Fig. 5.12 that the model captures at least a part of the drag forces, and, more importantly, that it predicts cycle-averaged values that are close to the measurements. For many (control) applications, instantaneous values for lift are of more interest than ones for drag [21, 28, 29].

The parameter estimates, shown in Table A.3, are in a plausible order of magnitude and the translatory and rotational circulation coefficients approximately agree with similar results in the literature [40, 72]. Correlations between parameters were mostly found to be sufficiently low (below 0.5), and estimated errors (Cramér-Rao lower bounds) were likewise low (cf. Fig. 5.14). These points suggest an effective estimation process and reliable results. Further, a correlation was observed between parameters and flight regimes. In particular, C_l increases with lower flapping frequencies and higher forward velocities, which can be explained by the increased airflow over the wings leading to increased lift production, whereas C_F increases with higher flapping frequencies and lower forward velocities, which can be explained by the prevalence of unsteady wing-wing interaction effects closer to hover. While the similar order of magnitude of the parameters over different flight regimes suggests that the initial model structure already partly adjusts the model to the spe-

Table 5.7: Parameters estimated from each set of estimation data

Param.	Test #								Avg.	St. dev.
	1	2	3	4	5	6	7	8		
C_l	0.89	1.22	1.20	1.24	1.43	0.90	1.37	2.02	1.28	28%
C_r	1.49	1.45	1.45	1.44	1.39	1.39	1.41	1.57	1.45	4%
C_F	1.69	1.57	1.55	1.58	1.61	1.66	1.43	0.67	1.47	23%

cific test condition, the trends of some of the parameters with the flight conditions further suggest that the final accurate result is attained partly by means of the parameters. These trends also suggest that with a smaller number of parameters, common to all flight conditions, a global model of the flapping aerodynamics could be obtained that covers all flight regimes. This is discussed further in Sec. 5.4.4.

5.4.3. FREQUENCY CONTENT EVALUATION
Fig. 5.13 provides an example of how the model compares to the less filtered wind tunnel data (67Hz cutoff) including five harmonics of frequency content. This allows for a closer evaluation of the model. Note that the drag force contains significant higher-frequency content, which is difficult to distinguish from noise. In view of this, and previous observations on the limitations of the drag modelling, further evaluations are focused on the lift component.

Firstly, it can be seen that the model cannot fully capture the fling effect. In particular, the additional fling-related force peak occurring in the 67Hz-filtered data at the beginning of the flap cycle (until $t^* \approx 0.17$, cf. Sec. 5.3.3) is not reproduced. From this perspective, the model follows the 40Hz-filtered data more closely. Here the fling peak is no longer visible, however its effect can be recognised in the phase shift of the first force peak, which, in this case, incorporates the first two peaks of the 67Hz-filtered data. The force peaks of the model are approximately aligned with the 40Hz-filtered data, and the amplitudes comparable to those in the data. Hence, although there are limitations connected to the quasi-steady model structure, the introduced fling term clearly accounts for a significant part of the overall fling effect.

Secondly, it can be observed that in a number of details of the force evolution, the model is in fact closer to the 67Hz-filtered data than to the 40Hz-filtered data. The troughs of the model, for instance, correspond more closely to those of the 67Hz-filtered data, dipping to lower values than those of the 40Hz-filtered data. The model also appears to echo the hint at a peak occurring in the 67Hz-filtered data at $t^* \approx 0.4$ of the flap cycle, corresponding to the time when the wings have moved apart (black circumference in Fig. 5.13(a)).

The right hand side plot in Fig. 5.13 shows the power spectral density (PSD) estimates of the model and the corresponding wind tunnel measurements. Here it can be seen that, while the lift model contains predominantly frequency content up to the third harmonic, there is still some higher-frequency content, at least up to the fifth harmonic. However, at these high frequencies the data are highly affected by noise, and a comparison to data filtered at 3 harmonics already provides a nearly complete evaluation of the model, as also shown in [66].

(a) Time domain   (b) Frequency domain
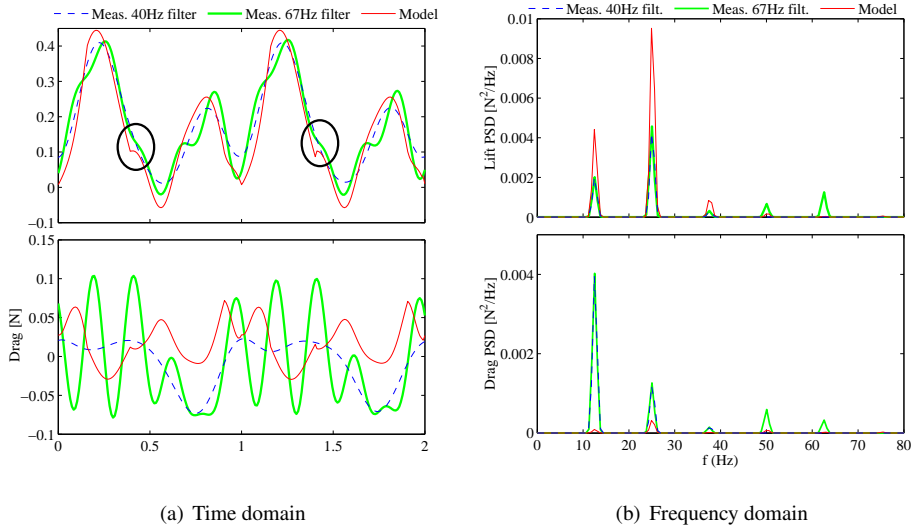
Figure 5.13: Model-predicted forces, and forces measured in the wind tunnel filtered at 40Hz and 67Hz, respectively, and corresponding power spectral densities, for test # 4. The circle in Fig.(a) highlights one of the additional peaks visible in the data filtered with a higher, 67Hz cutoff.

5.4.4. GLOBAL APPLICABILITY AND VALIDATION WITH FREE-FLIGHT DATA

The results discussed so far were obtained using different model parameters for each flight condition. This restricts the applicability domain of the model to the specific flight conditions used in the modelling process, for which data was available. Particularly from an application perspective, however, it is of interest to consider different conditions, ideally covering the flight envelope of a system. This is a crucial requirement for control and simulation applications, if the operating domain of the platform is not to be restricted, and also advantageous for design and performance studies, in order to make complete evaluations. In this context, an investigation was made into possibilities to apply the devised model globally, i.e., in different flight conditions, based on the currently available data.

For a model to be applicable in arbitrary conditions, any model parameters must be either constant for all conditions or a function of measurable input variables. To identify global applicability options for our model, we thus consider the parameters $(C_l, C_r, C_F,$ cf. Eqs. 5.3, 5.4, 5.7) estimated from the different available datasets, as described in Sec. 5.4.2. As pointed out previously, trends were observed between the estimated parameters and the flight regime of the data used to estimate them. These correlations are highlighted in Fig. 5.14. As forward velocity and body pitch attitude are highly correlated (R^2=0.94), only the latter variable is shown.

It can be observed that C_l decreases with increasing flapping frequency and decreasing body pitch angle (hence, increases with increasing forward velocity), while C_F displays opposite trends. The trends can be considered approximately linear, particularly in relation

to the flapping frequency. There are some slight outliers, which mostly correspond to flight regimes that themselves can be considered outliers (e.g., test condition # 6, unusually high flapping frequency for the resulting velocity), but also highlight the fact that the parameters are correlated to *both* the flapping frequency and the pitch angle (or velocity). Indeed, from Table 5.3 it can be seen that with the same flapping frequency it is possible to fly at different pitch attitudes (e.g., 65° in test condition #6 versus 83° in test condition #1). C_r, by contrast, does not vary significantly within the range of flight conditions considered (4% standard deviation, cf. Table A.3). Sensitivity studies confirm that changes in C_r within the range covered by the parameter estimates from the current tests have a negligible effect on the final result.

These trends suggest that the model can be adapted to cover a significant part of the flight envelope with only a small number of global parameters, rather than a different set of local parameters (C_l, C_r, C_F) for each flight regime. Based on the observations made, a 'global' model was computed by keeping C_r fixed at the average of the results from all test conditions (cf. Table A.3), and approximating C_l and C_F as a function of the flapping frequency f_f and the body pitch attitude Θ_b. Least squares parameter estimation was applied to compute this function, and a first-order polynomial was found to yield adequate results, while entailing a low computational load and simple model structure:

$$C_{\{l,F\},global} = C_{\{l,F\},global}(f_f, \Theta_b) = p_{\{l,F\},1} + p_{\{l,F\},2}f_f + p_{\{l,F\},3}\Theta_b$$

$$C_{r,global} = \frac{1}{n}\sum_{i}^{n} C_{r,local,i} \tag{5.24}$$

where i indicates the test condition number as defined previously and n is the total number of test cases, in this case $n=8$. The model that results from substituting the respectively relevant part of Eq. 5.24 into Eqs. 5.3, 5.4 and 5.7 is parameter-varying, with two of the original model parameters being a function of the states. Results can thus be computed in any arbitrary condition. However validation is required to evaluate the effectiveness of these results, and especially to verify whether it is acceptable to extrapolate to conditions outside the range considered in the original tests (e.g. $V > 2m/s$). Fig. 5.14 shows the model parameters computed from the above equation ('global') in comparison to the original parameters estimated from separate sets of estimation data collected in different flight conditions ('local'). It can be seen that the two sets of values are close (up to 8% difference between corresponding parameters).

The obtained 'global' model was first evaluated in the test conditions considered in the wind tunnel, as for example shown in Fig. 5.15. Here the output of the global model is compared to wind tunnel data, as well as to the corresponding local model identified specifically in the considered test condition (cf. Sec. 5.4.2). The figure additionally presents free-flight data collected in conditions approximately corresponding to those recreated in the respective wind tunnel test. Given that the final goal is to represent a free-flying vehicle, it is of interest that the model should be able to represent the behaviour occurring during flight. Before being compared to free-flight data, the model was filtered after the third harmonic. On the one hand, the current free-flight measurements yield no reliable information beyond the third harmonic [66], so it was considered more accurate and meaningful to validate a filtered version of the model with the filtered free-flight forces. On the other hand, the higher-frequency content (above 40Hz) is limited (cf. Sec. 5.4.2 and Fig. 5.13), and com-
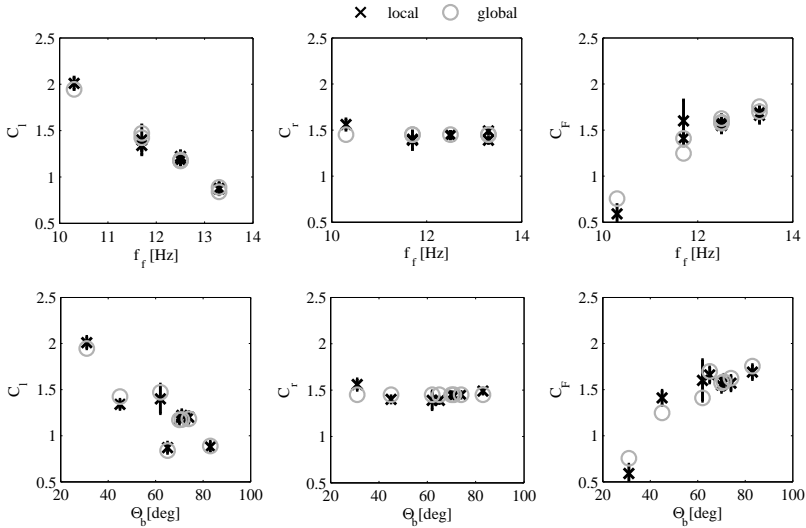
Figure 5.14: Model parameters (C_l, C_r, C_F) (i) estimated from each set of identification data (local, blue crosses), with corresponding estimated error bounds, and (ii) computed from the flapping frequency and body pitch attitude according to Eq. 5.24 (global, red circles).

paring filtered and unfiltered model results highlights that the difference is small, so that from a practical point of view using one or the other version is approximately equivalent.

Fig. 5.15 shows that the forces predicted by the global model are very close to those predicted by the separate local models for each flight condition. We also observe that the model can approximate the free-flight lift, albeit not as accurately as the wind tunnel lift. In this regard, it must be considered that, as discussed in Sec. 5.3.3, the free-flight and wind tunnel measurements differ somewhat. Hence, regardless of the theoretical quality of the model, its performance cannot be equally effective when it is applied in a free-flight situation, having been identified using wind tunnel data and not accounting for the tail. This limitation mainly affects the drag component, for which the model cannot be considered to provide reliable information beyond the average force, but also has some effect on lift: we see for instance that the free-flight lift in subfigure 5.15(a) has significantly smaller peaks than the wind-tunnel lift.

Lastly, Fig. 5.15 shows the output of an 'average' model, where all of the parameters are set to an average from the previous test results rather than computed from Eq. 5.24. It is clear that, to cover a wider range of conditions, the suggested parameter-varying approach yields more accurate results. Nonetheless, if a quick and approximate result is desired, or if only a small range is considered, an average model may also be an acceptable solution, requiring even less effort to implement.

The final stage in evaluating the model consists in validation with free-flight data representing flight regimes that were not reproduced in the wind tunnel and hence not considered at any stage of the modelling process. Fig. 5.16 shows the result of applying the model to free-flight data collected in two different test conditions not replicated in the wind tunnel.

(a) Test condition # 4   (b) Test condition # 8
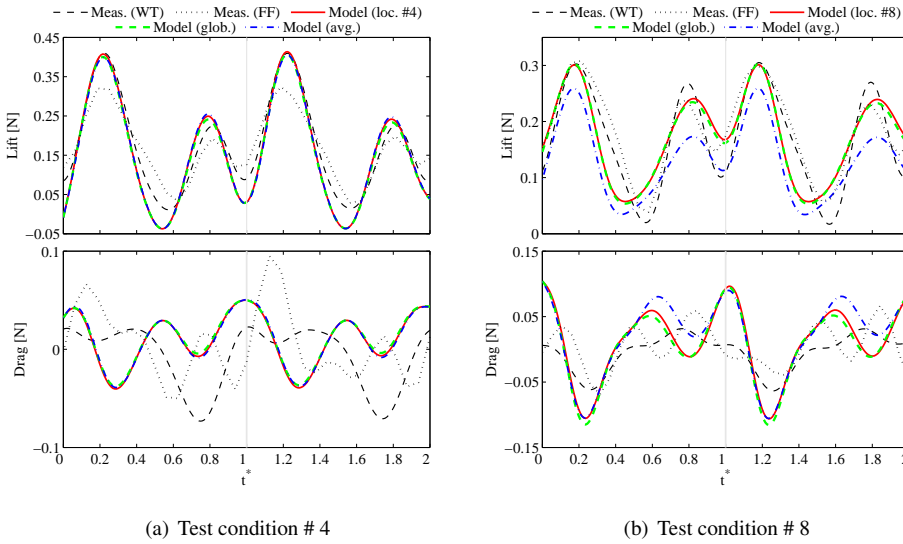
Figure 5.15: Global model evaluation in comparison to the two local models for test conditions #4 and #8. Wind tunnel (WT) and free-flight (FF) measurements versus model-predicted forces obtained from the 'local' models identified from each separate dataset, and from the 'global' model based on Eq. 5.24.

The lift force is still predicted with some accuracy: the sub-flap force evolution approximately corresponds to the measured one and the cycle-averaged forces are very close. There are some discrepancies, e.g., the model-predicted curves display larger peak amplitudes, but based on the previous remarks it is likely that these reflect differences between wind tunnel and free-flight measurements, rather than shortcomings of the model. It can be noted in particular, that the free-flight lift has slightly larger peaks in the higher-velocity condition in subfigure 5.15(b) than in the lower-velocity one in subfigure 5.15(a), whereas an opposite trend was observed in all wind tunnel tests. These observations suggest that a more accurate prediction of the free-flight lift would be obtained if the model coefficients were identified from free-flight data. However, in this case additional effects should be considered, particularly the tail, for which higher-quality measurements would be required. Nonetheless, the current model gives a first approximation and accurate cycle-average, also for the free-flight case, and can be considered accurate enough for simple design and control applications. At this stage, no suitable data was available to evaluate conditions outside the initial test range ($V > 2 m/s$): this will be investigated in future research.

In terms of on-board applicability, a possible limitation of the model is the requirement for forward velocity measurement, typically unavailable on FWMAV. However, it was found that up to forward velocities of 1m/s, the velocity induced by the flapping motion clearly predominates, meaning the total forces can be predicted with sufficient accuracy even if forward velocity is neglected [38]. Where a wider range of conditions is to be considered, a possibility is to approximately compute the velocity from the pitch attitude, given
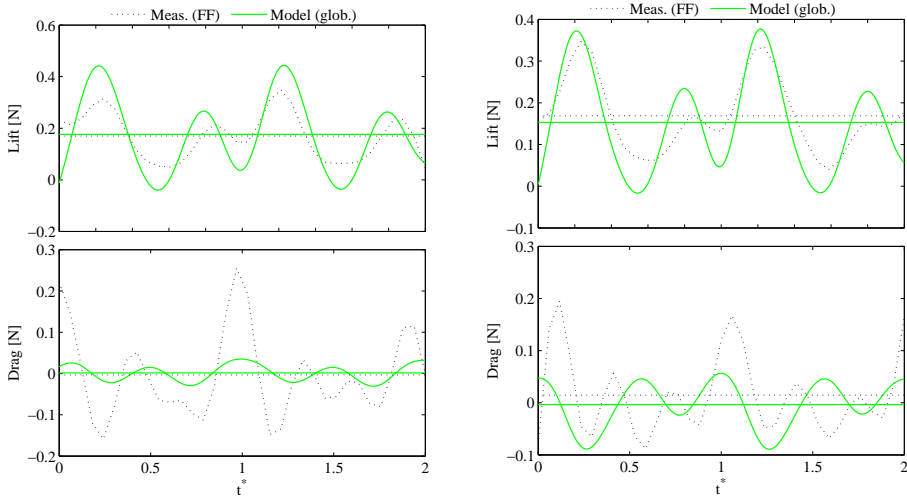
(a) Flight condition: $\theta = 79°, V = 0.44 m/s, f_f = 13.3 Hz$ (b) Flight condition: $\theta = 59°, V = 0.86 m/s, f_f = 12.5 Hz$

Figure 5.16: Global model validation examples. Free-flight measurements versus model-predicted forces computed according to Eq. 5.24, for two flight conditions not used in the modelling process. Cycle averages are also indicated for each force time history (horizontal lines).

that these two variables are strongly correlated ($R^2 = 0.94$) and for a vehicle that is capable of flying the specific correlation should be obtainable.

5.5. Conclusions

Quasi-steady models for flapping-wing aerodynamics available in the literature were extended to provide accurate modelling of the lift forces on clap-and-fling ornithopters. The proposed model accounts for centripetal, circulatory, viscous, added mass, and wing-wing interaction effects. Key additions to previous quasi-steady modelling approaches are the inclusion of a fling circulation factor to account for unsteady wing-wing interaction, the consideration of specific wing kinematics and geometry, and the consideration of different forward flight velocities. The aerodynamic coefficients in the proposed model structure were computed using parameter estimation techniques and wind tunnel measurements collected on a flapping-wing micro aerial vehicle (FWMAV) test platform. Validation tests were performed with both wind tunnel and free-flight data.

The resulting model was found to predict the lift forces of the test platform accurately, with output correlation coefficients of up to 0.97, and shows that accounting for wing-wing interaction is essential for accurate instantaneous force modelling when such effects are present, and that the proposed approach is effective. The drag forces are estimated less accurately, with correlation coefficients between 0.04 and 0.90. Better results would require accounting for the tail and using high-accuracy free-flight measurements, but consequently also a more complex model structure. This will be investigated in future research.

The model parameters were found to be either independent of the flight conditions or correlated to these, allowing for a global model to be developed, where the non-constant parameters are a first-order function of the flapping frequency and body pitch attitude. Thus, the same model can be used to represent different operating conditions of a vehicle and, if sufficient data is available, it could be possible to cover the full flight envelope in an analogous way. The global model computed for the test platform is very close to the local models for the flight regimes where the local models were computed. Additionally, validation tests with free-flight data show that the free-flight lift can be predicted with some accuracy also for flight conditions not used in the modelling process. This highlights the potential of the model for control applications.

The proposed model accurately represents a wide range of flight conditions, is computationally simple and requires few measurements (flapping frequency, pitch attitude and forward velocity). Its physically meaningful and yet simple model structure can be easily interpreted and is thus useful to obtain a better understanding of the platform and analyse its properties. These advantageous features make the model, on the one hand, a useful tool for preliminary analysis and design, even before a flight-capable platform is available and, on the other hand, a strong candidate for model-based control work and first step towards sub-flap cycle control. Future work will encompass evaluating different wing shapes, aspect ratios and kinematics, and validating the model for a wider range of different flight regimes including manoeuvring flight, using a higher data acquisition frequency.

REFERENCES

[1] S. F. Armanini, J. V. Caetano, G. C. H. E. de Croon, C. C. de Visser, and M. Mulder, *Quasi-steady aerodynamic model of clap-and-fling flapping MAV and validation with free-flight data,* Bioinspiration & Biomimetics **11**, 046002 (2016).

[2] W. Nachtigall and H. Rothe, *Nachweis eines "clap-and-fling-Mechanismus" bei der im Windkanal fliegenden Haustaube,* Journal of Ornithology **123**, 439 (1982).

[3] T. Weis-Fogh, *Quick estimates of flight fitness in hovering animals, including novel mechanisms for lift production,* Journal of Experimental Biology **59** (1973).

[4] T. Weis-Fogh, *Flapping flight and power in birds and insects, conventional and novel mechanisms*, edited by T. Y. Wu, C. J. Brokaw, and C. Brennen, Vol. 2 (Springer US, 1975) pp. 729–762.

[5] C. P. Ellington, *The aerodynamics of hovering insect flight. iii. kinematics,* Philosophical Transactions of the Royal Society of London B: Biological Sciences **305**, 41 (1984).

[6] L. A. Miller and C. S. Peskin, *Flexible clap and fling in tiny insect flight,* Journal of Experimental Biology **212**, 3076 (2009).

[7] R. A. Norberg, *The pterostigma of insect wings an inertial regulator of wing pitch,* Journal of Comparative Physiology **81**, 9 (1972).

[8] R. J. Cooter and P. S. Baker, *Weis-fogh clap and fling mechanism in locusta,* Nature **269**, 53 (1977).

[9] F.-O. Lehmann, *When wings touch wakes: understanding locomotor force control by wake–wing interference in insect wings,* Journal of Experimental Biology **211**, 224 (2007).

[10] L. Bennett, *Clap and fling aerodynamics-an experimental evaluation,* Journal of Experimental Biology **69**, 261 (1977).

[11] G. R. Spedding and T. Maxworthy, *The generation of circulation and lift in a rigid two-dimensional fling,* Journal of Fluid Mechanics **165**, 247 (1986).

[12] S. Sunada, K. Kawachi, I. Watanabe, and A. Azuma, *Fundamental analysis of three-dimensional 'near fling',* Journal of Experimental Biology **183**, 217 (1993).

[13] F.-O. Lehmann, S. P. Sane, and M. Dickinson, *The aerodynamic effects of wing–wing interaction in flapping insect wings,* Journal of Experimental Biology **208**, 3075 (2005).

[14] M. Groen, B. Bruggeman, B. Remes, R. Ruijsink, B. van Oudheusden, and H. Bijl, *Improving flight performance of the flapping wing MAV DelFly II,* in *International Micro Air Vehicle Conference and Competition (IMAV)* (2010).

[15] M. Perçin, Y. Hu, B. W. van Oudheusden, B. Remes, and F. Scarano, *Wing Flexibility Effects in Clap-and-Fling,* International Journal of Micro Air Vehicles **3**, 217 (2011).

[16] Q.-V. Nguyen, W. L. Chan, and M. Debiasi, *Design, Fabrication, and Performance Test of a Hovering-Based Flapping-Wing Micro Air Vehicle Capable of Sustained and Controlled Flight,* in *International Micro Air Vehicle Conference and Competition* (2014).

[17] S. Mao and Y. Xin, *Flows around two airfoils performing "fling and subsequent translation" and "translation and subsequent clap",* Acta Mechanica Sinica **19**, 103 (2003).

[18] L. A. Miller and C. S. Peskin, *A computational fluid dynamics of 'clap and fling' in the smallest insects,* Journal of Experimental Biology **208**, 195 (2005).

[19] N. Arora, A. Gupta, S. Sanghi, H. Aono, and W. Shyy, *Lift-drag and flow structures associated with the clap and fling motion,* Physics of Fluids **26**, 071906 (2014).

[20] Y. Kawamura, S. Souda, S. Nishimoto, and C. P. Ellington, *Clapping-wing micro air vehicle of insect size,* in *Bio-mechanisms of Swimming and Flying*, edited by N. Kato and S. Kamimura (Springer Japan, 2008).

[21] S. S. Baek, *Autonomous ornithopter flight with sensor-based behavior,* Univ. California, Berkeley, Tech. Rep. UCB/EECS-2011-65 (2011).

[22] D. Prosser, *Flapping wing design for a dragonfly-like micro air vehicle*, Master's thesis, Rochester Institute of Technology (2011), accessed from http://scholarworks.rit.edu/theses/5804.

[23] G. C. H. E. de Croon, E. de Weerdt, C. de Wagter, B. D. W. Remes, and R. Ruijsink, *The appearance variation cue for obstacle avoidance,* IEEE Transactions on Robotics **28**, 529 (2012).

[24] T. Nakata, H. Liu, Y. Tanaka, N. Nishihashi, X. Wang, and A. Sato, *Aerodynamics of a bio-inspired flexible flapping-wing micro air vehicle,* Bioinspiration & Biomimetics **6** (2011).

[25] F. Y. Hsiao, T. M. Yang, and W. C. Lu, *Dynamics of flapping-wing MAVs: Application to the tamkang golden snitch,* Journal of Applied Science and Engineering **15**, 227 (2012).

[26] M. Perçin, H. E. Eisma, J. H. S. de Baar, B. W. van Oudheusden, B. Remes, R. Ruijsink, and C. de Wagter, *Wake reconstruction of flapping-wing MAV DelFly II in forward flight,* in *International Micro Air Vehicle Conference and Competition* (2012).

[27] S. Deng, M. Percin, B. van Oudheusden, B. Remes, and H. Bijl, *Experimental investigation on the aerodynamics of a bio-inspired flexible flapping wing micro air vehicle,* International Journal of Micro Air Vehicles **6**, 105 (2014).

[28] C. Rose and R. S. Fearing, *Comparison of ornithopter wind tunnel force measurements with free flight,* in *2014 IEEE International Conference on Robotics & Automation (ICRA)* (2014).

[29] Q.-V. Nguyen, W. L. Chan, and M. Debiasi, *An insect-inspired flapping wing micro air vehicle with double wing clap-fling effects and capability of sustained hovering,* in *SPIE Proceedings Bioinspiration, Biomimetics and Bioreplication*, Vol. 9429 (2015).

[30] G. Lim, S. Shkarayev, Z. Goff, and P. Beran, *Studies of flight kinematics of ornithopters,* in *International Competition and Conference on Micro Air Vehicles* (2012).

[31] J. Keshavan and N. M. Wereley, *Design and development of a high frequency biologically inspired flapping wing mechanism,* in *48th AIAA/ASME/ASCE/AHS/ASC Structures, Structural Dynamics, and Materials Conference, Structures, Structural Dynamics, and Materials Conference*, AIAA Paper 2007-1789 (2007).

[32] M. Keennon, K. Klingebiel, and H. Won, *Development of the nano hummingbird: A tailless flapping wing micro air vehicle,* in *50TH AIAA Aerospace Sciences Meeting incl. New Horizons Forum and Aerospace Exposition*, AIAA Paper 2012-0588 (2012).

[33] J. L. Verboom, S. Tijmons, C. De Wagter, B. Remes, R. Babuska, and G. C. H. E. de Croon, *Attitude and altitude estimation and control on board a flapping wing micro air vehicle,* in *IEEE International Conference on Robotics and Automation (ICRA)* (2015).

[34] J. V. Caetano, C. C. de Visser, G. C. H. E. de Croon, B. Remes, C. De Wagter, and M. Mulder, *Linear Aerodynamic Model Identification of a Flapping Wing MAV Based on Flight Test Data,* International Journal of Micro Air Vehicles (2013).

5

[35] J. Grauer, E. Ulrich, J. E. Hubbard, D. Pines, and J. S. Humbert, *Testing and System Identification of an Ornithopter in Longitudinal Flight,* Journal of Aircraft **48**, 660 (2011).

[36] S. F. Armanini, C. C. de Visser, and G. C. H. E. de Croon, *Black-box LTI Modelling of Flapping-wing Micro Aerial Vehicle Dynamics,* in *AIAA Atmospheric Flight Mechanics Conference* (2015) AIAA Paper 2015-0234.

[37] S. F. Armanini, C. C. de Visser, G. C. H. E. de Croon, and M. Mulder, *Time-varying model identification of flapping-wing vehicle dynamics using flight data,* Journal of Guidance, Control, and Dynamics **39**, 526 (2016).

[38] S. F. Armanini, J. V. Caetano, C. C. de Visser, G. C. H. E. de Croon, and M. Mulder, *Aerodynamic Model Identification of a Clap-and-Fling Flapping-Wing MAV : a Comparison between Quasi-Steady and Black-Box Approaches,* in *AIAA Atmospheric Flight Mechanics (AFM) Conference*, AIAA Paper 2016-0014 (2016).

[39] M. H. Dickinson, F.-O. Lehmann, and S. P. Sane, *Wing Rotation and the Aerodynamic Basis of Insect Flight,* Science **284**, 1954 (1999).

[40] S. P. Sane and M. H. Dickinson, *The aerodynamic effects of wing rotation and a revised quasi-steady model of flapping flight.* Journal of Experimental Biology **205**, 1087 (2002).

[41] U. Pesavento and Z. J. Wang, *Falling paper: Navier-Stokes solutions, model of fluid forces, and center of mass elevation,* Physical Review Letters **93**, 144501 (2004), the American Physical Society.

[42] Z. A. Khan and S. K. Agrawal, *Wing Force and Moment Characterization of Flapping Wings for Micro Air Vehicle Application,* in *Proceedings of the American Control Conference*, Vol. 3 (2005).

[43] M. Perçin and B. van Oudheusden, *Three-dimensional flow structures and unsteady forces on pitching and surging revolving flat plates,* Experiments in Fluids **56**, 47 (2015).

[44] J. V. Caetano, S. F. Armanini, C. C. de Visser, G. C. H. E. de Croon, and M. Mulder, *Data-Informed Quasi-Steady Aerodynamic Model of a Clap-and-Fling Flapping Wing MAV,* in *International Conference on Intelligent Unmanned Systems (ICIUS)* (2015).

[45] G. C. H. E. de Croon, M. Perçin, B. D. W. Remes, R. Ruijsink, and C. De Wagter, *The DelFly Design, Aerodynamics, and Artificial Intelligence of a Flapping Wing Robot* (Springer Netherlands, 2016).

[46] S. P. Sane, *The aerodynamics of insect flight,* Journal of Experimental Biology **206**, 4191 (2003).

[47] C. P. Ellington, *The Aerodynamics of Hovering Insect Flight. I. The Quasi-Steady Analysis,* Philosophical Transactions of the Royal Society B: Biological Sciences **305**, 1 (1984).

[48] H. E. Taha, M. R. Hajj, and P. S. Beran, *State-space representation of the unsteady aerodynamics of flapping flight,* Aerospace Science and Technology **34**, 1 (2014).

[49] H. E. Taha, M. R. Hajj, and A. H. Nayfeh, *Flight dynamics and control of flapping-wing MAVs: a review,* Nonlinear Dynamics **70**, 907 (2012).

[50] G. J. Berman and Z. J. Wang, *Energy-minimizing kinematics in hovering insect flight,* Journal of Fluid Mechanics **582**, 153 (2007).

[51] T. Theodorsen, *General theory of aerodynamic instability and the mechanism of flutter*, Technical Report 496 (NACA, 1935).

[52] D. Peters, *Two-dimensional incompressible unsteady airfoil theory - an overview,* Journal of Fluids and Structures **24**, 295 (2008).

[53] G. C. H. E. de Croon, M. A. Groen, C. de Wagter, B. D. W. Remes, R. Ruijsink, and B. W. van Oudheusden, *Design, aerodynamics and autonomy of the DelFly,* Bioinspiration & Biomimetics **7**, 025003 (2012).

[54] M. J. Lighthill, *On the Weis-Fogh mechanism of lift generation,* Journal of Fluid Mechanics **60**, 1 (1973).

[55] D. Kolomenskiy, H. K. Moffatt, M. Farge, and K. Schneider, *The Lighthill-Weis-Fogh clap-fling sweep mechanism revisited,* Journal of Fluid Mechanics **676**, 572 (2011).

[56] J. P. Whitney and R. J. Wood, *Aeromechanics of passive rotation in flapping flight,* Journal of Fluid Mechanics **660**, 197 (2010).

[57] C. Wang and J. Eldredge, *Low-order phenomenological modeling of leading-edge vortex formation,* Theoretical and Computational Fluid Dynamics **27**, 577 (2013).

[58] C. P. Ellington, *The aerodynamics of hovering insect flight. iv. aerodynamic mechanisms,* Philosophical Transactions of the Royal Society of London. Series B, Biological Sciences **305**, 79 (1984).

[59] R. Noda, T. Nakata, and H. Liu, *Effects of wing deformation on aerodynamic performance of a revolving insect wing,* Acta Mechanica Sinica **30**, 819 (2014).

[60] R. H. Edwards and H. K. Cheng, *The separation vortex in the weis-fogh circulation-generation mechanism,* Journal of Fluid Mechanics **120**, 463 (1982).

[61] J. C. Wu and H. Hu-Chen, *Unsteady aerodynamics of articulate lifting bodies,* in *2nd Applied Aerodynamics Conference, Fluid Dynamics and Co-located Conferences* (1984).

[62] S. P. Sane, *Steady or unsteady? uncovering the aerodynamic mechanisms of insect flight,* Journal of Experimental Biology **214**, 349 (2011).

[63] A. I. Korotkin, *Added Masses of Ship Structures*, 1st ed., 88, Vol. 1 (Springer Netherlands, 2009) pp. 37–38.

5

[64] I. H. A. Abbott and A. E. V. Doenhoff, *Theory of wing sections : including a summary of airfoil data* (Dover Publications, New York, 1959).

[65] J. V. Caetano, C. C. de Visser, B. D. W. Remes, C. de Wagter, and M. Mulder, *Modeling a Flapping Wing MAV: Flight Path Reconstruction of the DelFly II,* in *AIAA Modeling and Simulation Technologies Conference*, AIAA Paper 2013-4597 (2013).

[66] J. V. Caetano, M. Percin, B. W. van Oudheusden, B. D. W. Remes, C. de Wagter, G. C. H. E. de Croon, and C. C. de Visser, *Error analysis and assessment of unsteady forces acting on a flapping wing micro air vehicle: Free-flight versus wind tunnel experimental methods,* Bioinspiration & Biomimetics **10** (2015).

[67] J. V. Caetano, M. B. Weehuizen, C. C. de Visser, G. C. H. E. de Croon, and M. Mulder, *Rigid-Body Kinematics Versus Flapping Kinematics of a Flapping Wing Micro Air Vehicle,* Journal of Guidance, Control, and Dynamics **38**, 2257 (2015).

[68] M. Groen, B. Bruggeman, B. Remes, R. Ruijsink, B. van Oudheusden, and H. Bijl, *Improving flight performance of the flapping wing MAV DelFly II,* in *International Micro Air Vehicle Conference and Competition (IMAV)* (2010).

[69] M. W. Oppenheimer, D. B. Doman, and D. O. Sigthorsson, *Dynamics and Control of a Biomimetic Vehicle Using Biased Wingbeat Forcing Functions,* Journal of Guidance, Control, and Dynamics **34**, 204 (2011).

[70] R. Jategaonkar, *Flight Vehicle System Identification A Time Domain Methodology* (AIAA Progress in Astronautics and Aeronautics, Reston, VA, USA, 2006).

[71] V. Klein and E. Morelli, *Aircraft System Identification* (AIAA Education Series, 2006).

[72] A. Andersen, U. Pesavento, and Z. J. Wang, *Unsteady aerodynamics of fluttering and tumbling plates,* Journal of Fluid Mechanics **541**, 65 (2005).

5

6

WING WAKE-TAIL INTERACTION AND TAIL AERODYNAMIC MODELLING

In Chapter 5 a physically meaningful model of the wing aerodynamics was developed. Currently, however, many flapping-wing vehicles, including the test vehicle used in this thesis, include a conventional tailplane, such as is found on fixed-wing aircraft. Advantages include static stability, simple control mechanisms and easier design. While the tail produces small forces compared to the wings, it has a crucial effect on the dynamics. However, the interaction between unsteady wing wake and tail is highly complex and therefore generally not modelled explicitly. To complement the previous chapter and obtain a complete phenomenological model of the aerodynamics, in this chapter a novel approach is proposed to model the time-varying aerodynamic forces produced by the tailplane, considering the effect of the wing wake. Firstly, the wing wake itself is modelled from PIV data using a multivariate splines-based identification method, to predict the wing-induced flow on the tail. Secondly, the obtained information is introduced in a quasi-steady aerodynamic force model that also considers the free stream, to estimate the forces generated by the tail. The resulting aerodynamic model yields insight into the magnitude and spatio-temporal changes of the tail forces, thus providing new insight into the role of the tail and its interaction with the wing wake. A clear physical connection is retained, despite the inclusion of empirical components. The suggested approach allows for the wings and tail to be represented separately and can for instance be combined with the model described in Chapter 5 to yield a full and accurate model of the vehicle aerodynamics. The approach thus represents a useful basis for more advanced modelling, design and control work, for both the current robot and comparable vehicles.

Despite significant interest in tailless flapping-wing micro aerial vehicle designs, tailed configurations are often favoured, as they offer many benefits, such as static stability and a simpler control strategy, separating wing and tail control. However, the interaction between the wing wake and tail is complex, due to the unsteady wing aerodynamics, and is generally not modelled explicitly. We propose an approach to model the flapping-wing wake and tail-wing wake interaction in a tailed flapping-wing robot. First, the wake is modelled as a periodic function depending on wing flap phase and position with respect to the wings. The wake model is constructed out of six low-order sub-models representing the mean, amplitude and phase of the tangential and vertical velocity components. The parameters in each sub-model are estimated from stereo-PIV measurements using an identification method based on multivariate simplex splines. The computed model represents the measured wake with high accuracy, is computationally manageable and is applicable to a range of different tail geometries. The wake model is then used within a quasi-steady aerodynamic model, and combined with the effect of free-stream velocity, to estimate the forces produced by the tail. The results provide a basis for further modelling, simulation and design work, and yield insight into the role of the tail and its interaction with the wing wake in flapping-wing vehicles. It was found that due to the effect of the wing wake, the velocity seen by the tail is of a similar magnitude as the free stream and that the tail is most effective at 50-70% of its span.

6

6.1. INTRODUCTION

In nature many flapping-wing flyers operate taillessly, e.g., flies, bees, moths, etc.. Thanks to elaborate wing actuation mechanisms, they are able to achieve high-performance, efficient flight and stabilisation using only their wings. However, despite significant research into developing tailless flapping-wing robots [2–4], which potentially allow for maximal exploitation of the manoeuvrability associated with flapping-wing flight, many flapping-wing micro aerial vehicles (FWMAV) continue to be designed with a tail [5–8]. Tailed vehicles benefit from both (a) the flapping wings – which provide high manoeuvrability, hover capability and enhanced lift generation, thanks to unsteady aerodynamic mechanisms – and (b) a conventional tail – providing static and dynamic stability and simple control mechanisms. The combination of points (a) and (b) leads to overall favourable performance, as well as simpler design, modelling and implementation. While their increased stability comes at the cost or a slight reduction in manoeuvrability compared to tailless vehicles, tailed vehicles nonetheless achieve a high performance and retain the advantage of more straightforward development and easier application. The presence of a tail can be particularly advantageous for specific types of missions, e.g., ones where extended periods of flight are involved. Therefore, there is significant potential for such platforms in terms of applications. However, the simpler control and stabilisation mechanisms come at a price, as the interaction between tail and flapping wings must be carefully considered, and this poses an additional challenge in the modelling and design process. The location of the tail behind the wings implies that the flow on the tail is significantly influenced by the flapping of the wings, with the downwash from the wings leading to a complex, time-varying flow on the tail.

Flapping-wing flight on its own is already highly challenging to model, due to the un-

steady aerodynamics and complex kinematics. Significant effort has been spent on developing accurate aerodynamic models, particularly ones that are not excessively complex and can be applied for design, simulation and control. In an application context, the most widely used approach for this is simple, quasi-steady modelling [9–13], and, to a lesser extent, data-driven modelling [14–19]. However, the combination of wings and tail has not been widely studied, despite being used on many flapping-wing robots; instead the design of the tail in such vehicles so far has largely relied on an engineering approach. Dynamic models either consider the vehicle as a whole without distinguishing between tail and wings [16, 19, 20], or model the tail separately but without explicitly considering its interaction with the wings [21]. Not only is the wing-tail interaction highly complex, making a quasi-steady approach difficult but, additionally, only limited experimental data are available to support this type of analysis and potentially allow for data-driven approaches.

At present, no approach has been suggested specifically to model the forces acting on the tail in flapping-wing vehicles, particularly in a time-resolved perspective. Several studies have analysed the wake behind flapping wings experimentally in great detail, in both robotic [22–24] and animal [25–27] flyers. Altshuler et al. [28] have also conducted PIV measurements around hummingbird tails. However modelling efforts focused on the tail and tail-wing wake interaction have been scarce. Noteworthy among these, are the attempts to analyse the wake by means of actuator disk theory, adjusted to the flapping-wing case [29, 30], however this work mostly focuses on a flap cycle-averaged level and on analysis of the wing aerodynamics. A cycle-averaged result considering a single value for the wing-induced velocity is unlikely to capture the time-varying forces on the tail. Conversely, a high-fidelity representation accounting for the unsteady effects that are present would require highly complex models that may not be suitable for practical purposes, e.g., CFD-based models. In practice, an intermediate solution is required, providing sufficient accuracy without introducing excessive complexity.

This chapter proposes a simple approach to model the wake of the wing of a flapping-wing robot, and hence the time-varying aerodynamics of the vehicle's tail, starting from particle image velocimetry (PIV) data. The model is based on experimental observations, thus ensuring closeness to the real system, but avoids excessive complexity to allow for simulation and control applications. The modelling process comprises two steps: firstly, a model is developed for the flapping-wing wake, depending on the wing motion. The wake is represented as a periodic function, where the velocity at each position in the considered spatial domain depends on the position in relation to the wings, as well as on the wing flapping phase. The overall wake model is constructed out of six low-order sub-models representing, respectively, the mean, amplitude and phase of the two velocity components considered, with the parameters in each sub-model being estimated from PIV measurements. Secondly, the obtained wake model is used to compute the flapping-induced velocity experienced by the tail, considering the tail positioning and geometry, and incorporated in a standard aerodynamic force model to estimate the forces produced by the tail. Tail forces are predicted for different flight conditions, also considering the effect of free-stream velocity in forward flight. Aerodynamic coefficients are based on quasi-steady flapping wing aerodynamic theory, as the tail experiences a time-varying flow, similar to what it would experience if it were itself performing a flapping motion.

The obtained results provide a basis for advanced modelling and simulation work, rep-

resent a potentially helpful tool for design studies, and yield new insight into the role of the tail and its interaction with the wings in flapping-wing vehicles. It was for instance found that the induced velocity on the tail is of a comparable order of magnitude to the free-stream velocity, and established at what spanwise positions the tail is expected to be most effective. The overall insight obtained may be valuable for improved tailed FWMAV designs, as well as paving the way for the development of tailless vehicles in the future. Combining the resulting tail aerodynamics model with a model of the flapping wing aerodynamics will result in a full representation of the studied vehicle, constituting a useful basis for the development of a full simulation framework, at a high level of detail, and supporting novel controller development.

The remainder of this chapter is structured as follows. Section 6.2 provides an overview of the experimental data. Section 6.3 briefly outlines the overall modelling approach. Detailed explanation of the wing wake modelling, starting from analysis of the experimental data, is given in Section 6.4, while the model identification and results are discussed in Section 6.5. The proposed tail force model is presented in Section 6.6 and assessed using aerodynamic coefficients from the literature. Section 6.7 closes with the main conclusions.

6.2. EXPERIMENTAL DATA

The modelling approach suggested is based on experimental data collected on a robotic test platform. Stereo-PIV data were used to model the flapping-wing induced velocity on the tail. The test platform and experimental data are presented in the remainder of this section.

6.2.1. TEST PLATFORM

As in the remainder of this thesis, the FWMAV used as a test platform in this chapter is a DelFly II (configuration I from Table G.1). For a detailed description and geometric features, cf. Chapter 1 Sec. 1.4.1, Appendix G and, e.g., Fig. 2.1). The most relevant feature for this chapter is the inverted 'T' styrofoam tail, which provides static stability and allows for simple, conventional control mechanisms that can be separated from the wing-flapping. The tail is therefore an essential element of the current design. It is also worth recapitulating that the DelFly flaps at frequencies between 9Hz and 14Hz, and the upper and lower wings are in phase with each other. The upper and lower wing leading edges on either side meet at a dihedral of 13°, while the maximum opening angle between upper and lower wings, defining the flap amplitude, is of approximately 90°.

6.2.2. TIME-RESOLVED PIV MEASUREMENTS

To obtain insight into the wake behind the flapping wings and model it, a set of previously collected stereo-PIV (particle image velocimetry) measurements [31] was used. These measurements were conducted at two different flapping frequencies, 9.3Hz and 11.3Hz (with, respectively, Re=10000 and Re=12100), at 0m/s free-stream velocity (representing hover conditions), to obtain the 2D velocity profile in the wake of the flapping wings.

The experimental setup is shown in Fig. 6.1. Subfigure 6.1(a) indicates the positioning of the three high-speed cameras (Photron FASTCAM, SA 1.1), which allowed for the wing flap angle corresponding to each PIV image to be obtained in addition to the velocity vectors. The figure also clarifies the coordinate frame used as a reference in the wake mea-

(a) Photograph of the setup   (b) Front view (looking at the vehicle)   (c) Side view
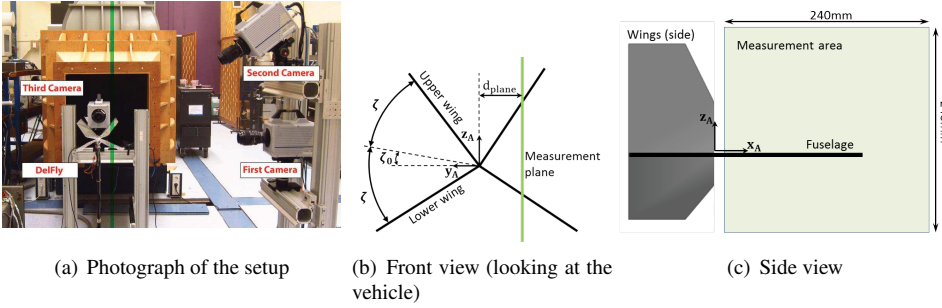
Figure 6.1: Experimental setup for PIV measurements; figures adapted from [31].

surements. Note that as the focus was on the wing wake, measurements were conducted on a simplified version of the test vehicle, consisting only of the wings and fuselage, and no tail. Fig. 6.2 clarifies the positioning of the measurement area with respect to the current tail of the studied FWMAV, and the coordinate frames used in this study.

Data were obtained at ten different spanwise positions (d_{plane}) to the right hand side of the fuselage, covering a range from 20mm to 200mm, in steps of 20mm. At each spanwise position, measurements were conducted in a 240mm×240mm chordwise oriented plane (aligned with the vehicle's XZ plane), positioned 10mm downstream of the wing trailing edges, as clarified by Figs. 6.1(b), 6.1(c) and 6.2. The planes were each centred around an axis 24mm above the fuselage, in order to capture the full wing stroke amplitude, considering the 13° wing dihedral of the platform. Double-frame images were captured at a recording rate of 200 Hz, and approximately 30-36 flap cycles (depending on the flapping frequency) were captured at each position. The post-measurement vector calculation [31] resulted in a spacing between measurement points of approximately 3.6mm in each direction. Measurements in the region closest to the wings were found to be unreliable due to laser reflection, hence data acquired in the 60mm of the measurement plane closest to the wings were discarded. Details on the PIV measurements, experimental setup and pre and post-processing can be found in Ref. [31].

6.3. MODELLING APPROACH OVERVIEW

We begin by considering a simplified 2D aerodynamic model, where the tail lift and drag forces are assumed to be described by the standard equations:

$$L_t = \frac{1}{2}\rho S_t V_t^2 C_{L,t}(\alpha_t), \tag{6.1}$$

$$D_t = \frac{1}{2}\rho S_t V_t^2 C_{D,t}(\alpha_t), \tag{6.2}$$

where ρ is the air density, S_t is the tail reference area, V_t is the flow velocity, α_t is the angle of attack (AOA) of the tail, and C_{Lt} and C_{Dt} are the lift and drag coefficients of the tail, respectively, as a function of tail AOA.

The AOA and velocity experienced by the tail are significantly affected by the down-

6

Figure 6.2: Top view on the FWMAV, showing the main tail geometric features and position, and the area covered by the wake model, in relation to the original region covered by the PIV measurements (measurements in mm).

wash from the flapping wings. As a consequence, they are time-varying and complex, and depend on both the wing kinematics, and the free-stream conditions. Additionally, the velocity and AOA perceived by the tail vary depending on the spanwise location that is considered. In view of the spanwise changes, a blade element modelling approach was opted for, using differential formulations of Eqs. 6.1–6.2 (cf. Eqs. 6.20, 6.21). This implies that three-dimensional effects are neglected, as discussed subsequently in Sec. 6.4.2. While quasi-steady blade-element modelling is a significantly simplified formulation, its use is widespread in the flapping-wing literature, where it has frequently been found to yield somewhat accurate approximations of unsteady flapping-wing aerodynamics [13, 32–34]. This type of formulation was therefore considered acceptable to approximate the aerodynamics of the tail, which can be seen as a flat plate in a time-varying flow.

According to blade-element theory, the local AOA and velocity experienced at each blade element can be expressed as follows:

$$\alpha_{t,loc} = \arctan\left(\frac{-w_{t,loc}}{u_{t,loc}}\right) \tag{6.3}$$

$$V_{t,loc} = \sqrt{u_{t,loc}^2 + w_{t,loc}^2} \tag{6.4}$$

where u and w are, respectively, the x and z components of the local velocity perceived by the tail blade element, according to the coordinate frame defined in Fig. 6.1. Each component includes the contribution of the free-stream velocity (V_∞), as well as the contribution of the wing flapping-induced velocity at the spanwise position considered, as explained in Sec. 6.6.1 (cf. Eq. 6.6.1). Fig. 6.3 illustrates the different flow velocities acting on a tail section (blade element), as a clarification, as well as the resulting flow velocity vector $V_{t,loc}$, given by the combination of free-stream and wing-induced velocities. Note that the horizontal tailplane has approximately no constructive incidence angle, as it is aligned with the xy-plane of the body (coordinate frame $B1$).

Since the free-stream contribution can be approximately computed from the flight conditions, the main unknown is the contribution of the wings. A realistic model of the aerodynamics of a tail positioned behind flapping wings requires representing the time-varying velocity profile that results from the unsteady wing aerodynamics. As a result, the first step in the modelling process is to represent the flapping-wing wake and deduce the resulting effective velocity and AOA on the tail. The second step is, then, to include the induced velocity predicted by the aforementioned model in the differential form of Eqs. 6.1 and 6.2. Additionally, there may be further effects that result specifically from the interaction of the free-stream and wake components: these require experimental data to be quantified, and are excluded at this stage.

The overall modelling approach is clarified by the diagram in Fig. 6.4. Throughout the remainder of this paper, this diagram will serve as a reference. The modelling process comprises the following main components, numbered so as to correspond to the numbers shown in the figure:

1. The necessary data must be obtained, i.e. the input to the model. The geometry and position of the tail are known for a given vehicle. The flight condition (velocity, wing flap phase and wing flapping frequency) can be determined through flight testing, if a flight-capable vehicle is already available, or otherwise based on similar vehicles.

(a) Tail section (blade element) definition

(b) Local velocities and angles at 2D section (blade element)
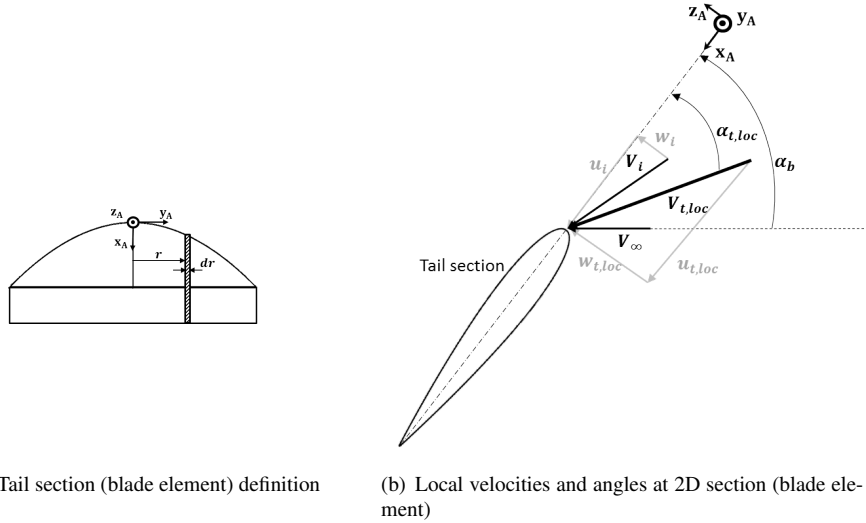
Figure 6.3: Flow velocities experienced at a spanwise tail section (not to scale). α_b indicates the angle of attack of the vehicle and V_∞ is the free-stream velocity (which approximately corresponds to the forward velocity of the vehicle). The wing-induced velocity experienced at the tail section is given by the vector V_i, while the total velocity experienced *locally* at the tail section is represented by the vector $V_{t,loc}$, obtained by summing V_i and V_∞. The components of each velocity vector along the x_A and z_A axes, respectively, are shown in grey. On the left, the definition of a blade element with respect to the whole tail is clarified.

If online application of the model is desired, the flight condition must be determined in flight.

2. The induced velocity components, arising from the placement of the tail in the wake of the flapping wings, must be computed. The wake modelling is presented in detail in Secs. 6.4 and 6.5, and yields the time-varying wing-induced velocity within a comprehensive area behind the wings. The induced velocity is expressed in components aligned with the x_A-axis (u_i) and with the z_A-axis (w_i), respectively, according to the coordinate system shown in Fig. 6.2.

3. From the wing-induced velocities (u_i, w_i) and the known free-flight conditions (V_∞), the resulting flow conditions at the tail (V_t, α_t) are computed, as explained in Sec. 6.6.1–6.6.3. Additionally, the aerodynamic force coefficients of the tail ($C_{L,t}, C_{D,t}$) are estimated, as explained in Sec. 6.6.2.

4. The final result of the modelling process is given by the tail aerodynamic forces (X_t, Z_t), discussed in Sec. 6.6.3.

The detailed modelling process is presented and discussed in the following sections.
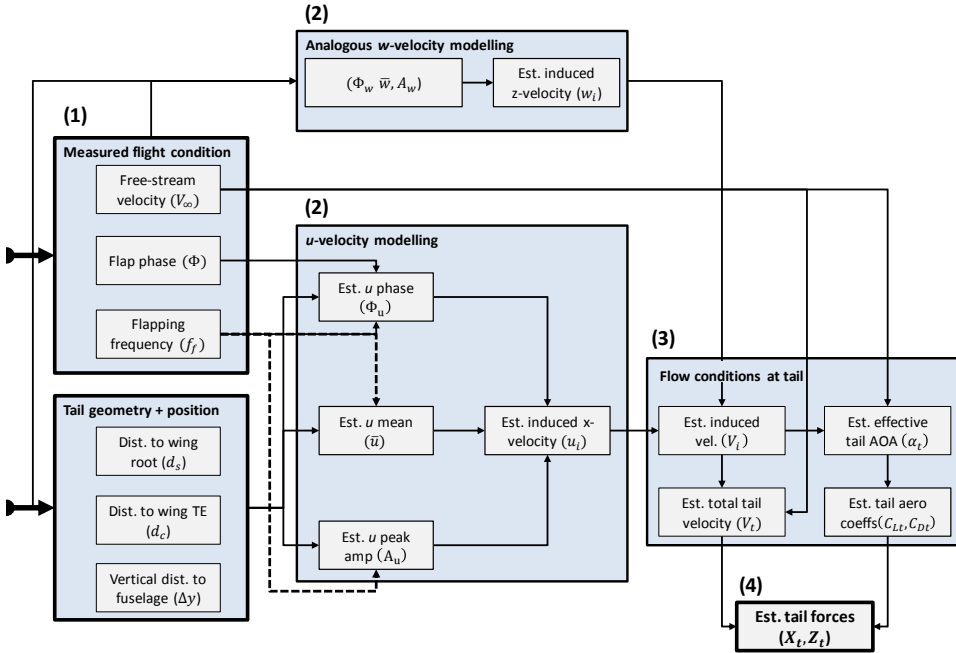
Figure 6.4: Diagram illustrating the overall modelling approach developed (est.=estimated).

6.4. WING WAKE MODELLING

6.4.1. EXPERIMENTAL EVALUATION OF THE WING WAKE

The velocity experienced by the tail in flapping-wing vehicles consists of a combination of free-stream velocity and induced velocity from the wings, where the latter component imparts a time-varying behaviour to the tail. It is of particular interest here because at the typical flight velocities of the FWMAV considered, the induced velocity is of a comparable order of magnitude to the free-stream velocity. Prior to modelling, the PIV data were analysed to establish the main trends and derive a suitable modelling approach.

Whilst initially all available measurements were considered, finally the focus was placed on those relevant for the current tail configuration and possible variations from it – i.e. data collected within a small area around the present tail configuration, as shown in Fig. 6.2. Therefore, only these data were used to model the wake. In spanwise (y_A in Fig. 6.1, or y_B in Fig. 6.2) direction, data collected at distances up to 85mm from the fuselage impinge upon the current tail design. As larger spans are being considered for future designs, data up to 100mm from the wing root were considered. Based on analogous considerations, in x_A (or x_B) direction, the domain of interest was reduced to the first 150mm behind the wing trailing edges.

In z_B direction, data for a small range of values above and below the fuselage were evaluated, to gain an idea of the variation of the flow in this direction (cf. Fig. 6.5). Although the tail essentially remains within approximately the same plane, it was considered useful to consider such changes because the tail has a thickness, and its position may vary slightly

(a) Mean of u

(b) Peak amplitude of u
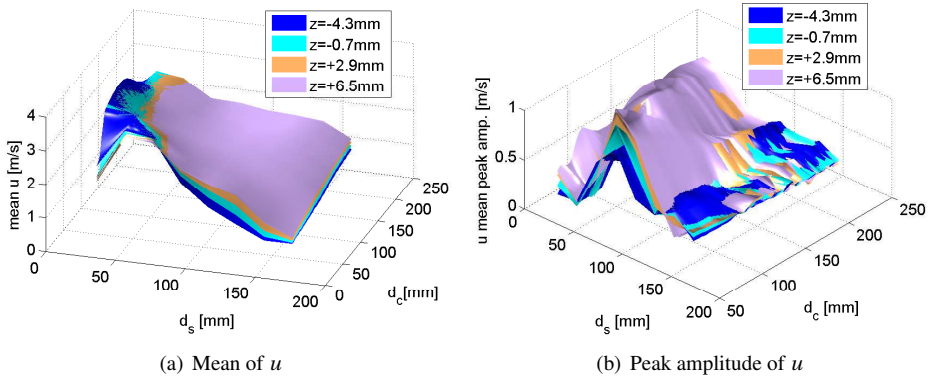
Figure 6.5: Velocity component u (mean and peak amplitude) obtained at different spanwise and chordwise positions, for 4 different vertical positions (z), at 11.2Hz flapping frequency.

with respect to the static case due to vibrations and bending of the fuselage during flight.

Short samples (3s) of the velocities in x_A and z_A direction (i.e. u and w, respectively) measured at each chordwise (d_c) and spanwise (d_s) position considered in the subsequent modelling process (cf. Sec. 6.4.3) are shown in Fig. 6.6. The definition of the wake positions with respect to the wings is clarified in Fig. 6.2. The data in Fig. 6.6 are discussed further in the remainder of this section. Additionally, an overlap of velocity measurements obtained at different chordwise distances from the wings and constant spanwise position is shown in Fig. 6.7 – here a qualitative idea can be obtained of the periodicity of the wake, and of the gradually increasing phase lag at increasing distances from the wing trailing edges. An initial assessment of the data allowed for the following three main observations.

Firstly, it was found that the induced velocity in x_A direction (u) is the main contributor to the average wake velocity, while the mean w velocities are much smaller, often close to zero (cf. Fig. 6.6). However, both components show significant oscillations during the wing flap cycle and hence both should be considered in a time-resolved model. The oscillations in w velocity also influence the local AOA on the tail (cf. Eq. 6.3).

Secondly, both the time histories (cf. Figs. 6.6, 6.7) and the discrete Fourier transforms (DFT) of the measurements reveal that the wake is highly periodic – with the exception of some isolated parts – and at fixed positions in the wake there is considerable agreement between separate flap cycles. This suggests that the velocity variations can be directly related to the wing flapping. Nonetheless, at some positions in the wake, the data become noisier and display more variation between cycles (e.g. at $d_c=80mm, d_s=20-40mm$). This may be due to additional complex interaction between the vortices in the wake [22], but also due to PIV imperfections. In the current study the wake is assumed to be periodic. This captures the main effects observed, while yielding less complex and more interpretable results.

Thirdly, it was found that in most of the domain relevant for the tail, the frequency content is largely concentrated at and around the flapping frequency (cf. Fig. 6.8). Thus, it was considered acceptable for a first approximation of the velocities on the tail, to low-pass
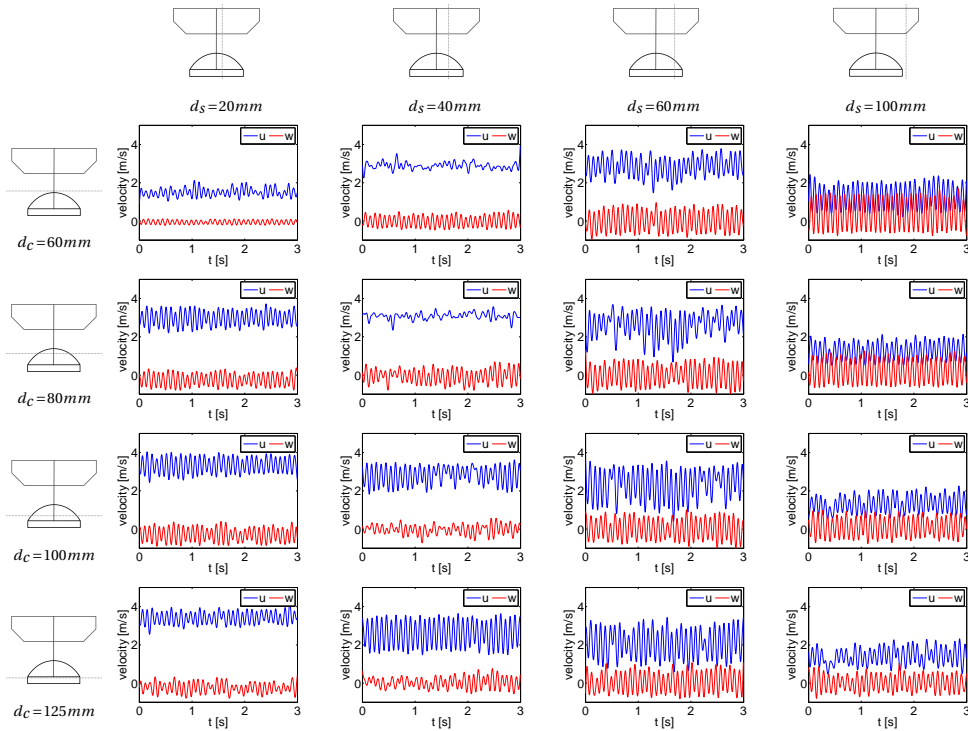
Figure 6.6: Measured wake u and w flow velocities at different chordwise (d_c) and spanwise (d_s) distances (data from Ref. [31]).

filter the data just above the flapping frequency. Nonetheless, there are isolated parts of the wake where this assumption becomes questionable, e.g., very close to both the wing trailing edges and the wing root. These are the same locations mentioned in the previous point. At these locations, it was also found that the frequency content shifts towards higher harmonics. This cannot be captured by the current model, but can be considered in future work.

As the velocities are mostly periodic, the amplitude and phase of the oscillations were considered next. Figs. 6.6 and 6.9 show that there are trends in the peak amplitude and phase of the wake velocity, with both the chordwise distance (d_c) from the wing trailing edges, and the spanwise distance (d_s) from the fuselage. The measurements obtained very close to both the wing root and the wing trailing edge are often less clean than those obtained elsewhere, possibly due to the complex aerodynamics resulting from the vicinity of the upper and lower wings to each other and their mutual interference. It is also possible that some of these effects are due to the wake not yet being fully developed very close to the wings. Similarly, the data obtained directly behind the wing tips are noisy and only barely periodic, possibly due to wake contraction [35], which implies that at increasing distances behind the flapping wings, the wing wake occupies an area that is increasingly narrower
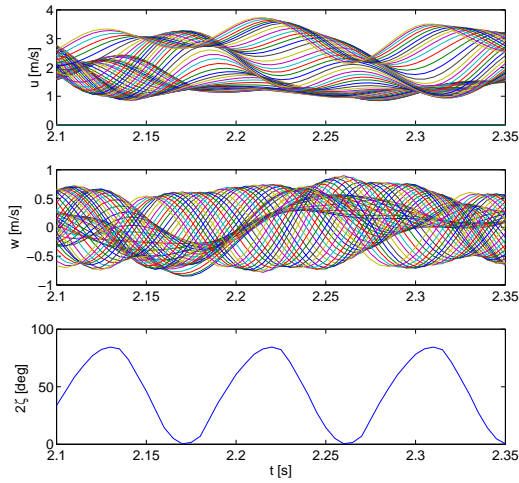
Figure 6.7: Overlapped measurements for velocity components u and w obtained at different chord-wise positions, at a fixed vertical position (approximately in the plane of the tail), for a spanwise position $d_s=60mm$; and corresponding angle between upper and lower wings, 2ζ (cf. Fig. 6.1(b)).

6

than the wing span, so that at some distance behind the wing tips, the wing wake has only a negligible effect. However, for the current FWMAV it is unlikely that even new tail designs would become as wide as the wings. Due to the described effects, the clearest measurements were obtained at intermediate spanwise distances (d_s), away from both the wing root and the wing tip, with some exceptions due to unsteady effects mentioned in the previous paragraphs. It is interesting to note that generally the mean u velocities initially increase, but then decrease with spanwise distance. This may be related to the specific vortex formations, but may also be enhanced by the dihedral of the wings. As the tail is aligned with the fuselage, at increasing spanwise distances from the wing root, the tail plane is increasingly less influenced by the main vortex formations.

In chordwise direction (d_c), the mean u values generally decrease farther away from the wing trailing edges, with the extent of this decrease varying depending on the spanwise position (d_s), while the w average velocities remain close to zero and show less clear trends. At large distances from the trailing edges, the peaks are small and tend to merge together, which complicates the recognition of patterns. This effect is further enhanced by the PIV settings, typically chosen so as to capture the highest velocity in the measurement plane effectively, to the detriment of lower velocities occurring simultaneously at other locations. In vertical (z_B) direction, changes were found to be small but noticeable in the mean u values, but only minor in the u peak amplitudes (cf. Fig. 6.5) and w velocities.

Comparing the data obtained at the two different flapping frequencies suggests that a higher flapping frequency leads to a higher mean velocity (mainly u), while not significantly affecting the peak amplitudes in the time-varying component. However, the availability of data for only two different flapping frequencies was considered insufficient for reliable

(a) u, time domain

(b) u, frequency domain

(c) w, time domain

(d) w, frequency domain
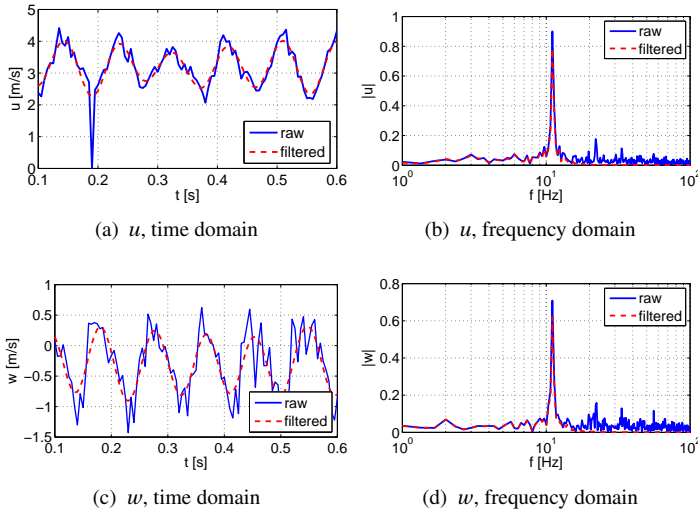
Figure 6.8: Example of the effect of low-pass filtering just above the flapping frequency ($\sim 12Hz$), in the time and frequency domain (wake position shown: $d_s = 20mm$, $d_c = 90mm$; DFT frequency resolution: 1.2Hz).

6

(a) Mean of u

(b) Peak amplitude of u
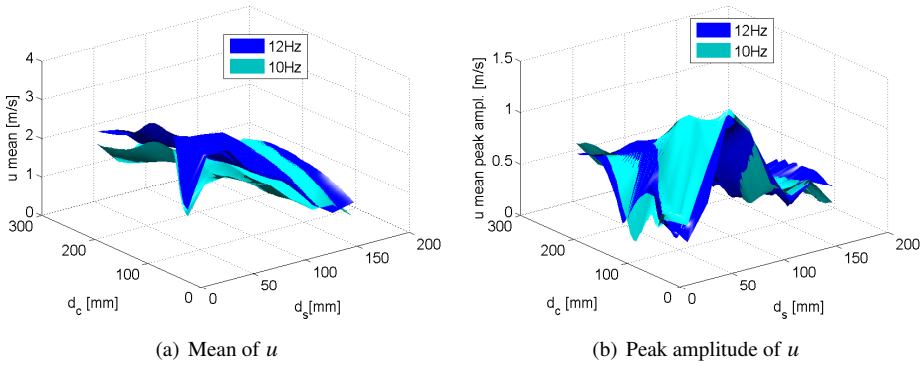
Figure 6.9: Velocity component u (mean and mean peak amplitude) obtained at different spanwise and chordwise positions and fixed vertical position, for two different flapping frequencies.

conclusions to be drawn, hence this likely dependency was not further considered in the modelling process, at this stage. Contrasting the PIV measurements for different flapping frequencies also reveals similar overall trends, suggesting a degree of reliability. In general, it should be considered that while a full aerodynamic interpretation requires extensive 3D data and analysis beyond the scope of this study, the unsteady processes involved imply that the observed trends may not always be intuitive. In this sense, the aforementioned similarity is a particularly useful indication.

The wing wake modelling approach was based on the preceding discussion and is outlined in the following section.

6.4.2. ASSUMPTIONS

The following assumptions and simplifications were made within the modelling process.

1. Based on the discussion in Sec. 6.4.1, the wing wake was assumed to be periodic. As mentioned previously, this is not always the case, nonetheless, even where there are additional effects, the periodic component remains significant, and is dominant in most cases, such that this assumption was considered acceptable for a first approximation.

2. Based on the frequency content analysis of the PIV data, it was decided to filter the wake velocities just above the first flapping harmonic.

3. The wing beat was assumed to be sinusoidal. While in the considered FWMAV the outstroke is slightly slower than the instroke [13], this difference is small and was considered negligible [13], particularly in view of the simplified nature of the aerodynamic model itself. More accurate mathematical representations of the kinematics, e.g., using a split-cycle piecewise representation [36], or different functions such as the hyperbolic tangent would have increased the model complexity and interpretability, and are left for future work.

4. Velocities in y_B (or y_A) direction were assumed to be negligible. While these velocities are of comparable magnitude to those in z_B direction, the blade element formulation adopted assumes that spanwise terms do not generate lift. The contribution of the aforementioned component is also assumed to be minor in a cycle-averaged sense because the platform is symmetrical around the $x_B z_B$ plane.

5. Three-dimensional effects, such as tail tip effects, were considered negligible, based on the results in [24] and [31] (cf. Figs. 5.3 and 5.4 in Ref. [31]). This assumption may become questionable in rapid manoeuvres, where the sudden change of AOA would induce 3D effects – this situation is not considered in the current formulation. Conducting PIV measurements on the wings alone, rather than on the full vehicle, also provides clearer insight into the wing wake propagation, as measuring on the full vehicle entails several additional challenges (discussed subsequently in Secs. 6.6.2 and 7.1.4).

6. It was assumed that the wing wake measured in hover conditions can provide information on the tail forces also for slow forward flight conditions, when combined in a simplified way with the free-stream effect (cf. Sec. 6.6). The wake vortices have different intensities and propagation rates depending on the free-stream velocity and flapping frequency [24], and the wake model is therefore likely inadequate for fast forward flight conditions. Nonetheless, the approach is deemed suitable to develop a low-order and physically representative model of the wake in slow forward flight regimes, which can be used to evaluate the effect of the wake on the tail and the magnitude of the tail forces. As shown in Table 6.2, the dynamic similarity parameters for the most commonly flown slow forward flight conditions ($V < 0.7$m/s) are comparable to the hover case. A more elaborate wake model could be obtained with an analogous approach as that proposed in this study, starting from PIV data collected in different flight regimes, however the result would be extremely complex and outside of the scope of the current feasibility study.

Finally, as a clarification: the wake models developed in this section predict the velocity *of the flow*, according to the coordinate system *A* shown in Figs. 6.1(b), 6.1(c) and 6.2.

The velocity that will be used to determine the tail forces in the subsequent section, is the velocity *of the respective tail section*, according to the coordinate system B shown in Fig. 6.2. As the x and z axes of the two systems are reversed (rotation by π rad about the y axis), the u and w components of the tail velocity have the same sign as the corresponding components of the flow velocity.

6.4.3. SINUSOIDAL MODEL STRUCTURE OF THE WING WAKE

The two components of the wake velocity (u, w) were approximated as cosine waves:

$$\hat{u}(d_s, d_c, \zeta) = \bar{u} + A_u(d_s, d_c) \cos(\Phi_u(d_s, d_c, \zeta)) \tag{6.5}$$

$$\hat{w}(d_s, d_c, \zeta) = \bar{w} + A_w(d_s, d_c) \cos(\Phi_w(d_s, d_c, \zeta)) \tag{6.6}$$

where d_c is the chordwise distance from the wing trailing edges, d_s is the spanwise distance from the wing root and ζ is the instantaneous wing flap angle. The six unknown parameters in the above model are: the mean velocities $(\bar{u}, \bar{w})$, the amplitudes of the oscillatory peaks with respect to the mean (A_u, A_w), and the phases with respect to the wing flap phase (Φ_u, Φ_w). Each parameter must be known at any position in the wake, within the range considered (cf. Fig. 6.2).

The phase of the induced velocities, in particular, must also be related to the wing flap phase, so that an accurate time-resolved model is obtained, that can predict the velocities in the wake any moment of the wing flap cycle. As mentioned previously, the wing flapping motion of the test platform is assumed to be sinusoidal. The magnitude of the angle of each wing with respect to the dihedral can thus be written as:

$$\zeta := \bar{\zeta} + A_\zeta \cos(2\pi t^*) \tag{6.7}$$

where t^* is non-dimensional time with respect to the wing flapping. If the beginning of the flap cycle is considered the moment when the wings are open, the phase corresponds to that of a pure cosine wave. The induced velocities are then waves with the same frequency as the wing flap angle, but phase shifted with respect to it. Φ_u and Φ_w in Eq. 6.5 can be formulated as:

$$\Phi_{u,w} = (2\pi(t^* + \Delta t_{u,w} f_f)) \tag{6.8}$$

where t is dimensional time, f_f is the wing flapping frequency, and Δt is the time difference between the start of the cycle (assumed to occur when the wings are open) and the time at which the peak of the considered wake velocity component occurs.

Applying this formulation requires knowing the time within the flap cycle (t^*). In practice, one possibility to do this is to use a sensor to register when the wings are at a particular position, measure the time with respect to this instant, and reset to zero every time the wings return to this position. If the flapping frequency is known, the non-dimensional time can be calculated, and the above equations can be applied once the time shift Δt is determined. An alternative is to find a function relating flap time to wing flap angle, and measuring the flap angle at each instant. As the same angles occur twice per flap cycle, the result is a piecewise function that also depends on the flap rate. Either way, it can be assumed that the time with respect to the wing flapping is known or measurable.

The relation of each of the six parameters in Eqs. 6.5 and 6.6 with position in the wake (d_c, d_s) and flap phase was estimated from the PIV data presented in Sec. 6.2.2. This

is discussed in the subsequent section. It should be noted that the parameters are likely to also depend on the flapping frequency, however this dependence cannot be determined conclusively with the current data, which only cover two different flapping frequencies. At present, results were determined only for the specific flapping frequencies for which data were available. As the procedure is analogous for different flapping frequencies, results are only presented for the 11.2Hz case.

6.5. MODEL IDENTIFICATION AND RESULTS

6.5.1. SUB-MODEL IDENTIFICATION

The unknown parameters $(\bar{u}, A_u, \Phi_u, \bar{w}, A_w, \Phi_w)$ in Eq. 6.5 (hereafter 'wake parameters') were determined from the PIV data presented in Sec. 6.2.2 using an identification method. In particular, a separate sub-model was developed to estimate each of the six original parameters (cf. Fig. 6.4). In an identification context, each of the wake parameters is therefore the output (z) of a separate sub-model. In view of the assumed wake periodicity, rather than using all measurements, the measured output at each wake position and non-dimensional time instant was defined as the mean over all flap cycles recorded at that particular position and time. Data for ten flap cycles were used to construct these models, to allow for validation of the results with the remaining data. Moreover, as discussed in Sec. 6.4.1, changes of the velocities in z_A direction are small but visible, and should be included in the model. Thus, instead of using measurements for the single particular z_A position closest to the tail plane, we computed the average of the velocities measured at the two closest measurement points above and below the tail plane. This covers a distance of approximately 8mm and should improve the reliability of the final force model results. Given the small magnitude and gradualness of the variation observed in this direction (cf. Fig. 6.5), using a larger number of points is not expected to change the results significantly.

As seen in Sec. 6.4.1, the wake parameters depend nonlinearly on chordwise and spanwise position with respect to the wings, and on the wing flap phase, hence the sub-models must depend on these variables. To obtain low-order models that nonetheless can represent these dependencies accurately, an identification method based on multivariate simplex B-splines was chosen. This allows for accurate global models to be obtained by combining low-order local ones, thus avoiding the typically high model orders required to cover the entire domain of a nonlinear system with a single polynomial model. A thorough explanation of the estimation method can be found in Refs. [37, 38], hence only a concise overview is given here.

Simplex splines are geometric structures minimally spanning a set of n dimensions. Each simplex t_j has its own local barycentric coordinate system, and supports a local polynomial that can be written (in so-called B-form) as:

$$p(x) = \begin{cases} \sum_{|\kappa|=d} c_\kappa^{t_j} B_\kappa^d(b_{t_j}(x)) & \text{for } x \in t_j, \\ 0 & \text{for } x \notin t_j \end{cases} \tag{6.9}$$

where $c_\kappa^{t_j}$ are the coefficients of the polynomial, known as B-coefficients, b_{t_j} are the barycentric coordinates of point x with respect to simplex t_j, d is the degree of the polynomial, $\kappa = (\kappa_0, \kappa_1, \ldots, \kappa_n)$ is a multi-index containing all permutations that sum up to d, and

$B_\kappa^d(b)$ are the local basis functions of the multivariate spline:

$$B_\kappa^d(b):=\frac{d!}{\kappa!}b^\kappa, \quad d\geq 0, \kappa\in\mathbb{N}^{n+1}, b\geq 0 \tag{6.10}$$

Polynomials of the form given in Eq. 6.9 can be used as a model structure for system identification. The underlying idea is that prior to estimation, the identification domain is divided into a net of non-overlapping simplices (triangulation), and a separate local model is identified for each simplex, using the datapoints contained in that simplex. In an identification framework, the basis functions in Eq. 6.9 represent the measurements used to model the chosen system output, whereas the B-coefficients are the model parameters to be estimated and locally control the structure of the polynomial.

In this study, an ordinary least squares estimator was used [37], hence, the output equation at each measurement point i is:

$$z_i = \sum_{|\kappa|=d} c_\kappa^{t_j} B_\kappa^d(b_{t_j}(x_i))+\epsilon_i, x\in t_j \tag{6.11}$$

Written in vector form, this is:

$$\mathbf{z}=\mathbf{Bc}+\boldsymbol{\epsilon}. \tag{6.12}$$

The sparse $\mathbf{B}$ matrix in the above equation contains the regressor measurements, converted to the barycentric coordinates of the simplex containing them. As each local model is constructed using only the data within a single simplex, the global B-matrix for the full triangulation is a block diagonal matrix constructed from the B-matrices of the J simplices:

$$\mathbf{B}_{glob}=diag(\mathbf{B}_{t1},\ldots,\mathbf{B}_{tJ}). \tag{6.13}$$

Given the B-matrix, an ordinary least squares (OLS) estimator can be defined for the B-coefficients in $\mathbf{c}$.

$$\hat{\mathbf{c}}=(\mathbf{B}^T\mathbf{B})^{-1}\mathbf{y}. \tag{6.14}$$

To ensure continuity between the separate models, continuity conditions of the following form can be defined between neighbouring simplices:

$$\mathbf{H}\cdot\mathbf{c}=\mathbf{0}, \tag{6.15}$$

where $\mathbf{H}$ is the smoothness matrix defining the continuity conditions. The estimator can then be reformulated to include these continuity conditions, e.g., as explained in Ref. [37].

The outlined approach was applied to estimate a model for each of the six wake parameters in Eq. 6.5, leading to six separate sub-models, that are finally combined to estimate the total time-resolved induced velocity components, as shown in Fig. 6.4. The output variable for each sub-model is thus one of the aforementioned parameters. In each case, an appropriate model structure and triangulation of the domain defined by the chordwise (d_c) and spanwise (d_s) positions in the wake were chosen, based on analysis of the input-output data. The chosen modelling setup for each case is shown in Table 6.1. In all cases, equally shaped and evenly distributed two-dimensional simplices were used. When comparable results were obtainable with different combinations of model order and triangulation density, the solution leading to the lowest model order was favoured, as it leads to a comparatively

Table 6.1: Modelling parameters for each output variable and performance of the resulting model.

output y	model deg. d	continuity	# simplices J	RMS	R^2
$\bar{u}$	2	0	8	$0.05\frac{m}{s}$	1.0
A_u	4	0	4	$0.01\frac{m}{s}$	1.0
Φ_u	2	0	8	$0.002s$	1.0
$\bar{w}$	2	0	8	$0.01\frac{m}{s}$	1.0
A_w	2	0	8	$0.01\frac{m}{s}$	1.0
Φ_w	2	0	2	$0.003s$	0.98

smaller number of coefficients and is less prone to numerical issues. Zero-order continuity[1] was considered sufficient at this stage, as the intended usage of the model does not require more.

Note that in the case of the phase, to facilitate the modelling, the time delay was formulated in a continuous way: starting from the time delay of the earliest occurring peak in the wake, other peaks are taken incrementally, going over into successive cycles, rather than restarting at zero when the delay becomes larger than the cycle period. However, in practice it is useful to know where the peaks in the wake are located at a particular moment in the (current) flap cycle, rather than with respect to the same particular flap cycle that may be more than one flapping period away. Thus, in a second moment, when going from the wave parameters to the actual wave, the phase model results were transformed back into the relative frame of a single flap cycle, to yield the relative time delay with respect to the most recent peak:

$$\Delta t_{rel} = \Delta t_{abs} \mod T_{cycle}, \tag{6.16}$$

where T_{cycle} is the flapping period.

6.5.2. WAKE MODELLING RESULTS

The obtained results are summarised in Figs. 6.10–6.15. It can be seen that in general the respective models represent the PIV-computed wake parameters with significant accuracy, mostly leading to small residuals and high R^2 values (cf. Table 6.1 and Figs. 6.10–6.15). The residuals generally tend to be larger close to the wing root, in agreement with the observations made earlier regarding more unsteady regions in the wake, where trends are more nonlinear. Nonetheless, even at these locations, the residuals remain small and the model accuracy high.

Evidently, however, the ultimate goal is to represent the actual wake velocities, and hence to evaluate the extent to which the suggested sinusoidal approximation of Eqs. 6.5–6.6 is itself acceptable. As observed in Sec. 6.4.1, the PIV data are predominantly periodic, and in some cases close to a perfect sine wave. Hence, a further evaluation of the obtained wake model was made by substituting the estimated parameters (i.e., the predicted output of the six sub-models) into Eq. 6.5 to compute the velocities as each considered position in the wake, and comparing the outcome to the direct PIV measurements. In particular,

---

[1]Neighbouring pieces of the simplex spline function are equal at their shared edge, but continuity is not guaranteed for their derivatives.

(a) Measured data surface (b) Model surface (c) Measured and model-predicted output (d) Residual surface
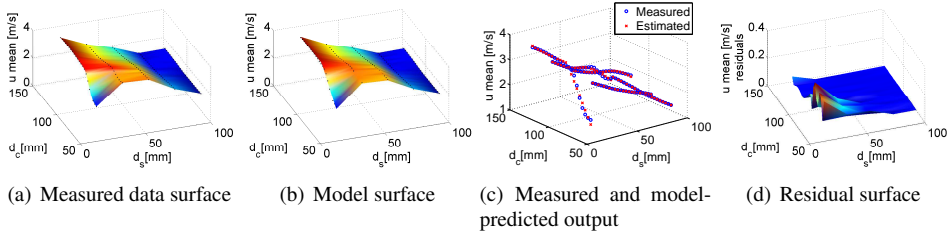
Figure 6.10: Model: u mean parameter

(a) Measured data surface (b) Model surface (c) Measured and model-predicted output (d) Residual surface
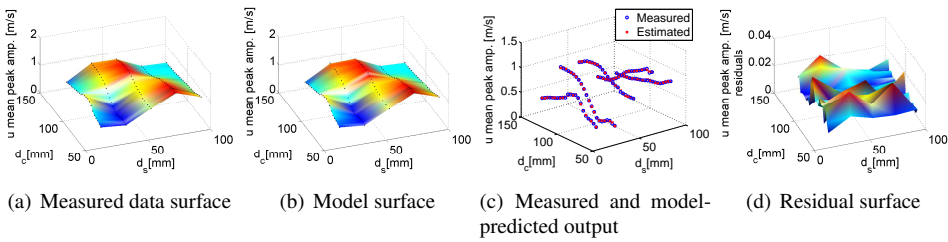
Figure 6.11: Model: u peak amplitude parameter

(a) Measured data surface (b) Model surface (c) Measured and model-predicted output (d) Residual surface
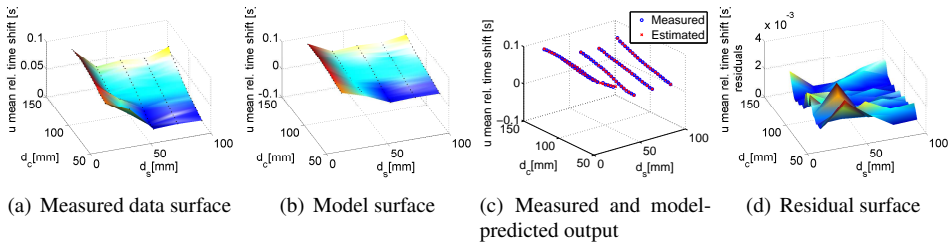
Figure 6.12: Model: u phase delay parameter

(a) Measured data surface   (b) Model surface   (c) Measured and model-predicted output   (d) Residual surface
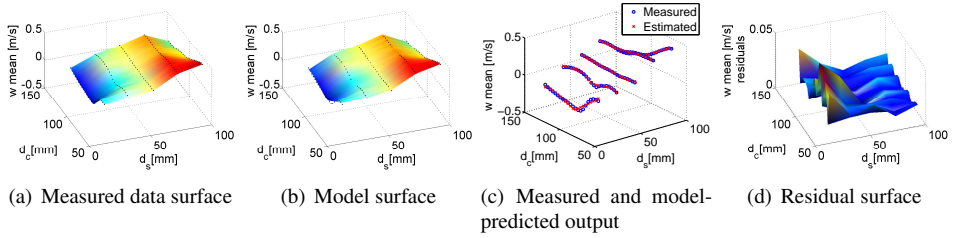
Figure 6.13: Model: w mean parameter

(a) Measured data surface   (b) Model surface   (c) Measured and model-predicted output   (d) Residual surface
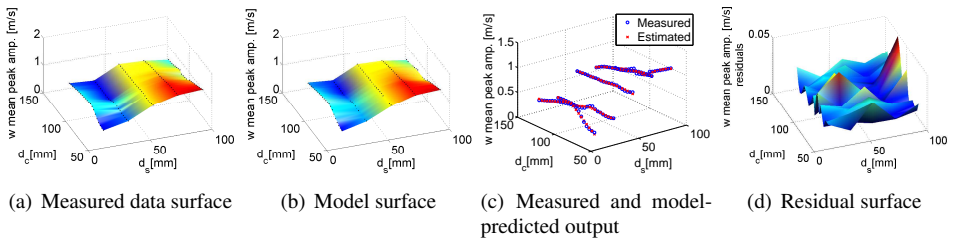
Figure 6.14: Model: w peak amplitude parameter

(a) Measured data surface   (b) Model surface   (c) Measured and model-predicted output   (d) Residual surface
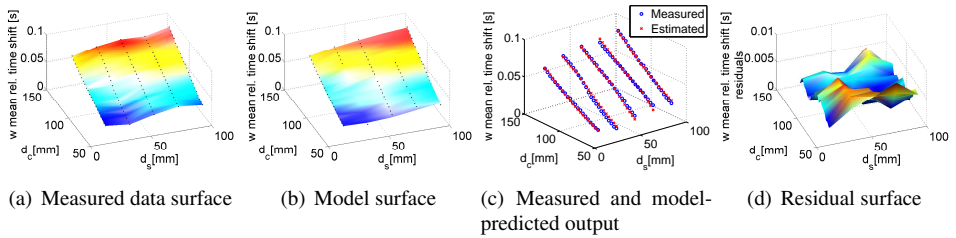
Figure 6.15: Model: w phase delay parameter

the PIV data used in this evaluation were not used in the identification process, hence this comparison constitutes an independent validation of the wake model.

Fig. 6.16 shows several examples of the model validation process. It can be observed that, as expected from the PIV data and the highly accurate estimates of the wake parameters, the agreement is generally significant, especially in mean and amplitude, which are mostly very close to those of the data. The amplitude shows some discrepancies, mostly related to the modelling assumption of periodicity, which, as discussed previously, is not always fully valid, rather than to the identified model itself. As discussed in Sec. 6.4.1, these assumptions are particularly questionable close to the wings. Overall, the most notable discrepancies are found in the phase, which in some cases is not fully in agreement, as seen in Fig. 6.16 (e.g., at position d_c=80mm, d_s=60mm). This may be a result of insufficient accuracy in determining the flapping frequency, which in some cases varies slightly throughout the data samples. Indeed, it appears that the frequency itself is not always identical, rather than the phase delay. As a small discrepancy in phase may add up to a large error over time, it is especially important that the frequency is determined accurately, and this should be ensured when applying this model.

On a final note, it should be considered that although a relatively large number of parameters (B-coefficients of the sub-models) is required to achieve sufficient accuracy over the entire domain considered, the model structure itself is based on low-order components and does not require heavy computations to implement. Additionally, applying the model for tail force estimation requires only knowing the geometry of the vehicle, and very few measurements, viz. flapping frequency and wing flap angle or timing of each cycle. The model also allows for reasonable estimates to be made for in-between positions in the wake, where no direct measurements were available, thus providing more flexibility, for instance facilitating the use of blade element approaches to compute the tail forces. However, as the flapping-wing wake is unsteady, further analysis may be advisable to confirm what occurs at unobserved positions in the wake. With the available data, the current model provides an effective starting point to represent the wake in a realistic but manageable way.

6
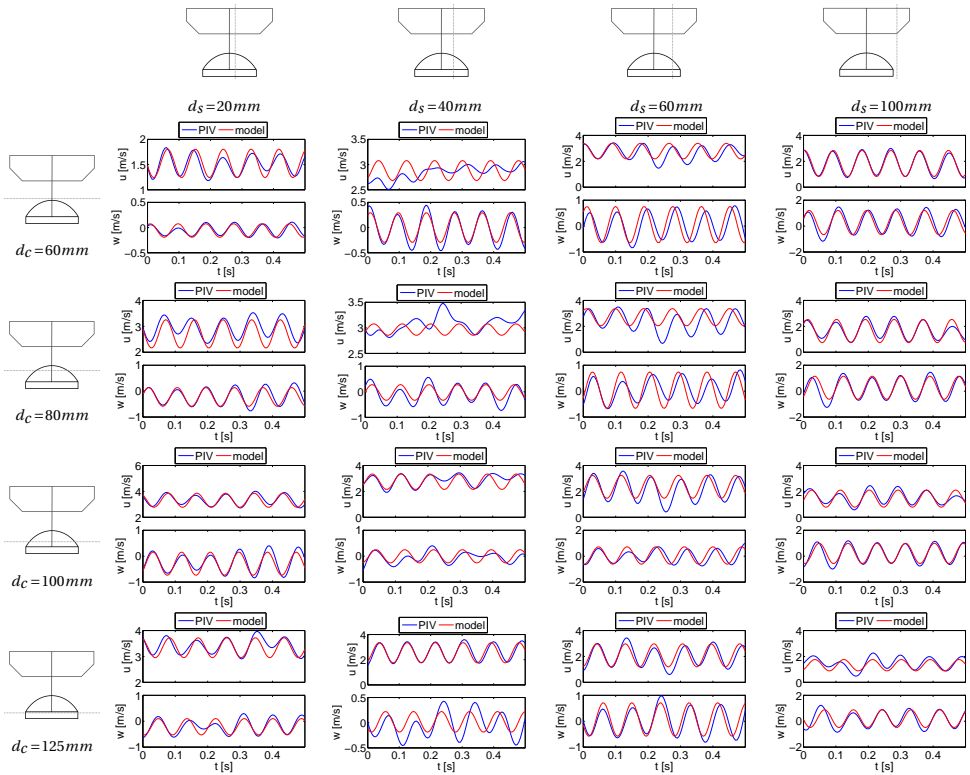
Figure 6.16: Validation example: model-predicted and measured wake velocities u and w at different wake locations, using Eq. 6.5 and the parameters estimated with the sub-models presented in Sec. 6.4.3 (PIV data from Ref. [31]).

6.6. TAIL FORCE MODELLING

6.6.1. EFFECTIVE VELOCITY AND ANGLE OF ATTACK ON THE TAIL

The flapping-induced flow velocity models developed in the previous section can be used within a blade element model of the tail aerodynamics. For this it is necessary to determine the specific velocities experienced along the tail leading edge. Fig. 6.2 shows the planform of the test platform tail. The developed wake model allows for the local induced velocities to be determined anywhere along the tail leading edge, as a function of instantaneous flap phase and spanwise and chordwise position of the point considered. The averaging introduced in vertical direction accounts for small variations and inaccuracies in the nominal z_B positioning of the tail. The suggested model provides a continuous mathematical description of the entire wake in the relevant domain, hence it is possible to determine the induced u and w velocities at any point and, consequently, to define blade elements with an arbitrarily close spacing. Fig. 6.3 clarifies the different velocity components acting at each tail section.

Assuming the vehicle is moving with a forward velocity V, hence is affected by a free-stream velocity V_∞, the body-frame u and w velocities experienced by a particular blade element, and resulting total velocity, are given by:

$$\hat{u}_{t,loc} = \hat{u}_i + V_\infty \cos \alpha_b, \tag{6.17}$$

$$\hat{w}_{t,loc} = \hat{w}_i + V_\infty \sin \alpha_b, \tag{6.18}$$

$$\hat{V}_{t,loc} = \sqrt{\hat{u}_{t,loc}^2 + \hat{w}_{t,loc}^2} \tag{6.19}$$

where α_b is the body AOA, the subscript i indicates induced velocities, a hat superscript indicates model-estimated values, and variables without superscript are assumed to be known.

The local AOA and velocity experienced at each blade element can then be computed using Eq. 6.3, and the lift and drag forces at each blade element can be determined using differential formulations of Eqs. 6.1 and 6.2:

$$dL_t(r,t) = \frac{1}{2}\rho c_t(r)\hat{V}_{t,loc}^2(r,t)C_{L,t}(\hat{\alpha}_{t,loc}(r,t))dr \tag{6.20}$$

$$dD_t(r,t) = \frac{1}{2}\rho c_t(r)\hat{V}_{t,loc}^2(r,t)C_{D,t}(\hat{\alpha}_{t,loc}(r,t))dr \tag{6.21}$$

where r is the spanwise distance from the wing root to the middle of the considered blade element, and $c_t(r)$ is the tail chord at this position. Note that while the variables are expressed as functions of r, to underline that the equation is evaluated at every spanwise blade element, in fact the local velocity and AOA are a function of *both* the spanwise and the chordwise position of the tail with respect to the wings, as clarified by eqs. 6.5 and 6.6.

Given that each blade element may have a different orientation, due to the temporally and spatially varying flow, the local definition of lift and drag has a different orientation at each station. Hence, in order to integrate the local forces, the differential forces are first transformed to the body coordinate system, based on the local AOA at each blade element. Integrating these components then yields the contribution of the tail to the body-frame X and Z forces.

Note that, as evident from Eqs. 6.20 and 6.21, the aerodynamic forces were assumed to depend only on the instantaneous AOA. It is known that when a wing simultaneously

translates and rotates about a spanwise axis, the aerodynamic effects acting on it (rotational forces, Wagner effect, added mass, clap-and-peel) are also affected by the wing rotation velocity and, hence, the AOA rate of change. However, calculating rotational circulation is not trivial, due to the lack of physical insight on the phenomenon and the influence of other parameters (Reynolds number and reduced frequency), and wing rotation effects are often studied numerically [39]. The explicit inclusion of such phenomena in the proposed model would hence add significant complexity, with no a priori justification for the specific flight regimes studied. Furthermore, as observed in Ref. [40] (table 1), the dominant component in the force generation process is the leading edge vortex, which is included in the suggested model. In view of these points, the influence of the AOA rate of change was neglected, allowing for a simple, yet physically representative model to be developed.

6.6.2. AERODYNAMIC COEFFICIENTS

The remaining unknowns in Eqs. 6.20 and 6.21 are the lift and drag coefficients. Several options can be considered for these parameters, starting from a simple linear theory approach, where $C_{L,t} = 2\pi\alpha_{t,loc}$ and $C_{D,t} = C_{D0} + kC_{Di}^2$. However, it was considered a more realistic alternative to assume that, as the tail experiences a time-varying flow, its lift and drag coefficients take one of the harmonic formulations typically assumed for flapping wings (e.g. cf. Refs. [10, 40–42]), and in particular, that stall is delayed due to the unsteady flow on the tail.

Evidently, the most realistic approach to determine the aforementioned coefficients is an experimental approach, however this was found to pose a challenge. On the one hand, flapping-wing vehicles are typically very small, so their tails generate very small forces that may be difficult to measure even with highly accurate force sensors. This makes it particularly difficult to carry out measurements on the tail alone. On the other hand, clamping the full FWMAV in the wind tunnel results in vibrations, especially in z_B direction, that are not observed in free flight [43] – a significant problem because this is the direction the tail is expected to contribute to most. Obtaining realistic data, that would allow for both the aerodynamic coefficients, and the estimated forces themselves to be validated, would therefore require free-flight PIV measurements (a technique that has recently been demonstrated for the first time [44], but only for measurements at a distance behind the test vehicle). An additional problem encountered during preliminary wind tunnel tests with the full vehicle was the interference of the strut on which the vehicle is clamped: while this is typically not an issue, the normal flight attitude of the FWMAV used in this study – like that of many insects in slow or hovering flight – involves a high body pitch attitude, which leads to the entire tail being positioned behind the aforementioned strut. Moreover, the strut is shaped in an aerodynamically favourable way, minimising its impact on the flow, only in its uppermost part. The normal flight attitude of the studied test platform leads to the tail being positioned further down, where the strut affects the flow on the tail.

Typically, the formulations proposed in the literature specifically for flapping wings and for flat plates performing analogous motions, are empirical and contain vehicle-specific parameters that must be determined experimentally or somehow estimated [40–42]. Given the aforementioned experimental challenges, experimental values from the flapping-wing literature were selected to represent the aerodynamic coefficients, allowing for an approximate, qualitative evaluation of the modelling approach to be made. In particular, we opted
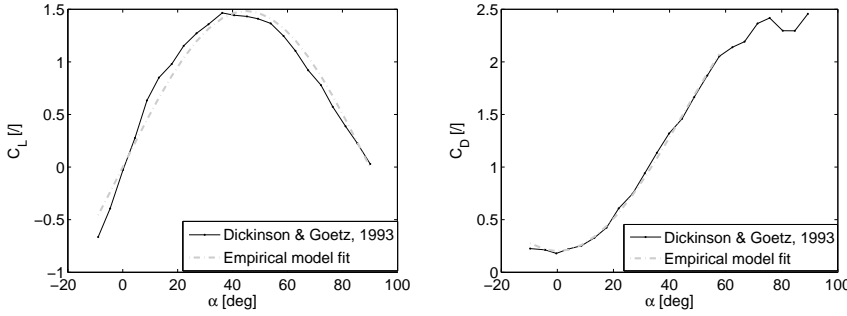
Figure 6.17: Empirical functions representing the aerodynamic coefficients obtained experimentally in Ref. [45], used in this study.

to use the coefficients measured by Dickinson & Götz [45] in their experimental study on translating model wings. These data were considered a realistic starting point because: (i) end plates were used to reduce 3D effects, hence the obtained coefficients are applicable to wing sections, allowing for a blade element approach such as that proposed in the current study; and (ii) the model wings and experimental setup used can be considered reasonably comparable to the tail studied here, i.e., involving non-rotating, rigid, flat-plate wings, translating at low Reynolds numbers. Nonetheless, it should be considered that the Reynolds numbers occurring at the tailplane (taking an average over the span and over the flap cycle, $Re_t \approx 8000$–10000 for $V_\infty = 0.3$–1.0m/s) are higher than those in the aforementioned study, and therefore the coefficients only allow for an approximation. Accurate results will require refining these values based on experimental measurements on the specific test platform, although studies have suggested that differences in coefficients are limited for $Re \approx 10^2$–0^5 [46], and the result obtained with the current coefficients may therefore also provide some quantitative information.

Empirical functions were fitted through the measurements in Ref. [45] (cf. Fig. 4 in [45]). In particular, the following functions were found to yield an accurate approximation, as shown in Fig. 6.17:

$$C_{L,t} = C_l \sin 2\alpha_{t,loc}, \tag{6.22}$$

$$C_{D,t} = C_{d0} \cos^2 \alpha_{t,loc} + C_{d\frac{\pi}{2}} \sin^2 \alpha_{t,loc}, \tag{6.23}$$

where C_l, C_{d0} and $C_{d\frac{\pi}{2}}$ are constants, which were set to the following values, obtained via least squares regression: $C_l = 1.6$, $C_{d0} = 0.2$, $C_{d\frac{\pi}{2}} = 2.8$. It is worth noting that functions of the same form have been used previously to model the aerodynamic coefficients of flapping wings or plates, however these were derived from measurements performed on finite-span, rotating plates/wings [11].

A full validation will involve adjusting the aerodynamic coefficients to the specific test platform, which in turn will require more extensive wind tunnel testing, with a considerably more elaborate setup, and will be considered in future work. Despite the limitations mentioned, the aerodynamic coefficients from the literature provide the means for an initial computation of the tail forces.

6.6.3. LOCAL FLOW AND TAIL FORCE PREDICTION

Results were computed in four different forward flight conditions, chosen to correspond to conditions previously measured in free flight with the same vehicle [47], and shown in Table 6.2[2]. The properties of the PIV test conditions are also shown.

Test condition	V_∞[m/s]	α_b[deg]	f_f[Hz]	Re	k
PIV 1	0	N/A	9.3	10000	0.28
PIV 2	0	N/A	11.3	12100	0.28
1	0.3	83	13.3	14500	0.28
2	0.5	74	12.5	14100	0.27
3	0.7	62	11.7	14200	0.25
4	1.0	45	10.3	14700	0.21

Table 6.2: Flight conditions the tail force model was tested for, corresponding to conditions determined in free-flight tests on the same vehicle [47]; and corresponding Reynolds numbers (Re) and reduced frequencies k ($k = \frac{\omega \bar{c}}{2 V_{ref}}$). The PIV measurement conditions are shown additionally – these correspond to the pure hover case and do not directly correspond to free-flight conditions, hence the corresponding body angle of attack α_b is not known.

Prior to discussing the forces, it is interesting to consider the effective AOA and velocity resulting at the tail from the suggested modelling approach, and the variation of these values both within the flap cycle and along the tail span. The flow conditions depend solely on the proposed wake model and are not affected by the assumptions on the aerodynamic coefficients. It can be observed that the local AOA at the tail is lowered significantly by the velocity induced by the flapping wings, which leads to values within the typical linear regime of a flat plate for a significant part of the tail ($d_s \approx 20-70mm$), as highlighted in Figs. 6.18(a) and 6.19(a). This may help to explain why the tail still generates forces at AOAs that are clearly outside the range that leads to force generation on a flat plate, even though presumably a significant part of the forces is also caused by unsteady mechanisms. Additionally, this suggests that the simplified lift and drag formulations (Eqs. 6.1, 6.2) chosen may indeed be acceptable for a first approximation, despite being unable to capture all effects.

Fig. 6.18(a) shows that the cycle-averaged local velocity at the tail first increases, reaching a maximum between approximately 40mm and 60mm from the wing root (corresponding to $\sim 50-70\%$ of the tail span) and then decreases again outwards along the tail leading edge towards the tip of the tail (cf. Fig. 6.19(a)). This behaviour is in agreement with experimental studies on birds [29], and has a considerable impact on the force production. It us therefore useful for design purposes, and may help to explain the large differences observed between short and long tails of similar area or aspect ratio [48]. The effective cycle-averaged AOA behaves in a complementary way, first decreasing and then increasing. This is consistent with the variation in flapping-induced velocity: where there is less induced velocity, the AOA is closer to the AOA of the wings/body and the contribution of the free stream becomes relatively more important compared to that of the flapping. The

---

[2]Note that the reference velocity considers both the flapping and the forward motion of the body, as for instance explained in Appendix E.
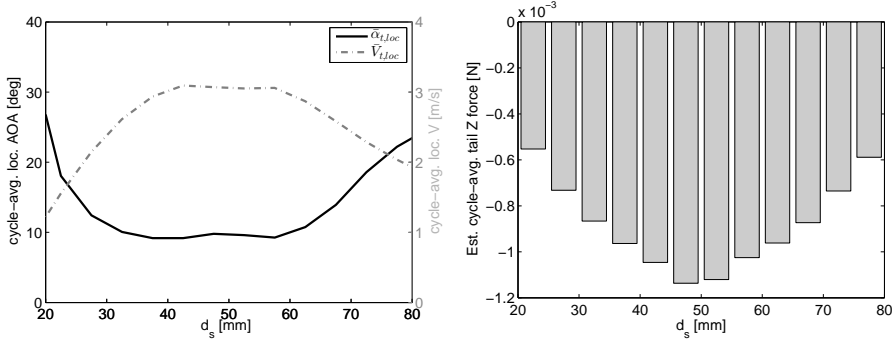
(a) Local cycle-averaged AOA and velocity along tail leading edge

(b) Local cycle-averaged Z-force at each tail blade element

Figure 6.18: Local flow conditions and Z-force on the tail at each section along the leading edge, for $V_\infty = 0.5m/s$. Note that the velocity and AOA are instantaneous variables, which take on a specific value at every spanwise position, but the resulting force is an integral along the span, hence the force at each spanwise position depends on the – in practice finite – blade element size. This explains the different subplot representations.

trends also agree somewhat with experimental measurements conducted in the near wake of bats [29].

The spanwise variation is particularly interesting in terms of design, because it already suggests that the central-outer part of the tail is more critical for force production. This for instance implies that increasing the span is highly effective up to a certain point, and then rapidly decreases in effectiveness. In turn, this may be helpful when designing the shape of a new tail and deciding how to distribute the surface area in particular. While the induced velocity is not the only important factor to consider, it does provide important hints.

At time-resolved level, a gradual phase advance can be observed in Fig. 6.19(a), with movement towards the tip. Moreover, the oscillatory component increases in the same direction (i.e., larger peaks), echoing the increased peaks particularly in w-velocity along the same direction (e.g., cf. Fig. 6.6).

With increasing forward velocity of the body, the general trends remain similar, however the peaks and troughs move closer together, leading to less variation in the time-varying component. This may be due to the smaller contribution of the free-stream velocity to the w-component at higher velocities. The mean local AOA increases at higher free-stream velocities, but not to a significant extent. While at higher forward velocities the flapping-induced velocity becomes less important compared to the free-stream velocity, hence the mean local AOA should be closer to that of the body, at the same time the body is at a lower pitch attitude to begin with, so the overall effect is partly cancelled out. By contrast, at very low forward velocities (cf. Fig. 6.19(a)), some of the local AOA values are even temporarily negative during the flap cycle, which is possible due to the w-component of the induced velocity, which varies in direction, and during the flap cycle can reach a similar magnitude to u.

Initial results for the tail forces were obtained using the proposed aerodynamic coeffi-

(a) Local angle of attack.   (b) Local lift coefficient.
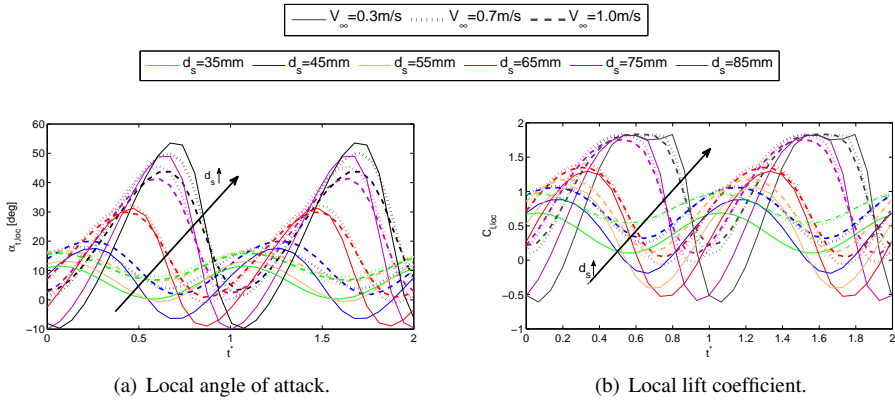
Figure 6.19: Local lift coefficient and AOA at different positions along the tail, for different free-stream velocities.

cient formulations (Eqs. 6.22–6.23). Fig. 6.19(b) shows the resulting local lift coefficients at different sections along the tail leading edge. Coefficients are shown for the three different flight conditions shown in Fig. 6.19(a), and presented in a single plot to allow for easier comparing of the impact of the free-stream velocity on the phase and amplitude of the local coefficients. It can be observed that the coefficients largely replicate the trends in the local tail AOA, with the phase advancing and the oscillatory peaks growing in amplitude at further outboard sections. The mean lift coefficients also generally increase with increasing free-stream velocity, and the trend is more evident than in the AOA. It seems that at higher velocities, the effect of the larger free stream experienced by the tail, due to the higher velocity and lower body pitch, dominates over the slight decrease in induced velocity from the wings.

The tail forces predicted by the suggested model are shown in Fig. 6.20, for two wing flap cycles. Given the approximate values chosen for the aerodynamic coefficients, at this stage the results are mainly evaluated qualitatively. As expected, the contribution in x_B direction is minor (approximately 10 times smaller than in z_B direction), and tends to zero particularly at low forward velocities, where it mainly represents parasitic drag and friction. In the case of elevator deflection – in free flight – the X force is expected to increase in magnitude (i.e., become more negative), resulting in an increment in the control moment. The contribution to the Z force is more significant. While the values are small ($\sim 0.01 - 0.03N$), it should be considered that for the present platform this would constitute up to 20% of the weight force (16g mass), and hence is not negligible. The signs are negative as expected, given that the tail would mainly produce a force upwards, i.e., in negative z_B direction. With increasing forward flight velocities, the tail produces more force, in an absolute sense, which reflects the free-stream effect. Moving outwards along the tail leading edge, the cycle-averaged tail forces largely echo the trends in the total velocity (cf. Fig. 6.18(a)), i.e., they first increase significantly, peak between 50-70% of the span, then decrease again. The most noticeable difference is that towards the tail tip, the tail force decreases more than would be expected from the induced velocity evolution: this is due to

the gradual reduction in surface area towards the tip (cf. Fig. 6.2), which results in less force being generated here. As expected, the large variation in flow conditions along the tail has a considerable impact on the force production, and the observed effect and the modelling of it may be useful for design purposes.

(a) *X*-force   (b) *Z*-force
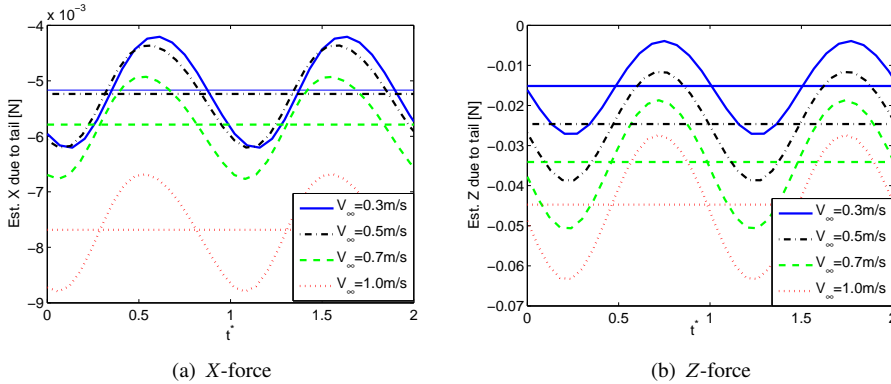
Figure 6.20: Preliminary tail force results, expressed in body frame, computed using aerodynamic coefficients from the literature. Results are shown for four different free-stream velocities. In addition to the time-resolved forces, the flap cycle-averaged forces are shown as horizontal lines.

While the values of the forces need to be validated using the actual aerodynamic coefficients of the test platform, their order of magnitude is highly plausible (e.g., based on the weight, flight behaviour and wing forces of the vehicle), and remains similar if the aerodynamic coefficients are varied within the range typically encountered in the flapping-wing literature. Additionally, the current model contains a significant amount of information that is based on real data obtained on the test platform, such as the geometry, the test conditions (based on free flight) and, especially, the wake model, which has been validated. Combined, these points suggest that the approach is promising.

On a final note, it should be remarked that the interaction between free stream and wing wake is likely to be more complex than a mere addition, as an increasing free-stream velocity may decrease the vorticity observed in the wake in hover conditions, affecting the wing wake – this will be explored in future work. Nonetheless, the proposed model includes the most significant effects and provides a first approach to characterise and quantify the role of the tail.

6.6.4. EVALUATION OF MAIN RESULTS
The proposed model represents the time-varying flow and forces on the tail, based on real data, and provides insight into how these vary, both along the span and within the flap cycle. It thus offers the possibility of predicting the flow conditions and forces produced by the tail, and their spatio-temporal variation. This, for instance, allows for accurate time-resolved modelling of the forces of the entire vehicle, if the proposed model is combined with a model of the wing aerodynamics [13]. Additionally, if the model is precise enough and suitable for the considered application, it could provide a basis for (sub-flap) control, for

instance, timing the input signals for more effectiveness, or counteracting flapping-induced oscillations.

The model is also useful for tail design studies as it shows where and when the expected forces are highest, hence where and when the tail should be most effective. This in turn can be used to shape and position the tail, and possibly the actuators. Finally, the model can provide some indication of how much effect the tail has on the stability, in terms of how much force it can generate but also more generally if the model is combined with a model of the wing aerodynamics. This gives a more flexible and still physically meaningful overall model, which is for instance at an advantage compared to black-box models that do not distinguish between the tail and wings.

In particular, the developed model remains directly applicable as long as the wings – and the flow conditions – stay the same, thus it constitutes a helpful tool for comparing different tail designs within a certain design space, once the wing design has been established. This may help to select candidates for the final configuration, or to devise different configurations for different purposes, especially before a flight-capable FWMAV exists. It must be noted that to apply the approach to other platforms (with different wings and/or tails) and varying flight conditions, it is necessary to ensure that the flow conditions and vehicle configuration are comparable to those studied here, and that similar modelling assumptions can be made. Some parts of the high-level approach may be transferable also to more widely differing vehicles, e.g., the wing wake modelling approach. As for any data-driven approach, ideally new measurements are required for an accurate result. Once the required data are available, however, the proposed model can be easily applied to different (but comparable) vehicles and extended to account for additional effects (e.g., different flapping frequencies).

The proposed model could be improved in accuracy and comprehensiveness by dispensing with some of the assumptions introduced in Sec. 6.4.2 and considering additional effects, e.g., three-dimensional effects. A more thorough investigation of the interaction between wing wake and free stream is particularly advocated. However, obtaining meaningful measurements for such an investigation is challenging (cf. Sec. 6.6.2). Moreover, while the same modelling methodology can technically be applied to measurements obtained in different flight regimes, constructing a model directly based on all of these data would lead to a significant increase in complexity and consequent decrease in applicability. It would thus be advantageous, prior to extending the model, to investigate how representative the current approach is, through further extensive experimental analysis.

The validation of the aerodynamic coefficients and resulting forces (cf. Secs. 6.6.2 and 6.6.3) was found to pose a major challenge, and this represents a limitation of the current study. As discussed in Sec. 6.6.2, a complete and realistic quantitative validation of the tail forces will require novel, more advanced experimental techniques, that allow for measurements on the full vehicle (including the wings and tail) in free-flight conditions (e.g., free-flight PIV). Future work will therefore focus on investigating such approaches, which would also be highly useful to better evaluate the tail-wake interaction itself. Using CFD approaches for comparison may also provide added confidence in the results, albeit not strictly constituting a validation. Finally, an improved physical understanding of the flow in the wake may also improve the current results.

6.7. CONCLUSION

This study proposed a modelling approach based on novel multivariate simplex splines and basic quasi-steady aerodynamic theory, to estimate the time-resolved aerodynamic forces produced by the tail of a clap-and-peel FWMAV during flight, under the influence of the wing wake. Particle image velocimetry (PIV) techniques were used to characterise the flow-field in the wake, as a function of spatial position and wing flap phase. After modelling the wake, the model output was validated by comparing the identified model to PIV data not used in the modelling process, revealing significant accuracy. The obtained wake representation was then used to compute the flow conditions at the tail, and the resulting aerodynamic forces acting on the tail, using a standard aerodynamic model and a quasi-steady assumption. It was observed that the local flow conditions on the tail are significantly altered by the presence of the flapping wings, and typically pushed closer to the linear steady regime for a significant part of the span, which may help to explain why tails on FWMAVs are so effective. The spanwise evolution of the flow conditions was found to impact the resulting force production very significantly. Based on the known mass and flight properties of the test platform, the resulting forces have a plausible order of magnitude when complemented with aerodynamic coefficients from the literature. A full quantitative validation will require further research into new experimental methods allowing for accurate time-resolved force measurements on the full vehicle in realistic free-flight conditions. Future work will hence focus on determining more accurate tail forces and validating these, thus closing the research loop. The proposed tail model represents the time-varying flow and forces on the tail based on real data, and thus provides useful insight as well as practical benefits. A combination of the resulting model with a model of the flapping wings has the potential of fully representing the studied vehicle, constituting a useful basis for development of a complete simulation framework, and supporting novel controller development. Furthermore, the developed modelling approach can be a helpful tool for basic design considerations, for instance to predict the effectiveness of a new tail or compare different tails design within the considered design range. The modelling approach can be applied to other comparable vehicles, if wing data are available and sufficient aerodynamic similarity is ensured. Qualitatively, the observations made may also apply to other comparable vehicles, with analogous clap-and-peel mechanism.

REFERENCES

[1] S. F. Armanini, J. V. Caetano, C. C. de Visser, M. D. Pavel, G. C. H. E. de Croon, and M. Mulder, *Modelling wing wake and wake-tail interaction for a flapping-wing aircraft,* International Journal of Micro Air Vehicles (2018), (submitted).

[2] M. Keennon, K. Klingebiel, H. Won, and A. Andriukov, *Development of the Nano Hummingbird: A tailless flapping wing micro air vehicle,* in *50th AIAA Aerospace Sciences Meeting* (2012).

[3] K. Ma, P. Chirarattananon, S. Fuller, and R. Wood, *Controlled flight of a biologically inspired, insect-scale robot,* Science **340**, 603 (2013).

[4] N. Gaissert, R. Mugrauer, G. Mugrauer, A. Jebens, K. Jebens, and E. M. Knubben, *Inventing a micro aerial vehicle inspired by the mechanics of dragonfly flight,* in *To-*

wards Autonomous Robotic Systems. TAROS 2013., Lecture Notes in Computer Science, Vol. 8069, edited by A. Natraj, S. Cameron, C. Melhuish, and M. Witkowski (Springer, Berlin, Heidelberg, 2014) pp. 90–100.

[5] G. C. H. E. de Croon, K. M. E. de Clercq, R. Ruijsink, B. D. W. Remes, and C. de Wagter, *Design, aerodynamics, and vision-based control of the DelFly,* International Journal of Micro Air Vehicles **1**, 71 (2009).

[6] P. Zdunich, D. Bilyk, M. MacMaster, D. Loewen, J. DeLaurier, R. Kornbluh, T. Low, S. Stanford, and D. Holeman, *Development and Testing of the Mentor Flapping-Wing Micro Air Vehicle,* Journal of Aircraft **44**, 1701 (2007).

[7] C.-K. Hsu, J. Evans, S. Vytla, and P. Huang, *Development of flapping wing micro air vehicles - design, CFD, experiment and actual flight,* in *48th AIAA Aerospace Sciences Meeting Including the New Horizons Forum and Aerospace Exposition* (2010).

[8] F. Y. Hsiao, T. M. Yang, and W. C. Lu, *Dynamics of flapping-wing MAVs: Application to the tamkang golden snitch,* Journal of Applied Science and Engineering **15**, 227 (2012).

[9] C. P. Ellington, *The Aerodynamics of Hovering Insect Flight. I. The Quasi-Steady Analysis,* Philosophical Transactions of the Royal Society B: Biological Sciences **305**, 1 (1984).

[10] S. P. Sane and M. H. Dickinson, *The aerodynamic effects of wing rotation and a revised quasi-steady model of flapping flight.* Journal of Experimental Biology **205**, 1087 (2002).

[11] G. J. Berman and Z. J. Wang, *Energy-minimizing kinematics in hovering insect flight,* Journal of Fluid Mechanics **582**, 153 (2007).

[12] T. Nakata, H. Liu, and R. J. Bomphrey, *A cfd-informed quasi-steady model of flapping-wing aerodynamics,* Journal of Fluid Mechanics **783**, 323 (2015).

[13] S. F. Armanini, J. V. Caetano, G. C. H. E. de Croon, C. C. de Visser, and M. Mulder, *Quasi-steady aerodynamic model of clap-and-fling flapping MAV and validation with free-flight data,* Bioinspiration & Biomimetics **11**, 046002 (2016).

[14] B. M. Finio, N. O. Perez-Arancibia, and R. J. Wood, *System identification and linear time-invariant modeling of an insect-sized flapping-wing micro air vehicle,* in *2011 IEEE/RSJ International Conference on Intelligent Robots and Systems (IROS)* (2011).

[15] J. Grauer, E. Ulrich, J. E. Hubbard, D. Pines, and J. S. Humbert, *Testing and System Identification of an Ornithopter in Longitudinal Flight,* Journal of Aircraft **48**, 660 (2011).

[16] J. V. Caetano, C. C. de Visser, G. C. H. E. de Croon, B. Remes, C. De Wagter, and M. Mulder, *Linear Aerodynamic Model Identification of a Flapping Wing MAV Based on Flight Test Data,* International Journal of Micro Air Vehicles (2013).

6

[17] A. N. Chand, M. Kawanishi, and T. Narikiyo, *Parameter Estimation for the Pitching Dynamics of a Flapping-Wing Flying Robot,* in *IEEE International Conference on Advanced Intelligent Mechatronics (AIM)* (2015).

[18] S. F. Armanini, C. C. de Visser, and G. C. H. E. de Croon, *Black-box LTI Modelling of Flapping-wing Micro Aerial Vehicle Dynamics,* in *AIAA Atmospheric Flight Mechanics Conference* (2015) AIAA Paper 2015-0234.

[19] S. F. Armanini, C. C. de Visser, G. C. H. E. de Croon, and M. Mulder, *Time-varying model identification of flapping-wing vehicle dynamics using flight data,* Journal of Guidance, Control, and Dynamics **39**, 526 (2016).

[20] S. Baek and R. Fearing, *Flight forces and altitude regulation of 12 gram i-bird,* in *IEEE RAS and EMBS International Conference on Biomedical Robotics and Biomechatronics (BioRob)* (2010).

[21] J. Grauer, E. Ulrich, J. H. Jr, D. Pines, and J. S. Humbert, *Model Structure Determination of an Ornithopter Aerodynamics Model from Flight Data,* in *48th AIAA Aerospace Sciences Meeting Including the New Horizons Forum and Aerospace Exposition* (2010).

[22] M. Perçin, H. Eisma, B. van Oudheusden, B. Remes, R. Ruijsink, and C. de Wagter, *Flow Visualization in the Wake of the Flapping-Wing MAV 'DelFly II' in Forward Flight,* in *AIAA Applied Aerodynamics Conference* (2012).

[23] H. Ren, Y. Wu, and P. G. Huang, *Visualization and characterization of near-wake flow fields of a flapping-wing micro air vehicle using PIV,* Journal of Visualization **16**, 75 (2012).

[24] M. Perçin, B. van Oudheusden, H. Eisma, and B. Remes, *Three-dimensional vortex wake structure of a flapping-wing micro aerial vehicle in forward flight configuration,* Experiments in Fluids **55** (2014).

[25] A. Hedenström, M. Rosén, and G. R. Spedding, *Vortex wakes generated by robins erithacus rubecula during free flight in a wind tunnel.* Journal of the Royal Society Interface **3**, 263 (2006).

[26] G. R. Spedding, *The wake of a kestrel (falco tinnunculus) in flapping flight.* Journal of Experimental Biology **127**, 59 (1987).

[27] R. J. Bomphrey, P. Henningsson, D. Michaelis, and D. Hollis, *Tomographic particle image velocimetry of desert locust wakes: instantaneous volumes combine to reveal hidden vortex elements and rapid wake deformation,* Journal of the Royal Society Interface **9**, 3378 (2012).

[28] D. L. Altshuler, M. Princevac, H. Pan, and J. Lozano, *Wake patterns of the wings and tail of hovering hummingbirds,* Experiments in Fluids **46**, 835 (2009).

6

[29] F. T. Muijres, G. R. Spedding, Y. Winter, and A. Hedenstr om, *Actuator disk model and span efficiency of flapping flight in bats based on time-resolved piv measurements,* Experiments in Fluids **51**, 511 (2011).

[30] S. Shkarayev and D. Silin, *Applications of actuator and disk theory and to membrane and flapping wings,* AIAA Journal **48** (2010).

[31] M. Perçin, *Aerodynamic Mechanisms of Flapping Flight*, Ph.D. thesis, Delft University of Technology (2015).

[32] U. Pesavento and Z. J. Wang, *Falling paper: Navier-Stokes solutions, model of fluid forces, and center of mass elevation,* Physical Review Letters **93**, 144501 (2004), the American Physical Society.

[33] A. Andersen, U. Pesavento, and Z. J. Wang, *Unsteady aerodynamics of fluttering and tumbling plates,* Journal of Fluid Mechanics **541**, 65 (2005).

[34] C. Ellington, *The aerodynamics of hovering insect flight. i. the quasi-steady analysis,* Philosophical Transactions of the Royal Society of London. B, Biological Sciences **305**, 1 (1984).

[35] B. Cheng, J. Roll, Y. Liu, D. R. Troolin, and X. Deng, *Three-dimensional vortex wake structure of flapping wings in hovering flight,* Journal of the Royal Society Interface **91** (2014).

[36] M. W. Oppenheimer, D. B. Doman, and D. O. Sigthorsson, *Dynamics and Control of a Biomimetic Vehicle Using Biased Wingbeat Forcing Functions,* Journal of Guidance, Control, and Dynamics **34**, 204 (2011).

[37] C. C. de Visser, J. A. Mulder, and Q. P. Chu, *Global nonlinear aerodynamic model identification with multivariate splines,* in *AIAA Atmospheric Flight Mechanics Conference*, AIAA Paper 2009-5726 (2009).

[38] C. C. de Visser, *Global Nonlinear Model Identification with Multivariate Splines*, Ph.D. thesis, Delft University of Technology (2011).

[39] M. Sun and J. Tang, *Unsteady aerodynamic force generation by a model fruit fly wing in flapping motion,* Journal of Experimental Biology **205**, 55 (2002).

[40] H. E. Taha, M. R. Hajj, and P. S. Beran, *State-space representation of the unsteady aerodynamics of flapping flight,* Aerospace Science and Technology **34**, 1 (2014).

[41] Z. J. Wang, *Dissecting Insect Flight,* Annual Review of Fluid Mechanics **37**, 183 (2005).

[42] M. H. Dickinson, F.-O. Lehmann, and S. P. Sane, *Wing Rotation and the Aerodynamic Basis of Insect Flight,* Science **284**, 1954 (1999).

6

[43] J. V. Caetano, M. Percin, B. W. van Oudheusden, B. D. W. Remes, C. de Wagter, G. C. H. E. de Croon, and C. C. de Visser, *Error analysis and assessment of unsteady forces acting on a flapping wing micro air vehicle: Free-flight versus wind tunnel experimental methods,* Bioinspiration & Biomimetics **10** (2015).

[44] M. Karásek, M. Percin, T. Cunis, B. W. van Oudheusden, C. D. Wagter, B. D. W. Remes, and G. C. H. E. de Croon, *First free-flight flow visualisation of a flapping-wing robot,* arXiv preprint: 1612.07645 (2017).

[45] M. Dickinson and K. G. Götz, *Unsteady aerodynamic performance of model wings at low reynolds numbers,* Journal of Experimental Biology **174**, 45 (1993).

[46] J. R. Usherwood, *The aerodynamic forces and pressure distribution of a revolving pigeon wing,* Experiments in Fluids **46**, 991 (2009).

[47] J. V. Caetano, C. C. de Visser, B. D. Remes, C. De Wagter, E.-J. Van Kampen, and M. Mulder, *Controlled Flight Maneuvers of a Flapping Wing Micro Air Vehicle: a Step Towards the Delfly II Identification,* AIAA Atmospheric Flight Mechanics Conference (2013).

[48] F. G. J. Rijks, M. Karásek, S. F. Armanini, and C. C. de Visser, *Studying the effect of the tail on the dynamics of a flapping-wing mav using free-flight data,* in *AIAA Atmospheric Flight Mechanics Conference*, AIAA Paper 2018-0524 (2018).

6

7

CONCLUSIONS

Biologically-inspired flapping-wing micro aerial vehicles (FWMAVs) are emerging as a promising new category of unmanned aerial vehicle (UAV). Thanks to their potentially remarkable performance at low Reynolds numbers, such vehicles would be extremely valuable for flight in complex, tight environments, where fixed-wing, and even rotary-wing, solutions become inadequate. The aim of this thesis was to address some of the main theoretical and practical challenges that currently prevent FWMAVs from being used beyond the research domain. In particular, the primary research question formulated in Chapter 1 was:

> **Research question**
>
> How can experimental data be used to model the complex, time-varying flight mechanics of flapping-wing micro aerial vehicles in a way that is accurate, insightful, and suitable for simulation, control and design problems?

A number of different answers to this question were put forth in the previous chapters, guided by the more specific sub-questions formulated in Chapter 1. This final chapter summarises the main results and contributions of this thesis, and presents the main conclusions drawn. The proposed models and methodologies are evaluated and compared, in terms of their respective advantages, limitations and potential applications, and the main insight obtained in the process is recapitulated. Finally, recommendations are formulated for extensions to the work in this thesis as well as further research in the field.

7.1. MAIN FINDINGS AND CONCLUSIONS

7.1.1. FLIGHT TESTING

System identification of small, unusual and under-studied flying vehicles, especially flapping-wing ones, is an active field of research where limited experience has been accumulated, and where the methods derived for conventional aircraft may not be directly applicable.

Chapter 2 investigated some of the methodologies required for system identification and experimental analysis of FWMAVs.

SENSOR FUSION

Motivated by the lack of informative high-frequency data in free-flight and manoeuvring conditions, and by the noise amplification issues associated with optical tracking [1], this thesis proposed a sensor fusion approach, merging external motion tracking and on-board inertial measurements to yield improved flight data for flapping-wing vehicles. The algorithm, presented in Chapter 2, involves extended Kalman filtering and time synchronisation, and accounts for specific details of the setup, such as the positioning of the sensors.

In addition to an improved reliability, the suggested method provides more informative free-flight data, achieving a quality shown to be comparable to that attainable in wind tunnel tests[1] and considerably improving on previous data obtained via motion tracking alone [2]. Without the hindrances introduced by tethering [1], more realistic experiments can be conducted, which can involve manoeuvring and different flight regimes, while concurrently a high level of detail is maintained. Considering manoeuvres is particularly advantageous as manoeuvrability is a key asset of FWMAVs. The more extensive insight provided into the motion and forces within each flap cycle renders the fusion approach valuable also for fundamental studies. Examples would be the analysis of the sub-flap cycle aerodynamics in realistic flight conditions, or the investigation of unsteady mechanisms that are more clearly discernible at high frequencies, e.g., clap-and-fling [3]. Compared to motion tracking data[2], significantly more detail is achieved and the noise amplification issues arising from numerical differentiation [1] are avoided. Compared to IMU data, the high noise, drift and bias issues are resolved. The filter yields more effective velocity estimates than either of the sensors separately, and allows for accurate attitude estimation even for very small vehicles, where motion tracking is affected by resolution limitations.

The methodology is considered applicable and beneficial not only for a wide range of FWMAVs, but also for non-flapping MAVs, and is furthermore expected to remain effective at smaller scales. While the Kalman gains must be tuned anew for different platforms, recommendations were made on the tuning procedure to facilitate this process and make the method more easily applicable to other vehicles. One limitation identified in the current setup was the attachment of the IMU to the body, which was found to have some effect on the measurements during large-amplitude manoeuvres, due to remaining underdamped structural vibrations. It is thus recommended to determine better ways to attach the IMU or account for such effects in the fusion process.

EXPERIMENT DESIGN

The flapping motion can significantly influence the identification process, especially when it is of a similar order of magnitude as the time-averaged body motion. It was established that the input signal used for excitation should allow for the time-averaged body motion to be distinct from the flapping-related motion. This may call for large-amplitude and/or long-duration input signals, which may infringe certain modelling assumptions, such as

---

[1]For frequencies up to five times the flapping frequency.

[2]Evidently the result depends on the specific motion tracking setup used, however the currently available systems typically have a relatively low bandwidth compared to on-board sensors.

linearity. If the focus is on the time-averaged dynamics, the flapping-related content can be filtered out of the data in the post-processing phase, as suggested in Chapter 3. This was found to yield effective identification results and preserve a sufficiently high signal-to-noise ratio in the identification data without requiring excessively large input signals. Filtering below the flapping frequency is thus preferable when linear models are used. If flapping effects are to be modelled, however, this solution is only viable if the flapping can be considered independently, e.g., as in Chapter 3. Moreover, filtering is undesirable for online identification due to the resulting time lag.

On the practical side, the restricted space typically available when flight testing FW-MAVs introduces several constraints, especially in conjunction with linear modelling approaches, which require a steady condition prior to each test manoeuvre. Reaching a steady condition is challenging for continually oscillating FWMAVs and the limited physical space implies frequent turns, which continually move the vehicle away from its equilibrium. Maximising the time during which the input signal is effective conflicts with ensuring that the initial condition is as steady as possible, hence short and small input signals were found to be preferable, which however may clash with the flapping-related limitations discussed above. Evidently, these issues become increasingly problematic at higher flight speeds, further limiting the flight conditions that can be tested. Practical constraints are therefore important to bear in mind when designing experiments.

The most suitable type of input clearly depends on the platform and especially on its actuation mechanisms. For tailed vehicles, multistep signals were found to constitute an effective compromise between adequate excitation, ease of design, implementation and execution, and compatibility with the practical boundary conditions of FWMAV testing, i.e., the aforementioned space constraints, but also potentially limited actuation mechanisms and input programming possibilities. Particularly doublet signals were found suitable due to their short duration but the nonetheless effective excitation resulting. Input signal tuning was discussed in consideration of the aforementioned challenges, providing guidelines for testing FWMAVs comparable to the DelFly.

7.1.2. GREY-BOX DYNAMIC MODELLING
The modelling approach propounded in the first part of this thesis focused on an overall system level, with the aim of modelling FWMAV dynamics based on flight data. The resulting methods and models, presented in Chapters 3 and 4, contribute to the recently emerging field of FWMAV system identification.

TIME-VARYING LOCAL MODELLING
In Chapter 3, a grey-box formulation was devised to locally model time-varying flapping-wing dynamics. The suggested modelling approach is based on time-scale separation and is novel in combining the time-averaged and time-varying dynamics in a simple way, while maintaining a high degree of realism thanks to the derivation from flight data. To implement the approach, a decomposition of the identification data into high-frequency and low-frequency components by means of filtering was introduced, which allowed for the separate time scales to be modelled separately first, and then combined in a final step.

The proposed approach was demonstrated on the DelFly, and is considered an effective solution to represent the time-varying forward flight dynamics of a range of comparable

FWMAVs based on free-flight data. The chosen linear time-invariant (LTI) model structure and the Fourier series accurately approximate the time-averaged and time-varying dynamics, respectively, within the proposed identification framework. The model is computationally light and well-suited for simulation and control work, while the explicit inclusion of flapping effects is useful for the designing and testing of on-board instrumentation or guidance and control algorithms. The formulation was also shown to be valuable as a tool for analysis, e.g., to evaluate the system dynamics in different flight conditions (Chapter 4) or for different tail designs (Appendix B). On a more immediate level, the model improves on the previously available models of the DelFly [4], being simulation-capable, accurate for both the aerodynamics and the flight dynamics, and including time-varying effects.

Time-scale separation was found to be an acceptable assumption for the DelFly, despite its flapping frequency being low compared to its body mode frequencies (the former is approximately ten times the latter, at the limit of what is considered acceptable [5]). For overall system analysis, basic simulations and controller development, the time-averaged component is deemed sufficient. Nonetheless, indications of possible interactions were identified between the time-averaged and time-varying components, particularly during manoeuvres (eg. cf. Fig. 3.13). Whether the observed effects can be traced back to data acquisition issues, or whether they are in fact caused by interactions between the flapping and the body dynamics, needs to be established more definitively. In any case, it was concluded that time-scale coupling should be investigated further for in-depth understanding of the vehicle.

GLOBAL DYNAMICS AND MODELLING

Chapter 4 addressed the problem of global modelling of flapping-wing dynamics. The aim was to develop a global modelling approach for the test platform and comparable FWMAVs, and additionally determine how and how much the dynamics of the DelFly vary across the flight envelope. A linear parameter-varying (LPV) approach was formulated for identification of the global time-averaged dynamics, starting from flight data collected in a range of different conditions, covering a significant part of the flight envelope achievable without altering the vehicle's configuration. Local LTI models were first identified from each of the collected datasets, using the approach set forth in Chapter 3; a set of scheduling functions was then determined to represent the dependency of these models on the flight condition.

The resulting global model requires few measurements and has a simple and easily interpretable structure. Across the considered domain, it achieves an only slightly lower accuracy than the set of local models it is based on, while using a considerably lower number of parameters and offering the important advantage of continuous coverage, as opposed to a set of disjoint local models. The modelling approach is suitable to represent the time-averaged dynamics of FMWAVs that can locally be modelled linearly. While the nonlinearity of the DelFly was found to be limited in the explored flight envelope, the approximately constant model accuracy up to the edges of the considered domain suggests that some degree of extrapolation may be possible. The approach itself should also be applicable to represent more significant variations as long as local linearity is preserved.

The combined analysis of the flight data, the local models and the LPV model additionally yielded further insight into the dynamic properties of the test platform, thus demonstrating the value of the models as analysis tools. Next to determining how the stability

and natural frequencies of the vehicle vary, it was also possible to distinguish more clearly between kinematic and aerodynamic effects. The main limitation identified in this study was the fact that while the observed changes in the dynamics are significant, they are small on an absolute scale. The small overall scale of FWMAV work implies that small changes can be meaningful – and experience confirms that they are noticeable when flying – but also that these changes are often close in magnitude to the modelling and data acquisition errors. Hence it can be challenging to achieve a high accuracy and reliability in modelling MAVs, and effective measurement and flight testing are essential. Improvements to the global modelling may thus be obtainable through the use of more comprehensive, informative and accurate data. Moreover, extending the model to cover different configurations is expected to be feasible and would exploit the benefits of the LPV approach more fully.

7.1.3. TIME-VARYING NONLINEAR AERODYNAMIC MODELLING

The second part of this thesis focused specifically on the short time-scale, time-varying aerodynamics, with the aim of obtaining more detailed and physically insightful models, that might be useful both in a theoretical sense, and for design problems and potentially advanced sub-flap cycle control. In view of these objectives, the wings and tail are modelled separately.

WING AERODYNAMICS

With the aim of modelling the wing aerodynamics of FWMAVs affected by wing-wing interaction, Chapter 5 extended quasi-steady aerodynamic modelling theory to account for clap-and-fling effects, hence yielding a more accurate model for the forces generated by flyers making use of such mechanisms, such as the DelFly. Additionally, vehicle-specific wing kinematics were incorporated in the model, as opposed to prescribed, ideal kinematics, and different forward flight velocities were explicitly considered.

Clap-and-fling was modelled using a semi-empirical circulatory term that acts during the first part of the flap cycle, while the upper and lower wings are interacting. This addition to the model was found to significantly affect the accuracy of the predicted lift forces, improving considerably on the performance of existing models, which were found to underestimate the lift during the clap-and-fling phase. It was therefore concluded that in flyers where clap-and-fling occurs, this effect is important to model, especially when the sub-flap cycle forces are considered. The model parameters were initially estimated from wind tunnel data in several different flight regimes. Subsequently, a function was found expressing the model parameters as a function of the considered flight regime: this resulted in a single set of parameters covering a wide range of flight regimes. While using free-flight data to estimate the model parameters would yield more realistic results, validation tests with flight data showed that the lift force model is already highly accurate, and suggested that interpolation between the test conditions is feasible. By contrast, an accurate prediction of the drag force was concluded to require free-flight data as a basis due to the effects of tethering [1].

The aerodynamic model is accurate over a range of flight conditions, computationally light and requiring few measurements. The possibility of predicting the lift force accurately in different conditions is useful for control, while at the same time the model yields insight into the aerodynamic force generation process and may be useful for design studies. Given that the estimated parameters agreed considerably with analogous parameters reported in

the literature, such a model may be helpful for preliminary analysis even before a vehicle is flight-capable. Finally, applying a quasi-steady model to the DelFly showed that such a formulation can in some cases still be applicable at relatively high reduced frequencies.

Tail aerodynamics

Chapter 6 addressed the previously unconsidered problem of estimating the time-resolved aerodynamic forces produced by the tail of an FWMAV. A modelling approach was introduced to estimate these forces, considering the effect of the flapping-wing wake, based on a combination of quasi-steady aerodynamic theory and data-driven empirical modelling. In addition to representing an approach to predict the tail forces, the modelling process yielded insight into the tail-wing wake interaction and the tail aerodynamics. The wing wake was modelled as a periodic function of spatial position and wing flap phase, with coefficients estimated from PIV measurements conducted in the wake of the wings. The resulting model was validated with additional PIV data and shown to be highly accurate. The wake model was then used to compute the wing-induced flow on the tail, which in turn was introduced in a quasi-steady aerodynamic model, and combined with the effect of the free stream, to predict the tail forces. The modelling approach was demonstrated on the DelFly, using aerodynamic coefficients from the literature.

It was shown that the flow conditions on the tail are significantly influenced by the flapping wings and brought close to the linear steady regime for a large part of the tail span, which may partly explain why FWMAV tails can be effective at very high pitch attitudes (exceeding 70°). The cycle-averaged local velocity and angle of attack at the tail have a peak and trough, respectively, at approximately ~50-70% of the tail span and, consequently, the tail forces peak at a similar location. It thus appears that the central-outer part of the tail generates comparatively more force, which for instance suggests that increasing the tail span beyond a certain width yields no significant performance improvement. While the forces must be validated using the aerodynamic coefficients of the test platform, their magnitude is plausible, with the dominant force component, i.e., the force perpendicular to the tail, being predicted to comprise up to 20% of the vehicle's weight.

The modelling approach is highly effective at representing the wing wake, which gives insight into the flow conditions at the tail, and appears promising for predicting the tail forces. The resulting model is detailed, based on experimental data, and maintains a physical link despite the empirical component. While a relatively large number of parameters are needed to represent the wake, the model is constructed out of low-order components and does not require heavy computations or extensive measurements when implemented. The approach is considered helpful for further modelling and control work and, additionally, yielded insight into the role of the tail and its interaction with the wings. The wake model could also be used to define a rough prescribed wake for similar clap-and-fling vehicles, to obtain an initial idea of the resulting tail forces.

A limitation of the current formulation is the simplified representation of the interaction between free stream and wing wake. Furthermore, the aerodynamic coefficients must be determined specifically for the test platform to validate the computed forces. Validation was found to represent a major experimental challenge, ideally requiring free-flight PIV tests. Nonetheless, a simple and functioning approach was provided to make initial evaluations and quantify the role of the tail.

7.1.4. FURTHER DISCUSSION

Following the discussion of each chapter in the previous sections, this section makes an overall appraisal of the developed models and approaches, particularly in comparison to each other. The general applicability of each model is also discussed. Note that to be fully comparable to the grey-box models developed in the first part of this thesis, the aerodynamic models developed in the second part would need to be integrated into a set of equations of motion. Given that even in the grey-box models, however, only the aerodynamics are estimated, while the dynamics are assumed a priori, a comparison is considered feasible.

MODEL COMPARISON

The grey-box model structure suggested in the first part of this thesis clearly presents considerable practical advantages, particularly when flapping effects are neglected. LTI models are computationally inexpensive, easily interpretable and readily applicable for stability analysis. A vast selection of control and analysis techniques are available for systems represented in this form. Even if time-varying effects are included in the grey-box models, their structure remains uncomplicated, as the flapping is assumed to have no influence on the body dynamics. The main drawback of the grey-box models is the limited physical insight they offer. Although the model structures are derived from physical considerations, they reduce the system to broad correlations. Nonetheless, there is some insight to be gained: as shown in Chapters 3 and 4, data-driven models are helpful to characterise the dynamics of a system and establish key physical relations, even if these cannot be explained and investigated in depth. This type of approach is a useful first step in evaluating new systems, where the physical mechanisms have not yet been fully studied, as was the case with the DelFly.

In terms of physical insight, the aerodynamic models devised in the second part of this thesis are superior. Despite involving some empirical components, they are closely related to the physics of the system and include meaningful physical details. The price for this is a somewhat higher complexity. While still computationally light, these models have more intricate structures and require more effort to be developed, interpreted, implemented and adapted to different vehicles. The physical information they incorporate makes them adaptable to some configuration changes (e.g., changes in the wing kinematics), but accounting for these changes can be complicated in practice, especially if a high accuracy is striven for, which requires conducting new experiments to re-estimate the model parameters.

The availability of suitable experimental data can generally be seen as the cardinal point upon which all the developed methods hinge. A particular complication in this regard, is the fact that some of the required data are only obtainable once a vehicle is flight-capable. This is another aspect differentiating the proposed approaches. The quasi-steady aerodynamics models mainly rely on wind tunnel tests that do not strictly require a flight-capable vehicle. In some cases, it may even be possible to make preliminary evaluations without any experiments: e.g., to obtain a rough idea of a new design it is possible to use model parameters from similar vehicles. Hence, if some accuracy is sacrificed, the models are applicable even in the design phase. By contrast, the identification models rely on free-flight testing and hence require a flight-capable vehicle. It may be possible to integrate further geometric information in the models, such that simple predictions can be made for limited configuration changes, however flight testing remains an indispensable starting point. This said, once a flight-capable FWMAV is available, the grey-box model building process is

easier and more rapid to implement and adapt, e.g., as shown in Appendix B, where the same approach is applied to model different configurations. The aerodynamic models are more challenging to develop, even without considering that they still need to be combined with dynamics equations before they can provide a full representation of the system.

Concerning applicability, it is additionally important to consider the computational cost and the measurements required to *use* the models once developed. On both fronts, all the developed models display a favourable performance, requiring light computations and relatively few measurements, with the aerodynamic models at a slight disadvantage as the required measurements, e.g., various wing angles, may be more difficult to acquire accurately. Considerations of this sort are especially important if the models are to be used online, as FWMAVs have very limited computational capacity and instrumentation on board. The former is not expected to be a problem with the suggested models, but the latter may require adaptations. Online applicability is a crucial point to consider in further work.

The preceding discussion highlights that, predictably, the most suitable model depends on the application. One important factor to consider, for instance, is the desired level of accuracy. In many cases a small improvement in accuracy comes at the cost of a significant increase in complexity, which may be unnecessary. The most accurate model is not the optimal solution for all problems. In this sense, the grey-box models are recommended for most control applications, but all the suggested models seem applicable for control system design, and possibly for use with a model-based control system. While the state-space models, based on linear aerodynamics, are easier to handle, the quasi-steady aerodynamics models potentially allow for more detail and may be usable for sub-flap cycle controllers in the future. The suggested Fourier series representation could also be used for this, but would need to be improved, e.g., to account for phase information, irregularities introduced by manoeuvres, and potential flight regime-dependent changes. The quasi-steady aerodynamics models are advocated for theoretical analysis, in-depth comparison of different platforms, and preliminary design studies. For simulations, both types of models can be used. The result may be more flexible and insightful if based on the time-resolved, quasi-steady aerodynamics models, which would allow for physical parameters to be altered and for the effects of such changes to be observed. For sub-flap modelling specifically, the quasi-steady aerodynamics models are preferable, although the Fourier series are also usable. For rapid evaluations, the basic grey-box models are sufficient. In general, when a flight-capable vehicle is available, grey-box modelling – possibly with the addition of model structure optimisation – is suggested as an effective approach to gain initial qualitative insight, particularly for new and unconventional vehicles. Finally, a combination of different modelling approaches is considered helpful for a comprehensive evaluation.

General applicability

The work presented in this thesis was implemented on a specific test vehicle, the DelFly II, however, the obtained results can to some extent be generalised and thus also represent a step ahead in the FWMAV modelling field.

The time-scale separation approach is applicable, in terms of both model structure and identification process, to any vehicle where the flapping is largely decoupled from the body motions, while the body oscillations are still of interest. The global modelling approach, including the scheduling formulation and model structure determination, can be applied to

both flapping-wing and fixed-wing MAVs, as long as local linear modelling is effective, while the flight envelope definition and choice of scheduling variables may be interesting for similar FWMAVs more specifically.

The suggested quasi-steady model, with its clap-and-fling extension, is applicable for most vehicles exhibiting significant clap-and-fling effect, especially for flexible wings ('clap-and-peel'). The inclusion of the measured wing kinematics is generalisable also to more widely differing FWMAVs. In general, the quasi-steady model is applicable to similar FW-MAVs if both the wing kinematics and the aerodynamic coefficients are known or can be estimated. Similarly, the tail modelling approach can be applied to other tailed FWMAVs, if wing wake measurements are available and aerodynamic coefficients are known or can be estimated. For this model the vehicle does not need to be flight-capable a priori. For FWMAVs similar to the DelFly, especially in terms of their wing geometry and flapping mechanism, simple qualitative evaluations may even be feasible using the current wake.

In addition to the models, also the experimental methods are expected to be applicable to a range of other vehicles. The data fusion framework is considered a helpful tool in FWMAV and MAV research. It can be useful to study other vehicles with similar instrumentation, including non-flapping ones, which may benefit from, e.g., effective velocity estimation, reduction of noise amplification issues and avoidance of resolution problems. Similarly, some of the recommendations made for flight testing apply to MAVs in general.

7.2. Main contributions

Following the above discussion, this section summarises the main contributions made in this thesis. The resulting publications were mentioned in the corresponding chapters and are listed fully in an annex to this thesis.

- Fusion of on-board and off-board sensor measurements for a FWMAV, allowing for reconstruction of high-fidelity and high-resolution states and forces (Chapter 2).

- Development of system identification, flight testing, input design and data processing methods and recommendations for FWMAVs (Chapters 2, 3).

- Accurate, low-order grey-box model identification of flapping-wing dynamics using free-flight data, yielding models amenable for simulation and controller synthesis (Chapter 3).

- Inclusion of time-varying flapping effects in low-order state-space flapping-wing dynamics models using a time-scale separation-based system identification approach (Chapter 3).

- Analysis of the dynamic properties of a FWMAV in different flight regimes using data-derived models (Chapter 4).

- Application of an LPV identification approach for global modelling of unconventional flapping-wing vehicle dynamics (Chapter 4).

- Extension of existing quasi-steady flapping-wing aerodynamics modelling approaches to include: clap-and-fling, real wing kinematics and different flight conditions (Chapter 5).

- Analysis and modelling of the flapping-wing wake based on experimental data (Chapter 6).

- Modelling of the time-varying tail aerodynamics of a tailed FWMAV, considering the effect of the wing wake (Chapter 6).

As discussed in Sec. 7.1.4, while the models and methods developed in this thesis were implemented on the DelFly II, they are to some extent expected to be applicable to other FWMAVs and the aim was to generalise as much as possible. At the same time, however, the computed models represent a useful contribution to support further work on the DelFly specifically. In particular, the following models were obtained, that were not previously available: (i) an accurate and simulation-capable model of the dynamics, explicitly including time-varying effects; (ii) an initial global dynamic model; (iii) a quasi-steady model of the wing aerodynamics, including clap-and-peel effect and covering different flight regimes; (iv) a time-varying model of the tail aerodynamics.

7.3. RECOMMENDATIONS FOR FUTURE WORK

This thesis provides answers to the research questions posed in Chapter 1 and addresses some of the challenges in the FWMAV modelling field, however the results obtained also open up new questions and can be extended and improved. Some of the main recommendations are summarised in this section.

FLIGHT TESTING AND EXPERIMENTAL CHALLENGES

Flight testing was found to be a significant challenge, with many of the practical problems encountered either leading to additional modelling requirements, or deriving from pre-existent modelling requirements. Regarding data acquisition, the attachment of the IMU to the body was found to have some influence on the sensor fusion results. Extensive calibration tests should therefore be performed to better evaluate this effect and counter it, e.g., by finding an alternative method to attach the IMU, minimising the aforementioned effects, or by modelling these effects and accounting for them in the sensor data.

Another challenge is the typically limited space available when flight testing FWMAVs, which is especially relevant when considering fast forward flight regimes. Investigating and modelling a more extensive flight envelope is for instance heavily reliant on the possibility of collecting data at higher velocities. When insufficient space is available, it may be possible to resort to free-flight testing in the wind tunnel [6], or, alternatively, to conduct outdoor tests using exclusively on-board measurements, which however would require new online sensor fusion approaches to be developed. Both options should be explored to allow for more complete models to be developed and validated.

Further experimental challenges were encountered when modelling the aerodynamics in more detail (Part II of the thesis). Two overarching issues here are the limitations entailed by tethering and the small magnitude of the measured quantities. The difference between free-flight and tethered testing, and the impossibility of considering manoeuvres in the latter type of setup, ideally calls for free-flight testing. However, in free flight it is very difficult to achieve the same level of detail and accuracy as when tethering, as the test environment is less controlled and the forces – which are very small – are not directly measured. Furthermore, free flight only allows for measurements to be made on the full vehicle, which

for instance does not allow for the wings and tail to be separated. Hence, further effort should be expended in finding suitable experimental processes for aerodynamic modelling, depending on the specific requirements. The proposed sensor fusion may allow for some additional tests to be conducted in free flight. Additionally, it would be opportune to consider alternative options, e.g. free-flight wind tunnel tests or a systematic combination of tethered and free-flight tests. This issue is discussed further subsequently in this section, when discussing the aerodynamic modelling specifically.

DYNAMIC MODELLING

The dynamic modelling approach can be enhanced, both as a general method and in its application to the test platform. Aspects to consider include: improving the accuracy and level of detail, extending the flight envelope and enhancing the applicability of the models.

In terms of accuracy, some model components are still lacking, especially the lateral dynamics, which are challenging to model in FWMAVs, like the DelFly, where the roll and yaw axes are tightly coupled and cannot be excited independently. On the practical side, it is recommended to invest more work on input design, e.g., exploiting optimal input design methods [7, 8] to ensure adequate excitation. Alternative model structures may likewise lead to improvements in less well-estimated components, and may furthermore become indispensable if more complex parts of the dynamics are considered (roll-yaw coupling, body-flapping coupling, extreme manoeuvres, etc.). Including some of the effects currently neglected, such as the aforementioned ones, may also itself increase the accuracy. The effect of flapping frequency variation would be particularly useful to consider as it constitutes a link between the time-averaged body dynamics and the flapping dynamics.

In terms of coverage, it would be useful to consider more extreme flight conditions (fast forward flight, hover) and more aggressive manoeuvres (steep turns, dives, etc.), and to assess to what extent these can be represented by the suggested LPV model. Current results suggest that, for the considered test platform and flight domain, a more advanced model identification approach, e.g., using neural networks [9] or splines [10], is not necessary, however this may no longer be the case if more extreme conditions and manoeuvres are considered. Aggressive manoeuvres are not widely studied in the FWMAV modelling literature, and, given that manoeuvrability and versatility are crucial advantages of flapping-wing flyers, this aspect calls for further investigation. Extending the model coverage will in turn require more extensive flight testing and, hence, tackling practical challenges such as limited testing space (cf. previous subsection)

Further, it would be desirable for the developed model to be somewhat adaptable. FWMAVs are mostly constructed manually, hence different specimens of the same vehicle are never identical and unintended changes can often even occur between separate flights, e.g., following reparation work. Moreover some vehicles, such as the DelFly, can only achieve their full flight envelope with different configurations, e.g., by actively varying the centre of gravity (CG) position [11]. Accounting for CG shifts, or other common and measurable variations in configuration – e.g., using an LPV approach with configuration-specific parameters as additional scheduling variables – would yield a more generalisable model, as well as allow for a wider flight envelope coverage for the DelFly specifically.

Based on the model identification results, it is also recommended that coupling effects between body and flapping dynamics should be further investigated, for the DelFly and

any platform where the flapping frequency is of a similar order of magnitude as the natural body mode frequencies. The regime of low flapping frequencies, where the body and flapping dynamics interact, has not yet been widely explored in the FWMAV literature. While challenging to model, due to its high complexity, it may also bring advantages of its own.

AERODYNAMIC MODELLING

On the aerodynamic modelling side, the current results successfully demonstrate new approaches, however the models should be more fully validated and refined. The wing model could be enhanced by considering additional effects, including wing flexibility and the wing 'clap' effect, which is less dominant than the 'fling' in the DelFly, but not necessarily negligible. It would also be of interest to evaluate different wing geometries and kinematics. Embedding further geometric parameters in the model structure would for instance support design studies and make the model easier to adapt to different platforms. In terms of validation, further comparison of the model with free-flight data would be desirable to better evaluate its performance. The suggested sensor fusion algorithm (Chapter 2) may even allow for the model parameters to be estimated from free-flight data, which may yield a more realistic outcome and potentially allow for consideration of manoeuvring flight. Free-flight estimation data may also allow for more effective modelling of the drag, which cannot be measured realistically in wind tunnel experiments. However, free-flight testing would require explicitly considering the tail: this may be feasible using the developed tail model (Chapter 6), but would first require further assessing and validating the said model.

The tail aerodynamic model requires further validation before it can be fully exploited. As discussed in Chapter 6, validating the tail forces is not trivial from an experimental point of view. Obtaining suitable data ideally requires conducting tests with the tail placed in the unsteady wing wake. In the wind tunnel, measuring on the full, flapping vehicle is problematic due to the flapping-induced vibrations of the vehicle, which lead to unrealistic force measurements. Separately measuring the tail forces is also challenging because these forces appear to be close to the typical sensor resolutions. A possible solution may be free-flight PIV testing [6], allowing for realistic measurements but requiring high-precision control to be implemented accurately. It may also be possible to cut the fuselage and clamp the wings and tail separately, to reduce the effect of vibrations and allow for separate force measurements; or to generate a prescribed time-varying flow around the self-standing tail, e.g., based on the current wing wake model. The tail model would also benefit from further exploration of the interaction between free stream and wing wake. PIV measurements in forward flight conditions would help to evaluate to what extent the suggested modelling approach is effective. Such data could also be used to derive wake models at different velocities, using the same method as in Chapter 6, and combine these into a single free stream-dependent wake model. For the reasons mentioned previously, however, obtaining adequate data for these evaluations is likewise challenging, and hence further research on the experimental side is especially recommended.

Combining the aerodynamic models of wings and tail would yield a complete and detailed model of the vehicle's aerodynamics. Extending this model to include the effects of control inputs, and combining it with a suitable formulation for the body dynamics, would in turn yield a full *dynamic* model of the system, significantly more physically meaningful than the grey-box models proposed alternatively. The explicit separation of the wings

and tail may also yield new insight into the vehicle's flight properties and provide ideas for improved simplified grey-box model structures where the effect of the tail can be isolated.

OUTLOOK: APPLICATIONS

Ultimately, models are tools – an important next step in this research will hence be the application of the developed models. Preliminary examples were given in this thesis, where the LTI models are applied to analyse a system that is not fully known (Chapter 4) and to guide a design study (Appendix B). The phenomenological aerodynamic models could be used in a similar way, but before a flight-capable vehicle is available. One use of the models would therefore be to analyse new vehicles or configurations, which for instance may support the design of improved configurations. Additionally, it is now possible to explore more advanced control options (e.g., as shown in Ref. [12]) and to develop full simulation environments. In particular, the models pave the way for new control possibilities specific to flapping-wing flight. Knowing the temporal variation of the tail forces, it may for instance be possible to time the control surface deflections in a targeted manner, e.g., so as to improve their effectiveness or minimise oscillations of the body. Analogously, the time-varying wing forces could be exploited, particularly on FWMAVs that are controlled mainly through the wings, e.g., tailless platforms. Systematically exploiting the time-varying effects would be a further step towards emulating the flight performance of insects and birds, opening up many novel and exciting opportunities.

REFERENCES

[1] J. V. Caetano, M. Percin, B. W. van Oudheusden, B. D. W. Remes, C. de Wagter, G. C. H. E. de Croon, and C. C. de Visser, *Error analysis and assessment of unsteady forces acting on a flapping wing micro air vehicle: Free-flight versus wind tunnel experimental methods,* Bioinspiration & Biomimetics **10** (2015).

[2] J. V. Caetano, C. C. de Visser, B. D. Remes, C. De Wagter, E.-J. Van Kampen, and M. Mulder, *Controlled Flight Maneuvers of a Flapping Wing Micro Air Vehicle: a Step Towards the Delfly II Identification,* AIAA Atmospheric Flight Mechanics Conference (2013).

[3] S. F. Armanini, J. V. Caetano, G. C. H. E. de Croon, C. C. de Visser, and M. Mulder, *Quasi-steady aerodynamic model of clap-and-fling flapping MAV and validation with free-flight data,* Bioinspiration & Biomimetics **11**, 046002 (2016).

[4] J. V. Caetano, C. C. de Visser, G. C. H. E. de Croon, B. Remes, C. De Wagter, and M. Mulder, *Linear Aerodynamic Model Identification of a Flapping Wing MAV Based on Flight Test Data,* International Journal of Micro Air Vehicles (2013).

[5] G. K. Taylor and A. L. R. Thomas, *Dynamic flight stability in the desert locust Schistocerca gregaria,* Journal of Experimental Biology **206**, 2803 (2003).

[6] T. Cunis, M. Karásek, and G. C. H. E. de Croon, *Precision Position Control of the DelFly II Flapping-wing Micro Air Vehicle in a Wind-tunnel,* in *International Micro Air Vehicle Conference and Competition (IMAV)* (2016).

[7] E. Morelli, *Flight test validation of optimal input design and comparison to conventional inputs,* in *AIAA Atmospheric Flight Mechanics Conference* (1997).

[8] R. K. Mehra, *Optimal inputs for linear system identification,* IEEE Trans. Autom. Control **19**, 192 (1974).

[9] J. Sjöberg, H. Hjalmarsson, and L. Ljung, *Neural networks in system identification,* IFAC Proceedings Volumes **27**, 359 (1994).

[10] C. C. de Visser, *Global Nonlinear Model Identification with Multivariate Splines*, Ph.D. thesis, Delft University of Technology (2011).

[11] J. A. Koopmans, S. Tijmons, C. de Wagter, and G. C. H. E. de Croon, *Passively stable flapping flight from hover to fast forward through shift in wing position,* in *International Micro Air Vehicles Conference* (2015).

[12] M. W. Goedhart, E.-J. van Kampen, S. F. Armanini, C. C. de Visser, and Q. P. Chu, *Machine learning for flapping wing flight control,* in *AIAA Intelligent Systems Conference*, AIAA Paper 2018-2135 (2018).

7

A

COMPARISON OF QUASI-STEADY AND BLACK-BOX AERODYNAMIC MODELS

This appendix compares two different models to describe the time-resolved aerodynamics of a clap-and-fling flapping-wing micro aerial vehicle (the DelFly II), with an outlook on control. The first model is a quasi-steady model based on blade element theory, and constitutes a precursor to the model developed in Chapter 5, which does not yet consider clap-and-fling. The second model is a black-box model based on Fourier series expansion, analogous to the time-varying component of the model proposed in Chapter 3. The unknown parameters in the models are computed from wind tunnel force data using maximum likelihood estimation. The advantages and limitations of each model are discussed, including their ability to represent transient effects such as clap-and-fling. Additionally, the changes in sub-flap aerodynamics with different steady flight conditions are evaluated, and the possibilities of developing a global flight envelope model with the suggested approaches are investigated.

A

A.1. INTRODUCTION

For purposes of model-based control, aerodynamic models of FWMAVs should be simple and computationally efficient, while nonetheless capturing a significant part of the aerodynamic behaviour. For this reason, quasi-steady formulations have found a wide application [2–7]. However, while quasi-steady models are fairly computationally efficient and interpretable, one of their limiting aspects is their incapability to represent unsteady flap cycle-resolved aerodynamics, such as clap-and-fling (cf. Chapter 1, Sec. 1.2.3). In the platform studied in this thesis, the DelFly II [8], clap-and-fling is significant due to the biplane configuration of the wings, and is indeed one of the most dominant unsteady effects observed in flight and in experiment [9]. An alternative to the quasi-steady approach that allows for equally – and potentially more – computationally light models is system identification used in conjunction with experimental data [10–12]. This approach typically involves either partially physical (grey-box) or black-box model structures, and has the advantage that the resulting models are relatively easy to adapt to a specific platform if data are obtainable. However this also limits the possibilities of using such models in a more general approach, given their connection with the specific ornithopter and specific flight regime used for identification.

This appendix compares two different approaches to model the sub-flap evolution of the aerodynamic forces generated by a clap-and-fling FWMAV (the DelFly II). The first approach involves quasi-steady modelling, based on the work of Berman and Wang [7] and adapted to the current FWMAV by considering the four wings and real wing kinematics [13]. The resulting model is a precursor of the model developed in Chapter 5: the most important differences are that the model developed here does not account for clap-and-fling and does not consider the forward velocity of the vehicle. The second model is a purely data-driven black-box model based on a Fourier series expansion [12], analogous to the approach used in Chapter 3 to represent the time-varying component. The unknown parameters of both models are identified using the forces generated by the FWMAV, as determined from wind tunnel measurements. The models are evaluated separately in comparison with experimental data, as well as compared to each other, with the goal of assessing the advantages of each for global modelling and possible applications. I that although both models are preliminary and/or simplified versions of the models developed in the main body of this thesis, many of the observations made in comparing them apply equally to the more advanced models developed in this thesis.

This appendix is structured as follows. Section A.2 concisely describes the test platform and the experimental data used in this study. Section A.3 outlines the two modelling approaches applied and the parameter estimation method used to obtain the parameters within each model. Section A.4 presents the results obtained and evaluates and compares the two models, and Section A.5 concludes with final remarks.

A.2. EXPERIMENTAL SETUP

The platform used in this study was described in Chapter 1 (Sec. 1.4.1). The coordinate frame used and properties of the specific vehicle used were shown and described in Chapter 5 (Sec. 5.3.1). The experimental data were obtained from wind tunnel tests, described extensively in Chapter 5.

A.3. AERODYNAMIC MODELS

This section presents the two different aerodynamic modelling approaches, and the parameter estimation method used to determine the model parameters.

A.3.1. QUASI-STEADY AERODYNAMIC MODEL

The forces acting on each flapping wing are modelled based on the quasi-2D force model of Caetano et al.[13]. This model builds on the model initially devised by Pesavento and Wang [6], and extended by Berman and Wang [7], who combined it with blade element theory and applied it to a flapping wing with three degrees of freedom. The model was further adapted to use real wing kinematics and to be applicable to a four-winged FWMAV [13]. The resulting equations are,

$$dF_{x_w} = [(\frac{c(r)}{\bar{c}R} M_{wing} + m_{22}) v_{z_w} \dot{\theta} - \rho_f \Gamma v_{z_w} - m_{11} a_{x_w}] dr - dF_x^v \tag{A.1}$$

$$dF_{z_w} = [-(\frac{c(r)}{\bar{c}R} M_{wing} + m_{11}) v_{x_w} \dot{\theta} + \rho_f \Gamma v_{x_w} - m_{22} a_{z_w}] dr - dF_z^v \tag{A.2}$$

$$\Gamma = \frac{1}{2} C_T c(r) |V| \sin 2\alpha + \frac{1}{2} C_R c^2(r) \dot{\theta} \tag{A.3}$$

$$\mathbf{F}^v = \frac{1}{2} \rho_f c(r) [C_{D_0} \cos^2 \alpha + C_{D_{\frac{\pi}{2}}} \sin^2 \alpha] |V| (v_{x_w}, v_{z_w}) dr \tag{A.4}$$

$$m_{11} = \frac{1}{4} \pi \rho_f b^2, \quad m_{22} = \frac{1}{4} \pi \rho_f c^2(r) \tag{A.5}$$

$$v_{x_w} = r_i \dot{\zeta} \cos \theta_w \quad , \quad v_{z_w} = -r_i \dot{\zeta} \sin \theta_w - dc \dot{\theta_w} \tag{A.6}$$

Eqs. A.1 and A.2 represent the total force acting on a single wing along the $\mathbf{x}_W$ and $\mathbf{z}_W$ axis (cf. Fig. 5.11 in Chapter 5), respectively, for each blade element. Eq. 5.2 represents the circulatory components of the forces, including translational (C_T) and rotational (C_R) circulation. Eq. A.4 represents the viscous forces, which are affected by the drag coefficients for zero (C_{D_0}) and 90°($C_{D_{\frac{\pi}{2}}}$) angle of attack of the wing. The centripetal forces and added mass effect are represented by the first and penultimate term in Eqs. A.1 and A.2, respectively.

Eq. A.6 defines the relative velocities on the wings. Here the location of the wing rotation axis, d, determines the impact of the passive wing rotation on the relative velocity perceived by the wings. It must be noted that the model discussed here does not consider the forward velocity of the FWMAV. This is because the primary goal was to consider models that can be applied for control, thus ideally on board. Given that at present on-board velocity measurements are not available on the considered platform, nor indeed on most FWMAVs, the forward velocity component was neglected. In this regard it should also be considered that the contribution of the forward velocity is small compared to the very high velocities related to the flapping motion.

The total forces acting on the wing are computed by integrating the forces on each blade element along the wing span, considering the wing shape and real flapping kinematics. Further details on the underlying model can be found in Ref. [13] and in Chapter 5, which presents an extension of the model developed here.

Most of the parameters in the above equations were obtained from the wing kinematics [14]. The remaining parameters, viz. $C_T, C_R, C_{D_0}, C_{D_{\frac{\pi}{2}}}$ and d, were estimated from the force data, as explained in Sec. A.3.3.

A.3.2. FOURIER SERIES

As an alternative to the previously presented quasi-steady aerodynamic model, a black-box model was developed, according to the approach taken in Ref. [12] (Chapter 3). This model was considered to provide a useful comparison for the physically-derived model presented in the previous section, but also an alternative practical solution in its own right. Whilst physical meaning is desirable, for many applications an accurate model of any sort is useful.

As evident from experimental data (Fig. 5.7(b)), the flapping motion of the wings leads to highly periodic sub-flap cycle aerodynamic force evolution, particularly in the X component. Hence a trigonometric Fourier series expansion can be considered a suitable model structure to represent the X force over the flap cycle, i.e.,

$$X(t) = a_0 + \sum_{n=1}^{h} \left(a_n \sin\left(2\pi n f t\right)\right) + \sum_{n=1}^{h} \left(b_n \cos\left(2\pi n f t\right)\right), \tag{A.7}$$

where h is the number of harmonics in the model, f is the fundamental frequency, which is chosen to be equal to the flapping frequency, t is time, and a_n and b_n are the nth Fourier coefficients. Only one constant term, a_0, is left in the series to avoid redundant parameters. This term represents the average of the forces. An analogous approach was found previously [12] to be suitable to model the flapping-related component in free-flight data at a typical flight condition, and was therefore considered likely to be effective also for other flight regimes.

In view of the structure of Fourier series, it is logical to select a Fourier series containing the same number of harmonics as are left in the estimation data after filtering. Hence the driving factor in selecting the number of harmonics for the model was the choice of filter cutoff for the estimation data.

Fourier series up to the third and fifth harmonic h were initially investigated. Filtering out frequency content above the third harmonic still allows for the main component of the force evolution to be seen, therefore establishing a model for the first three harmonics is already useful. An additional advantage is that the first three harmonics are also clearly recognizable in free-flight data, which allows for models to also be identified and validated with flight data.

On the other hand, filtering above the fifth harmonic allows for the clap-and-fling effect to be captured more thoroughly, and generally permits a higher accuracy. This comes at the cost of a larger number of parameters, however the resulting structure is still manageable and computationally simple. Furthermore, given that the parameters have no physical significance, a larger number of these is not as crucial an issue as it would be in a physical model, in terms of interpretation of the model. Hence, in the final instance, a fifth order model was selected.

The final model structure depends only on the flapping frequency, which can be measured in flight. The flapping frequency ensures that the Fourier series periods correspond to the flap cycles, and this is the only physical information flowing into the model. This implies that the model is easy to apply, but lacks adaptability. One reason for this formulation

was the observation that in non-manoeuvring flight the sub-flap time-progression of the X force does not appear to vary significantly with different conditions. Thus, an additional goal was to investigate for what range of different steady flight conditions the X force can be represented by the same model.

A.3.3. PARAMETER ESTIMATION

The unknown parameters in the previously presented model structures (cf. Eqs. A.1–A.7) were estimated using a maximum likelihood (ML) estimator. The estimation process has been described, and applied to similar model types, in Chapters 3 and 5 – an analogous procedure was used in this study. Initial guesses for the parameters were based on literature values for the quasi-steady aerodynamic models [5, 7] (Table A.1), and obtained using linear regression for the Fourier series models.

The output equations can be directly inferred from the aerodynamic models in Secs. A.3.1 and A.3.2. In fact, although the evolution of the aerodynamic forces is a dynamic process, given that measurements of all required variables were obtainable, there was no need to include any dynamics in the estimation process. Rather, the output is a direct function of the input, and can be directly computed from the measurements at each time step.

The output z for both models is the aerodynamic force X, which is in each case a function of a different set of parameters and measurements. In the Fourier series models, the parameters to be estimated are the Fourier coefficients in Eq. A.7, i.e.

$$\Theta_{Fourier} = \begin{bmatrix} a_0 \ a_1 \ \dots \ a_5 \ b_1 \ b_2 \ \dots b_5 \end{bmatrix}, \tag{A.8}$$

These parameters bear no physical meaning, and simply yield a mathematical description of the output. The required inputs are the flapping frequency, constant over the cycle for the wind tunnel tests, and the non-dimensional cycle time t^*. The output equation is given by Eq. A.7.

In the quasi-steady model the parameters to be estimated are [13],

$$\Theta_{QS} = \begin{bmatrix} C_T \ C_R \ d \end{bmatrix}. \tag{A.9}$$

Initially two additional parameters, C_{D_0} and $C_{D_{\frac{\pi}{2}}}$ were also estimated. However, while the model-predicted output was fairly accurate, implausible values were estimated for these two parameters, and it was therefore decided to fix them at literature-based values, and only estimate the parameters given in A.9, to maintain as physically realistic a result as possible. A likely reason is that $C_{D_{\frac{\pi}{2}}}$ has no significant effect on the X force component and therefore cannot be identified effectively from X force data, while C_{D0} is typically very close to zero and hence difficult to estimate with accuracy.

The physical meaning of the parameters has been discussed in Sec. A.3.1, and the output equation is obtained from Eqs. A.1 and A.2. Note that the equations are given for a single blade element, therefore obtaining the actual output requires integrating the forces over the full span. For this model, the required measurements are the flap angle and its derivative, the wing pitch angle and its first and second derivatives, and the flapping frequency. All of these measurements were obtainable from the wind tunnel experiments.

A

Table A.1: Initial guesses for the parameters in the quasi-steady model, based on values in the literature[5, 7]. In the final model, the parameters C_{D0} and $C_{D\frac{\pi}{2}}$ were fixed at the values given in the table; the remaining parameters were estimated.

Parameter	Initial value before estimation
C_T	1
C_R	1.6
d	0.2
C_{D_0}	0.05
$C_{D_{\frac{\pi}{2}}}$	0.2

Table A.2: Statistical evaluation of computed models, compared to estimation data.

Test #	Quasi-steady model			Fourier-series model		
	RMSE[N]	R^2	Corr.	RMSE[N]	R^2	Corr.
1	0.022	0.478	0.740	0.005	0.998	0.999
2	0.018	0.515	0.768	0.003	0.997	0.999
3	0.017	0.608	0.819	0.003	0.999	1.000
4	0.017	0.614	0.821	0.006	0.997	0.998
5	0.016	0.585	0.798	0.007	0.996	0.998
6	0.017	0.548	0.797	0.037	0.921	0.960
7	0.014	0.563	0.787	0.005	0.998	0.999
8	0.010	0.519	0.752	0.004	0.999	0.999

A.4. RESULTS AND DISCUSSION

The two models were evaluated in terms of their effectiveness in representing the measured data, in statistical terms, and, in the case of the physically-derived model, in terms of the obtained parameter values. In the interest of clarity, only four test cases are shown, viz. the same ones as discussed earlier. They differ in flapping frequency as well as in flow velocity and angle of attack. Results show the total force generated by all four wings.

Fig. A.1 shows the model-predicted X force for each test case, in comparison with the corresponding wind tunnel measurements. Measurements filtered at 40Hz and at 67Hz are shown, to underline different effects, and both the quasi-steady and the Fourier series models are presented on the same plots, to facilitate their comparison. The corresponding statistical metrics (root mean square error, RMSE, coefficient of determination, R2, and correlation coefficient) quantifying the performance of each model are presented in Table A.2, whilst the parameter estimates can be found in Tables A.3 and A.4.

Both models are capable of capturing the main component of the force evolution, albeit to a different extent. The quasi-steady model is fairly effective at replicating the lower-frequency content in the measurements, in all test cases. The model-predicted values display an adequate agreement with the measurements in terms of phase, amplitude and average, and the overall shape of the force evolution is captured well, with the second peak

A

(a) Test condition # 1

(b) Test condition # 4

(c) Test condition # 7

(d) Test condition # 8
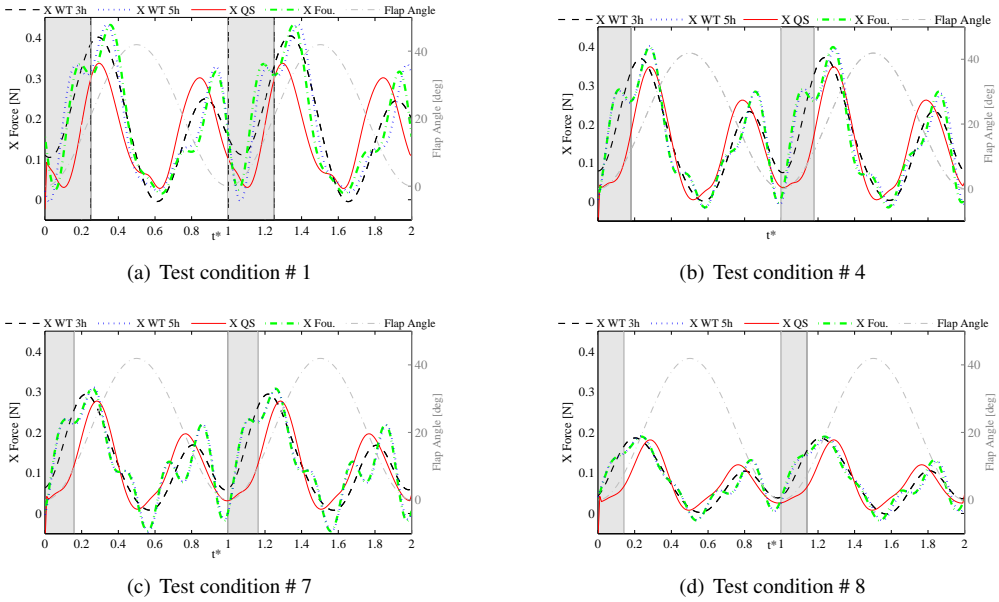
Figure A.1: Wind tunnel (WT) X-force measurements versus X forces predicted by quasi-steady (QS) and Fourier series (Fou.) models, for test cases #1, #4, #7, #8. Wind tunnel measurements are shown with filtering after the 3rd harmonic (3h) and after the 5th harmonic (5h).

Table A.3: Parameters estimated from each set of estimation data, for the quasi-steady model.

Param.	Test #1	Test #2	Test #3	Test #4	Test #5	Test #6	Test #7	Test #8	Avg.	Std.
C_T	3.033	2.703	3.330	3.471	3.090	2.556	2.560	2.020	2.795	0.497
C_R	0.683	0.050	0.165	0.112	-0.145	0.221	-0.042	-0.172	0.109	0.287
d	0.255	0.317	0.358	0.354	0.369	0.291	0.352	0.412	0.333	0.047

Table A.4: Parameters estimated from each set of estimation data, for the Fourier series model.

Param.	Test #1	Test #2	Test #3	Test #4	Test #5	Test #6	Test #7	Test #8	Avg.	Std.
a_0	0.130	0.083	0.145	0.165	0.172	0.191	0.161	0.161	0.151	0.033
a_1	0.071	0.046	0.070	0.084	0.097	0.116	0.088	0.083	0.082	0.021
b_1	0.039	0.030	0.053	0.054	0.038	0.013	0.047	0.050	0.040	0.014
a_2	-0.008	0.000	-0.007	-0.032	-0.024	-0.105	-0.008	-0.039	-0.028	0.034
b_2	-0.085	-0.053	-0.107	-0.107	-0.092	-0.045	-0.100	-0.100	-0.086	0.024
a_3	0.002	0.005	0.003	-0.007	-0.005	-0.027	-0.006	-0.012	-0.006	0.010
b_3	-0.024	-0.014	-0.033	-0.031	-0.013	0.009	-0.028	-0.032	-0.021	0.014
a_4	0.003	0.009	0.016	0.032	0.001	-0.046	0.006	0.022	0.005	0.023
b_4	-0.023	-0.011	-0.008	-0.020	-0.042	-0.023	-0.032	-0.027	-0.023	0.011
a_5	0.046	0.022	0.038	0.023	0.015	-0.048	0.022	0.010	0.016	0.028
b_5	-0.030	0.003	-0.014	-0.049	-0.051	0.010	-0.036	-0.041	-0.026	0.023

A

in each cycle being lower than the first. Particularly in comparison with the more heavily filtered (40Hz cutoff) data, where unsteady effects are less clearly visible, there is a good agreement.

Nonetheless, the force evolution is not fully replicated. In particular, given that unsteady effects are not inherently accounted for in the model, the clap-and-fling effect cannot be fully and accurately represented. The clap-and-fling effect can be visualised in the data filtered at the 5th harmonic, where it leads to an additional force peak at the start of the flap cycle (grey area in the plots). Comparing this to the model, it is clear that the model only captures the peak occurring *after* the clap-and-fling peak. In the more heavily filtered data, the clap-and-fling peak is no longer visible, however its effect is evident in the phase shifting and increased amplitude of the first force peak, which incorporates the first two peaks of the less filtered (67Hz cutoff) data. Thus, whilst the force evolution in the more filtered data has the same shape as in the model, and the amplitudes of the corresponding peaks are comparable, in the model the first peak of each cycle is phase shifted due to the neglecting of clap-and-fling.

In spite of this shortcoming, which is a consequence of the model definition and was thus expected, the performance of the model can be considered satisfactory, with output correlations up to 0.8 and R^2 values up to 0.6 (Table A.2). The adequate performance is particularly noteworthy in view of the small number of estimated parameters, which suggests that the underlying model structure is suitable. The estimation of platform-specific aerodynamic parameters rather than their theoretical derivation or literature-based calculation, ensures closeness to the real system and extracts an optimal solution from the chosen model structure.

The parameter values are plausible for C_T and d, however C_R estimates are small compared to typical literature values [5], and clearly correlated to the forward flight velocity and flapping frequency. The anomalous C_R values are likely a consequence of the neglected wing-wing interaction in the model, which the C_R coefficient appears to compensate for. This suggests a more physically realistic result would be obtained by adding a separate term to the model to account for wing-wing interaction, nonetheless the current solution yields a functional model, useful for the intended purpose. It should also be considered that the effect of forward flight velocity was neglected, as explained in Sec. A.3.1, so the parameters to some extent may be compensating also for this.

The Fourier series-based models can achieve a significantly higher accuracy than the quasi-steady models, for all test conditions considered here. For these models, the agreement between estimated and measured forces is remarkable, with the former almost perfectly replicating the latter. This behaviour is highlighted by the corresponding metrics: the residual errors are extremely low, approximately one order of magnitude smaller than in the quasi-steady case, whilst the output correlation coefficients and R^2 values are close to 1. The marked periodicity in the force evolution is clearly well-represented by this type of model structure. Furthermore, the model is not hindered by physical assumptions and hence can also capture unsteady effects. It can be observed that the clap-and-fling peak is reproduced effectively. The high accuracy also comes at a low computational cost and although the number of parameters is higher than in the quasi-steady case, the model structure remains simple and straightforward to implement.

However, the Fourier series models also present a number of limitations. Above all, the

(a) Test # 1

(b) Test # 7

(c) Test # 8
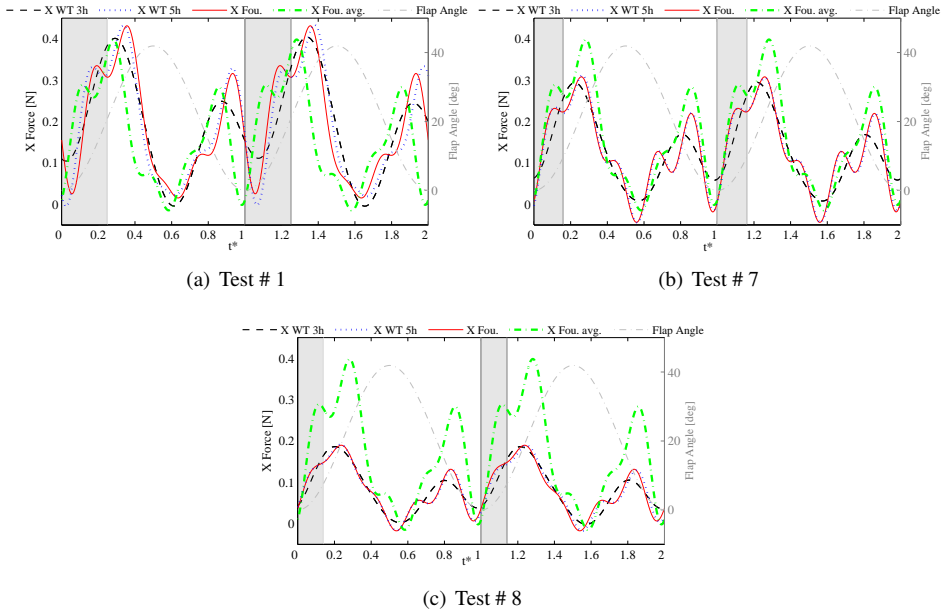
Figure A.2: Wind tunnel (WT) X-force measurements versus model-predicted X-forces. Evaluation of the Fourier series model obtained in a central part of the flight envelope (test #4, cf. Fig. A.1(b)) as a representative model to describe the X-force in all test conditions. Being the chosen reference average case, test # 4 is not shown here.

(a) Test # 1

(b) Test # 2

(c) Test # 7

(d) Test # 8
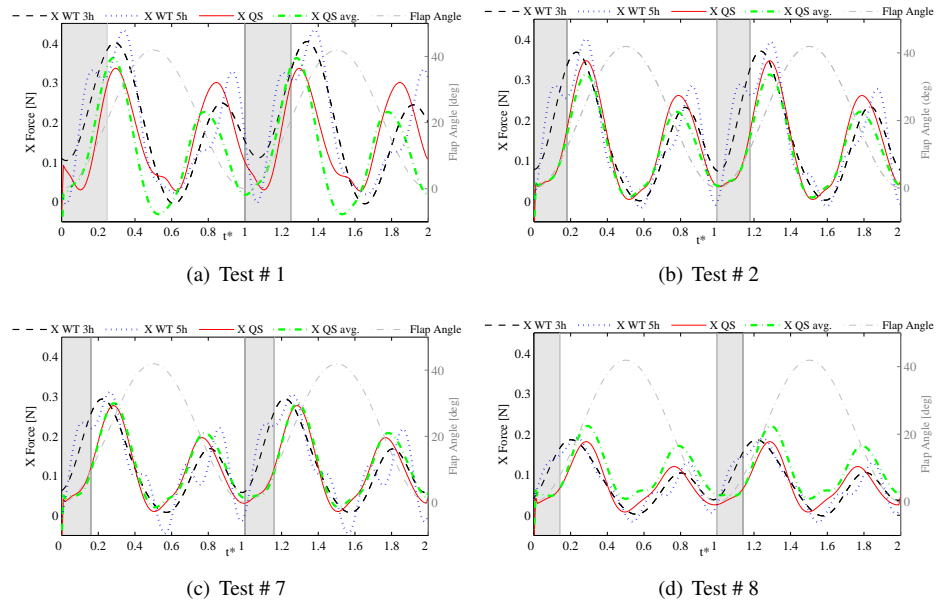
Figure A.3: Wind tunnel (WT) X-force measurements versus X-forces predicted by quasi-steady (QS) models. Evaluation of average quasi-steady model obtained by averaging each parameter over the values estimated from all 8 datasets.

A

models are tightly connected to the test condition they were estimated in. The only physical information contained in these models is the effect of the flapping frequency on the phase, whereas all other effects of different test conditions cannot be considered. This implies that each model is indeed highly accurate, but only in the test condition it was estimated for, and that hence these models cannot be easily extended to cover different flight conditions.

Computing an average model from the separate Fourier series models obtained in different test conditions is not effective or strictly justifiable, as each combination of parameters applies only to the particular test condition of the identification data and it is predominantly the parameters themselves that account for the differences between different flight conditions. Different combinations of parameters can lead to the same outcome, so that the parameters cannot be considered separately and the models essentially can only be considered as single entities. This is reflected in the often significant variation between estimates for the same parameter obtained from different datasets. Furthermore, given that the separate parameters cannot be attributed a physical meaning, a comparison between estimates for the same parameter obtained from different datasets is not meaningful.

Given that the focus of this study is on the sub-flap component, one possibility to cover more flight conditions with the Fourier series based approach, is to assume that the same approximate force evolution occurs in different test conditions, at least within a limited range. Fig. A.2 shows that applying the same model (in this case, the model estimated for test condition # 4, which can be considered representative for the 'central part' of the flight envelope) to different test conditions is in some cases acceptable, but in others inadequate. As expected, the residual RMS increases with the distance of the considered test condition from that the model was estimated in, ranging from 2% to over 50% (Fig. A.4). Clearly, although within a range of more typical flight conditions ($V \in [0.5, 1] m/s$), the X forces generated are fairly similar and the same model can be applied with reasonable accuracy, as soon as larger variations in conditions are introduced, this approach is no longer sufficient.

This approach evidently also implies erroneous cycle-averaged force predictions, hence a slight improvement would be to assume that the mean force can be predicted by other means, while only the *oscillatory* component of the aerodynamic force evolution remains the same in all flight conditions. In steady flight, the mean force can be approximately estimated from the vehicle mass and pitch attitude, while during manoeuvres a separate model for the cycle-averaged aerodynamic forces would be required [12]. Both approaches may be applicable on-board, particularly the former, as on several platforms pitch attitude can be estimated from sensor data [15] or computed from trim information [16]. Even with this adjustment, however, global modelling with a single Fourier series model could be useful only for basic evaluations, where a very approximate idea of the flapping motion is required. If the goal is to truly represent the differences in sub-flap progression between different flight conditions with a single model, then this approach is insufficient, especially near the edges of the flight envelope.

In this regard, the quasi-steady formulation has a clear advantage. Whereas the Fourier series models can be considered useful tools, but not a source of information, the quasi-steady model retains a clear connection to the real system and can provide insight and understanding, even considering the significant assumptions and simplifications it involves. This allows for an interpretation of obtained results and for application of the model for analysis purposes.

(a) Quasi-steady average model

(b) Fourier series average model
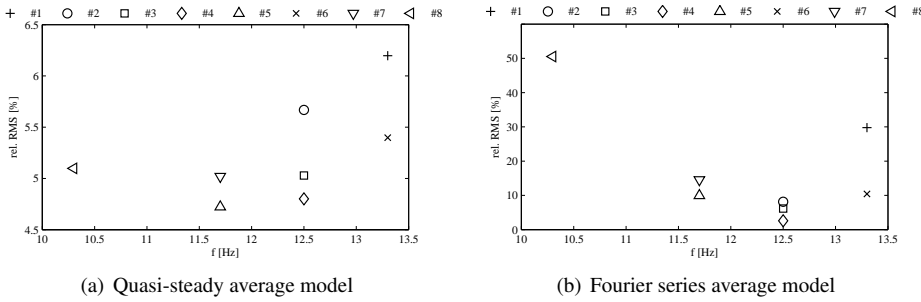
Figure A.4: Residual RMS of the 'average' quasi-steady and Fourier series models, respectively, when applied to each dataset (test #1–test #8). In view of the different modeling approaches, the average quasi-steady model is computed by averaging each parameter over all test cases, whereas the *average* Fourier series model is the model estimated for test condition # 4, considered representative for the 'central part' of the flight envelope.

Moreover, given that the quasi-steady model contains information on the particular test condition it describes and on the kinematics of the system, it should be able to adapt to different test conditions without relying entirely on the parameters. This expectation is confirmed by the computed parameter estimates. In fact, it can be seen that, with the exception of a few outliers, the parameters estimated from different datasets cover a relatively limited range. This firstly indicates an effective estimation process, and secondly suggests that a global model of this form can be computed and applied to all test conditions with effective results.

To test this, an average model was computed by taking the mean of each parameter over all test cases. The model was applied in all test conditions and found to have a reasonably good performance, as illustrated in Fig. A.3, so that it can be considered, in first approximation, a global model. The RMS remains within a narrow range (4.5%-6%, cf. Fig. A.4) for all cases. From this result it also appears that while neglecting forward velocity (cf. Sec. A.3.1) indubitably has an effect on the parameters, which are likely to vary more significantly to compensate for this, the effect is not detrimental to the outcome. Indeed, a well-performing global model can be obtained nonetheless, which may be somewhat less accurate but has the considerable advantage of being applicable on-board a typical platform.

In global terms, the use of a quasi-steady averaged model thus appears to be more effective and reliable than the use of a single Fourier series model as a global model, at least in the context of control. However, the Fourier series models retain the advantage of a higher achievable accuracy and the effortless inclusion of unsteady effects. For simulation applications, the Fourier series models would provide a more realistic result than the simplified quasi-steady ones. Furthermore, for accurate global simulation, a possible approach would be to combine the separate local models, all highly accurate, into one global model. This solution is not practical for FWMAV control or on-board applications, owing to the large number of parameters and increased computational load, but may be useful for high-fidelity simulation.

A

A.5. CONCLUSION

Two different models for the aerodynamics of a flapping-wing micro aerial vehicle (FW-MAV) were presented and compared. The first is based on quasi-steady aerodynamic modelling, while the second is a 5th-order Fourier series expansion. The parameters within the models were estimated using wind tunnel data and system identification methods. The models were applied to replicate the aerodynamic forces of the DelFly, a clap-and-fling FWMAV, and were evaluated and compared.

It was found that the quasi-steady model can represent a significant component of the force (X) component perpendicular to the wing stroke plane (relative RMS <9%), and is a useful basic description of the aerodynamics despite its inability to capture unsteady effects such as clap-and-fling. Using experimental data to estimate model parameters is an effective way of adapting the model to the platform and increasing the accuracy, while the fairly satisfactory results obtained using a very small number of parameters suggest that the model structure is adequate for the vehicle considered. Although this formulation has a limited accuracy, it has the advantage of being easily adapted to different flight conditions, without necessitating different parameters. An averaged model was found to provide a reasonably accurate description of the aerodynamics over the full flight envelope, which is useful for applications requiring basic but not highly accurate sub-flap simulation. Relying solely on measurements that are obtainable on-board FMWAVs, the model is also potentially useful for control applications. Furthermore, thanks to its physical significance, it is applicable for conceptual analysis and investigations.

By contrast, the Fourier series models were found to yield a highly accurate description of each test condition, including unsteady effects. However they depend entirely on the parameters to capture differences between different flight regimes, and therefore cannot be adapted to different conditions. This type of model is useful for high-accuracy simulation and control in limited parts of the flight envelope, and could be used for high-fidelity global simulations if a form of gain scheduling were employed to combine the separate models for different flight conditions. On-board usage, however, would require somehow including additional information on the flight conditions in the basic model structure, without excessively increasing the computational burden.

Due to their different properties, the models are better suited for different applications. However both have a useful level of accuracy, and are theoretically and computationally very simple. A more accurate description using physical models would require the explicit inclusion of the clap-and-fling effect. This could be done based on first principles, which however would require significant simplification for a practical solution to be obtained, or alternatively, the quasi-steady model could be combined with a black-box component accounting only for the unsteady effects.

REFERENCES

[1] S. F. Armanini, J. V. Caetano, C. C. de Visser, G. C. H. E. de Croon, and M. Mulder, *Aerodynamic Model Identification of a Clap-and-Fling Flapping-Wing MAV : a Comparison between Quasi-Steady and Black-Box Approaches,* in *AIAA Atmospheric Flight Mechanics (AFM) Conference*, AIAA Paper 2016-0014 (2016).

[2] S. P. Sane and M. H. Dickinson, *The control of flight force by a flapping wing: lift and*

drag production, Journal of Experimental Biology **2626**, 2607 (2001).

[3] S. P. Sane and M. H. Dickinson, *The aerodynamic effects of wing rotation and a revised quasi-steady model of flapping flight.* Journal of Experimental Biology **205**, 1087 (2002).

[4] A. Andersen, U. Pesavento, and Z. J. Wang, *Unsteady aerodynamics of fluttering and tumbling plates,* Journal of Fluid Mechanics **541**, 65 (2005).

[5] A. Andersen, U. Pesavento, and Z. J. Wang, *Analysis of transitions between fluttering, tumbling and steady descent of falling cards,* Journal of Fluid Mechanics **541**, 91 (2005).

[6] U. Pesavento and Z. J. Wang, *Falling paper: Navier-Stokes solutions, model of fluid forces, and center of mass elevation,* Physical Review Letters **93**, 144501 (2004), the American Physical Society.

[7] G. J. Berman and Z. J. Wang, *Energy-minimizing kinematics in hovering insect flight,* Journal of Fluid Mechanics **582**, 153 (2007).

[8] G. C. H. E. de Croon, K. M. E. de Clercq, R. Ruijsink, B. D. W. Remes, and C. de Wagter, *Design, aerodynamics, and vision-based control of the DelFly,* International Journal of Micro Air Vehicles **1**, 71 (2009).

[9] M. Perçin, Y. Hu, B. W. van Oudheusden, B. Remes, and F. Scarano, *Wing Flexibility Effects in Clap-and-Fling,* International Journal of Micro Air Vehicles **3**, 217 (2011).

[10] J. Grauer, E. Ulrich, J. H. Jr, D. Pines, and J. S. Humbert, *Model Structure Determination of an Ornithopter Aerodynamics Model from Flight Data,* in *48th AIAA Aerospace Sciences Meeting Including the New Horizons Forum and Aerospace Exposition* (2010).

[11] J. V. Caetano, C. C. de Visser, G. C. H. E. de Croon, B. Remes, C. De Wagter, and M. Mulder, *Linear Aerodynamic Model Identification of a Flapping Wing MAV Based on Flight Test Data,* International Journal of Micro Air Vehicles (2013).

[12] S. F. Armanini, C. C. de Visser, G. C. H. E. de Croon, and M. Mulder, *Time-varying model identification of flapping-wing vehicle dynamics using flight data,* Journal of Guidance, Control, and Dynamics **39**, 526 (2016).

[13] J. V. Caetano, S. F. Armanini, C. C. de Visser, G. C. H. E. de Croon, and M. Mulder, *Data-Informed Quasi-Steady Aerodynamic Model of a Clap-and-Fling Flapping Wing MAV,* in *International Conference on Intelligent Unmanned Systems (ICIUS)* (2015).

[14] J. V. Caetano, M. B. Weehuizen, C. C. de Visser, G. C. H. E. de Croon, and M. Mulder, *Rigid-Body Kinematics Versus Flapping Kinematics of a Flapping Wing Micro Air Vehicle,* Journal of Guidance, Control, and Dynamics **38**, 2257 (2015).

A

[15] J. L. Verboom, S. Tijmons, C. De Wagter, B. Remes, R. Babuska, and G. C. H. E. de Croon, *Attitude and altitude estimation and control on board a flapping wing micro air vehicle,* in *IEEE International Conference on Robotics and Automation (ICRA)* (2015).

[16] S. F. Armanini, J. L. Verboom, G. C. H. E. de Croon, and C. C. de Visser, *Determination of trim curves for a flapping-wing MAV,* in *International Micro Air Vehicle Conference and Competition (IMAV)* (Delft, 2014).

B

APPLICATION: EFFECT OF THE TAIL ON THE DYNAMICS

One aspect missing in the analysis presented in this thesis is the separate effect of the wings and tail on the vehicle dynamics. This type of information is not only important when evaluating the flight behaviour, but also essential for the designer, who can use it to direct the development process of new vehicles. Unlike the wings, the tail is largely unstudied in this context. In this appendix the role of the tail in tailed flapping-wing robot flight mechanics is explored, with the aim of further understanding such role, and deriving insight for improved vehicle design. This work relates to the tail aerodynamics analysis in Chapter 6, further exploring the role of the tail, but also represents a practical application of the modelling approach in Chapter 3, thus giving an example of how the different approaches presented in this thesis are connected. Rather than resorting to multi-body modelling and simulation tests, an experimental approach is taken. The effects of the horizontal tail on the longitudinal dynamics are studied by systematically varying the surface area, aspect ratio and longitudinal position of the tail – resulting in 48 different configurations – and identifying a local LTI model for each case. Based on a combined analysis of the flight data and the obtained models, correlations between tail geometry and resulting flight behaviour are assessed. Steady-state conditions are shown to be predictable from tail geometry, however accurate prediction of the dynamics based on tail geometry alone is found to be unreliable due to excessive error margins. Nonetheless, several trends are identified that provide new insight and may be useful for design work. Increasing the surface area or aspect ratio is shown to increase the steady-state velocity and improve the pitch damping. Results also suggest that the tail span is an important design parameter and significantly influences the damping. The effect of the span, in particular, appears to be connected to the distance between tail and wings, which is in agreement with the induced velocity profile observed in Chapter 6.

B

B.1. INTRODUCTION

As discussed in Chapter 6, at present most robotic flapping-wing flyers feature a tailplane to provide passive stability and easier actuation and control through conventional aerodynamic surfaces [2]. This comes at the cost of an increased size, higher gust sensitivity and reduced manoeuvrability, nonetheless, a tail can be beneficial in particular mission scenarios. During fast forward flight, for example, exploiting passive stability may be more energy-efficient than active wing control. Some birds also manipulate their tail geometry for flight control, a feat which may be interesting for future flapping-wing micro aerial vehicles (FWMAVs) [3]. Even though a tailplane has potential advantages, the effects of such a tailplane on flapping-wing flight mechanics have not been thoroughly studied [4, 5]. Numerical methods struggle to capture the complexity of the unsteady, time-varying aerodynamics and its interaction with a tail surface [6], while theoretical models developed to estimate bird tail aerodynamics have been found to be inaccurate when compared to experimental data [3, 7]. Most FWMAV models either do not explicitly account for the tail [8, 9] or omit the interaction with the flapping wings [10].

A time-resolved tail aerodynamics model was developed in Chapter 6 of this thesis, based on PIV (particle image velocimetry) measurements in the wake of the flapping wings. This model may be used to gain a better understanding of the role of the tail, however, to yield in-depth insight, the model must first be more thoroughly validated [11] and ideally integrated in a set of dynamic equations for the full vehicle, so that the resulting system dynamics can be evaluated. In this appendix, an alternative approach is proposed to evaluate the effects of the tail, based on the targeted application of system identification techniques, such as those developed in Chapters 3 and 4. In view of the highly complex, unsteady aerodynamics of flapping flight and the current lack of suitable theoretical models of tail aerodynamics, this type of approach is an attractive solution to study the tail.

A systematic experimental study was conducted to assess the effect of the horizontal tailplane on the flight dynamics of the DelFly II [5]. Given that the complete design space of tail geometries is vast, the scope was narrowed down by selecting three tail design parameters to focus on, viz. surface area, aspect ratio and longitudinal position with respect to the wings. To facilitate the adjustment of the tail and its positioning, a modified version of the DelFly II was designed appositely for this study, featuring a detachable modular tail. Free-flight system identification experiments were conducted and the thus obtained free-flight data were used to estimate longitudinal, decoupled linear time-invariant (LTI) models of the cycle-averaged dynamics of different designs of the test platform, featuring a wide range of different tail configurations. An analysis of the LTI models was then performed to gain insight into the effect of the horizontal tail on the dynamics of the ornithopter. The feasibility of using the observed trends in the models to predict dynamic properties of the vehicle when using arbitrary other tail configurations was assessed as well.

This appendix is structured as follows. Section B.2 discusses the experimental approach taken in this study, including a description of the test platform and a discussion on the experiment execution and data processing. This is followed by a discussion of the modelling approach in Section B.3, presenting the model structure, the parameter estimation method and the model validation approach. The results of the experiments are presented and discussed in Section B.4. Section B.5 summarises the most important findings and offers recommendations for future work.

(a) Base tail only.   (b) Base tail with standard tail attached.
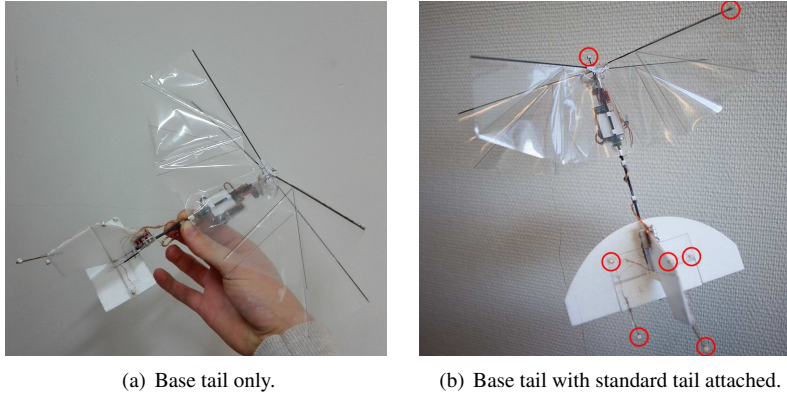
Figure B.1: Photographs of the FWMAV used in this study, illustrating the modular tail concept.

B.2. EXPERIMENTAL SETUP

B.2.1. TEST PLATFORM

The platform used in this study is a variation of the DelFly II (cf. Chapter 1 Sec. 1.4.1 for a description) and was equipped both with a Lisa/S autopilot, containing an IMU for data acquisition, and with active LED markers, indicated by red circles in Fig. B.1(b), for optical tracking purposes. The specific vehicle used in this study ranged in mass from $22.8g$ to $24.3g$, depending on the test configuration.

A number of changes were made to the standard design to facilitate the study of the effects of a varying tail geometry. The tail was redesigned as a modular part of the system, which can be fully detached from the fuselage. This allows for intermediate fuselage segments to be added or removed to adjust the longitudinal position of the tail. Furthermore, the tail itself was redesigned in a modular way. As illustrated in Fig. B.1, the horizontal tailplane consists of a so-called 'base tail', onto which additional components of different shapes and sizes can be attached so as to generate the desired overall tail geometry. The base tail and elevator surface are shown in Fig. B.1(a), while in Fig. B.1(b) the standard tail has been attached to the base tail, clarifying the aforementioned modular mechanism. Due to this design, the test platform features a smaller elevator surface than the standard DelFly II (cf. Table G.1), which, however, was still found to provide sufficient excitation for system identification during the free-flight experiments. Given that the tail test geometries must fit around the horizontal base piece, the minimum size of the tail geometries is constrained by the size of the base tail. Through flight experience it was found that the base tail alone is too small for stable flight, hence smaller tails are of no interest for an open-loop flight configuration and the lower bound in size imposed by the base tail did not impact the final results. The base tail has a total chord length of $48mm$ (including the elevator) and a span of $80mm$ (cf. Fig. B.2): this dimensioning was found to provide suitable support for the vertical tail whilst limiting the aforementioned constraints on the horizontal tail designs.

The fuselage was split into a front section and a tail section. Additionally, a middle segment can be included between the two to adjust the longitudinal position of the tail. The
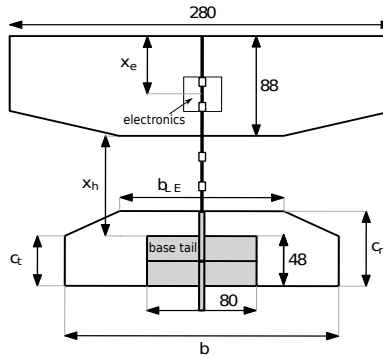
Figure B.2: Geometrical parameters used to manipulate the tail's geometry and position (figure not to scale, measurements in *mm*).

fuselage segments are connected using a guiding pin which slides inside the hollow cross-section of the fuselage, while a bracket prevents the segments from rotating with respect to each other.

B.2.2. TEST CONFIGURATIONS

In view of the very high number of conceivable tail geometries, the scope of this study was limited by focusing on the following three parameters:

1. Tail surface area (S). It is known that the force generated by an aerodynamic surface scales with its total surface area: in steady aerodynamics this relationship is linear [12], however this may not be the case for an aerodynamic surface in the wake of flapping wings.

2. Tail aspect ratio (AR). This parameter provides a measure of the aerodynamic efficiency of a wing, e.g., in steady aerodynamics, and is defined as [12]:

$$AR = \frac{b^2}{S} \tag{B.1}$$

3. Longitudinal position of the tail with respect to the wings (x_h). It transpires from previous studies that the interaction between flapping wings and tail is very complex [3, 6]. PIV experiments show that the wake structure of the DelFly is highly nonlinear and unsteady. Moreover, its strength and orientation vary with spanwise and chordwise position behind the wings [13], which in turn affects the induced velocity and thus the flow conditions at the tailplane [14]. This warrants an investigation into the effect of the longitudinal position of the tail on the dynamic behaviour of the FWMAV.

The aforementioned variables were varied systematically to study their effect on the system dynamics. The surface area and AR are directly related, hence to study these variables each of the two was manipulated while keeping the other constant. Fig. B.2 shows the
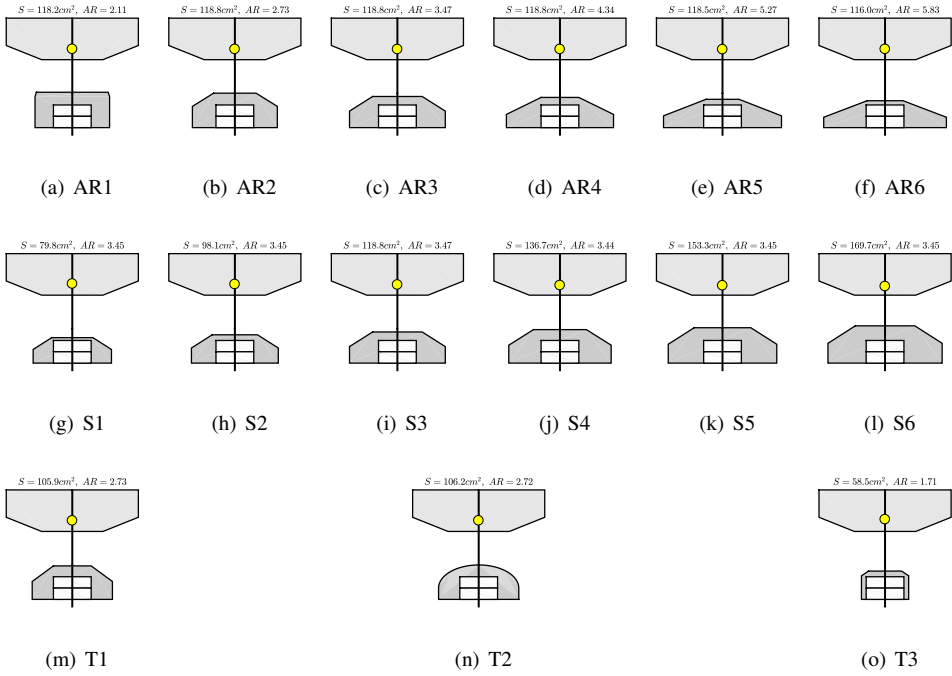
Figure B.3: Tail geometries used in this study. Dot represents the estimated CG position.

physical parameters manipulated to control the AR, surface area and longitudinal position of the tail. Note that in the figure x_e denotes the position of the electronics assembly containing the battery and the Lisa/S autopilot. This assembly can slide along the fuselage to provide additional control over the longitudinal position of the vehicle's centre of gravity (CG).

Fig. B.3 shows the tail geometries used in this study, in schematic form. The corresponding physical dimensions are provided in Table B.2. In the remainder of this appendix, configurations are denoted by a tail and fuselage identifier, e.g., configuration S3c represents tail S3 at a longitudinal position $x_h = 126mm$. Two series of tail geometries were defined to study the surface area and aspect ratio and, for each of these series, different longitudinal positions of the tail were considered. The tail configurations used to test the effect of the surface area have a fixed aspect ratio of $AR \approx 3.45$, which was found to result in a good range of surface areas that could be covered given the limitations imposed by the base tail. S6 has slightly more than twice the surface area of S1 (cf. Figs. B.3(g)–B.3(l)). The aspect ratio tails all have a surface area of $S \approx 118.2cm^2$. Again this provided the possibility of testing a large range of aspect ratios whilst maintaining the same surface area. The tested aspect ratios range from 2.11 (AR1) to 5.83 (AR6) (cf. Figs. B.3(a)–B.3(f)). Note that configurations AR3 and S3 share the same geometry and are part of both test series (i.e. the test series focused on the surface area and on the AR, respectively). Table B.1 gives an overview of the four different fuselage lengths that were used and the corresponding tail

Table B.1: Fuselage configurations used in the experiments.

Fuselage identifier	a	b	c	d
x_h (mm)	57	98	126	114

positions, x_h, defined as the distance from the flapping-wing trailing edge to the leading edge of the base tail, cf. Fig. B.2.

Figs. B.3(m), B.3(n) and B.3(o) show three additional tails that were tested and were not part of either the 'S' or the 'AR' series. Tail T2, in Fig. B.3(n), is the original tail used in the standard design of the DelFly II. Tail T1 has approximately the same aspect ratio and surface area as T2, but sharp edges instead of the original elliptical shape. This tail was used to assess the effect of changing the leading edge shape to a non-elliptical one, a design modification introduced in this study to facilitate the systematic manipulation of the geometric features of the tail. The flight behaviour of the vehicle with each of these two tail configurations was found to be almost identical, justifying the use of sharp edges for all other evaluations in this work. Finally, tail T3 (Fig. B.3(o)) was used to assess at which point the ornithopter started to display an unstable dynamic behaviour.

Table B.2: Physical dimensions of the tail geometries used in the experiments.

Parameter	S1	S2	S3/AR3	S4	S5	S6	AR1	AR2	AR4	AR5	AR6	T1	T2	T3
b (mm)	166	184	203	217	230	242	158	180	227	250	260	170	170	100
b_{LE} (mm)	87	96	105	112	120	126	152	90	80	70	76	80	-	70
c_r (mm)	54	60	66	71	75	79	75	73	64	60	57	71	73	60
c_t (mm)	29	32	35	38	40	42	66	45	28	25	22	38	24	50
AR (−)	3.45	3.45	3.47	3.44	3.45	3.45	2.11	2.73	4.34	5.27	5.83	2.73	2.72	1.71
S (cm^2)	79.8	98.1	118.8	136.7	153.3	169.7	118.2	118.8	118.82	118.5	116.0	105.9	106.2	58.5

(Tail identifier header spans all tail columns)

B.2.3. FLIGHT TESTING

As discussed previously in this thesis (e.g., Sec. 1.4.2), wind tunnel experiments have a number of limitations and cannot be used to realistically assess the dynamic stability characteristics of a particular configuration [15, 16]. For this reason, free-flight experiments were used in this study. Flight tests were conducted in the TU Delft *CyberZoo* optical motion tracking facility (cf. Chapter 1 Sec. 1.4.2), using the same data acquisition and processing setup as described in Chapter 2. The locations of the LED markers on the ornithoper, chosen for this flight test campaign, are indicated by circles in Fig. B.1(b). Throughout this study, coordinate system *B*2, as defined in Chapter 1 Sec. 1.4.3, was used; the coordinate system is also shown again in Fig. B.5.

The FWMAV was flown manually, while the identification manoeuvres were pre-programmed and performed automatically when triggered by the operator, as discussed in Chapter 2. This ensured a consistent excitation of the dynamics and increased the likelihood of repeatable results. For each configuration a single flight was performed with an average flight time of approximately 5-6 minutes, resulting in an average of 21 manoeuvres per flight. These manoeuvres were assumed to constitute independent experiments in the subsequent analysis phase. During the experiments the electronics assembly and battery were fixed in

B

position ($x_e \approx 52mm$) to minimise changes to the vehicle.

Doublet pulses on the elevator were used as input signals, for the reasons discussed in Chapter 2, with the duration and amplitude being tuned for the specific requirements of this study. In particular, through flight testing with the largest and smallest tail geometries it was found that a 65% elevator deflection with 0.33 second pulses provides sufficient excitation for larger tail geometries whilst not destabilising most of the smaller ones. Experiments for configuration T3 were performed with a 30% deflection doublet as this was the only configuration that was destabilised by the previously described input signal.

The data processing preceding the analysis phase was conducted according to the procedures laid forth in Chapter 2, involving time-synchronisation, sensor fusion and low-pass filtering. As in Chapter 3, a fourth-order low-pass Butterworth filter with $5Hz$ cutoff frequency was used for filtering, and, in view of the focus on the time-averaged dynamics, only the low-frequency component was used for identification. Manoeuvres were automatically isolated using the elevator servo command signal, logged on board. Specifically, the data segments used for identification were defined to start 0.5 seconds prior to the beginning of the manoeuvre and last until a rudder deflection (i.e., a turn) was detected.

B.3. DYNAMIC MODELLING

B.3.1. MODEL IDENTIFICATION

The model structure used in this study is that used in Chapters 3 and 4 to model the time-averaged longitudinal dynamics (Eq. 4.1). As shown in the aforementioned chapters, around steady flight conditions the time-averaged dynamics of the test platform can be approximated effectively using LTI models. Additionally, LTI models are easy to use for obtaining new insight into a previously unexplored effect, such as that considered in this study. Next to their limited validity range, the chosen LTI models have the drawback – for this particular study – that they do not contain terms explicitly modelling the effect of the tail or incorporating tail geometry specifications. Thus, it cannot be known with certainty whether a particular change in the model parameters is the result of a change in tail geometry. Nonetheless, for an initial study of the tail effect on the dynamics, the LTI model structure was considered sufficient and tail effects could be to some extent inferred.

The flapping frequency was initially added to the model structure in Eq. 4.1, as a second input variable. However, this did not yield significant improvements in model accuracy and provided little additional insight into the effect of the tail because responses to throttle input varied only very little between configurations. Furthermore, as discussed previously, elevator manoeuvres provide more suitable excitation to study the effect of the tail as they are direct pitching moment disturbances. Hence, the flapping frequency was omitted in the final tests, leading to the same model structure as used previously in this thesis.

As in Chapter 3, the unknown parameters of the LTI model were estimated using a combination of ordinary least squares (OLS) estimation and a maximum likelihood (ML) optimisation step (cf. Secs. 3.4.2 and C.4 for details). Models were estimated for each of the manoeuvres conducted in each flight (~21 per flight). Typically 0–2 datasets per tail configuration led to failed convergence of the ML estimator.

B.3.2. AVERAGE MODEL DEFINITION

To compare the dynamic behaviour of the tail geometries it is more convenient to estimate a single, representative model for each tail configuration. Thus, three different approaches were defined to estimate such an average model.

B

MEAN PARAMETER MODEL

The most straightforward approach to estimate an average model for a particular configuration is to take, for each parameter, the mean of the estimates obtained from all the individual identification manoeuvres. Since the input used to excite the dynamics was pre-programmed and remained unchanged for all experiments conducted with the same configuration, the excitation of the system was very consistent. This led to a similar response for each excitation sequence and was thus expected to yield consistent models. Analysing the mean of the model parameters is hence considered a plausible approach to determine a representative model. Nonetheless, small disturbances experienced in flight lead to some variation in the individual models. One approach to assess the reliability of a particular parameter is to consider the standard deviation of said parameter over all the individual models. The mean and standard deviations of the parameters over the set of individual models can also give an indication of the relative impact of each particular parameter on the system dynamics.

WEIGHTED MEAN (WM) MODEL

Taking a simple mean of all the parameters may not be the most accurate method to estimate a representative model, as it assumes that the parameter estimates obtained from all of the separate identification experiments were equally successful. Due to the nature of the ML optimisation step in the parameter estimation process, this is not necessarily the case. Ljung proposes a method to compute a weighted mean (WM) of the parameters by taking into account the covariance matrix of the estimation [17]. Given multiple parameter estimates, obtained from n independent datasets, the following equation provides an average parameter set, weighted according to the estimated covariance matrices:

$$\hat{\theta} = P \cdot \sum_{i=1}^{n} \left(\left[P^{(i)} \right]^{-1} \cdot \hat{\theta}^i \right), \text{ with } P = \left[\sum_{i=1}^{n} \left[P^{(i)} \right]^{-1} \right]^{-1}. \tag{B.2}$$

In the above expression, $\hat{\theta}^i$ represents the parameter estimate for dataset i.

This method takes into account that not all estimations are equally reliable. According to Ljung, the parameter estimate resulting from Eq. B.2 should be the minimum covariance parameter estimate [17].

AVERAGED TIME-RESPONSE (RA) MODEL

Lastly, an average model was computed by overlaying all the datasets collected using the same tail geometry, computing the mean time-response, and estimating a single representative model using the averaged response as identification data. This approach was assumed to be justifiable in view of the high consistency between individual manoeuvres performed during the same flight test (i.e., with the same tail configuration). Furthermore, the time-varying, flapping-related content in the data was not taken into account when averaging. In the remainder of this appendix, this type of model is denominated response-averaged (RA) model.

Table B.3: Model validation metrics.

Metric	Threshold
RMSE	$RMSE \geq 80$ %tile
output correlation	$\text{mean}(corr) \leq 0.70$
parameter covariance	$\left\lvert \frac{\text{cov}(\hat{\theta})}{\hat{\theta}} \right\rvert > 1$

B.3.3. MODEL VALIDATION

APPROACH

Model validation was performed on two levels. First the quality of each individual model was assessed by simulating its response to the measured input. Comparing the model-predicted states to the measured states gives a measure of accuracy for the particular model considered. Then, the aforementioned averaged models (cf. Sec. B.3.2) were estimated, using a selection of the 'accepted' datasets, and evaluated using validation data (i.e., data not used to estimate the averaged models). Three metrics were used to evaluate the quality of individual models, viz.: (i) the root mean squared error (RMSE) between measured and model-predicted states; (ii) the correlation coefficient between measured and model-predicted states (corr); and (iii) the covariance of the parameter estimates. For each validation metric, a suitable threshold was defined and used to determine whether or not each model was considered acceptable. The resulting thresholds are given in Table B.3. Note that covariance flags were normalised by the total number of parameters, and the RMSE threshold was defined such that the models with the highest 20% of RMSE values (amongst all models for the same tail configuration) were flagged.For each model, each of the chosen metrics was computed and each state or parameter exceeding any one of the chosen threshold was flagged. This evaluation resulted in a summed flag value for each model: if the flag value of a model exceeded 1, the model was rejected and not used to compute average models for the corresponding configuration.

After evaluating the individual models based on the criteria in Table B.3, 70% of the data (corresponding to 70% of the individual models) were selected at random for the calculation of averaged models, whilst the remaining 30% of the data were used for validation.The different types of averaged models described in Sec. B.3.2 were then evaluated using the validation data to find the most representative among them. To evaluate the averaged models, two metrics were used: the mean RMSE and the mean correlation. These metrics were computed for each tail configuration and each validation dataset, and the model scoring best on the highest number of datasets was considered to be the most representative model for the particular tail configuration considered. The highest fitness models for each tail configuration were then used to compare the dynamic characteristics of different tail geometries.

RESULTS

The models for all configurations were validated using the aforementioned approach. Fig. B.4 shows an example of the results for configuration S1b: these results are representative for the bulk of the tail configurations considered. Table B.4 gives an overview of the validation results for all configurations.

Fig. B.4(a) shows the model-predicted and measured time responses for the chosen ex-

B

(a) Time response (b) Eigenvalues
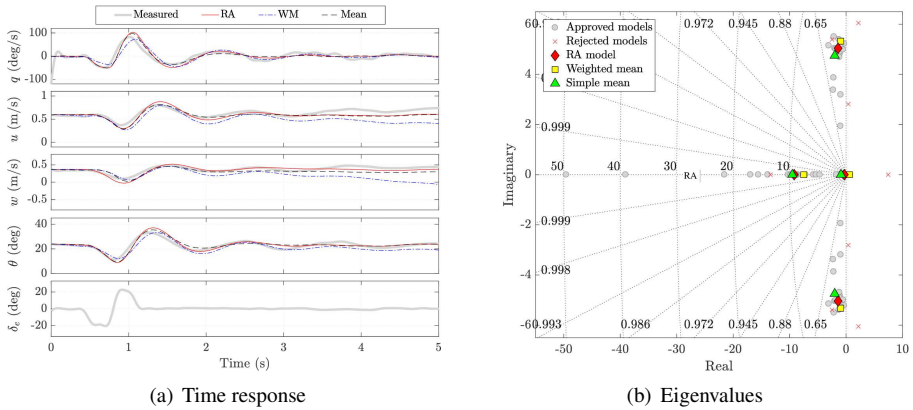
Figure B.4: Example of validation results for configuration S1b

ample tail configuration and validation dataset. It can be observed that all three models predict the measured states with significant accuracy. There is, however, a slight instability in the weighted mean (WM) model, caused by a positive real eigenvalue. Fig. B.4(b) shows the system eigenvalues: a clear clustering can be observed, particularly for the complex conjugate eigenvalues. The averaged models display a high consistency in the complex conjugate pair of eigenvalues, and their eigenvalues are also located around the aforementioned cluster of the individual model eigenvalues, providing some confidence in the methods used to obtain the average models. The real eigenvalues are less consistent and show more spread, already in the individual models. As discussed in Chapters 3 and 4, this was also the case in previous system identification work for this FWMAV and is most likely caused by a lack of excitation in the body z_B-axis [18].

Fig. B.4(b) also shows the poles of rejected models, which were not used for estimation or validation of the averaged models, based on the thresholds in Table B.3. For the example case (i.e., configuration) considered, the rejected models with unstable complex conjugate pole pairs were the result of ML identification divergence. In most cases, however, model rejection was a result of the ML estimation converging to a local minimum, hence yielding sub-optimal results. Typically less than four individual models were rejected, leaving an average of 12 independent datasets to estimate average models from, suggesting that the experiment execution and estimation process were generally successful.

The three averaged models generally display a high performance for the given, representative example, however the weighted mean model has a tendency to be drawn towards unstable real poles if such poles are present in any of the individual models used to estimate the WM model. It appears that the model parameters of models with an unstable real pole had lower covariances, which in turn gave them a high weighting in the computation of the WM model. As a result, the WM model has a slight instability, visible in the time response in Fig. B.4(a). For this configuration, all three average models have a significant accuracy, with a mean $corr > 0.80$, and mean $RMSE = 0.11$ for the RA and mean model. However, the slight instability in the WM model clearly results in higher RMSE (0.16) and lower

correlation (0.64) values. The RA model scores best overall and is therefore considered the most representative model for configuration S1b.

For some configurations the weighted mean model was drawn significantly towards an unstable pole due to more than one individual model with a positive real eigenvalue. In some cases this led to poor validation results for the weighted mean model (cf. Table B.4). The simple mean model and the RA model are much less sensitive to individual models featuring positive real eigenvalues. Overall, the RA model scored highest for a majority of the configurations tested. This confirms the consistency of the dynamic excitation and provides additional confidence in a proper experiment execution.

B

Table B.4: Mean validation scores, standard deviation in brackets. Note: not all configurations were tested; and for T3b and T3c, modelling was unsuccessful.

| Tail | Model | Fuselage configuration | | | | | | | |
| | | a (x_h=57mm) | | b (x_h=98mm) | | c (x_h=126mm) | | d (x_h=114mm) | |
		RMSE	corr.	RMSE	corr.	RMSE	corr.	RMSE	corr.
S1	RA	0.12 (0.02)	0.88 (0.03)	0.11 (0.01)	0.87 (0.05)	0.10 (0.01)	0.86 (0.02)	0.11 (0.02)	0.84 (0.05)
	WM	0.12 (0.02)	0.87 (0.02)	0.16 (0.02)	0.64 (0.11)	0.11 (0.01)	0.85 (0.05)	0.13 (0.01)	0.84 (0.04)
	Mean	0.12 (0.01)	0.86 (0.05)	0.11 (0.01)	0.83 (0.06)	0.09 (0.01)	0.88 (0.05)	0.13 (0.03)	0.77 (0.11)
S2	RA	0.10 (0.02)	0.84 (0.09)	0.11 (0.02)	0.86 (0.05)	0.10 (0.01)	0.83 (0.09)	-	-
	WM	0.12 (0.02)	0.72 (0.12)	0.14 (0.01)	0.78 (0.05)	0.20 (0.03)	0.63 (0.13)		
	Mean	0.10 (0.02)	0.81 (0.11)	0.12 (0.01)	0.80 (0.05)	0.10 (0.02)	0.79 (0.04)	-	-
S3/AR3	RA	0.12 (0.02)	0.78 (0.08)	0.09 (0.01)	0.87 (0.03)	0.10 (0.01)	0.80 (0.06)	0.09 (0.01)	0.90 (0.06)
	WM	0.17 (0.02)	0.62 (0.14)	0.10 (0.02)	0.81 (0.07)	0.11 (0.01)	0.75 (0.06)	0.13 (0.02)	0.73 (0.12)
	Mean	0.12 (0.02)	0.75 (0.07)	0.10 (0.01)	0.86 (0.03)	0.10 (0.01)	0.79 (0.05)	0.09 (0.01)	0.90 (0.05)
S5	RA	0.09 (0.04)	0.86 (0.07)	0.08 (0.02)	0.88 (0.03)	0.09 (0.02)	0.79 (0.04)	0.11 (0.03)	0.80 (0.08)
	WM	0.11 (0.04)	0.82 (0.06)	0.11 (0.01)	0.76 (0.05)	0.12 (0.02)	0.59 (0.07)	0.16 (0.02)	0.48 (0.09)
	Mean	0.09 (0.04)	0.85 (0.07)	0.09 (0.02)	0.84 (0.04)	0.10 (0.02)	0.71 (0.07)	0.12 (0.02)	0.76 (0.11)
S6	RA	0.09 (0.03)	0.89 (0.05)	-	-	-	-	-	-
	WM	0.11 (0.02)	0.85 (0.05)	-	-	-	-	-	-
	Mean	0.09 (0.03)	0.89 (0.05)	-	-	-	-	-	-
AR1	RA	0.14 (0.05)	0.78 (0.27)	0.12 (0.02)	0.86 (0.01)	0.13 (0.01)	0.86 (0.04)	0.14 (0.02)	0.84 (0.06)
	WM	0.15 (0.04)	0.73 (0.24)	0.18 (0.01)	0.59 (0.06)	0.16 (0.05)	0.78 (0.13)	0.13 (0.04)	0.84 (0.07)
	Mean	0.14 (0.05)	0.75 (0.29)	0.12 (0.02)	0.83 (0.03)	0.18 (0.02)	0.75 (0.07)	0.14 (0.03)	0.81 (0.11)
AR2	RA	0.10 (0.04)	0.89 (0.05)	0.11 (0.03)	0.87 (0.07)	0.08 (0.02)	0.89 (0.04)	-	-
	WM	0.13 (0.03)	0.80 (0.06)	0.12 (0.03)	0.82 (0.09)	0.09 (0.02)	0.85 (0.05)	-	-
	Mean	0.10 (0.03)	0.87 (0.05)	0.11 (0.03)	0.85 (0.06)	0.08 (0.02)	0.88 (0.04)	-	-
AR5	RA	0.12 (0.03)	0.85 (0.05)	0.10 (0.02)	0.83 (0.08)	0.11 (0.01)	0.70 (0.15)	0.12 (0.03)	0.82 (0.02)
	WM	0.18 (0.03)	0.72 (0.07)	0.12 (0.01)	0.75 (0.07)	0.13 (0.01)	0.53 (0.07)	0.13 (0.03)	0.76 (0.08)
	Mean	0.10 (0.03)	0.86 (0.06)	0.10 (0.03)	0.78 (0.09)	0.11 (0.01)	0.65 (0.19)	0.13 (0.04)	0.73 (0.11)
AR6	RA	0.11 (0.02)	0.85 (0.05)	-	-	-	-	-	-
	WM	0.12 (0.02)	0.80 (0.07)	-	-	-	-	-	-
	Mean	0.10 (0.02)	0.87 (0.06)	-	-	-	-	-	-
T1	RA	0.11 (0.03)	0.88 (0.06)	0.10 (0.03)	0.88 (0.05)	0.14 (0.03)	0.76 (0.07)	-	-
	WM	0.75 (0.65)	0.44 (0.23)	0.15 (0.04)	0.74 (0.10)	0.29 (0.09)	0.32 (0.28)	-	-
	Mean	0.11 (0.03)	0.87 (0.04)	0.10 (0.03)	0.87 (0.06)	0.13 (0.04)	0.76 (0.10)	-	-
T2	RA	0.10 (0.01)	0.86 (0.03)	0.11 (0.05)	0.90 (0.06)	0.67 (0.61)	0.47 (0.30)	-	-
	WM	0.17 (0.03)	0.75 (0.07)	0.15 (0.03)	0.75 (0.11)	0.19 (0.03)	0.68 (0.18)	-	-
	Mean	0.12 (0.01)	0.83 (0.04)	0.13 (0.05)	0.82 (0.08)	0.17 (0.03)	0.67 (0.16)	-	-
T3	RA	0.29 (0.13)	0.87 (0.12)	-	-	-	-	-	-
	WM	1.16 (0.85)	0.44 (0.21)	-	-	-	-	-	-
	Mean	0.34 (0.10)	0.67 (0.09)	-	-	-	-	-	-

B.4. RESULTS AND DISCUSSION

B.4.1. EFFECT ON STEADY STATE

The tail geometry is expected to affect the magnitude of the tail force F_h. Assuming the force generated by the flapping wings (F_w) initially remains unchanged, a different tail force should result in a different moment equilibrium and therefore different steady-state

B

(a) $x_h = 57mm$ (b) $x_h = 98mm$ (c) $x_h = 126mm$
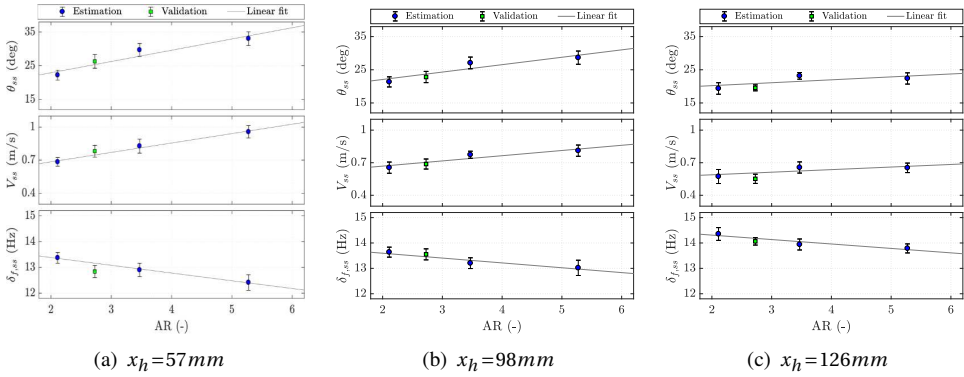
Figure B.6: Steady state as a function of tail aspect ratio (1σ error bars shown).

conditions (for the same elevator deflection, i.e., in this case none), as clarified by Fig. B.5.
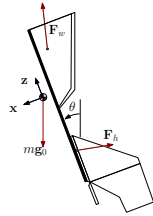
Figure B.5: Free-body diagram of the DelFly in typical slow forward flight attitude, showing the body-fixed reference frame ($\mathbf{y}_B$ is positive towards the left hand side wing).

The effects of the horizontal tail aspect ratio and surface area on the vehicle's steady-state conditions are shown in Figs. B.6 and B.7, respectively. Linear fits were estimated using three of the configurations, while one additional configuration was used to validate the results and test whether the steady-state conditions can be predicted based on the tail geometry. It can be observed that increasing the aspect ratio increases the force generated by the tail and thus causes a larger

body pitch angle. This in turn tilts the wing force F_w (cf. Fig.B.5) and leads to a higher steady-state velocity. This effect becomes less pronounced when the tail is moved farther away from the flapping wings, as indicated by the less steep slope in the trend line in Fig. B.6(c) in comparison to Fig. B.6(a). Increasing the surface area has a similar effect on the steady state as increasing the aspect ratio, however the effect of the surface area seems to be less significant. Moreover, the slopes of the linear fits in Figs. B.7(a) and B.7(c) are very similar, suggesting that the overall effect of surface area on the steady-state conditions does not vary with longitudinal position.

In Fig. B.8, the steady-state conditions are plotted as a function of the longitudinal position of the tail. Increasing the separation from the wings decreases the steady-state velocity and pitch angle. This is not fully in line with expectations: moving the tail farther away from the main wings increases the moment arm of the tail force with respect to the CG (cf. Fig.B.5), which would suggest that the tail generates more nose-down moment, resulting in a faster steady-state configuration. The probable reason for the observed result is a CG shift. In fact, changing the longitudinal position from $x_h = 57mm$ to $x_h = 126mm$ produces an average CG shift of $15.1mm$, depending on the tail used, and thus causes a

(a) $x_h = 57mm$ (b) $x_h = 98mm$ (c) $x_h = 126mm$
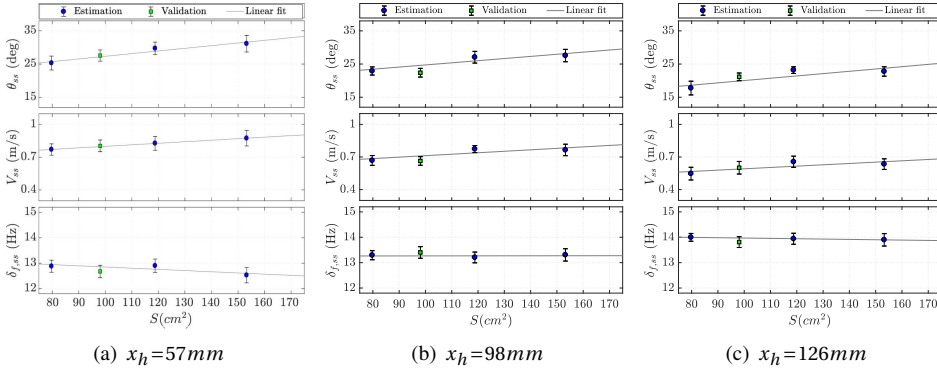
Figure B.7: Steady-state conditions as a function of tail surface area (1σ error bars shown).

(a) For varying AR   (b) For varying S
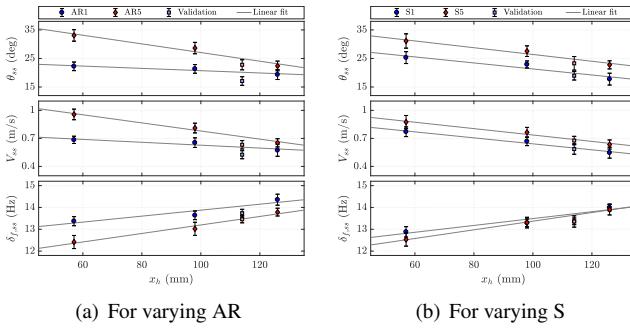
Figure B.8: Influence of the longitudinal position of the tail on the vehicle's steady-state conditions (1σ error bars shown).

mean increase of the tail moment arm of approximately 74%. However, assuming F_w acts at the wing quarter chord point, the wing moment arm also increases by approximately 40%. According to earlier wind tunnel results, the wings of this vehicle produce a small, negative contribution in force perpendicular to the fuselage (here, X), thus generating a nose-up pitching moment [19, 20]. The steady-state trends observed in Fig. B.8 imply that the wing contribution is dominant in establishing the moment equilibrium. Comparing Fig. B.8 to Figs. B.6 and B.7 also shows that, overall, the geometry of the tail has less impact on the steady-state conditions than its longitudinal position.

As mentioned earlier, the effect of the tail position on the vehicle's steady state appears to be the same for configurations S1 and S5, as indicated by the near-parallel linear fits in Fig. B.8(b), however Fig. B.8(a) shows that the difference in steady-state condition between AR1 and AR5 decreases when x_h increases. Hence, it appears that close to the flapping wings increasing the AR brings a more pronounced aerodynamic advantage than increasing the surface area. By contrast, this aerodynamic advantage seems to diminish when moving away from the wings. At increased x_h, the free-stream velocity is expected

B

(a) Function of tail AR.   (b) Function of tail S.
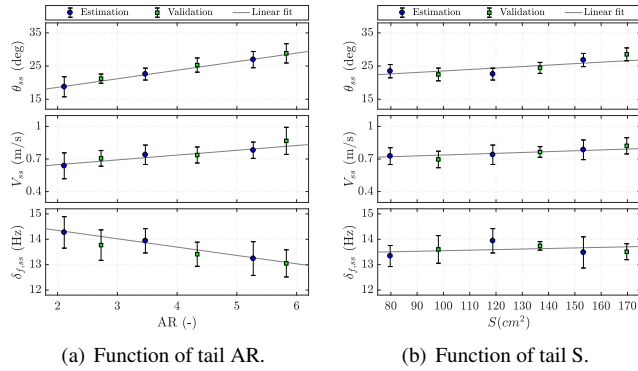
Figure B.9: Steady-state conditions versus surface area and AR: results of additional experiments performed to evaluate whether steady-state conditions can be accurately predicted based on tail geometry (x_h=57mm, 1σ error bars shown).

to become increasingly dominant over the flapping wing-induced velocity. Since the steady-state attitude is likely determined in part by the total drag of the system, this result implies that for large x_h the tail is mainly producing a drag force, which is determined mostly by its surface area. Given that AR1 and AR5 in Fig. B.8(a) have the same surface area, they eventually converge to almost the same resulting steady-state condition as the longitudinal distance between tail and wings increases.

The experiments for configurations AR1d, AR5d, S1d and S5d (e.g., the validation points in Fig. B.8 obtained for x_h=114mm) were conducted at a later time than the original experiments. Inevitably small changes occurred in the system during the intermittent time (cf. discussion on repeatability of experiments in Chapter 2). Since the FWMAV is very light and vibrates continuously during flight, such changes are inevitable and can have a significant impact on the steady-state conditions. This means that an accurate comparison of the steady-state conditions is not possible when measurements are not taken consecutively. Additional data points were required to investigate whether the steady-state conditions can be predicted based on tail geometry parameters. For this purpose, four additional tail configurations (AR4, AR6, S4, S6) were constructed after the initial experiments. To minimise the effect of the aforementioned unforeseeable changes in the system, which can affect the steady-state conditions, as observed in Fig. B.8(b), steady-state experiments for x_h=57mm were repeated on a single day. The results of these experiments are shown in Fig. B.9. On-board data were not logged during these flights to reduce the testing time, as optical tracking was deemed sufficient for this particular evaluation.

Comparing the steady-state conditions in Fig. B.9(a) to the previously obtained ones in Fig. B.6 confirms that the steady-state conditions can vary significantly over time, and generally highlights the difficulty of finding universally valid models for FWMAVs. Especially the results for configuration AR5a (AR=5.27) changed significantly between the two flight testing campaigns. If experiments are performed in succession, with minimal changes made to the system in between, it is possible to accurately predict steady-state conditions as a simple, linear function of the tail aspect ratio or surface area. It can also be observed

Table B.5: Result of predicting steady-state conditions using linear fits, based on the results in Fig. B.9 (additional set of flight tests).

Tail	θ_{ss}(deg)				V_{ss}(ms^{-1})				$\delta_{f,ss}$(Hz)			
	x_m	$\hat{x}$	$\|x_m-\hat{x}\|$	$\left\|\frac{x_m-\hat{x}}{\sigma(x)}\right\|$	x_m	$\hat{x}$	$\|x_m-\hat{x}\|$	$\left\|\frac{x_m-\hat{x}}{\sigma(x)}\right\|$	x_m	$\hat{x}$	$\|x_m-\hat{x}\|$	$\left\|\frac{x_m-\hat{x}}{\sigma(x)}\right\|$
AR2a	21.20	20.48	0.74	0.54	0.71	0.67	0.03	0.36	13.77	14.11	0.34	0.57
AR4a	25.30	24.61	0.69	0.32	0.74	0.75	0.01	0.19	13.41	13.58	0.17	0.36
AR6a	28.83	28.45	0.37	0.13	0.87	0.82	0.05	0.40	13.05	13.09	0.04	0.07
S2a	22.46	23.43	0.97	0.50	0.70	0.74	0.04	0.21	13.60	13.54	0.06	0.10
S4a	24.45	25.14	0.69	0.42	0.76	0.77	0.01	0.29	13.74	13.63	0.11	0.66
S6a	28.53	26.60	1.93	1.00	0.82	0.79	0.03	0.06	13.51	13.70	0.19	0.61

(a) x_h=57mm (b) x_h=114mm (c) x_h=126mm
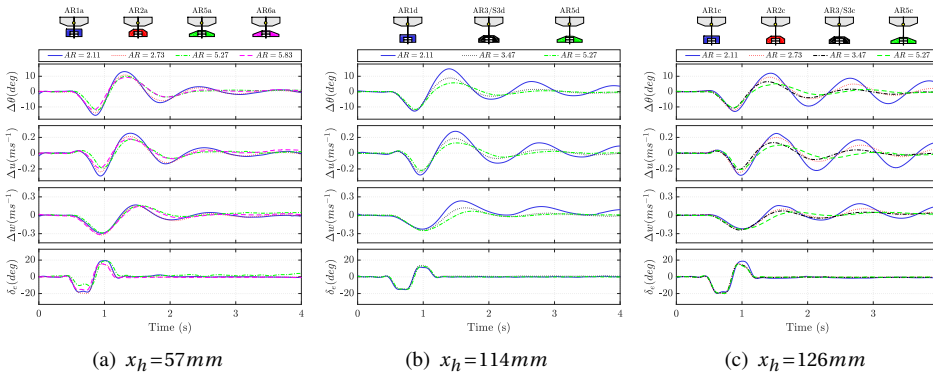
Figure B.10: Influence of tail aspect ratio on average time response to elevator doublet.

that the trends emerging from the two sets of experiments (cf. Figs. B.9, B.6 and B.7) are qualitatively the same, suggesting that the observed correlation between tail geometry and steady-state conditions is valid. The prediction errors are summarised in Table B.5, showing that the predictions are less than one standard deviation from the measurements. It is even possible to extrapolate the trends a little beyond the original estimation range and still predict the steady-state conditions with good accuracy, which provides interesting opportunities for future design tools. The significant impact that minor changes in the geometry have on the quantitative trends implies that a full evaluation requires extensive testing, and it may for instance be advisable – eventually – to conduct a large number of tests at intervals to try and determine the range within which values vary. Nonetheless, qualitative trends can be clearly determined, and the order of magnitude of these trends provides at least an approximate quantitative indication.

B.4.2. EFFECT ON DYNAMIC BEHAVIOUR

During the flight experiments, differences in the system response were clearly noticeable for the different configurations. Analysing the time response of each configuration was thus expected to provide additional insight into the effect of the tail. Fig. B.10 shows the average time responses for different *AR* tails. The average response is computed over all the manoeuvres performed during an experiment. The results show that an increased aspect ratio

B
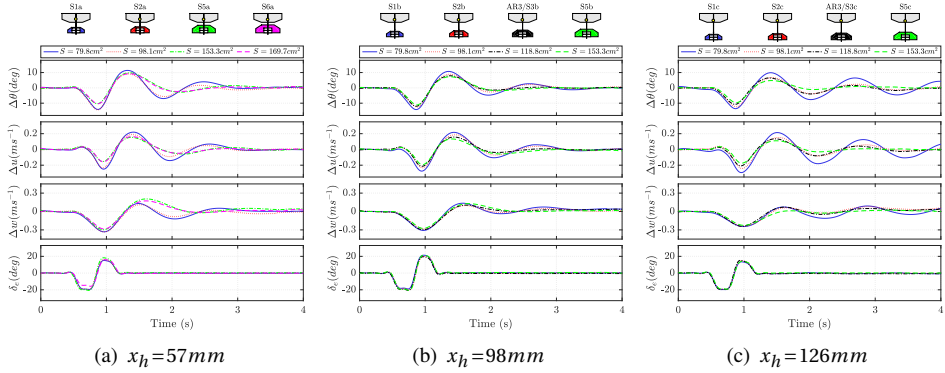
Figure B.11: Influence of tail surface area on average time response to elevator doublet.

has a positive effect on damping capabilities and slightly reduces the natural frequency of the oscillation. This may be partially caused by the larger span width of AR3 and AR5, which gives these configurations effective surface area in a spanwise region which experiences a high induced velocity wake, based on the PIV measurements and analysis conducted in Chapter 6 (cf. Fig. 6.18(a) in Chapter 6 or Fig. 14 in Ref. [6]). Note that apparent differences in the input signal in Fig. B.10 and other time response figures are caused by tracking problems with the elevator marker and subsequent averaging over multiple data segments. The results in Fig. B.10 also show that the responses vary significantly with a changing longitudinal tail position. When the distance to the flapping wings is small (Fig. B.10(a)), increasing the aspect ratio seems to have a slightly more significant effect on the natural frequency of the oscillation but the responses are in fact quite similar. In Fig. B.10(b), the differences in average response are far more evident and clearly show a higher damping for configurations AR3d and AR5d. Though the initial responses are almost identical, the peak at $t \approx 1.4s$ decreases considerably in magnitude for high AR configurations. These differences in damping are also apparent in Fig. B.10(c). In fact, increasing x_h beyond $114mm$ appears to drastically reduce the damping capabilities of configuration AR1c, and to lesser extent AR2c, but it does not affect AR3c and AR5c in a similar way.

Fig. B.11 shows the average time responses for tails of different surface areas. Differences in damping again become more apparent for increasing longitudinal distance of the tail from the wings (cf. Fig.B.11(c)). From Fig. B.11(a) it seems that increasing the surface area beyond $S = 153.3cm^2$, i.e., from S5a to S6a, does not produce any significant change in the dynamic response. A larger surface area seems to have some effect on the natural frequency of the oscillation when the tail is close to the flapping wings, based on the time responses in Fig. B.11(a), though the oscillations in Fig. B.11(c) are almost entirely in-phase, showing only differences in damping. The damping is reduced for configuration S1c in comparison to S1b. This is unexpected, since the tail moment arm increases from $x_h = 98mm$ to $x_h = 126mm$. As for the steady-state results in Fig. B.8, this may be due to the wing force also generating a larger, destabilising moment when the CG is moved further aft.

From Figs. B.10 and B.11 it is apparent that the longitudinal position of the tail has

(a) S1 (S=79.8cm^2, AR=3.45) (b) AR3/S3 (S=118.8cm^2, AR= 3.47) (c) AR1 (S=118.2cm^2, AR= 2.11)
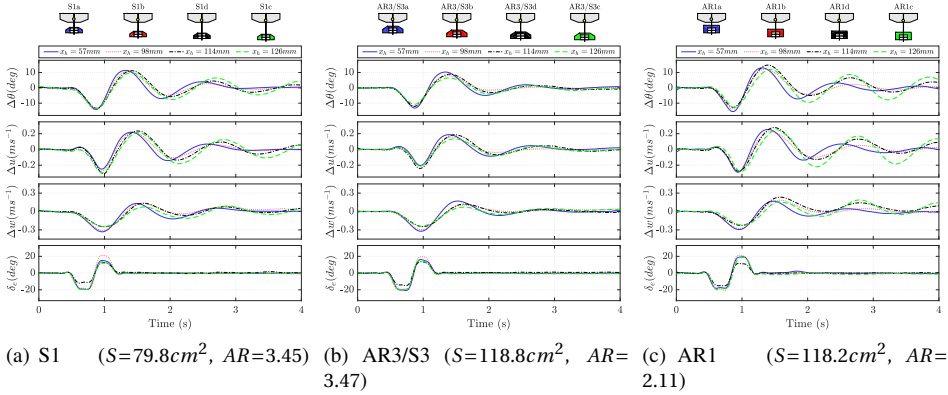
Figure B.12: Influence of longitudinal position on average time response to elevator doublet.

a significant impact on the dynamic behaviour of the FWMAV for a given tail geometry. This is visualised more clearly in Fig. B.12, which shows the results for tail configurations with varying longitudinal position. Fig. B.12(c) shows that the damping increases for longitudinal positions up to x_h=98mm, but decreases significantly when the tail position is increased beyond this for configuration AR1. The same can be observed for configuration S1, cf. Fig. B.12(a), although the difference is smaller than for AR1. By contrast, Fig. B.12(b) shows that for configuration AR3/S3 the damping of the oscillation remains high even up to x_h=126mm. Increasing the distance between the tail and the flapping wings is expected to improve the damping, as the moment arm of the tail force increases (cf. Fig. B.5). However, given that configuration S3/AR3 matches the aspect ratio of configuration S1 and the surface area of configuration AR1, the decrease in damping at high x_h, for configurations AR1c and S1c, cannot be linked directly to either the surface area or the aspect ratio of the tail.

It is hypothesised that the maximum span width of the tail plays a role in the explanation of this result. Configurations S1 and AR1 feature relatively small span widths of 158mm and 166mm, respectively, whereas configuration S3 has a larger span width of 203mm. The results observed in Fig. B.12 could be explained by the typical induced velocity profile of flapping wings, which experiences peaks at 60−70% of the flapping-wing span [14, 21] (cf. Chapter 6). In the wake of flapping wings, energy dissipates when moving downstream in chordwise direction, decreasing the magnitude of the induced velocity. The region of high induced velocity was also found to decrease in spanwise direction when moving farther away from the flapping wings, resembling a bell shape (cf. Fig. 6.5 in Chapter 6). In view of these observations, tails with a smaller span may no longer be seeing the aforementioned high induced velocity field when x_h is large, which would considerably reduce their effectiveness when the longitudinal position exceeds 98mm.

The time responses indicate changes in damping and natural frequency of the oscillatory eigenmode of the FWMAV, which can be further studied by analysing the eigenvalues of the estimated models. Fig. B.13 shows the results for varying tail aspect ratios. The plots illustrate the eigenvalues of the most representative averaged model for each configu-

(a) $x_h = 57mm$ (b) $x_h = 98mm$ (c) $x_h = 114mm$ (d) $x_h = 126mm$
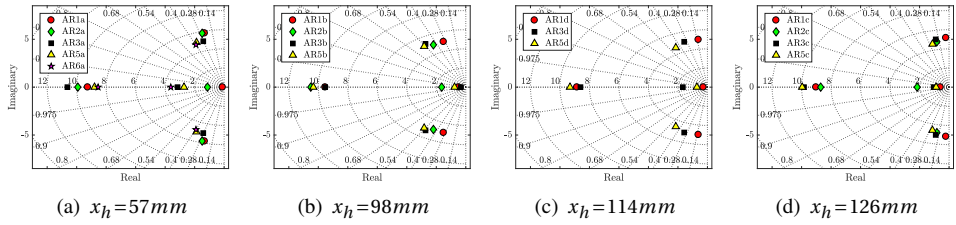
Figure B.13: Pole plots illustrating the effect of the tail aspect ratio on the system eigenvalues.

(a) $x_h = 57mm$ (b) $x_h = 98mm$ (c) $x_h = 114mm$ (d) $x_h = 126mm$
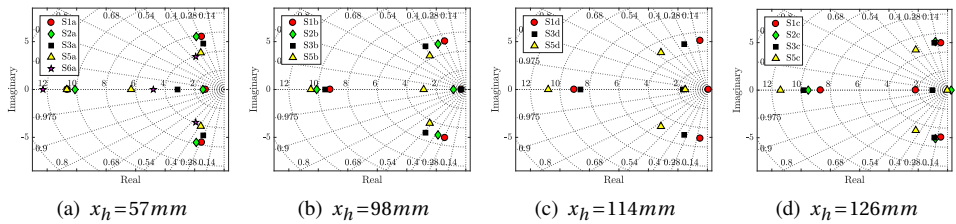
Figure B.14: Pole plots illustrating the effect of the tail surface area on the system eigenvalues.

ration, based on the validation results (cf. Table B.4). There is a clear trend in the complex conjugate pair of eigenvalues, while the real eigenvalues show less consistent trends. As discussed in Sec. B.3.3, the real eigenvalues of the individual models were generally less consistent than the complex conjugate eigenvalues (cf. Fig. B.4(b)), although it is clear that the ornithopter has two aperiodic eigenmodes with eigenvalues at approximately -1 and -10 (cf. Chapter 4).

In line with the time response results in Fig. B.10, increasing the tail AR slightly reduces the natural frequency of the response and has a slight positive effect on the damping for $x_h = 57mm$ (cf. Fig. B.13(a)). For $x_h = 114mm$ and higher, Figs. B.13(c) and B.13(d) show that increasing the AR leads to significant improvements in damping but hardly affects the natural frequency.

Fig. B.14 shows the pole-zero plots for different tail surface areas. The results are similar to those obtained for a varying AR and are again in agreement with what was observed in the average time responses in Fig. B.11. The complex conjugate eigenvalues for the two largest tail configurations, S5a and S6a in Fig. B.14(a), are in fact very similar, which echoes the marginal difference in the time response observed in Fig. B.11(a).

By contrast, the longitudinal position of the tail has a less straightforward but nonetheless significant effect on the system. For $x_h = 57mm$ (Fig. B.14(a)), a larger surface area mainly affects the natural frequency of the response; whereas for $x_h = 98mm$ (Fig. B.14(b)), $x_h = 114mm$ (Fig. B.14(c)) and $x_h = 126mm$ (Fig. B.14(d)) an increase in surface area mainly results in an increase in damping. These results imply that the behaviour of the system changes significantly for longitudinal tail positions between $98-114mm$. It can also be observed that configurations S1 and S3 lose considerable damping capabilities between these two fuselage lengths (cf. Figs. B.14(b) and B.14(c)). This may be related to

Table B.6: Estimated stability derivatives and standard deviations for varying S (x_h=98mm).

Param	S1b $\hat{\theta}$	S1b $100\|\hat{\sigma}/\hat{\theta}\|$	S2b $\hat{\theta}$	S2b $100\|\hat{\sigma}/\hat{\theta}\|$	S3b $\hat{\theta}$	S3b $100\|\hat{\sigma}/\hat{\theta}\|$	S5b $\hat{\theta}$	S5b $100\|\hat{\sigma}/\hat{\theta}\|$
M_q	-4.41e-04	0.48	-6.46e-04	0.57	-7.30e-04	0.49	-9.03e-04	0.54
M_u	-1.90e-03	0.45	-1.79e-03	0.64	-2.06e-03	0.67	-1.70e-03	0.66
M_w	-3.76e-05	23.30	-7.91e-04	2.05	-6.59e-04	1.56	-1.27e-03	0.82
X_q	1.89e-02	0.77	1.85e-02	1.05	2.93e-02	0.47	3.15e-02	0.50
X_u	-1.30e-01	0.56	-1.26e-01	0.45	-1.34e-01	0.34	-1.43e-01	0.23
X_w	-1.13e-02	6.06	-4.13e-02	1.57	-2.12e-02	1.56	-3.06e-02	0.98
Z_q	-1.26e-03	19.63	1.79e-03	24.20	1.36e-03	29.17	-2.22e-03	11.04
Z_u	1.84e-02	4.56	1.78e-02	5.96	-7.86e-04	123.50	1.58e-02	3.67
Z_w	-1.07e-02	4.16	-9.43e-03	8.10	2.05e-03	23.80	-1.79e-02	2.71

the strength of the flapping-wing wake, and in particular to the free-stream velocity becoming dominant over the flapping wing-induced velocity at larger distances from the flapping wings. This implies that at larger distances from the wings the horizontal tail most likely acts as a flat plate translating at high angle of attack, which in turn causes a significant decreases in aerodynamic force generation [12]. The wake modelling study conducted in Chapter 6 for the same test platform indeed confirms that overall the wing-induced velocity decreases significantly with increasing distance from the flapping wings. Nonetheless, more advanced wake modelling is recommended to further investigate the interaction between free stream and wing-induced flow, and particularly to determine at what distance from the flapping wings the free-stream component starts to become dominant.

The ability to design configurations with specific dynamic properties based on the tail geometry would be an asset for FWMAV development. To some extent, this could be done based on the previously discussed trends in the eigenvalues (or, equivalently, in the system damping and natural frequencies). Alternatively, a perhaps more flexible approach would be to exploit correlations between specific model parameters and tail geometry-related variables. In addition to considering the dynamics, a brief evaluation was hence made of the individual model parameters.

As an example, Table B.6 shows the estimated stability derivatives, and corresponding standard deviations, for varying surface area. These are the model parameters of the most representative average models, which for all the configurations in this example was the RA model. The parameter values in Table B.6 are in the same order of magnitude as those found in previous system identification work performed for this FWMAV (cf. Chapter 3 or Ref. [9]). In agreement with previous results in this chapter and throughout this thesis, the parameters related to the body z_B-axis and to the w velocity component have higher estimated standard deviations, however, overall the standard deviations are low and do not highlight any issues in the estimation process. Nonetheless, Table B.6 does not immediately reveal clear trends in the model parameters with the surface area, and, in general, identifying trends in the model parameters based on the tail geometry proved to be difficult using the current models. This is likely due to the small scale issues discussed in Chapter 4, which imply that small errors in the data and models have a significant effect, and that trends in the dynamics may not be as clearly visible in the separate parameters. Furthermore, the model structure used in this study was not optimised in any way, and therefore it is likely that some parameters are superfluous and may additionally render the trends in the remaining

(a) As a function of AR.

(b) As a function of surface area.
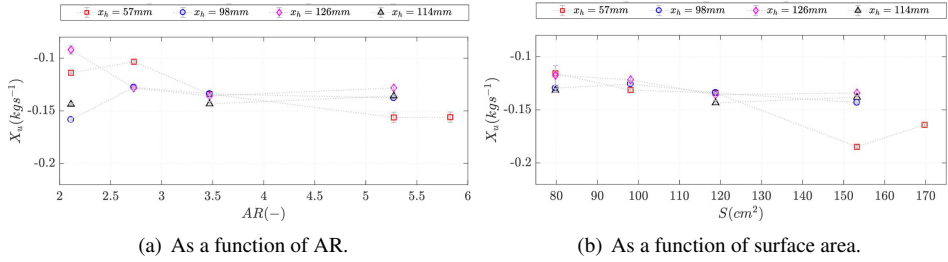
Figure B.15: Effect of tail geometry on X_u, estimated from free-flight and wind tunnel data.

(a) As function of AR.

(b) As function of S.
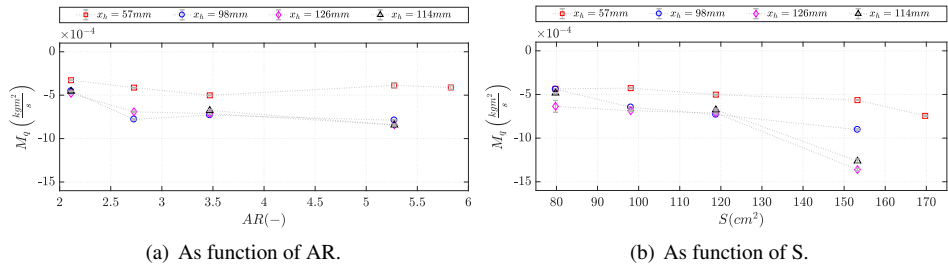
Figure B.16: Effect of tail geometry on $\mathbf{M_q}$.

parameters less clear.

Despite the aforementioned limitations, the parameters expected to be most dominant in determining the overall system dynamics and/or most connected to the tail, were evaluated individually, i.e., X_u, M_q, M_u and X_q. For the sake of clarity, only the parameter values from the most representative model were considered for each configuration.

X_u is a measure of the drag force resulting from changes in forward velocity. Fig. B.15 shows that X_u is approximately constant for different aspect ratios, whereas it displays a slight upward trend with an increasing tail surface area. This is in line with expectations, as a larger surface area translating through air leads to a higher drag force. However, the obtained results show only vague trends that were considered insufficiently reliable and clear for a model of X_u as a function of tail surface area to be developed.

M_q determines the corrective moment generated in response to pitch disturbances, and should be negative for dynamic stability. Fig. B.16 shows the obtained estimates as a function of tail geometry. Again, the surface area appears to have more effect on this parameter, however a trend can also be recognised with the aspect ratio. Increasing the AR or surface area leads to an increase in the magnitude of M_q, in line with earlier results showing an increase in damping with increased tail surface area or AR (cf. Figs. B.13 and B.14). As observed previously, the surface area appears to affect the damping capabilities of the tail surface more than the aspect ratio (larger increase in magnitude of M_q in Fig. B.15(b)), especially for configuration S5 ($S=153.3cm^2$). The obtained results suggest that increasing the aspect ratio and/or surface area increases the tail force F_h, which in turn leads to a larger stabilising moment being generated by the tail (cf. Fig. B.5). Additionally, the added mass

(a) As function of AR.

(b) As function of S.
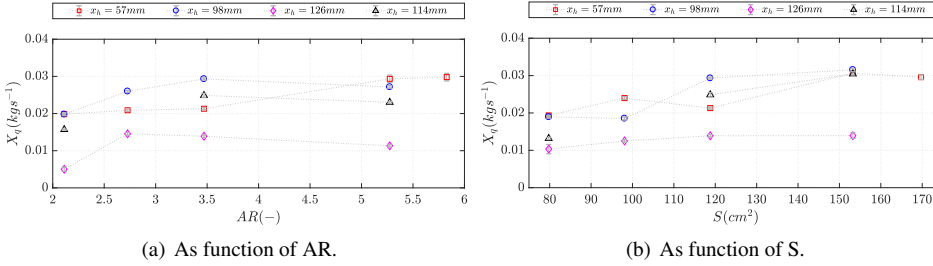
Figure B.17: Effect of tail geometry on $\mathbf{X_q}$.

force may also play a role: as the ornithopter experiences accelerations, it is subjected to a reaction force of the accelerated fluid surrounding it. In Chapter 5, the added mass of the wing was modelled as that of a flat plate, i.e., as a quadratic function of the chord length integrated along the span [20]. Assuming the same formulation for the tail would help explain the larger variation in M_q for increasing surface area, as the S-series tails feature a larger variation in chord length (cf. Table B.2). It can also be observed in Fig. B.16 that M_q is not significantly influenced by the longitudinal position of the tail. This suggests that changes in damping for a specific tail at different longitudinal positions may result more from an increase in inertia (I_{yy}) than from changes in the aerodynamic effect of the tail. Increasing the longitudinal position of the tail from $x_h=57mm$ to $x_h=126mm$ increases the inertia moment I_{yy} by an average of 150%. The results in B.16 indicate that the aerodynamic damping capabilities of most tail geometries increase up to $x_h=98mm$, while inertia effects become dominant when the distance between tail and wings is increased further.

The cross-coupling terms M_u and X_q are also important parameters in determining the oscillatory response of the system. As shown in Fig. B.17, increasing the tail aspect ratio or surface area leads to a slight increase in X_q, hence improving the damping capability of the tail. The longitudinal position also appears to influence the magnitude of X_q, however there is no clear trend. X_q increases in magnitude with increasing longitudinal position up to $x_h=98mm$ and then decreases again for $x_h \geq 114mm$ (this is especially clear in the results for $AR=3.47$ in Fig. B.17(a)). Fig. B.18 does not highlight any significant effect of the tail geometry on the magnitude of M_u. There is however a visible trend with the longitudinal position of the tail. In particular, the results indicate that coupling between the velocity along the x_B-axis and the pitching moment increases when the tail is moved farther away from the wings. This can be explained by the increase in the moment arm of *both* the wings and the tail with increasing x_h. The negative sign of M_u indicates that an increase in body velocity u leads to a negative, i.e., pitch up, moment change. This, and the fact that M_u does not appear to change significantly with tail geometry, implies that the wing force is dominant in contributing to M_u.

In general, despite the similar predicted system dynamics, the averaged models for a given configuration were found to display significant variations in model parameters. This suggests that some model parameters, such as Z_u and X_w, have little effect on the pitch dynamics. The results in Table B.6 support this hypothesis, as the relatively high standard deviations of some of the parameters do not have a significant impact on the overall per-

(a) As function of AR.

(b) As function of S.
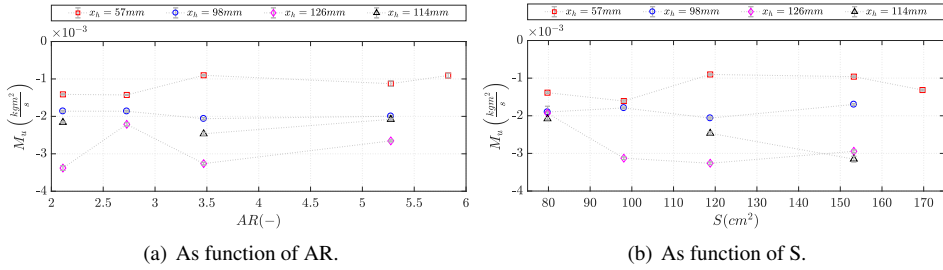
Figure B.18: Effect of tail geometry on $\mathbf{M_u}$.

formance of the models. For a better understanding of the individual model parameters and specific effects it is advisable to further investigate the model structure. It may for instance be beneficial to use a similar approach as in Chapter 4 to determine a more suitable structure, or even directly to use the simplified model structure from Chapter 4.

B.4.3. EFFECT OF TAIL SPAN WIDTH

From the results in Fig. B.12, the hypothesis arose that the span width of the horizontal tail has a significant effect on the dynamic behaviour of the test platform (and, presumably, of similar FWMAVs). As discussed, the behaviour of tail configurations with the same AR and surface area seems to vary significantly when the distance between the tail and the flapping wings is large. This prompted further investigation of the effect of the tail span. To illustrate this effect more clearly, Fig. B.19 for instance shows the time responses for several different tails as a function of their maximum span. It can be observed that there is a considerable difference in response between configurations T3a and S1a in Fig. B.19(a): the response for T3a starts oscillating heavily about its steady condition even under the influence of a smaller elevator input, while configuration S1a is well-damped. Configurations T3b and T3c even tended to be destabilised by 30% elevator deflections, making it difficult to accurately estimate LTI models for these configurations. The difference in response behaviour seen in Fig. B.19(a) is more extreme than expected from the difference in surface area and aspect ratio alone, based on the results in Figs. B.10 and B.11. It is thus hypothesised that the increased span width of configuration S1a may be contributing to the aforementioned significant increase in damping, since the induced velocity in the in-board region of the tail decreases significantly [6, 14, 21] (cf. also Chapter 6).

This hypothesis is supported by Figs. B.19(b) and B.19(c), which show results for two configurations with similar maximum span (S1 and AR1) and one configuration with a wider span (AR3/S3), at two different longitudinal positions x_h. Despite differences of 63.6% and 48.2% in AR and surface area, respectively, between configurations S1 and AR1, the responses of these configurations are very similar, especially in terms of damping. Configuration AR3c, which has a larger maximum span width, shows significantly better damping capabilities despite having the same aspect ratio as configuration S1 and the same surface area as configuration AR1. The aerodynamic importance of maximum span width has previously been noted by Thomas in his study of bird tail aerodynamics [3].

Given that the AR, surface area and span width are all related through Eq. B.1, it is im-
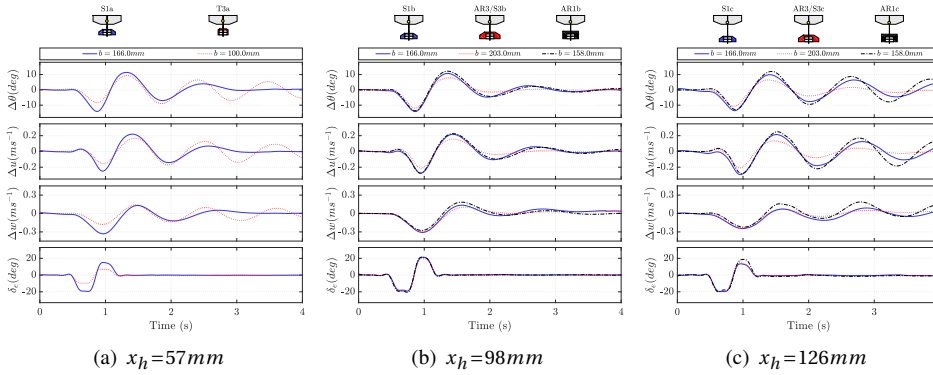
Figure B.19: Effect of tail span width on average time response.

possible to isolate the contribution of any one of these parameters to the system dynamics. Therefore additional research is needed to draw definitive conclusions about the role of the maximum span width. More advanced wake modelling studies, building on the research presented in Chapter 6 may yield better insight into the flow conditions at the tail and may thus help to quantify and assess the effect of the tail span width on the resulting system behaviour.

B.5. CONCLUSION

This appendix discussed a systematic study into the effect of the horizontal tail on the time-averaged dynamics of a flapping-wing micro aerial vehicle (FWMAV), the DelFly II. In particular, the surface area, aspect ratio and longitudinal position of the tail were varied in order to investigate their effect on the flight behaviour. It was found that increasing the surface area and aspect ratio both result in a larger pitch down moment, thus increasing the steady-state velocity, and suggesting that the tail force increases in magnitude with increased surface area and aspect ratio. It was additionally shown that the steady-state conditions of the vehicle can be predicted from the tail geometry using simple linear relations, which may be useful for future FWMAV platform design tools. Increasing the longitudinal distance of the tail from the wings decreases the steady-state velocity, most likely due to the concurrent shift in CG position. The forces generated by the wings were found to be dominant in determining the moment equilibrium and therefore the increased moment arm of the wings results in slower flight. Results also suggest that the effectiveness of the tail decreases with increased distance to the flapping wings, possibly due to less energy being available in the wing wake. Increasing the tail aspect ratio and surface area generally increases the damping of the periodic, oscillatory eigenmode and slightly decreases the natural frequency. For increased distance to the flapping wings, the effect on the natural frequency becomes less pronounced but significant changes in damping were observed. Some tail geometries experienced a significant decrease in damping capabilities at longitudinal positions exceeding $98mm$. This appears to be connected to the span width of the tail surface rather than its surface area or aspect ratio only. More research into the effect

of maximum tail span width is thus recommended. Trends were identified in some stability derivatives (M_q, X_q, M_u and X_u), however, the current confidence level is not considered sufficient to allow for prediction of the dynamics based on the tail geometry. In future studies, it is recommended to focus more on the system identification cycle to improve model accuracy, e.g., by optimising the model structure or the input signals. In the context of novel FWMAV platform designs, it is suggested to systematically study the effect of a non-zero angle of the horizontal tail with respect to the fuselage. Some birds tilt their tails for flight control purposes and it should be interesting to study the potential benefits of such a feature for robotic flappers. Future research may also focus on the vertical tail surface and its effects on the lateral dynamics of the ornithopter. Finally, further insight in the tail aerodynamics and its interaction with the flapping wing wake may provide a better understanding of the tail and allow for more quantitative conclusions to be drawn.

REFERENCES

[1] F. G. J. Rijks, M. Karásek, S. F. Armanini, and C. C. de Visser, *Studying the effect of the tail on the dynamics of a flapping-wing mav using free-flight data,* in *AIAA Atmospheric Flight Mechanics Conference*, AIAA Paper 2018-0524 (2018).

[2] G. C. H. E. de Croon, K. M. E. de Clercq, R. Ruijsink, B. D. W. Remes, and C. de Wagter, *Design, aerodynamics, and vision-based control of the DelFly,* International Journal of Micro Air Vehicles **1**, 71 (2009).

[3] A. Thomas, *On the aerodynamics of birds' tails,* Philos. Trans. R. Soc. London, Ser. B **340**, 361 (1993).

[4] D. D. Chin and D. Lentink, *Flapping wing aerodynamics: from insects to vertebrates,* Journal of Experimental Biology **219**, 920 (2016).

[5] G. C. H. E. de Croon, M. Perçin, B. D. W. Remes, R. Ruijsink, and C. De Wagter, *The DelFly Design, Aerodynamics, and Artificial Intelligence of a Flapping Wing Robot* (Springer Netherlands, 2016).

[6] W. Tay, H. Bijl, and B. van Oudheusden, *Biplane and Tail Effects in Flapping Flight,* in *42nd AIAA Fluid Dynamics Conference and Exhibit* (2012).

[7] W. Maybury, J. Rayner, and L. Couldrick, *Lift generation by the avian tail,* Philosophical Transactions of the Royal Society of London, Series B: Biological Sciences **268**, 1443 (2001).

[8] J. V. Caetano, C. C. de Visser, G. C. H. E. de Croon, B. Remes, C. De Wagter, and M. Mulder, *Linear Aerodynamic Model Identification of a Flapping Wing MAV Based on Flight Test Data,* International Journal of Micro Air Vehicles (2013).

[9] S. F. Armanini, C. C. de Visser, G. C. H. E. de Croon, and M. Mulder, *Time-varying model identification of flapping-wing vehicle dynamics using flight data,* Journal of Guidance, Control, and Dynamics **39**, 526 (2016).

B

[10] J. Grauer, E. Ulrich, J. E. Hubbard, D. Pines, and J. S. Humbert, *Testing and System Identification of an Ornithopter in Longitudinal Flight,* Journal of Aircraft **48**, 660 (2011).

[11] S. F. Armanini, J. V. Caetano, C. C. de Visser, M. D. Pavel, G. C. H. E. de Croon, and M. Mulder, *Modelling wing wake and wake-tail interaction for a flapping-wing aircraft,* International Journal of Micro Air Vehicles (2018), (submitted).

[12] J. D. Anderson, *Fundamentals of Aerodynamics*, 5th SI units ed., edited by J. D. Anderson (McGraw Hill, 2011).

[13] M. Perçin, H. Eisma, B. van Oudheusden, B. Remes, R. Ruijsink, and C. de Wagter, *Flow Visualization in the Wake of the Flapping-Wing MAV 'DelFly II' in Forward Flight,* in *AIAA Applied Aerodynamics Conference* (2012).

[14] S. F. Armanini, J. V. Caetano, C. C. de Visser, and G. C. H. E. de Croon, *Modelling wing wake and tail-wake interaction of a clap-and-peel flapping-wing MAV,* in *AIAA Modeling and Simulation Technologies Conference* (2017).

[15] J. V. Caetano, M. Percin, B. W. van Oudheusden, B. D. W. Remes, C. de Wagter, G. C. H. E. de Croon, and C. C. de Visser, *Error analysis and assessment of unsteady forces acting on a flapping wing micro air vehicle: Free-flight versus wind tunnel experimental methods,* Bioinspiration & Biomimetics **10** (2015).

[16] C. Rose and R. S. Fearing, *Comparison of ornithopter wind tunnel force measurements with free flight,* in *2014 IEEE International Conference on Robotics & Automation (ICRA)* (2014).

[17] L. Ljung, *System Identification Theory for the User*, 2nd ed. (Prentice Hall, Upper Saddle River, NJ, 1999).

[18] S. F. Armanini, M. Karásek, C. C. de Visser, G. C. H. E. de Croon, and M. Mulder, *Flight testing and preliminary analysis for global system identification of ornithopter dynamics using on-board and off-board data,* in *AIAA Atmospheric Flight Mechanics Conference*, AIAA Paper 2017-1634 (2017).

[19] J. V. Caetano, S. F. Armanini, C. C. de Visser, G. C. H. E. de Croon, and M. Mulder, *Data-Informed Quasi-Steady Aerodynamic Model of a Clap-and-Fling Flapping Wing MAV,* in *International Conference on Intelligent Unmanned Systems (ICIUS)* (2015).

[20] S. F. Armanini, J. V. Caetano, G. C. H. E. de Croon, C. C. de Visser, and M. Mulder, *Quasi-steady aerodynamic model of clap-and-fling flapping MAV and validation with free-flight data,* Bioinspiration & Biomimetics **11**, 046002 (2016).

[21] F. Muijres, G. Spedding, Y. Winter, and A. Hedenström, *Actuator disk model and span efficiency of flapping flight in bats based on time-resolved PIV measurements,* Experiments in Fluids **51**, 511 (2011).

C

BLACK-BOX MODELLING OF TIME-AVERAGED DYNAMICS

This appendix presents a set of black-box linear state-space models of flapping-flight dynamics, obtained by means of system identification techniques from the same flight data used in Chapter 3. These models, which cover both the longitudinal and the lateral time-averaged dynamics of the test platform, are the precursors of the models developed in Chapter 3. Representing a starting point for all further investigations, this study involved no assumptions on the model structure, aside from the selection of states to include. This means that kinematic dependencies are implicitly incorporated in the resulting models and not all model terms are physically meaningful. On the positive side, however, these models are easy to implement and to use, especially for control applications. The exploratory results summarised in this appendix showed that LTI model structures can accurately represent the dynamics of the test platform in forward flight, and may therefore be a suitable choice to model flapping-wing dynamics, for both the DelFly and other similar vehicles. Establishing a more meaningful physical connection in the model structure was nonetheless concluded to be desirable for further work, which explains the adjusted model structure used in Chapters 3 and 4. Accurate models were obtained for both the longitudinal and the lateral dynamics and shown to predict the response to validation inputs with considerable accuracy, thus allowing for a simulation of the DelFly near the stationary points considered. The identified dynamics are stable and thus in agreement with the observed behaviour of the DelFly in the considered flight regime.

C.1. INTRODUCTION

As discussed throughout this thesis, the development of flapping-wing micro aerial vehicles (FWMAVs) poses a considerable challenge owing to the complex nature of flapping-wing flight, and the consequent difficulty of developing effective models for such vehicles. Accurate aerodynamic and dynamic models are however essential in the development of new vehicles as well as to enhance the performance, reliability and – ultimately – autonomy of these vehicles. In the context of control system design and stability analysis, simple models are desirable, and hence highly simplified models have been applied to flapping-wing flyers. These models frequently use averaging to cancel out time-varying sub-flap cycle effects [2–4] and are often linear time-invariant (LTI) [5–8]. As discussed in Chapter 1, if flight data are obtainable, an attractive method to obtain accurate, low-order and easily applicable models is system identification. In this context, this appendix describes an initial investigation of the system identification approach to FWMAV modelling, constituting the preliminary basis for the work discussed in the main body of this thesis.

At the same time, the work presented constitutes the first formulation of a complete and simulation-capable dynamic model for the studied test vehicle, building on earlier work by Caetano et al. [9]. In Ref. [9], the body dynamics of the DelFly were modelled with a standard rigid-body fixed-wing aircraft formulation, and the aerodynamics were represented by an arbitrary linear model with parameters estimated from free-flight data. However, the chosen approach was found to have a number of limitations. While the estimation results predicted the aerodynamic forces with accuracy, the moments were predicted less accurately and simulations of the full system diverged within less than half a second [9]. Hence, one additional goal of this study was to obtain a simulation-capable model that accurately represents the dynamics of the system as a whole. Compared to earlier work, the proposed approach tackles the modelling problem from a different side, by laying emphasis on obtaining a full and functional model, which closely represents the dynamics as observed from flight data, without separately addressing the complex aerodynamics. Additionally, in view of the still somewhat limited knowledge of flapping-wing dynamics, and particularly of the dynamics of the chosen test vehicle, this study was used to obtain initial insight into possible model structures, providing useful indications for the more in-depth modelling in Chapter 3.

This study thus presents a set of linear black-box state-space models for the time-averaged longitudinal and lateral flight dynamics of the DelFly FWMAV. The models were obtained by means of system identification techniques from flight data collected in a motion tracking chamber and provide an effective initial description of the FWMAV's dynamic behaviour in the vicinity of a steady forward flight condition. The obtained models are additionally intended to be used for simulation purposes, improving the currently limited simulation possibilities for the DelFly. As such, they are an important first step in the dynamic modelling of the DelFly.

The rest of this appendix is structured as follows. Section C.2 briefly presents the flight test data used for this investigation. Sections C.3 and C.4 describe the modelling approach and the parameter estimation techniques used, and Section C.5 presents the main results obtained. Section C.6 closes with a summary of the main conclusions.

C.2. PLATFORM AND EXPERIMENTAL DATA

The subject of these tests is the DelFly II, described in Chapter 1 (Sec. 1.4.1). Specifically, the same specimen was used as in Chapter 3. The vehicle and coordinate system used in this study (cf. frame $B1$ in Sec. 1.4.3) were shown in Chapter 3 (Fig. 3.2).

The flight data used for these experiments were recorded in the Vicon tracking chamber of the US Air Force Research Laboratory at Wright-Patterson Air Force Base [10]. The flight testing setup and process, and the pre-processing of these data, including filtering and state reconstruction, are described in previous work by Caetano et al [10, 11]. and summarised in Chapter 1 (Sec. 1.4.2) and Chapter 3. This study is based on the same data as Chapter 3, i.e., 16 data samples for slow forward flight, containing elevator and rudder manoeuvres, specifically doublets and 211 signals.

C.3. MODELLING APPROACH

Parameter estimation typically requires a model structure to be postulated for the system being analysed. In this study, a black-box approach was chosen to model the DelFly dynamics: whilst a type of model and a model order were chosen a priori, the internal structure of this model was not specified. The model is also considered a black box in the sense that no distinction is made between the aerodynamics and the dynamics. Rather, the aerodynamics are incorporated in the overall model, which describes the propagation of the system states in response to control inputs.

As discussed previously, flapping-wing dynamics are time-varying and typically non-linear. Nonetheless, it was assumed that linearisation can provide an acceptable initial approximation within limited regions of the flight envelope. Simplified models can be useful, for instance to develop basic and computationally efficient simulation frameworks. Furthermore, the DelFly has been found to be passively stable in forward flight, and consequently the use of linear models was expected to lead to models with a practical utility. Hence, the chosen approach was deemed a logical first step prior to attempting more advanced modelling techniques.

LTI state-space model structures were assumed for the dynamics, in the well-known form

$$\dot{\mathbf{x}} = \mathbf{A}\mathbf{x} + \mathbf{B}\mathbf{u}, \qquad (C.1)$$

where $\mathbf{A}$ and $\mathbf{B}$ are time-invariant matrices containing the unknown parameters to be estimated.

This model structure implies that only the time-averaged dynamics can be captured and that the resulting models are only valid in the proximity of a particular steady flight condition. The state matrices were assumed to be full and no assumptions were made on their internal structure. The advantage of this is a high degree of flexibility, which can be useful in cases such as this where the dynamics of the system are not known in great detail and may not be accounted for by a priori assumptions. On the other hand, this limits the possibility of evaluating the results. As in a standard small-perturbations approach, the separate matrix entries, i.e. the parameters, can be interpreted to each represent the effect of one of the states on one of the outputs. However, not all of the parameters necessarily describe real physical phenomena. Similarly, given the high number of parameters, it is likely that some of the these are in fact superfluous, which may lead to problems in the

estimation process and may cause dynamic effects to be misattributed. The chosen approach was considered useful to start with because the dynamics of the DelFly are not known in great detail, however in a successive stage, and based on the current results, the physically inexplicable components will be excluded from the model structure in subsequent work (cf. Chapter 3).

In a first instance, decoupled longitudinal and lateral dynamics were assumed, in view of the simplicity and reduced order of the resulting models. The following states and inputs were selected for the longitudinal and lateral dynamics respectively,

$$\mathbf{x}_{\text{lon}} = \begin{bmatrix} q\ u\ w\ \Theta \end{bmatrix}, \quad u_{\text{lon}} = \delta_e$$
$$\mathbf{x}_{\text{lat}} = \begin{bmatrix} p\ r\ v\ \Phi \end{bmatrix}, \quad u_{\text{lat}} = \delta_r.$$

Given the linear model structure, the values in fact represent perturbations from the initial stationary condition.

C.4. PARAMETER ESTIMATION APPROACHES

This section explains the techniques used for parameter estimation and their application within this appendix. The same methods were also used in Chapters 3 and 4, with minor adjustments, therefore this section also complements the main text with a more extensive explanation of the estimation techniques.

C.4.1. ORDINARY LEAST SQUARES

Ordinary least squares (OLS) estimation is based on minimising the difference between the measured and model-calculated output of a system, quantified in terms of the squared error in the system equations. For the formulation of OLS estimation, it is assumed that at each discrete time point each measured output z of the system is equal to a linear combination of the regressors x, added to some unknown error ϵ, assumed to be Gaussian white noise and independent of the model parameters. In vector form this can be written as,

$$\mathbf{z} = \mathbf{X}\mathbf{\Theta} + \boldsymbol{\epsilon}, \tag{C.2}$$

where $\boldsymbol{\epsilon}$ is the equation error vector, $\mathbf{z}$ is the output measurement vector, $\mathbf{X}$ is the matrix of measured regressors and $\mathbf{\Theta}$ is the vector of unknown parameters.

Given the above equations, a cost function can be defined in terms of the squared error in the state equations of the system,

$$J(\mathbf{\Theta}) = \frac{1}{2}\boldsymbol{\epsilon}^T\boldsymbol{\epsilon} = \frac{1}{2}[\mathbf{z} - \mathbf{X}\mathbf{\Theta}]^T[\mathbf{z} - \mathbf{X}\mathbf{\Theta}] \tag{C.3}$$

Minimising the cost function with respect to $\mathbf{\Theta}$ yields the OLS estimator for $\mathbf{\Theta}$.

$$\hat{\mathbf{\Theta}} = (\mathbf{X}^T\mathbf{X})^{-1}\mathbf{X}^T\mathbf{z} \tag{C.4}$$

OLS estimation was conducted using the combined states and inputs defined in Sec. C.3 as regressors, and the derivatives of the states as the system output. The unknown parameters contained in the vector Θ in the above equations are thus contained in the system matrices $\mathbf{A}$ and $\mathbf{B}$ in Eq. C.1.

If $\mathbf{A}$ and $\mathbf{B}$ are defined as

$$\mathbf{A}=[a_{ii}], \quad \mathbf{B}=[b_{ij}], \qquad i=1,2,\ldots,n_x, \quad j=1,2,\ldots,n_u, \tag{C.5}$$

where n_x is the number of states and n_u is the number of inputs in the state-space system, and the regressor matrix $\mathbf{X}$ is constructed from the combined states and inputs at all N measurement points considered,

$$\mathbf{X}=\begin{bmatrix} x_{1,1} & x_{2,1} & \ldots & x_{n_x,1} & u_{1,1} & u_{2,1} & \ldots & u_{n_u,1} \\ x_{1,2} & \ddots & & \vdots & u_{1,2} & \ddots & & \vdots \\ \vdots & & & & & & \vdots & \\ x_{1,n_k} & \ldots & & x_{n_x,n_k} & u_{1,n_k} & \ldots & & u_{n_u,n_k} \end{bmatrix}, \tag{C.6}$$

the estimation problem for each output z_i, i.e. each row in the original state-space system, can be formulated as,

$$\mathbf{z}_i := \begin{bmatrix} \dot{x}_{i,1} \\ \dot{x}_{i,2} \\ \vdots \\ \dot{x}_{i,n_k} \end{bmatrix} = \mathbf{X}\Theta + \begin{bmatrix} \epsilon_{i,1} \\ \epsilon_{i,2} \\ \vdots \\ \epsilon_{i,n_k} \end{bmatrix}, \quad \Theta := \begin{bmatrix} a_{i1} \\ a_{i2} \\ \ldots \\ a_{in_x} \\ b_{i1} \\ b_{i2} \\ \ldots \\ b_{in_u} \end{bmatrix}. \tag{C.7}$$

Each row in the regressor matrix thus represents the measurements for a separate time point. The elements inside the parameter vector represent the entries of the matrices $\mathbf{A}$ and $\mathbf{B}$ relevant to the considered output. OLS effectively treats the equation for each output separately, so each row i in the system matrices $\mathbf{A}$ and $\mathbf{B}$ is estimated separately, according to Eq. C.7.

Direct measurements of the state derivatives were not available, but were obtained via numerical differentiation of the state measurements, by means of a three-point difference technique. The hereby introduced noise was partly dealt with through additional filtering.

The main drawback of OLS, as apparent from Eq. C.2, is that the error term can only account for Gaussian white noise in the output measurements and that the regressor measurements must therefore be assumed to be error-free. Errors in the regressors can be considered using alternative techniques, such as total least squares or maximum likelihood-based estimation. Another possibility is to minimise the effect of measurement error by pre-processing the estimation data e.g. by means of state estimation techniques. This leads to the so-called two-step method [12]. As mentioned previously, the data used for these tests had been pre-processed in the context of earlier research [11]. The application of an OLS estimator was thus expected to lead to acceptable results. This estimation technique was also chosen in view of its computational and conceptual simplicity, which allows for a solution to be found in a single step and as long as the regressor matrix $\mathbf{X}$ is invertible. Furthermore, if the assumptions made on the error term (white Gaussian noise, uncorrelated with the regressors), the resulting parameter estimates are unbiased, consistent and efficient.

C.4.2. MAXIMUM LIKELIHOOD ESTIMATION

The ML estimator was used here within a formulation sometimes known as output error method (OEM), which allows for consideration of measurement error but not of process noise, and hence assumes the system to be deterministic. The cost function for this type of problem can be defined as the negative logarithm of the likelihood function expressing the probability p of an observation $\mathbf{z}$ occurring at a particular time point k, given the parameter vector Θ,

$$J(\mathbf{\Theta}, \mathbf{R}) = -\ln p(\mathbf{z}|\mathbf{\Theta}) = \frac{1}{2} \sum_{k=1}^{n_k} [\mathbf{z}(k) - \mathbf{y}(k)]^T \mathbf{R}^{-1} [\mathbf{z}(k) - \mathbf{y}(k)] + \frac{n_k}{2} \ln[\det(\mathbf{R})] + \frac{n_k n_y}{2} \ln(2\pi)$$

(C.8)

where $\mathbf{R}$ is the measurement noise covariance matrix, n_k is the number of data samples, n_y is the number of output variables measured, and $\mathbf{z}(k)$ and $\mathbf{y}(k)$ are the measured and model-predicted outputs, respectively, at time point k.

The error covariance matrix $\mathbf{R}$ appearing in the above expression was estimated separately from the parameters at the start of each iteration step. For this the parameters were fixed at the value found in the previous iteration and the cost function was minimised with respect to $\mathbf{R}$, which leads to the following expression [13],

$$\hat{\mathbf{R}} = \frac{1}{n_k} \sum_{k=1}^{n_k} [\mathbf{z}(k) - \mathbf{y}(k)][\mathbf{z}(k) - \mathbf{y}(k)]^T.$$

(C.9)

Substituting the above expression into the cost function in Eq. C.8 and omitting the constant terms yields a significantly reduced expression to calculate the cost at the current iteration step and determine whether the convergence criteria have been met.

$$J(\mathbf{\Theta}) = \det\{\mathbf{R}\}$$

(C.10)

To estimate a new set of parameters for the successive iteration step, the original cost function in Eq. C.8 must be considered again. The error covariance matrix has been determined from the previous set of parameters by means of Eq. C.9, and is therefore considered known and constant, whereas the model-predicted outputs are now a function of the unknown set of parameters for the coming iteration step. Hence, the second and third terms in Eq. C.8 are now constant and only the first term must be minimised with respect to the parameter vector, leading to the cost function,

$$J(\mathbf{\Theta}) = \frac{1}{2} \sum_{k=1}^{n_k} [\mathbf{z}(k) - \mathbf{y}(k)]^T \mathbf{R}^{-1} [\mathbf{z}(k) - \mathbf{y}(k)].$$

(C.11)

The above expression can be minimised by means of any suitable algorithm, and yields the parameter update step and thence a new set of parameters for the following iteration step. In this study, a Gauss-Newton technique was applied, which is based on approximating the cost function derivative with a second-order Taylor series expansion.

$$\left(\frac{\partial J}{\partial \mathbf{\Theta}}\right)_{i+1} \approx \left(\frac{\partial J}{\partial \mathbf{\Theta}}\right)_i + \left(\frac{\partial^2 J}{\partial \mathbf{\Theta}^2}\right)_i \Delta\mathbf{\Theta}$$

(C.12)

Equating the left hand side to zero to minimise the cost, yields a linear system of equations that can be solved for the parameter update step.

$$\Delta\mathbf{\Theta} = -\left(\frac{\partial^2 J}{\partial\mathbf{\Theta}^2}\right)^{-1}\left(\frac{\partial J}{\partial\mathbf{\Theta}}\right) \tag{C.13}$$

Substituting Equation C.11 into the Equation C.13 yields the following expressions for the first and second derivatives of the cost function.

$$\frac{\partial J}{\partial\mathbf{\Theta}} = -\sum_{k=1}^{n_k}\left[\frac{\partial\mathbf{y}(k)}{\partial\mathbf{\Theta}}\right]^T\mathbf{R}^{-1}\left[\mathbf{z}(k) - \mathbf{y}(k)\right] \tag{C.14}$$

$$\frac{\partial^2 J}{\partial\mathbf{\Theta}^2} = \sum_{k=1}^{n_k}\left[\frac{\partial\mathbf{y}(k)}{\partial\mathbf{\Theta}}\right]^T\mathbf{R}^{-1}\frac{\partial\mathbf{y}(k)}{\partial\mathbf{\Theta}} + \sum_{k=1}^{n_k}\left[\frac{\partial^2\mathbf{y}(k)}{\partial\mathbf{\Theta}^2}\right]^T\mathbf{R}^{-1}\left[\mathbf{z}(k) - \mathbf{y}(k)\right] \tag{C.15}$$

The derivatives of the model-predicted outputs with respect to the parameters can be obtained using a central difference technique, by perturbing the parameter vector in both directions and calculating the model-estimated outputs with each of the perturbed vectors.

Within this study, ML-based estimation was formulated using the states, as defined in Sec. C.3, as outputs, resulting in the output equation,

$$\mathbf{z} = \mathbf{I}\mathbf{x}. \tag{C.16}$$

The cost function was minimised at each iteration using a Gauss-Newton technique, as outlined above, and the convergence criterion was defined in terms of the relative change in cost for consecutive iterations. Previously obtained OLS results were used as initial guesses for the parameters.

C.5. RESULTS AND DISCUSSION

This section presents the main results obtained. The estimated models were initially evaluated separately, in terms of visual output matching, predictive capability, plausibility of the resulting estimates and dynamics and statistical metrics. Subsequently, a brief overall comparison was drawn between the models estimated from different estimation datasets, bearing in mind the differences between the separate estimation datasets and the limitations dictated by the chosen modelling approach.

C.5.1. DECOUPLED LONGITUDINAL AND LATERAL DYNAMICS MODELS

Taken on their own, several estimated models displayed favourable properties, including plausible responses to standard inputs and overall dynamic behaviour and a fairly good predictive capability.

An example of one of the estimated models for the longitudinal and lateral dynamics, respectively, is given in the following equations, where the bracketed values are the estimated standard deviations for each parameter estimate. The standard deviations are a wholly statistical metric referring specifically to the particular model presented and do not represent an average over multiple estimation runs. Both of these models were obtained

using ML-based estimation, in the form described in Sec. C.4. All following results in this section refer to these two models.

$$
\begin{bmatrix} \dot{q} \\ \dot{u} \\ \dot{w} \\ \dot{\Theta} \end{bmatrix} = \begin{bmatrix} 3.58(0.52) & 70.89(5.42) & -134.77(3.79) & -125.46(2.66) \\ 0.22(0.04) & -1.83(0.40) & -5.87(0.48) & -8.85(0.41) \\ 0.04(0.09) & 7.68(0.57) & -22.93(0.03) & -21.26(0.03) \\ 0.44(0.05) & -1.75(0.33) & 10.75(0.13) & 9.15(0.17) \end{bmatrix} \begin{bmatrix} \Delta q \\ \Delta u \\ \Delta w \\ \Delta \Theta \end{bmatrix} + \begin{bmatrix} -64.39(2.55) \\ -0.21(0.24) \\ -8.04(0.31) \\ 2.23(0.18) \end{bmatrix} \delta_e \qquad (C.17)
$$

$$
\begin{bmatrix} \dot{p} \\ \dot{r} \\ \dot{v} \\ \dot{\Phi} \end{bmatrix} = \begin{bmatrix} -13.86(1.54) & 48.29(6.91) & -108.30(15.30) & -28.96(5.23) \\ -2.14(0.27) & 4.70(1.39) & -24.89(2.32) & -2.04(0.82) \\ 0.72(0.07) & -2.78(0.38) & 0.66(0.61) & 1.85(0.22) \\ 0.93(0.17) & -0.68(0.89) & -0.33(1.40) & -0.38(0.51) \end{bmatrix} \begin{bmatrix} \Delta p \\ \Delta r \\ \Delta v \\ \Delta \Phi \end{bmatrix} + \begin{bmatrix} -110.50(9.44) \\ -24.14(0.99) \\ 0.99(0.19) \\ 0.48(0.59) \end{bmatrix} \delta_r \qquad (C.18)
$$

The most straightforward form of evaluation consists in assessing to what extent the estimated model can reproduce the measured data. This is an essential criterion, as ultimately the purpose of any model is to effectively represent reality. In particular, it is desirable for a model to be capable of accurately reproducing not only the estimation data, but any set of data obtained from the same system. To assess the predictive capability of the models, the datasets not used in the estimation of the particular model being analysed were used for validation purposes. A sample of results obtained from the models reported in Eqs. C.17 and C.18 above is presented as an example.

Fig. C.1 shows the measured and model-predicted values for the estimation dataset. It can be seen that there is a good agreement between the real and the simulated values, with only minor discrepancies, e.g. in the bank angle response, where the model is slightly quicker than the real system. A quantitative evaluation was also made in terms of the correlation between measured and model-estimated outputs, reported in Table C.1. It can be seen that the values mostly range approximately between 0.80 and 0.98, confirming the good agreement already established visually. The only exception to this is the relatively low correlation for the roll rate p. The obtained value of 0.597 is unexpected given the observed closeness of the model to the measurements. A possible explanation could be the larger amount of noise in said output, which the chosen metric would simply consider as system dynamics not captured by the model. This would also explain the comparatively low value obtained for the pitch rate q.

Table C.1: Correlation between measured and model-estimated outputs.

Output variable	q	u	w	Θ	p	r	v	Φ
Corr. coeff.	0.80	0.87	0.93	0.98	0.60	0.82	0.90	0.87

Two validation examples for the longitudinal and lateral model, respectively, are shown in Figs. C.2 and C.3. Overall, both models prove to be capable of providing reasonably good predictions of the validation data. Nonetheless, there are a few discrepancies between measured and simulated progressions. Most of these are likely to be related either to shortcomings in the estimation data or to limitations of the chosen modelling approach. The difference in yaw rate r response in the left hand plot of Fig. C.3 for instance suggests that
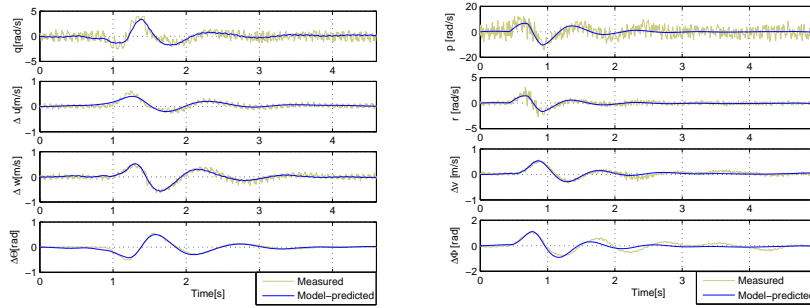
Figure C.1: Measured and model-estimated responses for the **identification** datasets: longitudinal model (left), lateral model (right).
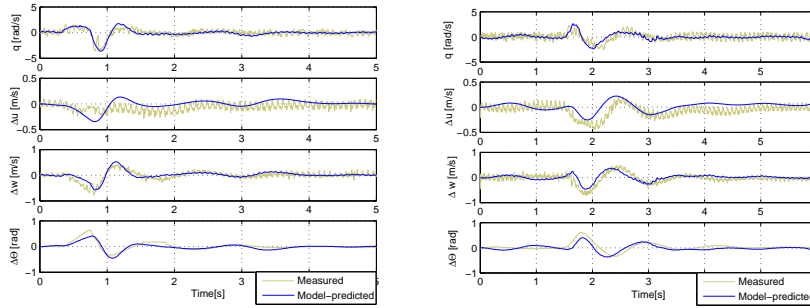
Figure C.2: Longitudinal model **validation**: measured and model-estimated responses for two validation datasets containing elevator 2-1-1 and doublet manoeuvres, respectively.
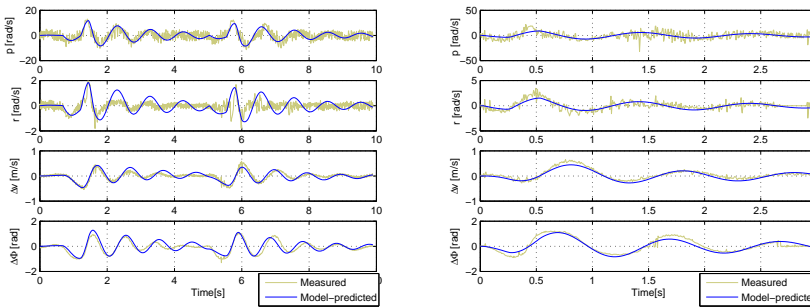
Figure C.3: Lateral model **validation**: measured and model-estimated responses for two validation datasets containing rudder 2-1-1 and doublet manoeuvres, respectively.

some component in the dynamics of the estimation data that was assumed to affect the yaw rate, has a diminished effect in the validation data, or may have been erroneously estimated to affect the yaw rate in the identification process. Something analogous appears to happen in the horizontal velocity u response. Despite the single shortcomings, the overall performance is considered effective, particularly considering the simplicity of the postulated model structure.

In statistical terms, the estimation process can be considered relatively effective, again particularly in view of the significant difference in complexity between model and real system. Most of the estimated standard deviation values shown in Eqs. C.17 and C.18 are small, typically below 20% of the estimate they refer to, and often significantly lower than this in the longitudinal model. The most notable exception to this are the relatively high standard deviations relating to the terms in the $\dot{\Phi}$ equation. Several of these are larger than the estimate values they refer to, suggesting that the corresponding parameters are badly estimated and may be superfluous. This could be explained by means of flight dynamics considerations; in fact it is evident that many of these terms have no physical meaning and could probably be omitted from the model. It can further be noted that these are the parameters with the smallest magnitudes, and thus would be difficult to estimate in any case since they have a comparatively small impact on the system dynamics. Hence the result suggests that certain parameters should be removed for an improved estimation performance.

The estimates themselves can also be evaluated qualitatively to some extent, based on what is known on FWMAV dynamics in general and DelFly dynamics specifically, as well as in terms of general flight dynamics theory, to the extent that it applies to flapping-wing vehicles. It is interesting to note that some of the obtained values do not correspond to what would be expected from standard flight dynamics and certain theoretically physically meaningless parameters take on quite significant values, e.g. some of the parameters theoretically representing an influence of the attitude on the moments. This is largely an inevitable consequence of the black-box approach, and simply suggests that all dynamic effects not captured by the physically meaningful parameters are attributed to the remaining ones, which however are not necessarily the origin for these. In spite of this, the majority of the obtained values seem plausible. The signs mostly correspond to what would be expected in a standard aircraft and some of the most notable differences in magnitude could be a consequence of the particular dynamics of the system at hand. For instance, the influence of the yaw rate r on the rolling moment equation and the influence of the roll rate p on the yawing moment equation (often referred to as dimensional stability derivatives L_r and N_p, respectively), are relatively large, but it is known that there is in fact a high degree of roll-yaw coupling in the DelFly II which may explain this.

A further evaluation was made in terms of the statistical correlation, which allows for excessive linear dependencies between separate parameters to be identified. From the correlation matrices it was found that most parameters are sufficiently independent, particularly in the longitudinal model, where most of the values are below 0.7. A small number of high correlation values (>0.9) were found, most of these referring to roll-yaw coupling terms. This again appears to underline the high degree of roll-yaw coupling and suggests that some of the affected parameters could perhaps be omitted from the current model.

Finally, the obtained systems were evaluated in terms of the resulting dynamics. The eigenvalues of the lateral and the longitudinal dynamics models presented in Eqs. C.17

and C.18 are reported in Table C.2. From the eigenvalues it transpires that both the lateral and the longitudinal dynamics are stable and are characterised by one slow and high-frequency oscillatory mode and two aperiodic motions. It is interesting to note that the lateral model in particular is fairly similar to a standard fixed-wing model. By contrast, the longitudinal model differs more significantly. Based on its frequency and damping, the oscillatory mode could be interpreted as an analogue to the short period mode, however the remaining eigenvalues are not as easily inserted in a fixed-wing dynamics framework. They could be considered an over-damped oscillation, which again would lead to a closeness to the fixed-wing case, or simply indicate dynamic characteristics that differ from those of typical fixed-wing systems. It should be borne in mind that the platform at hand significantly differs from conventional aircraft and therefore it is not unreasonable for the dynamics to differ to some extent. In this sense, the obtained results also provide insight into the specific dynamic properties of the DelFly II.

Table C.2: Eigenvalues for decoupled models in Eqs. C.17 and C.18

Longitudinal	Lateral
$-1.318 + 5.668i$	$-1.538 + 6.950i$
$-1.318 - 5.668i$	$-1.538 - 6.950i$
-0.383	-0.242
-9.018	-5.560

The system dynamics of the estimated models were also visualised in terms of step responses, as shown in Fig. C.4. Overall, the responses seem plausible, however there are a few exceptions, for instance the non-zero final value of the pitch rate, and the constant final value of the pitch attitude for constant pitch rate, both of which phenomena are not physically explicable. These effects are likely to be a consequence of the physically meaningless terms included in the attitude derivative equations. It is also worth noting the non-minimum-phase behaviour suggested by both models, however this result must be interpreted with caution given the black-box modelling approach.

Whilst a more accurate and detailed model would have to be nonlinear and ideally time-varying, the obtained results suggest that linear state-space models can provide a simple and effective representation of time-averaged flapping-wing flight dynamics around a stationary point. This is particularly remarkable in view of the elementary model structure assumed.

C.5.2. COMPARISON OF RESULTS GIVEN BY DIFFERENT DATASETS

Given the availability of several datasets and thus of several estimated models, an additional evaluation was made in the form of an overall comparison between the results obtained from different datasets. This highlighted a number of similarities in the overall dynamics of the obtained models, as well as a degree of variation, particularly in the estimates themselves, and to a lesser extent also in the overall dynamics.

The observed variation was largely expected, particularly in the separate estimates, given the black box approach and the high number of parameters. Furthermore, given that
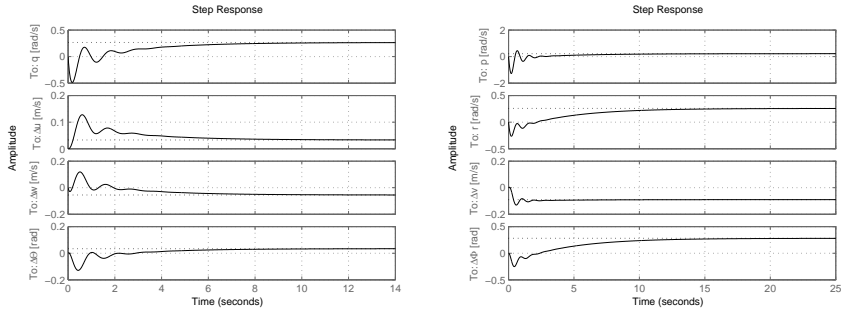
(a) Response of longitudinal dynamics model to a 5° elevator step input.

(b) Response of lateral dynamics model to a 5° rudder step input.

Figure C.4: Step responses of the model in Eqs. C.17 and C.18.

the model structure implied validity only around a specific steady flight condition, and that the different datasets were obtained around at least slightly different flight conditions and using different input manoeuvres, even in an ideal case the estimated models for different datasets would not have been identical. However, it was assumed that the overall dynamics would be at least approximately qualitatively comparable, since the different datasets were obtained in similar fast forward flight conditions and using comparable input manoeuvres. Thus the eigenmodes of the obtained models were compared. Fig. C.5 shows polar plots of the eigenvalues of all the lateral and longitudinal models estimated.
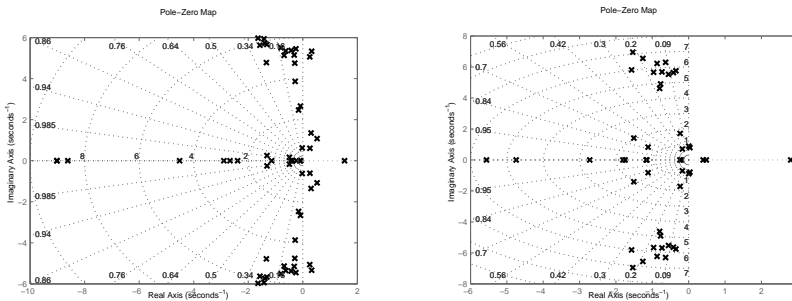
(a) Poles of estimated longitudinal dynamics models.

(b) Poles of estimated lateral dynamics models.

Figure C.5: Pole plots comparing the models estimated from different sets of estimation data.

It can be seen that although the results are somewhat scattered, the majority of the oscillatory poles are clustered within fairly small areas, in both the longitudinal and the lateral dynamics plots. This suggests that the majority of the models have similar oscillatory modes. The remaining eigenvalues are more scattered, with varying dynamic properties and in some cases varying stability. Regarding stability, it can however be observed that

the majority of the models are stable. Whilst this is not in itself an indication of model accuracy, it agrees with the observed flight behaviour of the DelFly, which indeed suggests a stable platform. Furthermore, the good performance of some of these models even when applied to validation data suggests that a stable model is adequate at least to capture the dynamics around stationary flight conditions.

C.5.3. COMPARISON OF DIFFERENT ESTIMATION APPROACHES

A number of differences were remarked between the results given by the two estimation approaches chosen. Many of these were expected in view of the different formulation of the two algorithms, nonetheless it is considered relevant to provide a brief overview of these.

In agreement with the theory, OLS results were obtained for all datasets considered and were generally more consistent across different datasets than their ML counterparts. By contrast, ML-based estimation led to a larger variation in results and entailed an inevitable uncertainty of getting a meaningful result in the first place. Given that ML estimation is an iterative minimum search, there is no guarantee that any solution will be found and no guarantee that an obtained solution is a global optimum. Several problems were encountered in the application of ML-based estimation, including failure to converge, and convergence to meaningless solutions. On the other hand, however, when ML results were obtained, they typically proved to be more effective than their OLS correspondents, as for instance shown in the example in Fig. C.6. This again was expected, as ML makes less restrictive assumptions than OLS, for instance in allowing for noise in the states.
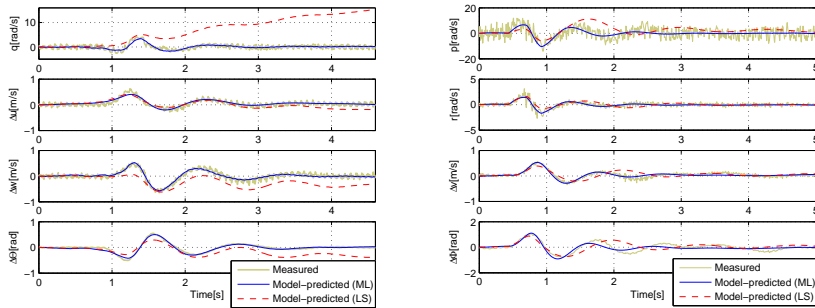
(a) Output match for longitudinal dynamics models.

(b) Output match for lateral dynamics models.

Figure C.6: Comparison of output match for OLS and ML-estimated models obtained from the same dataset.

Ultimately the chosen combination was found to be a good solution, as OLS estimation could be relied upon to yield results from all datasets and thus make use of all the available information, and ML could be used to obtain more accurate models where possible.

C.6. CONCLUSION

System identification methods were applied to free flight data to obtain black-box linear state-space models for the time-averaged longitudinal and lateral flight dynamics of an FW-MAV around steady conditions in fast forward flight. Estimation was conducted using both ordinary least squares and maximum likelihood estimators and thanks to the availability of several datasets recorded in similar flight conditions, a number of separate models could be estimated and compared. Several effective models were obtained, which were shown to have a good predictive capability and whose dynamic properties are considered plausible. The obtained LTI models both provide information about the flight dynamics of the DelFly and can be used in a first instance to effectively simulate the vehicle in reasonable proximity of steady forward flight conditions. This constitutes an enhancement to the current simulation capabilities, and may form a first step towards onboard attitude control. More advanced modelling will require the consideration of different flight conditions and will involve more complex model structures, for instance accounting for some of the nonlinear and time-varying effects. It will also be interesting to investigate the region of validity of the LTI models. Finally, the use of more physically meaningful model structures should be investigated further (e.g., cf. Chapters 3, 4).

REFERENCES

[1] S. F. Armanini, C. C. de Visser, and G. C. H. E. de Croon, *Black-box LTI Modelling of Flapping-wing Micro Aerial Vehicle Dynamics,* in *AIAA Atmospheric Flight Mechanics Conference* (2015) AIAA Paper 2015-0234.

[2] H. Rifai, N. Marchand, and G. Poulin, *Bounded control of a flapping wing micro drone in three dimensions,* in *IEEE International Conference on Robotics and Automation* (2008).

[3] Z. A. Khan and S. K. Agrawal, *Control of Longitudinal Flight Dynamics of a Flapping-Wing Micro Air Vehicle Using Time-Averaged Model and Differential Flatness Based Controller,* in *Proceedings of the 2007 American Control Conference* (2007).

[4] X. Deng, L. Schenato, W. C. Wu, and S. Shankar Sastry, *Flapping Flight for Biomimetic Robotic Insects : Part I - System Modeling,* IEEE Transactions on Robotics **22**, 776 (2006).

[5] R. C. Julian, C. J. Rose, H. Hu, and R. S. Fearing, *Cooperative Control and Modeling for Narrow Passage Traversal with an Ornithopter MAV and Lightweight Ground Station,* in *International Conference on Autonomous Agents and Multi-Agent Systems* (2013).

[6] G. K. Taylor and A. L. R. Thomas, *Dynamic flight stability in the desert locust Schistocerca gregaria,* Journal of Experimental Biology **206**, 2803 (2003).

[7] M. Sun and Y. Xiong, *Dynamic flight stability of a hovering bumblebee,* Journal of Experimental Biology **208**, 447 (2005).

[8] I. Faruque and J. Sean Humbert, *Dipteran insect flight dynamics. Part 1 Longitudinal motion about hover*. Journal of Theoretical Biology **264**, 538 (2010).

[9] J. V. Caetano, C. C. de Visser, G. C. H. E. de Croon, B. Remes, C. De Wagter, and M. Mulder, *Linear Aerodynamic Model Identification of a Flapping Wing MAV Based on Flight Test Data,* International Journal of Micro Air Vehicles (2013).

[10] J. V. Caetano, C. C. de Visser, B. D. Remes, C. De Wagter, E.-J. Van Kampen, and M. Mulder, *Controlled Flight Maneuvers of a Flapping Wing Micro Air Vehicle: a Step Towards the Delfly II Identification,* AIAA Atmospheric Flight Mechanics Conference (2013).

[11] J. V. Caetano, C. C. D. Visser, B. D. Remes, C. D. Wagter, and M. Mulder, *Modeling a Flapping Wing MAV : Flight Path Reconstruction of the Delfly II,* in *AIAA Modeling and Simulation Technologies Conference* (2013).

[12] J. Mulder, J. Sridhar, and J. Breeman, *Identification of Dynamic Systems - Applications to Aircraft Part 2: Nonlinear Analysis and Manoeuvre Design*, AGARD Flight Test Techniques Series, AGARD-AG-300 Vol.3 Part 2 (North Atlantic Treaty Organization, 1994).

[13] R. Jategaonkar, *Flight Vehicle System Identification A Time Domain Methodology* (AIAA Progress in Astronautics and Aeronautics, Reston, VA, USA, 2006).

C

D

RESIDUAL ANALYSIS FOR LOCAL LTI MODELS

This appendix provides a brief overview of the residual analysis that was conducted in order to better evaluate the model identification results in Chapters 3 and 4, in terms of both model performance and suitability of the chosen estimator for the identification problem studied. Given that the same type of evaluation was conducted for each identification dataset, and results were qualitatively comparable, the following analysis is outlined for a single example case, viz. the time-averaged longitudinal dynamics model derived in Chapter 3. Additionally, the average model residuals of the 46 models developed in Chapter 3 are presented in concise form in Fig. D.7, to provide a basic overview of the overall performance.

Given the measurement z and corresponding model-predicted output $\hat{y}$ at each measurement time t, given the parameter set $\hat{\theta}$, the model residuals are defined as:

$$\epsilon(t) = \epsilon(t, \hat{\theta}) = z(t) - \hat{y}(t|\hat{\theta}) \tag{D.1}$$

The residuals provide additional insight into the performance of the estimated model, and the suitability of the assumptions made in the estimation process. It can for instance be evaluated whether the model structure is adequate to approximate the data, and whether the assumptions made on the noise within the estimation process are acceptable. In addition to the magnitude and distribution of the residuals, it is common to consider the autocorrelation function:

$$\mathscr{R}_\epsilon^{n_k}(\tau) = \frac{1}{n_k} \sum_{t=1}^{n_k} \epsilon(t)\epsilon(t-\tau) \tag{D.2}$$

where n_k is the sample length, τ is the time lag, and ϵ denotes the residuals. The autocorrelation function shows to what extent the residuals are correlated to previous residuals in time. If the residuals depend on their own earlier values, this indicates that they are not a stochastic process but contain some deterministic component that the model does not capture.

Prior to evaluating the results, it is important to note that the low-pass filtering introduced in the time-averaged model identification process (e.g. filter cutoff of 6Hz in the current example/ Chapter 3) to limit the effects of flapping, has a significant influence on the data and hence on the residual analysis. Firstly, a significant part of the high-frequency noise is filtered out. Given that measurement noise tends to be more concentrated at higher frequencies, this means that in the data used for estimation there is comparatively less noise and more modelling error – which in turn leads to more coloured residuals. Secondly, low-pass filtering has a somewhat similar effect to oversampling, as the sampling rate (in this example, 200Hz) is extremely high compared to the information that is obtainable from the filtered data (i.e., compared to the frequency range the *time-averaged* model attempts to capture). Effectively, the same amount of information could have been obtained with a significantly lower sampling rate. This indirectly has some effect on the results. The confidence bounds used to evaluate the autocorrelation, for instance, depend on the sample size, which adversely affects the result if the sample size is 'larger than necessary' for the amount of information it contains. It can also be remarked that there is very little difference between adjacent residuals, as the time scale of the variation that can be captured after low-pass filtering is much slower than the time scale the sampling rate would allow to be captured. For the sake of completeness, this appendix also includes the results obtained when comparing the model to the unfiltered data, to provide further insight into the quality of the model and highlight some of the problems introduced by flapping.

Fig. D.1(b) shows, for each output variables, the residuals of the example model, normalised with the range of the corresponding measurement. The residuals mostly fall within the confidence bounds and are considered adequately small in magnitude, particularly considering the experimental limitations involved in the modelling process (cf. Chapter 2). It must be noted that the definition of what constitutes an acceptable set of residuals is to some extent arbitrary and depends on the required model accuracy and on the quality of the estimation data. As already discussed in the main text, while the developed model can

be improved, particularly in some components, the major trends in the data are captured accurately (cf. Chapter 3). This is also reflected in the residuals.

Next, it can be observed that the residuals have an approximately zero mean (cf. also Fig. D.7) – suggesting there is no significant bias that is unaccounted for in the estimation. At the same time, it is also apparent that the residuals are not white. This is unsurprising, given that a real, physical system is being modelled using simplified model structures and starting from real-world, noisy data. Nevertheless, it is useful to assess to what extent the model and identification approach are acceptable, and whether the estimated parameter covariances need to be adjusted to account for the non-white noise. To help establish these points, the distribution of the residuals is plotted in Fig. D.2, in comparison to an ideal normal distribution. It is clear that the obtained distributions are not perfectly normal, however they do not differ excessively from the normal curve, suggesting that the assumption of white noise is justifiable. The plot also highlights, again, that the mean is approximately zero.

Lastly, the autocorrelation of the residuals is shown in Fig. D.3. As expected, the functions for all states peak at zero and then drop, mostly remaining within the estimated confidence bounds, or in close proximity thereof. There are some peaks outside the bounds, again underlining that the residuals are not white, however, considering that a real physical system is being modelled and considering the previously discussed effects of filtering, the overall result suggests the assumptions made can be justified.

Together, the above observations indicate that there is a deterministic component left in the residuals, thus emphasising that the model structure can be improved and does not fully describe the true system. At the same time, the residuals, together with the results discussed in Chapters 3 and 4, suggest that the current models provide a suitable approximation and the estimation approach itself is justifiable. Ultimately, a model must be judged in view of its intended application: the overall performance of the current model was found to be improvable but already highly useful, particularly considering that a simple structure was one of the a priori requirements. An improved model structure could reduce the modelling error, however it may entail a high increase in complexity at a small benefit. Based on the preceding evaluation, and on the results discussed in Chapter 3, it is concluded that the chosen estimation approach can be justified, and the model structure is sufficient for simplified modelling. However, it is advisable to consider the fact that the residuals are coloured when evaluating the estimated variances of the parameter estimates. Different approaches have been suggested for this, e.g., simply multiplying all parameter covariances by an arbitrary 'fudge factor' (typically between 5 and 10) [1, 2], or reformulating the expression for the parameter covariance matrix to take into account the residual autocorrelation [3].

A number of additional observations can be made by considering the figures showing the comparison to unfiltered data. As a clarification, if must be noted that the high-frequency content appears much lower in the pitch attitude than in the other variables because all other variables were obtained via differentiation and hence suffered from noise amplification (cf. Chapter 3). Fig. D.1(c) shows that if the data are not filtered, the periodic, flapping-related content becomes the dominant component in the residuals and the deterministic modelling error becomes less evident (cf. also Fig. D.2(c)). The residuals are larger in magnitude, largely due to the flapping effect (rather than stochastic noise), which the time-averaged model is not intended to capture. The residual distribution is closer to

a normal one for the unfiltered data, and the autocorrelations are generally lower, suggesting that indeed a significant portion of the noise is concentrated at higher frequencies and removed by the low-pass filtering. This highlights once more that residual analysis based on filtered data tends to magnify the modelling error. It can further be observed that the flapping harmonics clearly emerge in the autocorrelation plot, in the form of peaks. While the statistical properties of the residuals are slightly better when the data are not filtered, presumably due to the reasons mentioned previously, the magnitude of the residuals is increased and using unfiltered data was found to yield less accurate modelling results and more frequent divergence of the estimator. One of the challenges in the studied vehicle is that the flapping frequency is very low and therefore filtering out the flapping frequency inevitably filters out a significant part of the noise, leaving behind only low-frequency noise in the same range as the modelling error.

In a practical sense, the essential requirement of a model is for it to replicate the real system. In this sense, it is also important to consider the output given by the model, particularly when compared with validation data. Figs. D.4–D.6 show the example model's residuals when tested against validation data (the same example as shown in Chapter 3). It can be seen that, overall, the performance is slightly less satisfactory than in the estimation data case, with the residual means moving slightly farther away from zero. There are also more residuals ranging outside the confidence bounds (which are estimated based on the estimation data). Nonetheless, the overall performance is comparable to the estimation data case, except for the u-velocity component (velocity parallel to the body fuselage), which is estimated with a considerable bias. As discussed in Chapter 3, this component proved the most difficult to estimated, and it was hypothesised that the data were not sufficiently informative for the purpose. Moreover, another problem is highlighted here: as clear from Fig. 3.7 in Chapter 3, the velocity does not begin at an entirely steady position and does not fully return to the initial condition after the manoeuvre, despite the signal being at zero. This suggests that there is some unconsidered effect, e.g., throttle or rudder input, or non-linearity in the dynamics. As already discussed in the text, the velocity estimation must therefore be improved in future work.

The mean residual for all models identified in Chapter 4 are presented in Fig. D.7. Qualitatively, results were similar as for the discussed example.

(b) Model versus filtered data.

(c) Model versus unfiltered data.
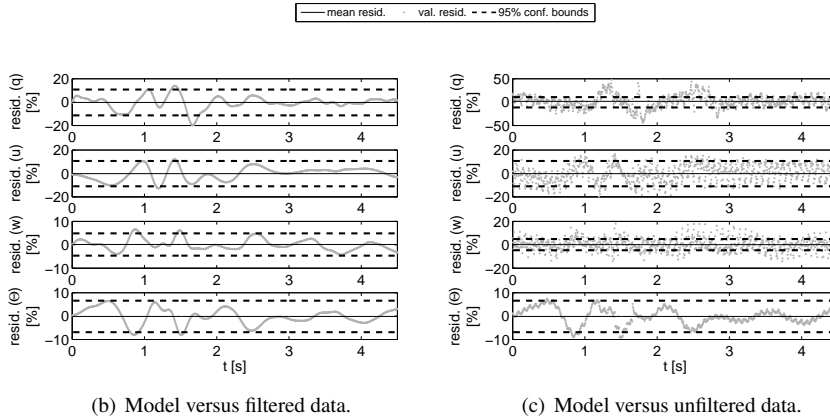
Figure D.1: Residuals of the longitudinal dynamics model identified in Chapter 3 (cf. Fig. 3.6).

(b) Model versus filtered data (as in estimation process).

(c) Model versus unfiltered data.
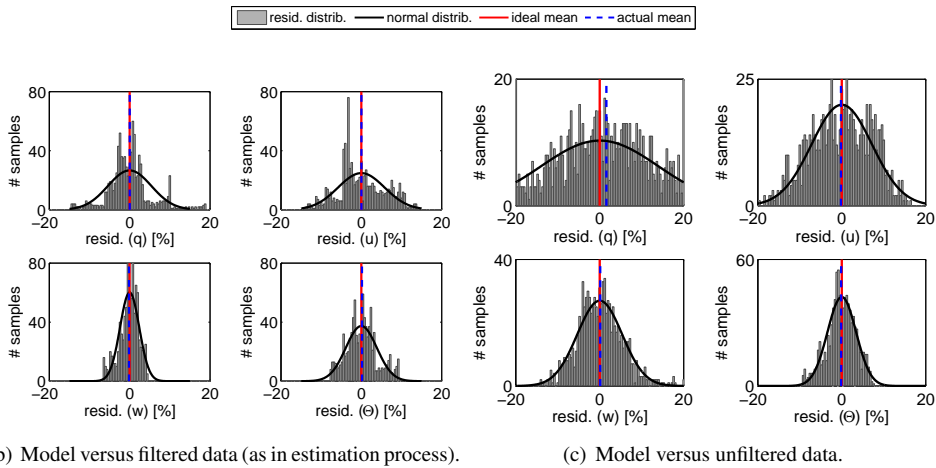
Figure D.2: Distribution of the residuals of the longitudinal dynamics model identified in Chapter 3 (cf. Fig. 3.6).

(a) Model versus filtered data.

(b) Model versus unfiltered data.
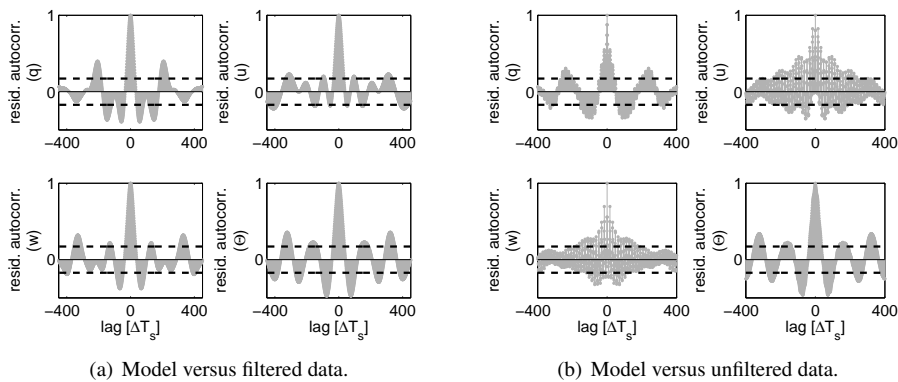
Figure D.3: Autocorrelation of the residuals of the longitudinal dynamics model identified in Chapter 3 (cf. Fig. 3.6); 99%-confidence bounds shown.
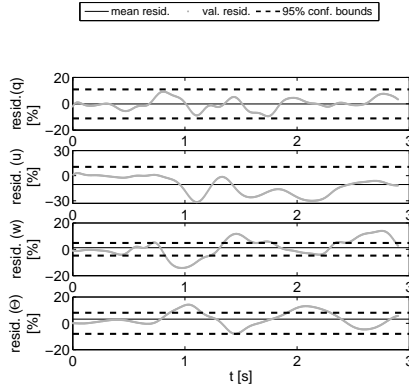
Figure D.4: Residuals of the time-averaged longitudinal dynamics model identified in Chapter 3, compared to validation data (cf. Fig. 3.7).
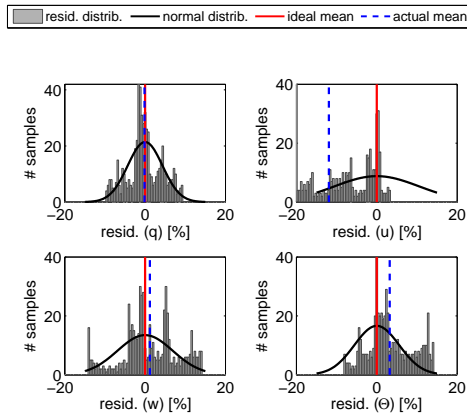
Figure D.5: Distribution of the residuals of the time-averaged longitudinal dynamics model identified in Chapter 3, compared to validation data (cf. Fig. 3.7).
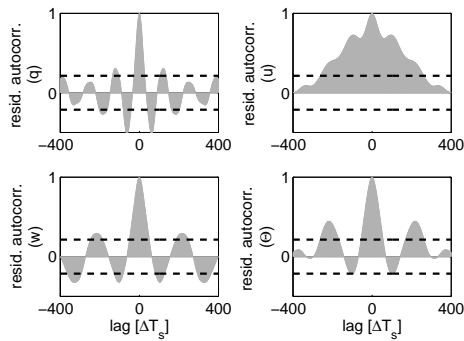
Figure D.6: Autocorrelation of the residuals of the time-averaged longitudinal dynamics model identified in Chapter 3, compared to validation data (cf. Fig. 3.7); 99%-confidence bounds shown.

(a) Overview   (b) Closer view
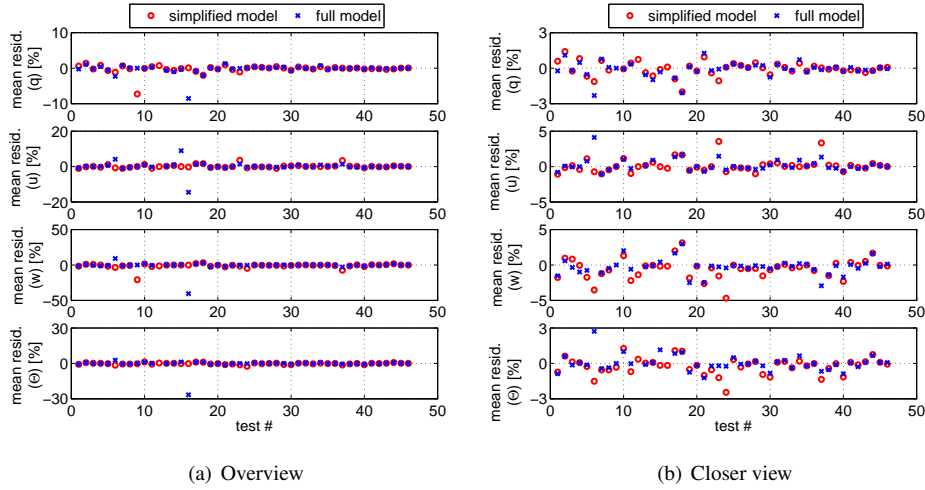
Figure D.7: Mean residuals of all local models identified in Chapter 4.

REFERENCES

[1] R. Jategaonkar, *Flight Vehicle System Identification A Time Domain Methodology* (AIAA Progress in Astronautics and Aeronautics, Reston, VA, USA, 2006).

[2] V. Klein and E. Morelli, *Aircraft System Identification* (AIAA Education Series, 2006).

[3] E. A. Morelli and V. Klein, *Determining the Accuracy of Maximum Likelihood Parameter Estimates With Colored Residuals*, NASA contractor report 194893 (NASA, 1994).

E

NON-DIMENSIONAL STABILITY AND CONTROL DERIVATIVES

In the flight dynamics domain, it is common to express the aerodynamic forces and moments in non-dimensional form, as a function of non-dimensional coefficients. The aim of this type of formulation is to facilitate the comparison between aircraft of different geometries and sizes. This appendix outlines the process of non-dimensionalising the parameters of the state-space models derived in Chapters 3 and 4 (i.e., the so-called 'stability and control derivatives'), allowing for easier comparison to results obtained on different flapping-wing flyers.

Non-dimensional stability and control derivatives for conventional, fixed-wing aircraft, are computed according to an established process, which involves normalising with the dynamic pressure and relevant geometric parameters. Essentially, an analogous process can be used in the flapping-wing case, however the reference velocity used for normalisation must be reconsidered. In fixed-wing aircraft, the steady-state forward velocity is used for normalisation, however in flapping-wing vehicles the forward velocity can be low and is often of the same order of magnitude as the flapping-induced velocity. As discussed in Chapter 1 in the context of aerodynamic similarity parameters, the notion of reference velocity is not well-defined in the flapping-wing case. In computing the Reynolds number for flapping-wing vehicles, it is common to use the forward velocity in forward flight conditions, and the mean wing tip velocity at hover. The main drawback to this solution is that it involves two different definitions, which implies that comparisons between forward flight and hover are not possible. Additionally, it can be argued that at very low forward velocities, using the wing tip velocity as a reference is more suitable – which however would require the definition of a 'cutoff' determining where one definition should start to be used rather than the other. Ultimately, the main purpose is to allow for comparison, and therefore, while the chosen approach should be meaningful, different approaches are possible, as long as they are clearly defined.

To select a suitable normalisation term, the body velocities and wing tip velocities due to flapping were compared for the flight conditions studied in this thesis. The mean wing tip velocity was defined as in Chapter 1, but considering the actual displacement of the wings over the flap cycle, resulting in the following equation:

$$V_{m,tip,0} = \frac{b}{2} f_{f0} (2\zeta_{max}) \tag{E.1}$$

where b is the wing span, f_{f0} is the steady-state flapping frequency (representing the considered steady flight condition), and ζ_{max} is the maximum flap amplitude of one wing.

For the most typical flight conditions of the DelFly, the wing-perceived velocity due to flapping was found to be somewhat larger than the body velocity. Specifically, for forward velocities ranging from 0 to 2m/s, the mean wing tip velocities range approximately from 3 to 2m/s. Given the comparable magnitude of the two types of velocities, the reference velocity for normalisation was defined to include both terms:

$$V_{ref} = \sqrt{V_0^2 + V_{m,tip,0}^2} \tag{E.2}$$

Another matter to consider is the presence of multiple wings. While in the case of the DelFly each wing flaps at the same frequency, and therefore should experience the same tip velocity, this neglects all interaction between the separate wings, and between the flapping motion and forward velocity. The large pitch attitude of the vehicle also implies that the bottom wings partly shield the top wings from the airflow. To allow for a somewhat meaningful but not overly complex non-dimensionalisation, it was nonetheless assumed that all wings perceive the same average velocity over a flap cycle. The aerodynamic reference surface was, analogously, defined as the sum of the areas of all four wings.

The nondimensional forces and moments were thus defined as:

$$C_x = \frac{X}{0.5\rho V_{ref}^2 S} \tag{E.3}$$

$$C_y = \frac{Y}{0.5\rho V_{ref}^2 S} \tag{E.4}$$

$$C_z = \frac{Z}{0.5\rho V_{ref}^2 S} \tag{E.5}$$

$$C_l = \frac{L}{0.5\rho V_{ref}^2 Sb} \tag{E.6}$$

$$C_m = \frac{M}{0.5\rho V_{ref}^2 S\bar{c}} \tag{E.7}$$

$$C_n = \frac{N}{0.5\rho V_{ref}^2 Sb} \tag{E.8}$$

where V_{ref} is the reference velocity defined by Eq. E.2 and S is the wing reference area, considering all four wings.

Assuming the model structure defined in Chapter 3, the forces and moments on the left hand side of Eqs. E.3–E.8 can also be expressed in terms of non-dimensional stability and control derivatives as:

$$C_x = \frac{c}{V_{ref}}C_{xq}q + \frac{1}{V_{ref}}C_{xu}u + \frac{1}{V_{ref}}C_{xw}w + C_{x\delta_e}\delta_e \tag{E.9}$$

$$C_y = \frac{b}{2V_{ref}}C_{yp}p + \frac{b}{2V_{ref}}C_{yr}r + \frac{1}{V_{ref}}C_{yv}v + C_{y\delta_r}\delta_r \tag{E.10}$$

$$C_z = \frac{c}{V_{ref}}C_{zq}q + \frac{1}{V_{ref}}C_{zu}u + \frac{1}{V_{ref}}C_{zw}w + C_{z\delta_e}\delta_e \tag{E.11}$$

$$C_l = \frac{b}{2V_{ref}}C_{lp}p + \frac{b}{2V_{ref}}C_{lr}r + \frac{1}{V_{ref}}C_{lv}v + C_{y\delta_r}\delta_r \tag{E.12}$$

$$C_m = \frac{c}{V_{ref}}C_{mq}q + \frac{1}{V_{ref}}C_{mu}u + \frac{1}{V_{ref}}C_{mw}w + C_{m\delta_e}\delta_e \tag{E.13}$$

$$C_n = \frac{b}{2V_{ref}}C_{np}p + \frac{b}{2V_{ref}}C_{nr}r + \frac{1}{V_{ref}}C_{nv}v + C_{y\delta_r}\delta_r \tag{E.14}$$

$$\tag{E.15}$$

The non-dimensional derivatives in the above equations are related to the dimensional derivatives used throughout this thesis through the following expressions, where $\bar{q}$ indicates the dynamic pressure ($\bar{q} = \frac{1}{2}\rho V_{ref}^2$):

$$C_{xq} = X_q \frac{V_{ref}}{\bar{q}S\bar{c}} \qquad C_{xu} = X_u \frac{V_{ref}}{\bar{q}S} \qquad C_{xw} = X_w \frac{V_{ref}}{\bar{q}S} \qquad C_{x\delta_e} = X_{\delta_e} \frac{1}{\bar{q}S}$$

$$C_{yp} = Y_p \frac{2V_{ref}}{\bar{q}Sb} \qquad C_{yr} = Y_r \frac{2V_{ref}}{\bar{q}Sb} \qquad C_{yv} = Y_v \frac{V_{ref}}{\bar{q}S} \qquad C_{y\delta_r} = Y_{\delta_r} \frac{1}{\bar{q}S}$$

$$C_{zq} = Z_q \frac{V_{ref}}{\bar{q}S\bar{c}} \qquad C_{zu} = Z_u \frac{V_{ref}}{\bar{q}S} \qquad C_{zw} = Z_w \frac{V_{ref}}{\bar{q}S} \qquad C_{z\delta_e} = Z_{\delta_e} \frac{1}{\bar{q}S}$$

$$C_{lp} = L_p \frac{2V_{ref}}{\bar{q}Sb^2} \qquad C_{lr} = L_r \frac{2V_{ref}}{\bar{q}Sb^2} \qquad C_{lv} = L_v \frac{V_{ref}}{\bar{q}Sb} \qquad C_{l\delta_r} = L_{\delta_r} \frac{1}{\bar{q}Sb}$$

$$C_{mq} = M_q \frac{V_{ref}}{\bar{q}S\bar{c}^2} \qquad C_{mu} = M_u \frac{V_{ref}}{\bar{q}S\bar{c}} \qquad C_{mw} = M_q \frac{V_{ref}}{\bar{q}S\bar{c}} \qquad C_{m\delta_e} = M_{\delta_e} \frac{1}{\bar{q}S\bar{c}}$$

$$C_{np} = N_p \frac{2V_{ref}}{\bar{q}Sb^2} \qquad C_{nr} = N_r \frac{2V_{ref}}{\bar{q}Sb^2} \qquad C_{nv} = N_v \frac{V_{ref}}{\bar{q}Sb} \qquad C_{n\delta_r} = N_{\delta_r} \frac{1}{\bar{q}Sb}$$

E

F

LOCAL LTI MODELS

This appendix lists the 46 local LTI models of the time-averaged longitudinal dynamics of the DelFly test platform, forming the basis of the analysis and global modelling in Chapter 4. Each model was identified using the procedures discussed in Chapter 3, and 46 models were obtained for each of two different model structures, viz. the original model introduced in Chapter 3 (Eqs. 3.7 and 4.1), and the simplified model introduced in Chapter 4 (Eq. 4.2). All results are shown in terms of the coordinate system used in Chapter 4, i.e. coordinate system $B2$, as defined in Chapter 1, Sec. 1.4.3. The tables list both the estimated parameters and (in brackets) the estimated standard deviations. The parameters are also reported in non-dimensional form, defined according to the procedure outlined in Appendix E.

Table F.1: Full local model: estimated parameters and standard deviations $(\hat{\theta}(\hat{\sigma}))$, cf. Chapter 4, Eq. 4.1 – Models # 1–16. Note: the estimator did not converge for flight test # 9.

Param.	Model #			
	1	2	3	4
$\mathbf{M_q}$	$-9.06\times10^{-2}(2.53\times10^{-2})$	$-5.24\times10^{-4}(3.67\times10^{-6})$	$-5.84\times10^{-4}(5.60\times10^{-6})$	$-5.78\times10^{-4}(3.90\times10^{-6})$
$\mathbf{M_u}$	$9.63\times10^{-1}(2.72\times10^{-1})$	$-1.93\times10^{-3}(2.29\times10^{-5})$	$-6.13\times10^{-4}(5.30\times10^{-5})$	$-1.60\times10^{-3}(2.44\times10^{-5})$
$\mathbf{M_w}$	$-1.99\times10^{0}(5.60\times10^{-1})$	$-1.16\times10^{-3}(5.21\times10^{-5})$	$-2.42\times10^{-3}(8.70\times10^{-5})$	$-1.61\times10^{-3}(4.56\times10^{-5})$
$\mathbf{M_{\delta e}}$	$1.88\times10^{-1}(5.22\times10^{-2})$	$1.98\times10^{-3}(1.47\times10^{-5})$	$2.00\times10^{-3}(1.13\times10^{-5})$	$1.87\times10^{-3}(1.44\times10^{-5})$
$\mathbf{X_q}$	$5.72\times10^{0}(1.58\times10^{0})$	$2.12\times10^{-2}(2.16\times10^{-4})$	$2.02\times10^{-2}(1.16\times10^{-4})$	$2.21\times10^{-2}(2.68\times10^{-4})$
$\mathbf{X_u}$	$-6.12\times10^{1}(1.69\times10^{1})$	$-1.40\times10^{-1}(1.10\times10^{-3})$	$-1.51\times10^{-1}(1.02\times10^{-3})$	$-1.04\times10^{-1}(1.15\times10^{-3})$
$\mathbf{X_w}$	$1.26E+02(3.49\times10^{1})$	$6.78\times10^{-4}(2.35\times10^{-3})$	$5.91\times10^{-3}(1.72\times10^{-3})$	$-4.99\times10^{-2}(2.12\times10^{-3})$
$\mathbf{X_{\delta e}}$	$-1.19\times10^{1}(3.25\times10^{0})$	$-6.48\times10^{-2}(8.28\times10^{-4})$	$-3.89\times10^{-2}(4.06\times10^{-4})$	$-7.20\times10^{-2}(9.13\times10^{-4})$
$\mathbf{Z_q}$	$-4.55\times10^{-1}(1.27\times10^{-1})$	$-2.64\times10^{-3}(2.79\times10^{-4})$	$1.04\times10^{-2}(5.00\times10^{-4})$	$-5.53\times10^{-3}(3.76\times10^{-4})$
$\mathbf{Z_u}$	$4.95\times10^{0}(1.36\times10^{0})$	$2.41\times10^{-2}(1.37\times10^{-3})$	$-2.19\times10^{-2}(1.93\times10^{-3})$	$2.06\times10^{-2}(1.45\times10^{-3})$
$\mathbf{Z_w}$	$-1.02\times10^{1}(2.80\times10^{0})$	$-4.55\times10^{-2}(2.74\times10^{-3})$	$6.34\times10^{-2}(3.09\times10^{-3})$	$-4.70\times10^{-2}(2.64\times10^{-3})$
$\mathbf{Z_{\delta e}}$	$9.06\times10^{-1}(2.62\times10^{-1})$	$-1.84\times10^{-2}(1.06\times10^{-3})$	$-3.87\times10^{-2}(1.51\times10^{-3})$	$-2.18\times10^{-3}(1.43\times10^{-3})$

Param.	Model #			
	5	6	7	8
$\mathbf{M_q}$	$-4.98\times10^{-4}(1.88\times10^{-6})$	$-2.07\times10^{-5}(1.11\times10^{-5})$	$-7.65\times10^{-4}(6.45\times10^{-6})$	$-7.20\times10^{-4}(4.50\times10^{-6})$
$\mathbf{M_u}$	$-1.64\times10^{-3}(9.81\times10^{-6})$	$-1.84\times10^{-3}(5.83\times10^{-5})$	$-1.69\times10^{-3}(2.01\times10^{-5})$	$-1.91\times10^{-3}(1.68\times10^{-5})$
$\mathbf{M_w}$	$-1.40\times10^{-3}(2.00\times10^{-5})$	$1.38\times10^{-3}(1.34\times10^{-4})$	$-1.97\times10^{-3}(4.15\times10^{-5})$	$-1.67\times10^{-3}(2.38\times10^{-5})$
$\mathbf{M_{\delta e}}$	$1.85\times10^{-3}(1.02\times10^{-5})$	$-2.63\times10^{-5}(2.29\times10^{-5})$	$2.56\times10^{-3}(2.26\times10^{-5})$	$2.27\times10^{-3}(1.61\times10^{-5})$
$\mathbf{X_q}$	$2.25\times10^{-2}(3.09\times10^{-4})$	$2.79\times10^{-2}(3.83\times10^{-4})$	$1.72\times10^{-2}(3.19\times10^{-4})$	$1.23\times10^{-2}(1.67\times10^{-4})$
$\mathbf{X_u}$	$-1.03\times10^{-1}(9.97\times10^{-4})$	$-1.31\times10^{-1}(2.13\times10^{-3})$	$-1.02\times10^{-1}(7.98\times10^{-4})$	$-1.31\times10^{-1}(7.35\times10^{-4})$
$\mathbf{X_w}$	$-3.06\times10^{-2}(1.53\times10^{-3})$	$3.82\times10^{-2}(4.93\times10^{-3})$	$-4.58\times10^{-2}(1.41\times10^{-3})$	$-3.37\times10^{-2}(9.72\times10^{-4})$
$\mathbf{X_{\delta e}}$	$-8.30\times10^{-2}(1.29\times10^{-3})$	$-7.77\times10^{-2}(9.60\times10^{-4})$	$-5.53\times10^{-2}(1.11\times10^{-3})$	$-4.44\times10^{-2}(6.05\times10^{-4})$
$\mathbf{Z_q}$	$-3.78\times10^{-3}(2.19\times10^{-4})$	$-6.79\times10^{-3}(5.92\times10^{-4})$	$-6.37\times10^{-3}(2.70\times10^{-4})$	$-5.85\times10^{-3}(2.04\times10^{-4})$
$\mathbf{Z_u}$	$6.28\times10^{-3}(6.95\times10^{-4})$	$6.09\times10^{-3}(2.99\times10^{-3})$	$2.03\times10^{-2}(6.83\times10^{-4})$	$1.78\times10^{-2}(6.88\times10^{-4})$
$\mathbf{Z_w}$	$-1.22\times10^{-2}(1.04\times10^{-3})$	$-4.26\times10^{-2}(6.26\times10^{-3})$	$-2.80\times10^{-2}(1.18\times10^{-3})$	$-3.14\times10^{-2}(8.62\times10^{-4})$
$\mathbf{Z_{\delta e}}$	$2.11\times10^{-2}(8.57\times10^{-4})$	$-5.57\times10^{-2}(2.10\times10^{-3})$	$-1.87\times10^{-2}(8.50\times10^{-4})$	$3.20\times10^{-3}(6.81\times10^{-4})$

Param.	Model #			
	9	10	11	12
$\mathbf{M_q}$	/	$-2.83\times10^{-4}(2.49\times10^{-6})$	$-5.97\times10^{-4}(5.99\times10^{-6})$	$-4.85\times10^{-4}(1.51\times10^{-5})$
$\mathbf{M_u}$	/	$-1.87\times10^{-3}(1.09\times10^{-5})$	$-1.05\times10^{-3}(3.11\times10^{-5})$	$-2.59\times10^{-4}(2.95\times10^{-5})$
$\mathbf{M_w}$	/	$-1.86\times10^{-4}(1.50\times10^{-5})$	$-2.16\times10^{-3}(5.57\times10^{-5})$	$-3.07\times10^{-3}(5.70\times10^{-5})$
$\mathbf{M_{\delta e}}$	/	$9.83\times10^{-4}(1.09\times10^{-5})$	$1.88\times10^{-3}(2.43\times10^{-5})$	$9.16\times10^{-3}(2.43\times10^{-5})$
$\mathbf{X_q}$	/	$1.91\times10^{-2}(1.77\times10^{-4})$	$1.86\times10^{-2}(2.07\times10^{-4})$	$2.55\times10^{-2}(1.11\times10^{-3})$
$\mathbf{X_u}$	/	$-1.64\times10^{-1}(9.10\times10^{-4})$	$-1.43\times10^{-1}(9.26\times10^{-4})$	$-3.04\times10^{-1}(2.54\times10^{-3})$
$\mathbf{X_w}$	/	$1.87\times10^{-2}(1.07\times10^{-3})$	$-9.82\times10^{-3}(1.66\times10^{-3})$	$2.42\times10^{-1}(4.18\times10^{-3})$
$\mathbf{X_{\delta e}}$	/	$-3.19\times10^{-2}(6.51\times10^{-4})$	$-3.71\times10^{-2}(6.74\times10^{-4})$	$-5.28\times10^{-4}(1.01\times10^{-4})$
$\mathbf{Z_q}$	/	$-6.66\times10^{-3}(3.92\times10^{-4})$	$-3.78\times10^{-4}(3.97\times10^{-4})$	$1.67\times10^{-2}(1.58\times10^{-3})$
$\mathbf{Z_u}$	/	$4.48\times10^{-2}(1.73\times10^{-3})$	$3.12\times10^{-2}(1.29\times10^{-3})$	$-1.74\times10^{-1}(2.87\times10^{-3})$
$\mathbf{Z_w}$	/	$-4.97\times10^{-2}(1.91\times10^{-3})$	$-2.14\times10^{-2}(2.09\times10^{-3})$	$2.94\times10^{-1}(5.97\times10^{-3})$
$\mathbf{Z_{\delta e}}$	/	$3.42\times10^{-2}(1.48\times10^{-3})$	$-1.13\times10^{-2}(1.35\times10^{-3})$	$1.64\times10^{-2}(1.88\times10^{-3})$

Param.	Model #			
	13	14	15	16
$\mathbf{M_q}$	$-5.54\times10^{-4}(3.43\times10^{-6})$	$-6.36\times10^{-4}(3.59\times10^{-6})$	$-4.23\times10^{-4}(1.14\times10^{-5})$	$-2.24\times10^{-4}(7.37\times10^{-6})$
$\mathbf{M_u}$	$-2.12\times10^{-3}(1.08\times10^{-5})$	$-2.40\times10^{-3}(2.64\times10^{-5})$	$-6.66\times10^{-3}(1.15\times10^{-4})$	$-4.44\times10^{-3}(7.49\times10^{-5})$
$\mathbf{M_w}$	$-5.68\times10^{-4}(1.61\times10^{-5})$	$-1.27\times10^{-3}(4.41\times10^{-5})$	$3.72\times10^{-3}(1.03\times10^{-4})$	$2.37\times10^{-3}(3.62\times10^{-5})$
$\mathbf{M_{\delta e}}$	$2.22\times10^{-3}(1.65\times10^{-5})$	$2.12\times10^{-3}(1.52\times10^{-5})$	$2.90\times10^{-3}(1.93\times10^{-5})$	$1.31\times10^{-3}(1.97\times10^{-5})$
$\mathbf{X_q}$	$1.99\times10^{-2}(1.15\times10^{-4})$	$2.37\times10^{-2}(2.93\times10^{-4})$	$1.20\times10^{-2}(7.35\times10^{-4})$	$1.09\times10^{-2}(2.17\times10^{-4})$
$\mathbf{X_u}$	$-1.47\times10^{-1}(5.87\times10^{-4})$	$-1.36\times10^{-1}(1.20\times10^{-3})$	$-3.36\times10^{-1}(6.65\times10^{-3})$	$-1.04\times10^{-1}(2.04\times10^{-3})$
$\mathbf{X_w}$	$-3.35\times10^{-3}(8.35\times10^{-4})$	$-3.29\times10^{-3}(1.58\times10^{-3})$	$1.48\times10^{-1}(5.60\times10^{-3})$	$-9.32\times10^{-2}(1.01\times10^{-3})$
$\mathbf{X_{\delta e}}$	$-4.66\times10^{-2}(5.40\times10^{-4})$	$-7.02\times10^{-2}(1.15\times10^{-3})$	$1.86\times10^{-2}(3.05\times10^{-3})$	$-2.53\times10^{-2}(6.23\times10^{-4})$
$\mathbf{Z_q}$	$-2.94\times10^{-3}(3.37\times10^{-4})$	$-1.73\times10^{-3}(1.74\times10^{-4})$	$2.24\times10^{-3}(5.81\times10^{-4})$	$-1.20\times10^{-3}(3.59\times10^{-4})$
$\mathbf{Z_u}$	$3.61\times10^{-2}(1.12\times10^{-3})$	$1.08\times10^{-2}(7.38\times10^{-4})$	$1.23\times10^{-1}(4.21\times10^{-3})$	$6.29\times10^{-2}(4.04\times10^{-3})$
$\mathbf{Z_w}$	$-2.36\times10^{-2}(1.07\times10^{-3})$	$4.23\times10^{-3}(8.19\times10^{-4})$	$-1.14\times10^{-1}(3.00\times10^{-3})$	$-7.34\times10^{-2}(2.00\times10^{-3})$
$\mathbf{Z_{\delta e}}$	$1.85\times10^{-2}(1.39\times10^{-3})$	$-4.89\times10^{-4}(5.96\times10^{-4})$	$-4.97\times10^{-2}(2.76\times10^{-3})$	$-5.28\times10^{-2}(1.23\times10^{-3})$

F

Table F.2: Full local model: estimated parameters and standard deviations ($\hat{\theta}(\hat{\sigma})$), cf. Chapter 4, Eq. 4.1 – Models # 17–32

Param.	Model #			
	17	18	19	20
M_q	$-4.90 \times 10^{-4} (3.13 \times 10^{-6})$	$-5.33 \times 10^{-4} (4.49 \times 10^{-6})$	$-7.31 \times 10^{-4} (6.32 \times 10^{-6})$	$-7.85 \times 10^{-4} (6.94 \times 10^{-6})$
M_u	$-1.55 \times 10^{-3} (1.23 \times 10^{-5})$	$-1.68 \times 10^{-3} (2.08 \times 10^{-5})$	$-1.49 \times 10^{-3} (5.01 \times 10^{-5})$	$-1.90 \times 10^{-3} (2.75 \times 10^{-5})$
M_w	$-6.52 \times 10^{-4} (1.58 \times 10^{-5})$	$-1.29 \times 10^{-3} (2.42 \times 10^{-5})$	$-1.57 \times 10^{-3} (5.59 \times 10^{-5})$	$-1.41 \times 10^{-3} (2.80 \times 10^{-5})$
M_{δ_e}	$1.76 \times 10^{-3} (1.38 \times 10^{-5})$	$2.16 \times 10^{-3} (1.86 \times 10^{-5})$	$2.38 \times 10^{-3} (2.09 \times 10^{-5})$	$2.64 \times 10^{-3} (2.24 \times 10^{-5})$
X_q	$1.94 \times 10^{-2} (1.83 \times 10^{-4})$	$2.20 \times 10^{-2} (1.74 \times 10^{-4})$	$2.45 \times 10^{-2} (5.29 \times 10^{-4})$	$2.00 \times 10^{-2} (3.32 \times 10^{-4})$
X_u	$-1.59 \times 10^{-1} (7.21 \times 10^{-4})$	$-1.59 \times 10^{-1} (8.15 \times 10^{-4})$	$-1.92 \times 10^{-1} (3.03 \times 10^{-3})$	$-1.56 \times 10^{-1} (1.20 \times 10^{-3})$
X_w	$-6.31 \times 10^{-3} (7.30 \times 10^{-4})$	$6.17 \times 10^{-3} (9.00 \times 10^{-4})$	$3.97 \times 10^{-2} (3.56 \times 10^{-3})$	$-1.04 \times 10^{-2} (1.15 \times 10^{-3})$
X_{δ_e}	$-4.66 \times 10^{-2} (7.72 \times 10^{-4})$	$-4.61 \times 10^{-2} (7.10 \times 10^{-4})$	$-3.45 \times 10^{-2} (1.63 \times 10^{-3})$	$-4.01 \times 10^{-2} (1.21 \times 10^{-3})$
Z_q	$-7.77 \times 10^{-4} (2.72 \times 10^{-4})$	$8.81 \times 10^{-4} (4.01 \times 10^{-4})$	$-1.02 \times 10^{-3} (7.88 \times 10^{-4})$	$-1.89 \times 10^{-3} (4.94 \times 10^{-4})$
Z_u	$7.59 \times 10^{-3} (9.43 \times 10^{-4})$	$3.59 \times 10^{-2} (1.44 \times 10^{-3})$	$2.00 \times 10^{-2} (2.87 \times 10^{-3})$	$4.31 \times 10^{-2} (1.07 \times 10^{-3})$
Z_w	$1.41 \times 10^{-2} (7.14 \times 10^{-4})$	$-1.33 \times 10^{-2} (1.59 \times 10^{-3})$	$-2.48 \times 10^{-2} (3.02 \times 10^{-3})$	$-3.31 \times 10^{-2} (1.21 \times 10^{-3})$
Z_{δ_e}	$7.02 \times 10^{-3} (9.92 \times 10^{-4})$	$-9.34 \times 10^{-3} (1.46 \times 10^{-3})$	$-1.97 \times 10^{-2} (2.44 \times 10^{-3})$	$-2.65 \times 10^{-3} (1.66 \times 10^{-3})$

Param.	Model #			
	21	22	23	24
M_q	$-6.62 \times 10^{-4} (8.90 \times 10^{-6})$	$-8.57 \times 10^{-4} (3.61 \times 10^{-6})$	$-7.20 \times 10^{-4} (8.89 \times 10^{-6})$	$-8.41 \times 10^{-4} (4.68 \times 10^{-6})$
M_u	$-1.57 \times 10^{-3} (4.29 \times 10^{-5})$	$-1.31 \times 10^{-3} (1.22 \times 10^{-5})$	$-2.80 \times 10^{-3} (3.89 \times 10^{-5})$	$-1.00 \times 10^{-3} (1.36 \times 10^{-5})$
M_w	$-1.52 \times 10^{-3} (3.23 \times 10^{-5})$	$-1.58 \times 10^{-3} (9.86 \times 10^{-6})$	$-6.17 \times 10^{-5} (2.83 \times 10^{-5})$	$-1.79 \times 10^{-3} (1.28 \times 10^{-5})$
M_{δ_e}	$1.48 \times 10^{-3} (2.12 \times 10^{-5})$	$3.21 \times 10^{-3} (1.46 \times 10^{-5})$	$3.68 \times 10^{-3} (3.32 \times 10^{-5})$	$2.82 \times 10^{-3} (1.68 \times 10^{-5})$
X_q	$2.27 \times 10^{-2} (3.52 \times 10^{-4})$	$2.23 \times 10^{-2} (2.76 \times 10^{-4})$	$1.54 \times 10^{-2} (3.69 \times 10^{-4})$	$2.30 \times 10^{-2} (2.83 \times 10^{-4})$
X_u	$-1.51 \times 10^{-1} (1.68 \times 10^{-3})$	$-1.74 \times 10^{-1} (1.45 \times 10^{-3})$	$-1.07 \times 10^{-1} (2.19 \times 10^{-3})$	$-1.48 \times 10^{-1} (9.04 \times 10^{-4})$
X_w	$-2.94 \times 10^{-2} (1.20 \times 10^{-3})$	$-5.25 \times 10^{-3} (1.07 \times 10^{-3})$	$-5.31 \times 10^{-2} (1.71 \times 10^{-3})$	$-3.31 \times 10^{-2} (8.15 \times 10^{-4})$
X_{δ_e}	$-4.05 \times 10^{-2} (8.97 \times 10^{-4})$	$-5.09 \times 10^{-2} (1.10 \times 10^{-3})$	$7.11 \times 10^{-2} (1.76 \times 10^{-3})$	$-4.72 \times 10^{-2} (9.59 \times 10^{-4})$
Z_q	$2.97 \times 10^{-4} (6.56 \times 10^{-4})$	$-5.60 \times 10^{-3} (1.99 \times 10^{-4})$	$-3.43 \times 10^{-4} (1.27 \times 10^{-4})$	$-3.31 \times 10^{-3} (2.47 \times 10^{-4})$
Z_u	$3.15 \times 10^{-2} (2.39 \times 10^{-3})$	$5.39 \times 10^{-2} (9.47 \times 10^{-4})$	$2.22 \times 10^{-2} (6.99 \times 10^{-4})$	$3.81 \times 10^{-2} (7.64 \times 10^{-4})$
Z_w	$-3.13 \times 10^{-2} (1.92 \times 10^{-3})$	$-4.99 \times 10^{-2} (7.11 \times 10^{-4})$	$-1.48 \times 10^{-2} (5.01 \times 10^{-4})$	$-3.38 \times 10^{-2} (6.69 \times 10^{-4})$
Z_{δ_e}	$-1.01 \times 10^{-2} (1.52 \times 10^{-3})$	$8.90 \times 10^{-3} (7.89 \times 10^{-4})$	$5.01 \times 10^{-3} (6.07 \times 10^{-4})$	$-7.17 \times 10^{-3} (7.81 \times 10^{-4})$

Param.	Model #			
	25	26	27	28
M_q	$-6.84 \times 10^{-4} (4.54 \times 10^{-6})$	$-7.64 \times 10^{-4} (4.48 \times 10^{-6})$	$-8.18 \times 10^{-4} (3.68 \times 10^{-6})$	$-9.29 \times 10^{-4} (9.30 \times 10^{-6})$
M_u	$-1.16 \times 10^{-3} (2.11 \times 10^{-5})$	$-1.75 \times 10^{-3} (1.45 \times 10^{-5})$	$-8.44 \times 10^{-4} (1.67 \times 10^{-5})$	$-1.19 \times 10^{-3} (6.01 \times 10^{-5})$
M_w	$-1.39 \times 10^{-3} (1.73 \times 10^{-5})$	$-1.19 \times 10^{-3} (1.25 \times 10^{-5})$	$-1.89 \times 10^{-3} (1.30 \times 10^{-5})$	$-2.21 \times 10^{-3} (4.87 \times 10^{-5})$
M_{δ_e}	$2.91 \times 10^{-3} (1.73 \times 10^{-5})$	$2.52 \times 10^{-3} (1.55 \times 10^{-5})$	$2.88 \times 10^{-3} (1.34 \times 10^{-5})$	$3.30 \times 10^{-3} (3.40 \times 10^{-5})$
X_q	$6.98 \times 10^{-3} (3.99 \times 10^{-4})$	$2.50 \times 10^{-2} (2.10 \times 10^{-4})$	$2.14 \times 10^{-2} (2.75 \times 10^{-4})$	$2.22 \times 10^{-2} (6.97 \times 10^{-4})$
X_u	$-9.76 \times 10^{-2} (1.63 \times 10^{-3})$	$-1.61 \times 10^{-1} (8.58 \times 10^{-4})$	$-1.74 \times 10^{-1} (1.31 \times 10^{-3})$	$-1.88 \times 10^{-1} (3.57 \times 10^{-3})$
X_w	$-7.52 \times 10^{-2} (1.30 \times 10^{-3})$	$-1.79 \times 10^{-2} (6.99 \times 10^{-4})$	$-1.11 \times 10^{-2} (9.90 \times 10^{-4})$	$5.09 \times 10^{-3} (2.85 \times 10^{-3})$
X_{δ_e}	$3.33 \times 10^{-3} (1.89 \times 10^{-3})$	$-4.92 \times 10^{-2} (7.12 \times 10^{-4})$	$-5.09 \times 10^{-2} (1.09 \times 10^{-3})$	$-4.17 \times 10^{-2} (2.94 \times 10^{-3})$
Z_q	$-8.27 \times 10^{-3} (2.63 \times 10^{-4})$	$-6.73 \times 10^{-3} (2.33 \times 10^{-4})$	$-1.99 \times 10^{-3} (2.59 \times 10^{-4})$	$-8.48 \times 10^{-3} (5.34 \times 10^{-4})$
Z_u	$3.83 \times 10^{-2} (1.02 \times 10^{-3})$	$4.07 \times 10^{-2} (9.06 \times 10^{-4})$	$1.83 \times 10^{-2} (7.16 \times 10^{-4})$	$5.13 \times 10^{-2} (2.04 \times 10^{-3})$
Z_w	$-4.39 \times 10^{-2} (8.45 \times 10^{-4})$	$-4.32 \times 10^{-2} (7.04 \times 10^{-4})$	$-2.14 \times 10^{-2} (6.94 \times 10^{-4})$	$-5.93 \times 10^{-2} (1.98 \times 10^{-3})$
Z_{δ_e}	$1.76 \times 10^{-2} (1.13 \times 10^{-3})$	$2.85 \times 10^{-3} (7.58 \times 10^{-4})$	$2.70 \times 10^{-3} (1.00 \times 10^{-3})$	$2.46 \times 10^{-3} (1.94 \times 10^{-3})$

Param.	Model #			
	29	30	31	32
M_q	$-8.34 \times 10^{-4} (5.34 \times 10^{-6})$	$-6.10 \times 10^{-4} (2.54 \times 10^{-6})$	$-8.45 \times 10^{-4} (4.64 \times 10^{-6})$	$-5.70 \times 10^{-4} (3.52 \times 10^{-6})$
M_u	$-1.25 \times 10^{-3} (1.14 \times 10^{-5})$	$-1.96 \times 10^{-3} (9.24 \times 10^{-6})$	$-1.40 \times 10^{-4} (1.21 \times 10^{-5})$	$-1.08 \times 10^{-3} (1.77 \times 10^{-5})$
M_w	$-1.50 \times 10^{-3} (1.11 \times 10^{-5})$	$-6.02 \times 10^{-4} (6.27 \times 10^{-6})$	$-1.98 \times 10^{-3} (1.19 \times 10^{-5})$	$-9.22 \times 10^{-4} (1.22 \times 10^{-5})$
M_{δ_e}	$3.20 \times 10^{-3} (2.14 \times 10^{-5})$	$2.39 \times 10^{-3} (9.72 \times 10^{-6})$	$2.83 \times 10^{-3} (1.58 \times 10^{-5})$	$2.39 \times 10^{-3} (1.50 \times 10^{-5})$
X_q	$2.60 \times 10^{-2} (3.07 \times 10^{-4})$	$1.81 \times 10^{-2} (1.71 \times 10^{-4})$	$5.61 \times 10^{-3} (4.58 \times 10^{-4})$	$2.35 \times 10^{-2} (2.62 \times 10^{-4})$
X_u	$-1.57 \times 10^{-1} (9.15 \times 10^{-4})$	$-1.65 \times 10^{-1} (8.60 \times 10^{-4})$	$-8.55 \times 10^{-2} (6.35 \times 10^{-4})$	$-1.96 \times 10^{-1} (1.66 \times 10^{-3})$
X_w	$-2.55 \times 10^{-2} (7.37 \times 10^{-4})$	$-2.74 \times 10^{-2} (5.06 \times 10^{-4})$	$-7.34 \times 10^{-2} (1.00 \times 10^{-3})$	$4.96 \times 10^{-5} (1.08 \times 10^{-3})$
X_{δ_e}	$-4.95 \times 10^{-2} (1.20 \times 10^{-3})$	$-2.90 \times 10^{-2} (7.02 \times 10^{-4})$	$-1.16 \times 10^{-2} (1.78 \times 10^{-3})$	$-4.35 \times 10^{-2} (1.06 \times 10^{-3})$
Z_q	$-3.75 \times 10^{-3} (3.15 \times 10^{-4})$	$7.66 \times 10^{-4} (1.11 \times 10^{-4})$	$6.58 \times 10^{-3} (3.06 \times 10^{-4})$	$-2.67 \times 10^{-3} (2.11 \times 10^{-4})$
Z_u	$3.15 \times 10^{-2} (7.21 \times 10^{-4})$	$3.36 \times 10^{-2} (5.69 \times 10^{-4})$	$-1.31 \times 10^{-2} (4.75 \times 10^{-4})$	$4.65 \times 10^{-2} (1.31 \times 10^{-3})$
Z_w	$-2.75 \times 10^{-2} (6.22 \times 10^{-4})$	$-2.14 \times 10^{-2} (2.93 \times 10^{-4})$	$-4.34 \times 10^{-3} (7.06 \times 10^{-4})$	$-3.87 \times 10^{-2} (8.40 \times 10^{-4})$
Z_{δ_e}	$4.50 \times 10^{-3} (1.22 \times 10^{-3})$	$-1.12 \times 10^{-2} (4.05 \times 10^{-4})$	$-1.77 \times 10^{-2} (1.15 \times 10^{-3})$	$4.25 \times 10^{-4} (8.43 \times 10^{-4})$

F

Table F.3: Full local model: estimated parameters and standard deviations $(\hat{\theta}(\hat{\sigma}))$, cf. Chapter 4, Eq. 4.1 – Models # 33–46

Param.	Model #			
	33	34	35	36
M_q	$-7.47\times10^{-4}(2.95\times10^{-6})$	$-5.52\times10^{-4}(3.14\times10^{-6})$	$-6.59\times10^{-4}(4.55\times10^{-6})$	$-7.87\times10^{-4}(5.37\times10^{-6})$
M_u	$-1.06\times10^{-3}(1.20\times10^{-5})$	$-8.74\times10^{-4}(2.41\times10^{-5})$	$-1.57\times10^{-3}(1.86\times10^{-5})$	$-5.14\times10^{-4}(2.59\times10^{-5})$
M_w	$-1.27\times10^{-3}(8.20\times10^{-6})$	$-7.92\times10^{-4}(1.40\times10^{-5})$	$-7.27\times10^{-4}(1.16\times10^{-5})$	$-2.00\times10^{-3}(2.11\times10^{-5})$
$M_{\delta e}$	$2.83\times10^{-3}(1.18\times10^{-5})$	$2.20\times10^{-3}(1.61\times10^{-5})$	$2.92\times10^{-3}(1.98\times10^{-5})$	$2.75\times10^{-3}(1.96\times10^{-5})$
X_q	$2.63\times10^{-2}(2.56\times10^{-4})$	$3.61\times10^{-2}(2.55\times10^{-4})$	$3.77\times10^{-2}(2.47\times10^{-4})$	$2.01\times10^{-2}(3.71\times10^{-4})$
X_u	$-2.10\times10^{-1}(1.49\times10^{-3})$	$-2.70\times10^{-1}(1.86\times10^{-3})$	$-2.14\times10^{-1}(1.53\times10^{-3})$	$-1.08\times10^{-1}(1.19\times10^{-3})$
X_w	$9.75\times10^{-3}(9.40\times10^{-4})$	$3.60\times10^{-2}(9.68\times10^{-4})$	$7.57\times10^{-3}(9.08\times10^{-4})$	$-4.68\times10^{-2}(1.15\times10^{-3})$
$X_{\delta e}$	$-5.53\times10^{-2}(1.02\times10^{-3})$	$-1.08\times10^{-1}(8.97\times10^{-4})$	$-1.01\times10^{-1}(1.14\times10^{-3})$	$-4.20\times10^{-2}(1.42\times10^{-3})$
Z_q	$-5.17\times10^{-3}(1.60\times10^{-4})$	$6.79\times10^{-3}(5.35\times10^{-4})$	$-7.77\times10^{-3}(2.32\times10^{-4})$	$-1.09\times10^{-3}(5.08\times10^{-4})$
Z_u	$4.91\times10^{-2}(9.32\times10^{-4})$	$9.27\times10^{-3}(2.45\times10^{-3})$	$2.55\times10^{-2}(9.31\times10^{-4})$	$1.92\times10^{-2}(1.22\times10^{-3})$
Z_w	$-4.37\times10^{-2}(5.92\times10^{-4})$	$-4.21\times10^{-3}(1.19\times10^{-3})$	$-3.91\times10^{-2}(6.04\times10^{-4})$	$-2.25\times10^{-2}(1.34\times10^{-3})$
$Z_{\delta e}$	$8.60\times10^{-3}(6.11\times10^{-4})$	$-2.26\times10^{-2}(2.22\times10^{-3})$	$1.16\times10^{-2}(1.05\times10^{-3})$	$-8.12\times10^{-3}(2.02\times10^{-3})$

Param.	Model #			
	37	38	39	40
M_q	$-9.75\times10^{-4}(6.80\times10^{-6})$	$-8.25\times10^{-4}(5.92\times10^{-6})$	$-6.99\times10^{-4}(4.51\times10^{-6})$	$-6.61\times10^{-4}(4.09\times10^{-6})$
M_u	$-3.52\times10^{-5}(3.62\times10^{-5})$	$-3.84\times10^{-4}(2.08\times10^{-5})$	$-1.94\times10^{-3}(2.71\times10^{-5})$	$-9.68\times10^{-4}(1.71\times10^{-5})$
M_w	$-1.61\times10^{-3}(1.68\times10^{-5})$	$-1.37\times10^{-3}(1.18\times10^{-5})$	$-6.79\times10^{-4}(1.03\times10^{-5})$	$-1.04\times10^{-3}(9.21\times10^{-6})$
$M_{\delta e}$	$3.68\times10^{-3}(2.70\times10^{-5})$	$2.95\times10^{-3}(2.18\times10^{-5})$	$2.44\times10^{-3}(1.65\times10^{-5})$	$2.37\times10^{-3}(1.56\times10^{-5})$
X_q	$3.72\times10^{-2}(5.61\times10^{-4})$	$3.49\times10^{-2}(8.74\times10^{-4})$	$3.35\times10^{-2}(3.72\times10^{-4})$	$2.69\times10^{-2}(2.44\times10^{-4})$
X_u	$-2.40\times10^{-1}(2.59\times10^{-3})$	$-2.12\times10^{-1}(2.87\times10^{-3})$	$-2.63\times10^{-1}(2.06\times10^{-3})$	$-2.18\times10^{-1}(1.15\times10^{-3})$
X_w	$1.37\times10^{-2}(1.32\times10^{-3})$	$-3.47\times10^{-4}(1.69\times10^{-3})$	$-4.35\times10^{-3}(7.12\times10^{-4})$	$-1.54\times10^{-2}(5.78\times10^{-4})$
$X_{\delta e}$	$-9.49\times10^{-2}(2.22\times10^{-3})$	$-7.72\times10^{-2}(3.12\times10^{-3})$	$-9.00\times10^{-2}(1.28\times10^{-3})$	$-6.60\times10^{-2}(8.69\times10^{-4})$
Z_q	$-2.21\times10^{-2}(1.05\times10^{-3})$	$-5.98\times10^{-3}(6.36\times10^{-4})$	$-3.93\times10^{-3}(7.00\times10^{-4})$	$-6.78\times10^{-3}(4.45\times10^{-4})$
Z_u	$1.06\times10^{-1}(2.91\times10^{-3})$	$2.85\times10^{-2}(1.35\times10^{-3})$	$6.44\times10^{-2}(2.16\times10^{-3})$	$7.02\times10^{-2}(1.60\times10^{-3})$
Z_w	$-7.69\times10^{-2}(1.78\times10^{-3})$	$-2.91\times10^{-2}(1.05\times10^{-3})$	$-3.34\times10^{-2}(8.88\times10^{-4})$	$-3.94\times10^{-2}(8.04\times10^{-4})$
$Z_{\delta e}$	$7.43\times10^{-2}(4.19\times10^{-3})$	$2.45\times10^{-2}(2.26\times10^{-3})$	$1.18\times10^{-2}(2.40\times10^{-3})$	$1.09\times10^{-3}(1.56\times10^{-3})$

Param.	Model #			
	41	42	43	44
M_q	$-6.77\times10^{-4}(9.50\times10^{-6})$	$-7.91\times10^{-4}(4.37\times10^{-6})$	$-8.15\times10^{-4}(8.00\times10^{-6})$	$-8.51\times10^{-4}(9.19\times10^{-6})$
M_u	$3.04\times10^{-4}(7.84\times10^{-5})$	$-5.14\times10^{-4}(1.70\times10^{-5})$	$2.59\times10^{-5}(4.66\times10^{-5})$	$4.24\times10^{-4}(5.20\times10^{-5})$
M_w	$-1.42\times10^{-3}(4.07\times10^{-5})$	$-1.14\times10^{-3}(8.75\times10^{-6})$	$-1.70\times10^{-3}(2.90\times10^{-5})$	$-1.58\times10^{-3}(2.99\times10^{-5})$
$M_{\delta e}$	$2.96\times10^{-3}(3.70\times10^{-5})$	$3.08\times10^{-3}(1.85\times10^{-5})$	$3.38\times10^{-3}(3.58\times10^{-5})$	$3.47\times10^{-3}(3.67\times10^{-5})$
X_q	$3.05\times10^{-2}(2.89\times10^{-4})$	$3.25\times10^{-2}(2.46\times10^{-4})$	$4.35\times10^{-2}(9.27\times10^{-4})$	$4.02\times10^{-2}(4.43\times10^{-4})$
X_u	$-2.49\times10^{-1}(2.29\times10^{-3})$	$-2.29\times10^{-1}(1.11\times10^{-3})$	$-2.84\times10^{-1}(5.89\times10^{-3})$	$-2.42\times10^{-1}(2.37\times10^{-3})$
X_w	$1.55\times10^{-2}(1.21\times10^{-3})$	$-9.59\times10^{-5}(5.40\times10^{-4})$	$5.76\times10^{-2}(3.45\times10^{-3})$	$2.44\times10^{-2}(1.40\times10^{-3})$
$X_{\delta e}$	$-7.81\times10^{-2}(1.11\times10^{-3})$	$-6.99\times10^{-2}(9.61\times10^{-4})$	$-1.06\times10^{-1}(4.19\times10^{-3})$	$-8.95\times10^{-2}(1.76\times10^{-3})$
Z_q	$-1.47\times10^{-2}(1.42\times10^{-3})$	$2.07\times10^{-2}(4.47\times10^{-4})$	$-1.61\times10^{-2}(8.09\times10^{-4})$	$-7.95\times10^{-2}(9.64\times10^{-4})$
Z_u	$1.77\times10^{-1}(8.57\times10^{-3})$	$2.01\times10^{-2}(1.34\times10^{-3})$	$9.21\times10^{-2}(4.02\times10^{-3})$	$5.27\times10^{-2}(3.23\times10^{-3})$
Z_w	$-1.06\times10^{-1}(4.54\times10^{-3})$	$-1.83\times10^{-2}(7.43\times10^{-4})$	$-7.94\times10^{-2}(2.49\times10^{-3})$	$-5.20\times10^{-2}(2.20\times10^{-3})$
$Z_{\delta e}$	$1.86\times10^{-2}(6.24\times10^{-3})$	$-1.53\times10^{-2}(1.64\times10^{-3})$	$1.93\times10^{-2}(3.49\times10^{-3})$	$-1.22\times10^{-2}(3.89\times10^{-3})$

Param.	Model #	
	45	46
M_q	$-6.43\times10^{-4}(4.40\times10^{-6})$	$-6.63\times10^{-4}(3.68\times10^{-6})$
M_u	$-1.02\times10^{-3}(2.89\times10^{-5})$	$-1.84\times10^{-3}(2.10\times10^{-5})$
M_w	$-8.72\times10^{-4}(1.16\times10^{-5})$	$-6.74\times10^{-4}(9.92\times10^{-6})$
$M_{\delta e}$	$2.57\times10^{-3}(1.68\times10^{-5})$	$2.81\times10^{-3}(1.51\times10^{-5})$
X_q	$2.85\times10^{-2}(2.15\times10^{-4})$	$2.66\times10^{-2}(2.93\times10^{-4})$
X_u	$-2.02\times10^{-1}(1.54\times10^{-3})$	$-2.00\times10^{-1}(2.21\times10^{-3})$
X_w	$-3.00\times10^{-2}(5.94\times10^{-4})$	$-1.62\times10^{-2}(1.04\times10^{-3})$
$X_{\delta e}$	$-8.49\times10^{-2}(9.16\times10^{-4})$	$-6.01\times10^{-2}(1.22\times10^{-3})$
Z_q	$6.24\times10^{-3}(7.17\times10^{-4})$	$-6.47\times10^{-3}(1.80\times10^{-4})$
Z_u	$-3.22\times10^{-2}(2.10\times10^{-3})$	$3.00\times10^{-2}(9.99\times10^{-4})$
Z_w	$-1.25\times10^{-2}(9.18\times10^{-4})$	$-3.88\times10^{-2}(3.92\times10^{-4})$
$Z_{\delta e}$	$-3.70\times10^{-2}(3.05\times10^{-3})$	$2.64\times10^{-3}(7.18\times10^{-4})$

Table F.4: Simplified local model: estimated parameters and standard deviations ($\hat{\theta}(\hat{\sigma})$), cf. Chapter 4, Eq. 4.2 – Models # 1–16

Param.	Model #			
	1	2	3	4
M_q	$-5.43\times10^{-4}(3.89\times10^{-6})$	$-5.05\times10^{-4}(2.63\times10^{-6})$	$-5.26\times10^{-4}(2.28\times10^{-6})$	$-5.22\times10^{-4}(3.00\times10^{-6})$
M_u	$-1.66\times10^{-3}(2.78\times10^{-5})$	$-1.99\times10^{-3}(1.59\times10^{-5})$	$-1.27\times10^{-3}(1.00\times10^{-5})$	$-1.90\times10^{-3}(2.01\times10^{-5})$
M_w	$-2.26\times10^{-3}(6.44\times10^{-5})$	$-1.14\times10^{-3}(3.68\times10^{-5})$	$-1.35\times10^{-3}(1.31\times10^{-5})$	$-1.04\times10^{-3}(3.85\times10^{-5})$
M_{δ_e}	$2.13\times10^{-3}(1.77\times10^{-5})$	$1.93\times10^{-3}(1.38\times10^{-5})$	$2.12\times10^{-3}(1.13\times10^{-5})$	$1.73\times10^{-3}(1.34\times10^{-5})$
X_q	$1.97\times10^{-2}(1.49\times10^{-4})$	$2.20\times10^{-2}(1.24\times10^{-4})$	$2.10\times10^{-2}(8.10\times10^{-5})$	$2.44\times10^{-2}(2.26\times10^{-4})$
X_u	$-1.37\times10^{-1}(5.40\times10^{-4})$	$-1.33\times10^{-1}(4.33\times10^{-4})$	$-1.45\times10^{-1}(2.96\times10^{-4})$	$-1.28\times10^{-1}(7.97\times10^{-4})$
X_{δ_e}	$-6.45\times10^{-2}(7.98\times10^{-4})$	$-7.12\times10^{-2}(6.06\times10^{-4})$	$-4.60\times10^{-2}(4.29\times10^{-4})$	$-6.78\times10^{-2}(1.02\times10^{-3})$
Z_q	$-4.89\times10^{-3}(1.74\times10^{-4})$	$-5.92\times10^{-3}(1.36\times10^{-4})$	$7.86\times10^{-5}(1.80\times10^{-4})$	$-6.26\times10^{-3}(2.13\times10^{-4})$
Z_w	$-3.59\times10^{-2}(1.18\times10^{-3})$	$-3.24\times10^{-2}(8.76\times10^{-4})$	$8.30\times10^{-3}(5.41\times10^{-4})$	$-2.96\times10^{-2}(1.50\times10^{-3})$

Param.	Model #			
	5	6	7	8
M_q	$-4.88\times10^{-4}(1.96\times10^{-6})$	$-7.55\times10^{-4}(4.06\times10^{-6})$	$-7.80\times10^{-4}(7.29\times10^{-6})$	$-6.99\times10^{-4}(4.59\times10^{-6})$
M_u	$-1.69\times10^{-3}(1.30\times10^{-5})$	$-2.88\times10^{-3}(1.19\times10^{-5})$	$-1.89\times10^{-3}(2.06\times10^{-5})$	$-1.82\times10^{-3}(1.56\times10^{-5})$
M_w	$-1.25\times10^{-3}(2.84\times10^{-5})$	$-2.14\times10^{-4}(1.43\times10^{-5})$	$-2.35\times10^{-3}(3.72\times10^{-5})$	$-2.03\times10^{-3}(2.35\times10^{-5})$
M_{δ_e}	$1.85\times10^{-3}(1.01\times10^{-5})$	$2.56\times10^{-3}(1.19\times10^{-5})$	$2.68\times10^{-3}(2.45\times10^{-5})$	$2.13\times10^{-3}(1.52\times10^{-5})$
X_q	$2.10\times10^{-2}(2.65\times10^{-4})$	$2.02\times10^{-2}(1.24\times10^{-4})$	$2.23\times10^{-2}(1.99\times10^{-4})$	$1.47\times10^{-2}(1.43\times10^{-4})$
X_u	$-1.14\times10^{-1}(8.32\times10^{-4})$	$-1.26\times10^{-1}(5.07\times10^{-4})$	$-1.23\times10^{-1}(6.71\times10^{-4})$	$-1.50\times10^{-1}(5.64\times10^{-4})$
X_{δ_e}	$-5.78\times10^{-2}(8.49\times10^{-4})$	$-4.24\times10^{-2}(4.80\times10^{-4})$	$-6.02\times10^{-2}(8.05\times10^{-4})$	$-5.20\times10^{-2}(5.64\times10^{-4})$
Z_q	$-9.73\times10^{-4}(1.33\times10^{-4})$	$-4.66\times10^{-3}(1.08\times10^{-4})$	$-1.14\times10^{-2}(1.23\times10^{-4})$	$-5.76\times10^{-3}(9.45\times10^{-5})$
Z_w	$1.52\times10^{-3}(6.89\times10^{-4})$	$2.44\times10^{-3}(3.44\times10^{-4})$	$-2.73\times10^{-2}(4.42\times10^{-4})$	$-1.40\times10^{-2}(4.25\times10^{-4})$

Param.	Model #			
	9	10	11	12
M_q	$-6.29\times10^{-4}(3.25\times10^{-5})$	$-3.08\times10^{-4}(2.26\times10^{-6})$	$-5.12\times10^{-4}(3.83\times10^{-6})$	$-4.90\times10^{-4}(3.15\times10^{-6})$
M_u	$-1.11\times10^{-3}(1.70\times10^{-4})$	$-1.69\times10^{-3}(1.53\times10^{-5})$	$-1.03\times10^{-3}(2.53\times10^{-5})$	$-1.31\times10^{-3}(1.47\times10^{-5})$
M_w	$-6.58\times10^{-3}(1.94\times10^{-4})$	$-4.98\times10^{-4}(2.41\times10^{-5})$	$-2.41\times10^{-3}(4.08\times10^{-5})$	$-1.58\times10^{-3}(1.97\times10^{-5})$
M_{δ_e}	$1.60\times10^{-3}(7.54\times10^{-5})$	$1.16\times10^{-3}(9.48\times10^{-6})$	$1.66\times10^{-3}(1.37\times10^{-5})$	$1.81\times10^{-3}(1.30\times10^{-5})$
X_q	$6.38\times10^{-3}(6.36\times10^{-4})$	$1.66\times10^{-2}(1.49\times10^{-4})$	$1.92\times10^{-2}(1.20\times10^{-4})$	$1.58\times10^{-2}(1.20\times10^{-4})$
X_u	$-9.56\times10^{-2}(2.03\times10^{-3})$	$-1.53\times10^{-1}(6.17\times10^{-4})$	$-1.51\times10^{-1}(4.77\times10^{-4})$	$-1.40\times10^{-1}(4.94\times10^{-4})$
X_{δ_e}	$-2.89\times10^{-2}(1.97\times10^{-3})$	$-2.27\times10^{-2}(5.82\times10^{-4})$	$-3.46\times10^{-2}(5.37\times10^{-4})$	$-2.51\times10^{-2}(6.27\times10^{-4})$
Z_q	$-1.83\times10^{-2}(1.32\times10^{-3})$	$-3.19\times10^{-3}(3.05\times10^{-4})$	$-2.88\times10^{-3}(2.09\times10^{-4})$	$3.71\times10^{-4}(2.11\times10^{-4})$
Z_w	$-7.63\times10^{-2}(3.17\times10^{-3})$	$-2.33\times10^{-2}(1.08\times10^{-3})$	$-7.81\times10^{-3}(1.00\times10^{-3})$	$1.41\times10^{-2}(6.48\times10^{-4})$

Param.	Model #			
	13	14	15	16
M_q	$-5.36\times10^{-4}(2.75\times10^{-6})$	$-6.10\times10^{-4}(2.79\times10^{-6})$	$-7.96\times10^{-4}(5.43\times10^{-6})$	$-5.88\times10^{-4}(1.06\times10^{-5})$
M_u	$-2.03\times10^{-3}(1.22\times10^{-5})$	$-2.22\times10^{-3}(1.54\times10^{-5})$	$-1.11\times10^{-3}(1.92\times10^{-5})$	$-1.85\times10^{-3}(5.17\times10^{-5})$
M_w	$-8.08\times10^{-4}(1.69\times10^{-5})$	$-1.54\times10^{-3}(2.01\times10^{-5})$	$-2.77\times10^{-3}(2.80\times10^{-5})$	$-2.75\times10^{-3}(1.02\times10^{-4})$
M_{δ_e}	$2.13\times10^{-3}(1.38\times10^{-5})$	$2.06\times10^{-3}(1.40\times10^{-5})$	$2.51\times10^{-3}(2.01\times10^{-5})$	$1.57\times10^{-3}(1.93\times10^{-5})$
X_q	$1.83\times10^{-2}(9.88\times10^{-5})$	$2.51\times10^{-2}(2.30\times10^{-4})$	$2.52\times10^{-2}(3.55\times10^{-4})$	$2.13\times10^{-2}(1.34\times10^{-4})$
X_u	$-1.47\times10^{-1}(4.44\times10^{-4})$	$-1.36\times10^{-1}(1.00\times10^{-3})$	$-1.33\times10^{-1}(1.45\times10^{-3})$	$-1.51\times10^{-1}(6.02\times10^{-4})$
X_{δ_e}	$-4.09\times10^{-2}(4.53\times10^{-4})$	$-6.99\times10^{-2}(1.08\times10^{-4})$	$-7.31\times10^{-2}(1.61\times10^{-4})$	$-3.88\times10^{-2}(5.88\times10^{-4})$
Z_q	$5.17\times10^{-4}(2.30\times10^{-4})$	$-1.96\times10^{-3}(8.62\times10^{-5})$	$-3.61\times10^{-3}(1.21\times10^{-4})$	$-1.64\times10^{-2}(5.88\times10^{-4})$
Z_w	$4.41\times10^{-3}(8.45\times10^{-4})$	$1.22\times10^{-2}(4.72\times10^{-4})$	$-5.91\times10^{-3}(5.02\times10^{-4})$	$-9.14\times10^{-2}(3.32\times10^{-3})$

F

Table F.5: Simplified local model: estimated parameters and standard deviations $(\hat{\theta}(\hat{\sigma}))$, cf. Chapter 4, Eq. 4.2 – Models # 17–32

Param.	Model #			
	17	18	19	20
M_q	$-4.94\times10^{-4}(3.00\times10^{-6})$	$-4.95\times10^{-4}(3.61\times10^{-6})$	$-7.24\times10^{-4}(5.31\times10^{-6})$	$-6.12\times10^{-4}(4.52\times10^{-6})$
M_u	$-1.48\times10^{-3}(9.26\times10^{-6})$	$-1.43\times10^{-3}(1.82\times10^{-5})$	$-1.63\times10^{-3}(3.61\times10^{-5})$	$-1.90\times10^{-3}(2.38\times10^{-5})$
M_w	$-7.73\times10^{-4}(9.74\times10^{-6})$	$-1.64\times10^{-3}(2.05\times10^{-5})$	$-1.58\times10^{-3}(3.77\times10^{-5})$	$-1.41\times10^{-3}(1.68\times10^{-5})$
M_{δ_e}	$1.75\times10^{-3}(1.38\times10^{-5})$	$2.11\times10^{-3}(1.68\times10^{-5})$	$2.43\times10^{-3}(1.65\times10^{-5})$	$2.17\times10^{-3}(1.66\times10^{-5})$
X_q	$2.08\times10^{-2}(1.45\times10^{-4})$	$2.08\times10^{-2}(1.14\times10^{-4})$	$1.89\times10^{-2}(2.98\times10^{-4})$	$2.38\times10^{-2}(2.30\times10^{-4})$
X_u	$-1.62\times10^{-1}(6.29\times10^{-4})$	$-1.61\times10^{-1}(5.64\times10^{-4})$	$-1.60\times10^{-1}(1.12\times10^{-3})$	$-1.80\times10^{-1}(1.00\times10^{-3})$
X_{δ_e}	$-5.01\times10^{-2}(6.24\times10^{-4})$	$-4.09\times10^{-2}(5.86\times10^{-4})$	$-1.94\times10^{-2}(1.23\times10^{-3})$	$-4.99\times10^{-2}(7.12\times10^{-4})$
Z_q	$9.00\times10^{-4}(1.36\times10^{-4})$	$-9.19\times10^{-4}(1.97\times10^{-4})$	$-6.76\times10^{-3}(3.04\times10^{-4})$	$-2.31\times10^{-3}(1.80\times10^{-4})$
Z_w	$2.15\times10^{-2}(4.60\times10^{-4})$	$-5.21\times10^{-3}(6.70\times10^{-4})$	$-2.72\times10^{-2}(8.39\times10^{-4})$	$-1.41\times10^{-2}(3.53\times10^{-4})$

Param.	Model #			
	21	22	23	24
M_q	$-5.55\times10^{-4}(6.26\times10^{-6})$	$-7.44\times10^{-4}(3.31\times10^{-6})$	$-5.09\times10^{-4}(5.31\times10^{-6})$	$-8.52\times10^{-4}(5.53\times10^{-6})$
M_u	$-1.87\times10^{-3}(3.37\times10^{-5})$	$-1.40\times10^{-3}(1.15\times10^{-5})$	$-2.63\times10^{-3}(2.39\times10^{-5})$	$-6.71\times10^{-4}(2.55\times10^{-5})$
M_w	$-1.27\times10^{-3}(2.27\times10^{-5})$	$-1.49\times10^{-3}(9.91\times10^{-6})$	$9.76\times10^{-5}(1.19\times10^{-5})$	$-2.60\times10^{-3}(2.51\times10^{-5})$
M_{δ_e}	$1.27\times10^{-3}(1.76\times10^{-5})$	$2.78\times10^{-3}(1.38\times10^{-5})$	$2.54\times10^{-3}(2.00\times10^{-5})$	$2.82\times10^{-3}(1.62\times10^{-5})$
X_q	$2.98\times10^{-2}(2.51\times10^{-4})$	$2.00\times10^{-2}(1.79\times10^{-4})$	$9.98\times10^{-3}(3.03\times10^{-4})$	$2.93\times10^{-2}(2.00\times10^{-4})$
X_u	$-1.92\times10^{-1}(1.36\times10^{-3})$	$-1.69\times10^{-1}(8.51\times10^{-4})$	$-1.65\times10^{-1}(1.73\times10^{-3})$	$-1.60\times10^{-1}(8.24\times10^{-4})$
X_{δ_e}	$-5.69\times10^{-2}(7.41\times10^{-4})$	$-4.24\times10^{-2}(6.20\times10^{-4})$	$6.49\times10^{-2}(1.02\times10^{-3})$	$-6.33\times10^{-2}(8.17\times10^{-4})$
Z_q	$-2.58\times10^{-3}(2.68\times10^{-4})$	$-3.56\times10^{-3}(1.06\times10^{-4})$	$3.14\times10^{-3}(1.25\times10^{-4})$	$-8.00\times10^{-3}(1.74\times10^{-4})$
Z_w	$-2.74\times10^{-2}(7.57\times10^{-4})$	$-2.29\times10^{-2}(4.13\times10^{-4})$	$1.23\times10^{-2}(4.60\times10^{-4})$	$-3.74\times10^{-2}(4.00\times10^{-4})$

Param.	Model #			
	25	26	27	28
M_q	$-5.87\times10^{-4}(3.91\times10^{-6})$	$-7.12\times10^{-4}(4.32\times10^{-6})$	$-7.75\times10^{-4}(3.21\times10^{-6})$	$-7.77\times10^{-4}(6.19\times10^{-6})$
M_u	$-1.34\times10^{-3}(2.00\times10^{-5})$	$-1.81\times10^{-3}(1.50\times10^{-5})$	$-8.26\times10^{-4}(1.62\times10^{-5})$	$-1.20\times10^{-3}(4.54\times10^{-5})$
M_w	$-1.25\times10^{-3}(1.67\times10^{-5})$	$-1.30\times10^{-3}(1.44\times10^{-5})$	$-1.93\times10^{-3}(1.26\times10^{-5})$	$-2.28\times10^{-3}(3.11\times10^{-5})$
M_{δ_e}	$2.32\times10^{-3}(1.65\times10^{-5})$	$2.30\times10^{-3}(1.51\times10^{-5})$	$2.72\times10^{-3}(1.15\times10^{-5})$	$2.78\times10^{-3}(2.06\times10^{-5})$
X_q	$2.25\times10^{-2}(3.19\times10^{-4})$	$2.59\times10^{-2}(1.49\times10^{-4})$	$2.29\times10^{-2}(2.04\times10^{-4})$	$2.45\times10^{-2}(4.76\times10^{-4})$
X_u	$-1.74\times10^{-1}(1.49\times10^{-3})$	$-1.73\times10^{-1}(6.89\times10^{-4})$	$-1.90\times10^{-1}(9.48\times10^{-4})$	$-2.17\times10^{-1}(2.58\times10^{-3})$
X_{δ_e}	$-4.35\times10^{-2}(1.67\times10^{-3})$	$-5.19\times10^{-2}(6.11\times10^{-4})$	$-5.57\times10^{-2}(9.12\times10^{-4})$	$-4.40\times10^{-2}(1.51\times10^{-3})$
Z_q	$-4.43\times10^{-3}(1.54\times10^{-4})$	$-5.25\times10^{-3}(1.10\times10^{-4})$	$-1.89\times10^{-3}(1.12\times10^{-4})$	$-7.68\times10^{-3}(1.86\times10^{-4})$
Z_w	$-1.96\times10^{-2}(5.51\times10^{-4})$	$-2.39\times10^{-2}(3.98\times10^{-4})$	$-1.57\times10^{-2}(2.92\times10^{-4})$	$-3.58\times10^{-2}(5.41\times10^{-4})$

Param.	Model #			
	29	30	31	32
M_q	$-8.14\times10^{-4}(5.41\times10^{-6})$	$-5.80\times10^{-4}(2.49\times10^{-6})$	$-7.96\times10^{-4}(3.74\times10^{-6})$	$-4.94\times10^{-4}(2.63\times10^{-6})$
M_u	$-1.21\times10^{-3}(1.39\times10^{-5})$	$-2.19\times10^{-3}(8.94\times10^{-6})$	$-2.83\times10^{-4}(1.74\times10^{-5})$	$-1.14\times10^{-3}(1.22\times10^{-5})$
M_w	$-1.72\times10^{-3}(1.44\times10^{-5})$	$-5.13\times10^{-4}(5.21\times10^{-6})$	$-2.02\times10^{-3}(1.34\times10^{-5})$	$-9.03\times10^{-4}(9.02\times10^{-6})$
M_{δ_e}	$3.07\times10^{-3}(2.15\times10^{-5})$	$2.29\times10^{-3}(9.28\times10^{-6})$	$2.70\times10^{-3}(1.34\times10^{-5})$	$2.03\times10^{-3}(1.28\times10^{-5})$
X_q	$2.81\times10^{-2}(2.27\times10^{-4})$	$2.10\times10^{-2}(1.65\times10^{-4})$	$1.98\times10^{-2}(4.30\times10^{-4})$	$2.44\times10^{-2}(1.72\times10^{-4})$
X_u	$-1.67\times10^{-1}(1.09\times10^{-3})$	$-1.84\times10^{-1}(9.56\times10^{-4})$	$-1.62\times10^{-1}(1.82\times10^{-3})$	$-1.95\times10^{-1}(8.51\times10^{-4})$
X_{δ_e}	$-5.73\times10^{-2}(8.77\times10^{-4})$	$-4.55\times10^{-2}(4.00\times10^{-4})$	$-4.89\times10^{-2}(1.15\times10^{-2})$	$-4.85\times10^{-2}(8.56\times10^{-4})$
Z_q	$-3.87\times10^{-3}(1.42\times10^{-4})$	$-3.19\times10^{-3}(7.68\times10^{-5})$	$-4.80\times10^{-3}(1.38\times10^{-4})$	$-1.65\times10^{-3}(1.41\times10^{-4})$
Z_w	$-2.20\times10^{-2}(3.19\times10^{-4})$	$-1.55\times10^{-2}(2.98\times10^{-4})$	$-1.90\times10^{-2}(3.22\times10^{-4})$	$-1.30\times10^{-2}(4.70\times10^{-4})$

F

Table F.6: Simplified local model: estimated parameters and standard deviations ($\hat{\theta}(\hat{\sigma})$), cf. Chapter 4, Eq. 4.2 – Models # 33–46

Param.	Model #			
	33	34	35	36
$\mathbf{M_q}$	$-6.82\times10^{-4}(2.41\times10^{-6})$	$-5.43\times10^{-4}(2.80\times10^{-6})$	$-6.35\times10^{-4}(3.49\times10^{-6})$	$-7.61\times10^{-4}(5.16\times10^{-6})$
$\mathbf{M_u}$	$-1.17\times10^{-3}(9.55\times10^{-6})$	$-8.18\times10^{-4}(1.89\times10^{-5})$	$-1.56\times10^{-3}(1.51\times10^{-5})$	$-3.54\times10^{-4}(2.95\times10^{-5})$
$\mathbf{M_w}$	$-1.21\times10^{-3}(7.38\times10^{-6})$	$-9.63\times10^{-4}(8.24\times10^{-6})$	$-7.86\times10^{-4}(8.60\times10^{-6})$	$-2.27\times10^{-3}(2.54\times10^{-5})$
$\mathbf{M_{\delta e}}$	$2.58\times10^{-3}(1.01\times10^{-5})$	$2.09\times10^{-3}(1.39\times10^{-5})$	$2.84\times10^{-3}(1.43\times10^{-5})$	$2.65\times10^{-3}(1.92\times10^{-5})$
$\mathbf{X_q}$	$2.11\times10^{-2}(1.82\times10^{-4})$	$2.94\times10^{-2}(2.22\times10^{-4})$	$3.68\times10^{-2}(2.00\times10^{-4})$	$2.99\times10^{-2}(2.69\times10^{-4})$
$\mathbf{X_u}$	$-1.82\times10^{-1}(8.21\times10^{-4})$	$-2.30\times10^{-1}(1.44\times10^{-3})$	$-2.14\times10^{-1}(1.03\times10^{-3})$	$-1.49\times10^{-1}(1.14\times10^{-3})$
$\mathbf{X_{\delta e}}$	$-3.56\times10^{-2}(5.62\times10^{-4})$	$-8.15\times10^{-2}(7.64\times10^{-4})$	$-1.02\times10^{-1}(9.06\times10^{-4})$	$-7.00\times10^{-2}(1.27\times10^{-3})$
$\mathbf{Z_q}$	$-2.28\times10^{-3}(9.14\times10^{-5})$	$-5.89\times10^{-4}(2.48\times10^{-4})$	$-5.07\times10^{-3}(1.28\times10^{-4})$	$-4.58\times10^{-3}(2.25\times10^{-4})$
$\mathbf{Z_w}$	$-1.94\times10^{-2}(2.81\times10^{-4})$	$-1.01\times10^{-2}(4.60\times10^{-4})$	$-2.86\times10^{-2}(3.58\times10^{-4})$	$-2.73\times10^{-2}(6.46\times10^{-4})$

Param.	Model #			
	37	38	39	40
$\mathbf{M_q}$	$-9.07\times10^{-4}(6.73\times10^{-6})$	$-7.74\times10^{-4}(5.00\times10^{-6})$	$-6.31\times10^{-4}(3.68\times10^{-6})$	$-6.23\times10^{-4}(4.23\times10^{-6})$
$\mathbf{M_u}$	$-4.02\times10^{-4}(3.98\times10^{-5})$	$-3.63\times10^{-4}(2.01\times10^{-5})$	$-1.78\times10^{-3}(2.44\times10^{-5})$	$-1.07\times10^{-3}(2.21\times10^{-5})$
$\mathbf{M_w}$	$-1.94\times10^{-3}(1.96\times10^{-5})$	$-1.39\times10^{-3}(1.18\times10^{-5})$	$-7.34\times10^{-4}(6.96\times10^{-6})$	$-1.25\times10^{-3}(1.27\times10^{-5})$
$\mathbf{M_{\delta e}}$	$3.15\times10^{-3}(1.63\times10^{-5})$	$2.73\times10^{-3}(1.80\times10^{-5})$	$2.28\times10^{-3}(1.55\times10^{-5})$	$2.22\times10^{-3}(1.47\times10^{-5})$
$\mathbf{X_q}$	$2.66\times10^{-2}(3.28\times10^{-4})$	$3.33\times10^{-2}(4.12\times10^{-4})$	$3.99\times10^{-2}(2.81\times10^{-4})$	$3.01\times10^{-2}(1.59\times10^{-4})$
$\mathbf{X_u}$	$-1.83\times10^{-1}(1.21\times10^{-3})$	$-2.10\times10^{-1}(1.99\times10^{-3})$	$-2.71\times10^{-1}(1.76\times10^{-3})$	$-2.43\times10^{-1}(9.73\times10^{-4})$
$\mathbf{X_{\delta e}}$	$-3.80\times10^{-2}(8.74\times10^{-4})$	$-7.02\times10^{-2}(1.80\times10^{-3})$	$-1.04\times10^{-1}(1.02\times10^{-3})$	$-7.69\times10^{-2}(6.79\times10^{-4})$
$\mathbf{Z_q}$	$-1.06\times10^{-2}(3.90\times10^{-4})$	$1.24\times10^{-3}(2.15\times10^{-4})$	$1.39\times10^{-3}(2.78\times10^{-4})$	$-7.85\times10^{-3}(2.27\times10^{-4})$
$\mathbf{Z_w}$	$-4.13\times10^{-2}(4.40\times10^{-4})$	$-1.46\times10^{-2}(3.21\times10^{-4})$	$-2.08\times10^{-2}(3.78\times10^{-4})$	$-3.17\times10^{-2}(3.58\times10^{-4})$

Param.	Model #			
	41	42	43	44
$\mathbf{M_q}$	$-4.97\times10^{-4}(3.56\times10^{-6})$	$-7.77\times10^{-4}(3.92\times10^{-6})$	$-6.98\times10^{-4}(4.29\times10^{-6})$	$-7.46\times10^{-4}(6.06\times10^{-6})$
$\mathbf{M_u}$	$-1.09\times10^{-3}(2.61\times10^{-5})$	$-5.43\times10^{-4}(1.82\times10^{-5})$	$-6.29\times10^{-4}(1.82\times10^{-5})$	$-9.33\times10^{-5}(3.38\times10^{-5})$
$\mathbf{M_w}$	$-7.71\times10^{-4}(1.33\times10^{-5})$	$-1.21\times10^{-3}(8.84\times10^{-6})$	$-1.44\times10^{-3}(1.38\times10^{-5})$	$-1.40\times10^{-3}(2.06\times10^{-5})$
$\mathbf{M_{\delta e}}$	$2.17\times10^{-3}(1.72\times10^{-5})$	$3.09\times10^{-3}(1.51\times10^{-5})$	$2.83\times10^{-3}(1.78\times10^{-5})$	$3.07\times10^{-3}(2.38\times10^{-5})$
$\mathbf{X_q}$	$2.73\times10^{-2}(1.40\times10^{-4})$	$3.27\times10^{-2}(1.53\times10^{-4})$	$2.82\times10^{-2}(3.27\times10^{-4})$	$3.27\times10^{-2}(2.12\times10^{-4})$
$\mathbf{X_u}$	$-2.21\times10^{-1}(7.73\times10^{-4})$	$-2.30\times10^{-1}(7.34\times10^{-4})$	$-1.70\times10^{-1}(1.51\times10^{-3})$	$-1.98\times10^{-1}(9.04\times10^{-4})$
$\mathbf{X_{\delta e}}$	$-6.63\times10^{-2}(6.78\times10^{-4})$	$-6.96\times10^{-2}(7.08\times10^{-4})$	$-5.35\times10^{-2}(9.03\times10^{-4})$	$-6.48\times10^{-2}(9.02\times10^{-4})$
$\mathbf{Z_q}$	$-9.46\times10^{-4}(3.67\times10^{-4})$	$-1.33\times10^{-3}(1.76\times10^{-4})$	$-9.55\times10^{-3}(2.01\times10^{-4})$	$-7.60\times10^{-3}(3.54\times10^{-4})$
$\mathbf{Z_w}$	$-1.58\times10^{-2}(8.34\times10^{-4})$	$-2.02\times10^{-2}(2.36\times10^{-4})$	$-3.18\times10^{-2}(3.92\times10^{-4})$	$-3.44\times10^{-2}(6.95\times10^{-4})$

Param.	Model #	
	45	46
$\mathbf{M_q}$	$-6.25\times10^{-4}(3.64\times10^{-6})$	$-6.70\times10^{-4}(3.04\times10^{-6})$
$\mathbf{M_u}$	$-1.67\times10^{-3}(3.04\times10^{-5})$	$-2.22\times10^{-3}(1.71\times10^{-5})$
$\mathbf{M_w}$	$-5.70\times10^{-4}(6.73\times10^{-6})$	$-5.81\times10^{-4}(8.09\times10^{-6})$
$\mathbf{M_{\delta e}}$	$2.50\times10^{-3}(1.94\times10^{-5})$	$2.76\times10^{-3}(1.18\times10^{-5})$
$\mathbf{X_q}$	$3.42\times10^{-2}(3.00\times10^{-4})$	$2.49\times10^{-2}(2.90\times10^{-4})$
$\mathbf{X_u}$	$-2.75\times10^{-1}(2.20\times10^{-3})$	$-2.19\times10^{-1}(1.89\times10^{-3})$
$\mathbf{X_{\delta e}}$	$-1.10\times10^{-1}(1.40\times10^{-3})$	$-5.26\times10^{-2}(1.22\times10^{-3})$
$\mathbf{Z_q}$	$3.31\times10^{-4}(3.49\times10^{-4})$	$-6.06\times10^{-3}(1.00\times10^{-4})$
$\mathbf{Z_w}$	$-1.89\times10^{-2}(5.74\times10^{-4})$	$-2.99\times10^{-2}(2.50\times10^{-4})$

F

Table F.7: Full local model: non-dimensional estimated parameters and standard deviations $(\hat{\theta}(\hat{\sigma}))$, cf. Chapter 4, Eq. 4.1 and Appendix E– Models # 1–16. Note: the estimator did not converge for test condition # 9.

Param.	Model #			
	1	2	3	4
C_{mq}	$-9.62\times10^{1}(2.69\times10^{1})$	$-5.53\times10^{-1}(3.88\times10^{-3})$	$-6.26\times10^{-1}(6.00\times10^{-3})$	$-6.00\times10^{-1}(4.05\times10^{-3})$
C_{mu}	$7.97\times10^{1}(2.25\times10^{1})$	$-1.59\times10^{-1}(1.89\times10^{-3})$	$-5.12\times10^{-2}(4.43\times10^{-3})$	$-1.30\times10^{-1}(1.98\times10^{-3})$
C_{mw}	$-1.65E+02(4.64\times10^{1})$	$-9.56\times10^{-2}(4.29\times10^{-3})$	$-2.02\times10^{-1}(7.27\times10^{-3})$	$-1.30\times10^{-1}(3.69\times10^{-3})$
$C_{m\delta_e}$	$5.17\times10^{0}(1.44\times10^{0})$	$5.39\times10^{-2}(4.00\times10^{-4})$	$5.60\times10^{-2}(3.17\times10^{-4})$	$4.92\times10^{-2}(3.79\times10^{-4})$
C_{mq}	$4.74E+02(1.66\times10^{1})$	$2.13\times10^{-1}(2.17\times10^{-3})$	$1.51\times10^{-1}(8.65\times10^{-4})$	$1.78\times10^{-1}(2.16\times10^{-3})$
C_{xu}	$-3.95E+02(1.09E+02)$	$-9.00\times10^{-1}(7.07\times10^{-3})$	$-9.84\times10^{-1}(6.65\times10^{-3})$	$-6.57\times10^{-1}(7.26\times10^{-3})$
C_{xw}	$8.14E+02(2.25E+02)$	$4.36\times10^{-3}(1.51\times10^{-2})$	$3.85\times10^{-2}(1.12\times10^{-2})$	$-3.15\times10^{-1}(1.34\times10^{-2})$
$C_{x\delta_e}$	$-2.55\times10^{1}(6.97\times10^{0})$	$-1.38\times10^{-1}(1.76\times10^{-2})$	$-8.50\times10^{-2}(8.87\times10^{-4})$	$-1.48\times10^{-1}(1.87\times10^{-2})$
C_{zq}	$-3.77\times10^{1}(1.05\times10^{1})$	$-2.17\times10^{-1}(2.30\times10^{-2})$	$8.69\times10^{-1}(4.18\times10^{-2})$	$-4.48\times10^{-1}(3.04\times10^{-2})$
C_{zu}	$3.20\times10^{1}(8.78\times10^{0})$	$1.55\times10^{-1}(8.80\times10^{-3})$	$-1.43\times10^{-1}(1.26\times10^{-2})$	$1.30\times10^{-1}(9.16\times10^{-3})$
C_{zw}	$-6.59\times10^{1}(1.81\times10^{1})$	$-2.92\times10^{-1}(1.76\times10^{-2})$	$4.13\times10^{-1}(2.01\times10^{-2})$	$-2.97\times10^{-1}(1.67\times10^{-2})$
$C_{z\delta_e}$	$1.94\times10^{0}(5.62\times10^{-1})$	$-3.91\times10^{-2}(2.25\times10^{-3})$	$-8.46\times10^{-2}(3.30\times10^{-3})$	$-4.47\times10^{-3}(2.93\times10^{-3})$

Param.	Model #			
	5	6	7	8
C_{mq}	$-5.15\times10^{-1}(1.95\times10^{-3})$	$-2.25\times10^{-2}(1.21\times10^{-2})$	$-8.42\times10^{-1}(7.10\times10^{-3})$	$-7.60\times10^{-1}(4.75\times10^{-3})$
C_{mu}	$-1.32\times10^{-1}(7.92\times10^{-4})$	$-1.56\times10^{-1}(4.94\times10^{-3})$	$-1.45\times10^{-1}(1.73\times10^{-3})$	$-1.57\times10^{-1}(1.38\times10^{-3})$
C_{mw}	$-1.13\times10^{-1}(1.61\times10^{-3})$	$1.17\times10^{-1}(1.14\times10^{-2})$	$-1.69\times10^{-1}(3.56\times10^{-3})$	$-1.37\times10^{-1}(1.96\times10^{-3})$
$C_{m\delta_e}$	$4.84\times10^{-2}(2.67\times10^{-4})$	$-7.58\times10^{-4}(6.60\times10^{-4})$	$7.57\times10^{-2}(6.69\times10^{-4})$	$6.17\times10^{-2}(4.38\times10^{-4})$
C_{mq}	$2.01\times10^{-1}(2.76\times10^{-3})$	$2.19\times10^{-1}(3.01\times10^{-3})$	$1.48\times10^{0}(2.74\times10^{-2})$	$1.01\times10^{0}(1.37\times10^{-2})$
C_{xu}	$-6.48\times10^{-1}(6.28\times10^{-3})$	$-8.66\times10^{-1}(1.41\times10^{-2})$	$-6.83\times10^{-1}(5.34\times10^{-3})$	$-8.41\times10^{-1}(4.72\times10^{-3})$
C_{xw}	$-1.93\times10^{-1}(9.63\times10^{-3})$	$2.52\times10^{-1}(3.26\times10^{-2})$	$-3.07\times10^{-1}(9.44\times10^{-3})$	$-2.16\times10^{-1}(6.24\times10^{-3})$
$C_{x\delta_e}$	$-1.69\times10^{-1}(2.63\times10^{-3})$	$-1.75\times10^{-1}(2.16\times10^{-3})$	$-1.28\times10^{-1}(2.56\times10^{-3})$	$-9.42\times10^{-2}(1.28\times10^{-3})$
C_{zq}	$-3.05\times10^{-1}(1.77\times10^{-2})$	$-5.75\times10^{-1}(5.02\times10^{-2})$	$-5.47\times10^{-1}(2.32\times10^{-2})$	$-4.82\times10^{-1}(1.68\times10^{-2})$
C_{zu}	$3.95\times10^{-2}(4.38\times10^{-3})$	$4.02\times10^{-2}(1.98\times10^{-2})$	$1.36\times10^{-1}(4.57\times10^{-3})$	$1.14\times10^{-1}(4.42\times10^{-3})$
C_{zw}	$-7.68\times10^{-2}(6.55\times10^{-3})$	$-2.82\times10^{-1}(4.14\times10^{-2})$	$-1.88\times10^{-1}(7.90\times10^{-3})$	$-2.02\times10^{-1}(5.53\times10^{-3})$
$C_{z\delta_e}$	$4.30\times10^{-2}(1.75\times10^{-3})$	$-1.25\times10^{-1}(4.72\times10^{-3})$	$-4.31\times10^{-2}(1.96\times10^{-3})$	$6.79\times10^{-3}(1.44\times10^{-3})$

Param.	Model #			
	9	10	11	12
C_{mq}	/	$-3.07\times10^{-1}(2.70\times10^{-3})$	$-6.54\times10^{-1}(6.56\times10^{-3})$	$-5.12\times10^{-1}(1.60\times10^{-2})$
C_{mu}	/	$-1.58\times10^{-1}(9.23\times10^{-4})$	$-8.98\times10^{-2}(2.66\times10^{-3})$	$-2.13\times10^{-2}(2.43\times10^{-3})$
C_{mw}	/	$-1.57\times10^{-2}(1.27\times10^{-3})$	$-1.85\times10^{-1}(4.76\times10^{-3})$	$-2.53\times10^{-1}(4.70\times10^{-3})$
$C_{m\delta_e}$	/	$2.83\times10^{-2}(3.13\times10^{-4})$	$5.51\times10^{-2}(5.07\times10^{-4})$	$2.50\times10^{-2}(6.62\times10^{-4})$
C_{mq}	/	$1.62\times10^{0}(1.50\times10^{-2})$	$1.59\times10^{0}(1.77\times10^{-2})$	$2.10\times10^{0}(9.15\times10^{-2})$
C_{xu}	/	$-1.08\times10^{0}(6.01\times10^{-3})$	$-9.53\times10^{-1}(6.17\times10^{-3})$	$-1.95\times10^{0}(1.63\times10^{-2})$
C_{xw}	/	$1.23\times10^{0}(7.07\times10^{-3})$	$-6.55\times10^{-2}(1.11\times10^{-2})$	$1.56\times10^{0}(2.69\times10^{-2})$
$C_{x\delta_e}$	/	$-7.16\times10^{-2}(1.46\times10^{-3})$	$-8.49\times10^{-2}(1.54\times10^{-3})$	$-1.12\times10^{-3}(2.15\times10^{-4})$
C_{zq}	/	$-5.64\times10^{-1}(3.32\times10^{-2})$	$-3.23\times10^{-2}(3.39\times10^{-2})$	$1.38\times10^{0}(1.30\times10^{-1})$
C_{zu}	/	$2.96\times10^{-1}(1.14\times10^{-2})$	$2.08\times10^{-1}(8.60\times10^{-3})$	$-1.12\times10^{0}(1.84\times10^{-2})$
C_{zw}	/	$-3.28\times10^{-1}(1.26\times10^{-2})$	$-1.43\times10^{-1}(1.39\times10^{-2})$	$1.89\times10^{0}(3.84\times10^{-2})$
$C_{z\delta_e}$	/	$7.67\times10^{-2}(3.32\times10^{-3})$	$-2.58\times10^{-2}(3.09\times10^{-3})$	$3.48\times10^{-2}(3.99\times10^{-3})$

Param.	Model #			
	13	14	15	16
C_{mq}	$-5.94\times10^{-1}(3.68\times10^{-3})$	$-6.50\times10^{-1}(3.67\times10^{-3})$	$-4.53\times10^{-1}(1.22\times10^{-2})$	$-2.31\times10^{-1}(7.61\times10^{-3})$
C_{mu}	$-1.77\times10^{-1}(9.03\times10^{-4})$	$-1.91\times10^{-1}(2.11\times10^{-3})$	$-5.56\times10^{-1}(9.60\times10^{-3})$	$-3.58\times10^{-1}(6.04\times10^{-3})$
C_{mw}	$-4.75\times10^{-2}(1.35\times10^{-3})$	$-1.01\times10^{-1}(3.52\times10^{-3})$	$3.11\times10^{-1}(8.60\times10^{-3})$	$1.91\times10^{-1}(2.92\times10^{-3})$
$C_{m\delta_e}$	$9.55\times10^{-3}(7.10\times10^{-5})$	$8.70\times10^{-3}(6.24\times10^{-5})$	$1.25\times10^{-2}(1.72\times10^{-4})$	$5.43\times10^{-3}(8.17\times10^{-5})$
C_{mq}	$1.66\times10^{0}(9.62\times10^{-3})$	$1.89\times10^{0}(2.34\times10^{-2})$	$1.00\times10^{0}(6.14\times10^{-2})$	$8.78\times10^{-1}(1.75\times10^{-2})$
C_{xu}	$-9.59\times10^{-1}(3.83\times10^{-3})$	$-8.46\times10^{-1}(7.46\times10^{-3})$	$-2.19\times10^{0}(4.33\times10^{-2})$	$-6.54\times10^{-1}(1.28\times10^{-2})$
C_{xw}	$-2.19\times10^{-2}(5.45\times10^{-3})$	$-2.05\times10^{-2}(9.83\times10^{-3})$	$9.64\times10^{-1}(3.65\times10^{-2})$	$-5.86\times10^{-1}(6.35\times10^{-3})$
$C_{x\delta_e}$	$-1.02\times10^{-1}(1.18\times10^{-3})$	$-1.40\times10^{-1}(2.29\times10^{-3})$	$4.06\times10^{-2}(6.65\times10^{-3})$	$-5.14\times10^{-2}(1.27\times10^{-3})$
C_{zq}	$-2.46\times10^{-1}(2.82\times10^{-2})$	$-1.38\times10^{-1}(1.39\times10^{-2})$	$1.87\times10^{-1}(4.85\times10^{-2})$	$-9.67\times10^{-2}(2.89\times10^{-2})$
C_{zu}	$2.35\times10^{-1}(7.31\times10^{-3})$	$6.72\times10^{-2}(4.59\times10^{-3})$	$8.01\times10^{-1}(2.74\times10^{-2})$	$3.95\times10^{-1}(2.54\times10^{-2})$
C_{zw}	$-1.54\times10^{-1}(6.98\times10^{-3})$	$2.63\times10^{-2}(5.09\times10^{-3})$	$-7.42\times10^{-1}(1.95\times10^{-2})$	$-4.61\times10^{-1}(1.26\times10^{-2})$
$C_{z\delta_e}$	$4.05\times10^{-2}(3.04\times10^{-3})$	$-9.73\times10^{-4}(1.19\times10^{-3})$	$-1.08\times10^{-1}(6.02\times10^{-3})$	$-1.07\times10^{-1}(2.50\times10^{-3})$

F

Table F.8: Full local model: non-dimensional estimated parameters and standard deviations ($\hat{\theta}(\hat{\sigma})$), cf. Chapter 4, Eq. 4.1 and Appendix E– Models # 17–32.

Param.	Model #			
	17	18	19	20
C_{mq}	$-5.32\times10^{-1}(3.40\times10^{-3})$	$-5.96\times10^{-1}(5.02\times10^{-3})$	$-8.03\times10^{-1}(6.94\times10^{-3})$	$-8.09\times10^{-1}(7.15\times10^{-3})$
C_{mu}	$-1.31\times10^{-1}(1.04\times10^{-3})$	$-1.46\times10^{-1}(1.81\times10^{-3})$	$-1.28\times10^{-1}(4.29\times10^{-3})$	$-1.53\times10^{-1}(2.21\times10^{-3})$
C_{mw}	$-5.52\times10^{-2}(1.34\times10^{-3})$	$-1.12\times10^{-1}(2.11\times10^{-3})$	$-1.35\times10^{-1}(4.79\times10^{-3})$	$-1.13\times10^{-1}(2.25\times10^{-3})$
$C_{m\delta_e}$	$7.67\times10^{-3}(6.01\times10^{-5})$	$9.69\times10^{-3}(8.34\times10^{-5})$	$7.01\times10^{-2}(6.16\times10^{-4})$	$6.85\times10^{-2}(5.81\times10^{-4})$
C_{mq}	$1.64\times10^{0}(1.55\times10^{-2})$	$1.92\times10^{0}(1.52\times10^{-2})$	$2.10\times10^{0}(4.53\times10^{-2})$	$1.61\times10^{0}(2.67\times10^{-2})$
C_{xu}	$-1.05\times10^{0}(4.76\times10^{-3})$	$-1.08\times10^{0}(5.54\times10^{-3})$	$-1.28\times10^{0}(2.03\times10^{-2})$	$-9.78\times10^{-1}(7.53\times10^{-3})$
C_{xw}	$-4.17\times10^{-2}(4.82\times10^{-3})$	$4.20\times10^{-2}(6.12\times10^{-3})$	$2.65\times10^{-1}(2.38\times10^{-2})$	$-6.52\times10^{-2}(7.21\times10^{-3})$
$C_{x\delta_e}$	$-1.05\times10^{-1}(1.73\times10^{-3})$	$-1.10\times10^{-1}(1.69\times10^{-3})$	$-7.93\times10^{-2}(3.75\times10^{-3})$	$-8.12\times10^{-2}(2.45\times10^{-3})$
C_{zq}	$-6.58\times10^{-2}(2.30\times10^{-2})$	$7.68\times10^{-2}(3.50\times10^{-2})$	$-8.74\times10^{-2}(6.75\times10^{-2})$	$-1.52\times10^{-1}(3.97\times10^{-2})$
C_{zu}	$5.01\times10^{-2}(6.23\times10^{-3})$	$2.44\times10^{-1}(9.79\times10^{-3})$	$1.34\times10^{-1}(1.92\times10^{-2})$	$2.70\times10^{-1}(6.71\times10^{-3})$
C_{zw}	$9.31\times10^{-2}(4.72\times10^{-3})$	$-9.04\times10^{-2}(1.08\times10^{-2})$	$-1.66\times10^{-1}(2.02\times10^{-2})$	$-2.08\times10^{-1}(7.59\times10^{-3})$
$C_{z\delta_e}$	$1.58\times10^{-2}(2.23\times10^{-3})$	$-2.22\times10^{-2}(3.47\times10^{-3})$	$-4.53\times10^{-2}(5.61\times10^{-3})$	$-5.36\times10^{-3}(3.36\times10^{-3})$

Param.	Model #			
	21	22	23	24
C_{mq}	$-7.76\times10^{-1}(1.04\times10^{-2})$	$-9.61\times10^{-1}(4.05\times10^{-3})$	$-7.95\times10^{-1}(9.82\times10^{-3})$	$-9.46\times10^{-1}(5.26\times10^{-3})$
C_{mu}	$-1.44\times10^{-1}(3.92\times10^{-3})$	$-1.15\times10^{-1}(1.07\times10^{-3})$	$-2.41\times10^{-1}(3.35\times10^{-3})$	$-8.77\times10^{-2}(1.19\times10^{-3})$
C_{mw}	$-1.39\times10^{-1}(2.95\times10^{-3})$	$-1.38\times10^{-1}(8.63\times10^{-4})$	$-5.32\times10^{-3}(2.44\times10^{-3})$	$-1.57\times10^{-1}(1.12\times10^{-3})$
$C_{m\delta_e}$	$4.97\times10^{-2}(7.11\times10^{-4})$	$9.86\times10^{-2}(4.48\times10^{-4})$	$1.10\times10^{-1}(9.89\times10^{-4})$	$8.71\times10^{-2}(5.19\times10^{-4})$
C_{mq}	$2.08\times10^{0}(3.22\times10^{-2})$	$1.95\times10^{0}(2.41\times10^{-2})$	$1.33\times10^{-1}(3.18\times10^{-2})$	$2.02\times10^{0}(2.48\times10^{-2})$
C_{xu}	$-1.08\times10^{0}(1.20\times10^{-2})$	$-1.19\times10^{0}(9.90\times10^{-3})$	$-7.19\times10^{-1}(1.47\times10^{-2})$	$-1.01\times10^{0}(6.19\times10^{-3})$
C_{xw}	$-2.10\times10^{-1}(8.56\times10^{-3})$	$-3.58\times10^{-2}(7.30\times10^{-3})$	$-3.57\times10^{-1}(1.15\times10^{-2})$	$-2.26\times10^{-1}(5.58\times10^{-3})$
$C_{x\delta_e}$	$-1.06\times10^{-1}(2.35\times10^{-3})$	$-1.22\times10^{-1}(2.64\times10^{-3})$	$1.65\times10^{-1}(4.09\times10^{-3})$	$-1.14\times10^{-1}(2.31\times10^{-3})$
C_{zq}	$2.72\times10^{-2}(6.00\times10^{-2})$	$-4.90\times10^{-1}(1.74\times10^{-2})$	$-2.96\times10^{-2}(1.09\times10^{-2})$	$-2.90\times10^{-1}(2.17\times10^{-2})$
C_{zu}	$2.25\times10^{-1}(1.70\times10^{-2})$	$3.68\times10^{-2}(6.46\times10^{-3})$	$1.49\times10^{-1}(4.70\times10^{-3})$	$2.61\times10^{-1}(5.23\times10^{-3})$
C_{zw}	$-2.23\times10^{-1}(1.37\times10^{-2})$	$-3.41\times10^{-1}(4.85\times10^{-3})$	$-9.95\times10^{-1}(3.37\times10^{-2})$	$-2.31\times10^{-1}(4.58\times10^{-3})$
$C_{z\delta_e}$	$-2.64\times10^{-2}(3.98\times10^{-3})$	$2.13\times10^{-2}(1.89\times10^{-3})$	$1.16\times10^{-2}(1.41\times10^{-3})$	$-1.73\times10^{-2}(1.88\times10^{-3})$

Param.	Model #			
	25	26	27	28
C_{mq}	$-7.50\times10^{-1}(4.98\times10^{-3})$	$-8.70\times10^{-1}(5.10\times10^{-3})$	$-8.86\times10^{-1}(3.99\times10^{-3})$	$-1.01\times10^{0}(1.01\times10^{-2})$
C_{mu}	$-9.92\times10^{-2}(1.81\times10^{-3})$	$-1.55\times10^{-1}(1.29\times10^{-3})$	$-7.13\times10^{-2}(1.41\times10^{-3})$	$-1.01\times10^{-1}(5.08\times10^{-3})$
C_{mw}	$-1.19\times10^{-1}(1.48\times10^{-3})$	$-1.06\times10^{-1}(1.11\times10^{-3})$	$-1.60\times10^{-1}(1.10\times10^{-3})$	$-1.87\times10^{-1}(4.12\times10^{-3})$
$C_{m\delta_e}$	$8.55\times10^{-2}(5.08\times10^{-4})$	$7.98\times10^{-2}(4.91\times10^{-4})$	$8.25\times10^{-2}(3.84\times10^{-4})$	$9.46\times10^{-2}(9.74\times10^{-4})$
C_{mq}	$5.97\times10^{-1}(3.41\times10^{-2})$	$2.22\times10^{0}(1.87\times10^{-2})$	$1.81\times10^{0}(2.32\times10^{-2})$	$1.88\times10^{0}(5.89\times10^{-2})$
C_{xu}	$-6.51\times10^{-1}(1.09\times10^{-2})$	$-1.12\times10^{0}(5.94\times10^{-3})$	$-1.15\times10^{0}(8.63\times10^{-3})$	$-1.24\times10^{0}(2.35\times10^{-2})$
C_{xw}	$-5.02\times10^{-1}(8.68\times10^{-3})$	$-1.24\times10^{-1}(4.84\times10^{-3})$	$-7.32\times10^{-2}(6.53\times10^{-3})$	$3.35\times10^{-2}(1.88\times10^{-2})$
$C_{x\delta_e}$	$7.63\times10^{-3}(4.33\times10^{-3})$	$-1.22\times10^{-1}(1.76\times10^{-3})$	$-1.14\times10^{-1}(2.44\times10^{-3})$	$-9.32\times10^{-2}(6.57\times10^{-3})$
C_{zq}	$-7.08\times10^{-1}(2.25\times10^{-2})$	$-5.98\times10^{-1}(2.07\times10^{-2})$	$-1.68\times10^{-1}(2.19\times10^{-2})$	$-7.17\times10^{-1}(4.51\times10^{-2})$
C_{zu}	$2.56\times10^{-1}(6.81\times10^{-3})$	$2.82\times10^{-1}(6.28\times10^{-3})$	$1.21\times10^{-1}(4.72\times10^{-3})$	$3.38\times10^{-1}(1.34\times10^{-2})$
C_{zw}	$-2.93\times10^{-1}(5.64\times10^{-3})$	$-2.99\times10^{-1}(4.88\times10^{-3})$	$-1.41\times10^{-1}(4.57\times10^{-3})$	$-3.91\times10^{-1}(1.31\times10^{-2})$
$C_{z\delta_e}$	$4.03\times10^{-2}(2.59\times10^{-3})$	$7.04\times10^{-3}(1.87\times10^{-3})$	$6.04\times10^{-3}(2.24\times10^{-3})$	$5.50\times10^{-3}(4.34\times10^{-3})$

Param.	Model #			
	29	30	31	32
C_{mq}	$-9.39\times10^{-1}(6.01\times10^{-3})$	$-6.86\times10^{-1}(2.86\times10^{-3})$	$-9.57\times10^{-1}(5.26\times10^{-3})$	$-6.48\times10^{-1}(4.00\times10^{-3})$
C_{mu}	$-1.10\times10^{-1}(1.00\times10^{-3})$	$-1.72\times10^{-1}(8.10\times10^{-4})$	$-1.24\times10^{-2}(1.07\times10^{-3})$	$-9.57\times10^{-2}(1.57\times10^{-3})$
C_{mw}	$-1.32\times10^{-1}(9.75\times10^{-4})$	$-5.28\times10^{-2}(5.50\times10^{-4})$	$-1.75\times10^{-1}(1.05\times10^{-3})$	$-8.17\times10^{-2}(1.08\times10^{-3})$
$C_{m\delta_e}$	$9.90\times10^{-2}(6.62\times10^{-4})$	$7.38\times10^{-2}(3.00\times10^{-4})$	$8.86\times10^{-2}(4.95\times10^{-4})$	$7.53\times10^{-2}(4.73\times10^{-4})$
C_{mq}	$2.28\times10^{0}(2.70\times10^{-2})$	$1.59\times10^{0}(1.50\times10^{-2})$	$4.96\times10^{-1}(4.05\times10^{-2})$	$2.08\times10^{0}(2.32\times10^{-2})$
C_{xu}	$-1.08\times10^{0}(6.27\times10^{-3})$	$-1.13\times10^{0}(5.88\times10^{-3})$	$-5.89\times10^{-1}(4.38\times10^{-3})$	$-1.35\times10^{0}(1.15\times10^{-2})$
C_{xw}	$-1.75\times10^{-1}(5.05\times10^{-3})$	$-1.87\times10^{-1}(3.46\times10^{-3})$	$-5.06\times10^{-1}(6.89\times10^{-3})$	$3.43\times10^{-4}(7.46\times10^{-3})$
$C_{x\delta_e}$	$-1.19\times10^{-1}(2.90\times10^{-3})$	$-6.98\times10^{-2}(1.69\times10^{-3})$	$-2.83\times10^{-2}(4.35\times10^{-3})$	$-1.07\times10^{-1}(2.61\times10^{-3})$
C_{zq}	$-3.29\times10^{-1}(2.77\times10^{-2})$	$6.72\times10^{-2}(9.74\times10^{-3})$	$5.81\times10^{-1}(2.70\times10^{-2})$	$-2.37\times10^{-1}(1.87\times10^{-2})$
C_{zu}	$2.16\times10^{-1}(4.94\times10^{-3})$	$2.30\times10^{-1}(3.89\times10^{-3})$	$-9.03\times10^{-4}(3.27\times10^{-3})$	$3.21\times10^{-1}(9.05\times10^{-3})$
C_{zw}	$-1.88\times10^{-1}(4.26\times10^{-3})$	$-1.46\times10^{-1}(2.00\times10^{-3})$	$-2.99\times10^{-2}(4.87\times10^{-3})$	$-2.67\times10^{-1}(5.81\times10^{-3})$
$C_{z\delta_e}$	$1.09\times10^{-2}(2.94\times10^{-3})$	$-2.70\times10^{-2}(9.75\times10^{-4})$	$-4.32\times10^{-2}(2.81\times10^{-3})$	$1.04\times10^{-3}(2.07\times10^{-3})$

F

Table F.9: Full local model: non-dimensional estimated parameters and standard deviations ($\hat{\theta}(\hat{\sigma})$), cf. Chapter 4, Eq. 4.1 and Appendix E– Models # 33–46.

Param.	Model #			
	33	34	35	36
C_{mq}	$-8.24\times10^{-1}(3.26\times10^{-3})$	$-6.33\times10^{-1}(3.60\times10^{-3})$	$-7.19\times10^{-1}(4.96\times10^{-3})$	$-8.71\times10^{-1}(5.94\times10^{-3})$
C_{mu}	$-9.12\times10^{-2}(1.03\times10^{-3})$	$-7.82\times10^{-2}(2.16\times10^{-3})$	$-1.34\times10^{-1}(1.58\times10^{-3})$	$-4.44\times10^{-2}(2.24\times10^{-3})$
C_{mw}	$-1.09\times10^{-1}(7.06\times10^{-4})$	$-7.09\times10^{-2}(1.25\times10^{-3})$	$-6.18\times10^{-2}(9.87\times10^{-4})$	$-1.73\times10^{-1}(1.82\times10^{-3})$
$C_{m\delta_e}$	$8.41\times10^{-2}(3.51\times10^{-4})$	$7.07\times10^{-2}(5.17\times10^{-4})$	$8.48\times10^{-2}(5.75\times10^{-4})$	$8.23\times10^{-2}(5.86\times10^{-4})$
C_{mq}	$2.26\times10^{0}(2.20\times10^{-2})$	$3.23\times10^{0}(2.28\times10^{-2})$	$3.21\times10^{0}(2.10\times10^{-2})$	$1.74\times10^{0}(3.20\times10^{-2})$
C_{xu}	$-1.41\times10^{0}(1.00\times10^{-2})$	$-1.88\times10^{0}(1.30\times10^{-2})$	$-1.42\times10^{0}(1.01\times10^{-2})$	$-7.27\times10^{-1}(8.01\times10^{-3})$
C_{xw}	$6.55\times10^{-2}(6.31\times10^{-3})$	$2.51\times10^{-1}(6.76\times10^{-3})$	$5.02\times10^{-2}(6.02\times10^{-3})$	$-3.15\times10^{-1}(7.74\times10^{-3})$
$C_{x\delta_e}$	$-1.28\times10^{-1}(2.37\times10^{-3})$	$-2.71\times10^{-1}(2.25\times10^{-3})$	$-2.29\times10^{-1}(2.58\times10^{-3})$	$-9.80\times10^{-2}(3.31\times10^{-3})$
C_{zq}	$-4.45\times10^{-1}(1.38\times10^{-2})$	$6.07\times10^{-1}(4.79\times10^{-2})$	$-6.61\times10^{-1}(1.97\times10^{-2})$	$-9.41\times10^{-2}(4.39\times10^{-2})$
C_{zu}	$3.30\times10^{-1}(6.26\times10^{-3})$	$6.47\times10^{-2}(1.71\times10^{-2})$	$1.69\times10^{-1}(6.18\times10^{-3})$	$1.29\times10^{-1}(8.22\times10^{-3})$
C_{zw}	$-2.93\times10^{-1}(3.97\times10^{-3})$	$-2.94\times10^{-2}(8.30\times10^{-3})$	$-2.59\times10^{-1}(4.01\times10^{-3})$	$-1.52\times10^{-1}(9.02\times10^{-3})$
$C_{z\delta_e}$	$1.99\times10^{-2}(1.42\times10^{-3})$	$-5.66\times10^{-2}(5.56\times10^{-3})$	$2.63\times10^{-2}(2.38\times10^{-3})$	$-1.89\times10^{-2}(4.71\times10^{-3})$

Param.	Model #			
	37	38	39	40
C_{mq}	$-1.11\times10^{0}(7.72\times10^{-3})$	$-9.52\times10^{-1}(6.83\times10^{-3})$	$-7.87\times10^{-1}(5.08\times10^{-3})$	$-7.44\times10^{-1}(4.60\times10^{-3})$
C_{mu}	$-3.12\times10^{-3}(3.21\times10^{-3})$	$-3.46\times10^{-2}(1.87\times10^{-3})$	$-1.70\times10^{-1}(2.38\times10^{-3})$	$-8.49\times10^{-2}(1.50\times10^{-3})$
C_{mw}	$-1.43\times10^{-1}(1.49\times10^{-3})$	$-1.23\times10^{-1}(1.06\times10^{-3})$	$-5.96\times10^{-2}(9.04\times10^{-4})$	$-9.13\times10^{-2}(8.08\times10^{-4})$
$C_{m\delta_e}$	$1.16\times10^{-1}(8.50\times10^{-4})$	$9.58\times10^{-2}(7.08\times10^{-4})$	$7.55\times10^{-2}(5.10\times10^{-4})$	$7.32\times10^{-2}(4.82\times10^{-4})$
C_{mq}	$0.00\times10^{0}(0.00\times10^{0})$	$0.00\times10^{0}(0.00\times10^{0})$	$0.00\times10^{0}(0.00\times10^{0})$	$0.00\times10^{0}(0.00\times10^{0})$
C_{xu}	$-4.90\times10^{-2}(5.29\times10^{-4})$	$-4.26\times10^{-2}(5.76\times10^{-4})$	$-5.50\times10^{-2}(4.31\times10^{-4})$	$-4.43\times10^{-2}(2.34\times10^{-4})$
C_{xw}	$9.46\times10^{-2}(9.12\times10^{-3})$	$-2.44\times10^{-3}(1.19\times10^{-2})$	$-2.98\times10^{-2}(4.88\times10^{-3})$	$-1.05\times10^{-1}(3.96\times10^{-3})$
$C_{x\delta_e}$	$-2.33\times10^{-1}(5.45\times10^{-3})$	$-1.96\times10^{-1}(7.91\times10^{-3})$	$-2.17\times10^{-1}(3.09\times10^{-3})$	$-1.59\times10^{-1}(2.09\times10^{-3})$
C_{zq}	$-5.78\times10^{-2}(2.75\times10^{-3})$	$-1.54\times10^{-2}(1.64\times10^{-3})$	$-1.05\times10^{-2}(1.88\times10^{-3})$	$-1.76\times10^{-2}(1.16\times10^{-3})$
C_{zu}	$2.16\times10^{-2}(5.94\times10^{-4})$	$5.72\times10^{-3}(2.71\times10^{-4})$	$1.35\times10^{-2}(4.52\times10^{-4})$	$1.43\times10^{-2}(3.25\times10^{-4})$
C_{zw}	$-1.57\times10^{-2}(3.63\times10^{-4})$	$-5.84\times10^{-3}(2.11\times10^{-4})$	$-6.99\times10^{-3}(1.86\times10^{-4})$	$-8.00\times10^{-3}(1.63\times10^{-4})$
$C_{z\delta_e}$	$1.82\times10^{-1}(1.03\times10^{-2})$	$6.21\times10^{-2}(5.73\times10^{-3})$	$2.85\times10^{-2}(5.79\times10^{-3})$	$2.63\times10^{-3}(3.76\times10^{-3})$

Param.	Model #			
	41	42	43	44
C_{mq}	$-7.71\times10^{-1}(1.08\times10^{-2})$	$-8.76\times10^{-1}(4.84\times10^{-3})$	$-8.99\times10^{-1}(8.82\times10^{-3})$	$-9.29\times10^{-1}(1.00\times10^{-2})$
C_{mu}	$2.70\times10^{-2}(6.97\times10^{-3})$	$-4.44\times10^{-2}(1.47\times10^{-3})$	$2.23\times10^{-3}(4.01\times10^{-3})$	$3.61\times10^{-2}(4.43\times10^{-3})$
C_{mw}	$-1.26\times10^{-1}(3.62\times10^{-3})$	$-9.84\times10^{-2}(7.56\times10^{-4})$	$-1.46\times10^{-1}(2.50\times10^{-3})$	$-1.34\times10^{-1}(2.55\times10^{-3})$
$C_{m\delta_e}$	$9.38\times10^{-2}(1.17\times10^{-3})$	$9.22\times10^{-2}(5.54\times10^{-4})$	$1.00\times10^{-1}(1.06\times10^{-3})$	$1.01\times10^{-1}(1.07\times10^{-3})$
C_{mq}	$0.00\times10^{0}(0.00\times10^{0})$	$0.00\times10^{0}(0.00\times10^{0})$	$3.74\times10^{0}(7.98\times10^{-2})$	$3.42\times10^{0}(3.77\times10^{-2})$
C_{xu}	$-4.93\times10^{-2}(4.54\times10^{-4})$	$-4.96\times10^{-2}(2.40\times10^{-4})$	$-6.26\times10^{-2}(1.30\times10^{-3})$	$-5.15\times10^{-2}(5.05\times10^{-4})$
C_{xw}	$1.07\times10^{-1}(8.39\times10^{-3})$	$-6.46\times10^{-4}(3.64\times10^{-3})$	$3.87\times10^{-1}(2.32\times10^{-2})$	$1.62\times10^{-1}(9.30\times10^{-3})$
$C_{x\delta_e}$	$-1.93\times10^{-1}(2.74\times10^{-3})$	$-1.63\times10^{-1}(2.24\times10^{-3})$	$-2.46\times10^{-1}(9.71\times10^{-3})$	$-2.03\times10^{-1}(3.99\times10^{-3})$
C_{zq}	$-3.73\times10^{-2}(3.61\times10^{-3})$	$5.74\times10^{-3}(1.24\times10^{-3})$	$-1.39\times10^{0}(6.96\times10^{-2})$	$-6.77\times10^{-1}(8.21\times10^{-2})$
C_{zu}	$3.51\times10^{-2}(1.70\times10^{-3})$	$4.35\times10^{-3}(2.90\times10^{-4})$	$6.18\times10^{-1}(2.70\times10^{-2})$	$3.50\times10^{-1}(2.14\times10^{-2})$
C_{zw}	$-2.10\times10^{-2}(9.00\times10^{-4})$	$-3.96\times10^{-3}(1.61\times10^{-4})$	$-5.33\times10^{-1}(1.67\times10^{-2})$	$-3.45\times10^{-1}(1.46\times10^{-2})$
$C_{z\delta_e}$	$4.60\times10^{-2}(1.54\times10^{-2})$	$-3.57\times10^{-2}(3.83\times10^{-3})$	$4.47\times10^{-2}(8.09\times10^{-3})$	$-2.77\times10^{-2}(8.82\times10^{-3})$

Param.	Model #	
	45	46
C_{mq}	$-7.10\times10^{-1}(4.86\times10^{-3})$	$-7.13\times10^{-1}(3.96\times10^{-3})$
C_{mu}	$-8.78\times10^{-2}(2.49\times10^{-3})$	$-1.54\times10^{-1}(1.76\times10^{-3})$
C_{mw}	$-7.51\times10^{-2}(9.99\times10^{-4})$	$-5.65\times10^{-2}(8.32\times10^{-4})$
$C_{m\delta_e}$	$7.65\times10^{-2}(5.00\times10^{-4})$	$7.93\times10^{-2}(4.26\times10^{-4})$
C_{mq}	$2.45\times10^{0}(1.85\times10^{-2})$	$2.23\times10^{0}(2.46\times10^{-2})$
C_{xu}	$-4.22\times10^{-2}(3.22\times10^{-4})$	$-4.45\times10^{-2}(4.92\times10^{-4})$
C_{xw}	$-2.01\times10^{-1}(3.99\times10^{-3})$	$-1.06\times10^{-1}(6.80\times10^{-3})$
$C_{x\delta_e}$	$-1.97\times10^{-1}(2.13\times10^{-3})$	$-1.32\times10^{-1}(2.68\times10^{-3})$
C_{zq}	$5.37\times10^{-1}(6.17\times10^{-2})$	$-5.42\times10^{-1}(1.51\times10^{-2})$
C_{zu}	$-2.16\times10^{-1}(1.41\times10^{-2})$	$1.96\times10^{-1}(6.53\times10^{-3})$
C_{zw}	$-8.39\times10^{-2}(6.16\times10^{-3})$	$-2.54\times10^{-1}(2.56\times10^{-3})$
$C_{z\delta_e}$	$-8.59\times10^{-2}(7.08\times10^{-3})$	$5.81\times10^{-3}(1.58\times10^{-3})$

F

Table F.10: Simplified local model: estimated non-dimensional parameters and standard deviations $(\hat{\theta}(\hat{\sigma}))$, cf. Chapter 4, Eq. 4.2 and Appendix E – Models # 1–16

Param.	Model #			
	1	2	3	4
Cmq	$-5.76\times10^{-1}(4.13\times10^{-3})$	$-5.33\times10^{-1}(2.78\times10^{-3})$	$-5.63\times10^{-1}(2.44\times10^{-3})$	$-5.42\times10^{-1}(3.11\times10^{-3})$
Cmu	$-1.37\times10^{-1}(2.30\times10^{-3})$	$-1.64\times10^{-1}(1.31\times10^{-3})$	$-1.06\times10^{-1}(8.36\times10^{-4})$	$-1.54\times10^{-1}(1.63\times10^{-3})$
Cmw	$-1.87\times10^{-1}(5.33\times10^{-3})$	$-9.39\times10^{-2}(3.03\times10^{-3})$	$-1.13\times10^{-1}(1.09\times10^{-3})$	$-8.42\times10^{-2}(3.12\times10^{-3})$
Cmδe	$5.86\times10^{-2}(4.87\times10^{-4})$	$5.26\times10^{-2}(3.76\times10^{-4})$	$5.94\times10^{-2}(3.17\times10^{-4})$	$4.55\times10^{-2}(3.53\times10^{-4})$
Cmq	$1.63\times10^{0}(1.23\times10^{-2})$	$1.81\times10^{0}(1.02\times10^{-2})$	$1.75\times10^{0}(6.77\times10^{-3})$	$1.98\times10^{0}(1.83\times10^{-2})$
Cxu	$-8.85\times10^{-1}(3.49\times10^{-3})$	$-8.55\times10^{-1}(2.78\times10^{-3})$	$-9.45\times10^{-1}(1.93\times10^{-3})$	$-8.08\times10^{-1}(5.03\times10^{-3})$
Cxδe	$-1.38\times10^{-1}(1.71\times10^{-3})$	$-1.51\times10^{-1}(1.29\times10^{-3})$	$-1.01\times10^{-1}(9.38\times10^{-4})$	$-1.39\times10^{-1}(2.09\times10^{-3})$
Czq	$-4.05\times10^{-1}(1.44\times10^{-2})$	$-4.88\times10^{-1}(1.12\times10^{-2})$	$6.57\times10^{-3}(1.50\times10^{-2})$	$-5.07\times10^{-1}(1.72\times10^{-2})$
Czw	$-2.32\times10^{-1}(7.62\times10^{-3})$	$-2.08\times10^{-1}(5.63\times10^{-3})$	$5.41\times10^{-2}(3.53\times10^{-3})$	$-1.87\times10^{-1}(9.47\times10^{-3})$

Param.	Model #			
	5	6	7	8
Cmq	$-5.05\times10^{-1}(2.03\times10^{-3})$	$-8.20\times10^{-1}(4.41\times10^{-3})$	$-8.59\times10^{-1}(8.02\times10^{-3})$	$-7.38\times10^{-1}(4.84\times10^{-3})$
Cmu	$-1.36\times10^{-1}(1.05\times10^{-3})$	$-2.44\times10^{-1}(1.01\times10^{-3})$	$-1.62\times10^{-1}(1.77\times10^{-3})$	$-1.50\times10^{-1}(1.28\times10^{-3})$
Cmw	$-1.01\times10^{-1}(2.29\times10^{-3})$	$-1.81\times10^{-2}(1.21\times10^{-3})$	$-2.02\times10^{-1}(3.19\times10^{-3})$	$-1.67\times10^{-1}(1.93\times10^{-3})$
Cmδe	$4.84\times10^{-2}(2.64\times10^{-4})$	$7.38\times10^{-2}(3.43\times10^{-4})$	$7.93\times10^{-2}(7.25\times10^{-4})$	$5.79\times10^{-2}(4.13\times10^{-4})$
Cmq	$1.69\times10^{0}(2.14\times10^{-2})$	$1.71\times10^{0}(1.05\times10^{-2})$	$1.91\times10^{0}(1.71\times10^{-2})$	$1.21\times10^{0}(1.18\times10^{-2})$
Cxu	$-7.18\times10^{-1}(5.24\times10^{-3})$	$-8.33\times10^{-1}(3.35\times10^{-3})$	$-8.24\times10^{-1}(4.49\times10^{-3})$	$-9.63\times10^{-1}(3.62\times10^{-3})$
Cxδe	$-1.18\times10^{-1}(1.73\times10^{-3})$	$-9.53\times10^{-2}(1.08\times10^{-3})$	$-1.39\times10^{-1}(1.86\times10^{-3})$	$-1.10\times10^{-1}(1.20\times10^{-3})$
Czq	$-7.85\times10^{-2}(1.07\times10^{-2})$	$-3.95\times10^{-1}(9.15\times10^{-3})$	$-9.79\times10^{-1}(1.06\times10^{-2})$	$-4.74\times10^{-1}(7.78\times10^{-3})$
Czw	$9.57\times10^{-3}(4.34\times10^{-3})$	$1.61\times10^{-2}(2.27\times10^{-3})$	$-1.83\times10^{-1}(2.96\times10^{-3})$	$-8.99\times10^{-2}(2.73\times10^{-3})$

Param.	Model #			
	9	10	11	12
Cmq	$-6.59\times10^{-1}(3.40\times10^{-2})$	$-3.34\times10^{-1}(2.45\times10^{-3})$	$-5.61\times10^{-1}(4.20\times10^{-3})$	$-5.18\times10^{-1}(3.33\times10^{-3})$
Cmu	$-9.07\times10^{-2}(1.39\times10^{-2})$	$-1.43\times10^{-1}(1.30\times10^{-3})$	$-8.80\times10^{-2}(2.16\times10^{-3})$	$-1.08\times10^{-1}(1.21\times10^{-3})$
Cmw	$-5.37\times10^{-1}(1.58\times10^{-2})$	$-4.22\times10^{-2}(2.04\times10^{-3})$	$-2.06\times10^{-1}(3.49\times10^{-3})$	$-1.30\times10^{-1}(1.62\times10^{-3})$
Cmδe	$4.28\times10^{-2}(2.02\times10^{-3})$	$3.34\times10^{-2}(2.73\times10^{-4})$	$4.87\times10^{-2}(4.02\times10^{-4})$	$4.93\times10^{-2}(3.54\times10^{-4})$
Cmq	$5.21\times10^{-1}(5.19\times10^{-2})$	$1.41\times10^{0}(1.26\times10^{-2})$	$1.64\times10^{0}(1.03\times10^{-2})$	$1.30\times10^{0}(9.89\times10^{-3})$
Cxu	$-6.09\times10^{-1}(1.29\times10^{-2})$	$-1.01\times10^{0}(4.07\times10^{-3})$	$-1.01\times10^{0}(3.18\times10^{-3})$	$-9.00\times10^{-1}(3.17\times10^{-3})$
Cxδe	$-6.04\times10^{-2}(4.11\times10^{-3})$	$-5.09\times10^{-2}(1.31\times10^{-3})$	$-7.91\times10^{-2}(1.23\times10^{-3})$	$-5.33\times10^{-2}(1.33\times10^{-3})$
Czq	$-1.49\times10^{0}(1.08\times10^{-1})$	$-2.70\times10^{-1}(2.58\times10^{-2})$	$-2.46\times10^{-1}(1.79\times10^{-2})$	$3.06\times10^{-2}(1.74\times10^{-2})$
Czw	$-4.86\times10^{-1}(2.02\times10^{-2})$	$-1.54\times10^{-1}(7.13\times10^{-3})$	$-5.21\times10^{-2}(6.67\times10^{-3})$	$9.06\times10^{-2}(4.16\times10^{-3})$

Param.	Model #			
	13	14	15	16
Cmq	$-5.75\times10^{-1}(2.95\times10^{-3})$	$-6.24\times10^{-1}(2.85\times10^{-3})$	$-8.52\times10^{-1}(5.81\times10^{-3})$	$-6.07\times10^{-1}(1.10\times10^{-2})$
Cmu	$-1.70\times10^{-1}(1.02\times10^{-3})$	$-1.77\times10^{-1}(1.23\times10^{-3})$	$-9.27\times10^{-2}(1.60\times10^{-3})$	$-1.49\times10^{-1}(4.17\times10^{-3})$
Cmw	$-6.76\times10^{-2}(1.41\times10^{-3})$	$-1.23\times10^{-1}(1.60\times10^{-3})$	$-2.31\times10^{-1}(2.34\times10^{-3})$	$-2.22\times10^{-1}(8.22\times10^{-3})$
Cmδe	$5.98\times10^{-2}(3.87\times10^{-4})$	$5.26\times10^{-2}(3.57\times10^{-4})$	$7.02\times10^{-2}(5.62\times10^{-4})$	$4.09\times10^{-2}(5.03\times10^{-4})$
Cmq	$1.53\times10^{0}(8.26\times10^{-3})$	$2.00\times10^{0}(1.83\times10^{-2})$	$2.10\times10^{0}(2.96\times10^{-2})$	$1.72\times10^{0}(1.08\times10^{-2})$
Cxu	$-9.59\times10^{-1}(2.90\times10^{-3})$	$-8.46\times10^{-1}(6.22\times10^{-3})$	$-8.66\times10^{-1}(9.44\times10^{-3})$	$-9.49\times10^{-1}(3.78\times10^{-3})$
Cxδe	$-8.95\times10^{-2}(9.92\times10^{-4})$	$-1.39\times10^{-1}(2.15\times10^{-3})$	$-1.59\times10^{-1}(3.51\times10^{-3})$	$-7.89\times10^{-2}(9.96\times10^{-4})$
Czq	$4.32\times10^{-2}(1.92\times10^{-2})$	$-1.56\times10^{-1}(6.87\times10^{-3})$	$-3.01\times10^{-1}(1.01\times10^{-2})$	$-1.32\times10^{0}(4.74\times10^{-2})$
Czw	$2.88\times10^{-2}(5.51\times10^{-3})$	$7.59\times10^{-2}(2.94\times10^{-3})$	$-3.85\times10^{-2}(3.27\times10^{-3})$	$-5.74\times10^{-1}(2.09\times10^{-2})$

F

Table F.11: Simplified local model: estimated non-dimensional parameters and standard deviations ($\hat{\theta}(\hat{\sigma})$), cf. Chapter 4, Eq. 4.2 and Appendix E – Models # 17–32

Param.	Model #			
	17	18	19	20
$\mathbf{C_{mq}}$	$-5.36 \times 10^{-1} (3.26 \times 10^{-3})$	$-5.53 \times 10^{-1} (4.04 \times 10^{-3})$	$-7.95 \times 10^{-1} (5.83 \times 10^{-3})$	$-6.31 \times 10^{-1} (4.66 \times 10^{-3})$
$\mathbf{C_{mu}}$	$-1.25 \times 10^{-1} (7.84 \times 10^{-4})$	$-1.25 \times 10^{-1} (1.59 \times 10^{-3})$	$-1.40 \times 10^{-1} (3.09 \times 10^{-3})$	$-1.53 \times 10^{-1} (1.91 \times 10^{-3})$
$\mathbf{C_{mw}}$	$-6.55 \times 10^{-2} (8.25 \times 10^{-4})$	$-1.43 \times 10^{-1} (1.79 \times 10^{-3})$	$-1.35 \times 10^{-1} (3.23 \times 10^{-3})$	$-1.13 \times 10^{-1} (1.35 \times 10^{-3})$
$\mathbf{C_{m\delta_e}}$	$5.04 \times 10^{-2} (3.97 \times 10^{-4})$	$6.44 \times 10^{-2} (5.12 \times 10^{-4})$	$7.16 \times 10^{-2} (4.86 \times 10^{-4})$	$5.63 \times 10^{-2} (4.31 \times 10^{-4})$
$\mathbf{C_{mq}}$	$1.76 \times 10^{0} (1.23 \times 10^{-2})$	$1.81 \times 10^{0} (9.94 \times 10^{-3})$	$1.62 \times 10^{0} (2.55 \times 10^{-2})$	$1.91 \times 10^{0} (1.85 \times 10^{-2})$
$\mathbf{C_{xu}}$	$-1.07 \times 10^{0} (4.15 \times 10^{-3})$	$-1.09 \times 10^{0} (3.84 \times 10^{-3})$	$-1.07 \times 10^{0} (7.49 \times 10^{-3})$	$-1.13 \times 10^{0} (6.27 \times 10^{-3})$
$\mathbf{C_{x\delta_e}}$	$-1.12 \times 10^{-1} (1.40 \times 10^{-3})$	$-9.73 \times 10^{-2} (1.39 \times 10^{-3})$	$-4.46 \times 10^{-2} (2.83 \times 10^{-3})$	$-1.01 \times 10^{-1} (1.44 \times 10^{-3})$
$\mathbf{C_{zq}}$	$7.62 \times 10^{-2} (1.15 \times 10^{-2})$	$-8.01 \times 10^{-2} (1.72 \times 10^{-2})$	$-5.79 \times 10^{-1} (2.61 \times 10^{-2})$	$-1.86 \times 10^{-1} (1.45 \times 10^{-2})$
$\mathbf{C_{zw}}$	$1.42 \times 10^{-1} (3.04 \times 10^{-3})$	$-3.54 \times 10^{-2} (4.56 \times 10^{-3})$	$-1.82 \times 10^{-1} (5.61 \times 10^{-3})$	$-8.84 \times 10^{-2} (2.21 \times 10^{-3})$

Param.	Model #			
	21	22	23	24
$\mathbf{C_{mq}}$	$-6.51 \times 10^{-1} (7.34 \times 10^{-3})$	$-8.35 \times 10^{-1} (3.71 \times 10^{-3})$	$-5.62 \times 10^{-1} (5.87 \times 10^{-3})$	$-9.58 \times 10^{-1} (6.22 \times 10^{-3})$
$\mathbf{C_{mu}}$	$-1.71 \times 10^{-1} (3.08 \times 10^{-3})$	$-1.22 \times 10^{-1} (1.01 \times 10^{-3})$	$-2.27 \times 10^{-1} (2.06 \times 10^{-3})$	$-5.89 \times 10^{-2} (2.24 \times 10^{-3})$
$\mathbf{C_{mw}}$	$-1.16 \times 10^{-1} (2.08 \times 10^{-3})$	$-1.30 \times 10^{-1} (8.67 \times 10^{-4})$	$8.41 \times 10^{-3} (1.03 \times 10^{-3})$	$-2.28 \times 10^{-1} (2.20 \times 10^{-3})$
$\mathbf{C_{m\delta_e}}$	$4.26 \times 10^{-2} (5.91 \times 10^{-4})$	$8.54 \times 10^{-2} (4.24 \times 10^{-4})$	$7.57 \times 10^{-2} (5.96 \times 10^{-4})$	$8.71 \times 10^{-2} (5.00 \times 10^{-4})$
$\mathbf{C_{mq}}$	$2.72 \times 10^{0} (2.30 \times 10^{-2})$	$1.75 \times 10^{0} (1.57 \times 10^{-2})$	$8.60 \times 10^{-1} (2.61 \times 10^{-2})$	$2.57 \times 10^{0} (1.75 \times 10^{-2})$
$\mathbf{C_{xu}}$	$-1.37 \times 10^{0} (9.70 \times 10^{-3})$	$-1.15 \times 10^{0} (5.81 \times 10^{-3})$	$-1.11 \times 10^{0} (1.16 \times 10^{-2})$	$-1.09 \times 10^{0} (5.64 \times 10^{-3})$
$\mathbf{C_{x\delta_e}}$	$-1.49 \times 10^{-1} (1.94 \times 10^{-3})$	$-1.02 \times 10^{-1} (1.49 \times 10^{-3})$	$1.51 \times 10^{-1} (2.37 \times 10^{-3})$	$-1.52 \times 10^{-1} (1.97 \times 10^{-3})$
$\mathbf{C_{zq}}$	$-2.36 \times 10^{-1} (2.45 \times 10^{-2})$	$-3.11 \times 10^{-1} (9.27 \times 10^{-3})$	$2.71 \times 10^{-1} (1.08 \times 10^{-2})$	$-7.02 \times 10^{-1} (1.53 \times 10^{-2})$
$\mathbf{C_{zw}}$	$-1.95 \times 10^{-1} (5.40 \times 10^{-3})$	$-1.56 \times 10^{-1} (2.82 \times 10^{-3})$	$8.27 \times 10^{-2} (3.09 \times 10^{-3})$	$-2.56 \times 10^{-1} (2.74 \times 10^{-3})$

Param.	Model #			
	25	26	27	28
$\mathbf{C_{mq}}$	$-6.44 \times 10^{-1} (4.29 \times 10^{-3})$	$-8.11 \times 10^{-1} (4.92 \times 10^{-3})$	$-8.40 \times 10^{-1} (3.48 \times 10^{-3})$	$-8.42 \times 10^{-1} (6.71 \times 10^{-3})$
$\mathbf{C_{mu}}$	$-1.15 \times 10^{-1} (1.71 \times 10^{-3})$	$-1.61 \times 10^{-1} (1.33 \times 10^{-3})$	$-6.98 \times 10^{-2} (1.37 \times 10^{-3})$	$-1.01 \times 10^{-1} (3.84 \times 10^{-3})$
$\mathbf{C_{mw}}$	$-1.07 \times 10^{-1} (1.43 \times 10^{-3})$	$-1.15 \times 10^{-1} (1.28 \times 10^{-3})$	$-1.63 \times 10^{-1} (1.06 \times 10^{-3})$	$-1.93 \times 10^{-1} (2.63 \times 10^{-3})$
$\mathbf{C_{m\delta_e}}$	$6.81 \times 10^{-2} (4.85 \times 10^{-4})$	$7.28 \times 10^{-2} (4.78 \times 10^{-4})$	$7.79 \times 10^{-2} (3.30 \times 10^{-4})$	$7.97 \times 10^{-2} (5.90 \times 10^{-4})$
$\mathbf{C_{mq}}$	$1.92 \times 10^{0} (2.73 \times 10^{-2})$	$2.30 \times 10^{0} (1.32 \times 10^{-2})$	$1.94 \times 10^{0} (1.72 \times 10^{-2})$	$2.07 \times 10^{0} (4.02 \times 10^{-2})$
$\mathbf{C_{xu}}$	$-1.16 \times 10^{0} (9.94 \times 10^{-3})$	$-1.20 \times 10^{0} (4.77 \times 10^{-3})$	$-1.25 \times 10^{0} (6.25 \times 10^{-3})$	$-1.43 \times 10^{0} (1.70 \times 10^{-2})$
$\mathbf{C_{x\delta_e}}$	$-9.97 \times 10^{-2} (3.83 \times 10^{-3})$	$-1.28 \times 10^{-1} (1.51 \times 10^{-3})$	$-1.25 \times 10^{-1} (2.04 \times 10^{-3})$	$-9.83 \times 10^{-2} (3.38 \times 10^{-3})$
$\mathbf{C_{zq}}$	$-3.79 \times 10^{-1} (1.32 \times 10^{-2})$	$-4.66 \times 10^{-1} (9.77 \times 10^{-3})$	$-1.60 \times 10^{-1} (9.46 \times 10^{-3})$	$-6.49 \times 10^{-1} (1.57 \times 10^{-2})$
$\mathbf{C_{zw}}$	$-1.31 \times 10^{-1} (3.68 \times 10^{-3})$	$-1.66 \times 10^{-1} (2.76 \times 10^{-3})$	$-1.03 \times 10^{-1} (1.92 \times 10^{-3})$	$-2.36 \times 10^{-1} (3.57 \times 10^{-3})$

Param.	Model #			
	29	30	31	32
$\mathbf{C_{mq}}$	$-9.16 \times 10^{-1} (6.09 \times 10^{-3})$	$-6.52 \times 10^{-1} (2.80 \times 10^{-3})$	$-9.02 \times 10^{-1} (4.24 \times 10^{-3})$	$-5.61 \times 10^{-1} (2.99 \times 10^{-3})$
$\mathbf{C_{mu}}$	$-1.06 \times 10^{-1} (1.22 \times 10^{-3})$	$-1.92 \times 10^{-1} (7.84 \times 10^{-4})$	$-2.50 \times 10^{-2} (1.54 \times 10^{-3})$	$-1.01 \times 10^{-1} (1.08 \times 10^{-3})$
$\mathbf{C_{mw}}$	$-1.51 \times 10^{-1} (1.26 \times 10^{-3})$	$-4.50 \times 10^{-2} (4.57 \times 10^{-4})$	$-1.78 \times 10^{-1} (1.18 \times 10^{-3})$	$-8.00 \times 10^{-2} (7.99 \times 10^{-4})$
$\mathbf{C_{m\delta_e}}$	$9.50 \times 10^{-2} (6.65 \times 10^{-4})$	$7.07 \times 10^{-2} (2.87 \times 10^{-4})$	$8.46 \times 10^{-2} (4.20 \times 10^{-4})$	$6.40 \times 10^{-2} (4.03 \times 10^{-4})$
$\mathbf{C_{mq}}$	$2.47 \times 10^{0} (1.99 \times 10^{-2})$	$1.84 \times 10^{0} (1.45 \times 10^{-2})$	$1.75 \times 10^{0} (3.80 \times 10^{-2})$	$2.16 \times 10^{0} (1.52 \times 10^{-2})$
$\mathbf{C_{xu}}$	$-1.14 \times 10^{0} (7.47 \times 10^{-3})$	$-1.26 \times 10^{0} (6.54 \times 10^{-3})$	$-1.12 \times 10^{0} (1.25 \times 10^{-2})$	$-1.35 \times 10^{0} (5.88 \times 10^{-3})$
$\mathbf{C_{x\delta_e}}$	$-1.38 \times 10^{-1} (2.12 \times 10^{-3})$	$-1.10 \times 10^{-1} (9.63 \times 10^{-4})$	$-1.19 \times 10^{-1} (2.81 \times 10^{-3})$	$-1.19 \times 10^{-1} (2.10 \times 10^{-3})$
$\mathbf{C_{zq}}$	$-3.40 \times 10^{-1} (1.25 \times 10^{-2})$	$-2.80 \times 10^{-1} (6.74 \times 10^{-3})$	$-4.24 \times 10^{-2} (1.22 \times 10^{-2})$	$-1.46 \times 10^{-2} (1.25 \times 10^{-2})$
$\mathbf{C_{zw}}$	$-1.51 \times 10^{-1} (2.18 \times 10^{-3})$	$-1.06 \times 10^{-1} (2.04 \times 10^{-3})$	$-1.31 \times 10^{-1} (2.22 \times 10^{-3})$	$-8.98 \times 10^{-2} (3.25 \times 10^{-3})$

F

Table F.12: Simplified local model: estimated non-dimensional parameters and standard deviations ($\hat{\theta}(\hat{\sigma})$), cf. Chapter 4, Eq. 4.2 and Appendix E – Models # 33–46

Param.	Model #			
	33	34	35	36
C_{mq}	$-7.53\times10^{-1}(2.66\times10^{-3})$	$-6.23\times10^{-1}(3.21\times10^{-3})$	$-6.92\times10^{-1}(3.81\times10^{-3})$	$-8.42\times10^{-1}(5.71\times10^{-3})$
C_{mu}	$-1.01\times10^{-1}(8.22\times10^{-4})$	$-7.32\times10^{-2}(1.69\times10^{-3})$	$-1.33\times10^{-1}(1.28\times10^{-3})$	$-3.06\times10^{-2}(2.55\times10^{-3})$
C_{mw}	$-1.04\times10^{-1}(6.35\times10^{-4})$	$-8.62\times10^{-2}(7.37\times10^{-4})$	$-6.68\times10^{-2}(7.31\times10^{-4})$	$-1.96\times10^{-1}(2.19\times10^{-3})$
$C_{m\delta_e}$	$7.67\times10^{-2}(3.00\times10^{-4})$	$6.71\times10^{-2}(4.47\times10^{-4})$	$8.24\times10^{-2}(4.15\times10^{-4})$	$7.93\times10^{-2}(5.74\times10^{-4})$
C_{mq}	$1.82\times10^{0}(1.57\times10^{-2})$	$2.63\times10^{0}(1.99\times10^{-2})$	$3.13\times10^{0}(1.70\times10^{-2})$	$2.58\times10^{0}(2.32\times10^{-2})$
C_{xu}	$-1.22\times10^{0}(5.51\times10^{-3})$	$-1.61\times10^{0}(1.00\times10^{-2})$	$-1.42\times10^{0}(6.83\times10^{-3})$	$-1.00\times10^{0}(7.68\times10^{-3})$
$C_{x\delta_e}$	$-8.26\times10^{-2}(1.30\times10^{-3})$	$-2.04\times10^{-1}(1.91\times10^{-3})$	$-2.31\times10^{-1}(2.05\times10^{-3})$	$-1.63\times10^{-1}(2.96\times10^{-3})$
C_{zq}	$-1.96\times10^{-1}(7.87\times10^{-3})$	$-5.27\times10^{-2}(2.22\times10^{-2})$	$-4.31\times10^{-1}(1.09\times10^{-2})$	$-3.95\times10^{-1}(1.94\times10^{-2})$
C_{zw}	$-1.30\times10^{-1}(1.89\times10^{-3})$	$-7.05\times10^{-2}(3.21\times10^{-3})$	$-1.90\times10^{-1}(2.37\times10^{-3})$	$-1.84\times10^{-1}(4.35\times10^{-3})$

Param.	Model #			
	37	38	39	40
C_{mq}	$-1.03\times10^{0}(7.64\times10^{-3})$	$-8.93\times10^{-1}(5.77\times10^{-3})$	$-7.10\times10^{-1}(4.14\times10^{-3})$	$-7.01\times10^{-1}(4.76\times10^{-3})$
C_{mu}	$-3.56\times10^{-2}(3.52\times10^{-3})$	$-3.27\times10^{-2}(1.81\times10^{-3})$	$-1.56\times10^{-1}(2.14\times10^{-3})$	$-9.39\times10^{-2}(1.94\times10^{-3})$
C_{mw}	$-1.72\times10^{-1}(1.74\times10^{-3})$	$-1.25\times10^{-1}(1.06\times10^{-3})$	$-6.44\times10^{-2}(6.11\times10^{-4})$	$-1.10\times10^{-1}(1.11\times10^{-3})$
$C_{m\delta_e}$	$9.92\times10^{-2}(5.13\times10^{-4})$	$8.87\times10^{-2}(5.85\times10^{-4})$	$7.05\times10^{-2}(4.80\times10^{-4})$	$6.86\times10^{-2}(4.54\times10^{-4})$
C_{mq}	$2.36\times10^{0}(2.90\times10^{-2})$	$3.00\times10^{0}(3.71\times10^{-2})$	$3.50\times10^{0}(2.47\times10^{-2})$	$2.64\times10^{0}(1.40\times10^{-2})$
C_{xu}	$-1.26\times10^{0}(8.36\times10^{-3})$	$-1.47\times10^{0}(1.40\times10^{-2})$	$-1.86\times10^{0}(1.21\times10^{-2})$	$-1.66\times10^{0}(6.66\times10^{-3})$
$C_{x\delta_e}$	$-9.33\times10^{-2}(2.15\times10^{-3})$	$-1.78\times10^{-1}(4.56\times10^{-3})$	$-2.51\times10^{-1}(2.46\times10^{-3})$	$-1.85\times10^{-1}(1.64\times10^{-3})$
C_{zq}	$-9.39\times10^{-1}(3.45\times10^{-2})$	$1.12\times10^{-1}(1.93\times10^{-2})$	$1.22\times10^{-1}(2.44\times10^{-2})$	$-6.89\times10^{-1}(1.99\times10^{-2})$
C_{zw}	$-2.85\times10^{-1}(3.04\times10^{-3})$	$-1.02\times10^{-1}(2.25\times10^{-3})$	$-1.42\times10^{-1}(2.59\times10^{-3})$	$-2.17\times10^{-1}(2.45\times10^{-3})$

Param.	Model #			
	41	42	43	44
C_{mq}	$-5.66\times10^{-1}(4.06\times10^{-3})$	$-8.60\times10^{-1}(4.34\times10^{-3})$	$-7.70\times10^{-1}(4.73\times10^{-3})$	$-8.14\times10^{-1}(6.61\times10^{-3})$
C_{mu}	$-9.68\times10^{-2}(2.32\times10^{-3})$	$-4.69\times10^{-2}(1.57\times10^{-3})$	$-5.41\times10^{-2}(1.57\times10^{-3})$	$-7.94\times10^{-3}(2.88\times10^{-3})$
C_{mw}	$-6.85\times10^{-2}(1.18\times10^{-3})$	$-1.04\times10^{-1}(7.63\times10^{-4})$	$-1.24\times10^{-1}(1.19\times10^{-3})$	$-1.19\times10^{-1}(1.75\times10^{-3})$
$C_{m\delta_e}$	$6.87\times10^{-2}(5.45\times10^{-4})$	$9.25\times10^{-2}(4.52\times10^{-4})$	$8.41\times10^{-2}(5.29\times10^{-4})$	$8.93\times10^{-2}(6.92\times10^{-4})$
C_{mq}	$2.43\times10^{0}(1.24\times10^{-2})$	$2.82\times10^{0}(1.32\times10^{-2})$	$2.43\times10^{0}(2.81\times10^{-2})$	$2.78\times10^{0}(1.80\times10^{-2})$
C_{xu}	$-1.53\times10^{0}(5.36\times10^{-3})$	$-1.55\times10^{0}(4.94\times10^{-3})$	$-1.14\times10^{0}(1.01\times10^{-2})$	$-1.31\times10^{0}(6.00\times10^{-3})$
$C_{x\delta_e}$	$-1.64\times10^{-1}(1.68\times10^{-3})$	$-1.62\times10^{-1}(1.65\times10^{-3})$	$-1.24\times10^{-1}(2.09\times10^{-3})$	$-1.47\times10^{-1}(2.05\times10^{-3})$
C_{zq}	$-8.41\times10^{-2}(3.26\times10^{-2})$	$-1.15\times10^{-1}(1.52\times10^{-2})$	$-8.22\times10^{-1}(1.73\times10^{-2})$	$-6.47\times10^{-1}(3.01\times10^{-2})$
C_{zw}	$-1.09\times10^{-1}(5.78\times10^{-3})$	$-1.36\times10^{-1}(1.59\times10^{-3})$	$-2.13\times10^{-1}(2.63\times10^{-3})$	$-2.28\times10^{-1}(4.61\times10^{-3})$

Param.	Model #	
	45	46
C_{mq}	$-6.90\times10^{-1}(4.02\times10^{-3})$	$-7.20\times10^{-1}(3.27\times10^{-3})$
C_{mu}	$-1.44\times10^{-1}(2.62\times10^{-3})$	$-1.86\times10^{-1}(1.43\times10^{-3})$
C_{mw}	$-4.91\times10^{-2}(5.79\times10^{-4})$	$-4.87\times10^{-2}(6.78\times10^{-4})$
$C_{m\delta_e}$	$7.44\times10^{-2}(5.77\times10^{-4})$	$7.78\times10^{-2}(3.33\times10^{-4})$
C_{mq}	$2.94\times10^{0}(2.58\times10^{-2})$	$2.09\times10^{0}(2.43\times10^{-2})$
C_{xu}	$-1.85\times10^{0}(1.48\times10^{-2})$	$-1.43\times10^{0}(1.24\times10^{-2})$
$C_{x\delta_e}$	$-2.55\times10^{-1}(3.25\times10^{-3})$	$-1.16\times10^{-1}(2.68\times10^{-3})$
C_{zq}	$2.85\times10^{-2}(3.00\times10^{-2})$	$-5.08\times10^{-1}(8.38\times10^{-3})$
C_{zw}	$-1.27\times10^{-1}(3.85\times10^{-3})$	$-1.96\times10^{-1}(1.63\times10^{-3})$

F

G

GEOMETRIC PROPERTIES OF THE DELFLY II

This appendix lists the main geometric properties of the DelFly II flapping-wing micro aerial vehicle used as test platform in this thesis. Due to their manual construction and varying instrumentation, different specimens of the same vehicle have slightly different properties. Additionally, the centre of gravity (CG) position must be shifted in order to achieve faster or slower forward flight velocities. Hence, three different configurations are described in the table below, corresponding to the vehicles used within this thesis. The table also highlights which configuration is used in which chapters.

Table G.1: Inertial and geometric properties of the DelFly II configurations used in this thesis.

	Property	Configuration I: Slow Flight, AFRL ($V \leq 1\,m/s$) (Ch. 3, 5)	Configuration II: Fast Flight, AFRL ($V \geq 1\,m/s$) (Ch. 5)	Configuration III: Cyberzoo ($V \leq 1.5\,m/s$) (Ch. 2, 4)
Full vehicle	Total mass [g]	17.4	18.4	23.5
	CG (from nose) ($\mathbf{x_{B1}}=\mathbf{z_{B2}}$) [mm]	-63.1	-37.1	-69.5
	CG (from nose) ($\mathbf{y_{B1}}=\mathbf{y_{B2}}$) [mm]	0.0	0.1	0.0
	CG (from nose) ($\mathbf{z_{B1}}=\mathbf{x_{B2}}$) [mm]	2.0	0.2	9.6
	Inertia $I_{xx,B1}=I_{zz,B2}$ [Nm²]	1.23E-5	0.19E-4	1.92E-5
	Inertia $I_{yy,B1}=I_{yy,B2}$ [Nm²]	9.64E-5	2.87E-4	6.55E-5
	Inertia $I_{zz,B1}=I_{xx,B2}$ [Nm²]	9.89E-5	7.97E-4	7.54E-5
Single wing	Mass [g]	0.29	0.29	0.29
	Span [mm]	274	274	274
	Root chord [mm]	85	85	85
	Tip chord [mm]	56	56	56
	Surface [m²]	2.11E-2	2.11E-2	2.11E-2
Horizontal Tail	Mass [g]	1.75	1.75	1.75
	Span [mm]	174	174	174
	Root chord [mm]	72	72	72
	Tip chord [mm]	22	22	22
	Total surface [m²]	9.79E-3	9.79E-3	9.79E-3
	Elevator chord [mm]	20	20	20
	Distance from nose [mm]	148	137	150
Vertical Tail	Mass [g]	0.8	0.8	0.8
	Height [mm]	54	54	54
	Total Surface [m²]	2.75E-3	2.75E-3	2.75E-3
	Rudder chord [mm]	20	20	20
	Distance from nose [mm]	148	137	150

G

SAMENVATTING

De toenemende interesse in onbemande vliegtuigen, voor een breed scala aan steeds uitdagendere toepassingen in zowel het militaire, commerciele en civiele domein, zorgt voor een drang naar innovatieve en onconventionele oplossingen. Een sterke trend is de toenemende vraag naar kleine, wendbare en daarmee veelzijdig inzetbare voertuigen, die geschikt zijn voor toepassing in complexe, nauwe en mogelijk gevaarlijke omgevingen. Conventionele bemande voertuigen kunnen niet aan deze vraag voldoen, dus zoeken ingenieurs naar inspiratie uit de natuur, wat heeft geleid tot de biologisch-geïnspireerde 'flapping-wing micro aerial vehicle', ofwel FWMAV (micro luchtvaartuigen met flappende vleugels). FWMAV's beschikken over opmerkelijke vliegprestaties bij lage snelheden en op kleine schaal, waarbij ze een hoge wendbaarheid, de mogelijkheid tot zweven ('hover') en een aanzienlijke potentie tot miniaturisatie etaleren. Ondanks deze gunstige eigenschappen worden FWMAV's bijna uitsluitend gebruikt als onderzoeksobjecten en blijft hun verdere ontwikkeling een aanzienlijke uitdaging vormen. Hoewel er inmiddels verscheidene FWMAV's bestaan, is onze kennis over hun vliegmechanica, en in het bijzonder de aerodynamica, beperkt. Dit hindert de ontwikkeling van effectieve (aero)dynamische modellen, die essentieel zijn voor realistische simulaties, efficiente ontwerpen en de ontwikkeling van geavanceerde vliegbesturingssystemen. Deze toepassingen zijn cruciaal voor de verdere verbetering van de prestaties en autonomie van FWMAV's. Tot op heden zijn er echter maar weinig modellen beschikbaar voor FWWAV's. De modellen die wel bestaan zijn of te complex voor praktische toepassingen, of te simpel voor de ontwikkeling van vliegbesturingssystemen, of niet volledig gevalideerd.

Dit proefschrift richt zich op de uitdaging van het modeleren van de tijds-variërende dynamica van flappende vleugels in FWMAV's op basis van data verzameld in zowel vrije vluchten als in experimenten in windtunnels. Het specifieke doel is de ontwikkeling van nieuwe modelleringstechnieken die meer inzage bieden in de vliegmechanica van FWMAV's. Deze modellen moeten nauwkeurig genoeg zijn voor toepassingen als simulatie en voor het ontwerp van vliegbesturingssystemen, maar moeten tegelijkertijd niet te complex en rekenintensief zijn. Dit proefschrift moet tevens bijdragen aan de verdere ontwikkeling van FWMAV's, om deze zo een stap dichterbij de volledige integratie in de luchtvaartsector te brengen. De gegevensgestuurde aanpak die hierin centraal staat zorgt er zowel voor dat er realistische resultaten verzameld worden, maar ook dat er inherente mogelijkheden tot validatie zijn. Ondanks een gebrek aan voorkennis over het bestudeerde systeem, biedt deze aanpak toch de mogelijkheid om tot nuttige inzichten te komen. Met het oog op de experimentele methodiek die centraal staat in dit proefschrift, is al het werk gebaseerd op een testvoertuig, namelijk de DelFly II, ontwikkeld aan de TU Delft. De aanpak rust in de eerste plaats op het grondig analyseren, modelleren en begrijpen van de vliegmechanica van een specifieke FWMAV. Vervolgens worden zowel de toegepaste methodiek als de verworven inzichten gegeneraliseerd zodat deze ook elders kunnen worden toegepast. Om aan deze doelstellingen te voldoen, worden er twee generieke modelleringsmethoden

315

ontwikkeld en behandeld in de twee delen van dit proefschrift.

De eerste modelleringsmethode is gebaseerd op systeemidentificatie op basis van vrije-vlucht data en leidt tot de ontwikkeling van lineair tijdsvariërende 'grey-box' toestands-modellen van de voertuigdynamica. Hierbij wordt gebruikt gemaakt van het principe van tijdschaal separatie, waarbij een modelstructuur dat bestaat uit twee delen wordt toegepast. Deze structuur ondersteund een decompositie in het frequentie-domein waarbij laag- en hoogfrequente signalen in de data van elkaar te onderscheiden zijn. Met deze techniek kunnen vervolgens de effecten van de tijdsvariërende dynamica van het vleugel-flappen worden toegevoegd aan het model. Deze effecten worden doorgaans verwaarloosd in FWMAV mo-dellen, maar hebben wel degelijk een toegevoegde waarde. Zo draagt kennis over deze effecten niet alleen bij aan een completere karakterisatie van het voertuig, maar ook voor het testen van nieuwe instrumentatie en besturings- en navigatiealgoritmes, waar een hoge precisie voor nodig is. Hoewel het tijdsvariënde model bewezen nauwkeurig is voor toe-passing op het bestudeerde onderzoeksplatform, zijn er tijdens manoeuvres ook effecten ge-vonden die het model niet kan verklaren. Deze effecten zijn klein, maar desondanks wordt geadviseerd om nader onderzoek te doen naar potentiele tijdschaal-koppelingen alvorens aan te nemen dat deze verwaarloosbaar zijn. Dit is met name het geval voor voertuigen als de DelFly, waar de frequentie van de dynamica van het flappen dichtbij de frequenties van de lichaamseigen dynamische modi ligt. De gekozen modelstructuur is verder afhankelijk van een klein aantal parameters en metingen en is nauwkeurig in het voorspellen van zowel gemiddelde als tijdsvariërende aerodynamische krachten en momenten. Daarnaast is het model te gebruiken voor nauwkeurige dynamische simulaties, warmee het bijdraagt aan de reeds bestaande resultaten die beschikbaar zijn voor de DelFly.

De op 'grey-box'-modellen gebaseerde aanpak is vervolgens toegepast op een reeks van verschillende vliegcondities en gebruikt om de voertuigdynamica van het testplatform completer te karakteriseren. Hierbij lag de nadruk met name op de belangrijke tijdsgemid-delde component. De resultaten van deze analyse zijn gebruikt om een lineair parameter-variërend (LPV) model te ontwikkelen, die de dynamica voor de gehele reeks reeds ver-kende vliegcondities beschrijft. Hiermee is een globale aanpak voor modelidentificatie toe-gepast op FWMAV's gedemonstreerd. Om deze globale aanpak te bewerkstelligen moest ook een reeks scheduling functies gedefineerd worden die de lokale modellen koppelen aan de corresponderende vliegcondities. Door gebruik te maken van een lage-orde en eenvoudig te interpreteren modelstructuur in combinatie met weinig parameters, is het LPV model in staat om een continue en nauwkeurige beschrijving van de voertuigdynamica te leveren die geldig is voor een aanzienlijk deel van de vluchtenvelop. Dit levert nieuwe mogelijkheden op voor toepassingen in besturing en simulatie en is een grote stap voorwaarts, aangezien reeds bestaand werk zich voornamelijk richt op modellen die slechts in een enkele vlucht-conditie geldig zijn. De globale modelleringsaanpak levert bovendien nieuwe kennis op over de voertuigdynamica, in het bijzonder over de veranderingen die optreden in verschil-lende vluchtcondities. Hoewel deze veranderingen zich op een kleine schaal voordoen in geval van de DelFly, zijn ze desondanks wel belangrijk. Zowel de lokale als de globale 'grey-box' modellen zijn bewezen nauwkeurig, rekenkundig efficiënt en eenvoudig te ver-krijgen, interpreteren en toe te passen. Hiermee zijn alle vooraf opgestelde doelstellingen behaald. De gedefinieerde modelstructuren en strategiën zijn bovendien toe te passen op andere FWMAV's met soortgelijke actuatiemechanismen en vliegeigenschappen.

Op het gebied van het vrije-vlucht systeemidentificatie proces dat is toegepast binnen de eerste modelleringsaanpak, was het tot op zekere hoogte nodig om bestaande vliegtest-, dataacquisitie- en dataverwerkingsmethoden aan te passen op vliegproeven met FWMAV's. Deze worden namelijk gekarakteriseerd door lage vliegsnelheden, periodische oscillaties van het lichaam, kleine omvangen en onconventionele vliegeigenschappen. Aanbevelingen voor het uitvoeren van effectieve vliegproeven met FWMAV's worden daarom ook in dit proefschrift aangedragen. Naast het ontwerp van de experimenten en richtlijnen voor het uitvoeren van de proeven, is ook een methode voor datafusie ontwikkeld die metingen combineert van inertiaalsensoren op het lichaam van het voertuig met externe metingen van optische positie sensoren. Deze fusie levert informatievere en betrouwbaardere metingen op in vergelijking met het afzonderlijke gebruik van de verschillende typen sensoren. Hiermee worden welbekende nadelen als ruisversterking, beperkte resolutie op kleine schaal, afwijkingen en afdrijven grotendeels vermeden. Een datakwaliteit die vergelijkbaar is met metingen uit een windtunnel is bovendien behaald zonder de nadelen van vastklemmen, wat met name bijzonder is gezien de hoge frequenties die typisch zijn voor FWMAV's. Bovendien zijn de metingen van hoge kwaliteit, ondanks dat deze in realistische vluchtcondities zijn genomen, zowel in manoeuvres als tijdens hoogfrequente bewegingen. De verzamelde data is niet alleen nuttig voor modelidentificatie, maar ook voor theoretische analyses zoals bijvoorbeeld tijdsgeresolveerde aerodynamica.

In het tweede deel van het proefschrift verschuift de nadruk van de overkoepelende systeemdynamica naar de aerodynamica, met bijzondere aandacht voor de variaties die optreden tijdens de afzonderlijke flap-cycli. Waar de eerste modelleringsaanpak zich met name richt op de ontwikkeling van lage-orde en eenvoudig toe te passen modellen, is het doel van de aanpak in het tweede deel van het proefschrift om fenomenologische modellen te verkrijgen. Deze moeten de voordelen van experimentele data benutten maar tegelijkertijd gedetailleerder, informatiever en fysisch geïnspireerd zijn. De vleugels en staart van het voertuig worden hierbij apart beschouwd, om zo hun respectievelijke effecten te isoleren en uiteindelijk beter te kunnen begrijpen. Om de benodigde detaillering mogelijk te maken, worden deze modellen afgeleid op basis van data die verkregen is in de windtunnel.

Een quasi-constant model is afgeleid om de aerodynamica van de vleugel te beschrijven, met bijzondere aandacht voor het belang van het zogeheten 'clap-and-fling' effect in FWMAV's. Hiervoor zijn bestaande quasi-constante formulaties uitgebreid met een extra circulatiecomponent die het 'clap-and-fling' effect vertegenwoordigd. Deze extra term heeft geleid tot een aanzienlijke verbetering in nauwkeurigheid ten opzichte van reeds bestaande formulaties. Hiermee is het belang om het 'clap-and-fling' mechanisme in aanmerking te nemen, indien deze aanwezig is, aangetoond. Het ontwikkelde model wijkt ook af van reeds bestaand werk omdat het is gebaseerd op tijdens de vlucht gemeten in plaats van voorgespecificeerde vleugelkinematica. Hiernaast is het model uitgebreid zodat het toepasbaar is in verschillende vluchtregimes. Dit is bewerkstelligd door de verandering van de krachten als functie van de voertuigstaat uit te drukken. Hiermee zijn nauwkeurige resultaten behaald zonder terug te vallen op excessieve complexiteit of lange rekentijden. Hoewel deze aanpak complexer is dan de in het eerste deel van het proefschrift beschreven 'grey-box' modellen, leidt het door de fysisch zinvollere structuur ook tot meer detail, inzicht en flexibiliteit. Tijdens het modelleringsproces is bovendien aangetoond dat een quasi-constante formulatie soms toepasbaar is bij relatief hoge gereduceerde frequenties,

wat suggereerd dat een doorgaans als acceptabel aangenomen bereik in specifieke gevallen opgerekent kan worden.

Om het hiervoor beschreven vleugelmodel aan te vullen, is tenslotte de aerodynamica van de staart beschouwd. Hoewel een meerderheid van de bestaande FWMAV's uitgerust zijn met een conventioneel staartvlak om te zorgen voor extra stabiliteit en om het actuatie-mechanisme te ondersteunen, wordt deze zelden expliciet in modellen opgenomen. Indien dit wel gebeurd wordt de interactie tussen het zog van de fladderende vleugel met de staart verwaarloosd of aanzienlijk versimpeld. Om de invloed van deze interactie te onderzoeken is een model van het zog geïdentificeerd op basis van PIV ('particle image velocimetry') data. Door zijn gesegmenteerde formulatie beschrijft het zogmodel de spatieel-temporale variatie van de luchtstroming achter de fladderende vleugel met een hoge nauwkeurigheid, zonder hierbij gebruik te maken van hogere-orde termen. De tijdsvariërende krachten op de staart zijn vervolgens gemodelleerd met behulp van een twee-dimensionaal quasi-constant aerodynamisch model. Hierin worden de lokale stromingscondities bij de staart uitgekerend op basis van het vleugelzog model gecombineerd met de invloed van de vrije luchtstroom. Het aerodynamische model van de staart is innovatief in de manier waarop het op een tijds-geresolveerd niveau rekening houdt met de invloed van de vleugel. Tegelijkertijd is het tot op zekere hoogte fysiek interpreteerbaar en rekenkundig efficiënt, terwijl de voorspelde krachten op het staartvlak van plausible orde van grootte zijn. De voorgestelde methode is kortom en effectieve methode om de krachten op het staartvlak van FWMAV's te voorspellen. Dit is nuttig voor het ontwikkelen van geraffineerde modellen, ontwerpen en vliegbesturingssystemen. Daarnaast draagt het model bij aan een beter begrip van de staart-vleugel zog interactie en de aerodynamica van de staart in het algemeen. Het is bovendien aangetoond dat de door de fladderende vleugel geïnduceerde stroming de luchtstroom rond de staart sterk beïnvloedt, zelfs tot op snelheden die van dezelfde orde van grootte zijn als de voorwaartse snelheid van het testplatform. De pieksnelheid op het staartvlak vind plaats op ongeveer 50-70% van de spanne, wat suggereerd dat het staartvlak in deze regio het meest effectief is.

Net zoals de in het eerste deel van dit proefschrift beschreven 'grey-box' modellen, zijn de voorgestelde fenomenologische aerodynamische modelleringsmethoden te generaliseren naar andere voertuigen wanneer, in dit geval, dynamische stabiliteit gegarandeerd is. Voorts is het uitvoeren van vliegproeven voor het verkrijgen van deze modellen niet strikt nood-zakelijk, wat ze op velerlei gebied eenvoudig toepasbaar maakt. Bovendien leveren deze modellen een uitgebreid en gedetailleerd fysisch inzicht in de werkzame aerodynamische processen. De prijs hiervoor is echter een complexere structuur, wat leidt tot een minder eenvoudige interpriatie en een hogere benodigde inspanning voor zowel de afleiding als de implementatie van het model. Doorgaans worden de 'grey-box' modellen, mede door hun algemene eenvoud, aanbevolen voor de meeste toepassingen in de ontwikkeling van vliegbesturingssystemen. Toepassingen op het gebied van geavanceerde vliegbesturingslogica hebben potentieel wel meer baat bij de fenomenologische modellen, omdat ze de tijdsvarierende mechanismes in deze modellen beter kunnen benutten. Deze modellen worden ook aanbevolen voor het verkrijgen van diepgaande theoretische analyses en ontwerpstudies die doorgaans worden uitgevoerd wanneer er nog geen luchtwaardig platform beschikbaar is. Echter, wanneer er wel een luchtwaardige FWMAV beschikbaar is, is de op 'grey-box' modellen gebaseerde aanpak aantrekkelijker. Deze modellen zijn namelijk eenvoudiger te

implementeren en leiden op een effectievere manier tot directe kwalitatieve inzichten over het nieuwe voertuig.

Hoewel de modelleringsmethoden die in dit proefschrift zijn ontwikkeld tot op zekere hoogte zijn te generaliseren, zijn ze vooralsnog alleen afgeleid op basis van metingen op de DelFly II. Hierdoor dragen ze voornamelijk bij aan een beter begrip van dit specifieke platform. In dat kader heeft het werk dat in dit proefschrift is beschreven geleid tot de ontwikkeling van een drietal modellen: (i) een nauwkeurig en voor simulaties geschikt dynamisch model die rekening houdt met tijdsvariërende effecten; (ii) een globaal dynamisch model; (iii) een quasi-constant aerodynamisch model van de vleugel, inclusief het 'clap-and-fling' effect; en (iv) een tijdsvariërend aerodynamisch model van de staart.

Op basis van de verkregen resultaten is het mogelijk om een aantal aanbevelingen voor toekomstig werk te formuleren. De 'grey-box' modellen zouden nog uitgebreid kunnen worden door het effect van de excitatie van de fladderfrequentie te beschouwen en ook kan de laterale component verbeterd worden. Vrije-vlucht proeven in de windtunnel zouden benut kunnen worden om de vliegenvelop verder te verkennen om zo een nog completer globaal model te verkrijgen. Daarnaast is het gunstig om tijdens het dynamische modelleringsproces expliciet rekening te houden met agressieve manoeuvres, aangezien manoeuvreerbaarheid een van de grootste troeven van FWMAV's is. In het licht van de doorgaans handmatige constructie van de meeste FWMAV's is het ook handig om rekening te houden met kleine variaties binnen hetzelfde voertuig. Dit kan bijvoorbeeld door geometrische parameters in te bouwen in de modelstructuur. Vanuit een meer theoretisch oogpunt suggereren de huidige resultaten dat potentiele koppelingen tussen het lichaam en de fladderdynamica nader onderzocht moeten worden voor voertuigen waar de fladderfrequentie en de frequenties van de lichaamsmodi van ongeveer gelijke grootte zijn.

Het quasi-constante aerodynamische model van de vleugel kan verder worden uitgebreid door de flexibiliteit van de vleugel en het zogeheten 'clap' effect nader te beschouwen. Het zou ook interessant zijn om verschillende vleugelgeometriën en kinematica te evalueren, om zo de generaliseerbaarheid van het model beter te kunnen inschatten. Het afleiden van model parameters op basis van vrije-vlucht data zou daarnaast kunnen leiden tot realistischere resultaten en een betere schatting van de luchtweerstand. Het krachtenmodel voor de staart heeft een omvangrijkere validatie nodig, wat enkele experimentele uitdagingen met zich mee brengt. Verder kan het staartmodel ook verbeterd worden door de interactie tussen de vrije luchtstroom en het vleugelzog nader te onderzoeken. Dit kan bijvoorbeeld met behulp van PIV metingen in voorwaartse vlucht. Dergelijke metingen kunnen ook bijdragen aan een beter theoretisch begrip van de complexe staart-vleugelzog interactie in FWMAV's. Het combineren van de aerodynamische modellen van de vleugel en staart, rekening houdend met het effect van stuurcommando's, en het resultaat vervolgens op een passende manier verwerken in de bewegingsvergelijkingen zou leiden tot een volledig fenomenologisch systeemdynamisch model. Dit model kan dan gebruikt worden als alternatief op de 'grey-box' modellen.

Tot slot, alle in de proefschrift ontwikkelde modellen maken de weg vrij voor nieuw werk binnen het ontwerp, simulatie, besturing en andere potentieel beoogde toepassingen in het domein van FWMAV's. In het bijzonder kunnen nu nieuwe vliegbesturingstechnieken worden verkend, bijvoorbeeld technieken die expliciet gebruik maken van het flappende-vleugel mechanisme om zo betere prestaties te behalen.

ACKNOWLEDGEMENTS

Endings are unsettling because they are followed by novelty and change, but they also make us look back and realise just how good (or bad) a time we had. The past four years have been an exhilarating scientific and personal adventure, and this is in no small measure due to the amazing people I have had around me during this time. It therefore gives me great pleasure to conclude this book – the end product of my adventure – with a heartfelt thank you to them.

My first thanks goes to my promotor, Prof. Max Mulder, for giving me the opportunity to pursue this PhD. Max, thank you for your high-level 'GNC' and support over the past years. Your critical and insightful remarks significantly improved my work, and I invariably took fresh ideas and motivation away from our meetings. It is still a source of wonder to me how you always found time in your bulging agenda to answer questions, review papers or arrange meetings, even at a short notice. You were always available and approachable, and I am truly grateful not only for your professional guidance, but also for all the research-unrelated advice and encouragement you gave me. Hartelijk dank.

My deepest appreciation, next, to my copromotor, Dr Coen de Visser. Coen, thanks for the valuable input and feedback, the interesting discussions, the many questions answered and asked. I found I could seek your advice anytime, whether on scientific or on practical matters. The good mood and positive atmosphere of our meetings made for a fantastic working environment – your enthusiasm was infectious and you managed to make me feel more confident about my own work. Thanks above all for giving me freedom in my research, and constantly encouraging me to take charge and take on new challenges, as a researcher and as a person. I hope we will continue to collaborate, so do not be too relieved to be getting no more lengthy reading material from me!

I would also like to thank my co-supervisor, Dr Guido de Croon, for reviewing many papers, providing different angles on problems, and keeping me connected to the DelFly world. You were always available when needed, and our occasional discussions left me with interesting suggestions and new questions to think about. I will also remember – though you may not – some excellent advice you once gave me on dealing effectively with uncooperative colleagues!

Throughout my PhD-time I have had the good fortune of working not only with my supervisors, but also with several other colleagues, and for this I would like to acknowledge them. Thank you to now-Dr João Caetano, my DelFly-modelling big brother (no pun intended), for a productive collaboration, which he managed to keep up even after leaving Delft. Our many written and verbal exchanges, though often disrupted by technological shortcomings, have been stimulating and enjoyable, and have enriched my work and widened my outlook. To Dr Matej Karásek, thanks for the discussions, suggestions, hardware explanations and, especially, for the flight testing help. I thoroughly enjoyed working with you and valued your insightful technical input, but also your extraordinary availability and efficiency, and the way you always made time to help out. I am also grateful to Dr Mar-

Ivan, for translating my summary into Dutch, and Yazdi, for turning my vague ideas into a superb cover for this book. I also thank all the other colleagues at C&S for the great everyday atmosphere, which made coming to work a pleasure, regardless of how my research was going. A particular thanks to Bertine Markus, for always being extremely helpful in all practical matters; to Xander in 't Veld and Hans Mulder, for the unique opportunity of helping with the flight practicals and the parabolas that came with it; and to Daan Pool, for organising the N-team games.

To all the friends I made here in the Netherlands, I am grateful for the welcome distraction and good times, which provided an essential counterweight to my work. Tommaso, Tao, Jaime, Matej, Isabel, Kim, Kirk, João, Dyah, short Ye, tall Jan, slightly-less-tall Jan and all other colleague-friends – thanks for the fun outside the office, conferencing, travelling, musicking, sporting, eating, drinking – as well as for the advice, encouragement, reassurance... Special mention to my skiing and après-skiing companions, Jamie, Tommaso, Matej, Isabel and Kim – I look forward to more repeats of our snowy adventures. I would also like to express an extra thanks to Jaime, Tommaso and Tao, who shared these entire four years with me, at work, at choir, and in between. Thanks for your friendship and support, and the many memorable (and not-so-memorable) times spent together – I cannot imagine what these years would have been like without you. Thanks/ grazie/ 谢谢. Moving away from the C&S epicentre, many thanks to Zhou, for the many long conversations, day trips and fun nights out; to Daan, Ranko, Aleksey, Jacqueline and all my fellow (ex-)Krashnese, for the musical and non-musical delectation; to my former rowing group, for the refreshing times on the water and improving my Dutch conversation and shouting skills; to Farid, Wenjing, Tamás, Tatiana and all other friends whose paths crossed mine during this time, making it more pleasant and colourful.

I cannot forget my 'old' friends further afield, Michaela, Elizabeth, Germano, Krish, Marine, Clervie, Giulio, Sala, Crystal and Philippe: thanks once again for always being there for me and reminding me to take things easy. Our countless hours (literally) of talking and laughing at sometimes strange times of day and night, your good company and your immense patience have continued to be very precious. Particular thanks to Phil, for helping me settle in in Delft and being so supportive in the first stages of my PhD.

Last but not least, my final thanks goes to my family. I have been somewhat far away from my family for the past ten years, but they have ignored this complication and continued to be my greatest support, and for this I thank them. It is with great pleasure, in particular, that I express my heartfelt appreciation to my parents. Thanks for putting up with my complaining, providing advice and believing in me all the time, especially when I myself do not. Your support, care and boundless optimism have been invaluable, not only during my PhD but always. Thank you. *È il fine* (sic)! I conclude with a word of sincere thanks to my grandfather, who has inspired me by example to always look on the bright side of things – a valuable skill for PhDing, as for everything else in life!

I will remember these four years as one of the most intense and happy times I have ever had. Delft is not home but none of my part-time-homes have felt like home as much as Delft. Thank you all very much.

Delft, November 2017

CURRICULUM VITÆ

Sophie Franziska ARMANINI

26-01-1990   Born in Padua, Italy

EDUCATION

2013-2017   PhD Aerospace Engineering
                 Technische Universiteit Delft, Delft, The Netherlands
                 Thesis: Identification of time-varying models for flapping-wing micro aerial vehicles

2007–2013   Dipl.-Ing. Aerospace Engineering
                 Technische Universität München, Munich, Germany
                 Thesis: Parameter identification of the DA-42 aircraft from flight test manoeuvres

2005–2007   International Baccalaureate Diploma
                 The English International School of Padua, Padua, Italy

EXPERIENCE

2017   Visiting researcher
                 Cornell University, Ithaca, NY, USA
                 Research focus: Fruit fly dynamics and control

2012–2013   Intern
                 AOS Pty., Melbourne, Australia

2011–2012   Visiting research student
                 Cranfield University, Cranfield, UK
                 Research focus: Decision-making for unmanned flight in icing conditions

AWARDS

2015   ICIUS conference best paper award

LIST OF PUBLICATIONS

JOURNAL ARTICLES

6. **Armanini, S. F.**, Karásek, M. and de Visser, C. C. *Global linear parameter-varying model identification of flapping-wing dynamics using flight data.*, Journal of Guidance, Control and Dynamics. (under review)

5. **Armanini, S. F**, Caetano, J. V., de Visser, C. C., Pavel, M. D., de Croon, G. C. H. E. and Mulder, M. *Modelling wing wake and wake-tail interaction for a flapping-wing MAV*, International Journal of Micro Air Vehicles. (submitted)

4. **Armanini, S. F.**, Karásek, M., de Croon, G. C. H. E. and de Visser, C. C. *Onboard/ offboard sensor fusion for high-fidelity flapping-wing robot flight data*, Journal of Guidance, Control and Dynamics, Vol. 40, No. 8, 2017.

3. **Armanini, S. F.**, Caetano, J. V., de Croon, G. C. H. E., de Visser, C. C. and Mulder, M. *Quasi-steady aerodynamic model of clap-and-fling flapping MAV and validation with free-flight data*, Bioinspiration & Biomimetics, Vol. 11, 046002, 2016.

2. **Armanini, S. F.**, de Visser, C. C., de Croon, G. C. H. E. and Mulder, M. *Time-varying model identification of flapping-wing micro aerial vehicle dynamics using flight data*, Journal of Guidance, Control and Dynamics, Vol. 39, No. 3, 2016.

1. **Armanini, S. F.**, Polak, M., Gautrey, J. E., Lucas, A. and Whidborne, J. F. *Decision-making for unmanned aerial vehicle operation in icing conditions*, CEAS Aeronautical Journal, Vol. 7, No. 4, 2016.

CONFERENCE PROCEEDINGS

14. **Armanini, S. F.**, Karásek, M. and de Visser, C. C. *Global LPV model identification of flapping-wing dynamics using flight data*, AIAA Modeling and Simulation Technologies Conference, Kissimmee FL, USA, 2018.

13. Goedhart, M. W., van Kampen, E-J., **Armanini, S. F.**, de Visser, C. C. and Chu, Q. P. *Machine learning for flapping wing flight control*, AIAA Intelligent Systems Conference, Kissimmee FL, USA, 2018.

12. Rijks, F. G. J., Karásek, M., **Armanini, S. F.** and C. C. de Visser, C. C. *Studying the effect of the tail on the dynamics of a flapping-wing MAV using free-flight data*, AIAA Atmospheric Flight Mechanics Conference, Kissimmee FL, USA, 2018.

11. Caetano, J. V. **Armanini, S. F.** and Karásek, M. *In-flight data acquisition and flight testing for system identification of flapping-wing MAVs*, IEEE International Conference on Unmanned Aerial Systems (ICUAS), Miami FL, USA, 2017.

10. **Armanini, S. F.**, Karásek, M., de Visser, C. C., de Croon, G. C. H. E. and Mulder, M., *Flight testing and preliminary analysis for global system identification of ornithopter dynamics using on-board and off-board data*, AIAA Atmospheric Flight Mechanics Conference, Grapevine TX, USA, 2017.

9. **Armanini, S. F.**, Caetano, J. V., de Visser, C. C. and de Croon, G. C. H. E., *Modelling tail-wake interaction of a clap-and-peel flapping-wing MAV*, AIAA Modeling and Simulation Technologies Conference, Grapevine TX, USA, 2017.

8. Karásek, M., Koopmans, A. J. **Armanini, S. F.**, Remes, B. D. W. and de Croon, G. C. H. E. *Free flight force estimation of a 23.5g flapping wing MAV using an on-board IMU*, IEEE International Conference on Intelligent Robots and Systems (IROS), Deajeon, Korea, 2016.

7. **Armanini, S. F.**, Caetano, J. V., de Visser, C. C., de Croon, G. C. H. E. and Mulder, M., *Aerodynamic model identification of a clap-and-fling flapping-wing MAV: a comparison between quasi-steady and black-box approaches*, AIAA Atmospheric Flight Mechanics Conference, San Diego, USA, 2016.

6. **Armanini, S. F.**, de Visser, C. C., de Croon, G. C. H. E. and Mulder, M., *A time-scale separation approach for time-varying model identification of a flapping-wing micro aerial vehicle*, AIAA Atmospheric Flight Mechanics Conference, San Diego, USA, 2016.

5. Caetano, J. V., **Armanini, S. F.**, de Visser, C. C., de Croon, G. C. H. E. and Mulder, M., *Data-informed quasi-steady aerodynamic model identification of a clap-and-fling flapping-wing MAV*, International Conference on Intelligent Unmanned Systems (ICIUS), Bali, Indonesia, 2015.

4. **Armanini, S. F.**, de Visser, C. C. and de Croon, G. C. H. E., *Black-box LTI modelling of flapping-wing micro aerial vehicle dynamics*, AIAA Atmospheric Flight Mechanics Conference, Kissimmee FL, USA, 2015.

3. **Armanini, S. F.**, Polak, M., Gautrey, J. E., Lucas, A. and Whidborne, J. F., *Decision-making for unmanned flight in icing conditions*, CEAS Air & Space Conference, Delft, The Netherlands, 2015.

2. Lucas, A., Whidborne, J. F. and **Armanini, S. F.**, *The Challenge - UAS Operations in known icing conditions*, AAUS Conference, Avalon, Australia, 2015.

1. **Armanini, S. F.**, Verboom, J. L., de Croon, G. C. H. E., and de Visser, C. C., *Determination of trim curves for flapping-wing MAVs*, International Micro Air Vehicles Conference, Delft, The Netherlands, 2014.